Dissertation zur Erlangung des Doktorgrades
der Fakultät für Chemie und Pharmazie
der Ludwig-Maximilians-Universität München

A quantitative FRET approach to characterize protein-protein interactions in living cells

Elisabeth Susanna Butz
aus
Worms, Deutschland

2017

Erklärung

Diese Dissertation wurde im Sinne von § 7 der Promotionsordnung vom 28. November 2011 von Herrn Prof. Dr. Christian Wahl-Schott betreut.

Eidesstattliche Versicherung

Diese Dissertation wurde eigenständig und ohne unerlaubte Hilfe erarbeitet.

München, den 21.09.2017

_____

(Elisabeth S. Butz)

Dissertation eingereicht am 21.09.2017

1. Gutachter: Prof. Dr. Christian Wahl-Schott
2. Gutachter: Prof. Dr. Martin Biel

Mündliche Prüfung am 20.11.2017

meinen Eltern

Reid, Robert, Artist, photographer by Highsmith, Carol M.
[Second Floor, North Corridor.
Mural depicting Understanding by Robert Reid.
Library of Congress Thomas Jefferson Building, Washington D.C.].
Photograph. Retrieved from the Library of Congress,
<https://www.loc.gov.item/2007684512/>.

Wisdom is the principal thing;

therefore get wisdom; and with all thy getting, get understanding.

Proverbs 4:7

Table of contents

1 Abbreviations and symbols

Abbreviations

Ca^{2+}	calcium
CaM	calmodulin
CFP	cyan fluorescent protein
CNG	cyclic nucleotide-gated channel
CNGB1	cyclic nucleotide-gated channel subunit B1
EGF	epidermal growth factor
EGFR	epidermal growth factor receptor
Em	emission
ES	endolysosomal system
Ex	excitation
FRET	Förster resonance energy transfer
GFP	green fluorescent protein
HEK	human embryonic kidney
Kv7.2	voltage-gated potassium channel 7.2
L-opsin	long wavelength opsin
LDL	low density lipoprotein
mTOR	mechanistic target of rapamycin
mTORC1	mechanistic target of rapamycin complex 1
NAADP	nicotinic acid adenine dinucleotide phosphate
NAFLD	non alcoholic fatty liver disease
nm	nano meter
OS	outer segment
PDGFR β	platelet-derived growth factor receptor β
PIP_2	phosphatidylinositol 4,5-bisphosphate
$PI(3,5)P_2$	phosphatidylinositol 3,5-bisphosphate
rAAV	recombinant adeno-associated virus
SE	sensitized emission
S-opsin	short wavelength opsin
SNARE	soluble N-ethylmaleimide-sensitive factor attachment receptor
Stx	syntaxin

TEM	transmission electron microscopy
TM	transmembrane domain
TPC	two-pore channel
TRP	transient receptor potential
TRPML	mucolipin family of TRP channels
YFP	yellow fluorescent protein

Symbols

$\varepsilon_{CFP}(436)$	molar extinction coefficient of CFP at 436 nm
$\varepsilon_{YFP}(436)$	molar extinction coefficient of YFP at 436 nm
A_b	fraction of acceptor molecules bound by donor
A_{free}	fraction of unbound acceptor molecules
CFP_{EST}	estimated number of CFP molecules
CFP_{FRET} (436, 535, direct)	fluorescence signal from a CFP molecule acquired through the FRET cube
D_b	fraction of donor molecules bound by acceptor
D_{free}	fraction of unbound donor molecules
E	true or efficient FRET efficiency
E_A	apparent FRET efficiency as determined by SE-FRET
E_D	apparent FRET efficiency as determined by E-FRET
E_{MAX}	maximal FRET efficiency
F_C	measure of sensitized emission
G	calibration constant; ratio between sensitized emission and donor dequenching
$K_{d,EFF}$	dissociation constant
M_A	proportionality constant relating to the acceptor pathway
M_D	proportionality constant relating to the donor pathway
R_{A1}	constant relating to the spectral properties of YFP
R_{D1}	constant relating to the spectral properties of CFP
S_{CFP} (D, 436, 480)	fluorescence measurement from a donor-only sample acquired through the CFP cube
S_{CFP} (DA, 436, 480)	fluorescence measurement from a sample expressing both donor and acceptor acquired through the CFP cube

S_{FRET} (A, 436, 535)	fluorescence measurement from an acceptor-only sample acquired through the FRET cube
S_{FRET} (D, 436, 535)	fluorescence measurement from a donor-only sample acquired through the FRET cube
S_{FRET} (DA, 436, 535)	fluorescence measurement from a sample expressing both donor and acceptor acquired through the FRET cube
S_{YFP} (A, 500, 535)	fluorescence measurement from an acceptor-only sample acquired through the YFP cube
S_{YFP} (DA, 500, 535)	fluorescence measurement from a sample expressing both donor and acceptor acquired through the YFP cube
YFP_{EST}	estimated number of YFP molecules
YFP_{FRET} (436, 535, direct)	fluorescence signal from a YFP molecule acquired through the FRET cube

2 List of manuscripts

This thesis is based on the following publications, which are referred to in the text by their roman numerals (I-VIII):

I. **Elisabeth S. Butz***, Manu Ben-Johny*, Michael Shen, Philemon S. Yang, Lingjie Sang, Martin Biel, David T. Yue, Christian Wahl-Schott
Quantifying macromolecular interactions in living cells using FRET two-hybrid assays
2016, **Nature Protocols**, 11(12): 2470-2498
** equal contribution*

II. Araitz Alberdi*, Carolina Gomis-Perez*, Ganeko Bernardo-Seisdedos, Alessandro Alaimo, Covadonga Malo, Juncal Aldaregia, Carlos Lopez-Robles, Pilar Areso, **Elisabeth S. Butz**, Christian Wahl-Schott, Alvaro Villarroel
Uncoupling PIP_2-calmodulin regulation of Kv7.2 channels by an assembly destabilizing epileptogenic mutation
2015, **Journal of Cell Science**, 128(21), 4014-4023
** equal contribution*

III. Christian Grimm, Lesca M. Holdt*, Cheng-Chang Chen*, Sami Hassan*, Christoph Müller, Simone Jörs, Hartmut Cuny, Sandra Kissing, Bernd Schröder, **Elisabeth S. Butz**, Bernd Northoff, Jan Castonguay, Christian A. Luber, Markus Moser, Saskia Spahn, Renate Lüllmann-Rauch, Christina Fendel, Norbert Klugbauer, Oliver Griesbeck, Albert Haas, Matthias Mann, Franz Bracher, Daniel Teupser, Paul Saftig, Martin Biel, Christian Wahl-Schott
High susceptibility to fatty liver disease in two-pore channel 2-deficient mice
2014, **Nature Communications**, 5:4699
** equal contribution*

IV. Yu-Kai Chao*, Verena Schludi*, Cheng-Chang Chen, **Elisabeth S. Butz**, O.N. Phuong Nguyen, Martin Müller, Jens Krüger, Claudia Kammerbauer, Manu Ben-Johny, Angelika Vollmar, Carola Berking, Martin Biel, Christian Wahl-Schott, Christian Grimm

TPC2 polymorphisms associated with a hair pigmentation phenotype in humans result in gain of channel function by independent mechanisms

2017, **accepted in Proceedings of the National Academy of Sciences**

** equal contribution*

V. Elvir Becirovic*, O.N. Phuong Nguyen*, Christos Paparizos, **Elisabeth S. Butz**, Gabi Stern-Schneider, Uwe Wolfrum, Stefanie M. Hauck, Marius Ueffing, Christian Wahl-Schott, Stylianos Michalakis, Martin Biel

Peripherin-2 couples rhodopsin to the CNG channel in outer segments of rod photoreceptors

2014, **Human Molecular Genetics**, 23(22), 5989-5997

** equal contribution*

VI. O.N. Phuong Nguyen, Sybille Böhm, Andreas Gießl, **Elisabeth S. Butz**, Uwe Wolfrum, Johann H. Brandstätter, Christian Wahl-Schott, Martin Biel, Elvir Becirovic

Peripherin-2 differentially interacts with cone opsins in outer segments of cone photoreceptors

2016, **Human Molecular Genetics**, 25(12), 2367-2377

VII. Elvir Becirovic, Sybille Böhm, Ong N. P. Nguyen, Lisa M. Riedmayr, Verena Hammelmann, Christian Schön, **Elisabeth S. Butz**, Christian Wahl-Schott, Martin Biel, Stylianos Michalakis

AAV vectors for FRET-based analysis of protein-protein interactions in photoreceptor outer segments

2016, **Frontiers in Neuroscience**, 10:356

VIII. Sybille Böhm*, Lisa M. Riedmayr*, O.N. Phuong Nguyen, Andreas Gießl, Toni Liebscher, **Elisabeth S. Butz**, Christian Schön, Stylianos Michalakis, Christian Wahl-Schott, Martin Biel, Elvir Becirovic

Peripherin-2 and Rom-1 have opposing effects on rod outer segment targeting of retinitis pigmentosa-linked peripherin-2 mutants

2017, **Scientific Reports,** 7(1):2321

** equal contribution*

3 Summary

The ability of proteins to specifically interact with each other is a key feature in the regulation of biological processes. Knowledge about interaction partners and characterization of protein-protein interactions contribute to the understanding of proper protein function and cell physiology. In particular, Förster resonance energy transfer (FRET) is a suitable method to analyze interactions between proteins in living cells.

In my PhD thesis, I established a quantitative FRET approach that aims to evaluate binding curves for interaction partners. Moreover, I applied the quantitative FRET approach to study biological questions, including the investigation of putative interaction partners of the endolysosomal ion channel two-pore channel 2 (TPC2), the Kv7.2 potassium channel and the photoreceptor-specific transmembrane protein peripherin 2.

Diverse FRET approaches exist to date. However, while most protocols report the FRET efficiency to conclude whether or not two partners may interact with each other, the application described in **manuscript I** computes calibrated FRET efficiencies from fluorescent measurements using three-filter cubes and correlates the FRET efficiencies to the concentration of donor and acceptor molecules to determine binding curves, which bear information about maximal FRET efficiencies and relative binding constants for individual FRET pairings. Calibration factors that represent the optical properties of the imaging setup and the fluorophores are crucial for quantitative measurements. A detailed description how to assess these factors is provided. The quantitative FRET approach is very robust as both donor-centric (E-FRET) and acceptor-centric (SE-FRET) efficiencies are obtained simultaneously from multiple cells.

The method was further applied to investigate protein-protein interactions of membrane proteins.

First of all, in **manuscript II**, an epilepsy-causing mutation in the Kv7.2 potassium channel was shown to be implicated in a reduced calmodulin binding affinity to the channel, which affects channel regulation.

A second study identified SNARE proteins, such as syntaxin 7 and syntaxin 6, as novel interaction partners of the intracellular ion channel TPC2 (**manuscript III**), revealing TPC2 as a putative member of the late endosome-lysosome fusion machinery. In **manuscript IV**, the impact of polymorphic variants of TPC2 on channel dimerization and mTOR binding was investigated.

Furthermore, in a study covered by **manuscripts V and VI,** rhodopsin as well as S- and M-opsins were identified as novel interaction partners of the retinal protein peripherin 2 in rods and cones, respectively. The binding domain underlying the interaction between peripherin 2 and rhodopsin, could be assigned to the fourth transmembrane domain of peripherin 2. Moreover, it could be demonstrated that disease-associated mutations in peripherin 2 attenuated this particular binding, suggesting differential pathophysiological consequences of disrupted interactions in rods and cones. In **manuscript VIII**, peripherin 2 and its homolog Rom-1 were shown to have opposing effects on rod outer segment targeting of disease-linked peripherin 2 mutants by evaluating their binding affinities. Peripherin 2 is a scaffold protein exclusively expressed in outer segments of rods and cones. As photoreceptors are polarized cells, FRET measurements were not only performed on transfected HEK293 cells but also on acutely isolated outer segments of virally transduced murine photoreceptors (**manuscript VII**).

In summary, this thesis provides a general approach to robustly quantify interactions between FRET protein pairings and demonstrates that this quantitative FRET approach could successfully be applied to study protein-protein interactions in biological contexts. More specifically, novel interaction partners of TPC2 and peripherin 2 were identified. In addition, disease-associated mutations in peripherin 2 and Kv7.2 were shown to affect protein binding affinities.

The results gained in this thesis demonstrate that protein interactions play a crucial role in the regulation of proper protein function. Loss of binding partners or a reduced binding affinity to particular proteins may result in pathophysiological conditions. A deeper knowledge about molecular interactions will contribute to the understanding of cellular mechanisms, etiology of diseases and may further evaluate putative targets of pharmacological interest.

Zusammenfassung

Eine fundamentale Eigenschaft von Proteinen in der Regulation biologischer Prozesse ist es, spezifisch miteinander wechselzuwirken. Kenntnisse über Interaktionspartner und die Charakterisierung von Protein-Protein Wechselwirkungen tragen somit zum Verständnis von Proteinfunktion und Zellphysiologie bei. Die Förster Energie Resonanztransfer (FRET, *Förster Resonance Energy Transfer*) stellt eine besonders geeignete Anwendung dar, um Proteinwechselwirkungen in lebenden Zellen zu untersuchen.

In der vorliegenden Dissertation, wurde eine quantitative FRET Methode entwickelt, mit dem Ziel, Bindungskurven für Proteininteraktionspartner zu erstellen. Darüber hinaus wurde die quantitative FRET Methode angewendet, um biologischen Fragestellungen nachzugehen. Im Besonderen wurden mögliche Interaktionspartner des endolysosomalen Zwei-Poren-Ionenkanals TPC2 (*two-pore channel 2*), des spannungsaktivierten Kaliumkanals $K_v7.2$ (*voltage-gated potassium channel 7.2*) und des Photorezeptor-spezifischen Transmembranproteins Peripherin 2 untersucht.

Bislang gibt es verschiedene FRET Anwendungen. Während die meisten Anwendungen die bloße FRET Effizienz ausgeben, um zu beurteilen, ob Proteine miteinander wechselwirken oder nicht, wird in **Manuskript I** eine Anwendung beschrieben, bei der kalibrierte FRET Effizienzen von 3-Filter Fluoreszenzmessungen berechnet werden. Diese FRET Effizienzen können mit den Konzentrationen von Donor und Akzeptor Molekülen korreliert werden, um Bindungskurven zu erstellen, die Informationen über maximale FRET Effizienzen und relative Bindungsaffinitäten einzelner FRET Interaktionspartner enthalten. Kalibrationsfaktoren, die optische Eigenschaften des FRET Gerätes und der Fluoreszenzproteine enthalten, sind unerlässlich für quantitative Messungen. Eine ausführliche Beschreibung wie diese Faktoren bestimmt werden, wird in dieser Arbeit geboten. Die quantitative FRET Methode ist sehr robust, da sowohl Donor-bezogene (E-FRET) als auch Akzeptor-bezogene (SE-FRET) Effizienzen simultan von mehreren Zellen gemessen werden.

Die Methode wurde des Weiteren angewendet, um Protein-Protein Interaktionen zwischen Membranproteinen zu untersuchen. Zunächst konnte in **Manuskript II** gezeigt werden, dass eine Epilepsie verursachende Mutation im Kaliumkanal $K_v7.2$ eine verminderte Calmodulin-Bindung an diesen zur Folge hat, was die Regulation des Kanals beeinträchtigt.

In einer zweiten Studie konnten die SNARE Proteine Syntaxin 6 und Syntaxin 7 als direkte Interaktionspartner des intrazellulären Ionenkanals TPC2 identifiziert werden (**Manuskript III**). Diesese Ergebnisse legen nahe, dass TPC2 ein Mitglied der endolysosomalen Fusionsmachinerie ist. In **Manuskript IV** wurden die Auswirkungen zweier Polymorphismen im TPC2 Ionenkanal auf die Dimerisierung des Kanals sowie auf dessen Bindungsaffinität zu mTOR untersucht.

In einer weiteren Studie, die die **Manuskripte V und VI** umfasst, wurden sowohl Rhodopsin in Stäbchen als auch S- und M-Opsine in Zapfen als neue Interaktionspartner des retinalen Proteins Peripherin 2 identifiziert. Als Bindungsdomäne, die der Interaktion zwischen Rhodopsin und Peripherin 2 unterliegt, konnte die vierte Transmembrandomäne von Peripherin 2 ermittelt werden. Darüber hinaus konnte gezeigt werden, dass krankheitsassoziierte Mutationen in Peripherin 2 Wechselwirkungen abschwächen, was möglicherweise pathologische Konsequenzen in Stäbchen bzw. Zapfen zur Folge haben kann. In **Manuskript VIII** konnten Peripherin 2 und dem homologen Protein Rom-1 gegensätzliche Rollen beim Transport von krankheitsassoziierten Peripherin 2 Mutanten in die Außensegmente von Stäbchen-Photorezeptoren zugewiesen werden. Peripherin 2 is ein „Gerüstprotein“, das einzig in den Außensegmenten von Photorezeptoren vorkommt. Photorezeptoren sind polarisierte Zellen. Daher wurden FRET Messungen nicht nur in HEK293 Zellen durchgeführt, sondern auch in akut isolierten Außensegmenten von viral transduzierten Mausphotorezeptoren (**Manuskript VII**).

Zusammenfassend bietet die vorliegende Arbeit eine allgemeine Anwendung, um robuste Wechselwirkungen zwischen FRET Proteinpartnern zu charakterisieren. Es konnte außerdem gezeigt werden, dass die quantitative FRET Methode erfolgreich angewendet werden kann, um Proteinwechselwirkungen im biologischen Kontext zu untersuchen. Neue Interaktionspartner von TPC2 und Peripherin 2 konnten identifiziert werden. Des Weiteren, konnte gezeigt werden, dass krankheitsassoziierte Mutationen in Peripherin 2 und dem Kv7.2 Kanal Proteinbindungen abschwächen.

Die Ergebnisse dieser Arbeit zeigen, dass Proteininteraktionen eine entscheidende Rolle in der Regulation von spezifischen Proteinfunktionen haben. Ein Verlust von Bindungspartnern oder eine Reduktion der Bindungsaffinität zu bestimmten Proteinen kann möglicherweise pathophysiologische Konsequenzen haben. Ein tieferes Verständnis von Interaktionen auf molekularer Ebene wird zur Aufklärung zellulärer Mechanismen und Krankheitsursachen führen und wird weiterhin mögliche Ziele von pharmakologischem Interesse hervorbringen.

4 Introduction

Since its initial description by Theodor Förster in 1948 (Förster, 1948), Förster resonance energy transfer (FRET) has become an invaluable tool for the evaluation of molecular distance between specific pairs of cellular proteins. Förster proposed that the rate of resonance energy transfer depends on the sixth power of the donor-to-acceptor separation distance. It is this strong dependence on separation distance that makes FRET imaging suitable to detect molecular interactions on a 1 nm – 10 nm scale (Förster, 1948; Stryer and Haugland, 1967; Vogel et al., 2006). This resolution is substantially higher than that of conventional fluorescence microscopy (Hell, 2006; Lakowicz, 2006).

Accompanied by the advent of suitable genetically encoded green fluorescent protein (GFP) color mutants (Miyawaki et al., 1997; Patterson et al., 2001; Shaner et al., 2005) that can be fused to the protein of interest, the FRET methodology has become a widely used tool to study protein-protein interactions.

In the following, I will introduce a novel approach to characterize FRET interactions quantitatively. It measures the apparent FRET efficiency and correlates it to the fraction of donor and acceptor molecules in a cell. Considering a large cohort of cells with excess donor and excess acceptor molecules, respectively, the approach allows to decipher binding curves and to robustly quantify the maximal FRET efficiency for a given interaction pair. In the end, three projects will be introduced, in which the FRET approach was applied.

4. 1 Principles of SE-FRET and E-FRET

FRET occurs when a donor fluorophore is excited and nonradiatively transfers energy to a nearby acceptor molecule (physical principles are nicely summarized in Clegg, 1992; Jares-Erijman and Jovin, 2003; Kenworthy, 2001). Three prerequisites concerning fluorescent proteins must be fulfilled in order for FRET to occur (Vogel et al., 2006): First, the emission spectrum of the donor must overlap the excitation spectrum of the acceptor. A typical pair of fluorescent proteins is CFP and YFP or optimized color mutants of those, respectively. (Patterson et al., 2001; Patterson et al., 2000). Fluorescence spectra of CFP and YFP are illustrated in figure 1. Secondly, the fluorophores need to be located within a distance of less than 2 times the Förster distance, typically less than 10 nm. Finally, the emission dipole moment of the donor and the excitation dipole moment of the acceptor must be

appropriately oriented to each other: FRET declines when the dipole moments are not oriented in parallel and eventually becomes zero when the dipole moments are perpendicular to each other.

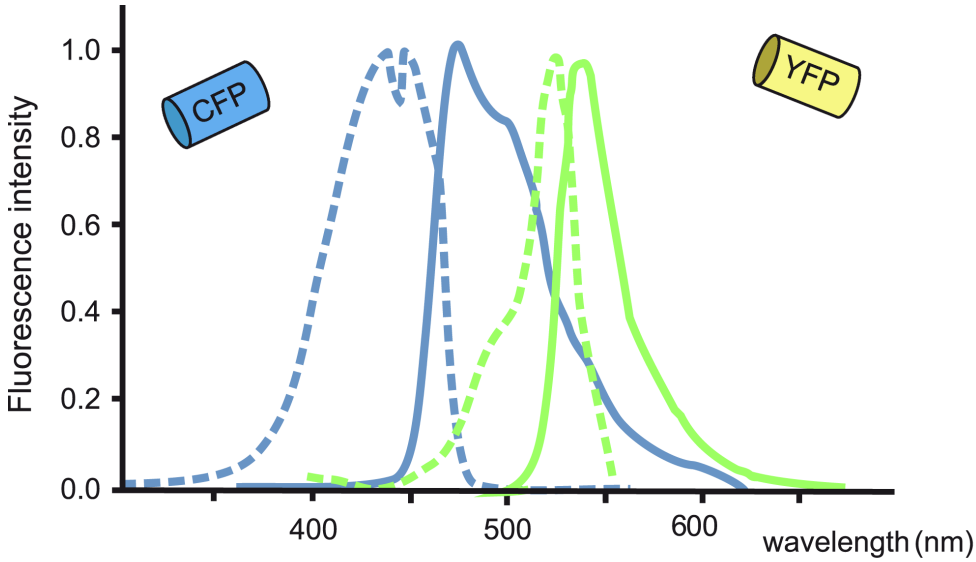

Figure 1 | Excitation (dashed lines) and emission (solid lines) spectra of CFP (cyan) and YFP (green). The emission spectrum of CFP overlaps the excitation as well as the emission spectrum of YFP.

In the presence of FRET, a characteristic double-peaked spectrum arises from a sample expressing both binding partners at the same time (Figure 2A). The energy transfer from donor to acceptor is reflected in the decrease of donor emission (‚donor quenching') as well as in an increase of acceptor emission (‚sensitized emission').

Hence, there are two ways to quantify FRET: For SE-FRET measurements, the increase in acceptor emission, e.g. YFP, is quantified. As this approach focusses on changes in acceptor emission, it is an acceptor-centric approach. Accordingly, the efficiency of FRET transfer can be expressed related to SE. In that case, the apparent FRET efficiency (E_A) is given by the amount of measured SE in relation to maximal SE that occurs for a FRET efficiency of 1. Alternatively, the FRET efficiency can be quantified from donor quenching. The apparent FRET efficiency (E_D) is then given by the ratio of the amount of measured donor quenching in relation to the total CFP fluorescence after photobleaching. This approach is termed E-FRET, and represents a donor centric approach focusing on the decrease in donor emission.

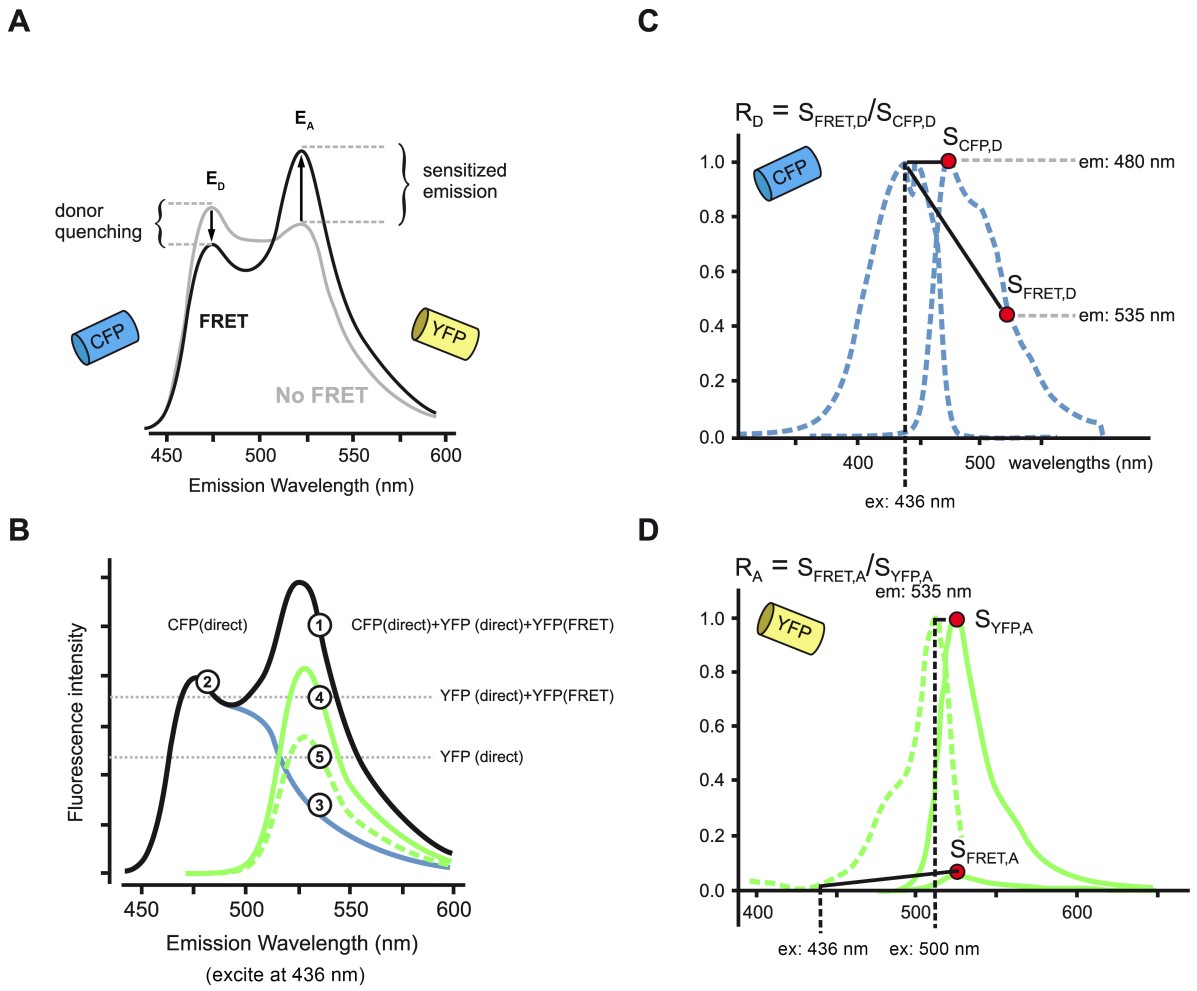

Figure 2 | Spectral properties of FRET (**A**) Shown is the emission spectrum that arises from a specimen, in which CFP and YFP are coexpressed, in the presence (black line) and absence (gray line) of FRET. FRET results in a decreased donor fluorescence (donor quenching) as well as in an increased acceptor fluorescence (sensitized emission). (**B**) Illustration of components that contribute to the fluorescence signal at 535 nm emission. Total emission at 535 nm is composed of direct CFP emission (point 3), direct YFP emission (point 5) and YFP emission due to FRET (points 4 -5). CFP emission is maximal at 440 nm (point 2). (**C**) Excitation (dashed line) and emission (solid line) spectra of CFP. S_{CFP} and S_{FRET} indicate CFP emission in response to excitation at 436 nm when measured through the CFP or FRET cube, resp. (**D**) Excitation (dashed line) and emission (solid line) spectra of YFP. S_{YFP} and S_{FRET} indicate YFP emission measured though the YFP cube (excitation at 500 nm) or FRET cube (excitation at 436 nm), resp..

Determination of FRET as „real“ net increase in acceptor fluorescence is considerably complicated, as several components contribute to the detectable acceptor emission (Figure 2B). The emission at 535 nm, the peak of YFP emission (Point 1), is the sum of direct CFP emission (donor bleed-through, Point 3) and YFP emission (Point 4), which in turn comprises YFP emission due to direct excitation (acceptor cross-excitation, Point 5) and YFP emission due to FRET (sensitized emission, Point 4 – 5).

The fluorescence measurements required for the computation of SE-FRET and E-FRET are obtained using three fluorescent filter cubes. Two of the filter sets are optimized to acquire

specific donor (CFP cube) or acceptor (YFP cube) emission when illuminated at the peak of the respective excitation spectrum. A third cube allows the detection of acceptor's emission following excitation of the donor (FRET cube).

For the derivations, I will use the following definitions of fluorescence signals: a fluorescence signal measured through a particular cube is defined as S_{CUBE}(DA, Ex, Em) where „cube" denotes CFP, YFP or FRET cube; „D" indicates donor, „A" acceptor and „AD" denotes both; „Ex" indicates excitation wavelength, „Em" denotes emission wavelength. A fluorescence signal from a particular CFP or YFP molecule is denoted as XFP_{CUBE}(Ex, Em, Direct/ FRET) where „Ex" indicates excitation wavelength and „Em" represents emission wavelength. „Direct/FRET" corresponds to the mode of excitation of the given molecule.

The expected donor bleed-through (Figure 2B; Point 3), i.e. the CFP fluorescence in the emission channel of the acceptor (535 nm) due to the overlap in the emission spectra of CFP and YFP, can be quantified using a predetermined spectral constant R_{D1} (Figure 2C). This constant is derived from cells expressing donor molecules only.

$$R_{D1} = \frac{CFP_{emission\ at\ 535}}{CFP_{emission\ at\ 480}} = \frac{S_{FRET}\ (D, 436, 535)}{S_{CFP}\ (D, 436, 480)}$$

The ratio of CFP emission at 535 nm and CFP emission at 480 nm is the same in every sample that expresses CFP. Hence, the ratio R_{D1} can be used to optically isolate the pure CFP signal at 535 nm in a sample expressing both donor and acceptor when knowing the CFP emission at 480 nm.

Accordingly, donor bleed-through can be quantified by the equation:

$$CFP_{FRET}(436, 535, direct) = R_{D1} \cdot S_{CFP}(DA, 436, 480)$$

Furthermore, excitation at 436 nm light through the FRET cube induces a small fraction of YFP emission at 535 nm. Since excitation at 500 nm only excites YFP but not CFP, direct YFP excitation can be determined using the YFP cube and a predetermined spectral ratio R_{A1} (Figure 2D), which is measured from cells expressing acceptor molecules only. The shape of the emission spectrum is independent of excitation wavelength and intensity: only the amplitude of the emission spectrum changes over excitation wavelength (shape invariance of emission spectrum) (Lakowicz, 2006). Accordingly, the ratio R_{A1} is defined as the fractional excitation of YFP through the FRET cube relative to the YFP cube:

$$R_{A1} = \frac{YFP_{emission\ at\ 535\ with\ 436\ excitation}}{YFP_{emission\ at\ 535\ with\ 500\ excitation}} = \frac{S_{FRET}\ (A, 436, 535)}{S_{YFP}\ (A, 500, 535)}$$

Consequently, the cross-excitation of YFP through the FRET cube in cells expressing both YFP and CFP may be revealed by the equation:

$$YFP_{FRET}(436, 535, direct) = R_{A1} \cdot S_{YFP}(DA, 500, 535)$$

In summary, R_{D1} and R_{A1} are determined in cells in which acceptor or donor alone are expressed and then applied to transform signals obtained from cells in which a mixture of acceptor and donor are expressed. The ratios depend only on the spectral properties of donor and acceptor molecules, and are independent of the excitation power, the concentrations of donor or acceptor in the field of view and the possibility of binding and FRET between donor and acceptor molecules.

Finally, the contribution of sensitized emission of YFP through the FRET cube can be calculated as

$$F_C = S_{FRET}(DA, 436, 535) - R_{D1} \cdot S_{CFP}(DA, 436, 480) - R_{A1} \cdot S_{YFP}(DA, 500, 535)$$

The fluorescence intensities measured with the three cubes contain not only information about the amount of FRET in the sample but are also dependent on the instrumentation used (filters, objectives, detectors etc.). Thus, the F_C signal obtained is not necessarily comparable to that gained in experiments performed using other equipment (Vogel et al., 2006). Hence, the measurement of F_C needs to be converted into an universal FRET efficiency, which should be the same for a particular sample regardless of the instrumentation used.

To this end, two more instrument-specific calibration constants, i.e. G and ε_{YFP} (436)/ ε_{CFP} (436), need to be determined from FRET experiments using a set of CFP-YFP dimers (see below, Figure 4). ε_{YFP} (436)/ ε_{CFP} (436) represents the ratio of acceptor to donor fluorescence intensity for equimolar concentrations in the absence of FRET. G is defined as the ratio of sensitized acceptor emission to the amount of donor dequenching and depends on the spectral properties of the fluorophores as well as the optical components

installed in the FRET imaging setup, including excitation light source, filter cubes and objective (Figure 3). However, G is constant for a particular fluorophore pair and imaging setup (Chen et al., 2006).

The FRET efficiency E_A is linearly related to F_C and is computed as the ratio of sensitized emission (Figure 2B; Point 4) to the emission of YFP due to direct excitation (Figure 2B; Point 5), corrected by the calibration constant ε_{YFP} (436)/ ε_{CFP} (436):

$$E_{\mathrm{A}} = E \cdot A_{\mathrm{b}} = \frac{F_{\mathrm{C}}}{R_{\mathrm{A1}} \cdot S_{\mathrm{YFP}}(\mathrm{DA},500,535)} \frac{\varepsilon_{\mathrm{YFP}}(436)}{\varepsilon_{\mathrm{CFP}}(436)}$$

The very same fluorescence intensity measurements can be used to nondestructively calculate the net decrease in donor fluorescence due to FRET. As mentioned above, the quenching of CFP is expressed as the FRET efficiency E_D. E_D can be computed from F_C and the calibration constant G:

$$E_{\mathrm{D}} = E \cdot D_{\mathrm{b}} = \frac{F_{\mathrm{C}}}{F_{\mathrm{C}} + G \cdot R_{\mathrm{D1}} \cdot S_{\mathrm{CFP}}(\mathrm{DA},436,480)}$$

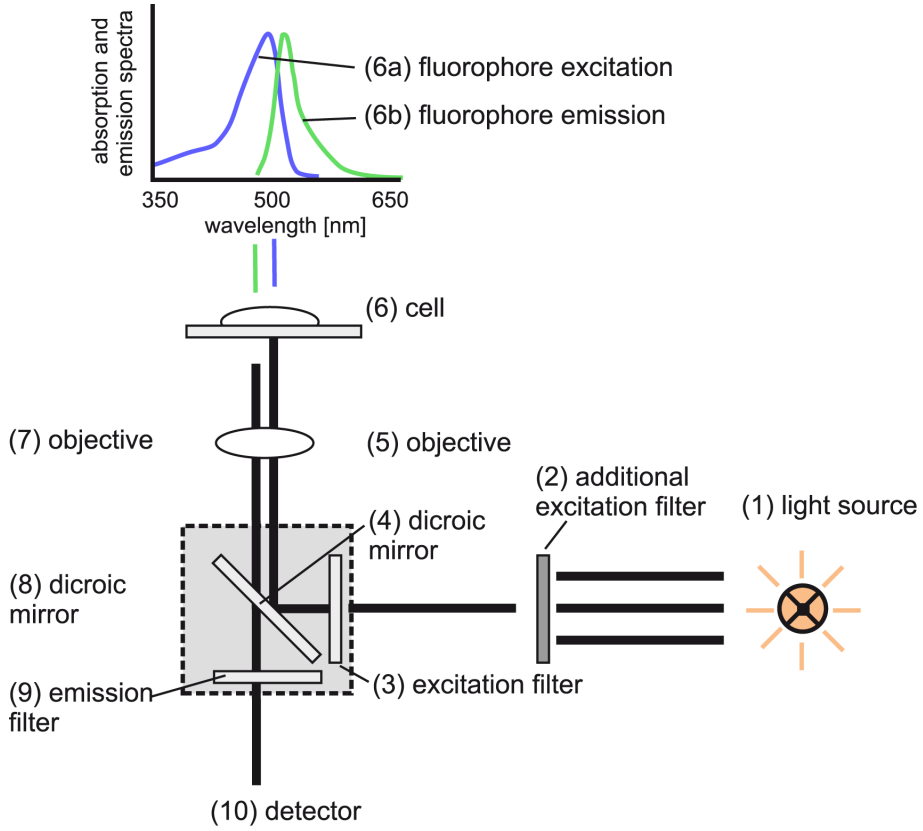

Figure 3 | Schematic illustration of optical components of a typical FRET imaging setup. All essential optical components within the excitation pathway (1 – 6a) as well as the emission pathway (6b – 10) are shown. Excitation light from a light source (1) passes excitation filters (2 and 3), a dichroic mirror (4) and an objective (5) before it excites a fluorescent specimen (6) with a particular excitation spectrum (6a). The emission pathway comprises the emission spectrum of the fluorophore (6b), an objective (7), a dichroic mirror (8), an emission filter (9) and the detector (10).

As mentioned above, G and ε_{YFP} (436)/ ε_{CFP} (436) are determined in experiments using a set of dimer constructs, in which CFP and YFP molecules are connected by a linker with variable size (Figure 4A). For each dimer construct, CFP and YFP molecules become expressed in a strict 1:1 ratio and interact with defined efficiency. Accordingly, sensitized emission equals the amount of donor dequenching, i.e. E_A equals E_D. Equations for E_A and E_D (see previous page) can be combined and a rearrangement yields the following equation:

$$\frac{F_C}{R_{A1} \cdot S_{YFP}(\mathrm{DA},500,535)} = -G\frac{R_{D1} \cdot S_{CFP}(\mathrm{DA},436,480)}{R_{A1} \cdot S_{YFP}(\mathrm{DA},500,535)} + \frac{\varepsilon_{CFP}(436)}{\varepsilon_{YFP}(436)}$$

The equation has the form of a straight line, y = mx + b, where x and y can be experimentally determined from direct fluorescent measurements (Figure 4B). The y-intercept of this relation corresponds to the three cube FRET calibration constant

ε_{YFP} (436)/ ε_{CFP} (436), whereas the slope determines the E-FRET calibration constant G. By using a set of dimers with different efficiencies, both calibration constants can be reliably calculated.

Alternatively, both constants can be computed based on the known optical properties of the imaging setup, including transmission rates of filter cubes and spectral properties of the fluorophores. Both approaches are specified in detail in manuscript I.

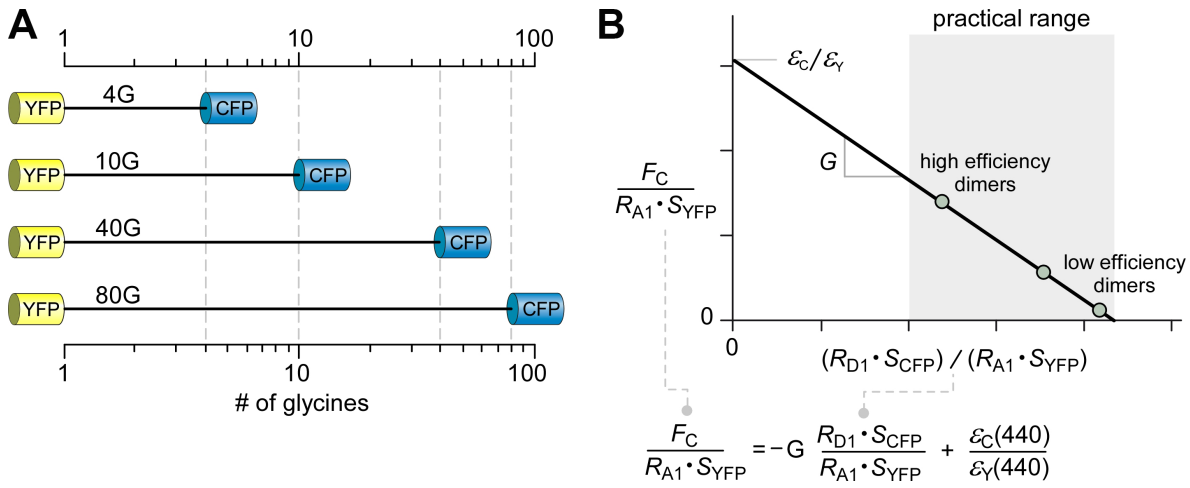

Figure 4 | Experimental determination of calibration constants G and ε_{YFP} (436)/ ε_{CFP} (436). (**A**) Schematic illustration of CFP-YFP dimer constructs harboring a defined number of glycines (G) as a linker. The individual distance between both fluorophores results in different FRET efficiencies. (**B**) Each dimer gives rise to $F_C/(R_{A1} \cdot S_{YFP})$ and $(R_{D1} \cdot S_{CFP}) /(R_{A1} \cdot S_{YFP})$ coordinates that can be plotted onto the y-axis and x-axis of the graph, resp.. The graph is fitted by a straight line. G can be calculated from the slope of the line, whereas the y-intercept yields information about the calibration constant ε_{YFP} (436)/ ε_{CFP} (436).

It is important to emphasize that E_A and E_D depend on the fraction of acceptor molecules that are bound to donor molecules (A_b) and the fraction of donor molecules with an associated acceptor (D_b), respectively. In other words, E_A and E_D would change with different A_b and D_b, respectively. The true or genuine FRET efficiency (E) is obtained if A_b or D_b equals 1 (as it is true for dimers), as given by the following equations:

$$E_A = E \cdot A_b = E = E \cdot D_b = E_D$$

This relation can be utilized to calculate binding curves for FRET pairings as outlined in the next paragraph.

4. 2 Calculation of binding curves

A very powerful application of quantitative FRET measurements arises from the possibility to determine the fraction of bound donor and acceptor molecules within a single cell. The measured FRET efficiencies (both E_A and E_D) obtained from multiple cells can then be displayed as a function of the concentration of CFP-tagged or YFP-tagged molecules allowing to calculate individual binding curves for putative interaction partners (Ben Johny et al., 2013; Erickson et al., 2001; Erickson et al., 2003).

In order to determine the concentration of donor and acceptor, it is essential to estimate the total number of donor (CFP_{EST}) and acceptor (YFP_{EST}) molecules for a given cell from three cube FRET measurements. In principle, the concentration is proportional to the total YFP and CFP fluorescence corrected for FRET.

These calculations require two more constants, G and ε_{YFP} (436)/ ε_{CFP} (436) (see paragraph 4.1). G incorporates information about light attenuation within the acceptor pathway (M_A constant) as well as within the donor pathway (M_D constant) by the equation:

$$G = \frac{M_A}{M_D} \cdot \frac{\varepsilon_{CFP}\,(436)}{\varepsilon_{YFP}\,(436)}$$

The ratio M_A/M_D can be experimentally determined using a set of CFP-YFP dimers as shown in figure 4. Alternatively, individual values for both M_A and M_D can be theoretically calculated based on the optical properties of an imaging setup, i.e. transmission rates of excitation and emission filter, intensity profile of the lamp, quantum yields and fluorescent spectra of the fluorophores.

Although the ratio M_A/ M_D, instead of their precise absolute values, is relevant for the purpose of obtaining relative binding affinities, it is necessary to look at them individually when converting fluorescence measurements into total number of YFP (YFP_{EST}) and CFP molecules (CFP_{EST}). The fluorescence signal measured using the YFP cube is free of any contribution from CFP. As M_A is a measure of the attenuation of brightness of YFP (when viewed through the FRET cube), the total number of YFP molecules can be estimated by:

$$YFP_{\mathrm{EST}} = \frac{YFP_{\mathrm{FRET}}(436,535,\mathrm{direct})}{M_{\mathrm{A}}} = \frac{R_{\mathrm{A1}} \cdot S_{\mathrm{YFP}}(\mathrm{DA},500,535)}{M_{\mathrm{A}}}$$

It is more complex to estimate the total number of CFP molecules from CFP intensity, as a considerable portion of CFP fluorescence is quenched during the FRET measurement. The expected CFP intensity after photobleaching can be estimated by dividing the CFP intensity measured through the CFP cube before photobleaching by the apparent E-FRET efficiency:

$$CFP_{\text{postbleach}}(436,535,\text{direct}) = \frac{CFP_{\text{prebleach}}(436,535,\text{direct})}{1-E_{\text{D}}} = \frac{R_{\text{D1}} \cdot S_{\text{CFP}}(\text{DA},436,480)}{1-E_{\text{D}}}$$

In analogy to YFP_{EST} calculation, the total number of CFP molecules in a given cell is related to the corrected total CFP intensity in the absence of FRET by the proportionality constant M_D, thus:

$$CFP_{\text{EST}} = \frac{R_{\text{D1}} \cdot S_{\text{CFP}}(\text{DA},436,480) + E_{\text{A}} \cdot R_{\text{A1}} \cdot S_{\text{YFP}}(\text{DA},500,535)}{M_{\text{D}}}$$

For the evaluation of a binding curve, it is necessary to obtain FRET efficiencies from a large cohort of cells expressing the fluorophore-tagged interaction partners with different levels of protein expression. The FRET efficiencies E_A and E_D depend on the fractional binding of acceptor and donor, respectively, which differ among individual cells with concentrations of the molecules. Thus, each cell gives rise to a single apparent E_A and E_D value (along with individual concentrations of donor and acceptor) and measurements from many cells are required to collect data points that populate each segment of a binding curve (Figure 5). Although a broad range of donor and acceptor concentrations may result already from stochastic expression in a cell population, one can evoke various ratios in CFP to YFP expression by adjusting the transfection ratios or by the choice of different promoters (Erickson et al., 2003). For binding curves, E_A is plotted as a function of free donor concentration (D_{free}) or E_D is plotted as a function of free acceptor concentration (A_{free}). Both D_{free} and A_{free} are computed based on estimates of CFP_{EST} and YFP_{EST}. The binding curve is then calculated by imposing a simple binding model and by performing a data fitting including all acquired measurements.

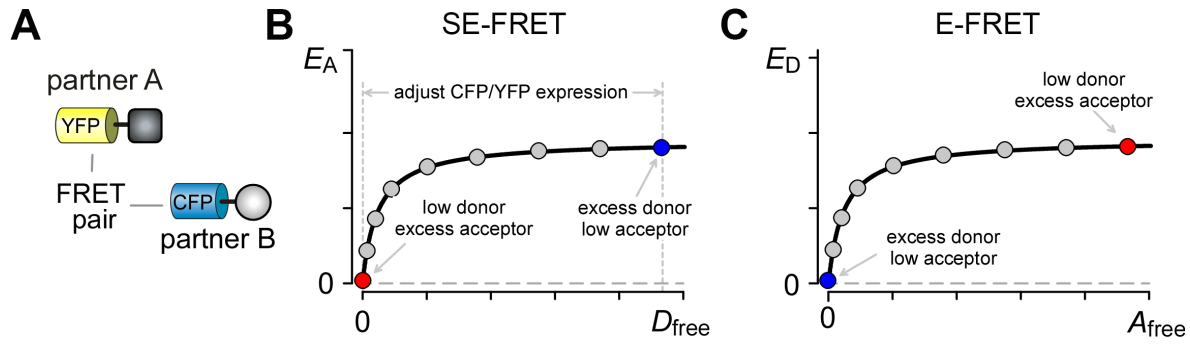

Figure 5 | Schematic representation of binding curves (**A**) Putative interaction partners tagged to CFP and YFP fluorophores, resp.. (**B, C**) Binding curves obtained by SE-FRET (**B**) and E-FRET (**C**) measurements. FRET efficiencies E_A and E_D are plotted against the fraction of free donor (D_{free}) and free acceptor (A_{free}), resp.. One dot represents data obtained from an individual cell. The black line results from curve fitting. Binding isotherms reach a saturating plateau with increasing free donor and acceptor concentration that bears information about maximal FRET efficiency E_{MAX}. Note that points at low D_{free} in panel B correspond to points at high A_{free} in panel C (red circles). Likewise, blue circles in panel B and C correspond to each other.

Based on a bimolecular binding reaction where a 1:1 complex is formed,

$$D + A \underset{K_{d,EFF}}{\rightleftharpoons} DA$$

the experimentally determined apparent SE-FRET (E_A) and E-FRET (E_D) efficiencies are linked to the free concentrations of donor (D_{free}) and acceptors (A_{free}) by the following relations:

$$E_A = E_{max} \cdot A_b = E_{max} \cdot \frac{D_{free}}{D_{free} + K_{d,EFF}}$$

$$E_D = E_{max} \cdot D_b = E_{max} \cdot \frac{A_{free}}{A_{free} + K_{d,EFF}}$$

The maximal efficiency (E_{MAX}) equals the true efficiency (E) and should be, as it is true for $K_{d,EFF}$, the same for a 1:1 binding interaction, regardless whether resulting from SE-FRET or E-FRET calculations (Ben Johny et al., 2016). Accordingly, with CFP_{EST} and YFP_{EST}, A_{free} and D_{free} can be computed as follows:

$$A_{free} = \frac{YFP_{EST} - K_{d,EFF} - CFP_{EST} + \sqrt{(YFP_{EST} - K_{d,EFF} - CFP_{EST})^2 + 4 \cdot K_{d,EFF} \cdot CFP_{EST}}}{2}$$

$$D_{\text{free}} = \frac{CFP_{\text{EST}} - K_{\text{d,EFF}} - YFP_{\text{EST}} + \sqrt{(CFP_{\text{EST}} - K_{\text{d,EFF}} - YFP_{\text{EST}})^2 + 4 \cdot K_{\text{d,EFF}} \cdot YFP_{\text{EST}}}}{2}$$

Initially, guessed values for E_{MAX} and $K_{d,EFF}$ are required to solve this expressions. Subsequently, data from various cells are fitted iteratively using a nonlinear least-squares regression analysis to estimate D_{free} and A_{free} in individual cells. The parameters E_{MAX} and $K_{d,EFF}$ are then adjusted until the squared errors ($(E_{A,\text{ predicted}} - E_A)^2$ and $(E_{D,\text{ predicted}} - E_D)^2$) are minimized.

Figure 5 illustrates typical binding curves resulting from SE-FRET and E-FRET measurements. The slope, in particular $K_{d,EFF}$, bears information about the relative binding affinity between two binding partners, whereas the saturating portion of the curve represents E_{MAX}, the true efficiency, which is required to calculate the molecular distance between two FRET partners.

4. 3 Application of FRET to identify intermolecular interaction partners

The method was implemented using Calmodulin (CaM) and two of its known interaction partners as model (Figure 6).

CaM is a small protein that regulates numerous calcium-mediated processes. It has two lobes (C- and N-domain), each containing two high affinity calcium-binding sites. Upon calcium binding, CaM undergoes a conformational change, which regulates subsequent CaM-binding to different target proteins (Chin and Means, 2000).

Initially, the interaction between CaM and Myosin V was investigated (Figure 6A). Myosin V is a motor protein that transports cargo in non-muscle cells, such as melanocytes, epithelial cells and neurons (Trybus, 2008). As characteristic for myosins, it possesses four structural domains, a motor domain containing the actin and ATP-binding site, a lever arm that is composed of six CaM-binding motifs (IQ domains), and an alpha-helical rod region followed by a globular tail, which is important for cargo binding (Houdusse et al., 2006; Trybus, 2008). In the absence of calcium, each IQ motif is bound to an apo-CaM (calcium-free) molecule (Houdusse et al., 1996), thus stabilizing the motor protein. From structural studies it is well known that a single CaM molecule binds to an IQ motif (Houdusse et al., 2006) resulting in a strict 1:1 binding stoichiometry. Low calcium levels lead to a conformational change in CaM accompanied by an activation of myosin, whereas high calcium levels inhibit motility and processive movements by dissociating CaM from one or more of the IQ domains (Houdusse et al., 2006).

For FRET measurements, only a fragment of myosin V, a single IQ domain, was used as FRET partner (Figure 6A) and measurements were performed under low calcium levels. The IQ domain was fused to YFP and coexpressed with CFP tagged CaM in HEK293 cells. Figure 6A shows SE-FRET as well as E-FRET binding curves arising from the interaction between CaM and $IQ_{MYOSINV}$. Apparent FRET efficiencies E_A and E_D were plotted as a function of the corresponding fraction of free donor and acceptor, respectively. Each gray dot represents a single cell. It is important to emphasize that three cube measurements from an individual cell were used to calculate both the apparent FRET efficiencies E_A (for SE-FRET) and E_D (for E-FRET). The whole data set was subsequently used to determine a binding relation for the FRET partners.

For a 1:1 binding interaction, the binding relation obtained by SE-FRET equals the one obtained by E-FRET (Ben-Johny et al., 2016). Accordingly, the maximal or true FRET

efficiency for CaM-CFP and $IQ_{MYOSINV}$-YFP could robustly be quantified from the saturating portion of the binding curve and was calculated to be $E_{MAX} = 0.21$.

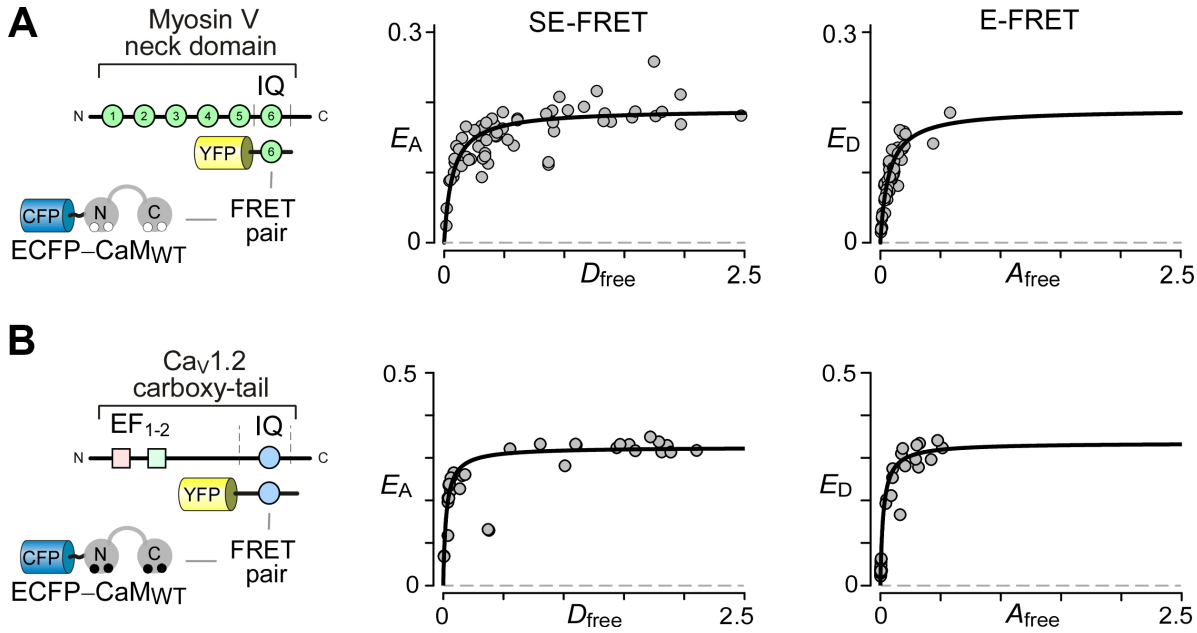

Figure 6 | Binding curves arising from CFP-tagged calmodulin (CaM) and YFP-tagged isolated IQ-domain of the myosin V neck domain (**A**) and the voltage-gated $Ca_v1.2$ channel (**B**). In both panels, interaction partners are schematically shown on the left, appendant SE-FRET and E-FRET measurements are shown in the middle and on the right, resp.. Gray dots represent measurements from individual cells and the black curve indicates the binding relation between the interaction partners, as calculated based on the Langmuir relation. Note that the same raw data, i.e. fluorescence intensity measurements, were used to calculate SE-FRET (E_A) and E-FRET (E_D) efficiencies. Further note, that the fitted binding curve (black curve) obtained by SE-FRET equals the one obtained by E-FRET (see manuscript I).

Next, the binding between CaM and the IQ domain of the voltage-gated calcium channel $Ca_v1.2$ was studied (Figure 6B). $Ca_v1.2$ is a L-type calcium channel, most important in cardiac myocytes and various neuronal cells (Ben-Johny and Yue, 2014; Minor and Findeisen, 2010). It possesses an intracellular C-terminal domain consisting of an EF hand and an IQ domain. Under calcium free conditions, apo-CaM is associated with the IQ domain. Upon calcium binding to CaM, its interaction with the IQ domain gets stronger. Elevated intracellular calcium concentrations lead to a conformational change in CaM rendering the $Ca_v1.2$ channel inactive. This feedback regulation mechanism, called CDI – calcium dependent inactivation, is common for various voltage-gated calcium channels (reviewed in Ben-Johny and Yue, 2014).

Binding curves resulting from interaction between CaM and $IQ_{CAv1.2}$ are shown in figure 6B. FRET measurements were done under high intracellular calcium-conditions upon application of ionomycin. CaM was tagged to CFP, whereas $IQ_{CAv1.2}$ was fused to YFP. As the $IQ_{CAv1.2}$ domain is only a C-terminal fragment of the channel, its expression resulted in a cytosolic distribution. CaM and the $IQ_{CAv1.2}$ domain interact in a 1:1 binding stoichiometry (Ben Johny et al., 2012). Indeed, the binding relation obtained by SE-FRET equals the one obtained by E-FRET and E_{MAX} = 0.35 could be calculated for CaM-CFP and $IQ_{CAv1.2}$-YFP (Figure 6B).

In conclusion, the novel FRET approach presented in this thesis can readily be used to quantitatively characterize protein interactions. It was consequently applied – with project-related modifications – in several individual projects, which will be introduced in the following sections.

4. 3. 1 An epilepsy-causing mutation in Kv7.2 affects calmodulin binding

Encouraged by the achievements in quantitatively detecting FRET interactions, CaM regulation of Kv7.2 potassium channel was further investigated.

The Kv7.2 channel belongs to the family of Kv voltage-gated potassium channels that comprises five members (Kv7.1 – Kv7.5), encoded by the mammalian *KCNQ1-5* genes. Kv7.1 and Kv7.4 subunits are mainly expressed in the heart and inner ear, respectively, whereas Kv7.2, Kv7.3 and Kv7.5 subunits are highly expressed in the brain and peripheral nervous system (reviewed in Brown and Passmore, 2009; Jentsch, 2000). In neurons, Kv7.2 subunits can homotetramerize or form heterotetramers with Kv7.3 and Kv7.5 subunits (Brown and Passmore, 2009). Neuronal Kv channels are especially important in regulating the excitability of neurons since they potently suppress repetitive firing of action potentials (Brown and Passmore, 2009; Robbins, 2001). Consistent with this, they suppress seizures, and dysfunctions of neuronal Kv channels are implicated in various neurological diseases such as epilepsy, autism and schizophrenia (Jentsch, 2000)

The common core structure of Kv channels is composed of six transmembrane segments with a voltage-sensing domain (S1-S4), a pore domain (S5-S6) and intracellular N- and C-terminal regions (Figures 7A, B). The large intracellular C-terminus harbors four helical regions (denoted as A-D domains) and is critical for assembly, trafficking and interaction with various signaling proteins (Chung, 2014; Haitin and Attali, 2008). The AB domain is

important for channel gating. It binds some lipids and several proteins, including CaM. Helix D is suggested to be crucial for oligomerization of the channel subunits, whereas helix C is supposed to be a structural linker.

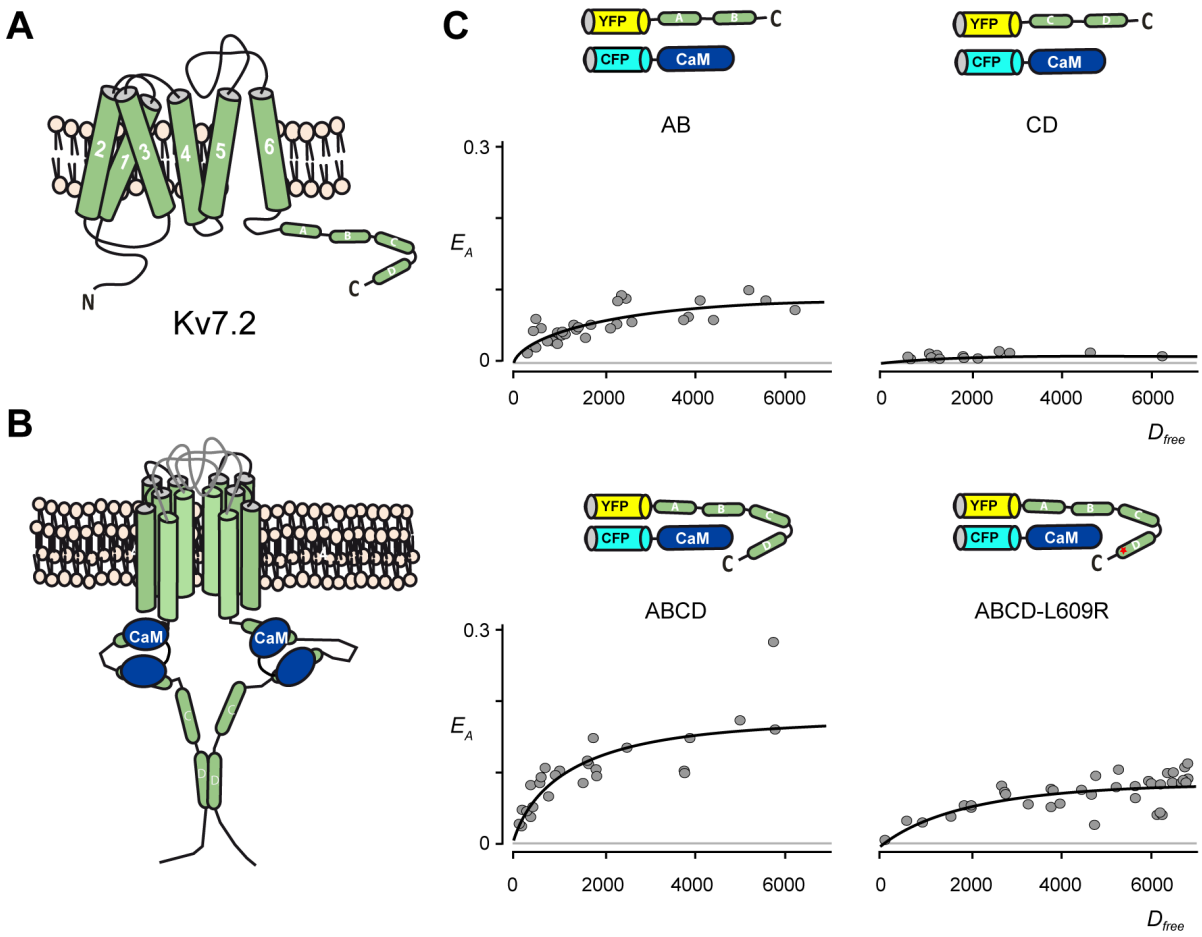

Figure 7 | Identification of an epileptogenic mutation as destabilizer for the calmodulin assembly to the voltage-gated potassium channel Kv7.2 (**A**) Graphical illustration of Kv7.2. The large intracellular C-terminus harbors 4 helical regions (denoted as A-D) with distinct functions. (**B**) Graphical illustration of a calmodulin (CaM) bound channel assembly. Note that only two subunits are represented. (**C**) Three cube FRET measurements evaluating the binding between CFP-tagged CaM and schematically indicated YFP-tagged truncated proteins. The reported binding between AB and CaM could be confirmed (left, positive control), while CD and CaM showed no specific binding (middle left, negative control). The high FRET efficiency between ABCD and CaM (middle right) was attenuated upon insertion of an epilepsy-causing mutation (L609R) in helix D (right), suggesting a destabilizing effect of L609R on channel oligomerization with functional consequences (see manuscript II).

In this study, the role of an epileptogenic mutation in the Kv7.2 C-terminal D domain in CaM binding was investigated using FRET.

To this end, C-terminal fragments containing either the AB domain, CD domain, wildtype full length C-terminus or the full length C-terminus bearing an epilepsy-causing L609R mutation (Richards et al, 2004) were fused to YFP and the binding to CaM, tagged to CFP, for each fragment was investigated in HEK293 cells (Figure 7B).
CaM binding to the AB domain could be confirmed (Sachyani et al., 2014; Villarroel et al., 2014), whereas no FRET between CaM and the CD domain occurred. This is in line with previous studies that rule out a role for CD helices in CaM binding (Sachyani et al., 2014; Yus-Najera et al., 2002). The binding relation obtained for the full length C-terminal fragment and its interaction partner CaM was very strong, even stronger than that between the single AB domain and CaM. This suggests an enhanced binding affinity mediated by the presence of the CD domains and concomitant tetramerization of the channel subunits, causing a subsequent clustering of donor and acceptor molecules. The mutation within the D domain of the channel destabilized the tetramerization of the channel and resulted in a substantial loss of CaM binding affinity.
These results strongly support the hypothesis that impaired CaM-binding to the channel contributes to the pathophysiology in epilepsy. Beside its physiological impact, the study validated the application of the FRET approach in a novel study.

4. 3. 2 Two-pore channel 2 and its role in the endolysosomal system

The FRET approach was moreover applied to study putative binding partners of the ion channel TPC2. FRET measurements were thereby challenged as the channel is intracellularly located within the endolysosomal system (ES).

The ES is specialized for the breakdown of proteins, lipids and other molecules and present in all mammalian cells (Figure 8A). The ES comprises intracellular membrane-enclosed compartments such as early and late endosomes, recycling endosomes, lysosomes and lysosome-related organelles (Grant and Donaldson, 2009; Luzio et al., 2007b; Repnik et al., 2013). Each organelle is suggested to be a transient, but distinct, compartment that elaborates into the next stage by maturation (e.g. early to late endosome) or fusion (e.g. late endosome to lysosome). Each stage is thereby characterized by a unique set of biomolecules resulting particularly in different pH environments and protein-activity states and, accordingly, in diverse organelle-associated functions (Bonifacino and Glick, 2004; Huotari and Helenius, 2011; Luzio et al., 2007a; Luzio et al., 2000). The lysosome is the terminal

degradation organelle (Xu and Ren, 2015). Moreover, it plays a role in sensing nutrient availability and autophagy (Cang et al., 2013; Medina et al., 2015).

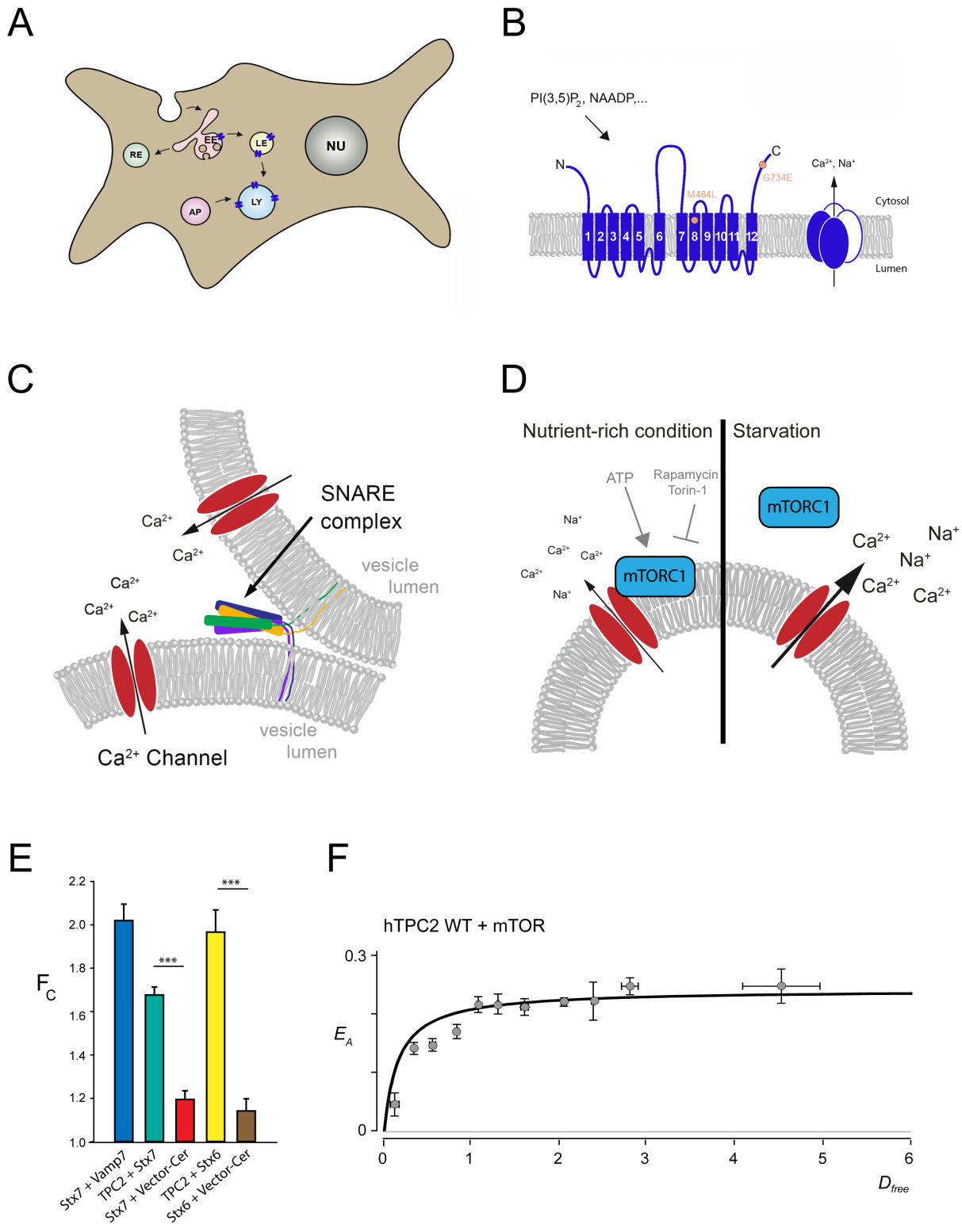

Figure 8 | TPC2 and the endolysosomal system (**A**) The endolysosomal system comprises vesicles such as early and late endosomes (EE and LE), recycling endosomes (RE), lysosomes (LY) and lysosome-related

(*Figure 8 continued*) organelles (e.g. autophagosomes (AP)). NU: Nucleus (**B**) Two-pore channel 2 (TPC2) has 12 transmembrane domains and two pore domains on each subunit. Two subunits assemble to build a functional channel. **(C)** Graphical illustration of a fusion event between endolysosomal vesicles. SNARE proteins from different membranes assemble upon a local increase in cytosolic calcium concentration. The calcium channel which provides calcium has not been identified so far. (**D**) Under nutrient-rich conditions, mTORC1 blocks TPC2 activity by direct interaction. Upon starvation, mTORC1 translocates from the lysosome resulting in increased TPC2 activity. (**E**) FRET measurements evaluating the interaction between TPC2 and Stx6 and Stx7, resp. Shown are average Fc values obtained from HEK293 cells overexpressing the indicated FRET pairs. (**F**) Representative binding curve arising from quantitative FRET measurements on cerulean-tagged TPC2 and citrine-tagged mTOR. FRET efficiencies (E_A) were plotted as a function of the corresponding free donor fraction. Clustered values from 3-6 individual cells were binned, gray dots represent the average values (± S.E.M.). (Manuscripts III and IV).

Two-pore channels (TPCs) have recently emerged as a group of endolysosomal cation channels (Grimm et al., 2017; Patel, 2015). Their name refers to two pore domains that are found on each subunit (Figure 8B). TPCs belong to the family of transient receptor potential (TRP) channels and are distantly related in particular to the mucolipin family of TRP channels (TRPML channels). Two TPC members, TPC1 and TPC2, are encoded by the human and murine genome.

Different findings hint at a role for TPC2 in endolysosomal trafficking, in particular lysosomal fusion (Grimm et al., 2014; Hockey et al., 2015; Lin-Moshier et al., 2014; Ruas et al., 2014). TPC2 is implicated in trafficking defects of the bacterial cholera toxin B (Ruas et al., 2010), EGF/EGFR and LDL-cholesterol trafficking (Grimm et al., 2014) as well as delayed degradation of platelet-derived growth factor receptor β (PDGFR β) (Ruas et al., 2014). Similarly, mice lacking both TPCs are resistant to Ebola virus infection, most probably due to defective fusion between endosomal membrane and viral membrane (Sakurai et al., 2015). Moreover, two independent interactome screens revealed putative interaction partners for TPC2 that are involved in intracellular vesicle trafficking and fusion processes, such as Rab- and soluble N-ethylmaleimide-sensitive factor attachment receptor (SNARE-) proteins (Grimm et al., 2014; Lin-Moshier et al., 2014).

Rab proteins are important for the initiation of a fusion event. They function as markers for membrane identity and recruit SNARE proteins (Jahn et al., 2003). SNARE proteins are the engines that drive membrane fusion. Each organelle is outfitted with a unique set of vesicle (v-)-SNARES and target (t-)-SNARES. Recruited by Rab proteins, a distinct v-SNARE assembles with a unique cognate t-SNARE at the appropriate target membrane (Chen and Scheller, 2001; Kummel and Ungermann, 2014). Once the SNARE complex is assembled, it generates the energy to overcome the energy barrier of lipid bilayer merging. Both homotypic and heterotypic fusion events in the ES require a local increase in cytosolic

calcium in order to occur (Luzio et al., 2007a; Pryor et al., 2000). The molecular identity of the calcium source remains to be identified (Figure 8C).

As it is true for TPC1, no disease has been associated with a mutation in the *TPCN2* gene so far. In humans, two TPC2 polymorphisms, namely M484L and G734E, are linked to pigmentation variants in hair color (Figure 8B) (Sulem et al., 2008). Recently, a direct role for TPC2 in pigmentation has been postulated (Ambrosio et al., 2016; Bellono et al., 2016). According to these studies, it is most likely that pH regulation and melanin production in melanocytes depend on the activation state of TPC2. TPC2-deficient melanosomes, the melanin producing organelles in melanocytes, showed an increase in pH and size, resulting most likely in an enhanced tyrosinase activity and increased melanin production. In contrast, TPC2 activation or overexpression had the opposite effect.
The activation mechanism of TPCs remains to be fully elucidated but has been reported to involve the second messenger nicotinic acid adenine dinucleotide phosphate (NAADP) and the endosomal membrane lipid phosphatidylinositol 3,5-bisphosphate ($PI(3,5)P_2$) (Brailoiu et al., 2009; Calcraft et al., 2009; Zong et al., 2009). The mechanism underlying NAADP activation is currently a matter of debate as NAADP-induced TPC calcium currents are not seen consistently (Ruas et al., 2015; Ruas et al., 2010; Wang et al., 2012). NAADP activation may be mediated by a yet unknown protein that binds to TPCs in order to open the channel (Grimm et al., 2017; Marchant et al., 2012).
Moreover, mechanistic target of rapamycin (mTOR) (Perl, 2015), part of the mTOR complex 1 (mTORC1), has been identified as a mediator that blocks TPC activation after ATP stimulation by direct protein-protein interaction (Cang et al., 2013). mTOR is a nutrient sensing kinase. Under nutrient-rich conditions, it is recruited to the lysosomal membrane, from where it is liberated upon starvation (Figure 8D) (Perl, 2016).
Polymorphic TPC2 variants in the context of channel gating and pigmentation have not yet been characterized.

FRET experiments accompanied two studies dealing with TPC2. First, it was investigated, whether TPC2 directly interacts with lysosome-associated SNARE proteins, such as syntaxin 6 (Stx6) or Stx7 (Figure 8C, E). Second, dimerization between wildtype TPC2 and its polymorphic variants as well as the binding to mTOR was assessed (Figure 8D, F).

FRET measurements on intracellular organelles are highly complex. The system is three-dimensional; endolysosomal vesicles are very motile and dynamic and undergo steadily homo- and heterotypic fusion events. Since TPC2 resides in diverse endolysosomal organelles, its interaction partner can be located on the same membrane structure or on different vesicles.

It is therefore of great importance to choose biological controls considering proteins with a similar physiological function and distribution. In case of the first study dealing with TPC2 and SNARE proteins (Figure 8E) the positive control was Stx7 and Vamp7, two SNARE proteins known to reside on the same vesicles and interact with each other (Bogdanovic et al., 2002; Pryor et al., 2004), while in the TPC2 polymorphism study, another lysosomal transmembrane protein (TMEM192) was used as negative control.

For the experiment shown in figure 8E, F_C values rather than universal FRET efficiency (E_A) values were calculated, as the set-up specific calibration constants G and $\varepsilon_{YFP}(436)/\ \varepsilon_{CFP}(436)$ were not yet implemented at that time point. The F_C values shown represent the average of F_C values obtained from multiple cells within a sample. F_C values (see page 5) are set-up specific. They contain information derived solely from intensity measurements without calibration, i.e. consideration of spectral properties of the fluorophore and light attenuation. Only when knowing the calibration constants, it is possible to determine the fraction of bound donor and bound acceptor molecules, respectively, and, accordingly, to determine robust binding curves. It is not ensured that F_C values represent the maximal FRET efficiency of a binding pair. Or simply said, it is not known which point of the binding curve is represented by the F_C value. However, it is valid to compare values between samples, provided that the cells were treated in the same way and that the expression ratio – ensured by the amount of cDNA transfection – of interaction partners (donor and acceptor) is the same in every condition.

Once the calibration constants G and ε_{YFP} (436)/ ε_{CFP} (436) were determined and the novel FRET approach was implemented on the imaging setup, it was possible to calculate binding curves from endolysosomal channel proteins as well. Figure 8E shows a representative binding curve for wildtype TPC2 and mTOR, where E_A is plotted as a function of D_{free}. Values populate each portion of the binding isotherm. For clarity, values for individual cells were binned and only the averaged values for the binned groups of cells are shown. However, the binding isotherm was calculated from raw data.

Data was measured under nutrient-rich conditions, when mTOR is supposed to be associated with the lysosomal membrane (Figure 8D).

4. 3. 3 Peripherin 2 and its role in photoreceptor outer segments

Furthermore, FRET was used to examine the role of peripherin 2 in photoreceptor outer segments (OS) (Figure 9). Peripherin 2 is a photoreceptor-specific scaffold protein located in the OS of both rods and cones (Figure 9A-D) (Stuck et al., 2016). The OS of photoreceptors are built up as a stack of membrane discs (Figure 9B). In rods, the discs are intracellular and thus physically separated from the plasma membrane. In cones, the discs are invaginations of the plasma membrane (Mustafi et al., 2009; Sung and Chuang, 2010). The region, where the lateral membrane segments of the disc membrane faces the plasma membrane is called rim region (Figure 9B, C). Here, the phototransduction cascade is anchored. There is evidence that peripherin 2 resides primarily in the rim region and structurally stabilizes the phototransduction cascade (Ding et al., 2015). Peripherin 2 plays a crucial role in the biogenesis of photoreceptors and is assigned to be important for membrane curvature (Arikawa et al., 1992; Ding et al., 2015) and membrane fusion (Boesze-Battaglia et al., 1997; Boesze-Battaglia et al., 1998) in photoreceptor disc formation. It has been shown that peripherin 2 binds to the beta-subunit of the rod cyclic nucleotide gated channel 1 (CNGB1) as well as to both isoforms of the glutamin acid-rich protein (GARP) (Poetsch et al., 2001; Ritter et al., 2011) suggesting a stabilizing role in connecting the plasma membrane to neighboring rim regions (Stuck et al., 2016). Furthermore, its homologue Rom-1 has been identified as an interaction partner (Bascom et al., 1992). In cones, however, peripherin 2 does not interact with the CNG channel (Conley et al., 2010) pointing to a differential role of peripherin 2 in rods and cones.
More than 100 disease-causing mutations in the human peripherin 2 gene (*PRPH2/RDS*) are known to date (Boon et al., 2008). The majority of the mutations are point mutations located in exon 2, which encodes for a part of a large extracellular/intradiscal loop as well as for a part of transmembrane domain 4 (TM4) (Figure 9D). Remarkably, some of the mutations lead to defects of rod photoreceptors in the affected individuals whereas others affect cones only (Boon et al., 2008; Wells et al., 1993). The molecular mechanisms underlying these distinct mutations have not been elucidated so far.

During the progress of this thesis, protein interactions between peripherin 2 and putative binding partners, with an emphasis on rhodopsin and cone opsins, were assessed. More specifically, the binding affinities of mutant peripherin 2 and the newly identified interaction partners were analyzed. In particular, the G266D, P210L and C214S mutations,

which are linked to retinitis pigmentosa (Sohocki et al., 2001) and the V268I mutation, associated with adult vitelliform macular dystrophy (Felbor et al., 1997) were investigated.

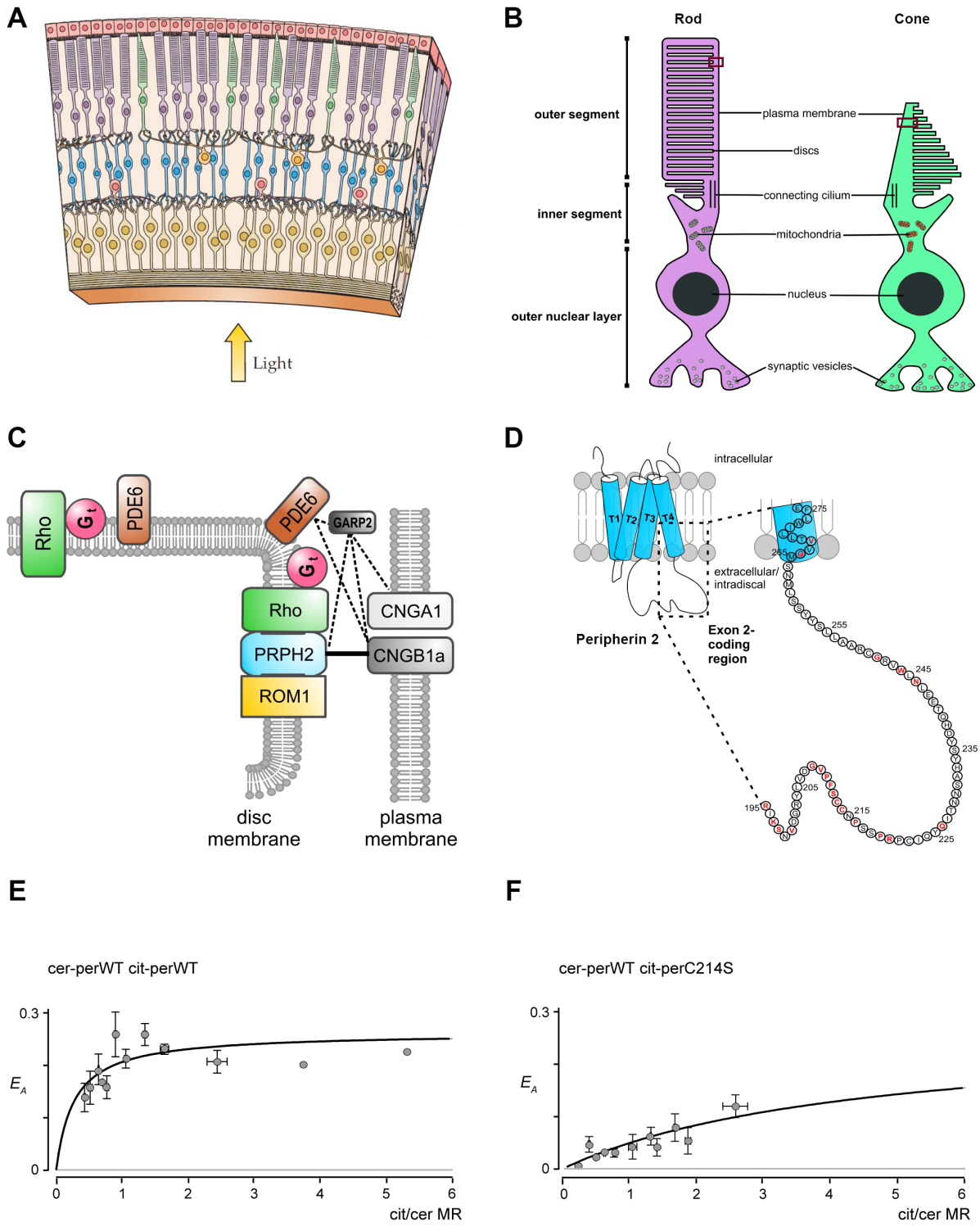

Figure 9 | Peripherin 2 is a scaffold protein in the outer segments (OS) of photoreceptors (**A**) The retina has a laminated structure and contains a variety of cell types. The outermost layer consists of photoreceptors, where the phototransduction takes place (Purves, 2001). (**B**) Rods and cones are highly polarized cells. The OS of photoreceptors are built up with a stack of membrane discs. The red boxes indicate the rim region.

(*Figure 9 continued*) (**C**) Illustration of proteins of the rod phototransduction cascade, including the photopigments or opsins (in rods: rhodopsin, in cones: M-opsin and S-opsin). Proteins are located in a disc membrane region facing to the plasma membrane, so called rim regions, or in the adjacent plasma membrane. (**D**) Peripherin 2 has four transmembrane domains. Most of disease-causing mutations are located in exon 2, which encodes a part of transmembrane 4 and part of the extracellular loop. Known amino acids that are linked to disease causing mutations are shown in red. (**E, F**) Representative binding curves obtained from FRET measurements in acutely isolated rod outer segments of retinas co-injected with (**E**) cerulean (cer)-tagged wildtype peripherin 2 (cer-perWT) and citrine (cit)-tagged wildtype peripherin 2 (cit-perWT) or (**F**) cer-perWT and cit-tagged mutant peripherin 2 (cit-perC214S). FRET efficiency E_A was plotted against the cer/cit molar ratio (MR) and a binding isotherme (black line) was iteratively fitted from single data points. Gray dots represent mean values of 1-7 single cells (+- S.E.M.).The two displayed binding curves reveal differential binding characteristics of corresponding FRET pairs. (Manuscripts V – VIII).

Given the postulated highly specialized scaffolding function of peripherin 2 in outer segments, it was necessary to perform FRET experiments not only in HEK293 cells but also in native outer segments of photoreceptors.

To this end, an approach was developed, where fluorophore-tagged binding partners were virally transduced into the retina of wildtype mice by subretinal injections. The outer segments were subsequently purified and FRET was measured *ex vivo* on either isolated cones or rods. This approach preserves not only the native environment of peripherin 2 but takes also the distinct protein composition of rods and cones into account.

For *ex vivo* experiments, the mouse retina was cotransduced with donor- and acceptor-tagged interaction partners. Additionally, mice with donor-tagged and acceptor-tagged only samples were examined to determine the amount of bleed through of the fluorophores.

Figure 9 shows representative binding curves obtained on acutely isolated photoreceptors for dimerization of wildtype peripherin 2 (Figure 9E) and peripherin 2 and its mutant variant C214S (Figure 9F). The FRET efficiency E_A is plotted as a function of the molar ratio of the fluorescent proteins cerulean/citrine rather than the fraction of free donor molecules. This modification was necessary as many endogenously expressed proteins, i.e. unlabeled proteins, are present in outer segments. Hence, one can expect a high number of binding events between endogenously expressed unlabeled and transduced fluorophore tagged molecules. A calculation of the fraction of bound donor and/ or acceptor molecules based on fluorescence intensity measurements as outlined in section 4.1 can therefore yield to inaccurate values. *In vivo* transduction efficiencies are usually not as high as transfection efficiencies in cultured cells, where the amount of transiently expressed, i.e. fluorophore tagged, proteins far exceeds the number of endogenously expressed proteins. The impact of binding events between fluorescence-tagged and unlabeled endogenous proteins can be neglected in case of transfected cultured cells.

Although information about donor and/ or acceptor concentrations is lacking, plotting E_A as a function of the molar ratio of cerulean/ citrine, i.e. the ratio of cerulean/ CFP and citrine/ YFP fluorescence, yields a saturating binding relation, which reveals information about relative binding affinities.

Altogether, protein-protein interactions could robustly be quantified, even in highly specialized cell types, such as photoreceptors.

5 Aims of the thesis

The objective of the present thesis was to learn more about protein-protein interactions using FRET. The focus was thereby on a quantitative FRET method originally developed by Erickson et al.. In 2010, the group of David T. Yue provided a nondestructive acceptor-centric method for detecting the strength of FRET interactions, termed FRET ratio, from fluorescent measurements obtained with three filter cubes. They furthermore provided a way to calculate the fraction of acceptor molecules bound to donor molecules in a cell.
However, a methodological approach how to convert FRET ratios into universal FRET efficiencies was lacking. Moreover, it was not clarified how to determine the fraction of bound acceptor without knowing detailed spectral properties of the particular imaging setup.

Aim 1 can consequently be specified as follows:

> *To establish a quantitative FRET approach that allows to determine both acceptor-centric and donor-centric FRET efficiencies and binding isotherms while including control of setup calibration and collisional FRET corrections.*

The thesis further aims (**Aim 2**)

> *to uncover molecular interactions in a biological context by applying quantitative FRET measurements*.

Specifically, the following questions were addressed:

(1) Can the FRET approach established in Aim 1 be validated in a biological context?
(2) Does an epileptogenic mutation affect the binding of calmodulin to Kv7.2 potassium channel?
(3) Does TPC2 interact with members of the endolysosomal fusion machinery? Do polymorphic variants of TPC2 affect binding characteristics as compared to wildtype TPC2?
(4) Does peripherin 2 in rod photoreceptors interact with other proteins of the phototransduction cascade except the rod CNGB1 channel subunit? Does peripherin 2 interact with proteins of the phototransduction cascade in cone photoreceptors? Do some disease-associated mutations affect peripherin 2 interactions?

6 Short summary of manuscripts

6. 1 Quantifying macromolecular interactions in living cells using FRET two-hybrid assays

Elisabeth S. Butz*, Manu Ben-Johny*, Michael Shen, Philemon S. Yang, Lingjie Sang, Martin Biel, David T. Yue, Christian Wahl-Schott

2016, **Nature Protocols**, 11(12): 2470-2498

**equal contribution*

This manuscript demonstrates a FRET approach to quantitatively assess binding affinities in living cells.

FRET-based assays have been employed to study molecular interactions of a broad range of biological molecules including ion channels, G-protein coupled receptors, immunoglobulins and cytosolic enzymes. Commonly, it is desired to quantify molecular interactions by determining binding constants and true FRET efficiencies for these interactions. However, such experiments require quantification of relative concentrations of interacting proteins and thus quantitative FRET microscopic approaches.

In this study, we describe an approach for robust quantification of relative binding affinities of protein-protein interactions by measuring FRET efficiency nondestructively. SE-FRET as well as E-FRET analysis can be performed on the same set of data, while control measurements allow to correct for collisional FRET.

The protocol includes a detailed step-by-step protocol comprising sample preparation, data aquisition and analysis. Furthermore, we outline in-depth how to calibrate the imaging setup and control for idiosyncrasies of the optical elements.

This manuscript is part of a collaboration with the group of Prof. David Yue (Johns Hopkins University, Baltimore, United States).

6. 2 Uncoupling PIP_2-calmodulin regulation of Kv7.2 channels by an assembly destabilizing epileptogenic mutation

Araitz Alberdi*, Carolina Gomis-Perez*, Ganeko Bernardo-Seisdedos, Alessandro Alaimo, Covadonga Malo, Juncal Aldaregia, Carlos Lopez-Robles, Pilar Areso, **Elisabeth S. Butz**, Christian Wahl-Schott, Alvaro Villarroel

2015, **Journal of Cell Science**, 128(21), 4014-4023

**equal contribution*

The publication deals with the calmodulin (CaM) regulation of the Kv7.2 potassium channel and shows that the phosphatidylinositol 4,5-bisphosphate (PIP_2) dependency of the channel is affected by the assembly of distant intracellular channel domains involving different CaM-binding modes.

With quantitative FRET measurements, in particular, we investigated the structural assembly of Kv7.2 and its influence on CaM binding. The channel has a large intracellular domain, containing four helical regions (A-D) and assembles as a tetramer with a coiled-coil formation between the distal D helices. It could be demonstrated that the CaM binding site is located within the AB helical regions, as the FRET efficiency between CaM and soluble CD fragments was completely lost. However, a disruption of the coiled-coil structure by an epilepsy-causing mutation within the D helix (L609R) abolished CaM interaction indicating that a coiled-coil formation is essential for CaM regulation of Kv7.2.

This study is part of a collaboration with Prof. Alvaro Villarroel and his group from University of Bilbao, Spain.

Declaration of Contribution: All quantitative FRET measurements shown in this paper, were conducted on our FRET imaging setup. I supervised Araitz Alberdi during a short term stay in our lab and conducted FRET measurements during the revision process of the publication. Additionally, I analyzed all FRET experiments.

Quantitative FRET experiments account for the substantial key statements of this publication.

6. 3 High susceptibility to fatty liver disease in two-pore channel 2-deficient mice

Christian Grimm, Lesca M. Holdt*, Cheng-Chang Chen*, Sami Hassan*, Christoph Müller, Simone Jörs, Hartmut Cuny, Sandra Kissing, Bernd Schröder, **Elisabeth S. Butz**, Bernd Northoff, Jan Castonguay, Christian A. Luber, Markus Moser, Saskia Spahn, Renate Lüllmann-Rauch, Christina Fendel, Norbert Klugbauer, Oliver Griesbeck, Albert Haas, Matthias Mann, Franz Bracher, Daniel Teupser, Paul Saftig, Martin Biel, Christian Wahl-Schott

2014, **Nature Communications**, 5:4699

**equal contribution*

TPC2 is a non-selective cation channel localized to vesicles along the endolysosomal pathway, which plays a crucial role in trafficking, breakdown and receptor-mediated recycling of macromolecules. In the liver, receptor-mediated uptake of low-density lipoproteins (LDLs) and subsequent endolysosomal transport is essential for hepatic cholesterol homeostasis and plasma lipoprotein metabolism and dysfunction within this pathway results in liver disease such as non-alcoholic fatty liver disease (NAFLD).

In this publication, we showed that a lack of TPC2 leads to an accumulation of LDL-cholesterol and EGF/EGF-receptor by conducting trafficking assays in mouse embryonic fibroblasts and hepatocytes derived from TPC2-deficient mice. The defects are most likely due to a failure in late endosome to lysosome fusion. On systemic level, TPC2-deficient mice are more susceptible to hepatic cholesterol overload and liver damage than wildtype mice as seen after a Western-type diet rich in cholesterol, which is consistent with NAFLD.

Our results render TPC2 as a key player for trafficking within the endolysosomal pathway that might be involved in the homeostatic control of macromolecules and cell metabolites.

Declaration of Contribution: I conducted all FRET measurements and concomitant analysis. I designed and engineered cDNA plasmids used in the study.

Quantitative FRET experiments revealed a direct interaction between TPC2 and Stx7, a SNARE protein crucial for homo- & heterotypic lysosomal fusion, indicating TPC2 as the putative Ca^{2+}-permeable channel that may provide local calcium for fusion.

6. 4 TPC2 polymorphisms associated with a hair pigmentation phenotype in humans result in gain of channel function by independent mechanisms

Yu-Kai Chao*, Verena Schludi*, Cheng-Chang Chen, **Elisabeth S. Butz**, O.N. Phuong Nguyen, Martin Müller, Jens Krüger, Claudia Kammerbauer, Manu Ben-Johny, Angelika Vollmar, Carola Berking, Martin Biel, Christian Wahl-Schott, Christian Grimm

2017, **accepted in Proceedings of the National Academy of Sciences**

**equal contribution*

Two human polymorphisms in the endolysosomal cation channel TPC2 (M484L and G734E) are associated with a shift from brown to blond hair color. On cellular level, this is most probably due to a regulatory role of TPC2 in pH and size of melanosomes, which controls the amount of melanin produced. However, a functional characterization of the polymorphic TPC2 variants was lacking.

In this study, we investigated the polymorphic channel characteristics. Both polymorphisms were found to lead to a gain of function by independent mechanisms. Whereas the M484L variant leads to an increased basal channel activity, the G734E variant is less prone to ATP inhibition.

Genotyping of more than 100 blond hair and brown/ black haired individuals confirmed that wildtype individuals are more brown haired, whereas polymorphic variants were predominantly found in blond haired individuals. Finally, in fibroblasts isolated from selected donors, the key electrophysiological in vitro findings were successfully validated.

Declaration of Contribution: I supervised Verena Schludi in FRET experiments and analyzed FRET data.

FRET experiments were conducted to assess the TPC2 wildtype and polymorphic variant dimerization and their binding to mTOR.

6. 5 Peripherin-2 couples rhodopsin to the CNG channel in outer segments of rod photoreceptors

Elvir Becirovic*, O.N. Phuong Nguyen*, Christos Paparizos, **Elisabeth S. Butz**, Gabi Stern-Schneider, Uwe Wolfrum, Stefanie M. Hauck, Marius Ueffing, Christian Wahl-Schott, Stylianos Michalakis, Martin Biel

2014, **Human Molecular Genetics**, 23(22), 5989-5997

**equal contribution*

Peripherin 2 is a tetraspanin transmembrane protein localized in the outer segments of photoreceptors. Mutations in peripherin 2 in rod photoreceptors are associated with retinitis pigmentosa in humans, a degenerative retinal disease eventually leading to blindness.

In this publication, we unraveled a direct interaction of peripherin 2 with two essential proteins of the rod phototransduction cascade, namely CNGB1a, a core subunit of the rod cyclic nucleotide-gated (CNG) channel, and rhodopsin, a light-sensitive protein, by employing *in vivo* and *in vitro* imaging, biochemical and immunoaffinity methods.

In order to identify components of the CNG channel complex, a preliminary affinity purification of mouse retinal proteins was followed by mass spectrometry. In combination with FRET measurements and co-immunoprecipitations, we consequently found that peripherin 2 links CNGB1a to rhodpsin. Moreover, FRET measurements utilizing C-terminally truncated peripherin 2 showed that transmembrane domain 4 (TM4) is central to the binding of the tetraspanin protein to rhodopsin. Interestingly, a retinitis pigmentosa associated mutation (G226D) found within TM4 selectively abolished the binding of peripherin 2 to rhodopsin.

In summary, the study sheds light on the role of peripherin 2 in the phototransduction complex and suggests a direct contribution of the protein to the pathophysiology of retinitis pigmentosa.

Declaration of Contribution: I performed and analyzed all *in vitro* in *in vivo* FRET measurements in HEK293 cells and in outer segments of native photoreceptors.

The results gained in the FRET experiments, highlight the physiological role of peripherin 2 and are central to the study.

6. 6 Peripherin-2 differentially interacts with cone opsins in outer segments of cone photoreceptors

O.N. Phuong Nguyen, Sybille Böhm, Andreas Gießl, **Elisabeth S. Butz**, Uwe Wolfrum, Johann H. Brandstätter, Christian Wahl-Schott, Martin Biel, Elvir Becirovic

2016, **Human Molecular Genetics**, 25(12), 2367-2377

In Becirovic et al., 2014 (Manuscript V, section. 6.5), we demonstrated a direct interaction between peripherin 2 and the rod opsin. However, the role of peripherin 2 in cone outer segments remained elusive.

In this study, we show that peripherin 2 localized in cone outer segments binds to both S-opsin and M-opsin with different affinities by using a combination of co-immunoprecipitation, quantitative FRET measurements and transmission electron microscopy (TEM) based immunolabeling experiments.

FRET measurements of the respective interactions revealed a reduced binding affinity of peripherin 2 to S-opsin compared to its interaction with M-opsin, which could be confirmed by subsequent TEM studies. Furthermore, quantitative FRET measurements in acutely isolated cone outer segments showed that the cone-degeneration causing V268I mutation in peripherin 2 selectively reduced binding to M-opsin without affecting the peripherin 2 interaction to S-opsin or rhodopsin.

These results point to a so far unknown role of peripherin 2 in cones and further underline the importance of direct interaction between the scaffold protein peripherin 2 and opsins.

Declaration of Contribution: I performed all *in vitro* in *in vivo* FRET measurements in HEK293 cells and in outer segments of native photoreceptors. I supervised Sybille Böhm in FRET experiments.

This publication represents a FRET-based study that reveals novel interaction partners of peripherin 2 in cone photoreceptors and examines the effect of peripherin 2 mutations on binding affinities.

6. 7 AAV Vectors for FRET-based analysis of protein-protein interactions in photoreceptor outer segments

Elvir Becirovic, Sybille Böhm, Ong N. P. Nguyen, Lisa M. Riedmayr, Verena Hammelmann, Christian Schön, **Elisabeth S. Butz**, Christian Wahl-Schott, Martin Biel, Stylianos Michalakis

2016, **Frontiers in Neuroscience**, 10:356

The successfully performed *ex vivo* FRET measurements on acutely isolated OS of photoreceptors in manuscripts V (Section 6.5) and VI (Section 6.6) resulted in the publication of a methodological paper, which describes for the first time how to combine AAV-vector mediated co-delivery of genetically encoded FRET partners in mouse models with subsequent quantitative FRET measurements. In this paper, a rapid and robust protocol for monitoring protein-protein interactions in acutely isolated photoreceptor OS of both rods and cones was established. Using recombinant adeno-associated virus (rAAV)-mediated gene transfer, fluorescently labeled FRET partners were delivered to their genuine expression locus. Critically, a high co-transduction efficiency is central for the success of the experiment. The procedure can be used to analyze protein-protein interactions of wild type or mutant OS proteins in their native environment. Moreover, the principal approach should be readily be transferable to other cell types.

Declaration of Contribution: I performed and analyzed the FRET experiments. In addition, I optimized sample preparation for FRET measurements and contributed to writing of the manuscript.

6. 8 Peripherin-2 and Rom-1 have opposing effects on rod outer segment targeting of retinitis pigmentosa-linked peripherin-2 mutants

Sybille Böhm*, Lisa M. Riedmayr*, O.N. Phuong Nguyen, Andreas Gießl, Toni Liebscher, **Elisabeth S. Butz**, Christian Schön, Stylianos Michalakis, Christian Wahl-Schott, Martin Biel, Elvir Becirovic

2017, **Scientific Reports,** 7(1):2321

**equal contribution*

Peripherin 2 forms homomeric protein complexes as well as heteromeric complexes with its homolog Rom-1 in photoreceptor OS. Mutations in the peripherin 2 gene are associated with autosomal dominant retinitis pigmentosa (adRP), whereas mutations in Rom-1 cause digenic RP only in combination with a heterozygous mutation in peripherin 2. Rom-1 is thus suggested to function as genetic modifier that influences disease progression. Until now it is not known how the different complexes assembled by various combinations of wildtype and mutant peripherin 2 or Rom-1, which can be formed in heterozygous patients, result in adRP.

In this study, two adRP-linked peripherin 2 mutants, namely P210L and C214S, were analyzed with regard to binding characteristics, subunit assembly, and rod OS targeting in heteromeric complexes containing wildtype, mutant peripherin 2 and/or Rom-1. These complexes can be formed in patients heterozygous for peripherin 2 mutations.

The results show that both mutants are misfolded and mislocalized. Moreover, their binding to wildtype peripherin 2 and Rom-1 was strongly decreased. Finaly, both mutants are preferentially forming non-covalent dimers with wildtype peripherin 2 and Rom-1. However, only complexes containing a wildtype peripherin 2 could be transported to the rod OS. Other complexes were retained in the inner segments.

In conclusion, the study reveals opposing roles of wildtype peripherin 2 and Rom-1 in rod OS targeting of adRP-linked peripherin 2 mutants.

Declaration of Contribution: I supervised Sybille Böhm in FRET experiments and analyzed part of the FRET data.

7 References

Ambrosio, A.L., Boyle, J.A., Aradi, A.E., Christian, K.A., and Di Pietro, S.M. (2016). TPC2 controls pigmentation by regulating melanosome pH and size. Proc Natl Acad Sci U S A *113*, 5622-5627.

Arikawa, K., Molday, L.L., Molday, R.S., and Williams, D.S. (1992). Localization of peripherin/rds in the disk membranes of cone and rod photoreceptors: relationship to disk membrane morphogenesis and retinal degeneration. J Cell Biol *116*, 659-667.

Bascom, R.A., Manara, S., Collins, L., Molday, R.S., Kalnins, V.I., and McInnes, R.R. (1992). Cloning of the cDNA for a novel photoreceptor membrane protein (rom-1) identifies a disk rim protein family implicated in human retinopathies. Neuron *8*, 1171-1184.

Bellono, N.W., Escobar, I.E., and Oancea, E. (2016). A melanosomal two-pore sodium channel regulates pigmentation. Sci Rep *6*, 26570.

Ben Johny, M., Yang, P.S., Bazzazi, H., and Yue, D.T. (2013). Dynamic switching of calmodulin interactions underlies Ca2+ regulation of CaV1.3 channels. Nat Commun *4*, 1717.

Ben-Johny, M., Yue, D.N., and Yue, D.T. (2016). Detecting stoichiometry of macromolecular complexes in live cells using FRET. Nat Commun *7*, 13709.

Ben-Johny, M., and Yue, D.T. (2014). Calmodulin regulation (calmodulation) of voltage-gated calcium channels. J Gen Physiol *143*, 679-692.

Boesze-Battaglia, K., Kong, F., Lamba, O.P., Stefano, F.P., and Williams, D.S. (1997). Purification and light-dependent phosphorylation of a candidate fusion protein, the photoreceptor cell peripherin/rds. Biochemistry *36*, 6835-6846.

Boesze-Battaglia, K., Lamba, O.P., Napoli, A.A., Jr., Sinha, S., and Guo, Y. (1998). Fusion between retinal rod outer segment membranes and model membranes: a role for photoreceptor peripherin/rds. Biochemistry *37*, 9477-9487.

Bogdanovic, A., Bennett, N., Kieffer, S., Louwagie, M., Morio, T., Garin, J., Satre, M., and Bruckert, F. (2002). Syntaxin 7, syntaxin 8, Vti1 and VAMP7 (vesicle-associated membrane protein 7) form an active SNARE complex for early macropinocytic compartment fusion in Dictyostelium discoideum. Biochem J *368*, 29-39.

Bonifacino, J.S., and Glick, B.S. (2004). The mechanisms of vesicle budding and fusion. Cell *116*, 153-166.

Boon, C.J., den Hollander, A.I., Hoyng, C.B., Cremers, F.P., Klevering, B.J., and Keunen, J.E. (2008). The spectrum of retinal dystrophies caused by mutations in the peripherin/RDS gene. Prog Retin Eye Res *27*, 213-235.

Brailoiu, G.C., Brailoiu, E., Parkesh, R., Galione, A., Churchill, G.C., Patel, S., and Dun, N.J. (2009). NAADP-mediated channel 'chatter' in neurons of the rat medulla oblongata. Biochem J *419*, 91-97, 92 p following 97.

Brown, D.A., and Passmore, G.M. (2009). Neural KCNQ (Kv7) channels. Br J Pharmacol *156*, 1185-1195.

Calcraft, P.J., Ruas, M., Pan, Z., Cheng, X., Arredouani, A., Hao, X., Tang, J., Rietdorf, K., Teboul, L., Chuang, K.T.*, et al.* (2009). NAADP mobilizes calcium from acidic organelles through two-pore channels. Nature *459*, 596-600.

Cang, C., Zhou, Y., Navarro, B., Seo, Y.J., Aranda, K., Shi, L., Battaglia-Hsu, S., Nissim, I., Clapham, D.E., and Ren, D. (2013). mTOR regulates lysosomal ATP-sensitive two-pore Na(+) channels to adapt to metabolic state. Cell *152*, 778-790.

Chen, H., Puhl, H.L., 3rd, Koushik, S.V., Vogel, S.S., and Ikeda, S.R. (2006). Measurement of FRET efficiency and ratio of donor to acceptor concentration in living cells. Biophys J *91*, L39-41.

Chen, Y.A., and Scheller, R.H. (2001). SNARE-mediated membrane fusion. Nat Rev Mol Cell Biol *2*, 98-106.

Chin, D., and Means, A.R. (2000). Calmodulin: a prototypical calcium sensor. Trends Cell Biol *10*, 322-328.

Clegg, R.M. (1992). Fluorescence resonance energy transfer and nucleic acids. Methods Enzymol *211*, 353-388.

Conley, S.M., Ding, X.Q., and Naash, M.I. (2010). RDS in cones does not interact with the beta subunit of the cyclic nucleotide gated channel. Adv Exp Med Biol *664*, 63-70.

Ding, J.D., Salinas, R.Y., and Arshavsky, V.Y. (2015). Discs of mammalian rod photoreceptors form through the membrane evagination mechanism. J Cell Biol *211*, 495-502.

Erickson, M.G., Alseikhan, B.A., Peterson, B.Z., and Yue, D.T. (2001). Preassociation of calmodulin with voltage-gated Ca(2+) channels revealed by FRET in single living cells. Neuron *31*, 973-985.

Erickson, M.G., Liang, H., Mori, M.X., and Yue, D.T. (2003). FRET two-hybrid mapping reveals function and location of L-type Ca2+ channel CaM preassociation. Neuron *39*, 97-107.

Felbor, U., Schilling, H., and Weber, B.H. (1997). Adult vitelliform macular dystrophy is frequently associated with mutations in the peripherin/RDS gene. Hum Mutat *10*, 301-309.

Förster, T. (1948). Intermolecular energy migration and fluorescence. Annalen der Physik *2*, 55-75.

Grant, B.D., and Donaldson, J.G. (2009). Pathways and mechanisms of endocytic recycling. Nat Rev Mol Cell Biol *10*, 597-608.

Grimm, C., Chen, C.C., Wahl-Schott, C., and Biel, M. (2017). Two-Pore Channels: Catalyzers of Endolysosomal Transport and Function. Front Pharmacol *8*, 45.

Grimm, C., Holdt, L.M., Chen, C.C., Hassan, S., Muller, C., Jors, S., Cuny, H., Kissing, S., Schroder, B., Butz, E.*, et al.* (2014). High susceptibility to fatty liver disease in two-pore channel 2-deficient mice. Nat Commun *5*, 4699.

Haitin, Y., and Attali, B. (2008). The C-terminus of Kv7 channels: a multifunctional module. J Physiol *586*, 1803-1810.

Hell, S. (2006). Handbook of biological confocal microscopy 3rd edn (New York: Springer Science + Buisness).

Hockey, L.N., Kilpatrick, B.S., Eden, E.R., Lin-Moshier, Y., Brailoiu, G.C., Brailoiu, E., Futter, C.E., Schapira, A.H., Marchant, J.S., and Patel, S. (2015). Dysregulation of lysosomal morphology by pathogenic LRRK2 is corrected by TPC2 inhibition. J Cell Sci *128*, 232-238.

Houdusse, A., Gaucher, J.F., Krementsova, E., Mui, S., Trybus, K.M., and Cohen, C. (2006). Crystal structure of apo-calmodulin bound to the first two IQ motifs of myosin V reveals essential recognition features. Proc Natl Acad Sci U S A *103*, 19326-19331.

Houdusse, A., Silver, M., and Cohen, C. (1996). A model of Ca(2+)-free calmodulin binding to unconventional myosins reveals how calmodulin acts as a regulatory switch. Structure *4*, 1475-1490.

Huotari, J., and Helenius, A. (2011). Endosome maturation. EMBO J *30*, 3481-3500.

Jahn, R., Lang, T., and Sudhof, T.C. (2003). Membrane fusion. Cell *112*, 519-533.

Jares-Erijman, E.A., and Jovin, T.M. (2003). FRET imaging. Nat Biotechnol *21*, 1387-1395.

Jentsch, T.J. (2000). Neuronal KCNQ potassium channels: physiology and role in disease. Nat Rev Neurosci *1*, 21-30.

Kenworthy, A.K. (2001). Imaging protein-protein interactions using fluorescence resonance energy transfer microscopy. Methods *24*, 289-296.

Kummel, D., and Ungermann, C. (2014). Principles of membrane tethering and fusion in endosome and lysosome biogenesis. Curr Opin Cell Biol *29*, 61-66.

Lakowicz, J.R. (2006). Principles of Fluorescence Spectroscopy (New York: Springer).

Lin-Moshier, Y., Keebler, M.V., Hooper, R., Boulware, M.J., Liu, X., Churamani, D., Abood, M.E., Walseth, T.F., Brailoiu, E., Patel, S.*, et al.* (2014). The Two-pore channel (TPC) interactome unmasks isoform-specific roles for TPCs in endolysosomal morphology and cell pigmentation. Proc Natl Acad Sci U S A *111*, 13087-13092.

Luzio, J.P., Bright, N.A., and Pryor, P.R. (2007a). The role of calcium and other ions in sorting and delivery in the late endocytic pathway. Biochem Soc Trans *35*, 1088-1091.

Luzio, J.P., Pryor, P.R., and Bright, N.A. (2007b). Lysosomes: fusion and function. Nat Rev Mol Cell Biol *8*, 622-632.

Luzio, J.P., Rous, B.A., Bright, N.A., Pryor, P.R., Mullock, B.M., and Piper, R.C. (2000). Lysosome-endosome fusion and lysosome biogenesis. J Cell Sci *113 (Pt 9)*, 1515-1524.

Marchant, J.S., Lin-Moshier, Y., Walseth, T.F., and Patel, S. (2012). The Molecular Basis for Ca2+ Signalling by NAADP: Two-Pore Channels in a Complex? Messenger (Los Angel) *1*, 63-76.

Medina, D.L., Di Paola, S., Peluso, I., Armani, A., De Stefani, D., Venditti, R., Montefusco, S., Scotto-Rosato, A., Prezioso, C., Forrester, A.*, et al.* (2015). Lysosomal calcium signalling regulates autophagy through calcineurin and TFEB. Nat Cell Biol *17*, 288-299.

Minor, D.L., Jr., and Findeisen, F. (2010). Progress in the structural understanding of voltage-gated calcium channel (CaV) function and modulation. Channels (Austin) *4*, 459-474.

Miyawaki, A., Llopis, J., Heim, R., McCaffery, J.M., Adams, J.A., Ikura, M., and Tsien, R.Y. (1997). Fluorescent indicators for Ca2+ based on green fluorescent proteins and calmodulin. Nature *388*, 882-887.

Mustafi, D., Engel, A.H., and Palczewski, K. (2009). Structure of cone photoreceptors. Prog Retin Eye Res *28*, 289-302.

Patel, S. (2015). Function and dysfunction of two-pore channels. Sci Signal *8*, re7.

Patterson, G., Day, R.N., and Piston, D. (2001). Fluorescent protein spectra. J Cell Sci *114*, 837-838.

Patterson, G.H., Piston, D.W., and Barisas, B.G. (2000). Forster distances between green fluorescent protein pairs. Anal Biochem *284*, 438-440.

Perl, A. (2015). mTOR activation is a biomarker and a central pathway to autoimmune disorders, cancer, obesity, and aging. Ann N Y Acad Sci *1346*, 33-44.

Perl, A. (2016). Activation of mTOR (mechanistic target of rapamycin) in rheumatic diseases. Nat Rev Rheumatol *12*, 169-182.

Poetsch, A., Molday, L.L., and Molday, R.S. (2001). The cGMP-gated channel and related glutamic acid-rich proteins interact with peripherin-2 at the rim region of rod photoreceptor disc membranes. J Biol Chem *276*, 48009-48016.

Pryor, P.R., Mullock, B.M., Bright, N.A., Gray, S.R., and Luzio, J.P. (2000). The role of intraorganellar Ca(2+) in late endosome-lysosome heterotypic fusion and in the reformation of lysosomes from hybrid organelles. J Cell Biol *149*, 1053-1062.

Pryor, P.R., Mullock, B.M., Bright, N.A., Lindsay, M.R., Gray, S.R., Richardson, S.C., Stewart, A., James, D.E., Piper, R.C., and Luzio, J.P. (2004). Combinatorial SNARE complexes with VAMP7 or VAMP8 define different late endocytic fusion events. EMBO Rep *5*, 590-595.

Purves (2001). Neuroscience. In Neuroscience, A.G. Purves D, Fitzpatrick D., ed. (Sunderland (MA): Sinauer Associates).

Repnik, U., Cesen, M.H., and Turk, B. (2013). The endolysosomal system in cell death and survival. Cold Spring Harb Perspect Biol *5*, a008755.

Ritter, L.M., Khattree, N., Tam, B., Moritz, O.L., Schmitz, F., and Goldberg, A.F. (2011). In situ visualization of protein interactions in sensory neurons: glutamic acid-rich proteins (GARPs) play differential roles for photoreceptor outer segment scaffolding. J Neurosci *31*, 11231-11243.

Robbins, J. (2001). KCNQ potassium channels: physiology, pathophysiology, and pharmacology. Pharmacol Ther *90*, 1-19.

Ruas, M., Chuang, K.T., Davis, L.C., Al-Douri, A., Tynan, P.W., Tunn, R., Teboul, L., Galione, A., and Parrington, J. (2014). TPC1 has two variant isoforms, and their removal has different effects on endo-lysosomal functions compared to loss of TPC2. Mol Cell Biol *34*, 3981-3992.

Ruas, M., Galione, A., and Parrington, J. (2015). Two-Pore Channels: Lessons from Mutant Mouse Models. Messenger (Los Angel) *4*, 4-22.

Ruas, M., Rietdorf, K., Arredouani, A., Davis, L.C., Lloyd-Evans, E., Koegel, H., Funnell, T.M., Morgan, A.J., Ward, J.A., Watanabe, K.*, et al.* (2010). Purified TPC isoforms form NAADP receptors with distinct roles for Ca(2+) signaling and endolysosomal trafficking. Curr Biol *20*, 703-709.

Sachyani, D., Dvir, M., Strulovich, R., Tria, G., Tobelaim, W., Peretz, A., Pongs, O., Svergun, D., Attali, B., and Hirsch, J.A. (2014). Structural basis of a Kv7.1 potassium

channel gating module: studies of the intracellular c-terminal domain in complex with calmodulin. Structure *22*, 1582-1594.

Sakurai, Y., Kolokoltsov, A.A., Chen, C.C., Tidwell, M.W., Bauta, W.E., Klugbauer, N., Grimm, C., Wahl-Schott, C., Biel, M., and Davey, R.A. (2015). Ebola virus. Two-pore channels control Ebola virus host cell entry and are drug targets for disease treatment. Science *347*, 995-998.

Shaner, N.C., Steinbach, P.A., and Tsien, R.Y. (2005). A guide to choosing fluorescent proteins. Nat Methods *2*, 905-909.

Sohocki, M.M., Daiger, S.P., Bowne, S.J., Rodriquez, J.A., Northrup, H., Heckenlively, J.R., Birch, D.G., Mintz-Hittner, H., Ruiz, R.S., Lewis, R.A.*, et al.* (2001). Prevalence of mutations causing retinitis pigmentosa and other inherited retinopathies. Hum Mutat *17*, 42-51.

Stryer, L., and Haugland, R.P. (1967). Energy transfer: a spectroscopic ruler. Proc Natl Acad Sci U S A *58*, 719-726.

Stuck, M.W., Conley, S.M., and Naash, M.I. (2016). PRPH2/RDS and ROM-1: Historical context, current views and future considerations. Prog Retin Eye Res *52*, 47-63.

Sulem, P., Gudbjartsson, D.F., Stacey, S.N., Helgason, A., Rafnar, T., Jakobsdottir, M., Steinberg, S., Gudjonsson, S.A., Palsson, A., Thorleifsson, G.*, et al.* (2008). Two newly identified genetic determinants of pigmentation in Europeans. Nat Genet *40*, 835-837.

Sung, C.H., and Chuang, J.Z. (2010). The cell biology of vision. J Cell Biol *190*, 953-963.

Trybus, K.M. (2008). Myosin V from head to tail. Cell Mol Life Sci *65*, 1378-1389.

Villarroel, A., Taglialatela, M., Bernardo-Seisdedos, G., Alaimo, A., Agirre, J., Alberdi, A., Gomis-Perez, C., Soldovieri, M.V., Ambrosino, P., Malo, C.*, et al.* (2014). The ever changing moods of calmodulin: how structural plasticity entails transductional adaptability. J Mol Biol *426*, 2717-2735.

Vogel, S.S., Thaler, C., and Koushik, S.V. (2006). Fanciful FRET. Sci STKE *2006*, re2.

Wang, X., Zhang, X., Dong, X.P., Samie, M., Li, X., Cheng, X., Goschka, A., Shen, D., Zhou, Y., Harlow, J.*, et al.* (2012). TPC proteins are phosphoinositide- activated sodium-selective ion channels in endosomes and lysosomes. Cell *151*, 372-383.

Wells, J., Wroblewski, J., Keen, J., Inglehearn, C., Jubb, C., Eckstein, A., Jay, M., Arden, G., Bhattacharya, S., Fitzke, F.*, et al.* (1993). Mutations in the human retinal degeneration slow (RDS) gene can cause either retinitis pigmentosa or macular dystrophy. Nat Genet *3*, 213-218.

Xu, H., and Ren, D. (2015). Lysosomal physiology. Annu Rev Physiol *77*, 57-80.

Yus-Najera, E., Santana-Castro, I., and Villarroel, A. (2002). The identification and characterization of a noncontinuous calmodulin-binding site in noninactivating voltage-dependent KCNQ potassium channels. J Biol Chem *277*, 28545-28553.

Zong, X., Schieder, M., Cuny, H., Fenske, S., Gruner, C., Rotzer, K., Griesbeck, O., Harz, H., Biel, M., and Wahl-Schott, C. (2009). The two-pore channel TPCN2 mediates NAADP-dependent Ca(2+)-release from lysosomal stores. Pflugers Arch *458*, 891-899.

8 Publications

Original Publications

Chen C-C*, **Butz ES***, Chao Y-K, Grishchuk Y, Becker L, Heller S, Slaugenhaupt SA, Biel M, Wahl-Schott C, Grimm C (2017) ***Small molecules for early endosome specific patch-clamping*** Cell Chem Biol 24(7):907-916.e4
* *Authors contributed equally*

Böhm S, Riedmayr LM, Nguyen O.N., Gießl A, Liebscher T, **Butz ES**, Schön C, Michalakis S, Wahl-Schott C, Biel M and Becirovic E (2017) ***Rom-1 prevents rod outer segment targeting of retinitis pigmentosa-linked peripherin-2 mutants.*** Sci Rep May 24:7(1):2321. doi: 10.1038/s41598-017-02514-5

Chen C-C*, Cang C*, Fenske S, **Butz E**, Chao Y-K, Biel M, Ren D, Wahl-Schott C, Grimm C (2017) ***Patch clamp technique to characterize ion channels in enlarged individual endolysosomes*** Nat Protoc 12(8):1639-1658

Butz ES*, Ben-Johny M*, Shen M, Yang PS, Sang L, Biel M, Yue DT, Wahl-Schott C (2016) ***Quantifying macromolecular interactions in living cells using FRET two-hybrid assays.*** Nat Protoc 11(12): 2470-2498
*** Authors contributed equally*

Becirovic E., Böhm S., Nguyen O.N., Riedmayr L.M., Hammelmann V., Schön C., **Butz E.S.**, Wahl-Schott C., Biel M., Michalakis S. (2016) ***AAV Vectors for FRET-Based analysis of protein-protein interactions in photoreceptor outer segments***., Front Neurosci. 28;10:356. doi: 10.3389/fnins.2016.00356.

Nguyen O.N., Böhm S., Gießl A., **Butz E.S.**, Wolfrum U., Brandstätter J.H., Wahl-Schott C., Biel M., Becirovic E. (2016) ***Peripherin-2 differentially interacts with cone opsins in outer segments of cone photoreceptors.*** Hum Mol Genet. 15;25(12):2367-2377

Alberdi A, Gomis-Perez C, Bernardo-Seisdedos G, Alaimo A, Malo C, Aldaregia J, Lopez-Robles C, Areso P, **Butz E**, Wahl-Schott C, Villarroel A. (2015) ***Uncoupling PIP2-calmodulin regulation of Kv7.2 channels by an assembly destabilizing epileptogenic mutation*.** J Cell Sci. 2015 Nov 1;128(21):4014-23. doi: 10.1242/jcs.176420.

Butz E., Peichl L., Müller B. (2014) ***Cone bipolar cells in the retina of the microbat Carollia Perspicillata*.** J Comp Neurol doi: 10.1002/cne.23726

Grimm C., Holdt L.M., Chen C.-C., Hassan S., Müller C., Jörs S., Cuny H., Kissing S., Schröder B., **Butz E.**, Northoff B., Castonguay J., Luber C.A., Moser M., Spahn S.,

Lüllmann-Rauch R., Fendel C., Klugbauer N., Griesbeck O., Haas A., Mann M., Bracher F., Teupser, D., Saftig P., Biel M., Wahl-Schott C. (2014) ***High susceptibility to fatty liver disease in two-pore channel 2-deficient mice***, Nature Commun., 5:4699. doi: 10.1038/ncomms5699

Becirovic E.*, Nguyen ON.*, Paparizos C., **Butz E.**, Stern-Schneider G., Wolfrum U., Hauck SM., Ueffing M., Wahl.Schott C., Michalakis S., Biel M. (2014) ***Peripherin-2 couples rhodopsin to the CNG channel in outer segments of rod photoreceptors*** Hum Mol Genet 23(22):5989-97. doi: 10.1093/hmg/ddu323

Müller B., **Butz E.**, Peichl L., Haverkamp S. (2013) ***The rod pathway of the microbat retina has bistratified rod bipolar cells and tristratified AII amacrine cells*,** J Neurosci, 33(3): 1014-1023; doi: 10.1523/JNEUROSCI.2072-12.2013

Weissbach A., Djarmati A., Klein C., Dragasević N., Zühlke C., Raković A:, Guzvić M., **Butz E.**, Tönnies H., Siebert R., Petrović I., Svetel M., Kostić V.S., Lohmann K. (2010) ***Possible genetic heterogeneity of spinocerebellar ataxia linked to chromosome 15*** Movement Disorders 25(11):1577-82 doi: 10.1002/mds.22857

Review

Grimm C., **Butz E.**, Chen C.C., Wahl-Schott C., Biel M. (2017) ***From mucolipidosis type IV to Ebola: TRPML and two-pore channels at the crossroads of endo-lysosomal trafficking and disease.,*** Cell Calcium Apr 23. pii: S0143-4160(17)30046-5. doi: 10.1016/j.ceca.2017.04.003.

Submitted manuscripts

Chao Y.K.*, Schludi V.*, Chen C.C., **Butz E.S.**, NguyenO.N.P., Müller M., Krüger J., Kammerbauer C., Ben-Johny M., Vollmar A., Berking C., Biel M., Wahl-Schott C., Grimm C. (2017) ***TPC2 polymorphisms associated with a hair pigmentation phenotype in humans result in gain of channel function by independent mechanisms.,*** submitted to Proceedings to the National Academy of Science (PNAS)

Conference participations and Poster

C.C. Chen, **E. Butz**, E. Plesch, Y.K. Chao, F. Bracher, C. Wahl-Schott, M. Biel, C. Grimm **Characterization of TRPML3 currents in endolysosomal system** *CRC/TRR152 Symposium*, 28. Sep. – 1. Oct. 2016, Herrsching

Butz E., Chen C.C., Hassan S., Armandi G., Griesbeck O., Wahl-Schott C., Biel M. **Neuronal phenotype of TPC2-deficient mice** *CRC/TRR152 Symposium*, 28. – 31. Oct. 2015, Herrsching

C. Grimm, **E. Butz**, C.C. Chen, M. Biel, C. Wahl-Schott **High susceptibility to non-alcoholic fatty liver disease in two-pore channel 2-deficient mice** (2940-POS) Biophysical Society 59th Annual Meeting, 7. – 11. Feb. 2015, Baltimore

E. Butz, M. Biel, C. Wahl-Schott **Quantitative FRET approach to monitor binding affinities between ion channesl and its putative interaction partners**, *Sommer School* 18. – 20. Jul. 2014, Frauenchiemsee

9 Acknowledgement

Hiermit möchte ich mich bei allen bedanken, die das Entstehen dieser Doktorarbeit möglich gemacht haben. Es war eine sehr prägende und lehrreiche Zeit für mich.

Mein aufrichtigster Dank gilt im Besonderen...

... **Prof. Dr. Martin Biel** für die Aufnahme in den Arbeitskreis, die andauernde Förderung und die finanzielle Unterstützung, die die Verwirklichung vieler Projekte erst möglich gemacht hat.
... **Prof. Dr. Christian Wahl** für die gute Betreuung, die stete Ermutigung und Förderung. Lieber Christian, vielen Dank für das Vertrauen, das Du in mich gesetzt hast!
... **Dr. Dr. Christian Grimm** für die kontinuierliche wissenschaftliche und moralische Unterstützung, die Geduld und gute Zusammenarbeit über das Dissertationsthema hinaus. Lieber Christian, es war immer sehr motivierend, mit Dir zu arbeiten!
... **Dr. Elvir Becirovic** für das Angebot, mich in seine Projekte einzubringen und das freundliche Überlassen einzelner Abbildungen. Danke, dass Du mich immer in die thematischen Hintergründe einbezogen hast!
... **Dr. Manu Ben Johny** für die interessante Zeit an der Johns Hopkins in Baltimore und den intensiven wissenschaftlichen Austausch.
... **Dr. Verena Hammelmann** für die vielen geduldigen und aufrichtigen Antworten auf all meine Fragen.
... **Dr. Cheng-Chang Chen** und **Yu-Kai Chao** für die gute Zusammenarbeit. It was a pleasure working with you!
... **Verena Schludi** für viele Jahre kollegiale Sitznachbarschaft, unermüdlichen Optimismus und gute Laune.
... meinen treuen Studenten **Renè Rötzer**, **Anna Rößing** und **Tamara Kiwitt** für ihre Hilfe, Unterstützung und Motivation in einer für mich sehr stressigen Zeit.
... den aktuellen wie auch ehemaligen **Kollegen des gesamten Arbeitskreises** für die angenehme Arbeitsatmosphäre, anregende Diskussionen und die Hilfsbereitschaft; viele lustige gemeinsame Abende und auch für das ein oder andere Gläschen Wein zur richtigen Zeit.

Von ganzem Herzen möchte ich meiner Familie, insbesondere meinen Eltern und Geschwistern, für ihre konstante Unterstützung und das große Vertrauen danken, das sie in mich setzen. Ohne euren Rückhalt hätte ich so einiges nicht geschafft!

10 Appendix

In the following, manuscripts I to VIII are reprinted:

I. **Butz et al.**, (2016) *Quantifying macromolecular interactions in living cells using FRET two-hybrid assays,* **Nature Protocols**, 11(12): 2470-2498

II. **Alberdi et al.**, (2015) *Uncoupling PIP_2-calmodulin regulation of Kv7.2 channels by an assembly destabilizing epileptogenic mutation,* **Journal of Cell Science**, 128(21), 4014-4023

III. **Grimm et al.**, (2014) *High susceptibility to fatty liver disease in two-pore channel 2-deficient mice*, **Nature Communications**, 5:4699

IV. **Chao et al.**, (2017) *TPC2 polymorphisms associated with a hair pigmentation phenotype in humans result in gain of channel function by independent mechanisms* 2017, **accepted in Proceedings of the National Academy of Sciences**

V. **Becirovic et al.**, (2014) *Peripherin-2 couples rhodopsin to the CNG channel in outer segments of rod photoreceptors* **Human Molecular Genetics**, 23(22), 5989-5997

VI. **Nguyen et al.**, (2016) *Peripherin-2 differentially interacts with cone opsins in outer segments of cone photoreceptors* **Human Molecular Genetics**, 25(12), 2367-2377

VII. **Becirovic et al.**, (2016) *AAV vectors for FRET-based analysis of protein-protein interactions in photoreceptor outer segments* **Frontiers in Neuroscience**, 10:356

VIII. **Böhm et al.**, (2017) *Peripherin-2 and Rom-1 have opposing effects on rod outer segment targeting of retinitis pigmentosa-linked peripherin-2 mutants* **Scientific Reports,** 7(1):2321

Quantifying macromolecular interactions in living cells using FRET two-hybrid assays

Elisabeth S Butz[1,3], Manu Ben-Johny[2,3], Michael Shen[2], Philemon S Yang[2], Lingjie Sang[2], Martin Biel[1], David T Yue[2] & Christian Wahl-Schott[1]

[1]Center for Integrated Protein Science CIPS-M and Zentrum für Pharmaforschung, Department Pharmazie; DZHK (German Center for Cardiovascular Research), partner site Munich Heart Alliance, Munich, Germany. [2]Calcium Signals Laboratory, Department of Biomedical Engineering, The Johns Hopkins University School of Medicine, Baltimore, Maryland, USA. [3]These authors contributed equally to this work. Correspondence should be addressed to M.B.-J. (manu@jhmi.edu) or C.W.-S. (Christian.Wahl@cup.uni-muenchen.de).

Published online 10 November 2016; corrected online 1 December 2016 (details online); doi:10.1038/nprot.2016.128

Förster resonance energy transfer (FRET) is a versatile method for analyzing protein–protein interactions within living cells. This protocol describes a nondestructive live-cell FRET assay for robust quantification of relative binding affinities for protein–protein interactions. Unlike other approaches, our method correlates the measured FRET efficiencies to relative concentration of interacting proteins to determine binding isotherms while including collisional FRET corrections. We detail how to assemble and calibrate the equipment using experimental and theoretical procedures. A step-by-step protocol is given for sample preparation, data acquisition and analysis. The method uses relatively inexpensive and widely available equipment and can be performed with minimal training. Implementation of the imaging setup requires up to 1 week, and sample preparation takes ~1–3 d. An individual FRET experiment, including control measurements, can be completed within 4–6 h, with data analysis requiring an additional 1–3 h.

INTRODUCTION

FRET is a powerful technique used to probe close-range molecular interactions and to estimate atomic-scale distances. Physically, the FRET phenomenon manifests as a dipole–dipole interaction between closely juxtaposed fluorescent molecules. For instance, after photoexcitation, a fluorophore may de-excite through direct emission of a photon of appropriate wavelength. However, in the presence of a nearby acceptor, the donor nonradiatively transfers energy to the acceptor molecule, resulting in quenched donor fluorescence—a phenomenon termed FRET. The excited acceptor molecule may subsequently emit a photon with a shifted spectrum. In principle, by monitoring the hue of the emitted photon, one can detect a molecular interaction and infer the approximate spatial arrangement of the two molecules. The physical principles underlying FRET and its application as a spectroscopic ruler have been reviewed at length in the past[1,2].

With the advent of an expanded color palette of genetically encoded fluorophores, the FRET methodology has garnered much interest in regard to studying biological systems[3]. To date, several strategies have been used to determine FRET efficiencies nondestructively[4–10]. Traditional approaches such as acceptor photobleaching quantify the donor fluorescence before and after photodestruction of the acceptor. This approach requires the sample to be exposed to high-intensity light, often resulting in cellular phototoxicity. The destructive nature of this popular approach means that only a single FRET measurement can be attained. Nondestructive assays assess FRET efficiency from brief low-intensity light pulses, enabling rapid and dynamic measurements with relatively minimal photodamage.

Development of the protocol

The FRET two-hybrid assay is a valuable method for detecting and quantifying binding interactions between biological macromolecules in living cells. A single cell is considered to be a 'biological cuvette', and FRET efficiency is systematically measured between pairs of fluorophore-tagged molecules from many single cells for quantitative determination of bimolecular interactions. The protocol presented here provides the theoretical and experimental framework to integrate two existing FRET two-hybrid approaches: 3^3-FRET and E-FRET. This analysis enables microscope-dependent calibration constants to be experimentally determined, apparent donor- and acceptor-centric FRET efficiencies to be computed, and robust, reproducible binding curves of high quality to be obtained—permitting rigorous biochemical analysis in living cells.

The methodology and formalism elaborated here is built upon work by Erickson *et al.* that was first applied to characterize the interaction of the Ca^{2+}-binding protein calmodulin with the L-type Ca^{2+} channel complex[9,10]. In this experimental paradigm, fluorescence measurements are obtained from three distinct filter cubes. The filters are chosen to specifically detect donor, acceptor and FRET signals. The use of three filter cubes allows for accurate dissection of the FRET signal from pure donor and acceptor signals, leading to its name 3^3-FRET. The 'sensitized emission' or the net increase in acceptor fluorescence due to FRET is computed from these measurements. Importantly, this metric corresponds to an acceptor-centric measurement of FRET, and the efficiencies computed are reported as 'E_A'. The very same measurements can be used to nondestructively calculate the net decrease in donor fluorescence due to FRET. This metric corresponds to FRET efficiencies obtained using donor dequenching or acceptor photobleaching methods. This methodology is termed 'E-FRET' and corresponds to a donor-centric FRET measurement denoted here as 'E_D'. Experimental determination of both 3^3-FRET and E-FRET efficiency measurements rely on two instrument-specific constants that need to be either computed based on the optical properties of the imaging system (**Supplementary Note 1**, **Supplementary Data 1**) or experimentally determined using a series of cyan fluorescent protein–yellow fluorescent protein (CFP–YFP) dimers ('Determination of calibration constants using dimers' section).

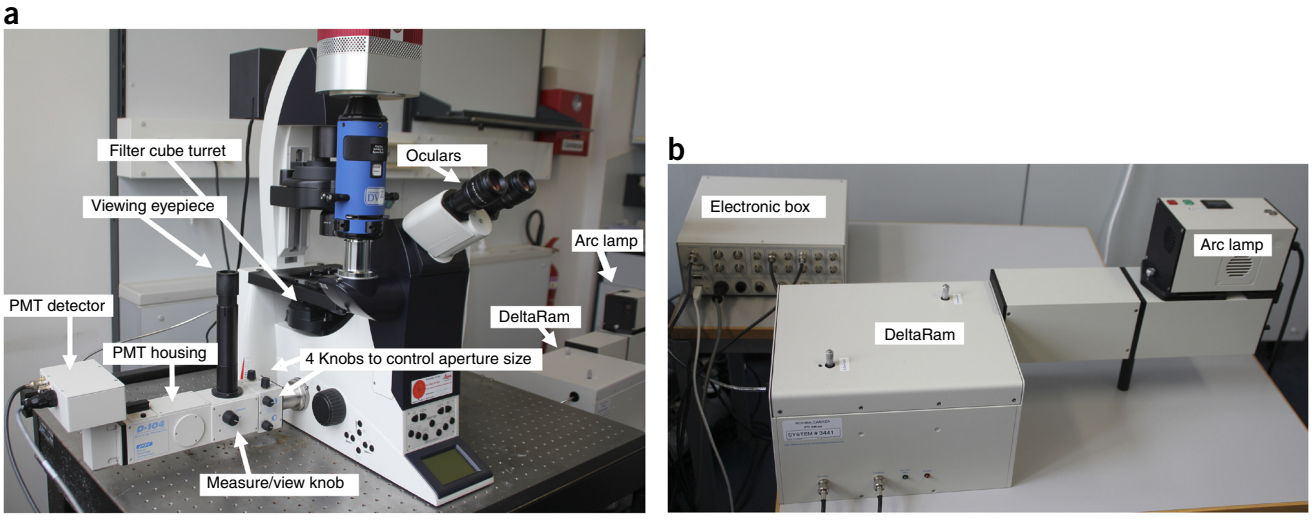

Figure 1 | Equipment setup for FRET imaging. (**a**) Photograph of the FRET setup comprising an inverted microscope and a photomultiplier detection system (PMT detector and PMT housing). The PMT housing contains an eyepiece and four knobs to control the aperture size. The measure/view knob is set to direct the light to either the eyepiece for visualization or the PMT for data acquisition. All major components are indicated. Note that the CCD camera connected to our microscope is not necessary to perform the FRET two-hybrid assays described here. (**b**) For excitation, a DeltaRam monochromator containing a xenon arc lamp is used; the one shown has knobs to adjust the slit width for excitation light.

Once 3[3]-FRET or E-FRET efficiencies are determined, the FRET two-hybrid assay correlates these efficiencies with the free concentrations of donor or acceptor molecules, respectively. The first important step in the workflow is the experimental determination of the total number of donor and acceptor proteins present in any given cell based on the total YFP and CFP fluorescence corrected for quenching due to FRET. Data from many single cells are then compiled to construct a single binding curve. In practice, the stochastic expression of CFP and YFP molecules in cells yields a broad range of free donor or acceptor concentrations, and each cell populates various segments of a binding curve.

Theoretical underpinnings of the FRET two-hybrid assay

For the illustrative experiments described in this protocol, the FRET measurement setup (**Fig. 1**) is composed of a wide-field fluorescence microscope, a xenon-lamp-based excitation system, a motorized turret containing three filter cubes and a photomultiplier-based detection system (**Figs. 1** and **2**). Any donor–acceptor fluorescent protein pairs that are suitable for FRET measurements, together with matched filter cubes, can be used for these experiments[11]. We will describe the method for the enhanced CFP–enhanced YFP (CFP–YFP) donor–acceptor pair, which is a popular choice for FRET. Three filter cubes are required: a CFP cube, a FRET cube and a YFP cube (**Table 1**). As the venus–cerulean FRET pairs are highly similar to CFP–YFP pairs, the same filter cubes can be used, although the instrument-specific calibration constants should be explicitly measured for these pairs, given their distinct quantum yields.

For typical FRET experiments, proteins of interest are fused to either CFP or YFP, and expressed pairwise in mammalian HEK293 cells. Fluorescence signal from each cell is analyzed using three filter cubes (**Table 1**) to compute apparent FRET efficiencies. Illumination of the sample at the peak of the donor excitation spectrum ($\lambda \sim 436$ nm) results in a double-peaked spectrum composed of CFP emission superimposed on YFP emission. In part, the net YFP fluorescence is the result of weak direct excitation by the 436-nm light (~1–3%). In addition, with FRET, CFP transfers energy to YFP, resulting in quenching of the CFP fluorescence (observed at ~480 nm) and an enhancement in the YFP fluorescence detected at ~535 nm (ref. 12). FRET can be measured either as the fractional increase in the acceptor intensity ('sensitized emission') or as the fractional decrease in the donor intensity ('donor quenching') (**Fig. 3a**). In the first case, the apparent FRET efficiency (E_A), is given by the amount of measured sensitized emission in relation to maximal sensitized emission that would be present for a FRET efficiency of 1. Alternatively, FRET can be measured using donor dequenching, in which case the apparent FRET efficiency (E_D), will be the ratio of the enhancement in CFP fluorescence acceptor photobleaching to the total CFP fluorescence after photobleaching (**Fig. 3b**). In this protocol, we use a nondestructive approach to determine E_D that uses an experimentally determined calibration constant (G factor) that relates the enhancement in YFP fluorescence to the decrease in CFP fluorescence (**Fig. 3**). In this protocol, we follow the mathematical conventions defined in Erickson *et al.*[9], and the fluorescence signal measured through a particular cube is defined as $S_{cube}(DA, \lambda_{ex}, \lambda_{em})$, where cube denotes a CFP, YFP or FRET cube; D denotes donor, A denotes acceptor and DA denotes both; λ_{ex} denotes excitation wavelength; and λ_{em} denotes emission wavelength. In addition, fluorescence signal from a particular CFP or YFP molecule may be represented as $XFP_{cube}(\lambda_{ex}, \lambda_{em}$, direct/FRET) when measured with excitation light of wavelength λ_{ex}, emission of wavelength λ_{em}. direct/FRET corresponds to the mode of excitation of the given molecule[9,10].

Determination of spectral factors R_{D1}, R_{D2} and R_{A1}. Calculation of E_A and E_D requires robust dissection of sensitized emission (**Fig. 4**). This determination is complicated by spectral overlap between donors (CFP) and acceptors (YFP) resulting from their broad excitation and emission spectra. Three confounding factors may obfuscate computation of FRET efficiencies (**Fig. 2**). First, the overlap in the emission spectra of CFP and YFP could lead

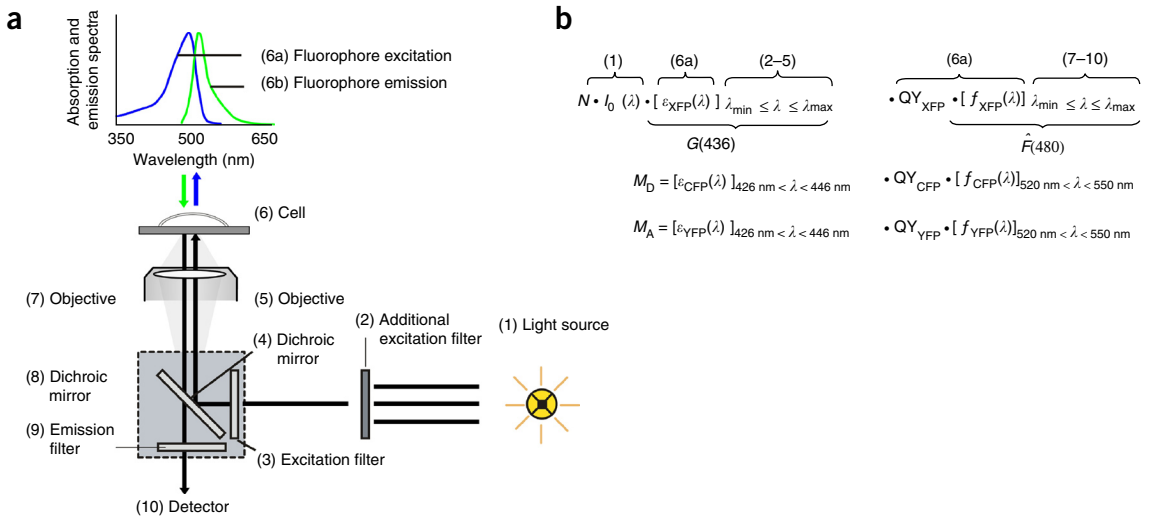

Figure 2 | Schematic of optical components of the FRET setup for a given filter cube and fluorophore. (**a**) The excitation pathway (1–6a) consists of the light source (1), excitation filters (2 and 3), a dichroic mirror that reflects the excitation light (4), a 40× objective (5) and the excitation spectrum of the fluorophore contained in a cell (6, 6a). The emission pathway (6b–9) consists of the emission spectrum and the quantum yield (QY) of the fluorophore expressed in the cell (6b), the objective (7), the dichroic that transmits the emission light (8), the emission filter (9) and the detector (10). (**b**) Top: Fluorescence intensity output can be calculated from setup-specific optical components in the excitation (1–6a) and emission pathways (6b–9) by multiplying together all relevant parameters: XFP is the fluorophore in question. N is the number of fluorophores excited, I_0 represents the overall intensity of the excitation lamp (over all wavelengths) and $\varepsilon_{XFP}(\lambda)$ represents the wavelength-dependent absorption properties of the fluorophore as given by the excitation spectrum of the fluorophore. The optical properties of the excitation pathway, such as the spectral properties of the excitation light source and the spectral properties of the excitation filter and dichroic mirror of the cube, are incorporated into the wavelength range depicted. $f_{XFP}(\lambda)$ and QY_{XFP} correspond to the emission spectrum and QY of the fluorophore. The spectral properties of the dichroic mirror and the emission filter of the FRET filter cube, as well as frequency-dependent sensitivity of the PMT detector, are incorporated into the wavelength range shown. M_D and M_A correspond to the brightness of a single donor and acceptor fluorophore.

to a small bleed-through of CFP fluorescence in the FRET cube (emission~535 nm). The expected bleed-through can be quantified from cells expressing CFP alone at the peak of their absorption spectrum (~436 nm) and computing the fractional emission through the FRET cube—$R_{D1} = S_{FRET}(D, 436, 535)/S_{CFP}(D, 436, 480)$. This strategy is effective, as CFP fluorescence can be isolated from cells expressing both CFP and YFP, using the CFP cube. The effective CFP fluorescence bleed-through in the FRET cube is then

$$CFP_{FRET}(436, 535, \text{direct}) = R_{D1} \cdot S_{CFP}(DA, 436, 480) \quad (1)$$

$R_{D1} \sim 0.25$ for our experimental setup. R_{D1} values are typically stable, as they probe the emission properties of CFP, and drastic changes in these values may signify changes in the detection subsystem such as diminished detector sensitivity or aging of emission filters.

Second, a small fraction of YFP is cross-excited by the 436-nm light through the FRET cube. The direct YFP signal can be optically isolated using the YFP cube with negligible CFP excitation (**Fig. 4**). The ratio R_{A1} is defined as the fractional excitation of YFP through the FRET cube relative to the YFP cube—$R_{A1} = S_{FRET}(A, 436, 535)/S_{YFP}(A, 500, 535)$. The cross-excitation of YFP through the FRET cube in cells expressing both YFP and CFP can be unmixed by computing:

$$YFP_{FRET}(436, 535, \text{direct}) = R_{A1} \cdot S_{YFP}(DA, 500, 535) \quad (2)$$

$R_{A1} \sim 0.03$ for our experimental setup. Experimentally, some day-to-day variability in R_{A1} values is observed due to changes in xenon arc lamp spectra or the excitation subsystem.

Third, a small fraction of CFP molecules may be directly excited through the YFP cube, leading to overestimation of the total YFP signal, $YFP_{YFP}(500, 535, \text{direct})$. R_{D2} is the ratio of CFP fluorescence output through the YFP cube relative to the CFP cube:

$$R_{D2} = S_{YFP}(D, 500, 535)/S_{CFP}(D, 436, 480) \quad (3)$$

The corrupting CFP signal through the YFP cube is then:

$$CFP_{YFP}(500, 535, \text{direct}) = R_{D2} \cdot S_{CFP}(DA, 436, 480) \quad (4)$$

In practice, the ratio R_{D2} is negligibly small (~0.009 for our experimental setup). This factor can be a concern in cells in which CFP values far exceed YFP values. FRET efficiency estimation is prone to substantial errors in this case.

In summary, R_{D1} and R_{A1} are determined in cells in which acceptor or donor alone are individually expressed and then applied to transform signals from different cells containing both acceptors and donors. Critically, these ratios are independent of the excitation intensity (I_0) and the number of donors (N_D) or acceptors (N_A) in the field of view; instead, they depend only on the spectral properties of the donor or acceptor, respectively (**Fig. 4**). These ratios can be used to optimize or troubleshoot the FRET experimental setup while establishing the method and testing associated hardware components.

Determination of FRET efficiencies. Once spectral ratios are determined, E_A and E_D can be calculated based on the fluorescence measurements from the CFP, YFP and FRET cubes according to equations (5–7) in **Box 1** (**Supplementary Note 2**).

TABLE 1 | Properties of the filter cubes present in the FRET rig.

Cube	Excitation	Dichroic	Emission
CFP	426–446 nm	T455lp	460–500 nm
YFP	490–510 nm	T515lp	520–550 nm
FRET	426–446 nm	T455lp	520–550 nm

The graphical interpretation of this computation is shown in **Figure 4a**. Sensitized emission of YFP is calculated by realizing that emission at 535 nm (**Fig. 4a**, point 1) is the sum of direct CFP emission (donor bleed-through; **Fig. 4a**, point 3), YFP emission due to direct excitation (acceptor cross-excitation; **Fig. 4a**, point 5) and YFP emission due to FRET excitation (F_C; **Fig. 4a**, points 4 and 5). The contribution of direct CFP emission at 535 nm (**Fig. 4a**, point 3) is computed based on CFP measurement using the CFP cube (**Fig. 4a**, point 2) and the spectral ratio R_{D1}. The contribution of YFP emission due to direct excitation (**Fig. 4a**, point 5) is determined based on YFP cube measurement (**Fig. 4d**) and the spectral ratio R_{A1}. The 3^3-FRET efficiency E_A is computed as the ratio of sensitized emission (**Fig. 4a**, points 4 and 5) to the emission of YFP due to direct excitation (**Fig. 4a**, point 5), corrected by a calibration constant that represents the ratio of extinction coefficients (**Box 1**). This latter factor ($R_{A1} \cdot S_{YFP}(DA, 500, 535) \cdot \varepsilon_{CFP}(436)/\varepsilon_{YFP}(436)$) is the maximal sensitized emission of YFP observable if $E_A = 1$. By contrast, the E-FRET computation converts the sensitized emission of YFP (F_C; **Fig. 4a**, points 4 and 5) to an equivalent quenching of CFP fluorescence due to FRET by the calibration constant G. E-FRET reports the ratio of the CFP quenching to total CFP output in the absence of FRET.

An important distinction is that E_A and E_D depend on the bound fraction of the donor (A_b) and acceptor (D_b), respectively. As A_b or D_b approaches 1, the apparent efficiency equals true efficiency (E). We will use a quantitative description of the total number of CFP and YFP molecules in a cell along with a 1:1 binding model to calculate D_b or A_b and to resolve a binding relation. The following section will define and outline the experimental strategy for determination of the instrument-specific calibration constants $\varepsilon_{YFP}(436)/\varepsilon_{CFP}(436)$ and G.

Determination of calibration constants for 3^3-FRET and E-FRET. The instrument-specific calibration constants ($\varepsilon_{YFP}(436)/\varepsilon_{CFP}(436)$ and G) can either be computed by analysis of the optical properties of the FRET experimental setup or be experimentally determined using CFP–YFP dimers tethered with variable size linkers (**Fig. 5a**). Here, we adopt the second approach, using four distinct CFP–YFP dimers to deduce these coefficients. The plasmids encoding various dimers have been deposited to Addgene[13]. The genetic fusion of CFP and YFP ensures that the stoichiometry is 1:1 and A_b=D_b=1. The apparent FRET efficiencies for these constructs, measured using 3^3-FRET and E-FRET, must equate:

$$E_A = E \cdot A_b = E = E \cdot D_b = E_D \quad (8)$$

Thus, rearranging equations (6 and 7) in **Box 1** yields equation (9), a convenient expression to experimentally determine the calibration constants.

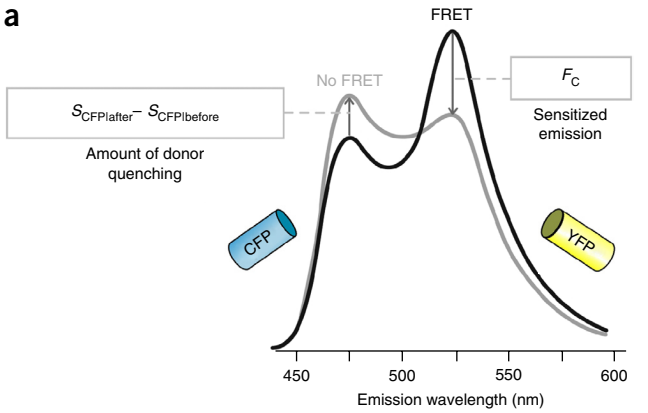

b

$$E_A = \frac{\text{Measured sensitized emission}}{\text{Maximal sensitized emission if } E = 1}$$

$$E_D = \frac{\text{Measured amount of donor quenching}}{\text{Total donor fluorescence in the absence of FRET}}$$

$$G = \frac{\text{Sensitized emission}}{\text{Amount of donor quenching}}$$

Figure 3 | Spectral properties of FRET. (**a**) Double-peaked spectrum arising from CFP and YFP coexpressing cells in the presence (black line) and absence of FRET (gray line). FRET reduces donor fluorescence (donor quenching) and increases acceptor fluorescence (sensitized emission). (**b**) Sensitized emission can be measured and converted into FRET efficiency using the general formula for E_A presented in **Box 1**. Sensitized emission can also be used for the determination of E_D by using a nondestructive FRET approach instead of acceptor photobleaching. This method requires the determination of the G factor, a factor that converts the amount of sensitized emission into donor dequenching (**Box 1**).

$$\frac{F_C}{R_{A1} \cdot S_{YFP}(DA, 500, 535)} = -G\frac{R_{D1} \cdot S_{CFP}(DA, 436, 480)}{R_{A1} \cdot S_{YFP}(DA, 500, 535)} + \frac{\varepsilon_{CFP}(436)}{\varepsilon_{YFP}(436)} \quad (9)$$

Here, $S_{YFP}(DA, 500, 535)$ and $S_{CFP}(DA, 436, 480)$ are direct measurements of the CFP–YFP dimer using the YFP and CFP cubes. F_C corresponds to sensitized emission of YFP, determined as described by equation (5) (**Box 1**), and R_{A1} and R_{D1} are spectral factors. Equation (9) in fact describes a straight line, $y = m \cdot x + b$ where

$$x = \frac{R_{D1} \cdot S_{CFP}(DA, 436, 480)}{R_{A1} \cdot S_{YFP}(DA, 500, 535)} \quad \text{and} \quad y = \frac{F_C}{R_{A1} \cdot S_{YFP}(DA, 500, 535)}$$

both experimentally determined. The intercept of this relation corresponds to the 3^3-FRET calibration constant $\varepsilon_{CFP}(436)/\varepsilon_{YFP}(436)$, whereas the slope determines the E-FRET calibration constant G (**Fig. 5b**). The x and y pair of values are computed individually for each cell for a given dimer, and the complete data set is plotted to obtain the calibration constants.

Calculation of the total number of CFP and YFP molecules. The apparent 3^3-FRET and E-FRET efficiencies depend on the bound fraction of acceptors (A_b) and donors (D_b) in a cell, respectively (**Box 2**, equations (10,12,15–23); **Supplementary Note 3**). To calculate the bound fractions, the total concentrations of CFP (CFP_{EST}) and YFP (YFP_{EST}) are estimated from single cells expressing an

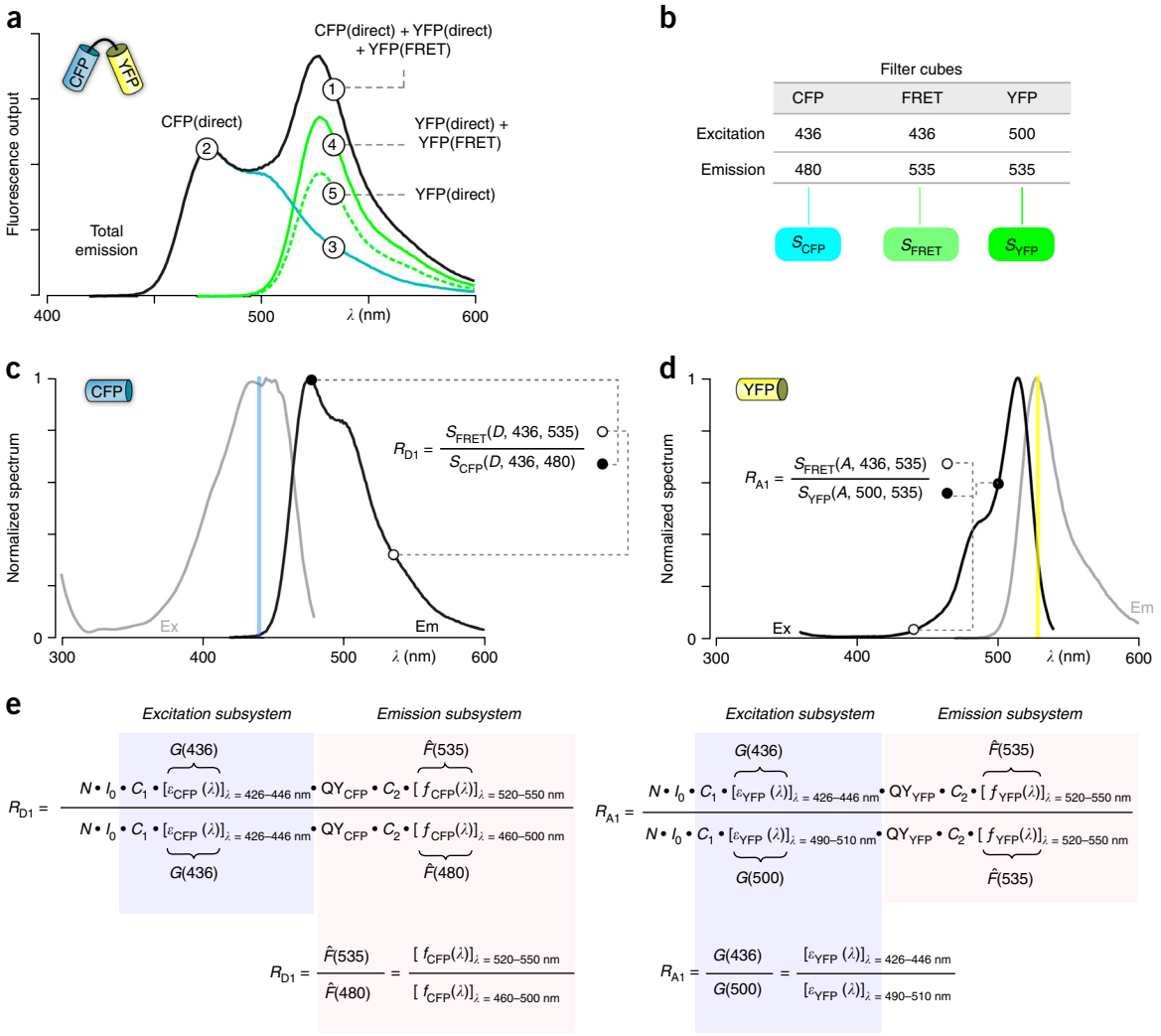

Figure 4 | Components of the fluorescence signal at 535-nm emission. (**a**) Combined emission spectrum of donor and acceptor. Maximal emission of CFP at 480 nm (point 2). The total fluorescence signal at 535 nm (point 1) is composed of donor bleed-through (point 3), fluorescence emission due to acceptor cross-excitation (point 5) and sensitized emission due to FRET (points 4 and 5). (**b**) Specifications of CFP, FRET and YFP filter cubes. Excitation: excitation wavelength, emission: emission wavelength. S_{CFP}, S_{FRET} and S_{YFP} are the output signals measured using the CFP, the FRET and the YFP filters, respectively. The detailed filter parameters are elaborated in **Table 1**. (**c**) Excitation (Ex) and emission (Em) spectra of CFP. $S_{FRET}(D, 436, 535)$ and $S_{CFP}(D, 436, 480)$ are the fluorescence signals measured at emission wavelengths of 535 nm and 480 nm, respectively, after excitation at 436 nm. From these signals, R_{D1} is calculated as indicated. (**d**) Excitation and emission spectra of YFP. $S_{FRET}(A, 436, 535)$ and $S_{YFP}(A, 500, 535)$ are the fluorescence signals measured at an emission wavelength of 535 nm after excitation at 436 nm or 500 nm, respectively. From these signals, R_{A1} is calculated as indicated. (**e**) R_{A1} and R_{D1} values mainly depend on the excitation lamp and detector response. Excitation subsystem: all parameters related to the excitation pathway. Emission subsystem: all parameters related to the emission pathway. Fluorescence intensity output is calculated according to the expression in **Figure 2b** (top). The ratio R_{D1} depends only on factors derived from the emission pathway; all factors from the excitation pathway cancel out. Therefore, R_{D1} reflects maturation of fluorescent proteins, which influences $f_{CFP}(535)$ and $f_{CFP}(480)$, as well as detector functions such as quantum efficiency, high voltage gain and stability of the detection. The ratio R_{A1} depends only on factors derived from the excitation pathway; all factors from the emission pathway cancel out. R_{A1} therefore reflects the number of fluorophores that may be affected by bleaching between the recordings of the two cubes, and fluctuations of the excitation lamp between the two recordings. Tabulation of R_{D1} and R_{A1} over a period of days and weeks (**Fig. 9a**,**b**) is very useful when establishing the method, as they serve to evaluate the stability of the light source (R_{A1}) and the detector (R_{D1}). FRET cannot be reliably measured until both values are stable. Differences between corresponding filters—e.g., the excitation filter of the CFP and the FRET cube or the excitation filter of the YFP and the FRET cube—are negligible. All variables are as defined in **Figure 2**.

interacting pair of donor and acceptor proteins. For noninteracting fluorophores, the fluorescence intensity is proportional to the total number of fluorophores in the given cell. As previously described by Erickson *et al.*[9], we use proportionality constants M_A and M_D for YFP and CFP molecules, respectively, to convert fluorescence intensities into the effective number of molecules[9,10]. These proportionality coefficients encode the brightness of the two fluorophores viewed using the FRET cube ($\lambda_{ex} \sim 436$ and $\lambda_{em} \sim 535$).

The fluorescence signal measured using the YFP cube ($S_{YFP}(DA, 500, 535)$) is devoid of any contribution from CFP. Thus, the total number of YFP molecules can be estimated as follows:

$$YFP_{EST} = \frac{YFP_{FRET}(436, 535, \text{direct})}{M_A} = \frac{R_{A1} \cdot S_{YFP}(DA, 500, 535)}{M_A} \quad (10)$$

Box 1 | Experimental computation of 3^3-FRET and E-FRET

The measurement of FRET efficiencies using 3^3-FRET and E-FRET for CFP–YFP FRET pairs relies on fluorescence measurements from three cubes: (1) S_{CFP}(DA, 436, 535) or the CFP cube; (2) S_{YFP}(DA, 436, 480) or the YFP cube; and (3) S_{FRET}(DA, 436, 535) or the FRET cube. These fluorescence measurements are then used to spectrally unmix the contribution of sensitized emission of YFP through the FRET cube using the spectral ratios R_{D1} and R_{A1} as follows:

$$F_C = S_{FRET}(DA, 436, 535) - R_{D1} \cdot S_{CFP}(DA, 436, 480) - R_{A1} \cdot S_{YFP}(DA, 500, 535) \quad (5)$$

The FRET efficiency as ascertained by the 3^3-FRET method is proportional to the ratio of sensitized emission to the direct excitation of YFP. Thus,

$$E_A = E \cdot A_b = \frac{F_C}{R_{A1} \cdot S_{YFP}(DA, 500, 535)} \frac{\varepsilon_{YFP}(436)}{\varepsilon_{CFP}(436)} \quad (6)$$

Similarly, the FRET efficiency as ascertained by the E-FRET method is given by the equation:

$$E_D = E \cdot D_b = \frac{F_C}{F_C + G \cdot R_{D1} \cdot S_{CFP}(DA, 436, 480)} \quad (7)$$

Computation of FRET efficiencies by both methods require the instrument-specific calibration constants $\varepsilon_{YFP}(436)/\varepsilon_{CFP}(436)$ and G. The procedure to experimentally determine these coefficients is outlined in Procedure Steps 78–99. These equations importantly assume a low-excitation limit at which the excitation power is low enough that there is no substantial ground-state depletion. Derivations for all equations are given in **Supplementary Note 2**.

$M_A = \varepsilon_{YFP}(436) \cdot f_{YFP}(535) \cdot QY_{YFP}$, where $\varepsilon_{YFP}(436)$ is the average molar extinction coefficient of YFP over the bandwidth of the FRET cube excitation filter (**Table 1**); $f_{YFP}(535)$ is the average YFP emission spectrum over the bandwidth of the FRET cube emission filter (**Table 1**); and QY_{YFP} is the quantum yield of YFP (0.61). The emission spectrum $f_{YFP}(\lambda)$ is normalized to have unitary area. The proportionality constant is related to the brightness of a single YFP molecule probed using the FRET cube. This approximation relies on the fact that optical transfer functions for the excitation and emission paths of the microscope are nearly constant over the respective bandwidths. Although the M_A value can be computed for any microscope system, the precise value is not essential.

By contrast, the estimation of the total number of CFP molecules from CFP intensity is more complex, as FRET results in quenching of the donor signal. There are two methods of compensating for this loss. First, FRET efficiency determined by the E-FRET method is equivalent to that determined by the donor dequenching method. Thus, the expected CFP intensity after acceptor photobleaching can be estimated by dividing the CFP intensity measured through the CFP cube before photobleaching by the apparent E-FRET efficiency, as shown in equation (11).

$$CFP_{postbleach}(436, 535, direct) = \frac{CFP_{prebleach}(436, 535, direct)}{1 - E_D} = \frac{R_{D1} \cdot S_{CFP}(DA, 436, 480)}{1 - E_D} \quad (11)$$

The total number of CFP molecules in a given cell is related to the corrected total CFP intensity in the absence of FRET ($CFP_{postbleach}$(436, 535, direct)) by proportionality constant M_D. Thus,

$$CFP_{EST} = \frac{R_{D1} \cdot S_{CFP}(DA, 436, 480)}{(1 - E_D) \cdot M_D} \quad (12)$$

Here, $M_D = \varepsilon_{CFP}(436) \cdot f_{CFP}(535)\ QY_{CFP}$, and $\varepsilon_{CFP}(436)$ is the average molar extinction coefficient of CFP over the excitation bandwidth of the FRET cube (**Table 1**); $f_{CFP}(535)$ is the average CFP emission over the emission bandwidth of the FRET cube (**Table 1**); and QY_{CFP} is the quantum yield of CFP (0.4).

A second strategy is to add the amount of fluorescence signal lost via FRET to the quenched CFP intensity by adding the term $E_A \cdot YFP_{FRET}(436, 535, direct) \cdot M_D/M_A$. This correction factor assumes a 1:1 donor–acceptor stoichiometry. The total number of CFP molecules is given by

$$CFP_{EST} = \frac{R_{D1} \cdot S_{CFP}(DA, 436, 480) + E_A \cdot R_{A1} \cdot S_{YFP}(DA, 500, 535)}{M_D} \quad (13)$$

The two strategies will yield similar estimates for CFP_{EST}, but equation (13) is valid only for a 1:1 interaction. For the purposes of obtaining relative binding affinities, calculating the precise value of M_A or M_D individually is not critical; however, the ratio of M_A to M_D is crucial. The parameter M_A/M_D can be obtained experimentally from the calibration constants for 3^3-FRET and E-FRET efficiency, as the ratio of slope to intercept from equation (9).

$$\frac{M_A}{M_D} = G \Big/ \frac{\varepsilon_{CFP}(436)}{\varepsilon_{YFP}(436)} \quad (14)$$

This relation depends upon the fact that $G = (f_{YFP}(535) \cdot QY_{YFP})/(f_{CFP}(535) \cdot QY_{CFP})$, which is the ratio of the quantum yields of the two fluorophores and the probability of emitting a photon of the given wavelength. Once M_A/M_D is determined, one possibility is to set $M_D = 1$. This maneuver would scale the relative binding affinities by an arbitrary scale factor. For our FRET setup, the M_A/M_D value was found to be 0.440. M_A and M_D can also be calculated based on the optical properties of the imaging system (**Fig. 2**).

The strategy for theoretical computation of M_A and M_D is outlined in **Supplementary Note 1** and **Supplementary Data 1**.

Calculation of binding curves. FRET efficiency measurements from many individual cells are collectively analyzed to deduce binding curves. The stochasticity in the expression of CFP- and YFP-tagged proteins among different cells allows for high variability in free donor and acceptor concentrations, yielding a saturating relationship for the apparent 3^3-FRET and E-FRET efficiencies. Accordingly, either E_A is plotted as a function of free donor concentration (D_{free}) or E_D is plotted as a function of free acceptor concentration (A_{free}). Both D_{free} and A_{free} are computed based on estimates of CFP and YFP concentrations (CFP_{EST} and YFP_{EST}, respectively) and by imposing a simple binding model on the entire data set. For a 1:1 binding interaction, the two curves should yield identical maximal efficiencies (E_{max} values) and relative binding affinities ($K_{d,EFF}$ values). The maximal FRET efficiency (obtained with either $D_b = 1$ or $A_b = 1$) reflects the overall spatial arrangement of the CFP and YFP molecules in the complex.

Procedurally for each individual cell, 3^3-FRET (E_A) and E-FRET (E_D) efficiencies are computed based on equations (6 and 7), respectively. YFP_{EST} and CFP_{EST} are determined using equations (10 and 12), respectively. The data from many cells are then fit iteratively using a nonlinear least-squares procedure that computes D_{free} and A_{free} values for each individual cell based on a simple Langmuir binding isotherm with the dissociation constant $K_{d,EFF}$. The equations used in this fitting procedure are provided in **Box 2**. Both D_{free} and A_{free}, the independent variables of the FRET two-hybrid binding curves, are computed based on the relative dissociation constant $K_{d,EFF}$, CFP_{EST} and YFP_{EST}, and requires an iterative nonlinear least-squares fitting procedure, as described in **Box 2** (equations (10,12,15–23)). Typically, fluorescence measurements from 20 to 30 cells are used to obtain an evenly sampled 'complete' binding relation. Once a fit is obtained, E_A and E_D are plotted against D_{free} and A_{free}, respectively. The maximal FRET efficiencies (E_{max} values), the saturating portion of the Langmuir relation, can often be estimated independently of the iterative fitting procedure. In general, $E_{A,max}$ (the maximal E_A value) and $E_{D,max}$ (the maximal E_D value) can be constrained to be between 0 and 1. Similarly, $K_{d,EFF}$ cannot be negative, and the practical upper limit is influenced by other factors (e.g., collisional FRET). These considerations provide constraints to obtain robust fits for both 3^3-FRET and E-FRET. **Figure 6** shows an example FRET two-hybrid binding curve.

Determination of spurious FRET. One additional confounding factor to consider when evaluating binding interactions using the FRET two-hybrid assay is the possibility of spurious FRET. When fluorophores are present at high bulk concentrations, a donor and an acceptor may be within the Förster distance by random chance and would undergo FRET even in the absence of a genuine underlying binding interaction. Accordingly, to obtain reliable 3^3-FRET or E-FRET binding curves, the contribution of spurious FRET must be subtracted. Unlike with binding interactions, spurious 3^3-FRET and E-FRET efficiencies are linearly proportional to the concentration of donors and acceptors, respectively. As the total fluorescence intensity from a single cell is proportional to the total number of CFP or YFP molecules in the cell, the magnitude

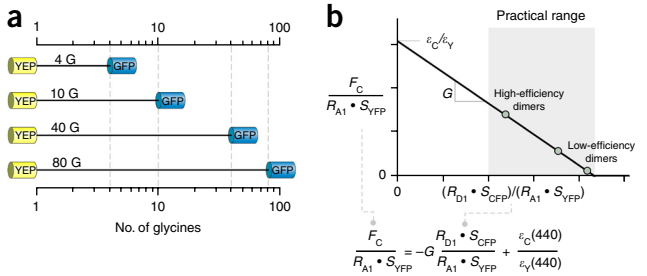

Figure 5 | Calibration experiments using cells expressing CFP–YFP dimers of high, intermediate and low FRET efficiency. (**a**) Schematic representation of individual dimers in which CFP and YFP are linked by a defined number of glycines (G), resulting in different FRET efficiencies. (**b**) For each dimer, $F_C/(R_{A1} \cdot S_{YFP})$ coordinates and $(R_{D1} \cdot S_{CFP})/(R_{A1} \cdot S_{YFP})$ coordinates are calculated and then plotted onto the graph. A higher FRET efficiency corresponds to higher donor quenching and a lower S_{CFP} values. Therefore, high-FRET-efficiency dimers are localized more to the left on the *x* axis with respect to lower-FRET-efficiency dimers. Similarly, a higher FRET efficiency implies higher sensitized emission. Therefore, high-FRET-efficiency dimers are localized more to higher values of the *y* axis with respect to lower-FRET-efficiency dimers. The gray area on the graph indicates the predicted range of possible FRET efficiencies, which is usually <40%. The graph is fit by a straight line. The slope of the line is $-G$ and the *y* intercept yields the excitation ratio of CFP and YFP: $\varepsilon_{CFP}(436)/\varepsilon_{YFP}(436)$.

of spurious FRET by the 3^3-FRET and E-FRET methods can be related to the measured CFP and YFP fluorescence intensity by the following equations[11]:

$$E_{A,spurious} = \frac{2}{3}\pi^2 \cdot R_0^3 \cdot 10^{-27} \cdot D = \frac{2}{3}\frac{\pi^2 \cdot R_0^3 \cdot 10^{-27}}{V_{cell}} \cdot \frac{R_{D1} S_{CFP}}{M_D} = m_{3^3\text{-FRET}} \cdot S_{CFP} \quad (24)$$

$$E_{D,spurious} = \frac{2}{3}\pi^2 \cdot R_0^3 \cdot 10^{-27} \cdot A = \frac{2}{3}\frac{\pi^2 \cdot R_0^3 \cdot 10^{-27}}{V_{cell}} \cdot \frac{R_{A1} S_{YFP}}{M_A} = m_{\text{E-FRET}} \cdot S_{CFP} \quad (25)$$

Here, R_0 corresponds to the Förster distance, V_{cell} is the volume of the cell, R_{D1} and R_{A1} are spectral factors and M_D and M_A are the calibration constants defined earlier. As CFP and YFP share a similar structure, the slopes of the two spurious FRET relations are related,

$$m_{\text{E-FRET}} = \frac{R_{A1}}{R_{D1}}\frac{M_D}{M_A} m_{3^3\text{-FRET}} \quad (26)$$

Empirically, spurious FRET can be obtained through fluorescence measurements from roughly 10–15 cells coexpressing untagged CFP and YFP molecules. As monomeric fluorescent proteins are typically used, the FRET efficiencies obtained correspond to spurious FRET and not to an underlying binding reaction. The 3^3-FRET efficiencies obtained are subsequently plotted against the CFP intensity, whereas the corresponding E-FRET efficiencies are plotted against the YFP intensities, and the respective slopes are estimated. Once the two relations are obtained, the FRET efficiencies obtained from each cell with the interacting

Box 2 | Determination of FRET binding curves

For a simple one-step bimolecular binding interaction with 1:1 stoichiometry,

$$D + A \underset{d,EFF}{\rightleftharpoons} DA$$

the experimentally measured apparent 3^3-FRET (E_A) and E-FRET (E_D) efficiencies must relate to the free concentrations of donors (D_{free}) and acceptors (A_{free}) by Langmuir isotherms:

$$E_A = E_{max} \cdot A_b = E_{max} \cdot \frac{D_{free}}{D_{free} + K_{d,EFF}} \quad (15)$$

$$E_D = E_{max} \cdot D_b = E_{max} \cdot \frac{A_{free}}{A_{free} + K_{d,EFF}} \quad (16)$$

For any given cell, the total number of YFP molecules is related to the YFP intensity through the YFP cube and is given by

$$YFP_{EST} = \frac{R_{A1} \cdot S_{YFP}(DA, 500, 535)}{M_A} \quad (10)$$

Note that M_A is a microscope-specific calibration constant. Similarly, the total number of CFP molecules in a given cell is related to the CFP intensity measured through the CFP cube and is given by

$$CFP_{EST} = \frac{R_{D1} \cdot S_{CFP}(DA, 436, 480)}{(1 - E_D) \cdot M_D} \quad (12)$$

To construct FRET two-hybrid binding curves, guessed E_{max} and $K_{d,EFF}$ values are initially used to estimate D_{free} and A_{free} concentrations for each individual cell, given the total YFP_{EST} and CFP_{EST} concentrations determined by the following equations:

$$D_{free} = \frac{CFP_{EST} - K_{d,EFF} - YFP_{EST} + \sqrt{(CFP_{EST} - K_{d,EFF} - YFP_{EST})^2 + 4 \cdot K_{d,EFF} \cdot YFP_{EST}}}{2} \quad (17)$$

Once D_{free} is estimated, A_{free} can be computed as

$$A_{free} = YFP_{EST} - (CFP_{EST} - D_{free}) \quad (18)$$

Alternatively, a symmetric formula for A_{free} based on equation (16) can be derived as follows:

$$A_{free} = \frac{YFP_{EST} - K_{d,EFF} - CFP_{EST} + \sqrt{(YFP_{EST} - K_{d,EFF} - CFP_{EST})^2 + 4 \cdot K_{d,EFF} \cdot CFP_{EST}}}{2} \quad (19)$$

The bound fraction of donor and acceptor molecules can be computed as follows:

$$D_b = 1 - D_{free} / CFP_{EST} \quad (20)$$

$$A_b = 1 - A_{free} / YFP_{EST} \quad (21)$$

Subsequently, predicted $E_{A,pred}$ and $E_{D,pred}$ values are determined for each cell by substituting computed D_{free} and A_{free} estimates with the guessed $K_{d,EFF}$ and E_{max} values into equations (14 and 15). Both E_{max} and $K_{d,EFF}$ are then iteratively optimized to simultaneously minimize the error in predicted E_A or E_D versus experimentally determined E_A or E_D for each cell i by a least-squares criteria:

$$\min_{K_{d,EFF},\, E_{max}} \sum_i (E^i_{A,pred} - E^i_A)^2 \quad (22)$$

$$\min_{K_{d,EFF},\, E_{max}} \sum_i (E^i_{D,pred} - E^i_D)^2 \quad (23)$$

Notice that the D_{free} and A_{free} values for each cell are recomputed after each iteration. Derivations for all equations are given in **Supplementary Text 2** and **3**.

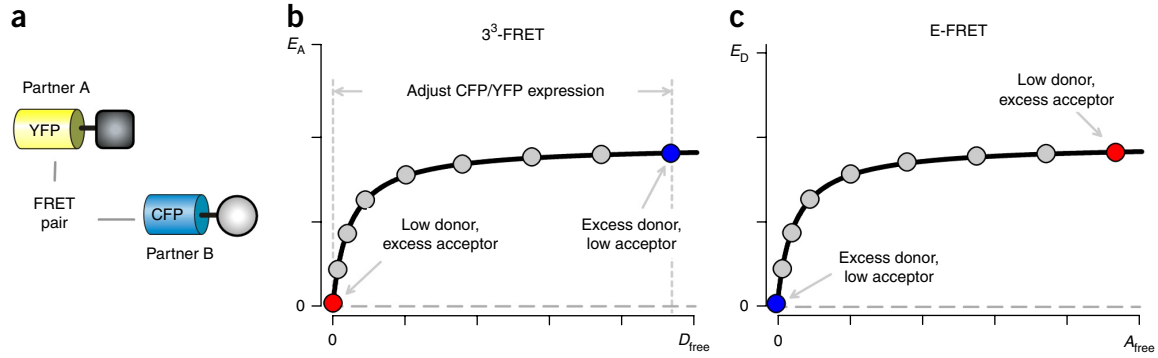

Figure 6 | Conceptual graph of FRET binding curves. (**a**) Diagram depicts hypothetical FRET binding partners A and B, tagged with YFP and CFP, respectively. Both molecules are coexpressed in single cells. (**b**) 3^3-FRET efficiency (E_A) values measured from single cells were plotted versus D_{free}, the concentration of free donor molecules (CFP—B molecules), to form a binding isotherm. The relative expression of CFP and YFP molecules in a cell is adjusted to attain a broad range of free donor concentrations. Cells with excess donor molecules will fall on the plateau of the isotherm. (**c**) E-FRET efficiency values (E_D) for single cells plotted versus A_{free}, the free concentration of acceptor molecules (YFP—A), also form a binding isotherm. Note that the point located at low D_{free} in panel **b** (red circle) corresponds to the point located at high A_{free} in panel **c**. Likewise, the point located at high D_{free} in panel **b** (blue circle) corresponds to the point located at low A_{free} in panel **c**.

pair of CFP- and YFP-tagged molecules is corrected for spurious FRET by the following equations:

$$E^i_{\mathrm{A,corrected}} = E^i_{\mathrm{A}} - m_{3^3\mathrm{-FRET}} \cdot S_{\mathrm{CFP}} \quad (27)$$

$$E^i_{\mathrm{D,corrected}} = E^i_{\mathrm{D}} - m_{\mathrm{E-FRET}} \cdot S_{\mathrm{YFP}} \quad (28)$$

One important consideration pertains to studying FRET between molecules residing in a restricted volume in certain subcellular localizations such as the plasma membrane. For such proteins, the slope of the spurious FRET relation can be unusually high, as the effective volume in the given compartment is smaller. One strategy for quantifying the magnitude of spurious FRET between proteins in such subcellular compartments is to localize CFP and YFP to these environments through appropriate targeting sequences. Importantly, FRET binding assays are suitable for studying the interaction of cytosolic binding partners with plasma membrane proteins such as voltage-gated Ca^{2+} channels[9,14]. For such experiments, a transmembrane binding partner such as the $Ca_V1.3$ pore-forming α-subunit is fused to YFP, and a cytosolic partner such as CaM is fused to CFP (ref. 14). Experimentally, the slope of the spurious FRET curve can be estimated by coexpressing CFP- or YFP-tagged membrane proteins with freely diffusing YFP or CFP. Practically, given this arrangement, the slope of the spurious FRET curve is quite similar to that obtained when CFP and YFP are freely diffusing entities[14] (**Supplementary Note 4**). Finally, for the interaction of two membrane-localized proteins, an important consideration is the relative size of the binding partners. As many transmembrane proteins, such as ion channels, are large in size, the tagged fluorophores tend to be further apart and less likely to interact by chance, resulting in low spurious FRET.

Estimation of FRET distance. The maximum FRET efficiencies for a given CFP–YFP dimer pair depend on a variety of factors, including the distance between the CFP and YFP molecules, an orientational factor (κ^2) and spectral overlap between the donor emission and acceptor excitation. FRET efficiency between a donor and an acceptor molecule is given by

$$E = \frac{1}{1+\left(\frac{R}{R_0}\right)^6} \quad (29)$$

where R is the distance of separation between the CFP and YFP molecules, and R_0 is the Förster distance where $E = 0.5$. Often, the two fluorophores are assumed to be randomly oriented with respect to each other, allowing for theoretical estimation of R_0 = 4.9 nm for a CFP–YFP pair. Thus, the approximate molecular distance between the donor and acceptor is

$$\Rightarrow R = R_0 \sqrt[6]{\left(\frac{1-E}{E}\right)} \quad (30)$$

For example, a FRET efficiency of 0.15 corresponds to a molecular distance of 6.5 nm between CFP and YFP. Maximal FRET efficiencies range between 0.10 and 0.40 for fluorescent proteins as the β-barrel structure impedes close apposition of the two fluorophores[15,16].

Overview of the procedure

An overview of the experimental design of the FRET assay is outlined in **Figures 7** and **8**. The first section of the protocol outlines the setup and calibration of the FRET microscope, including software customization for data acquisition (Steps 1–21), construction of a high-voltage-gain lookup table (HV-LUT; Steps 22–41) and other cell-based calibration measurements to ensure stable and reliable acquisition of FRET data (Steps 42–48). In the second section, we describe the steps for conducting routine FRET two-hybrid assays, including all control measurements (**Fig. 8**, Steps 100–128). A custom analysis sheet is provided, along with a detailed workflow for data analysis.

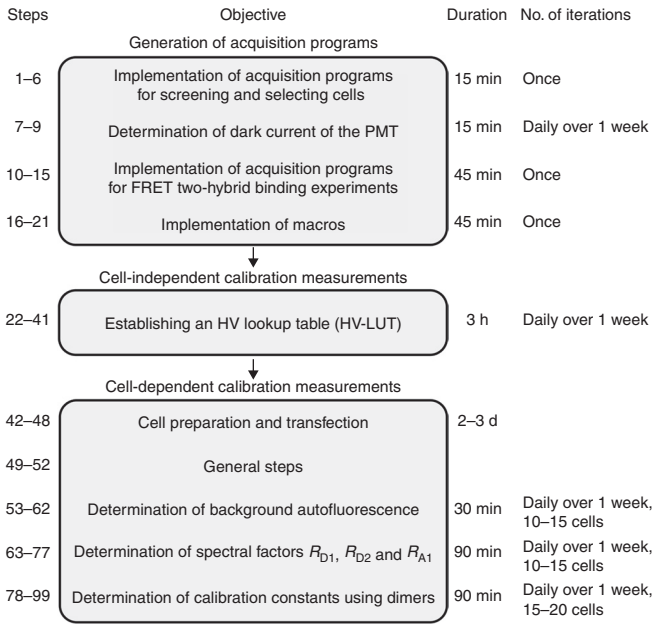

Figure 7 | Overview of the calibration phase of the FRET rig. Outline of the workflow for reliable calibration of the FRET rig. There are three major phases—generation of acquisition programs, cell-independent calibration measurements and cell-dependent calibration measurements.

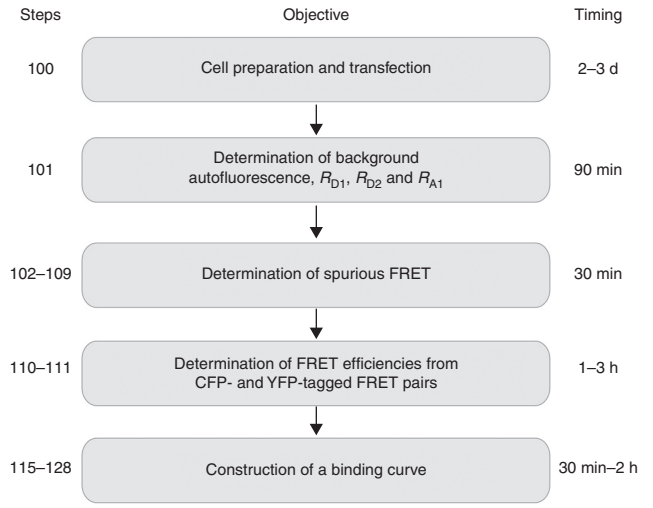

Figure 8 | Overview of a FRET two-hybrid binding experiment. Summary of steps required for conducting a single FRET two-hybrid experiment, along with the approximate timing for each step.

Software implementation. During the setup phase of the FRET rig, acquisition programs for obtaining fluorescence measurements are first configured. A typical experiment initiates with a visual screen for cells that are suitable for measurement. To select cells, two programs are required—(i) continuous excitation of CFP and (ii) continuous excitation of YFP. The actual FRET measurements are then performed using the CFP, FRET and YFP cubes with a brief excitation pulse. Two distinct excitation programs are required—(i) excitation using 436-nm-wavelength light for the CFP and FRET cubes and (ii) excitation using 500-nm-wavelength light for the YFP cube. Macros are defined that sequentially call the programs for the CFP, FRET and YFP cubes and store the acquired signals in a data file. All acquisition programs require subtraction of dark current.

Construction of an HV-LUT. One advantage of a photomultiplier tube (PMT) in fluorescence measurements is its ability to quantify intensities with high sensitivity and low noise over a broad range by controlling the high voltage set on the dynode. For FRET experiments, the donor and acceptor molecules are expressed at varying levels and require the use of multiple HV gains to detect fluorescence over a wide range. The light intensity reported by the photomultiplier detection system (PMT) follows a power-law relation with the HV gain. A lookup table is determined for a given microscope setup over limited HV gains used in FRET experiments. To construct an HV-LUT, we measure the fluorescence intensity of synthetic dyes mimicking spectral properties of CFP and YFP at different dilutions at predetermined HV gains. A standard HV gain is then chosen and the fluorescence intensities are normalized to the intensity at the standard HV gain. This procedure is performed during the setup phase of the FRET rig.

Cell-dependent calibration measurements. Both calibration constants (the G factor and the ratio of extinction coefficients) and spectral factors (R_{A1} and R_{D1}) differ for a given imaging setup by choice of fluorophores. These values have to be determined during the calibration phase of the setup from cells expressing CFP–YFP dimers, and donors or acceptors individually. Stability of all constants must be ascertained.

FRET two-hybrid binding experiments. Once the setup has been calibrated, robust FRET data can be obtained. For actual FRET experiments, six different cell samples are prepared that need to be measured on the day of the experiment: (i) nontransfected cells, for the determination of the background autofluorescence; (ii) cells expressing CFP alone, for the determination of the spectral factors R_{D1} and R_{D2}; (iii) cells expressing YFP alone, for the determination of the spectral factor R_{A1}; (iv) the CFP–YFP dimer, as a positive control; (v) cells expressing untagged CFP along with YFP, to determine spurious FRET; and (vi) cells expressing donor-tagged and acceptor-tagged binding pairs, for the actual FRET measurement. Background autofluorescence results from cell metabolites and weakly fluorescent amino acids. This value must to be subtracted for each of the three cubes (CFP, YFP and FRET cubes). Typically, the autofluorescence is <5% of the total signal through the cubes. The spectral ratios R_{A1}, R_{D1} and R_{D2} are determined before each FRET experiment from cells expressing YFP or CFP only. As a positive control, FRET efficiency is evaluated for a CFP–YFP dimer pair to evaluate daily performance of the microscope. Finally, spurious FRET and FRET efficiencies for the desired CFP- and YFP-tagged binding pairs are measured.

Workflow of data analysis. For data analysis, we provide a MATLAB script, which converts FelixGX data output to an input format suitable for Excel spreadsheets (**Supplementary Data 2**). In addition, a template Excel sheet is available (**Supplementary Data 3**). Alternatively, the analysis can be performed using software packages such as Origin or MATLAB. Once the raw data are acquired and filled in on the template Excel sheet, most of

the analysis is performed automatically, as the worksheets and relevant cells are linked with each other. The dimer analysis sheet calculates the *G* factor, the M_A/M_D ratio and the ratio of extinction coefficients. For the actual fitting procedure, points are calculated for each dimer, averaged across cells for each dimer and plotted on the graph. A least-squares linear fit is obtained by adjusting slope and *y* intercept. The sheet for the FRET two-hybrid binding data subtracts background signals and deposits the corrected signals in the binding curve sheet. This sheet calculates all FRET parameters with and without correction for spurious FRET, and it graphically displays binding curves for E_A versus D_{free} and E_D versus A_{free}. Finally, nonlinear curve fitting is performed in order to obtain the binding curves defined by the E_{max} and $K_{d,EFF}$ values.

Applications of the assay and target audience

The method is of interest to researchers characterizing protein–protein interactions within living cells, wherein such interactions correspond to cellular signaling events. As FRET efficiencies are obtained nondestructively, this methodology can be applied to quantitatively monitor both dynamic and steady-state aspects of binding interactions. FRET-based assays have been used to study a wide range of biological molecules, including ion channels, G-protein-coupled receptors, immunoglobulins and cytosolic enzymes such as protein kinase A and Ca^{2+}/calmodulin-dependent kinase II, as well as numerous other enzymes and receptors[9,17–19]. This methodology has been applied extensively to study the binding of voltage-gated Ca^{2+} channel holomolecules or subsegments with various channel-interacting proteins such as calmodulin[9,10,20,21], the auxiliary $Ca_V\beta$ subunit[22], G proteins[23,24] and members of the small GTPase family[25,26]. In addition, the comparative ease of obtaining relative binding affinities using the FRET two-hybrid assay has enabled systematic characterization of mutational effects on a binding interface such as the CaM-binding segment of the $Ca_V1.3$ channel[20,21]. FRET binding assays are also well suited for studying binding of molecules in distinct subcellular localizations such as the interaction between STIM1 in the ER membrane and Orai1 channel in the plasma membrane[27,28].

Advantages of the assay

This method has several advantages as compared with alternative FRET approaches. It is possible to quantitatively describe protein–protein interactions in living cells with binding curves from which relative affinities can be derived. Furthermore, the assay is robust because two independent metrics for FRET efficiencies (donor-centric and acceptor-centric) are determined and correlated. Molecular FRET distances can be calculated based on maximal FRET. Unlike acceptor photobleaching, the assay is completely nondestructive[9,13]. The specificity of the calculated FRET efficiencies is high, as spurious FRET is measured and subtracted from total binding curves[11,21]. Any cell type, such as cultured cells or primary cells, can be used[25,29–32]. These cells can be transfected by standard transfection or viral gene transfer[25]. Finally, this method can be readily translated to a dynamic FRET assay[28,33].

Technologically, one important advantage is that the approach can be highly automated and data acquisition and analysis is fast[34]. In principle, a single binding curve can be obtained within an hour, excluding time required for cell culture. Furthermore, the method exploits relatively inexpensive and widely accessible equipment, and therefore can be easily implemented. Minimally, a simple wide-field epifluorescence microscope including a motorized filter wheel, an excitation system composed of an optically stabilized xenon arc lamp, and a detection system consisting of a PMT and housing is sufficient.

TABLE 2 | Plasmids for FRET analysis.

Name	Description	Catalog number
ECFP	Untagged donor for spectral factors	84951
EYFP	Untagged acceptor for spectral factors	84952
YFP–G_4–CFP	Dimer for calibration	84953
YFP–G_{10}–CFP	Dimer for calibration	84954
YFP–G_{40}–CFP	Dimer for calibration	84955
YFP–G_{80}–CFP	Dimer for calibration	84956
ECFP–CaM_{WT}	Donor-tagged binding partner	84957
EYFP–Myosin Va IQ	Acceptor-tagged binding partner	84959
EYFP–$Ca_V1.2$ IQ	Acceptor-tagged binding partner	84958

Limitations of the assay

One disadvantage of the PMT-based system for determining FRET efficiencies is the lack of subcellular spatial resolution. For certain applications, determining spatial variation in FRET may lend important insights into biological function. This limitation can be overcome by using either a camera-based or a confocal imaging system. Such applications may require further calibration measurements to account for chromatic and spherical aberration of the objective and may require additional lookup tables to account for detector gains (e.g., for charge-coupled device (CCD) cameras). For confocal imaging, stability of optical parts and fluctuations of laser power may pose substantial challenges[35]. Confocal imaging setups may also be expensive. This approach is also less suited to high-throughput experiments. However, the method could potentially be implemented using a flow-cytometry-based system[34,36]. In addition, the current approach is not well suited to extremely fast and highly dynamic processes, as the time required to switch filter cubes can be hundreds of milliseconds. Faster imaging could be attained using multiple PMT detectors and filter wheels. Moreover, as changes in binding would alter only fluorescence measurements from the CFP and FRET cubes, only these measurements need to be obtained simultaneously and rapidly. Over a very short period of time, the changes in direct YFP fluorescence would be negligible. Thus, the protocol described here can be adapted to study fast time-scale events. Finally, the protocol assumes a single-step binding interaction with a 1:1 stoichiometry for determining relative dissociation constants. These constants could be experimentally ascertained if the maximal 3^3-FRET and E-FRET efficiencies are identical[37].

Comparison with alternative approaches

There are numerous methods available for detecting FRET efficiencies from biological systems that are suitable to a variety of applications[2]. Acceptor photobleaching or donor dequenching is a classic and widely used technique that measures the fractional enhancement in donor fluorescence upon photodestruction of the associated acceptor molecule. As such, this intensity-based technique does not require any instrument-specific calibration constants. Although simple to perform, this technique is destructive and is substantially more time-consuming. A second method of obtaining FRET efficiencies quantitatively is fluorescence lifetime imaging microscopy[38]. This technique measures changes in the fluorescence lifetime of donor molecules to infer FRET in a spatially resolved manner. Lifetime measurements can be attained using either a time-resolved fluorescence response to a brief pulse of light or through frequency domain measurements[39]. Moreover, it can be used in conjunction with multiphoton excitation to further enhance spatial resolution and sensitivity[39,40]. The use of multiphoton excitation could make this technique suitable to *in vivo* applications[40]. Although powerful for studying biological systems, one disadvantage is that this method requires expensive equipment that may preclude its widespread application[39]. In addition, many fluorescent proteins exhibit multiexponential fluorescence decays and may therefore confound accurate detection of fluorescence lifetimes[39]. Moreover, the concentration of acceptor molecules is generally not considered, and therefore this method is not typically used to quantitatively characterize the strength of binding interactions.

A key confounding factor in intensity-based measurements of FRET is the possibility of spectral cross talk as a consequence of the broad excitation and emission spectrum observed for typical fluorescent proteins. Spectral FRET measures the known spectrum of donor and acceptor molecules to unmix these confounding factors and estimate FRET efficiency by determining the full spectrum of the donor[41–44]. However, such measurements will also require expensive equipment to characterize fluorescence signals across a large spectrum.

Binding curves have been measured using approaches similar to the 3^3-FRET method described here[45–48]. First, plotting apparent acceptor-centric FRET efficiencies as a function of the ratio of CFP and YFP fluorescence intensity yields a saturating relationship that can be analyzed to determine changes in conformation or relative affinity[45,46]. A similar approach can be used to relate donor-centric FRET efficiencies as a function of the ratio of the number of YFP molecules to the number of CFP molecules in a cell by a saturating Langmuir relation[47]. However, the fitting constant in this method does not correspond to dissociation constants[47]. Moreover, this method also requires fluorescence lifetime imaging microscopy measurements for calibration[47,49]. Finally, the E-FRET (donor-centric) efficiencies can be correlated with the free concentration of acceptors to obtain a relative dissociation constant[48]. In all cases, a 1:1 binding stoichiometry is assumed.

Experimental design

Robust quantitative determination of FRET requires a well-calibrated microscope setup, a stable excitation source and a linear detection system, as described in the following section.

Setting up and calibrating the FRET rig. During the initial setup of the FRET rig, identical measurements required for routine FRET experiments (**Figs. 7** and **8**) are performed, generating large data sets from which the HV-LUT, the spectral factors and the FRET efficiency calibration constants are determined. The stability of these constants is confirmed over a period of a week. Large fluctuations in these constants will result in mis-estimation of FRET efficiency, adding to noise in FRET binding assays and often leading to irreproducible results.

Stability of the excitation light source. As FRET two-hybrid assay uses corrected total fluorescence output to estimate the concentrations of donors and acceptors, instability in the excitation source may lead to variable reporting of relative binding affinities. Commonly, xenon arc lamps are used for exciting fluorophores. An intrinsic problem of arc-lamp-based excitation systems is the short-term fluctuations of fluorescence output. Therefore, it is helpful to use xenon lamps equipped with a computer-controlled optical feedback system. Ideally, the feedback system measures lamp intensity output and adjusts any short-term fluctuations via a servo-controlled feedback system by regulating the power supply. Such systems are available from Newport (Oriel Research Xenon arc lamp (cat. no. 66477-150XF-R1) plus Light Intensity Controller LIK-LMP). Alternatively, a monochromator system that is driven by a stabilized power supply can be used in order to minimize intensity fluctuations. Furthermore, LED-based systems with or without optical feedback stabilization or temperature control are also available. Irrespective of the system used, excitation intensity output should be set to the low or middle dynamic range to minimize photobleaching. If necessary, neutral-density filters or optical grids (fluorescence intensity manager for Leica microscopes) can be used to reduce excitation intensity. We use a 150 W xenon arc lamp with slit widths of the monochromator output adjusted to 5 nm.

Stability of the emission light detector. Instability in the emission detector may also contribute to mis-estimation of total donors and acceptors, resulting in unreliable reporting of relative binding affinity. We use a PMT-based detection system. The advantage of the PMT is that the detection gain can be controlled over a wide range by changing the high voltage. Certain photodiode-based systems have a limited detection range and may necessitate further optimization. Another advantage of the photomultiplier system is that HV gain can be controlled by the software, which allows for very fast and automated data acquisition. CCD camera systems, which are also equipped with a gain control, are suitable for quantitative FRET experiments and require calibrations similar to those of PMT-based systems. However, FRET experiments using camera-based setups are more complex, as chromatic aberration may result in spatially varying spectral ratios[35].

Linear response of the emission light detector. Our FRET-based binding assay relies on robust determination of the number of donor and acceptor fluorophores in a given cell. It is therefore critical that fluorescence intensity measured using the PMT be linearly dependent on the concentration of fluorophores. In some cases, PMT detectors have been shown to respond nonlinearly to the intensity of the incident light[44,50,51], although some nonlinearities could be corrected[50]. Therefore, we confirmed a linear relation between the fluorescence intensity measured using the PMT and the concentration of fluorophores determined

by characterizing the fluorescence output of droplets of the synthetic dyes Alexa Fluor 514 and Proflavin, which mimic the spectral properties of YFP and CFP, respectively[35]. Indeed, the net fluorescence intensity was linearly dependent on the concentrations of Alexa Fluor 514 (**Supplementary Fig. 1a**) and Proflavin (**Supplementary Fig. 1b**). These results suggest that fluorescence intensity measured using our PMT setup is linearly proportional to the number of fluorophores in a cell.

MATERIALS

REAGENTS

- Sodium chloride (NaCl; VWR, cat. no. 27810)
- Potassium chloride (KCl; Carl Roth, cat. no. 6781)
- Magnesium chloride hexahydrate ($MgCl_2 \cdot 6H_2O$; Carl Roth, cat. no. 2189)
- Calcium chloride dihydrate ($CaCl_2 \cdot 2H_2O$; VWR, cat. no. 22317)
- Glucose monohydrate (Carl Roth, cat. no. 6887)
- HEPES (Sigma-Aldrich, cat. no. H3375)
- Sodium hydroxide (NaOH; VWR, 28244) **! CAUTION** Sodium hydroxide is a corrosive alkali. Wear protective gear while handling to avoid contact with skin and eyes.
- Poly-L-lysine hydrobromide (Sigma-Aldrich, cat. no. P2636)
- Polyethylenimine (PEI; Polysciences, cat. no. 23966-2)
- Cell sample of choice; here, we use the example of HEK293 cells (DSMZ, cat. no. ACC 305) **! CAUTION** For cell lines used in your research, it is essential to ensure that the cells are authentic and free from contamination such as mycoplasma.
- DMEM (low glucose) (Gibco, cat. no. 21885)
- FBS (Biochrom, cat. no. S 0615)
- Penicillin/streptomycin (P/S; Biochrom, cat. no. A2212)
- Alexa Fluor 514 succinimidyl ester (Molecular Probes, cat. no. A3-0002)
- Proflavin hemisulfate salt hydrate (Sigma-Aldrich, cat. no. P2508) **! CAUTION** Proflavin is toxic and an irritant. Wear appropriate eye shields and gloves when handling this compound.
- Plasmid constructs (see **Table 2**); all plasmids used in the PROCEDURE are available from Addgene (http://www.addgene.org)

EQUIPMENT

- Microtubes, 1.5 ml (e.g., Sarstedt, cat. no. 72.690.001)
- Glass-bottom dishes, 35 mm (In Vitro Scientific, cat. no. D35-20-1.5-N). **▲ CRITICAL** Cell culture dishes with glass bottoms are recommended for imaging. The glass bottom is optimized for minimal autofluorescence. For complete adherence of cells, it is recommended to coat dishes with poly-L-lysine (PLL; see Equipment Setup).
- Inverted fluorescence microscope (Leica, cat. no. DMI6000B)
- HC PL APO 40×/1.3 oil-immersion objective (Leica, cat. no. 11506329)
- CFP-filter cube, excitation: ET436/20×, dichroic: T455lp, emission: ET480/40 m, transmission rate 93–97% (Chroma Technology, cat. no. 49001)
- YFP-filter cube, excitation: ET500/20×, dichroic: T515lp, emission: ET535/30 m, transmission rate 93–97% (Chroma Technology, cat. no. 49003)
- FRET-filter-cube, excitation: ET436/20×, dichroic: T455lp, emission: ET535/30 m, transmission rate 93–97% (Chroma Technology, cat. no. 49052)
- DeltaRamX (Horiba)
- Xenon short arc lamp type (Ushio, model no. UXL-75XE)
- C-mount adaptor (specific for Leica microscope type)
- Microscope photometer (Horiba, model no. D-104 B)
- PMT housing (Horiba, model no. 914)
- PMT (Horiba, model no. R1527)
- FelixGX v4.3.6904 (Horiba)
- Excel 2013 (Microsoft Corporation)
- MATLAB vR2014b (MathWorks)

REAGENT SETUP

FRET imaging buffer For typical FRET two-hybrid assays, a bath (Tyrode's solution, containing 140 mM NaCl, 5 mM KCl, 1 mM $MgCl_2$, 2 mM $CaCl_2$, 10 mM glucose and 10 mM HEPES in ddH_2O) is used. Adjust the pH to 7.4 with 5 M NaOH. Prepare aliquots and store them at −20 °C for up to 1 year. Thawed aliquots can be stored at 4 °C for up to 1 week.

HEPES buffer Dissolve 2.38 g of HEPES in 1 liter of ddH_2O to attain a final concentration of 10 mM, and adjust the pH to 7.0 with 5 M NaOH. The buffer can be stored at 4 °C for up to 1 year.

Alexa Fluor 514 dye (1 mg/ml) Dissolve 1 mg in 1 ml of HEPES buffer and incubate the mixture overnight at room temperature (22 °C). The stock solution may be stored at 4 °C and is stable for several months. Prepare dilutions on the day of use with HEPES buffer. **▲ CRITICAL** It is important to protect this solution from light to prevent photobleaching.

Proflavin dye (100 mg/ml) Mix a total of 100 mg with 1 ml of HEPES buffer, and vortex and centrifuge the mixture for 1 min at 10,000*g* at room temperature to remove undissolved particles. This stock solution can be stored at 4 °C and is stable for several months. Prepare all dilutions freshly with HEPES buffer on the day of use. **▲ CRITICAL** It is important to protect this solution from light to prevent photobleaching.

Growth medium Supplement 450 ml of DMEM low-glucose medium with 50 ml of heat-inactivated FCS (10% (vol/vol) final) and 5 ml of P/S (1% (vol/vol) final). Store the medium at 4 °C for up to 4 weeks.

Transfection medium To 50 ml of unsupplemented DMEM low-glucose medium, add 250 µl of P/S (1% (vol/vol) final). Store the medium at 4 °C for up to 4 weeks.

Polyethylenimine transfection reagent Prepare 25 ml of a 1 mg/ml polyethylenimine (PEI) stock solution in endotoxin-free ddH_2O with pH adjusted to 7.0. Sterilize the solution using a 0.22-µm syringe filter, prepare aliquots and store them at −20 °C. A working stock can be stored at 4 °C for up to 4 weeks.

Poly-L-lysine stock (50 mg/ml) Dissolve 100 mg of PLL in 2 ml of ddH_2O for a poly-L-lysine (PLL) stock solution. The stock solution can be stored at 4 °C for up to 6 months.

EQUIPMENT SETUP

Preparation of imaging dishes Wash glass-bottom cell culture dishes with 80% (vol/vol) ethanol and let them dry completely. Coat each dish with 600 µl of 1:50,000 PLL dilution for 30 min at room temperature. Aspirate the PLL solution, wash twice with ddH_2O and allow the dishes to dry. Once dried, the dishes may be stored at room temperature for a few days.

Microscope Our measurements were obtained using a Leica DMI6000B inverted fluorescent microscope equipped with a motorized turret and a 40× objective (**Fig. 1**). The microscope is furnished with a motorized filter-wheel that enables rapid switching of filter cubes within 300 ms. If you are using filter cubes other than those listed in EQUIPMENT section, it is critical to ensure that the filter designs permit optimal transmission of desired optical signals.

Fluorescence excitation system We use a DeltaRamX monochromator containing a xenon short arc lamp (**Fig. 1**) for excitation. The excitation intensity of this light source can be adjusted by manually setting the slit control, which we typically set to 5 nm. For quantitative FRET microscopy, a stable excitation light source is essential. Arc-lamp-based excitation systems have the disadvantage of long-term decay in fluorescence output due to aging of the excitation lamp. To ensure long-term stability, the intensity of the lamp should be adjusted often to yield a target amount of YFP bleaching in a fixed time interval. For example, when the monochromator slits are opened to ~5 nm, the YFP bleaches to ~60% of initial intensity within 440 s. Repeat this measurement monthly and adjust the output of the xenon lamp, so that the reference value is reached. In practice, this adjustment can be attained by simply adjusting the slit width of the monochromator or by adjusting the power supply. Alternatively, excitation light intensity in the objective plane can be measured using a power intensity meter. The excitation light bulb needs to be replaced based on the lifetime of the light bulb used.

Fluorescence detection system The fluorescence intensity is detected by a PMT (Horiba) consisting of photometer housing and a PMT. In the analog mode, the PMT can operate at different HV gains, allowing for fluorescence measurement over a broad intensity range. The aperture can be adjusted by four aperture control knobs and, for the example used in PROCEDURE, is set to the size of a single HEK293 cell. A viewing scope enables control of

the aperture size and positioning of the relevant cell within the viewing area. Light beams arising from the sample can be directed to either the PMT or the eyepieces by toggling to the 'Measure' or 'View' position. To protect the PMT, the toggle is set to the 'Measure' position only when fluorescence signals are acquired.

Data acquisition and analysis We use FelixGX for signal acquisition and control of the monochromator and individual detector gains. Offline data analysis is performed with a custom-written MATLAB script and a customized Excel spreadsheet, which are provided as **Supplementary Data 2** and **3**, respectively. In principle, any commercially available image acquisition and data analysis software can be used. For automatization of the workflow, custom-written programs (e.g., with MATLAB) can be used to control all critical components of the system (e.g., light source, microscope, and filter cube turret).

PROCEDURE

Generation of acquisition programs for screening and selecting cells ● TIMING 15 min

▲ CRITICAL Steps 1–21 describe how to generate appropriate acquisition programs for FRET two-hybrid-binding assays using the FelixGX software. Alternatively, customized software (e.g., MATLAB) can be used to operate the monochromator. Independent of the data acquisition software used, key parameters such as the wavelength for excitation and emission, the duration of fluorescence recording and the sampling rate of data digitalization can be set as outlined here. Other parameters that are unique to the detection system or the excitation system may differ and will need to be specified according to the hardware used.

1| If you are using FelixGX for data acquisition, confirm that '914 default gain' is set to 950. This value is set incorrectly by the supplier and impedes the correct performance of the PMT. To set this value, start FelixGX and click the 'DeltaRamAnalog' tab (**Supplementary Fig. 2**) to open the hardware configuration window (**Supplementary Fig. 3a**). Set the parameter to 950. Then validate and close the window.

2| Create an acquisition program for continuous illumination of donor fluorescence (Steps 2–5). This program is suitable for screening and selecting fluorescent cells. In FelixGX, select the 'Setup' tab in the left lower corner of the main graphical user interface (**Supplementary Fig. 2**); this opens the 'Setup' window. The window has 10 tabs; choose the 'Acquisition Type' tab and select 'Timebased' (**Supplementary Fig. 3b**).

3| Select 'Acquisition Settings' from the 'Setup' window (**Supplementary Fig. 4a**) and specify the excitation wavelength for the CFP cube. The excitation wavelength needs to match the center wavelength of the individual excitation filter (e.g., 436 nm for CFP excitation). In the panel on the right side, set duration of the data acquisition to 600 s. The continuous illumination mode usually has an acquisition duration of 5–10 min. Set the sampling rate to 100 points per s and accept. All other settings can be left as default.

▲ CRITICAL STEP Users are encouraged to implement acquisition programs that match the properties of their given imaging setup. The sampling rate, acquisition duration and excitation wavelength may therefore be adjusted to yield good signals without inducing photobleaching.

4| Select 'PMTs' from the 'Setup' window (**Supplementary Fig. 4b**). Specify the gain voltage (e.g., 850 V) and accept. For screening of cells, it is convenient to use a standard HV gain of 850 V.

5| Save the program, e.g., as 'continuous CFP excitation'. This program will be invoked to screen for appropriate cells to collect FRET data and terminated after an appropriate cell is chosen. Note that the cells will never be exposed for the full acquisition duration, in order to avoid photobleaching effects.

6| Create an acquisition program for continuous illumination of acceptor fluorescence. Repeat Steps 2–5 and create a similar acquisition program for YFP illumination. Use the same settings, except for excitation wavelength, which should be set to match YFP excitation wavelength (e.g., 500 nm).

Determination of the dark current of the PMT ● TIMING 15 min

7| All specific programs require the dark current of the detector to be subtracted. To quantify the dark current, completely isolate the detector from incoming light by setting the photometer knob to 'View' (**Fig. 1**) and direct the light beam toward the oculars of the microscope. This blocks the light beam to the photometer and protects the PMT from saturation.

▲ CRITICAL STEP Daily measurements of dark current evaluate the stability of the detection pathway and are important during the setup phase of the FRET rig.

8| Place the CFP filter cube in the light beam. Start continuous CFP illumination (e.g., using the program set up in Steps 2–5) and record the signal for ~10 s.

9| Calculate the average signal of the trace acquired in Step 8. Using FelixGX, go to 'Math' → 'Trace Math' → 'Average' (**Supplementary Fig. 2**) and read out the value in the pop-up window. This value is the dark current of the PMT, which needs to be subtracted in all acquisition programs (Steps 12 and 13).

Generation of acquisition programs for FRET two-hybrid binding experiments ● TIMING 45 min

10| To conduct actual FRET measurements, create acquisition programs for the donor and acceptor using shorter acquisition durations (in the range of milliseconds to seconds). The pulse length needs to be adjusted so that it is long enough to have an optimal fluorescence signal without inducing photobleaching. To do this, repeat Steps 2 and 3 for excitation of CFP using the same settings, except for duration of acquisition, which should be set to 1 s (**Supplementary Fig. 4a**).

11| Set the gain voltage to '600', as described in Step 4.

12| Implement subtraction of dark current from the acquired signal, using the specific dark current value determined in Steps 7–9. In FelixGX, select 'Backgrounds' from the 'Setup' window (**Supplementary Fig. 4c**). Note that the term 'Background' used in this window refers to the dark current caused by spontaneous discharge of electrons by the PMT, whereas the term 'autofluorescence background' refers to fluorescence intensity of cells lacking fluorophores typically generated by cellular metabolites. The dark current signal defines the lower limit of the resolution of the detection system. To activate dark current subtraction, select 'Manual Input' and activate the option 'Use Background' by clicking the box and 'Accept'.

13| Select 'Traces' from the 'Setup' window (**Supplementary Fig. 4d**) and specify the dark current value obtained in Step 9 (−0.2957 mV, for our system). Specify a name for the acquisition program (e.g., 'CFP 600'), activate 'Visible Graph' by clicking the box and 'Accept'.

14| For the purpose of signal acquisition for binding curves, it is necessary to implement acquisition programs designated to detect signals with different detector gains. Usually, gains from 600 V to 1,150 V are in the operational range of the detector. Repeat Steps 10–13, but in Step 11 set the gain voltage to the desired value (e.g., '650'). Save the program with an appropriate name (e.g., 'CFP 650') and repeat this step for further HV gains. We recommend implementation of acquisition programs with intervals of 50 V. When this step has been successfully completed, 12 programs for specific HV gain will have been created.

15| Create analogous acquisition programs for YFP excitation by repeating Steps 10–14, but instead specify the excitation wavelength to be 500 nm for the YFP cube.

Generation of macros for FRET two-hybrid binding experiments ● TIMING 45 min

▲ **CRITICAL** Steps 16–21 describe how to use the FelixGX software to create separate macros for each HV gain (corresponding to 600–1150 V, in intervals of 50 V) using the acquisition programs created in Steps 10–15. Note that the acquisition protocol for donor excitation is suitable for fluorescence intensity readings using the CFP and FRET filter cubes, whereas the acquisition protocol for acceptor excitation is used to read signals using the YFP filter cube. An example macro sequence might be: donor excitation (CFP cube) → donor excitation (FRET cube) → acceptor excitation (YFP cube). Note that the HV gains used for donor excitation must be the same as those used for acceptor excitation.

16| On the main graphical user interface (**Supplementary Fig. 2**), select the 'Action' tab to open the 'Macro' window (**Supplementary Fig. 5**). Click the green '+' button in the upper left corner of the window to open the 'Macro Editor' window (**Supplementary Fig. 5a**).

17| To add a pause step to the macro, highlight 'Pause' from the list on the left side and click the 'Add' button (**Supplementary Fig. 5b**). This adds 'Pause [indefinite]' to the macro window (black panel) on the left side of the list. During an experiment, the pause point allows the appropriate filter cube to be brought into position.

18| Next, add the acquisition protocol for donor excitation at the first HV gain (e.g., 'CFP 600') to the macro by selecting 'Run Acquisition (existing)' from the list, and choosing the 'CFP 600' protocol from the pop-up list (**Supplementary Fig. 5c**).

19| Repeat Steps 17 and 18 to add pause steps and acquisition protocols for the FRET cube and the YFP cubes at HV gain of 600 V. Pause steps need to be added between each of the protocols for the three individual cubes and after the final acquisition protocol, as shown in **Supplementary Figure 5**, to allow switching of filter cubes when conducting a macro.

20| Save the macro with a name that specifies the HV gain—e.g., 'FRET 600'.

21| Repeat Steps 16–20 for all remaining gains. Once successfully completed, a total of 12 macros corresponding to each of the specific HV gains will have been created.

Establishment of an HV-LUT to normalize PMT gains ● TIMING 3 h daily over 1 week

22| Place an empty imaging dish on the microscope stage.

23| For background measurements, pipette 80 µl of HEPES buffer onto one edge of the empty dish.

24| Cover the dish with a lid in order to prevent rapid evaporation of the buffer.

25| Using bright-field illumination, navigate the objective to the border of the solution and focus. Subsequently, navigate toward the center of the solution and turn off bright-field illumination.

26| Direct the light beam to the PMT and obtain measurements using the 'FRET 600' macro. Repeat for all predetermined PMT HV gains. These measurements will give you 12 data points for each filter cube.

27| Rename the data set with a descriptive name and export as 'Export Group'. This creates a .txt file that can be read and converted to Excel-compatible data using the provided MATLB script (**Supplementary Data 2**).

28| Navigate to another region of the solution and repeat Steps 25–27 for at least 6–8 more spots of solution. Make sure to record several different positions in each dish.

29| Pipette 80 µl of a 1:10,000 dilution of Alexa Fluor 514 dye onto another edge of the imaging dish and ensure that the solutions remain well separated. Alternatively, a new imaging dish can be used.
▲ CRITICAL STEP Make sure that the dye solution is homogeneous and that no undissolved or contaminating particles reside in the light beam.

30| Collect fluorescence signals with all available gains, as described in Steps 25–27. Reject data if the fluorescence signal collected is beyond saturation of the PMT detector or if the signal-to-noise ratio is low.

31| Navigate carefully to another region of the dye solution, and repeat the measurement (as described in Step 30) for at least eight more regions.

32| Repeat Steps 29–31 using two more dilutions of the Alexa Fluor 514 dye—e.g. 1:2,000 and 1:50,000 dilutions. Using the three different dilutions, fluorescence signals will be obtained that cover a broad range of the PMT gains.
? TROUBLESHOOTING

33| Use a new imaging dish and repeat Steps 29–31 with 80 µl of Proflavin at a 1:10,000 dilution.

34| Collect data for 1:2,000 and 1:100,000 dilutions of Proflavin dye, as described in Steps 29–31. Again reject data by criteria set in Step 30.
? TROUBLESHOOTING

35| Export the data as 'Export Group'. For computation of the HV-LUT, read the exported data files derived from measurements of different dilutions of Proflavin and Alexa Fluor 514 dye and background measurements (Steps 27 and 35) using the provided MATLAB script (**Supplementary Data 2**), as described in Steps 36–41.

36| Subtract the background fluorescence from the dye measurements and use background-subtracted values for further calculations. The resulting table provides signal amplifications for each gain.

37| For Alexa Fluor 514 dye, use only signals that are measured using the FRET and YFP cubes. Similarly, for Proflavin dye, analyze only signals that are measured using the FRET and CFP cubes. Remove all other signals.

38| Normalize all signals to gain HV800 by dividing by the appropriate LUT factor. This yields the normalized amplification factor for each gain. The normalized amplification factor for gain HV800 will be 1.

39| For each dye dilution, average the normalized fluorescence signals from all three filter cubes. This gives signals for HV600–HV1150 for the CFP cube, the YFP cube and twice for the FRET cube.

40| Visualize the data for the CFP cube, the YFP cube and the FRET cube by plotting HV gains (*x* axis) against the normalized amplification factors. The power-law relation can be visualized on a logarithmic plot. In this case, the relation forms a straight line. Exclude outliers at the extreme gains for each dye concentration.

41| Average normalized signals from different dilutions for the CFP and YFP cubes. Pool FRET cube signals measured by either of the dyes and average. The outcome is the final HV-LUT.

Cell preparation and transfection for calibration of the setup ● TIMING 2–3 d

42| Seed HEK293 cells at a density of 1×10^5 to 5×10^5 cells in 2 ml of growth medium on a 35-mm glass-bottom dish at least 2 d before the experiment. Prepare at least one imaging dish per sample. Refer to the table below to assess the total number of cell dishes needed for setup calibration.

Sample	Purpose	Plasmid	Number of dishes to prepare
Background	Determining background fluorescence according to Steps 53–62	No transfection	1
Donor only	Determining R_{D1} and R_{D2} values according to Steps 63–73	Untagged CFP	1
Acceptor only	Determining R_{A1} value according to Steps 74–77	Untagged YFP	1
Dimer	Determining *G*-factor and M_A/M_D value according to Steps 78–99	YFP–G_4–CFP YFP–G_{40}–CFP YFP–G_{80}–CFP	3 (1 dish per dimer plasmid)

▲ **CRITICAL STEP** It is important that cells be well separated after seeding and after transfection. For FRET experiments, only single fluorescent cells are used, in order to avoid collection of light from adjacent cells.

43| Transfer cells to an incubator (37 °C and 10% CO_2 atmosphere) and allow them to grow overnight to a density of 60% confluence.

44| For transfection of cDNA plasmids, we use 25-kDa linear polymer PEI. Bring the transfection medium (serum free), transfection reagent PEI and relevant plasmids to room temperature and place them in a laminar flow work bench.

45| In a sterile 1.5-ml microtube, dilute 400–1,200 ng of appropriate cDNA plasmids in 200 µl of transfection medium.

46| Add PEI (1 mg/ml) to the diluted DNA mixture at a 3:1 ratio of total PEI (µg):total DNA (µg) to prepare DNA-containing liposomes. For example, for 1 µg of CFP plasmid, 3 µg of PEI would be added. The optimal PEI:cDNA ratio can vary between 1:1 and 3:1 and may need to be adjusted to obtain optimal protein expression.

47| Incubate the cDNA/PEI mixture for 5–15 min at room temperature, and subsequently add this mixture to the cells.

48| Incubate the cells for 24–72 h at 37 °C and 10% CO_2 atmosphere to allow for expression of the protein of interest. This time window needs to be individually adjusted to account for variability in rates of expression for proteins of interest.

Preparation for FRET two-hybrid binding experiments ● TIMING 20 min

49| Set the aperture of the adjustable pinhole or iris of the photometer (**Fig. 1**) to an appropriate size so as to acquire the fluorescence signal from an individual cell. In general, keep the size of the pinhole to a minimum; it should be just larger than a typical cell in order to reduce background fluorescence and enhance signal-to-noise ratio. This aperture is set before experimentation and maintained throughout the duration of each experiment. The pinhole is placed at the center of the field of view, as chromatic and spherical aberrations of the objective are least near the center of the optical axis. As a rule of thumb, only cells with a fluorescence signal at least seven times higher than background autofluorescence should be considered. This rule applies to the CFP and YFP cubes only, not to the FRET cube.

50| Turn on the fluorescence arc lamp at least 20 min before the experiment to ensure stable light output.

51| Open the FelixGX software or equivalent software to control the monochromator and to acquire fluorescence measurements.

52| Ensure that the 'Measure/View' knob of the photometer is set to 'View' mode at all times other than during data acquisition, in order to protect the PMT from saturation.

Determination of background autofluorescence ● TIMING 30 min daily over 1 week

53| Place a dish containing untransfected cells (background sample from Step 43) on the microscope stage.

54| Use bright-field illumination to bring a cell into focus (choose a cell with representative morphology).

55| Center the cell to the field of view of the pinhole by moving the microscope stage.

56| Toggle the photomultiplier to the 'Measure' position to enable fluorescence measurement.

57| Acquire fluorescence signals with all three filter cubes (CFP, FRET and YFP cubes) for all predetermined HV gains (i.e., 'FRET 600' macro to 'FRET 1150' macro). Start with the 'FRET 600' macro. Switch the filter cubes when prompted. For each cell, there will be 12 signals per filter cube.

58| Rename the data set with a unique descriptive notation (e.g., 'Cell 1') and export as 'Export Group'.

59| Repeat Steps 54–58 for 10–15 more cells and export the data.

60| For calculation of background autofluorescence, open MATLAB and execute the 'ReadFRETdata' script (**Supplementary Data 2**) for the data containing background measurements from Step 58. The MATLAB script converts the FelixGX data output to an input format suitable for Excel spreadsheets. The file exported in Step 58 contains data acquired from a single cell for the complete set of gains. The MATLAB script returns the average value of each trace for the fluorescence signals obtained with the CFP, FRET and YFP filter cubes. Alternatively, mean data can be computed with FelixGX or other software.

61| Open the Template Excel sheet provided as **Supplementary Data 3**. Start with 'Cell 1' and paste data from Step 60 into the 'Background' worksheet (**Supplementary Fig. 6**). In column D the HV gain is specified, and in columns E–G the fluorescence signals specified in the header are deposited.

62| Repeat Steps 60 and 61 for the remaining files containing background data (from Step 59) and paste them into the provided space for 'Cell 2', 'Cell 3' and so on. in the Excel sheet. In the 'Background' worksheet, the average value of all cells for each gain and filter cube is automatically calculated (column: K8–M19) and transferred to all other sheets except the 'HV lookup' worksheet. **? TROUBLESHOOTING**

Determination of the spectral factors R_{D1} and R_{D2} ● TIMING 45 min daily over 1 week

63| Place a dish containing cells expressing untagged CFP (donor sample, from Step 48) on the microscope stage. Move the CFP filter cube to within the light beam and start the 'Continuous CFP excitation' protocol.

64| Select an isolated fluorescent cell and place it into the field of view of the pinhole. Once a suitable cell is chosen, terminate the fluorescence illumination until you are ready to perform data measurement, in order to diminish photobleaching. If necessary, the bright-field light source can be used to position the cell.

65| Choose an appropriate HV gain for fluorescence measurement. The optimal HV gain depends on the expression level of the transfected plasmid and should match the brightness of the cell. Start with the 'FRET 800' macro when initially screening a sample. This standard gain is appropriate for intermediate-expressing cells. Switch to a higher or lower HV gain if necessary. For a sufficiently high signal-to-noise ratio, output signals between 100 mV and 4 V are required.

66| Load the appropriate macro, toggle the photomultiplier to the 'Measure' position and record data by starting the macro. Switch the filter cubes when prompted. You will obtain three fluorescence intensity signals from this measurement. The signal through the FRET cube yields $S_{FRET}(D, 436, 535)$, the signal through the CFP cube yields $S_{CFP}(D, 436, 480)$, and the signal through the YFP cube yields $S_{YFP}(D, 500, 535)$.

67| Rename the recording with an informative title and export as 'Export Group'.

68| Follow Steps 64–67 for an additional 10–15 individual cells. Select cells that express CFP at variable levels in order to collect data at different HV gains.

69| Calculate the spectral factors R_{D1} and R_{D2} from the data acquired in Steps 67 and 68 using the Template Excel sheet provided as **Supplementary Data 3,** or create your own analysis template. If you are using the Template Excel file, convert the data obtained in Step 67 using MATLAB as described in Step 60 and paste them into columns E–G (raw data) of the 'R_D value' worksheet (**Supplementary Fig. 7**). Continue for all cells acquired in Step 68.
▲ **CRITICAL STEP** The spectral ratios R_{D1} and R_{D2} are specific for a given FRET setup and need to be determined for each individual FRET setup. It is necessary to verify these values before daily experiments.
? TROUBLESHOOTING

70| For each cell, specify the HV gain at which the signal was recorded in column D.

71| Subtract background signals for the corresponding HV gain from each trace. In the 'R_D value' worksheet of the Excel spreadsheet, background subtraction is automatically performed (columns: I–K).

72| Calculate the R_{D1} value by dividing the background-subtracted FRET signal by the background-subtracted CFP signal ($R_{D1} = S_{FRET}(D, 436, 535)/S_{CFP}(D, 436, 480)$). This step is automatically performed in the Excel worksheet. The R_{D2} value is also calculated at this point ($R_{D2} = S_{YFP}(D, 500, 535)/S_{CFP}(D, 436, 480)$). For our setup, R_{D2} is so small that it will not be further considered.

73| Average the R_{D1} and R_{D2} values from single cells (data in column M) to obtain the overall R_{D1} and R_{D2} values (cells P9 and Q9). The calculated R_{D1} value is automatically transferred to the dimer sheet and the binding curve analysis ('BC analysis') sheet for further analysis.

Determination of the spectral factor R_{A1} ● TIMING 45 min daily over 1 week
74| For determination of spectral factor R_{A1}, use YFP-only-expressing cells (from Step 48) and follow Steps 63–68 using 500-nm excitation and 'Continuous YFP excitation' for selection of cells. Again, measure 10–15 individual cells.

75| Read out the data using MATLAB (Step 60), paste these values into columns E–G (raw data) of the 'R_A value' worksheet (**Supplementary Data 3**, **Supplementary Fig. 7**) and specify the HV gain in column D. The background is automatically subtracted (columns I–K).
▲ **CRITICAL STEP** The spectral ratio R_{A1} is specific to an individual FRET setup and needs to be determined for each individual FRET setup. It is necessary to verify the value before daily experiments.
? TROUBLESHOOTING

76| Calculate the R_{A1} ratio by dividing the background-subtracted FRET signal by the background-subtracted YFP signal ($R_{A1} = S_{FRET}(A, 436, 535)/S_{YFP}(A, 500, 535)$). The value is automatically computed in the Excel sheet, column M.

77| Average the R_{A1} values from single cells to obtain the mean R_{A1} value (cell P9). The calculated R_{A1} value is automatically transferred to the 'Dimer' sheet and the 'BC Analysis' sheet for further analysis.

Determination of calibration constants using dimers ● TIMING 90 min daily over 1 week
78| For determination of FRET efficiencies from dimers, place cells expressing a dimer plasmid (e.g., YFP–G_4–CFP, from Step 48) under the microscope.

79| Under continuous CFP illumination, select an isolated cell expressing the dimer at an intermediate level.

80| Switch to continuous YFP illumination and inspect the YFP expression of the cell.

81| Switch to bright-field illumination and center the cell in the visual field.

82| Direct the light beam to the photomultiplier and center the cell in the pinhole aperture of the photometer.

83| Record fluorescence intensities with an appropriate gain as described in Step 65. Choose a gain so that the signal falls into a range between 100 mV and 4 V.
? TROUBLESHOOTING

84| Export the data and repeat Steps 78–83 for at least 15 cells. Choose cells with different expression levels.

85| Collect data for multiple dimers (each dimer separately, for example Y–G_{40}–C, Y–G_{80}–C) by following Steps 78–84.
▲ **CRITICAL STEP** We recommend measuring three cube fluorescence measurements from all dimers across several days. Once a stable calibration curve is calculated, it is sufficient to determine FRET efficiencies for one dimer daily.
? TROUBLESHOOTING

86| For calculation of FRET efficiencies from dimers, read data files acquired in Step 84 using MATLAB and paste them into columns E–G of the 'Dimer' worksheet (**Supplementary Fig. 8**).

87| Specify the gain used for each cell in column D.

88| Subtract the corresponding background value from each measurement (columns J–L).

89| Calculate the $F_c/(R_{A1} \cdot S_{YFP})$ value according to equation (5) (**Box 1**) using the computed R_{D1} and R_{A1} values (Steps 73 and 77; Excel spreadsheet cell F2 and cell F3), respectively.

90| Continue with data from cells expressing each of the distinct dimers (Step 85) and repeat Steps 86–88 for analysis and calculate the $F_c/(R_{A1} \cdot S_{YFP})$ values of these dimers. The sheet calculates the average $F_c/(R_{A1} \cdot S_{YFP})$ value for each dimer and deposits it in column O in the cell indicated.

91| To analyze the dimer series experiment, open the 'Dimer Analysis' worksheet provided in the Excel spreadsheet (**Supplementary Fig. 9**).

92| Transfer the background-subtracted raw data (S_{CFP}FRET, S_{FRET}FRET, S_{YFP}FRET) from Steps 89 and 90 to the 'Dimer Analysis' worksheet, columns D–G.

93| For each cell from Step 92, compute F_C according to equation (5) and subsequently compute the F_c/S_{YFP} and S_{CFP}/S_{YFP} values using the background-subtracted raw data. This step is automated in the worksheet (columns H–J, subheader 'Calibration by Dimer Series').

94| Substitute actual R_{A1} and R_{D1} values measured daily (in contrast to dimers) in the equations $R_{D1}/R_{A1} \cdot S_{CFP}/S_{YFP}$ and $1/R_{A1} \cdot F_c/S_{YFP}$. These values represent the x and y coordinates for individual points (columns K,L) in the graph (top right).
▲ **CRITICAL STEP** For a FRET two-hybrid binding experiment, the R_{A1} and R_{D1} values should be updated each day, to account for daily fluctuations. By contrast, it is sufficient to use measurements from dimers acquired during the calibration phase of the rig.

95| Plot the data from Step 94 in a linear diagram. In the Excel sheet, data are automatically plotted in the top graph on the right-hand side. Data points for each dimer cluster together.

96| Calculate the mean $S_{CFP}/S_{YFP} \cdot R_{D1}/R_{A1}$ and $F_C/(R_{A1} \cdot S_{YFP})$ values for each dimer construct (columns M and N) and plot them into a graph, as shown in the lower graph on the right-hand side in the worksheet.

97| Compute a linear regression line for the data obtained in Step 96 and calculate both the y intercept and the slope of the regression. The values are used to determine the G factor and M_A/M_D value. Copy the y intercept and slope and paste them into cells T56 and T57, respectively, of the 'Dimer Analysis' worksheet. Please note that this step needs to be performed manually.

98| From the data obtained in Step 97, calculate the $\varepsilon_{YFP}(436)/\varepsilon_{CFP}(436)$ value by dividing 1 by the y intercept, and calculate the M_A/M_D value by dividing the negative slope (G factor) by the y intercept. These values should be pasted into cells W56 and W57. Please note that this step needs to be performed manually.

99| Set M_D to 1 in order to obtain M_A (M_A then equals the M_A/M_D ratio). Alternatively, the computed M_D value could be set here. In the latter case, the M_A value is then set such that M_A/M_D is as experimentally determined. Transfer the M_A/M_D ratio and the $\varepsilon_{YFP}(436)/\varepsilon_{CFP}(436)$ value to cells F7 and F10 of the 'BC Analysis' sheet. Please note that this step needs to be performed manually (**Supplementary Data 3**).

Cell preparation and transfection to perform a FRET two-hybrid experiment ● TIMING 2–3 d

100| For a FRET two-hybrid experiment, seed and transfect cells as described in Steps 42–48. The table below lists the samples required for an experiment. Prepare experimental cells as required according to the experimental design. Depending on the expression efficiency of the cDNA plasmids, it may be necessary to prepare more than one imaging dish for coexpression of interacting partners (biological samples), in order to achieve variable expression levels, which is fundamental to the outcome of the binding assay. We recommend starting with a 1:1 transfection (CFP-tagged protein:YFP-tagged protein) and to subsequently adjust the ratio to obtain varying ratios of donor and acceptor expression.

▲ **CRITICAL STEP** To obtain a completely populated binding curve, it is important to achieve variability in expression levels of interaction partners. In our experience, a PEI transfection reagent is best suited to obtaining heterogeneous expression levels. However, we encourage researchers to test other transfection reagents for their particular cDNA plasmid.

Sample	Purpose	Plasmid	Number of dishes to prepare
Control cells			
Background	Determining background fluorescence (Step 101)	No transfection	1
Donor only	Determining R_{D1} and R_{D2} values (Step 101)	Untagged CFP	1
Acceptor only	Determining R_{A1} value (Step 101)	Untagged YFP	1
Dimer (optional)	Positive control (Step 101)	e.g., YFP–G_4–CFP	1
Spurious FRET	Determining collisional FRET (Steps 102–109)	Cotransfect untagged CFP and untagged YFP	1
Experimental cells			
Biological samples	Determining the interaction of proteins	Cotransfect protein-tagged CFP and YFP	1 or more[a]
Control biological samples	Positive control		1 or more[a]

[a]Depending on experimental design.

Measurement of background, spectral factors R_{A1} and R_{D1}, and dimer control ● TIMING 90 min

101| Measure and analyze the control samples from Step 100 as described in Steps 53–84 in order to determine the following: background autofluorescence (background sample, Steps 53–62), R_{D1} and R_{D2} values (donor-only sample, Steps 63–73), R_{A1} value (acceptor-only sample, Steps 74–77) and the efficiency of one dimer to ensure stability of measurements between experimental days (dimer sample, Steps 78–84, for one dimer). It is recommended to include one dimer per experimental day in routine FRET experiments.

▲ **CRITICAL STEP** The background autofluoresence results from cellular metabolites and weakly fluorescent amino acids in proteins. These contaminating factors may vary daily depending on the cell conditions. It is therefore critical to measure autofluorescence background before each FRET experiment and use these values for analysis.

▲ **CRITICAL STEP** On a calibrated setup, it is sufficient to measure 5–8 cells, as the values are expected to be reasonably stable within a cell preparation. If the R_{A1} and R_{D1} values are not stable, FRET cannot be measured reliably.

Determination of spurious FRET ● TIMING 30 min

102| For the determination of spurious FRET, acquire fluorescence signals from cells expressing untagged CFP and YFP molecules (from Step 100) according to Steps 79–83.

103| Repeat signal acquisition for 10–15 cells and export data.

104| Use the MATLAB script to import the raw data obtained in Step 103 into columns D–F of the 'Spurious FRET' worksheet (**Supplementary Fig. 10**). In column C, specify the HV gain.

105| For each measurement, subtract the corresponding appropriate background value (columns H–J).

106| Calculate $F_c/(R_{A1} \cdot S_{YFP})$ (column K) and E_A (column M) according to equations (5 and 6), respectively. The values for R_{A1} and R_{D1} are picked from cells F3 and F4.

107| Determine CFP_{EST}, taking the HV-LUT (Sheet 9) into consideration to normalize for different HV gains. Calculate CFP_{EST} according to equation (12) (automatically performed in the Excel worksheet, column L). The R_{D1} and M_D values required for this calculation are chosen from cells F4 and F5.

108| Plot E_A as a function of CFP_{EST} and perform a linear regression on the data points (graph on the right-hand side in the worksheet).

109| Transfer the slope of the regression line to cell P7.

Determination of FRET efficiencies from CFP- and YFP-tagged FRET pairs ● TIMING 1–3 h

110| For the determination of FRET efficiencies from CFP- and YFP-tagged biomolecular interaction partners, record signals from at least 25 cells according to Steps 79–83. Perform measurements on imaging dishes transfected with different ratios of CFP- and YFP-tagged proteins, if necessary.

▲ **CRITICAL STEP** For binding analysis, it is necessary to choose cells with varying expression of CFP- and YFP-labeled proteins. Inspect the sample carefully under both CFP and YFP excitation, and preferentially include cells displaying varying ratios of CFP and YFP expression. This variability in cellular expression is critical to populating both the rising and saturating portions of the FRET two-hybrid binding curve (**Fig. 6**).

? TROUBLESHOOTING

111| To calculate the FRET efficiencies of CFP- and YFP-tagged interaction proteins, read fluorescence intensities obtained in Step 110 using MATLAB and paste the data into columns E–G of the 'Samples' worksheet.

112| Specify the gain used for each cell in column D.

113| From each measurement, subtract the corresponding appropriate background value (columns J–L).

114| Calculate $F_C/(R_{A1} \cdot S_{YFP})$ using the R_{A1} and R_{D1} values from cells G2 and G3, respectively. This is automated in the Excel template. These values are further used for construction of a binding curve and automatically linked to the 'BC Analysis' worksheet.

Construction of a binding curve ● TIMING 30 min–2 h

115| The table on the top left of the 'BC Analysis' worksheet is subdivided into three sections (**Supplementary Fig. 11**). The left part contains the FRET parameters. Here, R_{A1} (cell F4), R_{D1} (cell F5), M_A (F8) and the M_A/M_D ratio (F10) are collected from the linked worksheets. Calculate M_D (cell F9) according to **Supplementary Note 1** and **Supplementary Data 1** and transfer the $\varepsilon_{YFP}(436)/\varepsilon_{CFP}(436)$ value (cell F7) manually from the 'Dimer Analysis' worksheet. The middle part of the table contains parameters required for spurious FRET correction. Here, the slopes of the spurious FRET relations for 3^3-FRET (cell I5; SpFRET_E_3Cube) and EFRET (cell I6; SpFRET_E_EFRET) are tabulated. Confirm that the values in the left and the middle part of the table have been correctly transferred from the individual sheets linked to this table. The right part of the table contains parameters relevant for the fitting procedure (Steps 121–128).

116| Make sure that background-subtracted values, including the respective gains and the $F_C/(R_{A1} \cdot S_{YFP})$ values from Steps 113 and 114 are transferred from the 'Samples' worksheet into columns D–H of the 'BC Analysis' worksheet.

117| Calculate the E_A and E_D efficiencies according to equations (6 and 7) presented in **Box 1** and deposit the values in columns I and K, respectively. This step is automatically performed in the Excel sheet.

118| Correct the E_A and E_D efficiencies for spurious FRET (automated in columns J and L of the Excel sheet) according to equations (27 and 28), respectively, and the parameters presented in the top table in the 'BC Analysis' worksheet.

119| Total CFP_{EST} (column M) and YFP_{EST} (column N) are calculated according to equations (10 and 12), respectively, using parameters specified in the top table ('BC Analysis' worksheet). Ensure that both formulas are corrected for HV gain, that the background is subtracted from the raw signals and that efficiencies are corrected for spurious FRET.

120| Divide CFP_{EST} by YFP_{EST}. For dimers, this value is expected to be ~1 (column O).

▲ **CRITICAL STEP** For FRET-binding curves, only cells with a CFP/YFP ratio <20 are probed. Importantly, a CFP fluorescence value that is too large, in comparison with the YFP fluorescence value, could corrupt the measurement of sensitized emission

and lead to large errors in measured FRET efficiencies. These general criteria must be adjusted to account for the quantum yields of the fluorescent pairs and the microscopy setup.
? TROUBLESHOOTING

121| To fit a binding curve to FRET data, FRET efficiencies (E_A and E_D), as well as CFP_{EST} and YFP_{EST} values, have to be calculated for each individual cell as specified in Steps 115–120. For the fitting procedure, the right-hand side of the table ('BC Analysis' worksheet), the graphs titled 'three cube FRET' and 'E-FRET' ('BC Analysis' worksheet), and columns P–AA are relevant (**Supplementary Data 3**). Placeholders for $K_{d,EFF}$, $E_{A,max}$ and $E_{D,max}$ have been prepared in the right-hand side of the table. These parameters are called $K_{d,EFF}$, $E_{A,max}$ and $E_{D,max}$ and have been deposited in cells K4, K6 and K7, respectively. SUM_Err_3Cube (cell K8) and SUM_Err_EFRET (K9) represent the sum of squared error between predicted and experimentally observed E_A and E_D values. Total Error (K10) is the sum of both types of error (SUM_Err_3Cube + SUM_Err_EFRET).
The parameters N_D/N_A (K5) and N_D/N_A exp (K11) are the theoretical and the experimentally observed stoichiometries of the binding reaction and are assumed to be 1 in a 1:1 binding reaction, as presented in the example data set. The idea of the fitting procedure is as follows: By analyzing the entire data set, a nonlinear least-square fitting procedure is performed to obtain an estimate of the D_{free} and A_{free} values (columns P and Q), the maximal efficiencies $E_{A,max}$ and $E_{D,max}$ (K6 and K7), and the relative binding affinity $K_{d,EFF}$ of the binding reaction (K4). To obtain approximations of the parameters $E_{A,max}$ or $E_{D,max}$ and $K_{d,EFF}$ for the single-site binding model, a visual fit is performed first. Start with initial guesses for $K_{d,EFF}$ (cell K4), $E_{A,max}$ (K6) and $E_{D,max}$ (K7). The final fit for the binding curve is obtained following an iterative fitting procedure.

122| According to equations (17 and 19) in **Box 2**, estimate D_{free} and A_{free} and deposit the values in columns P and Q of the sheet. Both D_{free} and A_{free} change as $K_{d,EFF}$ changes. Thus, it is helpful to visualize the data points on the corresponding test binding curve during the fitting procedure. Accordingly, both 3^3-FRET (E_A) and E-FRET (E_D) are plotted against D_{free} and A_{free}, respectively (top graphs, middle and right). To build an intuition for the procedure, manually change the $K_{d,EFF}$ value and observe how the D_{free} and A_{free} values change. In addition to D_{free} and A_{free}, A_b and D_b are calculated according to equations (20 and 21) (**Box 2**) and deposited into columns R and S, respectively.

123| In parallel, predicted E_A and E_D values are calculated according to equations (6 and 7) (**Box 1**) and deposited into columns T and V. From predicted E_A and E_D values and experimentally determined E_A and E_D values, the errors 'E_A pred Error' (column U) and 'E_D pred Error' (column W) are calculated. The sums of 'E_D pred Error', 'E_A pred Error', and 'total error' are deposited in cells K8, K9 and K10, respectively.

124| Iteratively adjust the fitting parameters to obtain a best fit (lowest errors). Maximal FRET efficiencies and $K_{d,EFF}$ values should be identical for 3^3-FRET ($E_{A,max}$) and E-FRET ($E_{D,max}$) for a 1:1 binding stoichiometry.

125| Subsequently, use the Excel solver to optimize these parameters using the visual fit parameters from Steps 125–128 as initial guesses. Open the Excel solver by clicking 'Data' → 'Solver' (**Supplementary Fig. 12**)[52]. In case the Excel solver is not activated, activate it by clicking 'Folders' → 'Options' → 'Add-Ins'. Choose 'Excel-Add-Ins' in the 'Manage' drop-down menu, and hit the 'OK' button. In the 'Add-Ins' window, check the 'Solver' checkbox and click 'OK'. When asked to confirm, choose 'Yes'.

126| In the 'Solver Parameters' window, specify entries for 'Set Target Cell', 'Equal To', 'By Changing Variable Cells' and 'Subject to the Constraints'. **Supplementary Figure 12** shows how the parameters are set. 'Set Target Cell' determines which value is to be optimized. In the sample spreadsheet, this is set to cell K10 (**Supplementary Fig. 12a**), which is the total error (e.g., SumErr_3Cube plus SumErr_3Cube). In this case, 3^3-FRET and E-FRET curves are fitted simultaneously. If you would like to fit the 3^3-FRET graph alone, the target cell to be optimized needs to be set to cell K8 (SumErr_3Cube; **Supplementary Fig. 12b**); if you would like to fit the E-FRET curve alone, then set target cell to K9 (SumErr_ECube).

127| Set 'Min' in the 'Equal To' selection. 'By Changing Variable Cells' defines the adjustable parameters, which in our case are $K_{d,EFF}$, $E_{A,max}$ and $E_{D,max}$, contained in cells K4, K6 and K7, respectively. In 'Subject to the Constraints' impose constraints on the adjustable parameters. Here, it is useful to constrain $K_{d,EFF}$, $E_{A,max}$ and $E_{D,max}$ to ≥0.

128| In the 'Solver Parameters' window (**Supplementary Fig. 12**), click the 'Solve' button to initialize Solver.
Now, a prediction is calculated and the difference is calculated according to equations (22 and 23) (**Box 2**).
The solver now minimizes the sum-of-square errors between predicted and observed values. The results are deposited in cells K4, K6 and K7.

? TROUBLESHOOTING

Troubleshooting advice can be found in **Table 3**.

TABLE 3 | Troubleshooting table.

Step	Problem	Possible reason	Solution
32, 34	Not all HV gains are covered	Fluorescence intensity of the dyes does not match the detection range	Prepare new dilutions
62	Automated background subtraction is not correct	The link within the Excel sheet is not correctly defined	Check and redefine the lookup function in the Excel spreadsheet
69	Large intra-experimental fluctuations in R_{D1} values	Problem with detector	Check hardware settings; stabilize the detector
	Large interexperimental fluctuations in R_{D1} values	Problem with detector	Check hardware settings; stabilize the detector
		Filters are aging	Exchange filter sets
75	Large intra-experimental fluctuations in R_{A1} values	Unstable excitation lamp	Prewarm the excitation lamp; stabilize power supply; exchange lamp bulb
	Large interexperimental fluctuations in R_{A1} values	Unstable excitation lamp	Stabilize power supply; exchange lamp bulb
	Systematic shift and drift of R_{A1} value, which is not improved by changing the light bulb	Filters are aging	Exchange filter sets
83	PMT saturation	Fluorescence intensity is too high	Use a lower HV gain; retransfect cells
85	R_{A1} and R_{D1} values are stable but $F_C/R_{A1}*S_{YFP}$ and FRET efficiencies vary considerably for one dimer	Related to fluorophore maturation	Use cerulean and venus fluorescent proteins instead of CFP and YFP
110	Less variation in expression levels	Suboptimal transfection of cells	Transfect a smaller amount of cDNA; wait longer for expression
	Data points do not populate all phases of a binding curve	No variability in expression levels of interacting partners	Transfect different ratios of CFP- and YFP-tagged proteins
120	CFP_{EST}/YFP_{EST} ratio is much larger than 1 for dimers	Degradation of cDNA	Use another batch of plasmids

● TIMING

Implementation and calibration of the FRET imaging setup: 1-week period
Steps 1–6, generation of acquisition programs for screening and selecting cells: 15 min
Steps 7–9, determination of the dark current of the PMT: 15 min
Steps 10–15, generation of acquisition programs for FRET two-hybrid binding experiments: 45 min
Steps 16–21, generation of macros for FRET two-hybrid binding experiments: 45 min
Steps 22–41, establishment of an HV-LUT: 3 h daily over 1 week
Steps 42–48, cell preparation and transfection for calibration of the setup: 2–3 d
Steps 49–52, preparation for FRET two-hybrid binding experiments: 20 min
Steps 53–62, determination of background autofluorescence: 30 min daily over 1 week
Steps 63–77, determination of spectral factors R_{D1} and R_{D2}: 45 min daily over 1 week
Steps 74–77, determination of the spectral factor R_{A1}: 45 min daily over 1 week
Steps 78–99, determination of calibration constants using dimers: 90 min daily over 1 week
Step 100, cell preparation and transfection to perform a FRET two-hybrid experiment: 2–3 d
Step 101, measurement of background, spectral factors R_{A1} and R_{D1}, and dimer control: 90 min
Steps 102–109, determination of spurious FRET: 30 min

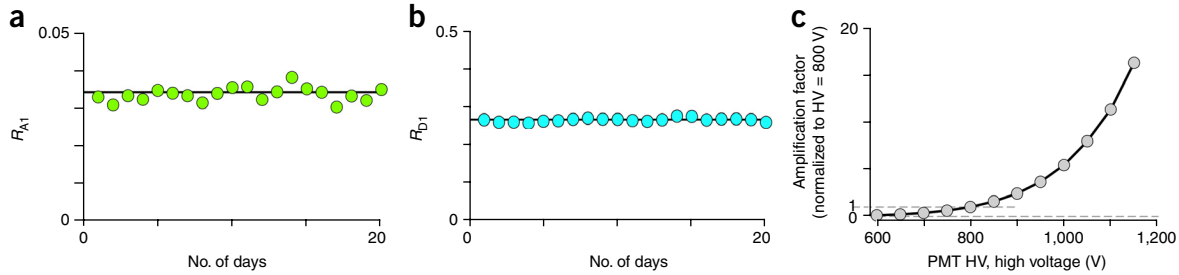

Figure 9 | Stability of spectral correction factors and amplification factors. (**a**) Typical daily variation in R_{A1} values observed over 20 experimental days. (**b**) Daily variation in R_{D1} values, observed over the same time period. (**c**) Plot of the normalized amplification factor (Step 41) obtained based on intensity measurements of fluorescent dyes versus high voltage shows a power-law relation. Amplification factors are normalized to a standard PMT HV gain of 800 V. PMT HV, photomultiplier tube high voltage.

Steps 110–114, determination of FRET efficiencies from CFP- and YFP-tagged FRET pairs: 1–3 h
Steps 115–128, construction of a binding curve: 30 min–2 h.

ANTICIPATED RESULTS

Indicators of a successful microscope setup

A stable FRET microscopy setup is critical for high-quality quantitative FRET experiments. The three key indicators of a successful setup are as follows:

- *Stability of the excitation light source indicated by stable* R_{A1}*values.* The R_{A1} value is mainly determined by the excitation system (**Fig. 4**) and is measured daily while establishing the FRET setup and during the course of FRET –two-hybrid experiments. Short-term (i.e., day-to-day and over the course of a single experiment) fluctuations in fluorescence output and/or intensity of the arc lamp are indicated by variability of R_{A1} values (**Fig. 9**; **Table 4**). For our setup, the range of R_{A1} values is 0.025–0.045 for YFP and should be stable in cells (**Fig. 9a**). R_{A1} measurements using dyes should also be very stable (for our setup, the range of R_{A1} values for Alexa514 dye was 0.049–0.058). An important cause of highly variable R_{A1} values is fluctuations of the excitation lamp caused by an unstable power supply or intensity fluctuations of the light bulb. When R_{A1} values are stable when measured using the Alexa Fluor 514 dye but unstable in cells, the problem may pertain to cell transfection and fluorophore maturation. Standardization of cell transfection and culture conditions will alleviate this potential problem. Long-term decay (i.e., over the course of several months) in fluorescence output due to aging of the excitation lamp is indicated by variation in R_{A1} values over the course of several months and needs to be compensated for, as outlined in Equipment Setup.
- *Stability of the detection system, indicated by* R_{D1}*values.* R_{D1} mainly depends on the emission pathway, in particular, on the detector (**Fig. 4**). Thus, stability of the emission light detector is indicated by low variability of R_{D1} values. However, for R_{D1} values to faithfully represent stability of the detection system, the following system parameters must be low: the dark current of the PMT; the noise level associated with empty glass imaging dishes; and background fluorescence in nontransfected cells. Representative and acceptable values for these parameters are given in **Table 4**. For our setup, the range of R_{D1} values obtained for Proflavin dye was 1.025–1.049, and the observed range of R_{D1} values for CFP was 0.24–0.27 (**Fig. 9b**). R_{D1} can be roughly calculated for the filter cubes used from the emission spectrum of CFP and also from the quantum

TABLE 4 | Background and R_{A1}, R_{D1} and R_{D2} values (at HV gain 800).

Entity	CFP cube	FRET cube	YFP cube
Blank cells (autofluorescence)	0.0129 mV (±0.0001)	0.0132 mV (±0.0001)	0.0097 mV (±0.0001)
Noise from empty imaging dish	0.0923 mV (±0.0001)	0.0729 mV (±0.0001)	0.0443 mV (±0.0001)
Noise from imaging buffer	0.0109 mV (±0.0001)	0.0093 mV (±0.0001)	0.0082 mV (±0.0001)
Dark current range	0.2957 mV (±0.005)	0.2957 mV (±0.005)	0.2957 mV (±0.005)
R_A, R_D values			
R_{D1} value	0.2651 (±0.0001)		
R_{D2} value	0.0008 (±3.8E-05)		
R_{A1} value	0.03394 (±5.079E-05)		

Values are means (n = 15) ± s.e.m.

efficiency of the detector used. Deviation of the experimentally determined R_{D1} value from the theoretical value suggests a likely malfunction of the detection system or the PMT. Possible causes of deviations include incorrect mode of operation for the PMT (photon counting instead of analog) or specific hardware settings in the configuration panel of the software. Importantly, the detector is nonlinear below a HV gain of 600 V and may contribute to unreliable measurements. We recommend recording of data from dim cells at a high HV gain. The optimal HV range is 600–1, 150 V. For very dim cells that may require an HV gain of 1,150 V or above, the signal-to-noise ratio decreases, which makes them are prone to measurement errors.

- *Stability of the HV-LUT for the PMT.* Stability of the HV-LUT is indicated by low fluctuations of individual values for a given gain, as presented in **Figure 9c** and **Table 5**. Before determination of the HV-LUT, it is absolutely required that R_{D1} and R_{A1} recordings be stable in cells throughout all HV gains. The lookup table is typically determined using fluorescence dyes and can be verified by measuring intensity signals from fluorescent cells using a range of HV gain settings during the calibration phase of the FRET rig (**Table 5**). In addition, intensity recordings from nontransfected cells should be used for validation of the table. Once the lookup table has been generated, it can be repeated yearly to confirm reproducibility of the system.

TABLE 5 | Lookup table for PMT HV gain factor.

PMT high-voltage HV (V)	Amplification factor S_X(HV)/S_X(800 V) (mean ± s.e.m.)
600	0.118 ± 0.001
650	0.214 ± 0.002
700	0.371 ± 0.002
750	0.617 ± 0.002
800	1
850	1.579 ± 0.003
900	2.420 ± 0.008
950	3.647 ± 0.013
1,000	5.427 ± 0.025
1,050	7.961 ± 0.050
1,100	11.306 ± 0.059
1,150	16.231 ± 0.140

Assessing the outcome of FRET –two-hybrid analysis

Once the R_{D1} and R_{A1} values are stable and an HV-LUT is obtained, actual FRET measurements can be performed. For FRET experiments, five controls are required in addition to the FRET measurements from CFP- and YFP-tagged binding pairs; these help gauge the validity of the FRET experiment:

- Background autofluorescence in untransfected cells
- R_{A1} values from YFP-only-expressing cells
- R_{D1} values from CFP-only-expressing cells
- Measurements from cells expressing CFP–YFP dimers to generate a calibration curve
- Measurement of spurious FRET from cells expressing CFP and YFP monomers

Background autofluorescence values in untransfected cells, R_{A1} values from YFP-only-expressing cells and R_{D1} values from CFP-only-expressing cells need to be stable, and there are four quality checks to ensure the validity of these measurements:

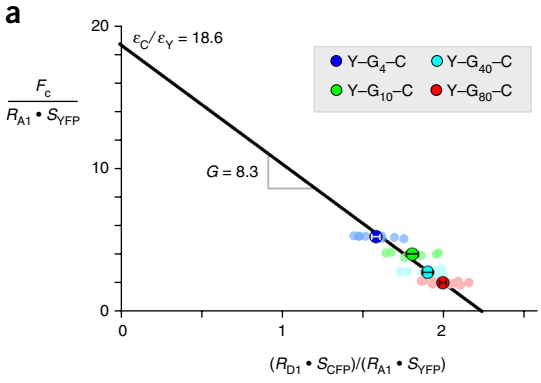

b

	E_A (mean ± s.e.m.)	E_D (mean ± s.e.m.)
YFP–G_4–CFP	0.296 ± 0.001	0.299 ± 0.004
YFP–G_{10}–CFP	0.228 ± 0.002	0.223 ± 0.003
YFP–G_{40}–CFP	0.156 ± 0.002	0.158 ± 0.002
YFP–G_{80}–CFP	0.116 ± 0.001	0.116 ± 0.002

Figure 10 | Determination of the *G* factor and the excitation ratio using dimers. (**a**) Calibration line obtained from CFP and YFP dimers connected by linkers of either 4, 10, 40 or 80 glycine (G) residues. Mean values are given by the larger colored circles. Individual data points are the smaller open colored points. From the linear regression line (black line), the *G* factor (slope) and the ratio of excitation coefficients (*y* intercept) are determined. (**b**) Table shows mean 3^3-FRET and E-FRET values experimentally determined for the various CFP–YFP dimers transfected into HEK293 cells, computed using equations for 3^3-FRET (E_A, equation 6) and E-FRET (E_D, equation 7) with experimentally determined calibration factors (n = 12–15).

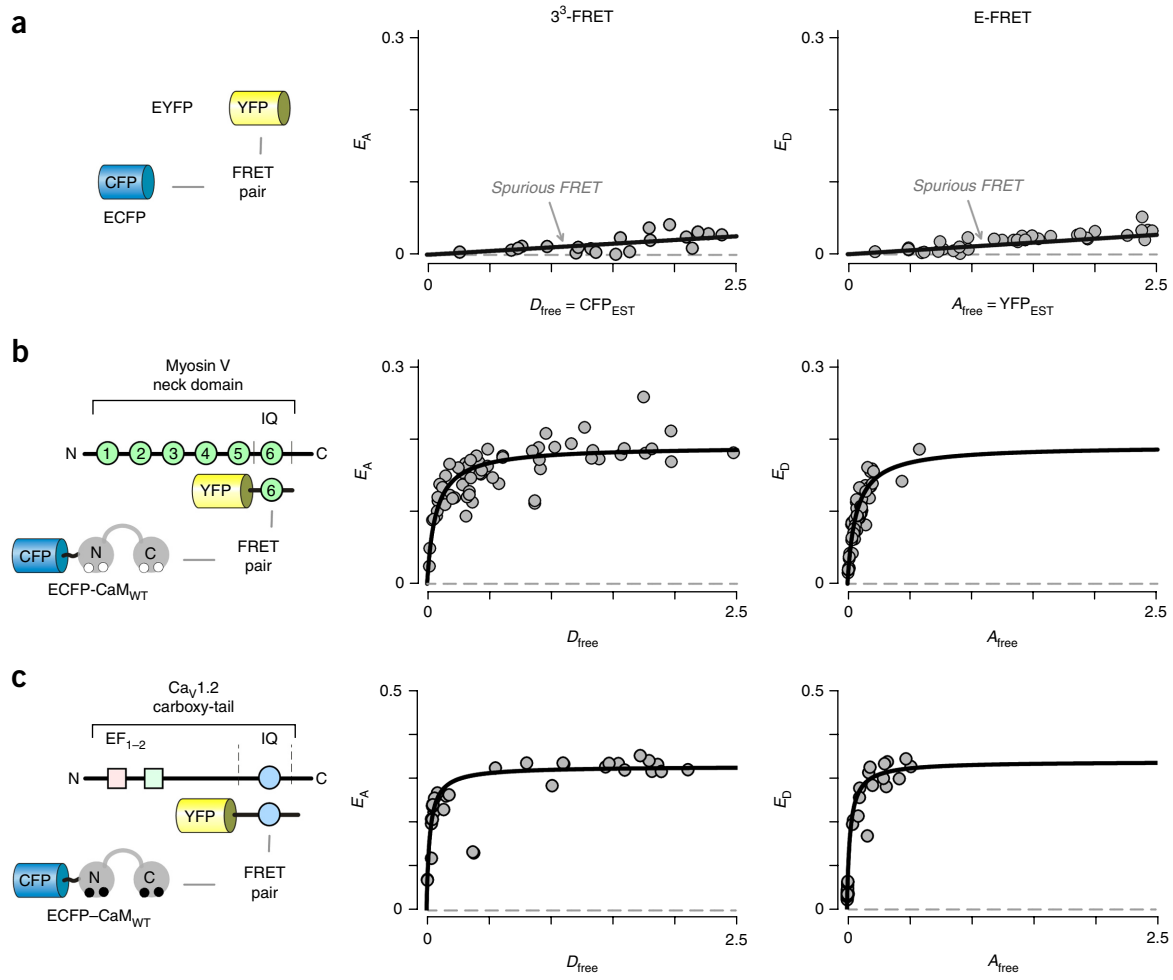

Figure 11 | Examples of spurious FRET and FRET two-hybrid binding curves. (**a**) Left, diagram illustrates untagged CFP and YFP FRET pair used to determine spurious FRET by 3^3-FRET (middle) and E-FRET (right). (**b**) Left, schematic of a FRET two-hybrid assay evaluating the binding of CFP-tagged calmodulin (CFP–CaM_{WT}) to the sixth YFP-tagged myosin Va IQ domain (YFP-IQ) at resting Ca^{2+} concentrations. Middle, 3^3-FRET computed from three cube fluorescence measurements from single cells expressing both YFP-IQ and CFP–CaM_{WT}, plotted against the free concentration of donor molecules (CFP–CaM_{WT}), reveal a robust binding curve. Right, E-FRET efficiency computed from the same fluorescence measurements is plotted against the free acceptor concentration (YFP-IQ). Note that estimates for the maximum or saturating FRET efficiency (E_{max}) and the relative binding affinity ($K_{d,EFF}$) are identical using the 3^3-FRET and E-FRET methods (D_{free} or A_{free} at half-saturation, respectively). (**c**) Robust binding of YFP-tagged IQ domain from the voltage-gated Ca^{2+} channel $Ca_V1.2$ to CFP–CaM_{WT} at elevated cellular Ca^{2+} conditions. Format as in panel **b**. Note again that the binding isotherms estimated are identical using the 3^3-FRET and E-FRET methods (black fit).

(1) Inspect R_{A1} values: if negative R_{A1} values are obtained ($R_{A1} < 0$), autofluorescence intensity recordings are not stable and are possibly overestimated.
(2) Inspect FRET efficiencies: efficiencies <0 suggest that R_{D1} values are not stable and may be overestimated.
(3) For YFP-only-expressing cells, FRET efficiency should equal 0. If not, R_{A1} has not been determined correctly.
(4) For CFP-only-expressing cells, $S_{FRET}(DA, 436, 453) - R_{D1} \cdot S_{CFP}(DA, 436, 480)$ should be zero. If not, R_{D1} has not been determined correctly.

The measurements of several CFP–YFP dimers are used to calculate a calibration curve from which the *G* factor and the excitation ratio are determined (**Fig. 10**). Depending on the donor and acceptor fluorophores used, the variation of individual data points of this curve is more or less pronounced. Given that R_{D1} and R_{A1} values are stable, variations in FRET efficiencies are larger for CFP and YFP dimers compared with cerulean and venus pairs. The cerulean and venus pairs may mature faster and more completely (~100%), resulting in more robust FRET measurements. For CFP–YFP dimers, E_A and E_D should be the same, and plotting E_D versus E_A should result in the line of unity. Furthermore, the experimentally determined CFP_{EST} (N_D) and YFP_{EST} (N_A) values should be equal, as the two fluorophores are tethered. Deviation from equality would suggest proteolysis or immature proteins. The range of FRET efficiencies for the set of dimers used is between 10 and 40%.

Spurious FRET is determined by using cells expressing CFP and YFP monomers (**Fig. 11a**) and plotting E_A and E_D versus CFP_{EST} and YFP_{EST}, respectively. The relationship should be linear. This value is subtracted from binding curves in order to

quantify FRET as a result of binding. Spurious FRET can also occur between two dimers. The amount of spurious FRET depends on the cell volume. As splitting of the cells during cell culture can change cell volume on a day-to-day basis, spurious FRET control experiments need to be performed daily.

Example results from two FRET two-hybrid binding assays are shown in **Figure 11b**,**c**. **Figure 11b** presents representative graphs for 3^3-FRET and E-FRET binding curves between myosin Va IQ peptide and calmodulin under low Ca^{2+} conditions. **Figure 11c** presents representative graphs for 3^3-FRET and E-FRET binding curves for interaction of $Ca_V1.2$ IQ peptide with calmodulin under elevated Ca^{2+} conditions. From the graph it is evident that all points are localized very closely to the fitted line, indicating low noise in FRET measurement. The results illustrate the high-affinity binding of calmodulin to the distal IQ segment of myosin Va (**Fig. 11b**) and the IQ domain of $Ca_V1.2$ (**Fig. 11c**) at basal cytosolic Ca^{2+} levels. The differences in maximal apparent FRET efficiencies for CaM binding to the two IQ domain peptides indicate that their binding conformations may be distinct. The high affinity binding for both IQ domain peptides fit with *in vitro* binding assays[53,54]. Together, these results demonstrate that FRET two-hybrid assays are well suited for in-depth quantification of macromolecular interactions in living cells.

Note: Any Supplementary Information and Source Data files are available in the online version of the paper.

ACKNOWLEDGMENTS We thank R. Rötzer, A. Rößing, T. Kiwitt and W. Yang for excellent technical support. This work was supported by funding from the German Research Foundation (SFB/TRR 152 TP12 to M.B., SFB/TRR 152 TP06 to C.W.-S. and SFB 870 TP B05 to C.W.-S.) and the National Institute of Mental Health (R01 MH065531 to D.T.Y. and M.B.-J.). D.T.Y. passed away on December 23, 2014. He was a remarkable teacher, inspirational scientist and a generous colleague. He pioneered the development and the usage of FRET two-hybrid assays to elucidate the mechanistic underpinnings of voltage-gated Ca^{2+} channels. His scientific brilliance and personal charm are greatly missed in the scientific community.

AUTHOR CONTRIBUTIONS E.S.B., M.B.-J., D.T.Y. and C.W.-S. developed and/or designed the study. E.S.B. and M.B.-J. collected and analyzed the data. M.S. and L.S. furnished initial experimental data for dimer calibrations. M.B.-J. and D.T.Y. provided theoretical derivations. M.S., M.B.-J. and P.S.Y. constructed YFP- and CFP-tagged constructs and dimers. E.S.B., M.B.-J. and C.W.-S. wrote the manuscript and created the figures. M.B. discussed and commented on the manuscript.

COMPETING FINANCIAL INTERESTS The authors declare no competing financial interests.

1. Clegg, R.M. Fluorescence resonance energy transfer and nucleic acids. *Methods Enzymol.* **211**, 353–388 (1992).
2. Jares-Erijman, E.A. & Jovin, T.M. FRET imaging. *Nat. Biotechnol.* **21**, 1387–1395 (2003).
3. Shaner, N.C., Steinbach, P.A. & Tsien, R.Y. A guide to choosing fluorescent proteins. *Nat. Methods* **2**, 905–909 (2005).
4. Berney, C. & Danuser, G. FRET or no FRET: a quantitative comparison. *Biophys. J.* **84**, 3992–4010 (2003).
5. Gordon, G.W., Berry, G., Liang, X.H., Levine, B. & Herman, B. Quantitative fluorescence resonance energy transfer measurements using fluorescence microscopy. *Biophys. J.* **74**, 2702–2713 (1998).
6. Xia, Z. & Liu, Y. Reliable and global measurement of fluorescence resonance energy transfer using fluorescence microscopes. *Biophys. J.* **81**, 2395–2402 (2001).
7. Youvan, D.C. & Marrs, B.L. Molecular genetics and the light reactions of photosynthesis. *Cell* **39**, 1–3 (1984).
8. Zal, T. & Gascoigne, N.R. Photobleaching-corrected FRET efficiency imaging of live cells. *Biophys. J.* **86**, 3923–3939 (2004).
9. Erickson, M.G., Alseikhan, B.A., Peterson, B.Z. & Yue, D.T. Preassociation of calmodulin with voltage-gated Ca(2+) channels revealed by FRET in single living cells. *Neuron* **31**, 973–985 (2001).
10. Erickson, M.G., Liang, H., Mori, M.X. & Yue, D.T. FRET two-hybrid mapping reveals function and location of L-type Ca2+ channel CaM preassociation. *Neuron* **39**, 97–107 (2003).
11. Erickson, M.G., Moon, D.L. & Yue, D.T. DsRed as a potential FRET partner with CFP and GFP. *Biophys. J.* **85**, 599–611 (2003).
12. Miyawaki, A. *et al.* Fluorescent indicators for Ca2+ based on green fluorescent proteins and calmodulin. *Nature* **388**, 882–887 (1997).
13. Chen, H., Puhl, H.L. III, Koushik, S.V., Vogel, S.S. & Ikeda, S.R. Measurement of FRET efficiency and ratio of donor to acceptor concentration in living cells. *Biophys. J.* **91**, L39–L41 (2006).
14. Yang, P.S., Johny, M.B. & Yue, D.T. Allostery in Ca(2)(+) channel modulation by calcium-binding proteins. *Nat. Chem. Biol.* **10**, 231–238 (2014).
15. Broussard, J.A., Rappaz, B., Webb, D.J. & Brown, C.M. Fluorescence resonance energy transfer microscopy as demonstrated by measuring the activation of the serine/threonine kinase Akt. *Nat. Protoc.* **8**, 265–281 (2013).
16. Ormo, M. *et al.* Crystal structure of the *Aequorea victoria* green fluorescent protein. *Science* **273**, 1392–1395 (1996).
17. Lohse, M.J., Nuber, S. & Hoffmann, C. Fluorescence/bioluminescence resonance energy transfer techniques to study G-protein-coupled receptor activation and signaling. *Pharmacol. Rev.* **64**, 299–336 (2012).
18. Zhang, J., Ma, Y., Taylor, S.S. & Tsien, R.Y. Genetically encoded reporters of protein kinase A activity reveal impact of substrate tethering. *Proc. Natl. Acad. Sci. USA* **98**, 14997–15002 (2001).
19. Takao, K. *et al.* Visualization of synaptic Ca2+/calmodulin-dependent protein kinase II activity in living neurons. *J. Neurosci.* **25**, 3107–3112 (2005).
20. Bazzazi, H., Ben Johny, M., Adams, P.J., Soong, T.W. & Yue, D.T. Continuously tunable Ca(2+) regulation of RNA-edited CaV1.3 channels. *Cell Rep.* **5**, 367–377 (2013).
21. Ben Johny, M., Yang, P.S., Bazzazi, H. & Yue, D.T. Dynamic switching of calmodulin interactions underlies Ca2+ regulation of CaV1.3 channels. *Nat. Commun.* **4**, 1717 (2013).
22. Takahashi, S.X., Miriyala, J., Tay, L.H., Yue, D.T. & Colecraft, H.M. A CaVbeta SH3/guanylate kinase domain interaction regulates multiple properties of voltage-gated Ca2+ channels. *J. Gen. Physiol.* **126**, 365–377 (2005).
23. Agler, H.L. *et al.* G protein-gated inhibitory module of N-type (ca(v)2.2) ca2+ channels. *Neuron* **46**, 891–904 (2005).
24. Karpenko, I.A. *et al.* Selective nonpeptidic fluorescent ligands for oxytocin receptor: design, synthesis, and application to time-resolved FRET binding assay. *J. Med. Chem.* **58**, 2547–2552 (2015).
25. Chang, D.D. & Colecraft, H.M. Rad and Rem are non-canonical G-proteins with respect to the regulatory role of guanine nucleotide binding in Ca 1.2 regulation. *J. Physiol.* **593**, 5075–5090 (2015).
26. Yang, T., Xu, X., Kernan, T., Wu, V. & Colecraft, H.M. Rem, a member of the RGK GTPases, inhibits recombinant CaV1.2 channels using multiple mechanisms that require distinct conformations of the GTPase. *J. Physiol.* **588**, 1665–1681 (2010).
27. Yamashita, M., Somasundaram, A. & Prakriya, M. Competitive modulation of Ca2+ release-activated Ca2+ channel gating by STIM1 and 2-aminoethyldiphenyl borate. *J. Biol. Chem.* **286**, 9429–9442 (2011).
28. Muik, M. *et al.* Dynamic coupling of the putative coiled-coil domain of ORAI1 with STIM1 mediates ORAI1 channel activation. *J. Biol. Chem.* **283**, 8014–8022 (2008).
29. Murphy, J.G. *et al.* AKAP-anchored PKA maintains neuronal L-type calcium channel activity and NFAT transcriptional signaling. *Cell Rep.* **7**, 1577–1588 (2014).

30. Ruiz-Velasco, V. & Ikeda, S.R. Functional expression and FRET analysis of green fluorescent proteins fused to G-protein subunits in rat sympathetic neurons. *J. Physiol.* **537**, 679–692 (2001).
31. Kern, A., Albarran-Zeckler, R., Walsh, H.E. & Smith, R.G. Apo-ghrelin receptor forms heteromers with DRD2 in hypothalamic neurons and is essential for anorexigenic effects of DRD2 agonism. *Neuron* **73**, 317–332 (2012).
32. Albizu, L. *et al.* Time-resolved FRET between GPCR ligands reveals oligomers in native tissues. *Nat. Chem. Biol.* **6**, 587–594 (2010).
33. Bazzazi, H. *et al.* Novel fluorescence resonance energy transfer-based reporter reveals differential calcineurin activation in neonatal and adult cardiomyocytes. *J. Physiol.* **593**, 3865–3884 (2015).
34. Lee, S.R., Sang, L. & Yue, D.T. Uncovering aberrant mutant PKA function with flow cytometric FRET. *Cell Rep.* **14**, 3019–3029 (2016).
35. Tadross, M.R., Park, S.A., Veeramani, B. & Yue, D.T. Robust approaches to quantitative ratiometric FRET imaging of CFP/YFP fluorophores under confocal microscopy. *J. Microsc.* **233**, 192–204 (2009).
36. Shrestha, D., Jenei, A., Nagy, P., Vereb, G. & Szollosi, J. Understanding FRET as a research tool for cellular studies. *Int. J. Mol. Sci.* **16**, 6718–6756 (2015).
37. Ben-Johny, M., Yue, D.N. & Yue, D.T. A novel FRET-based assay reveals 1:1 stoichiometry of apocalmodulin binding across voltage-gated Ca and Na ion channels. *Biophys. J.* **102**, 125a–126a (2012).
38. Koushik, S.V., Chen, H., Thaler, C., Puhl, H.L. III & Vogel, S.S. Cerulean, venus, and venusY67C FRET reference standards. *Biophys. J.* **91**, L99–L101 (2006).
39. Sun, Y., Day, R.N. & Periasamy, A. Investigating protein-protein interactions in living cells using fluorescence lifetime imaging microscopy. *Nat. Protoc.* **6**, 1324–1340 (2011).
40. Yasuda, R. Imaging spatiotemporal dynamics of neuronal signaling using fluorescence resonance energy transfer and fluorescence lifetime imaging microscopy. *Curr. Opin. Neurobiol.* **16**, 551–561 (2006).
41. Thaler, C., Koushik, S.V., Blank, P.S. & Vogel, S.S. Quantitative multiphoton spectral imaging and its use for measuring resonance energy transfer. *Biophys. J.* **89**, 2736–2749 (2005).
42. Zeug, A., Woehler, A., Neher, E. & Ponimaskin, E.G. Quantitative intensity-based FRET approaches—a comparative snapshot. *Biophys. J.* **103**, 1821–1827 (2012).
43. Leavesley, S.J., Britain, A.L., Cichon, L.K., Nikolaev, V.O. & Rich, T.C. Assessing FRET using spectral techniques. *Cytometry A* **83**, 898–912 (2013).
44. Mustafa, S., Hannagan, J., Rigby, P., Pfleger, K. & Corry, B. Quantitative Forster resonance energy transfer efficiency measurements using simultaneous spectral unmixing of excitation and emission spectra. *J. Biomed. Opt.* **18**, 26024 (2013).
45. Bykova, E.A., Zhang, X.D., Chen, T.Y. & Zheng, J. Large movement in the C terminus of CLC-0 chloride channel during slow gating. *Nat. Struct. Mol. Biol.* **13**, 1115–1119 (2006).
46. Takanishi, C.L., Bykova, E.A., Cheng, W. & Zheng, J. GFP-based FRET analysis in live cells. *Brain Res.* **1091**, 132–139 (2006).
47. Hoppe, A.D. & Swanson, J.A. Cdc42, Rac1, and Rac2 display distinct patterns of activation during phagocytosis. *Mol. Biol. Cell* **15**, 3509–3519 (2004).
48. Chen, H., Puhl, H.L. III & Ikeda, S.R. Estimating protein-protein interaction affinity in living cells using quantitative Forster resonance energy transfer measurements. *J. Biomed. Opt.* **12**, 054011 (2007).
49. Hoppe, A., Christensen, K. & Swanson, J.A. Fluorescence resonance energy transfer-based stoichiometry in living cells. *Biophys. J.* **83**, 3652–3664 (2002).
50. Chen, Y., Mauldin, J.P., Day, R.N. & Periasamy, A. Characterization of spectral FRET imaging microscopy for monitoring nuclear protein interactions. *J. Microsc.* **228**, 139–152 (2007).
51. Levy, S. *et al.* SpRET: highly sensitive and reliable spectral measurement of absolute FRET efficiency. *Microsc. Microanal.* **17**, 176–190 (2011).
52. Kemmer, G. & Keller, S. Nonlinear least-squares data fitting in Excel spreadsheets. *Nat. Protoc.* **5**, 267–281 (2010).
53. Findeisen, F. & Minor, D.L. Jr. Structural basis for the differential effects of CaBP1 and calmodulin on Ca(V)1.2 calcium-dependent inactivation. *Structure* **18**, 1617–1631 (2010).
54. Martin, S.R. & Bayley, P.M. Calmodulin bridging of IQ motifs in myosin-V. *FEBS Lett.* **567**, 166–170 (2004).

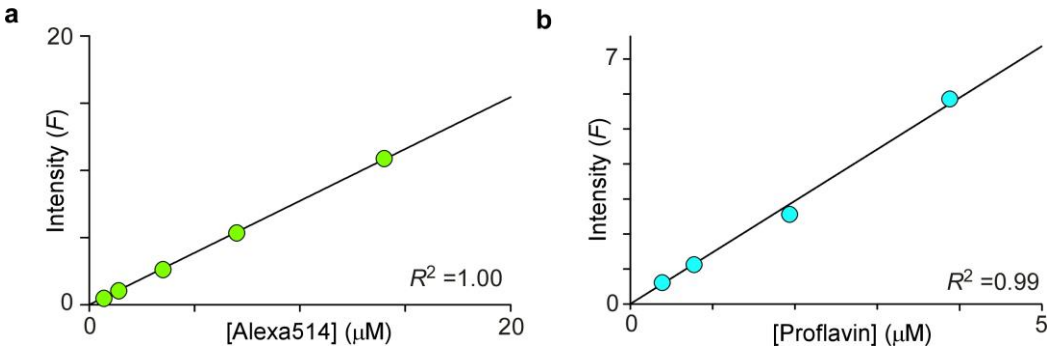

Supplementary Figure 1

Linearity of fluorescence detection subsystem

(a) Fluorescence intensity measured through the YFP cube is linearly proportional to the concentration of Alexa Fluor 514 dye. This result illustrates the linearity of the PMT detector enabling robust estimation of number of acceptor molecules. **(b)** Fluorescence intensity measured through the CFP cube is also linearly proportional to the concentration of Proflavin dye.

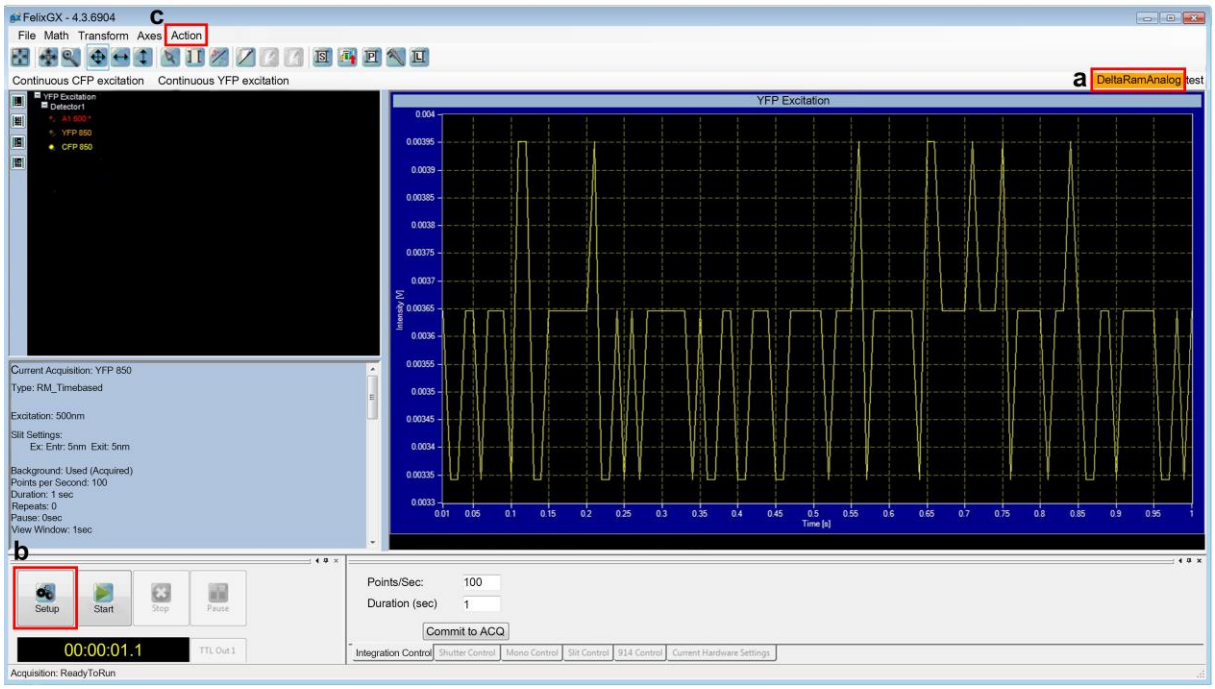

Supplementary Figure 2

Main graphical user interface of Felix GX

(a) The tab "*Delta Ram Analog*" (right upper corner) is clicked to open the "*Hardware Configuration*" window (Supplementary Fig. 2**a**). **(b)** The setup tab is selected (left lower corner) to open the "*Setup*" window (Supplementary Fig. 2**b**). **(c)** The "*Action*" tab opens the "Macro" window from which the "*Macro Editor*" window is opened (Supplementary Fig. 4).

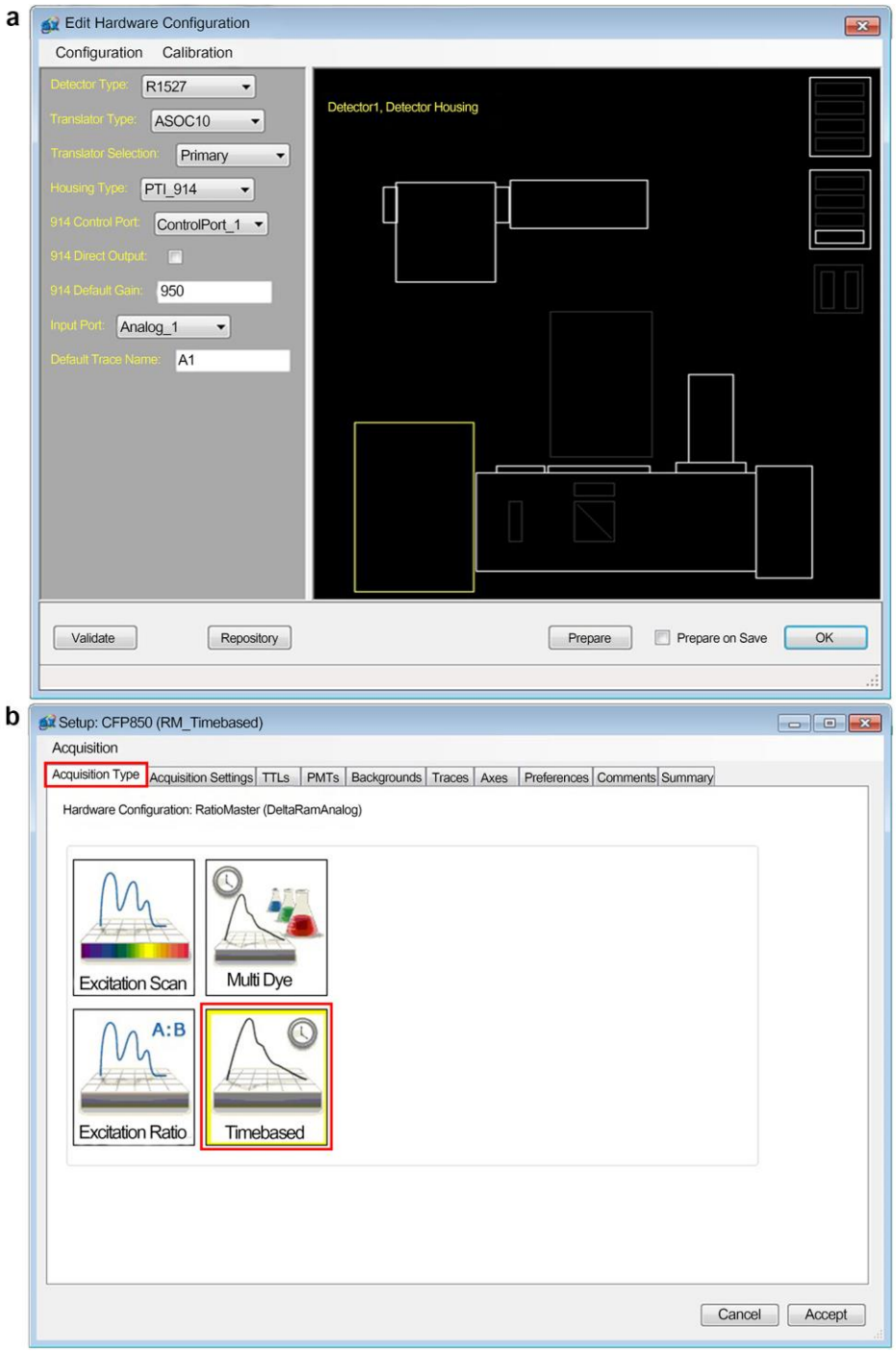

Supplementary Figure 3

The "*Hardware Configuration*" window and the "*Setup*" window.

(a) Settings for the "*Hardware Configuration*" window. **(b)** Settings for the "*Setup*" window. From the 10 tabs in the "*Setup*" window select "*Acquisition Type*" and click the option "*Timebased*".

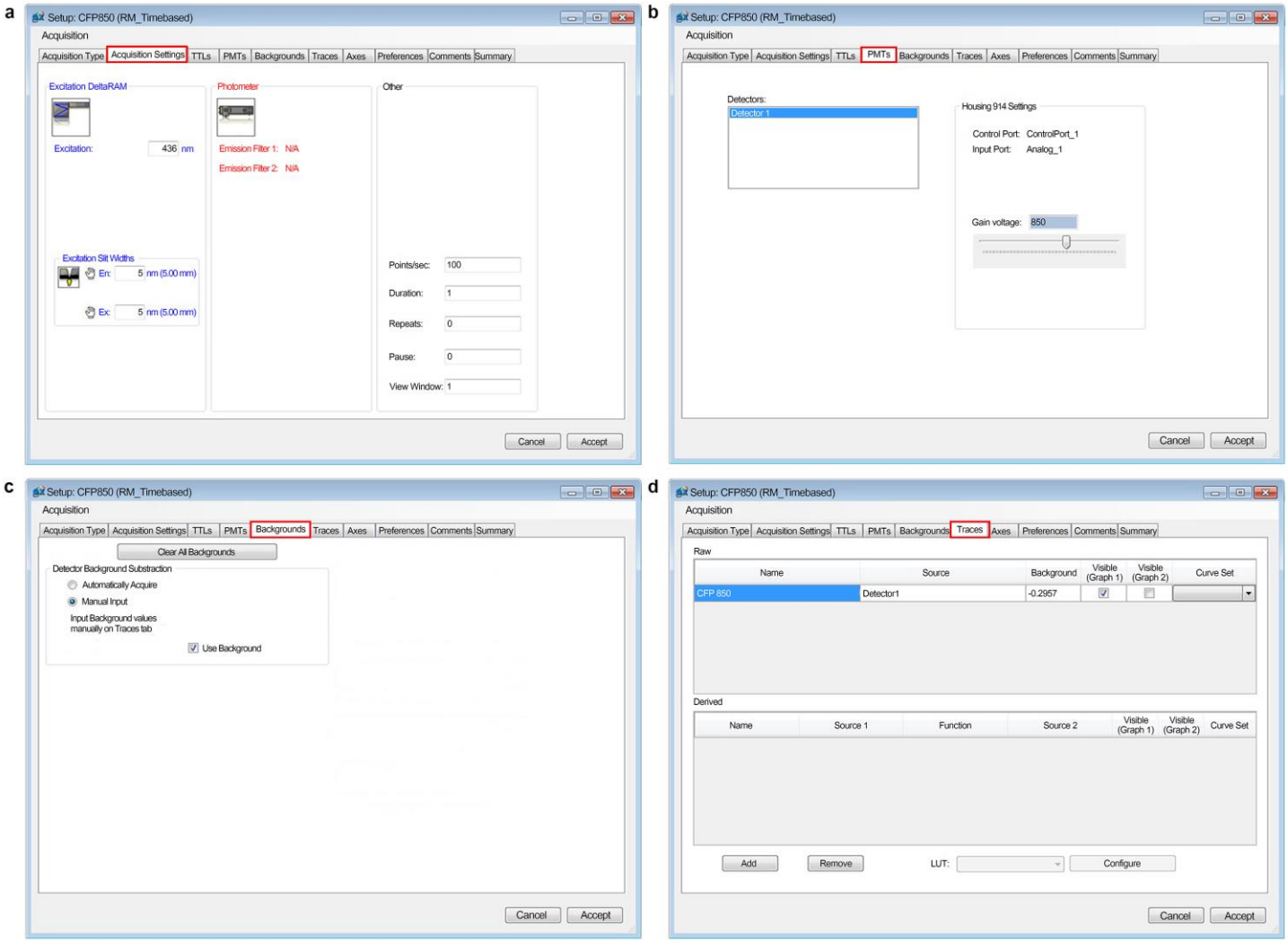

Supplementary Figure 4

Parameter settings specific for Timebased acquisition in the “Setup window”.

(a) Acquisition settings; **(b)** PMTs; **(c)** Backgrounds; **(d)** Traces tab.

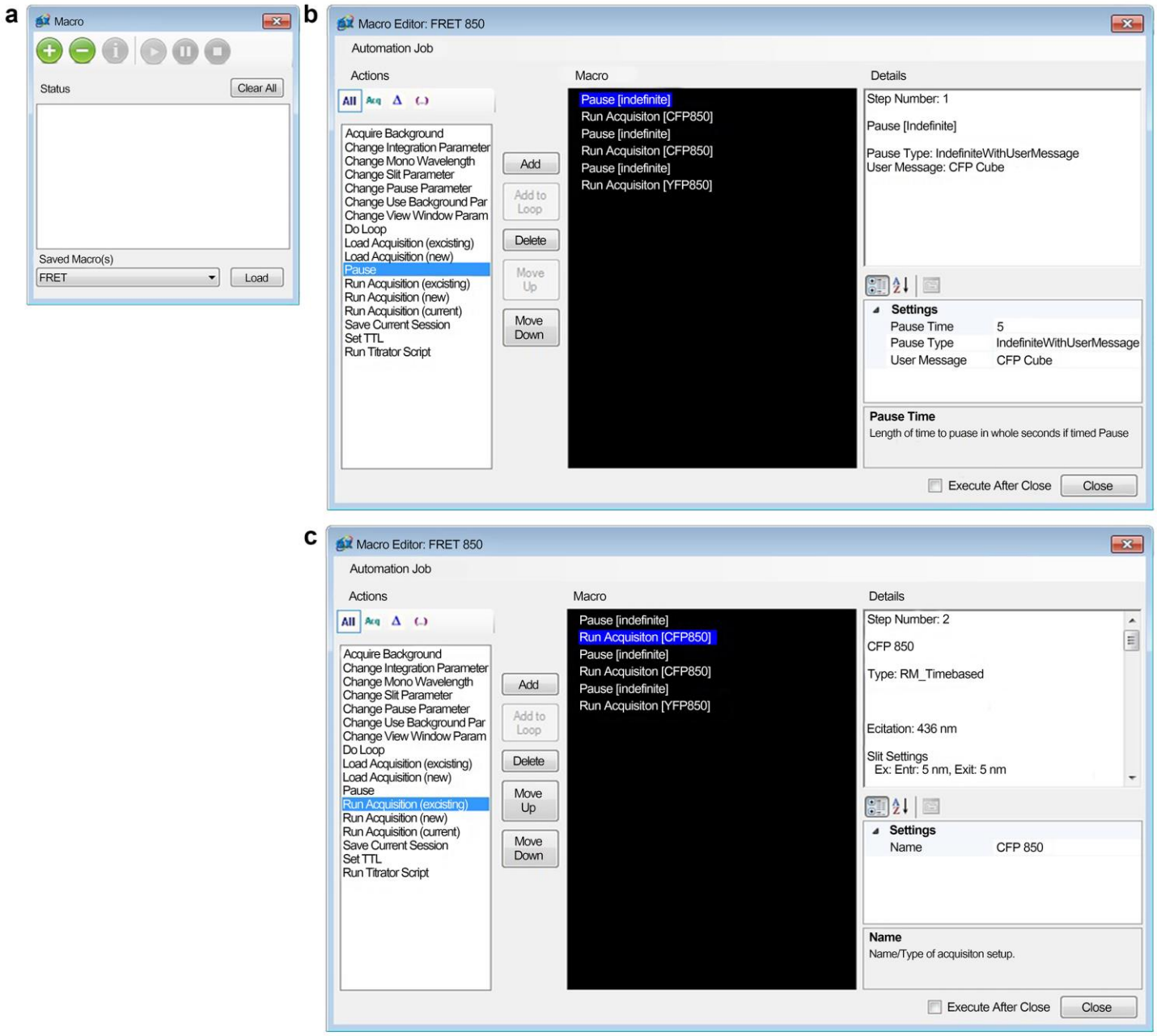

Supplementary Figure 5

Setup of Macros using the "*Macro*" and the "*Macro Editor*" window.

(a) Open the "*Macro*" window by clicking the "*Action*" tab in the main graphical user interface (Supplemental Fig. 1). Click the green "+" button to open the "*Macro Editor*" window (**b** and **c**). In this window, different actions (listed on the left hand side) can be added to the macro (list on the black panel on the right hand side). In this example, a pause step (**b**) and a protocol (*Run Acquisition*; **c**) is added to the macro by clicking the Add tab.

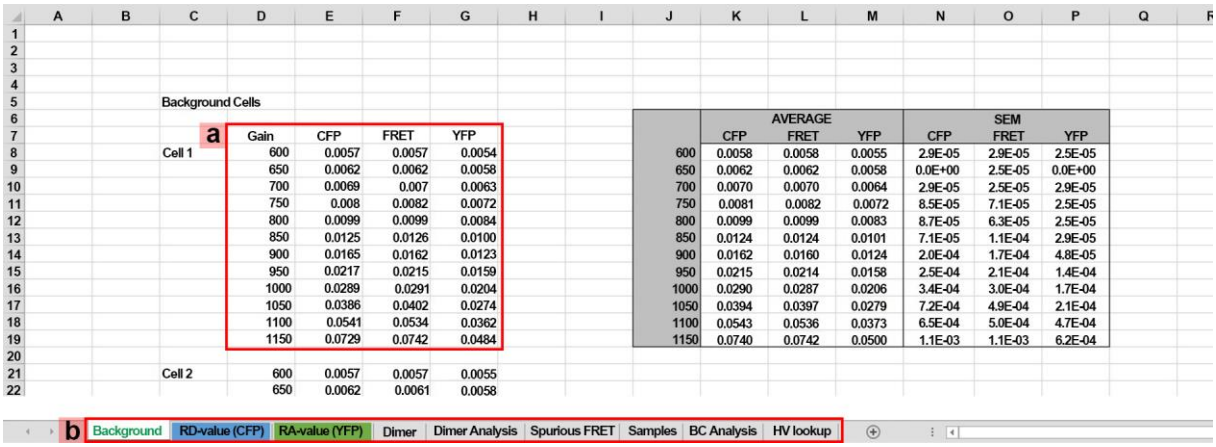

Background Cells

	Gain	CFP	FRET	YFP
Cell 1	600	0.0057	0.0057	0.0054
	650	0.0062	0.0062	0.0058
	700	0.0069	0.007	0.0063
	750	0.008	0.0082	0.0072
	800	0.0099	0.0099	0.0084
	850	0.0125	0.0126	0.0100
	900	0.0165	0.0162	0.0123
	950	0.0217	0.0215	0.0159
	1000	0.0289	0.0291	0.0204
	1050	0.0386	0.0402	0.0274
	1100	0.0541	0.0534	0.0362
	1150	0.0729	0.0742	0.0484
Cell 2	600	0.0057	0.0057	0.0055
	650	0.0062	0.0061	0.0058

	AVERAGE			SEM		
	CFP	FRET	YFP	CFP	FRET	YFP
600	0.0058	0.0058	0.0055	2.9E-05	2.9E-05	2.5E-05
650	0.0062	0.0062	0.0058	0.0E+00	2.5E-05	0.0E+00
700	0.0070	0.0070	0.0064	2.9E-05	2.5E-05	2.9E-05
750	0.0081	0.0082	0.0072	8.5E-05	7.1E-05	2.5E-05
800	0.0099	0.0099	0.0083	8.7E-05	6.3E-05	2.5E-05
850	0.0124	0.0124	0.0101	7.1E-05	1.1E-04	2.9E-05
900	0.0162	0.0160	0.0124	2.0E-04	1.7E-04	4.8E-05
950	0.0215	0.0214	0.0158	2.5E-04	2.1E-04	1.4E-04
1000	0.0290	0.0287	0.0206	3.4E-04	3.0E-04	1.7E-04
1050	0.0394	0.0397	0.0279	7.2E-04	4.9E-04	2.1E-04
1100	0.0543	0.0536	0.0373	6.5E-04	5.0E-04	4.7E-04
1150	0.0740	0.0742	0.0500	1.1E-03	1.1E-03	6.2E-04

Background | RD-value (CFP) | RA-value (YFP) | Dimer | Dimer Analysis | Spurious FRET | Samples | BC Analysis | HV lookup

Supplementary Figure 6

Data input field of the Background sheet.

(**a**) Raw data pasted into the respective columns from measurements using CFP- FRET- and YFP-cubes at a distinct HV gain. **(b)** The excel sheet contains 9 individual sub sheets (labeled from left to right: *Background*, *RD-value (CFP)*, *RA-value (YFP)*, *Dimer sheet*, *Dimer Analysis*, *Spurious FRET*, *Samples* (FRET sample data), *BC Analysis* and *HV lookup*.

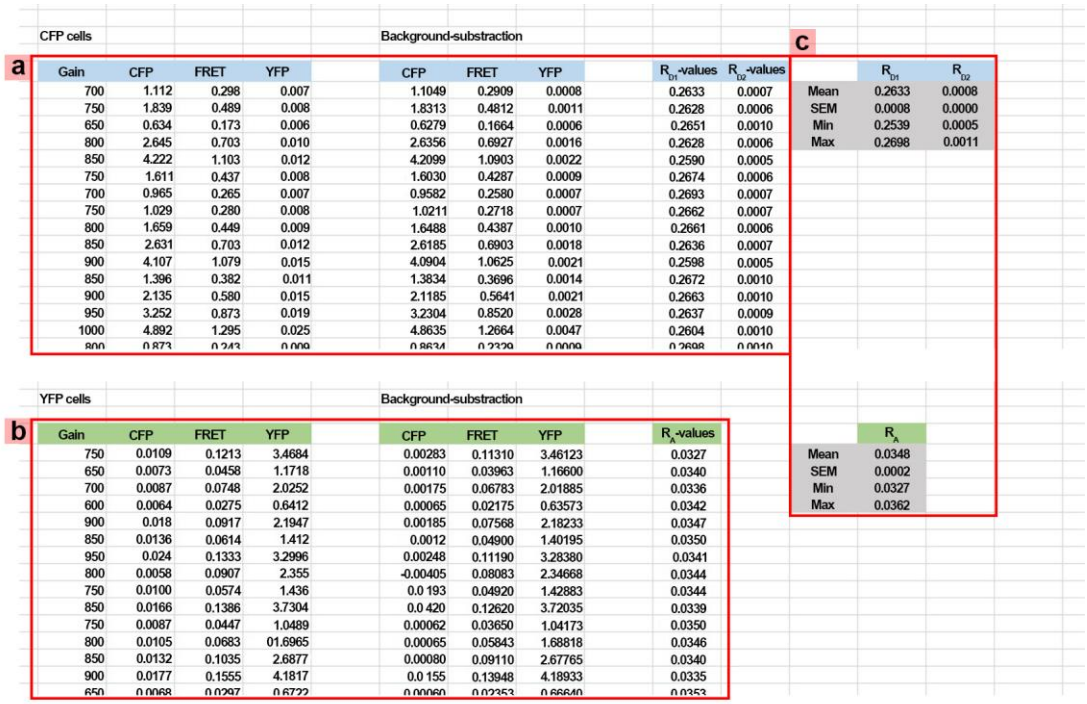

a

CFP cells

Gain	CFP	FRET	YFP	CFP	FRET	YFP	R_{D1}-values	R_{D2}-values
700	1.112	0.298	0.007	1.1049	0.2909	0.0008	0.2633	0.0007
750	1.839	0.489	0.008	1.8313	0.4812	0.0011	0.2628	0.0006
650	0.634	0.173	0.006	0.6279	0.1664	0.0006	0.2651	0.0010
800	2.645	0.703	0.010	2.6356	0.6927	0.0016	0.2628	0.0006
850	4.222	1.103	0.012	4.2099	1.0903	0.0022	0.2590	0.0005
750	1.611	0.437	0.008	1.6030	0.4287	0.0009	0.2674	0.0006
700	0.965	0.265	0.007	0.9582	0.2580	0.0007	0.2693	0.0007
750	1.029	0.280	0.008	1.0211	0.2718	0.0007	0.2662	0.0007
800	1.659	0.449	0.009	1.6488	0.4387	0.0010	0.2661	0.0006
850	2.631	0.703	0.012	2.6185	0.6903	0.0018	0.2636	0.0007
900	4.107	1.079	0.015	4.0904	1.0625	0.0021	0.2598	0.0005
850	1.396	0.382	0.011	1.3834	0.3696	0.0014	0.2672	0.0010
900	2.135	0.580	0.015	2.1185	0.5641	0.0021	0.2663	0.0010
950	3.252	0.873	0.019	3.2304	0.8520	0.0028	0.2637	0.0009
1000	4.892	1.295	0.025	4.8635	1.2664	0.0047	0.2604	0.0010
800	0.873	0.243	0.009	0.8634	0.2329	0.0009	0.2698	0.0010

c

	R_{D1}	R_{D2}
Mean	0.2633	0.0008
SEM	0.0008	0.0000
Min	0.2539	0.0005
Max	0.2698	0.0011

b

YFP cells

Gain	CFP	FRET	YFP	CFP	FRET	YFP	R_A-values
750	0.0109	0.1213	3.4684	0.00283	0.11310	3.46123	0.0327
650	0.0073	0.0458	1.1718	0.00110	0.03963	1.16600	0.0340
700	0.0087	0.0748	2.0252	0.00175	0.06783	2.01885	0.0336
600	0.0064	0.0275	0.6412	0.00065	0.02175	0.63573	0.0342
900	0.018	0.0917	2.1947	0.00185	0.07568	2.18233	0.0347
850	0.0136	0.0614	1.412	0.0012	0.04900	1.40195	0.0350
950	0.024	0.1333	3.2996	0.00248	0.11190	3.28380	0.0341
800	0.0058	0.0907	2.355	-0.00405	0.08083	2.34668	0.0344
750	0.0100	0.0574	1.436	0.0 193	0.04920	1.42883	0.0344
850	0.0166	0.1386	3.7304	0.0 420	0.12620	3.72035	0.0339
750	0.0087	0.0447	1.0489	0.00062	0.03650	1.04173	0.0350
800	0.0105	0.0683	01.6965	0.00065	0.05843	1.68818	0.0346
850	0.0132	0.1035	2.6877	0.00080	0.09110	2.67765	0.0340
900	0.0177	0.1555	4.1817	0.0 155	0.13948	4.18933	0.0335
650	0.0068	0.0297	0.6722	0.00060	0.02353	0.66640	0.0353

	R_A
Mean	0.0348
SEM	0.0002
Min	0.0327
Max	0.0362

Supplementary Figure 7

Data input field of the RD-value (CFP) and the RA-value (YFP) sheets.

Raw data are pasted into the respective columns on the left hand side from measurements in (**a**) CFP-only or **(b)** YFP-only expressing cells using CFP- FRET- and YFP-cubes at a distinct HV gain. Background subtraction and RA value calculation is performed automatically. **(c)** The mean R_D and R_A value, resp., is calculated on the right hand side (gray panel). Statistical values (Standard deviation of the mean (SEM), Minimum (Min) and Maximum (Max)) provide a useful tool to assess the variability of the values. Note that only the mean R_{D1} and R_{A1} values are used for subsequent analysis.

a

Dimer	Cell #	Gain	CFP	FRET	YFP
C4Y	1	900	0.4234	0.5803	2.1061
	2	900	0.5092	0.6984	2.5499
	3	800	0.4785	0.6734	2.4699
	4	850	0.4407	0.5675	2.055
C80Y	1	800	0.6354	0.4345	2.4701
	2	900	0.6364	0.4575	2.5399
	3	800	0.6185	0.3978	2.1493
	4	900	0.4866	0.3319	1.8246
C40Y	1	800	0.3944	0.3346	1.6917
	2	1050	0.5576	0.4311	2.0722
	3	850	0.4667	0.3915	1.9541
	4	850	0.5572	0.4394	2.1403
C10Y	1	800	0.4446	0.4777	1.9781
	2	950	0.5934	0.6414	2.6604
	3	950	0.5819	0.5818	2.3707
	4	950	0.5682	0.5776	2.3362
	5	850	0.4548	0.4615	1.883
	6	750	0.4941	0.467	1.8933
	7	900	0.6489	0.637	2.6496
	8	1000	0.5325	0.524	2.1987

b

Background substracted					
CFP	FRET	YFP	$F_c / R_{A1}*S_{YFP}$		
0.40725	0.564275	2.090075	**6.29**	Mean	**6.25**
0.49305	0.682375	2.533875	**6.27**	SEM	**0.023**
0.46865	0.663525	2.460025	**6.32**		
0.4283	0.5551	2.0426	**6.23**		
0.62555	0.424625	2.460225	**3.04**	Mean	**3.05**
0.62025	0.441475	2.523875	**3.17**	SEM	**0.022**
0.60865	0.387925	2.139425	**3.06**		
0.47045	0.315875	1.808575	**3.05**		
0.38455	0.324725	1.681825	**3.82**	Mean	**3.77**
0.51825	0.39145	2.03255	**3.61**	SEM	**0.035**
0.4543	0.3791	1.9417	**3.84**		
0.5448	0.427	2.1279	**3.83**		
0.43475	0.467825	1.968225	**5.17**	Mean	**5.05**
0.571875	0.62	2.639	**5.12**	SEM	**0.029**
0.560375	0.5604	2.3493	**5.06**		
0.546675	0.5562	2.3148	**5.12**		
0.4424	0.4491	1.8706	**5.12**		
0.486025	0.4588	1.8851	**5.05**		
0.63275	0.620975	2.633575	**4.96**		
0.50355	0.4953	2.17	**4.81**		

Supplementary Figure 8

Data input field of the Dimer sheet.

(a) Raw data are pasted into the respective columns on the left hand side from measurements in CFP-YFP dimer expressing cells using CFP- FRET- and YFP-cubes at a distinct HV gain. Raw data for individual cells are collected separately for a given dimer as indicated. **(b)** Background subtracted values are shown on the right. R_{A1} and R_{D1} values are automatically picked from RD-value (CFP) and the RA-value (YFP) sheets. Statistics are shown on the right hand side (Mean, SEM).

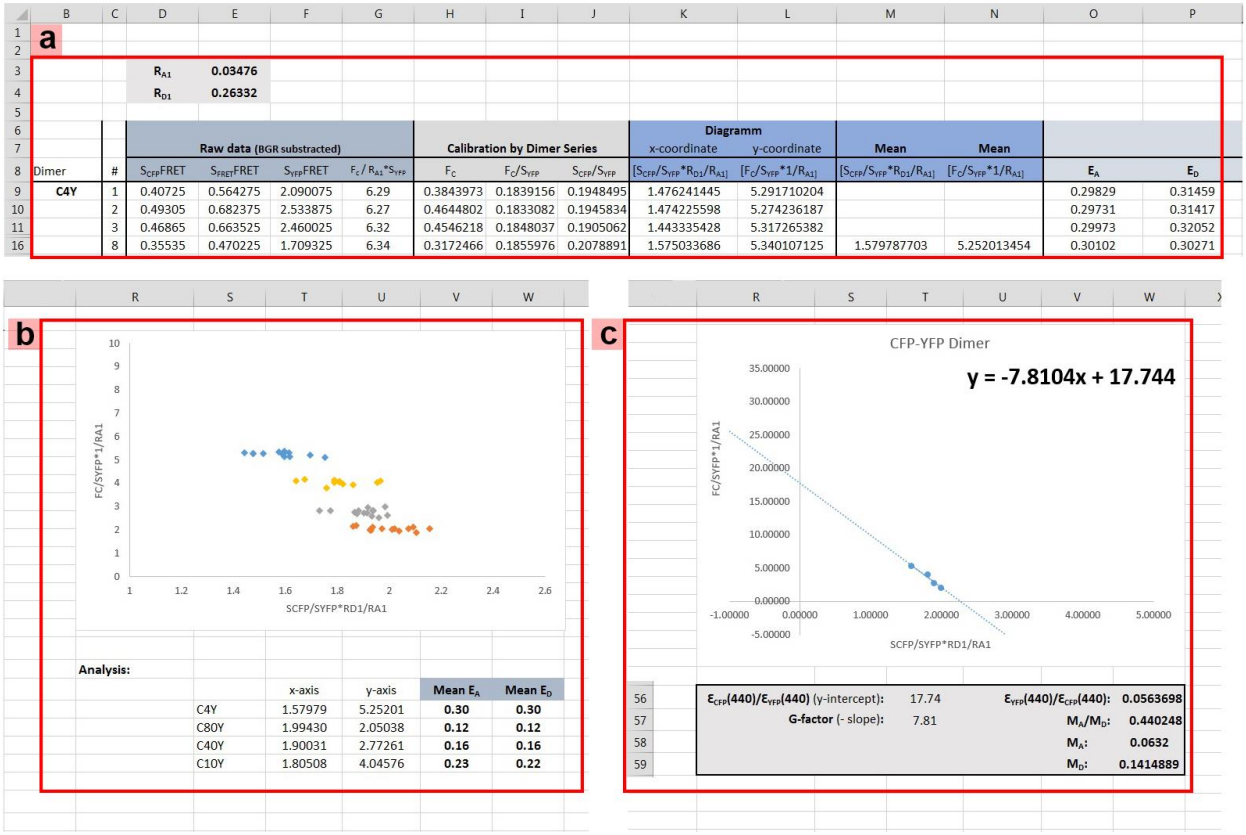

Supplementary Figure 9

Dimer analysis sheet.

(a) Columns D-G list background subtracted raw data from the "Dimer" sheet. Data for individual cells are collected separately for a given dimer as indicated in Column B. R_{A1} and R_{D1} values are automatically transferred from "RD-value (CFP)" and the "RA-value (YFP)" sheets (grey panel on the top, left). Columns H-P comprise calculations as outlined in Procedure Step 97. **(b)** The graph (column K plotted against column L) depicts data points for individual cells. For each dimer, cells cluster together. In the table below, the mean values of E_A and E_D for each dimer as well as mean values of the x- and y- coordinates (from columns M and N) are indicated. **(c)** The latter can be plotted in a new graph and analyzed by a linear regression line. In this template, the regression line is automatically computed and the resulting equation displayed in the graph. Note, that the y-intercept and the slope of this line is copied to cell T56 and T57 respectively for further analysis.

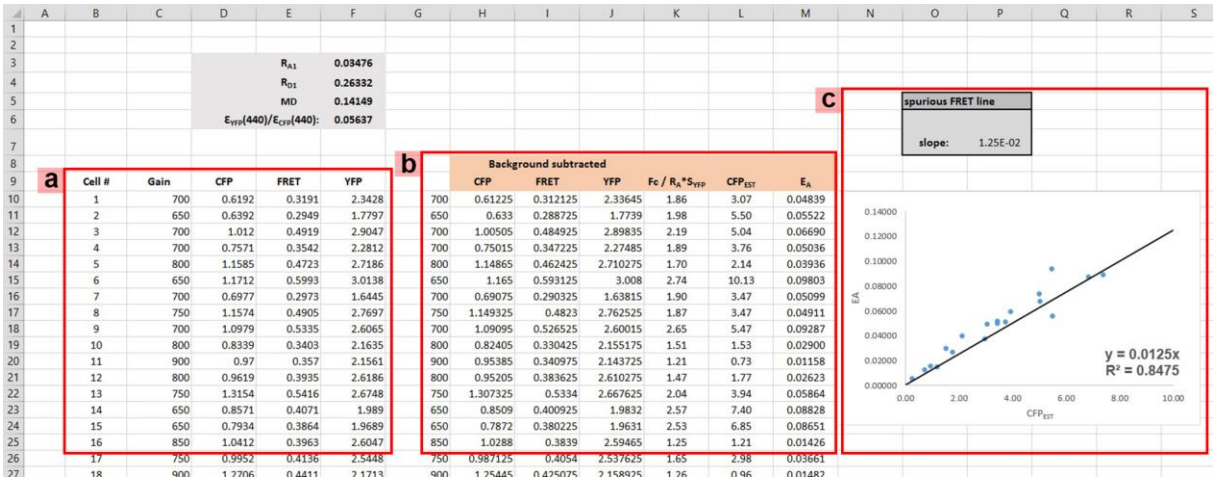

Supplementary Figure 10

Data input field of the "*Spurious FRET*" sheet.

(a) Raw data from cells expressing untagged eCFP and eYFP are transferred to respective cells in Columns C-G. **(b)** Background-subtraction as well as subsequent calculation of $F_c/(R_{A1}*S_{YFP})$, CFP_{EST} and E_A (columns K-M) is automatically performed referring to the constants in the gray panel at the upper left. **(c)** The graph at the right hand side, illustrates CFP_{EST} as a function of E_A. The slope of the regression line is used for spurious FRET correction in the "BC analysis sheet". The equation of the regression line is automatically displayed in the graph. The slope is subsequently entered into cell "P7" linked to the "*BC analysis*" sheet.

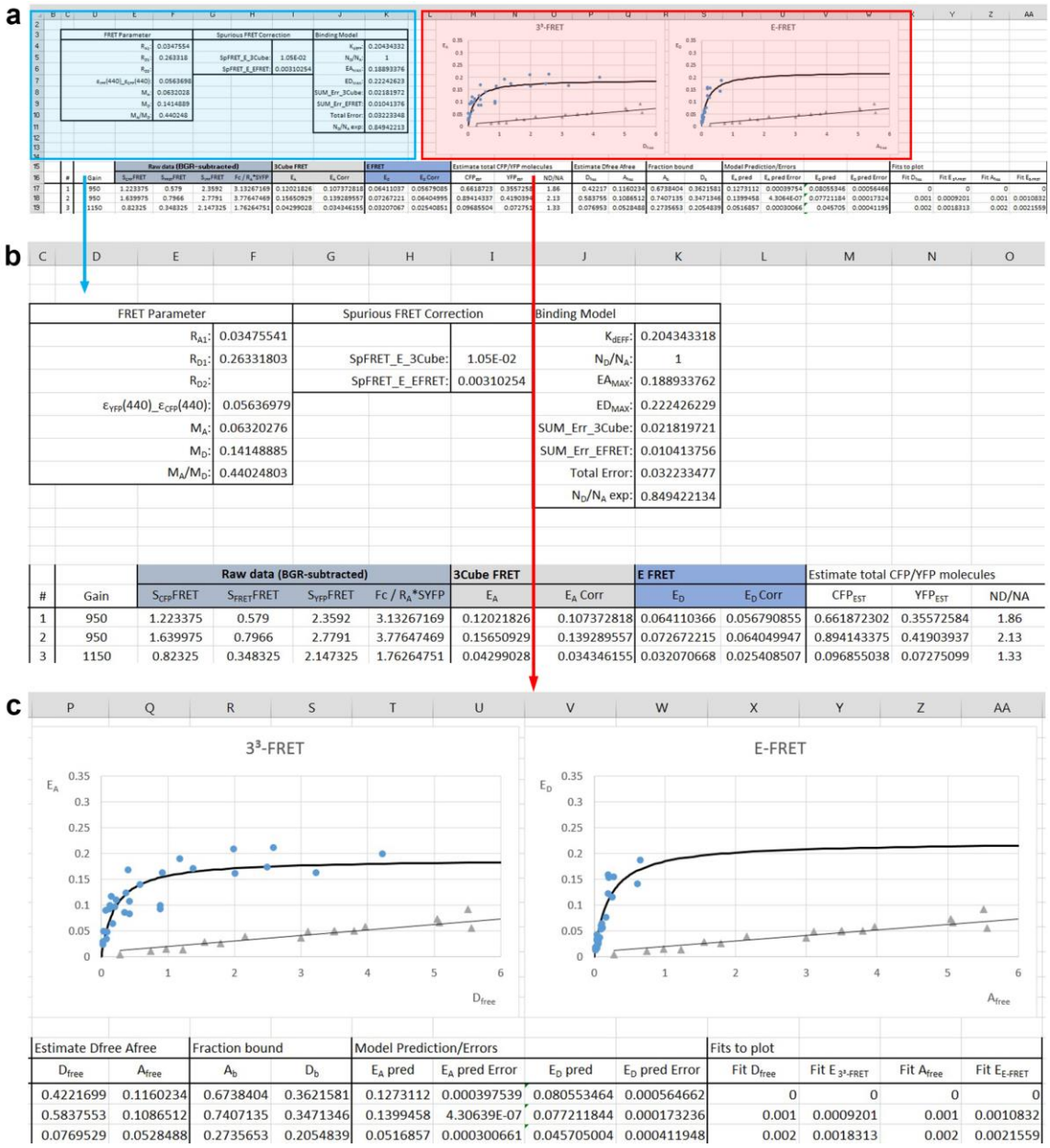

FRET Parameter		Spurious FRET Correction		Binding Model	
R_{A1}:	0.03475541			K_{dEFF}:	0.204343318
R_{D1}:	0.26331803	SpFRET_E_3Cube:	1.05E-02	N_D/N_A:	1
R_{D2}:		SpFRET_E_EFRET:	0.00310254	EA_{MAX}:	0.188933762
$\varepsilon_{YFP}(440)\_\varepsilon_{CFP}(440)$:	0.05636979			ED_{MAX}:	0.222426229
M_A:	0.06320276			SUM_Err_3Cube:	0.021819721
M_D:	0.14148885			SUM_Err_EFRET:	0.010413756
M_A/M_D:	0.44024803			Total Error:	0.032233477
				N_D/N_A exp:	0.849422134

		Raw data (BGR-subtracted)				3Cube FRET		E FRET		Estimate total CFP/YFP molecules		
#	Gain	S_{CFP}FRET	S_{FRET}FRET	S_{YFP}FRET	Fc / R_A*SYFP	E_A	E_A Corr	E_D	E_D Corr	CFP_{EST}	YFP_{EST}	ND/NA
1	950	1.223375	0.579	2.3592	3.13267169	0.12021826	0.107372818	0.064110366	0.056790855	0.661872302	0.35572584	1.86
2	950	1.639975	0.7966	2.7791	3.77647469	0.15650929	0.139289557	0.072672215	0.064049947	0.894143375	0.41903937	2.13
3	1150	0.82325	0.348325	2.147325	1.76264751	0.04299028	0.034346155	0.032070668	0.025408507	0.096855038	0.07275099	1.33

Estimate Dfree Afree		Fraction bound		Model Prediction/Errors				Fits to plot			
D_{free}	A_{free}	A_b	D_b	E_A pred	E_A pred Error	E_D pred	E_D pred Error	Fit D_{free}	Fit $E_{3^3\text{-FRET}}$	Fit A_{free}	Fit $E_{E\text{-FRET}}$
0.4221699	0.1160234	0.6738404	0.3621581	0.1273112	0.000397539	0.080553464	0.000564662	0	0	0	0
0.5837553	0.1086512	0.7407135	0.3471346	0.1399458	4.30639E-07	0.077211844	0.000173236	0.001	0.0009201	0.001	0.0010832
0.0769529	0.0528488	0.2735653	0.2054839	0.0516857	0.000300661	0.045705004	0.000411948	0.002	0.0018313	0.002	0.0021559

Supplementary Figure 11

Data input field of the binding curve analysis ("*BC analysis*") sheet.

(a) Background subtracted raw data (columns D-H) are automatically adopted from the "Samples" sheet. The principal calculation steps required in order to solve binding curves are automatically performed in columns I-W for each (biological) cell according Steps 117-130 outlined in the Procedure section. **(b)** The table in the upper left of the worksheet contains all parameters (columns F and I) necessary to correct for spectral properties and spurious FRET. Thereby, all values except the excitation ratio ($\varepsilon_{YFP}(440)/\varepsilon_{CFP}(440)$) are automatically transferred from previously analyzed sheets. Values for K_{dEff}, E_{Amax} and E_{Dmax} (Column K) are place holders that are adjusted during the fitting procedure. **(c)** Graphs shown displays data points for individual biological cells (blue dots) and the fitted binding isotherme (black lines). The graphs represent data for 3^3-FRET (D_{free} plotted against E_A) and E-FRET (A_{free} plotted against E_D) and allow a control of the fitting procedure.

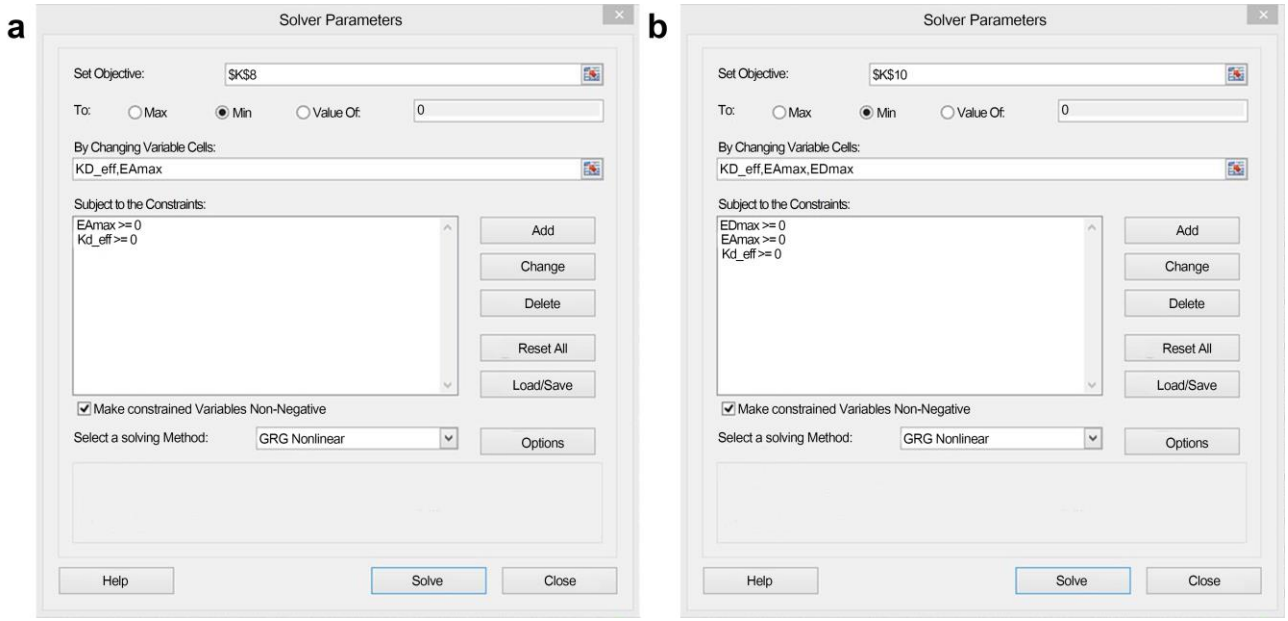

Supplementary Figure 12

Setting up Excel Solver for optimizing 3^3-FRET and E-FRET binding parameters.

(a) Least squares optimization of Cell K8 (*Sum_Err_3Cube*) by changing both KD_eff ($K_{D,EFF}$, relative affinity) and EAmax ($E_{A,max}$, maximum 3^3-FRET efficiency). In this scenario, two constraints are EAmax>0, and Kd_eff>0 in accordance with physical principles. **(b)** Least squares optimization of Cell K10 (*Total Error*) by changing both KD_eff ($K_{D,EFF}$, relative affinity), EAmax ($E_{A,max}$, maximum 3^3-FRET efficiency), and EDmax ($E_{D,max}$, maximum E-FRET efficiency). Three constraints are imposed: EDmax>0, EAmax>0, and Kd_eff>0.

Supplementary Note 1 | Theoretical calculation of M_D and M_A

The microscope specific calibration coefficients M_D and M_A correspond to the effective brightness of a single donor or acceptor molecule when observed through the FRET cube. Accordingly,

$$M_D = [\varepsilon_{CFP}]_{430\le\lambda\le450} \cdot [f_{CFP}]_{505\le\lambda\le575} \cdot QY_{CFP}$$

$$M_A = [\varepsilon_{YFP}]_{430\le\lambda\le450} \cdot [f_{YFP}]_{505\le\lambda\le575} \cdot QY_{YFP}$$

For the computation of these constants, spectra of CFP and YFP, the intensity profile of the xenon lamp as well as the transmission rates of the FRET filter cube provided in sheets 1-6 (Supplementary Data 1) are used. In this section, it is described how to use the FRET Excel spreadsheet to calculate M_D and M_A.

The Excel spreadsheet for theoretical calculation of M_D and M_A is composed of eight different worksheets (Supplementary Data 1). To activate these worksheets eight different tabs are present on the bottom of the excel sheet. In the input worksheets raw data are collected for the excitation and emission spectra of CFP and YFP (Sheet 1; labeled "1 ECFP Excitation Spectrum"; Sheet 2, labeled "2 ECFP Emission Spectrum"; Sheet 3 "3 EYFP Excitation Spectrum" and Sheet 4, labeled "4 EYFP Emission Spectrum"). The spectra of the fluorophores are experimentally determined from suspended HEK293 cells expressing ECFP and EYFP. The spectrum of the xenon arc lamp is deposited in Sheet 5 (labeled "5 Lamp profile"). The transmission spectrum of the emission filter and the excitation filter as well as the transmission and reflection spectrum of the dichroic mirror (all for the FRET filter cube) are collected in Sheet 6 (labeled "6 FRET Filter Cube"). Based on the data deposited in sheets 1-6, M_D and M_A are theoretically calculated in Sheet 7 (labeled "7 Calculation MD (CFP)") and Sheet 8 (labeled "8 Calculation MA (YFP)"), respectively

1 | In the Worksheet "1 ECFP Excitation Spectrum", the wavelength and intensity raw data of the CFP excitation spectrum are given in column A and B respectively. Table 1 is present in sheet 1-4 and is taken from (Patterson et al., 2001). In column C, the maximum peak (at 437 nm) of the excitation spectrum of CFP is scaled to the maximal molecular extinction coefficient for CFP ($\varepsilon_{max} = 26000 M^{-1}cm^{-1}$; red box in Table 1). In addition, the maximal peak of the CFP excitation spectrum is normalized to 1 (Column D). Values in Column D are transferred to sheet 7 (labeled "7 Calculation MD (CFP)"), column E.

2 | Worksheet "2 ECFP Emission Spectrum" contains raw fluorescence intensity data for CFP emission (Column B) for wavelengths ranging from 420nm – 600nm (Column A). Col D contains the CFP emission spectrum from column B and scaled to a maximum value of 1 at wavelength 475nm. The normalized spectrum is copied to column O of sheet 7. Col C contains the emission spectrum of CFP taken from column D and scaled in such a way that the integral equals the quantum yield of CFP (QY_{CFP} = 0.4; (Patterson et al., 2001)). This is done by integrating the normalized spectrum from Column D over the entire range of wave lengths yielding the value of 65.11. The value of the integral is deposited in the table of sheet 7 (Cell

Nature Protocols: doi:10.1038/nprot.2016.128

D4). The integral is then used to normalize the emission spectrum by dividing the entire spectrum by 65.11 and multiplying by the quantum yield of CFP (0.4; Column C).

3 | In the Worksheet "3 EYFP Excitation Spectrum", the wavelength and intensity raw data of the YFP excitation spectrum are given in column A and B respectively. In column C, the maximum peak of the excitation spectrum of YFP is scaled to the maximal molecular extinction coefficient for YFP ($\varepsilon_{\max} = 84000 M^{-1} cm^{-1}$; red box in Table 1). In addition, the maximal peak of the YFP excitation spectrum is normalize to 1 (Column D). Column D is transferred to sheet 8 (labeled "8 Calculation MA", column E).

4 | Worksheet "4 EYFP Emission Spectrum" contains raw fluorescence intensity data for YFP emission (Column B) for wavelengths ranging from 400nm – 700nm (Column A). Column D contains the YFP emission spectrum from column B and scaled to a maximum value of 1 at a wavelength of 527nm. The normalized spectrum is copied to column O of Sheet 8 ("8 Calculation MA"). Column C contains the emission spectrum of YFP taken from column D and scaled in such a way that the integral equals the quantum yield of YFP (QY_{CFP} = 0.61). This is done by integrating the normalized spectrum from Column D over the entire range of wave lengths yielding the value of 39.53. The value of the integral is deposited the table of sheet 8 (Cell D4). The integral is then used to normalize the emission spectrum by dividing the entire spectrum by 39.53 and multiplying by the quantum yield of YFP (0.61; Column C).

5 | In the worksheet "5 lamp profile" the wavelength and intensity raw data of the intensity spectrum of the excitation arc lamp are given in column A and B respectively. Column C contains the spectrum from column B normalized to a peak value of 1. Column C is transferred to column B in sheets 7 and 8.

6 | In worksheet "6 FRET filter cube" the wavelength (Column A) and intensity raw data of the transmission spectrum of the excitation filter (Column B), the emission filter (Column C) and the dichroic mirror (Column D) for the FRET cube are given. The reflection spectrum of the dichroic mirror is presented in column E. The spectra are all transferred to column C (excitation filter), column D (reflection of dichroic), column P (transmission of the dichroic) and column Q (emission filter) in sheets 7 and 8, resp..

7 | The top of sheet 7 contains the extinction coefficient for CFP (Cell D2) which is here $\varepsilon_{max} = 0.26\ \mu M^{-1} dm^{-1}$ (please note that units are different from (Patterson et al., 2001)) and the quantum yield of CFP (Cell D3). The value for the integral of the entire CFP emission spectrum normalized to maximum emission of 1 (Cell D4) is picked from Sheet 2 ("2 ECFP Emission Spectrum", cell D183). In addition, there are 5 place holders (D5-D9) for the excitation integral (D5; Ex integral), the emission integral (D6, Em integral), The M_D (D7) and the M_A value (D8), and the M_A/M_D ratio (D9). The calculation of these five parameters are given below.

8 | The lower part of sheet 7 contains spectral data for the excitation pathway (Column A-F) and the emission pathway (Column N-R). For the excitation pathway the data are the wavelengths (Column A), the intensity spectrum of the xenon arc lamp (Column B), the transmission spectrum of the excitation filter (Column C), the reflection spectrum of the dichroic (Column D)

Nature Protocols: doi:10.1038/nprot.2016.128

and the excitation spectrum for CFP (Column E). The spectra are all taken from sheets 1, 5 and 6 and represent the versions normalized to a maximum of one at the specified wavelength. They are plotted in graph A. Column F is calculated by multiplying together the values contained in column B-E. The result is plotted in graph B. For the emission pathway the data are the wavelengths (Column N), the emission spectrum for CFP (Column O), the transmission spectrum of the dichroic (Column P) and the emission filter (Column Q). The spectra are all taken from sheets 2 and 6 and represent the versions normalized to a maximum of one at the specified wavelength. They are plotted in graph C. Column R is calculated by multiplying together the values contained in columns O-Q. The result is plotted in Graph D.

9 | The excitation integral is calculated by integrating the data contained in Column F (Graph B) and deposited in Cell L7 and D5.

10 | The emission integral is calculated by integrating the data contained in Column R (Graph D) and deposited in Cell W7 and D6.

11 | M_D is calculated by scaling the excitation and emission integral (D5 and D6) by multiplying it by the maximal extinction coefficient (Cell D2) and by dividing it by the integral of the entire emission spectrum (Cell D4) times the quantum yield (Cell D3). The result is deposited in Cell D7.

12 | M_A is picked from cell D7 in sheet 8.

13 | M_A/M_D is calculated by dividing Cell D8 by Cell D7 and deposited in Cell D9.

14 | Sheet 8 ("8 Calculation MA") has an analogous design as Sheet 7. However, it contains spectral properties that are specific for YFP. The top of Sheet 8 contains the extinction coefficient for YFP (Cell D2) which is $\varepsilon_{max} = 0.84\ \mu M^{-1} dm^{-1}$ (please note that units are different from (Patterson et al., 2001)) and the quantum yield of YFP (Cell D3) picked from Table 1. The value for the integral of the entire YFP emission spectrum normalized to maximum emission of 1 (Cell D4) is picked from Sheet 4 ("4 EYFP Emission Spectrum", cell D134). In addition, there are 3 place holders (D5-D7) for the excitation integral (Cell D5; Ex integral), the emission integral (D6, Em integral) and the M_A value (D7). Excitation and emission spectra for YFP are deposited in columns E and O, respectively. The calculation of the values for the excitation integral and emission integral and the graphs are analogous as described for CFP.

Note that both M_A and M_D are independent of I_o, the overall intensity of the arc lamp, and the constant C that accounts for optical transmission properties of the microscope other than the filter cubes. For our setup, the calculated values are $M_A = 0.6320$ and $M_D = 0.14149$.

References

Patterson G, Day RN, Piston D (2001) Fluorescent protein spectra. J Cell Sci 114:837-838.

Nature Protocols: doi:10.1038/nprot.2016.128

Supplementary Note 2 | Determination of 3^3-FRET and E-FRET efficiencies

The experimental determination of 3^3-FRET and E-FRET efficiencies depend on the robust measurement of fluorescence intensities using three filter cubes as summarized in Box 1. Here, we present a formalism to model the fluorescence output from a single cell expressing two types of fluorophores, a donor assumed to be the cyan fluorescent protein (CFP) and an acceptor assumed to be the yellow fluorescent protein (YFP). In the dark, all fluorophores are assumed to be in their ground state (D, donor and A, acceptor) and upon photoexcitation convert to an excited state (D^* and A^*). Relaxation from the excited state results in the release of a photon. Each cell is assumed to contain N_D total donor molecules and N_A total acceptor molecules (**Supplementary Note 2 Fig. 1a**). Moreover, the fraction of donor molecules bound to an acceptor in each cell is given by D_b, and the fraction of acceptor molecules bound to a donor is given by A_b. Only the bound fraction of fluorophores is able to undergo FRET. The epifluorescence microscope setup measures the total fluorescence intensity from single cells using three filter cubes: the CFP cube (**Supplementary Note 2 Fig. 1b**), the YFP cube (**Supplementary Note 2 Fig. 1c**), and the FRET cube (**Supplementary Note 2 Fig. 1d**). There are two key sets of microscope specific parameters to define: (1) the wavelength-specific propensity of the excitation subsystem to excite a given fluorophore and (2) the wavelength-specific efficacy of the detection subsystem to detect the emitted photons.

First, we consider the propensity of a given fluorophore to be excited using the given microscope setup. For any filter cube x, the excitation rate (in units of transitions per second) of a single ground-state fluorophore is given by $I_0 \cdot G_x(y, \lambda_{ex,x})$. The variable I_0 denotes the intensity of the light emitted by the arclamp, y specifies the type fluorophore we are concerned with (either D or A), and $\lambda_{ex,x}$ denotes the particular wavelength of the excitation light used to excite the fluorophore. Notice that $G_x(D, \lambda_{ex,x})$ is a constant that incorporates the spectral properties of the lamp, optical properties of the excitation filter and dichroic mirror of the cube x, and the wavelength-dependent absorption properties of the fluorophore given by its molar extinction coefficient $\varepsilon_x(\lambda)$. For example, for the CFP cube $I_0 \cdot G_{CFP}(D, \lambda_{ex,CFP})$ signifies the rate of excitation for a single CFP fluorophore given the properties of the CFP filter cube.

Second, we introduce the term $F_x(y, \lambda_{em,x})$ to denote the fluorescence output of the photomultiplier tube (PMT) in response to photons emitted by the fluorophore y when measured using the filter cube x. Here, $F_x(y, \lambda_{em,x})$ is a constant that incorporates the emission spectrum of fluorophore within the wavelength limits specified by $\lambda_{em,x}$, the optical properties of the dichroic mirror and the emission filter of cube x, and the spectral response properties of the PMT detector. For example, $F_{CFP}(D, \lambda_{em,CFP})$ corresponds to the output transfer function for photons emitted from a single donor molecule (D) measured using the CFP cube. Figure Sxb-d provides a visual representation of these instrument specific constants. We now develop an explicit model for the donor and acceptor fluorescence output as a result of direct excitation or through FRET.

Nature Protocols: doi:10.1038/nprot.2016.128

Direct excitation of acceptor molecules

To deduce the fluorescence output of acceptor molecules when evaluated through the YFP cube, we consider the $YFP_X(\lambda_{ex,x}, \lambda_{em,x}, \text{direct})$ branch (pathway 3) of the state transition diagram shown in Fig. Sxe. The probability that an acceptor molecule is in the excited state is given by,

$$\frac{dP_A^*}{dt} = I_0 G_x(A, \lambda_{ex,x}) P_A - (k_A + k_{A,nr}) P_A^* \tag{S1.1}$$

In general, for the purposes of fluorescence measurements, the typical data acquisition times (several milliseconds) are substantially longer than the characteristic fluorescence relaxation time (several nanoseconds) such that the system could be assumed to have reached steady state. Moreover, in typical FRET experiments, the excitation power used is sufficiently low that there is minimal ground state depletion for either A fluorophores ($P_A \sim 1$). This assumption could be experimentally verified by testing for linearity of fluorescence output with respect to the excitation light intensity. Thus, the steady-state probability of an acceptor molecule occupying the excited state follows the relation,

$$\frac{dP_A^*}{dt} = 0 \Rightarrow P_A^* = \frac{I_0 G_x(A, \lambda_{ex,x})}{(k_A + k_{A,nr})} \tag{S1.2}$$

Next, we consider the emission-detection subsystem to estimate the rate of emission of photons from an excited acceptor and the efficacy by which such photons are detected. The rate of excited acceptor relaxations that result in the emission of a photon is given by $k_A P_A^*$. Thus, the total fluorescence output by all acceptor molecules in a cell is given by,

$$N_A \cdot k_A \cdot P_A^* \cdot \hat{F}_X(A, \lambda_{em,x}) \tag{S1.3}$$

Substituting S1.2 into S1.3 and exploting the fact the quantum yield of the acceptor is given by,

$$QY_A = \frac{k_A}{k_A + k_{A,nr}}$$

yields the relation,

$$YFP_x(\lambda_{ex,x}, \lambda_{em,x}, \text{direct}) = N_A \cdot I_0 \cdot G_x(A, \lambda_{ex,x}) \cdot F_X(A, \lambda_{em,x}) \tag{S1.4}$$

Note that the emission transfer function $F_X(A, \lambda_{em,x})$ now incorporates the QY_A of the acceptor, $F_X(A, \lambda_{em,x}) = QY_A \cdot \hat{F}_X(A, \lambda_{em,x})$. Note that this equation specifies the YFP intensity due to direct excitation through any filter cube. For example, the YFP intensity due to direct excitation through YFP cube would be given by, $YFP_{YFP}(505, 535, \text{direct}) = N_A \cdot I_0 \cdot G_{YFP}(A, 505) \cdot F_{YFP}(A, 535)$ Similarly, the YFP intensity due to direct excitation through the FRET cube is given by, $YFP_{FRET}(440, 535, \text{direct}) = N_A \cdot I_0 \cdot G_{FRET}(A, 440) \cdot F_{FRET}(A, 535)$

Nature Protocols: doi:10.1038/nprot.2016.128

Direct excitation of donor molecules

To model the fluorescence emission of donor molecules when evaluated through the CFP cube, we first consider the $CFP_X(\lambda_{ex,x}, \lambda_{em,x}$, direct) branch (pathway 1) of the complete state transition diagram shown in Fig. Sxe. Here, to obtain the total CFP emission due to direct excitation, we must consider two populations of CFP molecules: (1) the fraction of free donor molecules and (2) the fraction of donor molecules bound to an acceptor. As with acceptor molecule, we assume a low excitation limit such that there is minimal ground state depletion for donor (D) fluorophores ($P_D \sim 1$). Thus, for free donor molecules, the steady-state probability of occupying the excited state follows the relation,

$$\left.\frac{dP_D^*}{dt} = I_0 G_x(D,\lambda_{ex,x}) P_D - (k_D + k_{D,nr}) P_D^* \right\} \Rightarrow P_D^* = \frac{I_0 G_x(D,\lambda_{ex,x})}{(k_D + k_{D,nr})} \qquad \text{(pathway 1)} \qquad \text{(S1.5)}$$

However, as donor molecules bound to an acceptor can de-excite through FRET, the probability that such fluorophores are excited is governed by the equation,

$$\left.\frac{dP_D^*}{dt} = I_0 G_D(\lambda_{ex,x}) P_D - (k_D + k_{D,nr}) P_D^* = 0 \right\} \Rightarrow P_D^* = \frac{I_0 G_D(\lambda_{ex,x})}{(k_D + k_{D,nr})} \qquad \text{(pathway 2)} \qquad \text{(S1.6)}$$

$$\left.\frac{dP_D^*}{dt} = I_0 G_x(D,\lambda_{ex,x}) P_D - (k_D + k_{D,nr} + k_T) P_D^* \right\} \Rightarrow P_D^* = \frac{I_0 G_x(D,\lambda_{ex,x})}{(k_D + k_{D,nr} + k_T)}$$

Next, we consider the emission-detection subsystem to estimate the rate of emission of photons from an excited donor and the efficacy by which such photons are detected. The rate of excited donor relaxations that result in the emission of a photon is in general given by $k_D P_D^*$. Thus, the total fluorescence output by both free and bound donor molecules is given by,

$$N_D \cdot (1 - D_b) \cdot \frac{I_0 G_D(\lambda_{ex,x})}{(k_D + k_{D,nr})} \cdot k_D \cdot \hat{F}_X(D,\lambda_{em,x}) + N_D \cdot D_b \cdot \frac{I_0 G_x(D,\lambda_{ex,x})}{(k_D + k_{D,nr} + k_T)} \cdot k_D \cdot \hat{F}_X(D,\lambda_{em,x}) \qquad \text{(S1.7)}$$

Given that the quantum yield of the donor fluorophore is given by,

$$QY_D = \frac{k_D}{k_D + k_{D,nr}}$$

and by defining $F_X(D,\lambda_{em,x}) = QY_D \cdot \hat{F}_X(D,\lambda_{em,x})$, Eq. S1.7 simplifies to yield the equation,

$$CFP_x(\lambda_{ex,x}, \lambda_{em,x}, \text{direct}) = N_D \cdot I_0 \cdot G_x(D,\lambda_{ex,x}) \cdot F_X(D,\lambda_{em,x}) \cdot \left((1 - D_b) + D_b \frac{(k_D + k_{D,nr})}{(k_D + k_{D,nr} + k_T)} \right) \qquad \text{(S1.8)}$$

Nature Protocols: doi:10.1038/nprot.2016.128

Excitation of acceptor molecules as a result of FRET

The third key quantity of concern is YFP fluorescence output as a result of excitation by FRET or the $YFP_x(\lambda_{ex,x}, \lambda_{em,x}, \text{FRET})$ branch (pathway 2) of the complete state transition diagram in Fig Sxe. In order for YFP molecules to be excited by FRET, they have to be associated with CFP molecules. Moreover, as before we assume 'low-exciation limit' ($P_D \sim 1$, $P_A \sim 1$) and that the data acquisition time is long enough for the system to reach steady-state. First, we consider the probability of exciting a donor molecule,

$$\left.\frac{dP_D^*}{dt} = I_0 G_x(D, \lambda_{ex,x}) P_D - (k_D + k_{D,nr} + k_T) P_D^*\right\} \Rightarrow P_D^* = \frac{I_0 G_x(D, \lambda_{ex,x})}{(k_D + k_{D,nr} + k_T)} \quad \text{(S1.9)}$$

Next, we consider the rate of excitation of the bound acceptor molecule. At steady state,

$$\left.\frac{dP_A^*}{dt} = k_T P_D^* \cdot P_A - (k_A + k_{A,nr}) P_A^*\right\} \Rightarrow P_A^* = \frac{k_T}{(k_A + k_{A,nr})} P_D^* \quad \text{(S1.10)}$$

Substituting Eq. S1.9 in S1.10 yields,

$$P_A^* = \frac{1}{(k_A + k_{A,nr})} \frac{k_T}{(k_D + k_{D,nr} + k_T)} I_0 G_x(D, \lambda_{ex,x}) \quad \text{(S1.11)}$$

Next, we consider the emission-detection subsystem to estimate the rate of emission of photons from an excited acceptor and the efficacy by which such photons are detected. The rate of excited acceptor relaxations that result in the emission of a photon is in general given by $k_A P_A^*$. Thus, the total fluorescence output by YFP molecules excited by FRET is given by,

$$\begin{aligned} &N_D \cdot D_b \cdot P_A^* \cdot k_A \cdot \hat{F}_X(A, \lambda_{em,x}) \\ &= N_D \cdot D_b \cdot \frac{1}{(k_A + k_{A,nr})} \frac{k_T}{(k_D + k_{D,nr} + k_T)} I_0 \cdot G_x(D, \lambda_{ex,x}) \cdot k_A \cdot \hat{F}_X(A, \lambda_{em,x}) \end{aligned} \quad \text{(S1.12)}$$

Importantly, the total number of bound complexes is given by $N_D \cdot D_b = N_A \cdot A_b$. Moreover, the output transfer function is also defined as $F_X(A, \lambda_{em,x}) = QY_A \cdot \hat{F}_X(A, \lambda_{em,x})$. Substituting these identities into S1.12 yields,

$$YFP_x(\lambda_{ex,x}, \lambda_{em,x}, \text{FRET}) = N_A \cdot A_b \cdot \frac{k_T}{(k_D + k_{D,nr} + k_T)} I_0 \cdot G_x(D, \lambda_{ex,x}) \cdot F_X(A, \lambda_{em,x}) \quad \text{(S1.13)}$$

Equations S1.4, S1.8, and S1.13 form three master equations that could be used to deduce either the 3^3-FRET efficiency or the E-FRET efficiency as outlined in subsequent section.

Deducing 3^3-FRET efficiency

The 3^3-FRET efficiency measures sensitized emission or the fractional increase in acceptor intensity due to FRET. The term sensitized emission in Box 1 Eq. 5 corresponds to $YFP_x(\lambda_{ex,x}, \lambda_{em,x}, \text{FRET})$. Thus,

$$E_A = \frac{YFP_x(\lambda_{ex,x}, \lambda_{em,x}, \text{FRET})}{YFP_x(\lambda_{ex,x}, \lambda_{em,x}, \text{direct})} \cdot \frac{G_x(A, \lambda_{ex,x})}{G_x(D, \lambda_{ex,x})} \quad \text{(S1.14)}$$

Nature Protocols: doi:10.1038/nprot.2016.128

Notice, the factor $G_A(\lambda_{ex,x})/G_D(\lambda_{ex,x})$ is an instrument specific parameter that normalizes for the differences in the propensity for the donor and acceptor to absorb light. Substituting Eq. S1.13 and S1.4 into S1.14 yields,

$$E_A = \frac{N_A \cdot A_b \cdot \frac{k_T}{(k_D + k_{D,nr} + k_T)} I_0 \cdot G_x(D, \lambda_{ex,x}) \cdot F_X(A, \lambda_{em,x})}{N_A \cdot I_0 \cdot G_x(A, \lambda_{ex,x}) \cdot F_X(A, \lambda_{em,x})} \cdot \frac{G_x(A, \lambda_{ex,x})}{G_x(D, \lambda_{ex,x})} \quad \text{(S1.14)}$$

Simplifying this relation yields,

$$E_A = \frac{k_T}{(k_D + k_{D,nr} + k_T)} A_b = E \cdot A_b \quad \text{(S1.15)}$$

Thus, the apparent 3^3-FRET efficiency is the true FRET efficiency multiplied by the fraction of acceptor molecules that are bound. The experimental strategy to unscramble the parameter $YFP_x(\lambda_{ex,x}, \lambda_{em,x}, FRET)$ from corrupting factors is described in Box 1.

Nature Protocols: doi:10.1038/nprot.2016.128

Deducing E-FRET efficiency

E-FRET is a donor centric measure that estimates the fractional quenching of donor fluorescence due to FRET. Thus, the E-FRET efficiency corresponds to

$$E_{\mathrm{D}} = \frac{CFP_{\mathrm{FRET|after}} - CFP_{\mathrm{FRET|before}}}{CFP_{\mathrm{FRET|after}}} \tag{S1.16}$$

where $CFP_{\mathrm{FRET|before}}$ is the quenched CFP fluorescence intensity before acceptor molecules are photobleached and $CFP_{\mathrm{FRET|after}}$ is the intensity after all acceptor molecules are photobleached.

Importantly, $CFP_{\mathrm{FRET|after}}$ is an indirect measure that corresponds to the modified state transition diagram shown in Fig. 1f. For this modified system,

$$\left.\frac{dP_D^*}{dt} = I_0 G_{\mathrm{x}}(D,\lambda_{\mathrm{ex,x}})P_D - (k_{\mathrm{D}} + k_{\mathrm{D,nr}})P_D^*\right\} \Rightarrow P_D^* = \frac{I_0 G_{\mathrm{x}}(D,\lambda_{\mathrm{ex,x}})}{(k_{\mathrm{D}} + k_{\mathrm{D,nr}})} \tag{S1.17}$$

The fluorescence output for a single donor fluorophore would be proportional to $k_{\mathrm{D}}P_D^*$ the rate of excited donor relaxations that result in the emission of a photon. Accordingly, the total fluorescence output of $CFP_{\mathrm{FRET|after}}$ is given by,

$$CFP_{\mathrm{FRET|after}} = N_D \cdot P_{\mathrm{D}}^* \cdot k_D \cdot \hat{F}_{\mathrm{X}}(D,\lambda_{\mathrm{em,x}}) = N_D \cdot \frac{I_0 G_{\mathrm{x}}(D,\lambda_{\mathrm{ex,x}})}{(k_{\mathrm{D}} + k_{\mathrm{D,nr}})} \cdot k_D \cdot \hat{F}_{\mathrm{X}}(D,\lambda_{\mathrm{em,x}}) \tag{S1.18}$$

Utilizing the fact that $F_{\mathrm{X}}(D,\lambda_{\mathrm{em,x}}) = QY_{\mathrm{D}} \cdot \hat{F}_{\mathrm{X}}(D,\lambda_{\mathrm{em,x}})$, Eq. S1.17 simplifies to

$$CFP_{\mathrm{FRET|after}} = N_D \cdot I_0 \cdot G_{\mathrm{x}}(D,\lambda_{\mathrm{ex,x}}) \cdot F_{\mathrm{X}}(D,\lambda_{\mathrm{em,x}}) \tag{S1.19}$$

By contrast, $CFP_{\mathrm{FRET|before}}$ is a direct measure that corresponds to $\mathrm{CFP_X}(\lambda_{\mathrm{ex,x}}, \lambda_{\mathrm{em,x}}, \mathrm{direct})$ branch of state transition diagram in Fig. S1e. To relate $CFP_{\mathrm{FRET|after}}$ with $CFP_{\mathrm{FRET|before}}$, we reconsider Eq. S1.8,

$$\begin{aligned} CFP_{\mathrm{x}}(\lambda_{\mathrm{ex,x}},\lambda_{\mathrm{em,x}},\mathrm{direct}) &= N_D \cdot I_0 \cdot G_{\mathrm{x}}(D,\lambda_{\mathrm{ex,x}}) \cdot F_{\mathrm{X}}(D,\lambda_{\mathrm{em,x}}) \cdot \left((1-D_{\mathrm{b}}) + D_{\mathrm{b}} \frac{(k_{\mathrm{D}} + k_{\mathrm{D,nr}})}{(k_{\mathrm{D}} + k_{\mathrm{D,nr}} + k_{\mathrm{T}})} \right) \\ &= N_D \cdot I_0 \cdot G_{\mathrm{x}}(D,\lambda_{\mathrm{ex,x}}) \cdot F_{\mathrm{X}}(D,\lambda_{\mathrm{em,x}}) \cdot \left((1-D_{\mathrm{b}}) + D_{\mathrm{b}} \left(1 - \frac{k_{\mathrm{T}}}{(k_{\mathrm{D}} + k_{\mathrm{D,nr}} + k_{\mathrm{T}})} \right) \right) \end{aligned}$$

Simplifying this relation, we obtain

$$\begin{aligned} CFP_{\mathrm{x}}(\lambda_{\mathrm{ex,x}},\lambda_{\mathrm{em,x}},\mathrm{direct}) &= N_D \cdot I_0 \cdot G_{\mathrm{x}}(D,\lambda_{\mathrm{ex,x}}) \cdot F_{\mathrm{X}}(D,\lambda_{\mathrm{em,x}}) \\ &\quad - N_D \cdot I_0 \cdot G_{\mathrm{x}}(D,\lambda_{\mathrm{ex,x}}) \cdot F_{\mathrm{X}}(D,\lambda_{\mathrm{em,x}}) \cdot D_{\mathrm{b}} \cdot \frac{k_{\mathrm{T}}}{(k_{\mathrm{D}} + k_{\mathrm{D,nr}} + k_{\mathrm{T}})} \end{aligned} \tag{S1.20}$$

Substituting Eq. S1.19 to S1.20 yields,

$$\begin{aligned} CFP_{\mathrm{x}}(\lambda_{\mathrm{ex,x}},\lambda_{\mathrm{em,x}},\mathrm{direct}) &= CFP_{\mathrm{FRET|after}} \\ &\quad - N_D \cdot I_0 \cdot G_{\mathrm{x}}(D,\lambda_{\mathrm{ex,x}}) \cdot F_{\mathrm{X}}(D,\lambda_{\mathrm{em,x}}) \cdot D_{\mathrm{b}} \cdot \frac{k_{\mathrm{T}}}{(k_{\mathrm{D}} + k_{\mathrm{D,nr}} + k_{\mathrm{T}})} \end{aligned} \tag{S1.21}$$

Nature Protocols: doi:10.1038/nprot.2016.128

Also recall that the total number of bound complexes must be the same, therefore $N_D \cdot D_b = N_A \cdot A_b$. Thus,

$$CFP_x(\lambda_{ex,x}, \lambda_{em,x}, \text{direct}) = CFP_{FRET|after} - N_A \cdot A_b \cdot I_0 \cdot G_x(D, \lambda_{ex,x}) \cdot F_X(D, \lambda_{em,x}) \cdot \frac{k_T}{(k_D + k_{D,nr} + k_T)} \quad \text{(S1.22)}$$

Now, substituting S1.13 into Eq. S1.22 yields,

$$\begin{aligned} CFP_{FRET|before} &= CFP_x(\lambda_{ex,x}, \lambda_{em,x}, \text{direct}) \\ &= CFP_{FRET|after} - YFP_x(\lambda_{ex,x}, \lambda_{em,x}, FRET) \cdot \frac{F_X(D, \lambda_{em,x})}{F_X(A, \lambda_{em,x})} \end{aligned} \quad \text{(S1.23)}$$

Rearranging this equation yields,

$$CFP_{FRET|after} = CFP_{FRET|before} + YFP_x(\lambda_{ex,x}, \lambda_{em,x}, FRET) \cdot \frac{F_X(D, \lambda_{em,x})}{F_X(A, \lambda_{em,x})} \quad \text{(S1.24)}$$

Importantly, Eq. S1.24 confirms the intuition that CFP intensity after photobleaching is the sum of the quenched CFP intensity before photobleaching and amount of quenching reported as the sensitized emission corrected for emission properties of YFP molecules versus CFP molecules.

Substituting Eq. S1.24/S1.23 into S1.16, yields

$$E_D = \frac{CFP_{FRET|after} - CFP_{FRET|before}}{CFP_{FRET|after}} = \frac{YFP_x(\lambda_{ex,x}, \lambda_{em,x}, FRET) \cdot \frac{F_X(D, \lambda_{em,x})}{F_X(A, \lambda_{em,x})}}{YFP_x(\lambda_{ex,x}, \lambda_{em,x}, FRET) \cdot \frac{F_X(D, \lambda_{em,x})}{F_X(A, \lambda_{em,x})} + CFP_{FRET|before}}$$

Defining the microscope specific gain factor,

$$G = \frac{F_X(A, \lambda_{em,x})}{F_X(D, \lambda_{em,x})} \quad \text{(S1.25)}$$

yields the E-FRET equation shown in Box 1 Eq. 7,

$$E_D = \frac{YFP_x(\lambda_{ex,x}, \lambda_{em,x}, FRET)}{YFP_x(\lambda_{ex,x}, \lambda_{em,x}, FRET) + CFP_x(\lambda_{ex,x}, \lambda_{em,x}, direct) \cdot G} \quad \text{(S1.26)}$$

To deduce E_D in terms of fundamental parameters in Fig. Sxe, we substitute Eq. S1.13 and Eq S1.8 into Eq. S1.26 and further simplify to obtain,

$$\begin{aligned} E_D &= \frac{N_A \cdot A_b \cdot \frac{k_T}{(k_D + k_{D,nr} + k_T)} I_0 \cdot G_x(D, \lambda_{ex,x}) \cdot F_X(A, \lambda_{em,x})}{N_D \cdot I_0 \cdot G_x(D, \lambda_{ex,x}) \cdot F_X(A, \lambda_{em,x})} \\ &= \frac{N_D \cdot D_b}{N_D} \cdot \frac{k_T}{(k_D + k_{D,nr} + k_T)} = E \cdot D_b \end{aligned} \quad \text{(S1.27)}$$

Nature Protocols: doi:10.1038/nprot.2016.128

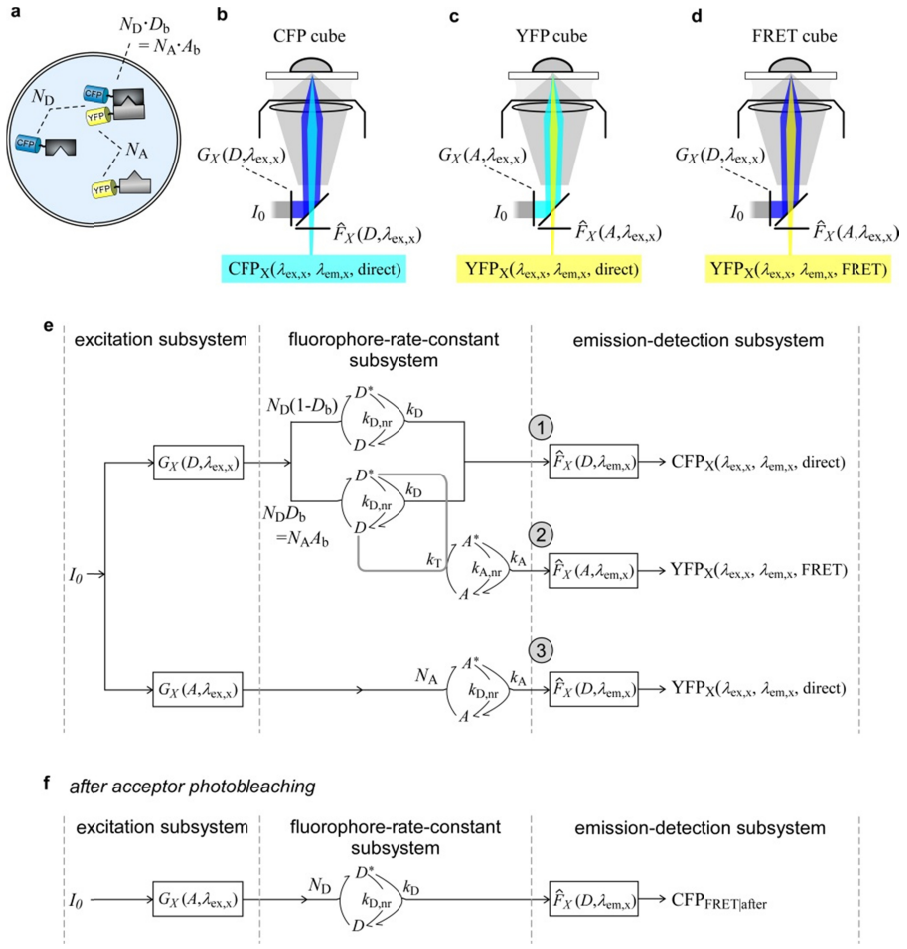

Supplementary Note 2 Figure 1 | Theoretical underpinnings of 3^3-FRET and E-FRET. **(a)** Diagram depicts a single cell containing binding partners tagged to CFP and YFP molecules. N_D corresponds to total number of donor molecules and N_A acceptor molecules. D_b corresponds to the fraction of donor molecule bound and A_b corresponds to fraction of acceptor molecules bound. **(b)** Diagram illustrates the input and output of the CFP cube. $G_X(D,\lambda_{ex,x})$ and $\hat{F}_X(D,\lambda_{ex,x})$ corresponds to microscope specific parameters. **(c – d)** Diagram illustrates input and output of the YFP and FRET cube. **(e)** Complete state transition diagram that specifies fluorescence output essential for computation of 3^3-FRET and E-FRET. **(f)** Diagram illustrates modified state transition diagram if acceptor molecules were photobleached.

Nature Protocols: doi:10.1038/nprot.2016.128

Supplementary Note 3| Determination of binding affinities from FRET measurements

As elaborated in Box 1, the 3^3-FRET and E-FRET efficiencies depend on the fraction of acceptor (A_b) and fraction of donor molecules (D_b) that are bound respectively. Both D_b and A_b in fact depend on the total number of donor and acceptor molecules and relative binding affinity. For typical FRET experiments, we consider a binding interaction with a 1:1 stoichiometry. Moreover, the bound state is assumed to conform to a unique with a characteristic FRET efficiency (E). These assumptions allow for fitting a simple Langmuir isotherm to the experimental data yielding an estimate for the binding affinity. Though more complex binding models can be evaluated using FRET, the increased number of states often implies the lack of a unique solution and multiple parameter sets may fit the data.

Consider the simple 1:1 binding model with dissociation constant K_d,

$$A + D \underset{K_d}{\rightleftharpoons} AD$$

As FRET experiments are typically conducted at steady-state,

$$\frac{[A_{free}][D_{free}]}{[AD]} = K_d \tag{S2.1}$$

Since, the total concentration of acceptor molecules $[A]_T = [A_{free}] + [AD]$, the fraction of bound acceptor molecules is given by,

$$A_b = \frac{[AD]}{[A]_T} = \frac{[AD]}{[A_{free}] + [AD]} = \frac{[D_{free}]}{[D_{free}] + K_d} \tag{S2.2}$$

The 3^3-FRET efficiency is thus,

$$E_A = E_{max} \cdot A_b = E_{max} \cdot \frac{[D_{free}]}{[D_{free}] + K_d} \tag{S2.3}$$

where E_{max} is the FRET efficiency when all acceptor molecules are bound.

Similarly, since the total concentration of donor molecules $[D]_T = [D] + [AD]$, the fraction of bound donor molecules is given by,

$$D_b = \frac{[AD]}{[D]_T} = \frac{[AD]}{[D_{free}] + [AD]} = \frac{[A_{free}]}{[A_{free}] + K_d} \tag{S2.4}$$

Thus, the E-FRET efficiency is given by,

$$E_D = E_{max} \cdot D_b = E_{max} \cdot \frac{[A_{free}]}{[A_{free}] + K_d} \tag{S2.5}$$

In both cases to obtain a binding relation, we must deduce the free concentration of donor and acceptor molecules.

Nature Protocols: doi:10.1038/nprot.2016.128

Importantly, fluorescence measurements from single cells are proportional to the total number of fluorophores. Accordingly, we restate Eq. S2.3 and Eq. S2.5 in terms of number of fluorophores. Thus,

$$A_{\mathrm{b}} = \frac{N_{D\mathrm{free}}}{N_{D\mathrm{free}} + K_{\mathrm{d}} \cdot V_{\mathrm{cell}} \cdot N_{\mathrm{avogadro}}} \tag{S2.6}$$

Similarly,

$$D_{\mathrm{b}} = \frac{N_{A\mathrm{free}}}{N_{A\mathrm{free}} + K_{\mathrm{d}} \cdot V_{\mathrm{cell}} \cdot N_{\mathrm{avogadro}}} \tag{S2.7}$$

Indeed, for a 1:1 stoichiometry interaction, the fraction of acceptors bound is given by, $A_{\mathrm{b}} = (N_{\mathrm{D}} - N_{\mathrm{Dfree}})/ N_{\mathrm{A}}$. Note that $N_{\mathrm{D}} - N_{\mathrm{Dfree}}$ corresponds to the number of bound donor-acceptor complexes. Thus, Eq. S2.6 can be rewritten as

$$\frac{N_{\mathrm{D}} - N_{D\mathrm{free}}}{N_{\mathrm{A}}} = \frac{N_{D\mathrm{free}}}{N_{D\mathrm{free}} + K_{\mathrm{d}} \cdot V_{\mathrm{cell}} \cdot N_{\mathrm{avogadro}}} \tag{S2.8}$$

Rearranging this equation,

$$N_{\mathrm{Dfree}}^2 - (N_{\mathrm{D}} - N_{\mathrm{A}} - K_{\mathrm{d}} \cdot V_{\mathrm{cell}} \cdot N_{\mathrm{avogadro}}) \cdot N_{\mathrm{Dfree}} - K_{\mathrm{d}} \cdot V_{\mathrm{cell}} \cdot N_{\mathrm{avogadro}} \cdot N_{\mathrm{D}} = 0 \tag{S2.9}$$

Solving this equation yields,

$$N_{\mathrm{Dfree}} = \frac{(N_D - N_{\mathrm{A}} - K_{\mathrm{d}} \cdot V_{\mathrm{cell}} \cdot N_{\mathrm{avogadro}})}{2} + \frac{\sqrt{(N_D - N_{\mathrm{A}} - K_{\mathrm{d}} \cdot V_{\mathrm{cell}} \cdot N_{\mathrm{avogadro}})^2 + 4 \cdot K_{\mathrm{d}} \cdot V_{\mathrm{cell}} \cdot N_{\mathrm{avogadro}} \cdot N_{\mathrm{D}}}}{2} \tag{S2.10}$$

Since the number of bound complexes are the same, $N_{\mathrm{A}} - N_{\mathrm{Afree}} = N_{\mathrm{D}} - N_{\mathrm{Dfree}}$. Thus,

$$N_{\mathrm{Afree}} = N_{\mathrm{A}} - N_{\mathrm{D}} + N_{\mathrm{Dfree}} \tag{S2.11}$$

Substituting Eq. S2.10 into Eq. S2.11 yields,

$$N_{\mathrm{Afree}} = \frac{N_A - N_{\mathrm{D}} - K_{\mathrm{d}} \cdot V_{\mathrm{cell}} \cdot N_{\mathrm{avogadro}}}{2} + \frac{\sqrt{(N_D - N_{\mathrm{A}} - K_{\mathrm{d}} \cdot V_{\mathrm{cell}} \cdot N_{\mathrm{avogadro}})^2 + 4 \cdot K_{\mathrm{d}} \cdot V_{\mathrm{cell}} \cdot N_{\mathrm{avogadro}} \cdot N_{\mathrm{D}}}}{2} \tag{S2.12}$$

Importantly, the total number of acceptor (N_{A}) and donor (N_{D}) molecules in a cell can be estimated based on fluorescence measurements as outlined below.

First, for YFP molecules the fluorescence intensity due to direct excitation viewed through the FRET cube can be obtained from Eq. S1.4 as,

$$YFP_{\mathrm{FRET}}(440, 535, \mathrm{direct}) = N_A \cdot I_0 \cdot G_{\mathrm{FRET}}(A, 436) \cdot F_{\mathrm{FRET}}(A, 535) \tag{S2.13}$$

The number of acceptor molecules is then,

$$I_0 \cdot N_A = YFP_{\mathrm{EST}} = \frac{YFP_{\mathrm{FRET}}(436, 535, \mathrm{direct})}{G_{\mathrm{FRET}}(A, 436) \cdot F_{\mathrm{FRET}}(A, 535)} \tag{S2.14}$$

Nature Protocols: doi:10.1038/nprot.2016.128

The factors, $G_{\mathrm{FRET}}(\mathrm{A},440)$ and $F_{\mathrm{FRET}}(\mathrm{A},535)$ correspond to microscope specific calibration factors. In cells that express both YFP and CFP, $\mathrm{YFP}_{\mathrm{FRET}}(440,535,\mathrm{direct})$ can be estimated from the YFP cube measurement by the relation,

$$YFP_{\mathrm{FRET}}(436,535,\mathrm{direct}) = R_{\mathrm{A1}} \cdot S_{\mathrm{YFP}}(\mathrm{DA},500,535) \tag{S2.15}$$

Thus,

$$I_0 \cdot N_A = YFP_{\mathrm{EST}} = \frac{R_{\mathrm{A1}} \cdot S_{\mathrm{YFP}}(DA,500,535)}{G_{\mathrm{FRET}}(A,436) \cdot F_{\mathrm{FRET}}(A,535)} = \frac{R_{\mathrm{A1}} \cdot S_{\mathrm{YFP}}(DA,500,535)}{M_{\mathrm{A}}} \tag{S2.16}$$

Similarly the total number of donor molecules (N_{D}) could be estimated based on the fluorescence intensity of CFP molecules through the FRET cube. However, one confounding factor is quenching of CFP fluorescence as a result of FRET to nearby YFP molecules. The amount of quenching could be corrected for based on Eq. S1.19. Here,

$$CFP_{\mathrm{FRET}}(436,535,\mathrm{direct}) = N_D \cdot I_0 \cdot G_{\mathrm{x}}(D,436) \cdot F_{\mathrm{X}}(D,535) \tag{S2.17}$$
$$- N_D \cdot I_0 \cdot G_{\mathrm{x}}(D,436) \cdot F_{\mathrm{X}}(D,535) \cdot D_{\mathrm{b}} \cdot \frac{k_{\mathrm{T}}}{(k_{\mathrm{D}} + k_{\mathrm{D,nr}} + k_{\mathrm{T}})}$$

Note that,

$$D_{\mathrm{b}} \cdot \frac{k_{\mathrm{T}}}{(k_{\mathrm{D}} + k_{\mathrm{D,nr}} + k_{\mathrm{T}})} = D_{\mathrm{b}} \cdot E = E_{\mathrm{D}} \tag{S2.18}$$

where E_{D} is the E-FRET efficiency. Thus, Eq. S2.17 simplifies to,

$$CFP_{\mathrm{FRET}}(436,535,\mathrm{direct}) = N_D \cdot I_0 \cdot G_{\mathrm{x}}(D,436) \cdot F_{\mathrm{X}}(D,535) \cdot (1 - E_{\mathrm{D}}) \tag{S2.19}$$

This expression can be rearranged to obtain,

$$I_0 \cdot N_D = CFP_{\mathrm{EST}} = \frac{CFP_{\mathrm{FRET}}(436,535,\mathrm{direct}) / (1 - E_{\mathrm{D}})}{G_{\mathrm{FRET}}(D,436) \cdot F_{FRET}(D,535)} \tag{S2.20}$$

Note once again the denominator corresponds to microscope specific calibration factors. Moreover, $CFP_{\mathrm{FRET}}(440,\ 535,\ \mathrm{direct})$ could be estimated based of fluorescence measurement from the CFP cube as follows:

$$CFP_{\mathrm{FRET}}(436,535,\mathrm{direct}) = R_{\mathrm{D1}} \cdot S_{\mathrm{CFP}}(\mathrm{DA},436,480) \tag{S2.21}$$

Eq. S2.21 could be substituted into Eq. S2.20 to obtain,

$$I_0 \cdot N_D = CFP_{\mathrm{EST}} = \frac{R_{\mathrm{D1}} \cdot S_{\mathrm{CFP}}(DA,436,480) / (1 - E_{\mathrm{D}})}{G_{\mathrm{FRET}}(D,436) \cdot F_{\mathrm{FRET}}(D,535)} = \frac{R_{\mathrm{D1}} \cdot S_{\mathrm{CFP}}(DA,436,480)}{M_{\mathrm{D}}(1 - E_{\mathrm{D}})} \tag{S2.22}$$

An alternative formulation is shown in main text Eq. 13 where the CFP signal lost due to FRET is added as a correction term.

Nature Protocols: doi:10.1038/nprot.2016.128

Both Eq. S2.16 and Eq. S2.22 provide experimentally determined estimates for total number of acceptor and donor molecules respectively. Thus, we now reconsider Eq. S2.10 by multiplying both RHS and LHS by I_0,

$$I_0 \cdot N_{\text{Dfree}} = \frac{(I_0 \cdot N_D - I_0 \cdot N_{\text{A}} - I_0 \cdot K_{\text{d}} \cdot V_{\text{cell}} \cdot N_{\text{avogadro}})}{2} + \frac{\sqrt{(I_0 \cdot N_D - I_0 \cdot N_{\text{A}} - I_0 \cdot K_{\text{d}} \cdot V_{\text{cell}} \cdot N_{\text{avogadro}})^2 + 4 \cdot I_0 \cdot K_{\text{d}} \cdot V_{\text{cell}} \cdot N_{\text{avogadro}} \cdot I_0 \cdot N_{\text{D}}}}{2} \quad \text{(S2.23)}$$

Now, we could redefine, Eq. S2.23 based on parameters experimentally determined (i.e. Eq. S2.16 and Eq. S2.22). If we define, $I_0 \cdot N_{\text{Dfree}} = D_{\text{free}}$, an effective concentration of free donor molecules and $K_{\text{d,EFF}} = I_0 \cdot K_{\text{d}} \cdot V_{\text{cell}} \cdot N_{\text{avo}}$, then

$$D_{\text{free}} = \frac{(CFP_{\text{EST}} - YFP_{\text{EST}} - K_{\text{d,EFF}}) + \sqrt{(CFP_{\text{EST}} - YFP_{\text{EST}} - K_{\text{d,EFF}})^2 + 4 \cdot K_{\text{d,EFF}} \cdot CFP_{\text{EST}}}}{2} \quad \text{(S2.24)}$$

Similarly, if $I_0 \cdot N_{\text{Afree}} = A_{\text{free}}$ then Eq. S2.11 could be rewritten as,

$$A_{\text{free}} = YFP_{\text{EST}} - CFP_{\text{EST}} + D_{\text{free}} \quad \text{(S2.25)}$$

These two equations, namely Eq. S2.24 and Eq. S2.25 allows one to determine the free concentrations of donor and acceptor molecules and effective binding affinities through the iterative procedure described in Box 2.

Notice that the computation of CFP_{EST} and YFP_{EST} requires the knowledge of both $M_{\text{D}} = G_{\text{FRET}}(D,436) \cdot F_{\text{FRET}}(D,535)$ and $M_{\text{A}} = G_{\text{FRET}}(A,436) \cdot F_{\text{FRET}}(A,535)$. However, only the ratio $M_{\text{A}}/M_{\text{D}}$ can be reliably determined experimentally using various CFP-YFP dimers. The individual values M_{A} and M_{D} are, in fact, calculated from the parameters of optical elements in the microscope. Reassuringly, our theoretical calculation yielded an $M_{\text{A}}/M_{\text{D}}$ ratio that was highly similar to the experimentally determined value. Even, since these values are computed based on manufacturer's specifications for various optical elements, they are only approximate. In our experiments, we followed a simple procedure whereby we computed the M_{D} value based on specifications of our optical elements, and then set the M_{A} value by multiplying this theoretically determined M_{D} value by the experimentally determined ratio $M_{\text{A}}/M_{\text{D}}$ (from dimer experiments). Here, we explore how a miscomputation of the theoretical M_{D} value may affect the measured $K_{\text{d,EFF}}$.

Suppose the true M_{D} value ($M_{\text{D}}^{\text{true}}$) relates to the estimated M_{D} value (M_{D}^{*}) by

$$M_{\text{D}}^{\text{true}} = M_{\text{D}}^{*} \cdot \eta \quad \text{(S2.26)}$$

Nature Protocols: doi:10.1038/nprot.2016.128

Here η is an error term. Since the M_A/M_D can be experimentally determined and therefore assumed to be ratio of the true M_A and M_D values (i.e. M_A^{true} / M_D^{true}), the estimated M_A value is given by,

$$M_A^* = M_D^* \cdot \left(\frac{M_A}{M_D} \right)_{experimental} = M_D^* \cdot \left(\frac{M_A^{true}}{M_D^{true}} \right) = \frac{M_A^{true}}{\eta} \tag{S2.27}$$

Reconsidering Eq. S2.16 and substituting in Eq. S2.27, we can relate the experimentally estimated YFP_{EST} (YFP_{EST}^*) to the true value YFP_{EST}^{true} as follows:

$$I_0 \cdot N_A = YFP_{EST}^{true} = \frac{R_{A1} \cdot S_{YFP}(DA,500,535)}{M_A^{true}} = \frac{R_{A1} \cdot S_{YFP}(DA,500,535)}{M_A^* \cdot \eta} = \frac{YFP_{EST}^*}{\eta} \tag{S2.28}$$

Similarly, we can relate the experimentally computed CFP_{EST} (CFP_{EST}^*) to the true value YFP_{EST}^{true} by substituting Eq. S2.26 into Eq. S2.22,

$$I_0 \cdot N_D = CFP_{EST} = \frac{R_{D1} \cdot S_{CFP}(DA,436,480)}{M_D^{true}(1-E_D)} = \frac{R_{D1} \cdot S_{CFP}(DA,436,480)}{M_D^* \cdot \eta \cdot (1-E_D)} = \frac{CFP_{EST}^*}{\eta} \tag{S2.29}$$

Now substituting Eqs. S2.28 and S2.29 into S2.23, we could determine the true free concentration of donor molecules, D_{free}^{true}, by the following equation:

$$I_0 \cdot N_{Dfree} = D_{free}^{true} = \frac{\left(\frac{CFP_{EST}^*}{\eta} - \frac{YFP_{EST}^*}{\eta} - K_{d,EFF} \right)}{2} + \frac{\sqrt{\left(\frac{CFP_{EST}^*}{\eta} - \frac{YFP_{EST}^*}{\eta} - K_{d,EFF} \right)^2 + 4 \cdot K_{d,EFF} \cdot \frac{CFP_{EST}^*}{\eta}}}{2} \tag{S2.30}$$

Rearranging this equation,

$$I_0 \cdot \eta \cdot N_{Dfree} = \eta \cdot D_{free}^{true} = \frac{\left(CFP_{EST}^* - YFP_{EST}^* - \eta K_{d,EFF} \right)}{2} + \frac{\sqrt{\left(CFP_{EST}^* - YFP_{EST}^* - \eta K_{d,EFF} \right)^2 + 4 \cdot \eta \cdot K_{d,EFF} \cdot CFP_{EST}^*}}{2} \tag{S2.31}$$

We could in fact redefine $K_{d,EFF}^* = \eta \cdot K_{d,EFF}^{true}$ and $D_{free}^* = \eta \cdot D_{free}^{true}$, yielding

$$I_0 \cdot \eta \cdot N_{Dfree} = D_{free}^* = \frac{\left(CFP_{EST}^* - YFP_{EST}^* - K_{d,EFF}^* \right)}{2} + \frac{\sqrt{\left(CFP_{EST}^* - YFP_{EST}^* - K_{d,EFF}^* \right)^2 + 4 \cdot K_{d,EFF}^* \cdot CFP_{EST}^*}}{2} \tag{S2.32}$$

Nature Protocols: doi:10.1038/nprot.2016.128

Experimentally, then the error in estimation of M_D by factor η would simply result in a scaled relative dissociation constant,

$$K^{*}_{\mathrm{d,EFF}} = \eta \cdot K^{\mathrm{true}}_{\mathrm{d,EFF}} = \eta \cdot I_0 \cdot V_{\mathrm{cell}} \cdot N_{\mathrm{avo}} \cdot K_{\mathrm{d}} \quad (2.33)$$

But this ambiguity is computationally no different than lacking knowledge of the I_0 value. In the extreme case, if we do not have an estimate of M_D, we could simply set $M^{*}_{\mathrm{D}} = 1$. Thus, $\eta = M^{\mathrm{true}}_{D}$, and the measured relative affinity is $K^{*}_{\mathrm{d,EFF}} = M^{\mathrm{true}}_{\mathrm{D}} \cdot I_0 \cdot V_{\mathrm{cell}} \cdot N_{\mathrm{avo}} \cdot K_{\mathrm{d}}$. Finally to compare across experimental setups, we could compare measured affinities for a robust construct and deduce the pertinent scaling factors.

Nature Protocols: doi:10.1038/nprot.2016.128

Supplementary Note 4 | Theoretical basis of concentration-dependent FRET

One important challenge for robust analysis of binding interactions using FRET 2-hybrid is that of concentration-dependent or spurious FRET. If the bulk concentrations of expressed fluorescent proteins are high, then a freely-diffusing donor molecule may, by chance, be sufficiently close to a freely-diffusing acceptor molecule to elicit FRET despite the absence of a specific binding interaction. How do we account for concentration dependence of spurious FRET? Empirically, if CFP and YFP fluorophores are co-expressed in HEK293 cells, the 3^3-FRET and E-FRET efficiencies appear to be linearly dependent on the total concentration of CFP (CFP_{EST}) or YFP (YFP_{EST}) respectively (Supplementary Fig. 1). In this section, we furnish a theoretical analysis that supports the linear dependence of spurious FRET efficiency on the total concentration of fluorophores. This discussion follows the derivation presented in Erickson *et al*[1].

For 3^3-FRET, consider an acceptor molecule at position $r = 0$ as shown in Supplementary Note 4 Fig. 1**a**. The probability that a donor molecule (D) resides within a spherical shell of radius r and $r + dr$ of the acceptor molecule is given by,

$$P_{\mathrm{D}}(r)\cdot dr = [\mathrm{D}]\cdot N_{\mathrm{avo}}\cdot 4\pi r^2\cdot dr\cdot(10^{-27}\ \mathrm{L/\AA^3}) \tag{S3.1}$$

Here, [D] denotes the (molar) concentration of donor molecule, N_{avo} represents Avogadro's number. The shell radius r is assumed to be in units of angstrom. The expected FRET efficiency ($\bar{E}_{\mathrm{A}}$) for randomly dispersed donors at all distances is given by,

$$\bar{E}_{\mathrm{A}} = \int_0^\infty P_{\mathrm{D}}(r)\cdot\frac{R_0^6}{R_0^6+r^6}\cdot dr \tag{S3.2}$$

Note that the two fluorophores are assumed to be of negligible molecular size and therefore can be infinitesimally close to each other. Substituting S3.1 into S3.2 yields,

$$\begin{aligned}\bar{E}_{\mathrm{A}} &= \int_0^\infty [\mathrm{D}]\cdot N_{\mathrm{avo}}\cdot 4\pi r^2\cdot(10^{-27}\ \mathrm{L/\AA^3})\cdot\frac{R_0^6}{R_0^6+r^6}\cdot dr \\ &= [\mathrm{D}]\cdot N_{\mathrm{avo}}\cdot 4\pi\cdot(10^{-27}\ \mathrm{L/\AA^3})\cdot R_0^6\int_0^\infty\frac{r^2}{R_0^6+r^6}\cdot dr\end{aligned} \tag{S3.3}$$

Simplifying this expression,

$$\begin{aligned}\bar{E}_{\mathrm{A}} &= [\mathrm{D}]\cdot N_{\mathrm{avo}}\cdot 4\pi\cdot(10^{-27}\ \mathrm{L/\AA^3})\cdot R_0^6\cdot\frac{1}{3R_0^3}\arctan\left(\frac{r^3}{R_0^3}\right)\Bigg|_0^\infty \\ &= [\mathrm{D}]\cdot N_{\mathrm{avo}}\cdot\frac{4}{3}\pi\cdot(10^{-27})\cdot R_0^3\cdot\left(\frac{\pi}{2}-0\right) = [\mathrm{D}]\cdot N_{\mathrm{avo}}\cdot\frac{2}{3}\pi^2\cdot(10^{-27})\cdot R_0^3\end{aligned} \tag{S3.4}$$

Nature Protocols: doi:10.1038/nprot.2016.128

As shown in main text Eq. 24, the fluorescence intensity of the donor fluorophore is proportional to concentration of donors ([D] = N_D / ($N_{avo} \cdot V_{cell}$) = (($R_{D1} \cdot S_{CFP}$) / M_D) / ($N_{avo} \cdot V_{cell}$), thus,

$$\bar{E}_A = \frac{R_{D1} S_{CFP}}{M_D} \cdot \frac{\frac{2}{3}\pi^2 \cdot (10^{-27}) \cdot R_0^3}{V_{cell}} = S_{CFP} \cdot \frac{2\pi^2 \cdot (10^{-27}) \cdot R_{D1} \cdot R_0^3}{3 \cdot M_D \cdot V_{cell}} = S_{CFP} \cdot m_{3^3\text{-FRET}} \quad \text{(S3.5)}$$

Hence, the spurious FRET efficiency is linearly proportional to the fluorescence intensity of the donor molecules in the given cell. Note that the estimate here is an upper limit for the spurious FRET efficiency as the donor and acceptor molecules were assumed to be of negligible size. Nonetheless, the slope of the spurious FRET curve could be estimated experimentally.

A similar relation could be determined for spurious FRET between a membrane-localized acceptor fluorophore and a cytosolic donor fluorophore. Consider the fluorophore arrangement shown in Supplementary Note 4 Fig. 1**b**. By symmetry, the probability of finding a donor fluorophore within distance *r* and *dr* would be exactly half as in Supplementary Note 4 Fig. 1**a**. Therefore, the spurious FRET slope would be half that of Eq. S3.5 but nonetheless linear with respect to the fluorescence intensity of the donor molecule.

Finally, in the case that both donor and acceptor fluorophores are tethered to membrane proteins, these molecules are restricted to the membrane as shown in Supplementary Note 4 Fig. 1**c**. Thus, the probability of finding a donor molecule within the distance *r* and *r* + *dr* can be obtained by considering the thin cylindrical shell,

$$P_D(r) \cdot dr = D_{surface} \cdot 2\pi r \cdot dr \cdot (10^{-8}\ \mu m^2/Å^2) \quad \text{(S3.6)}$$

Note that $D_{surface}$ is the surface density of the donor fluorophore in the membrane (units of number of molecules / μm^2). The expected FRET efficiency ($\bar{E}_A$) for randomly dispersed donors at all distances is given by,

$$\bar{E}_A = \int_0^\infty P_D(r) \cdot \frac{R_0^6}{R_0^6 + r^6} \cdot dr \quad \text{(S3.7)}$$

$$= \int_0^\infty D_{surface} \cdot 2\pi r \cdot (10^{-8}\ \mu m^2/Å^2) \cdot \frac{R_0^6}{R_0^6 + r^6} \cdot dr$$

$$= D_{surface} \cdot 2\pi \cdot (10^{-8}\ \mu m^2/Å^2) \cdot R_0^6 \cdot \int_0^\infty \frac{r}{R_0^6 + r^6} \cdot dr$$

$$= D_{surface} \cdot \eta \cdot 2\pi \cdot (10^{-8}\ \mu m^2/Å^2) \cdot R_0^2 \cdot \left(\frac{\sqrt{3}}{9} \pi \right) \quad \text{(S3.8)}$$

Nature Protocols: doi:10.1038/nprot.2016.128

The fluorescence intensity of the donor fluorophore is proportional to the number of donors in the membrane, thus $D_{\text{surface}} = N_{\text{D}} / SA_{\text{mem}} = ((R_{\text{D1}} \cdot S_{\text{CFP}}) / M_{\text{D}}) / SA_{\text{mem}}$,

$$\bar{E}_{\text{A}} = \frac{R_{\text{D1}} S_{\text{CFP}}}{M_{\text{D}}} \cdot \frac{2\pi^2 \cdot (10^{-8}\ \mu\text{m}^2/\text{Å}^2) \cdot R_0^2 \cdot \left(\frac{\sqrt{3}}{9}\right)}{SA_{mem}} = S_{\text{CFP}} \cdot \hat{m}_{3^3\text{-FRET}} \qquad \text{(S3.10)}$$

Again, notice that the spurious 3^3-FRET efficiency is linearly proportional to the fluorescence intensity of the CFP molecule. Importantly, as the molecules are constrained to the membrane the slope of the spurious FRET efficiency may be prohibitively large. Intuitively, this result stems from the enhanced crowding of fluorophores as a result of restricted planar diffusion. Experimentally, this large spurious FRET may be estimated by localizing donor and acceptor fluorescent proteins to the membrane by lipidation.

Nature Protocols: doi:10.1038/nprot.2016.128

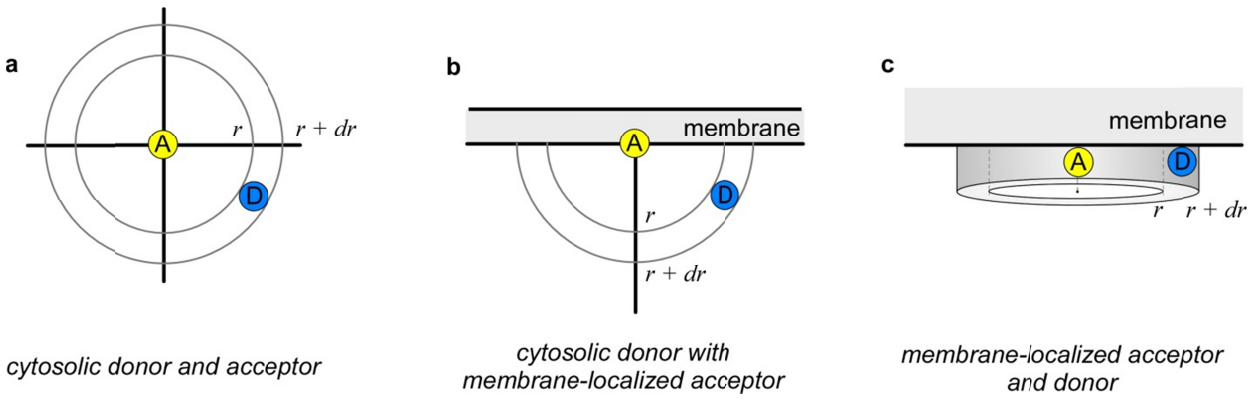

Supplementary Note 4 Figure 1 | Geometric arrangement of donor and acceptor fluorophores for theoretical analysis of spurious FRET relations. **(a)** Here, both donor and acceptor molecules are localized to the cytosol. Thus, we consider the probability of finding a donor molecule within a thin spherical shell of radius *r* and thickness *dr* **(b)** If the acceptor molecule is localized to the membrane, we consider probability of finding a donor molecule in the thin hemispherical shell of radius *r* and thickness *dr*. **(c)** If both donor and acceptor fluorophores are restricted to the membrane, then to estimate spurious FRET relations, we would consider the thin cylindrical shell of radius *r* and thickness *dr*.

Nature Protocols: doi:10.1038/nprot.2016.128

© 2015. Published by The Company of Biologists Ltd | Journal of Cell Science (2015) 128, 4014-4023 doi:10.1242/jcs.176420

RESEARCH ARTICLE

Uncoupling PIP_2-calmodulin regulation of Kv7.2 channels by an assembly destabilizing epileptogenic mutation

Araitz Alberdi[1,*], Carolina Gomis-Perez[1,*], Ganeko Bernardo-Seisdedos[1], Alessandro Alaimo[1], Covadonga Malo[1], Juncal Aldaregia[1], Carlos Lopez-Robles[1], Pilar Areso[2], Elisabeth Butz[3], Christian Wahl-Schott[3] and Alvaro Villarroel[1,‡]

ABSTRACT

We show that the combination of an intracellular bi-partite calmodulin (CaM)-binding site and a distant assembly region affect how an ion channel is regulated by a membrane lipid. Our data reveal that regulation by phosphatidylinositol(4,5)bisphosphate (PIP_2) and stabilization of assembled Kv7.2 subunits by intracellular coiled-coil regions far from the membrane are coupled molecular processes. Live-cell fluorescence energy transfer measurements and direct binding studies indicate that remote coiled-coil formation creates conditions for different CaM interaction modes, each conferring different PIP_2 dependency to Kv7.2 channels. Disruption of coiled-coil formation by epilepsy-causing mutation decreases apparent CaM-binding affinity and interrupts CaM influence on PIP_2 sensitivity.

KEY WORDS: Coiled-coil, Leucine zipper, Calmodulin, PIP_2, KCNQ, Epilepsy, M-current, Allosteric

INTRODUCTION

Phosphatidylinositol(4,5)bisphosphate (PIP_2) is a minor (<1%) acidic phospholipid found in the inner leaflet of the cell membrane and plays a vital part in cellular signaling by directly interacting with membrane proteins, including Kv7 potassium channels (Gamper and Shapiro, 2007; Suh and Hille, 2008; Hille et al., 2014; Zaydman and Cui, 2014). Function of Kv7 channels is absolutely dependent on PIP_2 (Zaydman and Cui, 2014) and activation of phospholipase C, and subsequent PIP_2 hydrolysis causes downregulation of their activity, which in turn lowers the threshold for activity (Brown et al., 2007), orchestrating excitability in brain, heart, skeletal muscle and inner ear. Related diseases encompass epilepsy, autism, schizophrenia, cardiac arrhythmias, hearing loss and sudden death (Soldovieri et al., 2011; Dvir et al., 2014a; Maljevic and Lerche, 2014).

The five members of the Kv7 family of non-inactivating voltage-dependent potassium channels share a common architecture, differing from that of Kv1–Kv4 channels in lacking an N-terminal T1 tetramerization domain. Instead, and in common with a large group of channels, such as Eag, Erg, SK, CNG and TRP channels, present multiple calmodulin (CaM; Uniprot P62161)-binding domains followed by a tetrameric coiled-coil segment (Jenke et al., 2003; Tsuruda et al., 2006). Kv7 channels have a large intracellular C-terminal region, ranging from 320 to 500 residues in size, containing four helical regions (A–D), which can be conceptually divided into three parts. Immediately after the last S6 transmembrane segment, the intracellular membrane proximal half (AB) is important for CaM binding and channel gating. Three-dimensional (3D) reconstitution locates the intracellular distal part (helix D) far from the membrane (Dvir et al., 2014b), which directs oligomerization and partner specificity (Yus-Nájera et al., 2002; Howard et al., 2007; Haitin and Attali, 2008). The AB and D helices are connected by helix C, indispensable for function, and a linker of variable length. Mutagenesis suggests that, in addition to the S4–S5 linker and the proximal C-terminus, helix C contributes to PIP_2 regulation (Dvir et al., 2014b; Zaydman and Cui, 2014). CaM binding is essential for Kv7 channels to exit from the endoplasmic reticulum, and influences heteromeric assembly of Kv7.2/3 channels and subsequent enrichment at the axonal initial segment (Yus-Nájera et al., 2002; Devaux et al., 2004; Chung et al., 2006; Etxeberria et al., 2008; Haitin and Attali, 2008; Alaimo et al., 2009; Cavaretta et al., 2014; Chung, 2014; Liu and Devaux, 2014). CaM regulatory mechanisms that change the gating behavior proceed through an effect on sensitivity to PIP_2 (Kosenko et al., 2012; Kosenko and Hoshi, 2013; Zaydman et al., 2013; Kang et al., 2014). The interlinker between helices A and B is not essential for function, although it plays a critical role in PIP_2 regulation for Kv7.3, but not in Kv7.1 and Kv7.2 channels (Hernandez et al., 2008; Aivar et al., 2012; Sachyani et al., 2014).

In contrast to the obligatory role of helices ABC for Kv7.2 channel function, helix D is dispensable (Schwake et al., 2006; Nakajo and Kubo, 2008). The helix D coiled-coil bundle has been largely considered as a passive stitch, with little active role other than to convey stability to the tetramer and specificity during the formation of heteromeric assemblies (Schmitt et al., 2000; Jenke et al., 2003; Maljevic et al., 2003; Schwake et al., 2006; Howard et al., 2007). Whilst this is undoubtedly part of its function, we find that this structure has a more active role by indirectly influencing PIP_2 dependency.

Here, we identified a mechanism to modulate, at a distance, regulation by PIP_2. We monitored the relative distance/orientation of the ABCD domain by live-cell fluorescence resonance energy transfer (FRET) assays in conjunction with analysis of whole-cell currents. The observations we made explain how the tetrameric conformation of helix D can functionally influence CaM binding to a distal site, and, in turn, how a pathological mutation affecting tetramer stability modifies Kv7.2 activity.

RESULTS

Calmodulin binds to Kv7.2 AB with a 1:1 stoichiometry

Calmodulin is a bi-functional protein, with two highly homologous lobes (N and C) joined by a flexible linker, each capable of engaging

[1]Unidad de Biofísica, Consejo Superior de Investigaciones Científicas, CSIC, UPV/EHU, Barrio Sarriena s/n, Leioa 48940, Spain. [2]Departament de Farmacología, UPV/EHU, Universidad del País Vasco, Barrio Sarriena s/n, Leioa 48940, Spain. [3]Department of Pharmacy, Center for Drug Research and Center for Integrated Protein Science Munich (CIPSM), Ludwig-Maximilians-Universität, München 81377, Germany.
*These authors contributed equally to this work

‡Author for correspondence (alvaro.villarroel@csic.es)

Received 24 June 2015; Accepted 9 September 2015

Journal of Cell Science (2015) 128, 4014-4023 doi:10.1242/jcs.176420

targets adopting an α-helix configuration (Villarroel et al., 2014). Helix A of Kv7.2 presents a marked preference for fetching the C-lobe, whereas helix B anchors more favorably to the N-lobe (Alaimo et al., 2014) and these features are present on the crystallographic Kv7.1 [AB/CaM] complex (Sachyani et al., 2014). To place the data of this report into physical perspective, Fig. 1 shows a tentative disposition of CaM on Kv7.2 forming a ring under the pore that complies with numerous restrictions from different studies (Mruk et al., 2012; Xu et al., 2013; Alaimo et al., 2014; Sachyani et al., 2014) (see Materials and Methods). One important feature derived from the 3D structure of the Kv7.1 [ABCD/CaM] complex is that the helix D coiled-coil is separated from the membrane by the CaM ring (Sachyani et al., 2014) (Fig. 1A).

To investigate in more detail the interaction with the Kv7.2 CaM-binding domain, we co-expressed CaM and a construct bearing the Kv7.2 CaM-binding elements (helices A and B, residues G313–R530) to produce the recombinant complex in bacteria. The intervening A–B linker (residues Y372–T501), which is not essential for Kv7.2 function (Aivar et al., 2012), was removed to improve protein yield. We found by size exclusion chromatography (SEC) that the purified material migrated with an apparent molecular mass of 35.3 kDa, which is close to the expected size for a 1:1 [CaM/AB] globular complex (16.7 +13.6=30.3 kDa; Fig. 1C). Thus, similar to Kv7.1 or Kv7.4 [AB/CaM] complexes studied *in vitro* (Wiener et al., 2008; Xu et al., 2013), the Kv7.2 [AB/CaM] complex adopts a 1:1 stoichiometry in solution.

The helix D L609R mutation disrupts coiled-coil formation

We studied next the consequences of the helix D L609R mutation [equivalent to L637R in the long Kv7.2 splice variant (Richards et al., 2004)] found in patients with hereditary benign familial convulsions (Richards et al., 2004), which is predicted to interrupt coiled-coil formation (Lupas and Gruber, 2005; Schwake et al., 2006) (Fig. 1B). To this end, non-tagged CaM and ABCD C-terminally tagged with a fluorescent protein were co-expressed in bacteria, and the resulting complexes were purified and analyzed. The SEC elution volume was consistent with a 4:4 [ABCD/CaM] globular complex. In contrast, the larger elution volume of the L609R mutant indicated that no stable tetramers were formed (Fig. 1C). In addition, the fastest non-denaturing electrophoretic pattern of [ABCD-L609R/CaM] compared with [ABCD/CaM] indicates disruption of the complex (Fig. 1D). Thus, the L609R mutation impedes the adoption of a stable tetrameric coiled-coil configuration.

Helices CD do not interact with calmodulin and the [ABCD/calmodulin] complex is compact

It has been suggested that FRET results between isolated domains of Ca^{2+} voltage-dependent channels and CaM can be applied to the entire protein (Ben Johny et al., 2013). Inspired by this precedent,

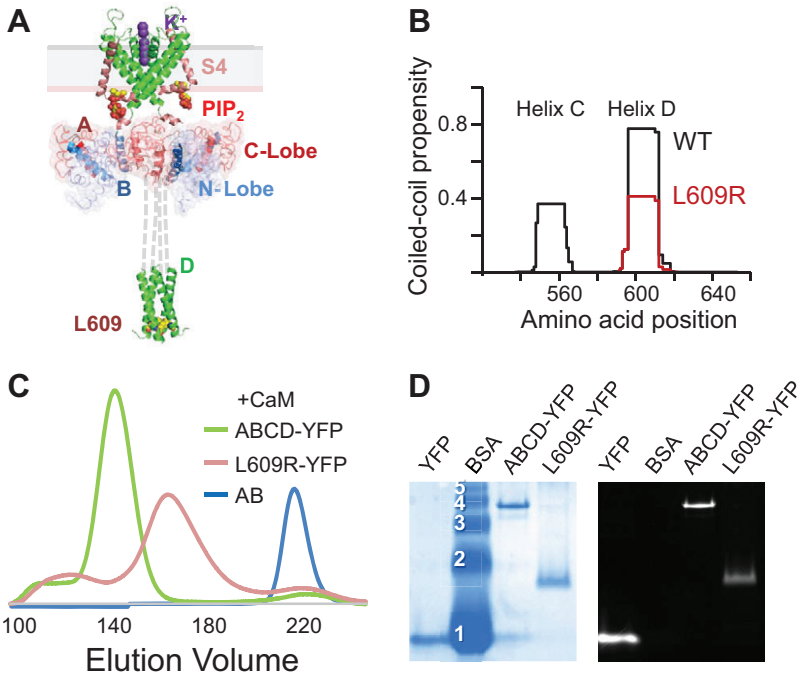

Fig. 1. The L609R mutation disrupts coiled-coil formation. (A) Structural model of the CaM ring under the membrane based on the crystallographic co-ordinates and synchrotron X-ray data of the [AB/CaM] Kv7.1 and [ABCD/CaM] Kv7.1 complexes, respectively (Sachyani et al., 2014), the [B/CaM] Kv7.4 complex (Xu et al., 2013), helix D Kv7.4 and Kv7.1 tetrameric bundles (Howard et al., 2007; Wiener et al., 2008), and the model derived from internal TEA-CaM blockade (Mruk et al., 2012). The disposition of helix C and the CD linker are unknown (dashed lines). Only the selectivity filter, the S4 (salmon), S5 and S6 segments (green), S4–S5 linker (salmon) and post-S6 segment (salmon) of two potassium channel subunits are shown for clarity. The distance between the inner leaflet of the membrane and L609 is ~10 nm in this model. (B) Coiled-coil probabilities of helices C and D for wild-type Kv7.2 and the L609R mutant computed using COILS (http://www.ch.embnet.org/software/COILS_form.html). (C) Size exclusion chromatography of the indicated constructs. Normalized absorbance is plotted against elution volume. All samples were loaded at a concentration of 20 µM. Theoretical molecular masses (in kDa) are: 103 for [ABCD-YFP/CaM], 412 for [ABCD-YFP/CaM]$_4$, 206 for [ABCD-YFP/CaM]$_2$ and 30 for [AB/CaM]. (D) Gel electrophoresis of the indicated samples in the absence of SDS. YFP (29 kDa) and BSA (66.5 kDa), which present different degrees of oligomerization, served as a ruler for molecular mass. On top of the BSA bands the presumed number of molecules in the oligomer is indicated (Friedman et al., 1993). The computed molecular mass of the ABCD-YFP construct is 57 kDa and that of CaM is 17 kDa. The fluorescence image of the same gel is shown on the right.

Journal of Cell Science (2015) 128, 4014-4023 doi:10.1242/jcs.176420

the interaction between CaM and the C-terminal Kv7.2 domain was analyzed by FRET in living cells. Cyan fluorescent protein (CFP) and yellow fluorescent protein (YFP) exhibit 50% energy transfer at a distance of ∼5 nm and measurable transfer up to 8 nm (Patterson et al., 2000). The ratio of the integral of CFP/YFP emission isolated after spectral unmixing is directly proportional to the FRET efficiency. The FRET index between CaM and helices AB was important (Fig. 2A,E), whereas between helices CD and CaM it was insignificant (Fig. 2B,E,G). These data reinforce the initial conclusion, based on yeast two-hybrid interaction trap and pull-down assays, that helices CD do not contribute directly to CaM binding (Yus-Nájera et al., 2002). Similarly, a role of CD helices has been discarded for CaM binding to Kv7.4 and Kv7.1 channels (Xu et al., 2013; Sachyani et al., 2014). In contrast, an increased FRET index compared with that of AB was observed between CFP-CaM and YFP-ABCD (Fig. 2C,E), which is an expected consequence of having multiple donors and acceptors within the FRET distance [<8 nm (Patterson et al., 2000; Vogel et al., 2006); Fig. 2F]. Based on the structure of the related Kv1.2 channel (Long et al., 2005), two fluorescent proteins in the same channel should be ∼5.6 nm apart (assuming they are in adjacent subunits) or 7.9 nm apart (assuming they are in non-adjacent subunits). In agreement with this interpretation, disruption of helix D coiled-coil by the L609R mutation resulted in a FRET index comparable to that of AB (Fig. 2D,E). The differences in FRET efficiency were apparent at low free donor or acceptor concentrations, where collisional or spurious FRET is negligible (Fig. 2G; Figs S1, S2). Thus CaM and AB from different subunits are within FRET distance in the tetrameric complex brought together by helix D.

Tetramerization of the distal helix D positions A helices from different subunits within FRET distance

To gain further insights into the [Kv7.2/CaM] complex, the impact of tetramerization on the separation between A helices of neighboring subunits was gauged by FRET analysis, attaching CFP or YFP at the N-terminus, upstream of helix A. This configuration allowed the assessment of the transfer of energy between adjacent subunits, which was virtually undetectable

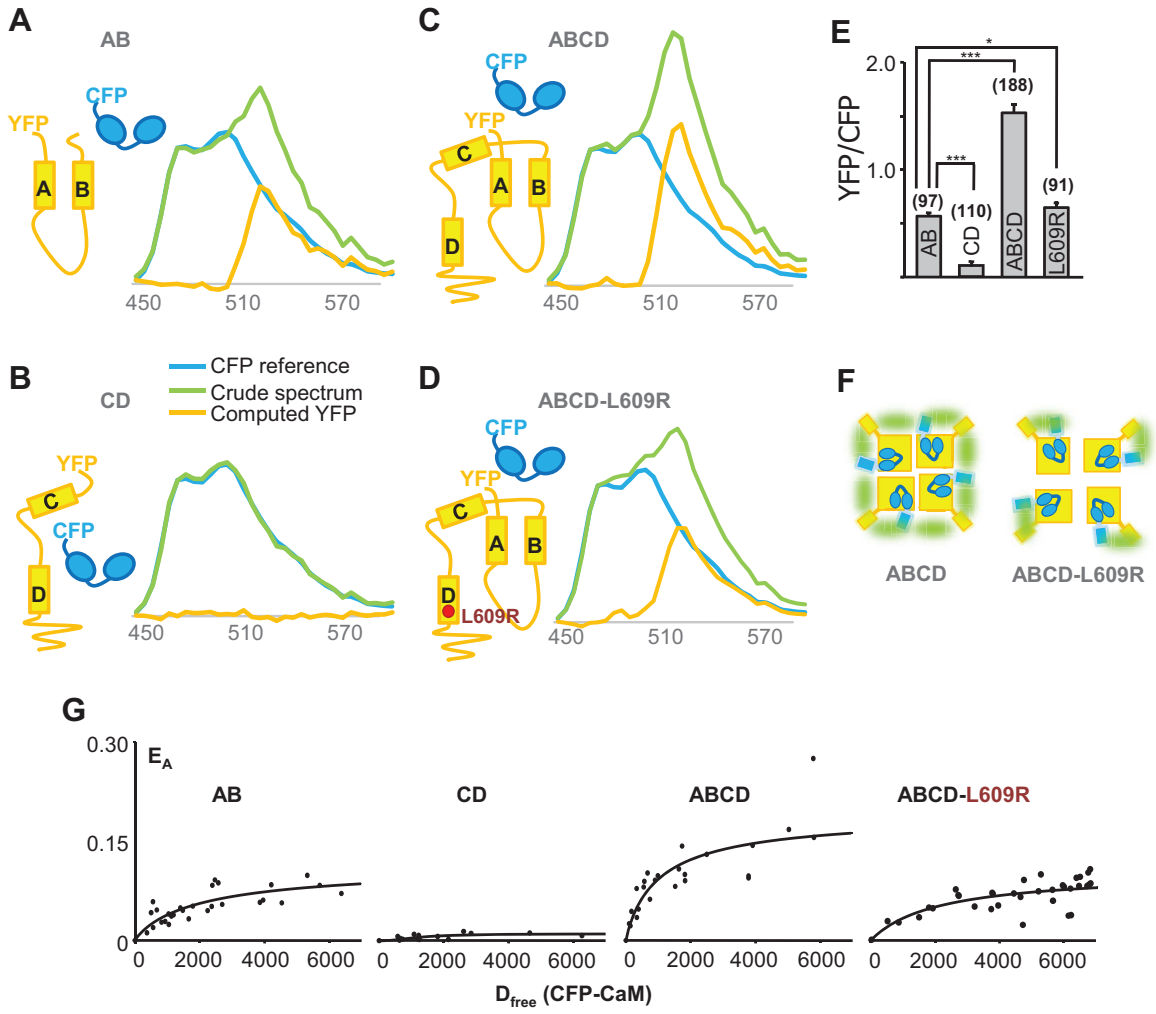

Fig. 2. FRET between calmodulin and ABCD is reduced by the helix D L609R mutation. (A–D) Emission spectra (green) after excitation at 405 nm from cells expressing CFP-CaM and YFP-target protein. The orange trace is the computed FRET emission from the YFP-tagged target protein and the cyan plot is the reference emission of CFP. Note in B the negligible bleed through due to direct excitation of YFP at 405 nm. (E) FRET indexes between CFP-CaM and the indicated constructs. (F) Cartoon illustrating how, as a result of tetramerization, each donor could be within FRET distance of two or more acceptors. Disruption of coiled-coil formation would cause separation/re-orientation of the donor–acceptor pairs, which now would function as independent entities. (G) Binding curve in which the FRET strength between CFP-CaM and the indicated YFP-labeled proteins is plotted versus concentration of free CFP-CaM from each individual cell (Ben et al., 2013) (n>25). E_A, acceptor-centric FRET efficiency; D_{free}, free donor concentrations in arbitrary units.

Journal of Cell Science (2015) 128, 4014-4023 doi:10.1242/jcs.176420

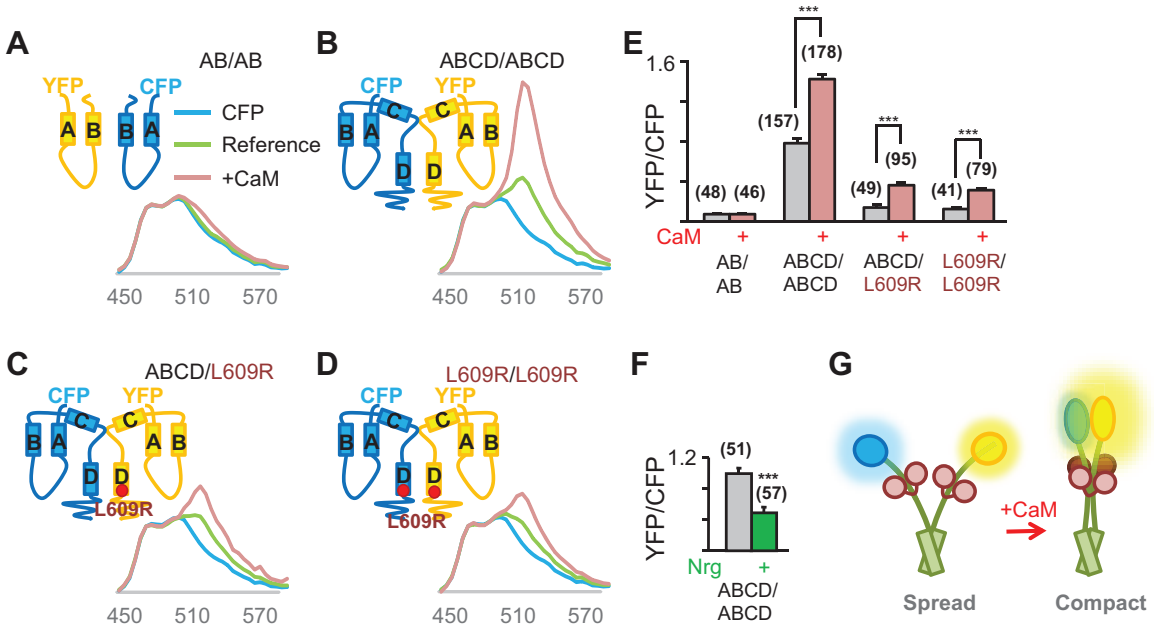

Fig. 3. Elevation of calmodulin levels leads to increased FRET in tetrameric ABCD. (A–D) Comparison of the impact of elevation of CaM levels on the emission spectra (green versus salmon) after excitation at 405 nm from cells co-expressing the indicated regions of Kv7.2 tagged with CFP and YFP at the N-termini. The reference CFP emission spectrum is plotted in blue. The deviation of the green and salmon traces from the blue plot provides a visual indication of changes in FRET. (E) Summary of FRET indexes measured under normal (gray) and elevated (salmon) CaM conditions. (F) Comparison of the impact of overexpression of Neurogranin (Nrg, green) to reduce CaM levels on spectral FRET between CFP-ABCD and YFP-ABCD. (G) Cartoon illustrating how CaM engaging AB in an additional binding mode could form a sort of 'lock washer' that compacts the proximal region of ABCD, bringing together donors and acceptors from different subunits.

between CFP-AB and YFP-AB (Fig. 3A, compare cyan and green traces). In contrast, a clear FRET signal was detected between CFP-ABCD and YFP-ABCD (Fig. 3B,E), indicating that the separation of the N-termini is below 8 nm in the tetrameric complex. Disruption of the helix D coiled-coil formation by the L609R mutation resulted in a large reduction of the FRET index (Fig. 3C,D), reinforcing the view that helix D is critical for bringing A helices close together.

Calmodulin re-orients the A helices of neighboring subunits

Three-dimensional structural data indicate that the ABCD domain can be envisioned as a flower bouquet with the tetrameric coiled-coil helix D corresponding to the pedestal (Sachyani et al., 2014) (Fig. 1). We can imagine the bunch in two extreme situations: in a compact arrangement or with flaccid stacks positioning the flowers towards the periphery (Fig. 3G). FRET can distinguish between closed and spread configurations, because in the first case donors and acceptors from neighboring [CaM/AB] complexes will be within FRET distance. With this idea in mind, the impact of elevating CaM levels was monitored. The FRET index recorded after disruption of tetramerization by the L609R mutation was low, and increased after CaM elevation (Fig. 3C,D; compare green and salmon plots), whereas no significant changes were revealed when helix D was missing (Fig. 3A). In contrast, a prominent FRET index was obtained for the CFP-ABCD and YFP-ABCD pair, which almost doubled with elevated CaM levels (Fig. 3B). Thus CaM leads to a rearrangement, probably by compaction (Fig. 3G), of the disposition of helix A in the ABCD complex. This compaction also takes place for the L609R mutant, but it does not reach the distant/orientation values of the ABCD complex. Furthermore, the FRET index was significantly reduced in cells overexpressing neurogranin, an apo-calmodulin-binding protein (Villarroel et al., 2014) that is expected to diminish CaM availability (Fig. 3F). These results suggest that CaM favors, by mass action, the adoption of a novel organization of the ABCD domain, and that this new configuration is favored by helix D acquiring a tetrameric coiled-coil formation.

Coiled-coil formation by helix D increases calmodulin-binding affinity

The changes on FRET suggest that CaM can bind to ABCD in at least two different configurations, resulting in an equilibrium scheme between a minimum of three states (Fig. 4A). A testable consequence of the incorporation of an additional binding mode is that the apparent binding affinity should decrease after disruption of helix D-mediated tetramer formation by L609R (Fig. 4). Using e-FRET methodology (Chen et al., 2006) we resolved the binding curve in which the FRET strength between CFP-CaM and YFP-ABCD is plotted cell-by-cell versus concentration of free YFP-ABCD (Ben Johny et al., 2013). This revealed that, besides decreasing maximal FRET, the L609R mutation led to a reduction in apparent binding affinity (Fig. 4B). To further evaluate the impact of this mutation in CaM binding in a more controlled *in vitro* setting, recombinant ABCD and ABCD-L609R proteins were produced in bacteria and purified in the absence of CaM (Alaimo et al., 2009). The refolded monodisperse CaM-binding domains were subsequently assayed *in vitro* for binding to dansylated CaM (D-CaM) (Alaimo et al., 2013b; Bonache et al., 2014). In accordance with theory and with results obtained by using live cells, the elimination of the presumed additional binding mode was accompanied by a clear decrease in apparent binding affinity for the L609R mutant (Fig. 4C,D). In the tetramer, the packing suggests that binding of one CaM might affect binding to another CaM. However, the Hill coefficient (Edelstein and Le, 2013) of the dose–

Journal of Cell Science (2015) 128, 4014-4023 doi:10.1242/jcs.176420

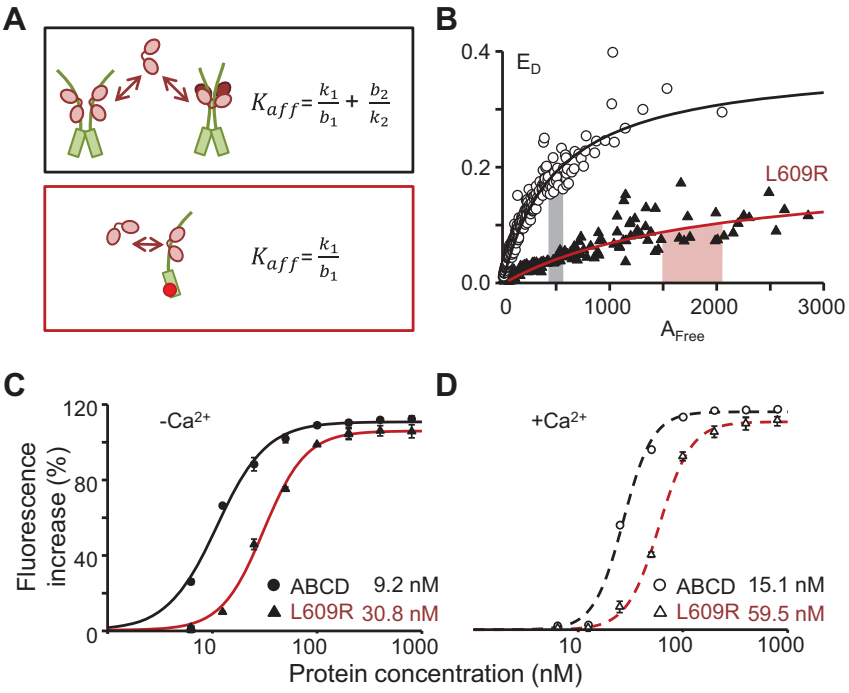

Fig. 4. Disruption of coiled-coil formation results in reduced calmodulin-binding affinity. (A) Scheme illustrating how coiled-coil formation can lead to a three-state binding model (top) compared with a two-state model in the absence of tetramerization (bottom). (B) The binding curve in which the FRET strength between CFP-CaM and YFP-ABCD (black line) or YFP-ABCD-L609R (red line) is plotted cell-by-cell versus concentration of free YFP-ABCD. The shaded boxes indicate the concentration range in arbitrary units producing half-maximal e-FRET. E_D, donor-centric FRET efficiency; A_{free}, free acceptor concentrations in arbitrary units. (C) Dose–response relationship of normalized D-CaM fluorescence emission increases with purified monodisperse recombinant GST-ABCD proteins in the absence of Ca^{2+}. The lines are the result of fitting a Hill equation to the data, and the EC_{50} from the fit is indicated in the figure. Hill coefficients for ABCD and L609R were 1.80±0.15 and 2.15±0.17, respectively (n=3). (D) Dose–response relationship of normalized D-CaM fluorescence emission increase in the presence of 3.9 µM free Ca^{2+}. The lines are the result of fitting a Hill equation, and the EC_{50} values from the fit are indicated in the figure. Hill coefficients for ABCD and L609R were 3.07±0.39 and 2.83±0.18, respectively (n=3).

responses did not change as a consequence of coiled-coil disruption, suggesting that tetramerization has minor or no effect on potential co-operativity between CaM molecules (Fig. 4C).

The effect of elevated calmodulin on PIP_2 dependency differs between WT and L609R mutant channels

Cells expressing Kv7.2, complemented or not with CaM, were examined by whole-cell recording (Fig. 5A,B) to explore the functional consequences of the tetramerization-disrupting mutation on CaM-dependent function, such as current density and PIP_2 dependency. Current density was not significantly affected by this mutation (Fig. 5), whereas there was a remarkable 18 mV right shift of the conductance–voltage relationship (Fig. 5C). The decrease in CaM-binding affinity caused by the L609R mutation should tend to reduce the ensemble occupancy of the four CaM-binding sites on a Kv7.2 channel. A similar decline in the steady-state occupancy

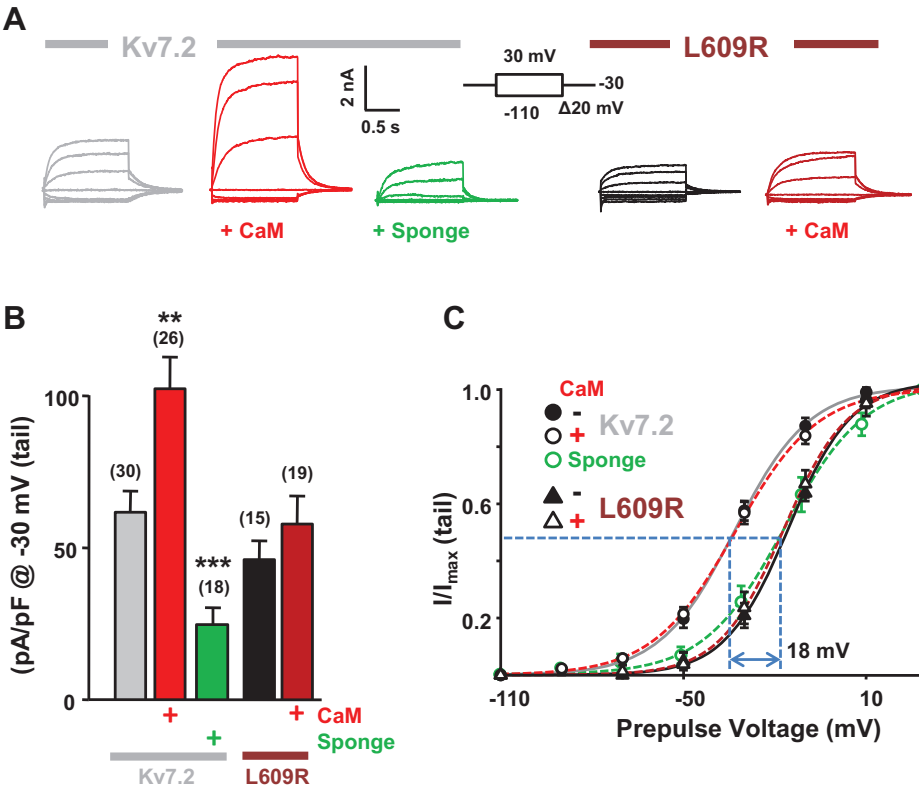

Fig. 5. The L609R mutation causes a right shift of the voltage dependency and precludes the effect of elevated calmodulin in current density. (A) Exemplar whole-cell current relaxations evoked at different potentials for the indicated channels under resting (gray), elevated CaM (red) and reduced (green) conditions. CaM availability was reduced with a CaM sponge. (B) Summary of current densities computed at −30 mV as the difference in quasi-instantaneous current after a prepulse to −110 mV (all channels closed) and +30 mV (all channels opened). Note that this protocol is insensitive to voltage-dependent shifts within a broad voltage range. (C) Normalized tail I–V relationship. The lines are fits of Boltzmann relationships to the data with the following parameters ($V_{½}$, slope in mV): wt, −33.2±1.0, 12.3±0.8; wt+CaM, −32.9±1.0, 13.5±0.9; wt+sponge, −15.6±2.1, 13.3±1.6; L609R, −15.5±1.1, 10.4±0.9; L609R+CaM, −17.4±1.6, 10.5±1.2.

Journal of Cell Science (2015) 128, 4014-4023 doi:10.1242/jcs.176420

should occur when the concentration of free CaM is critically low. To test this idea, the properties of Kv7.2 channels in a low CaM environment were evaluated. Under reduced CaM conditions there was a significant decrease in current density, consistent with the role of CaM on Kv7.2 trafficking (Etxeberria et al., 2008). Remarkably, there was a 17 mV right shift of the conductance–voltage relationship (Fig. 5). Similar effects were observed in cells expressing neurogranin ($n \geq 12$, not shown). Thus both disruption of coiled-coil formation and low CaM availability led to similar changes in the conductance–voltage relationship, with a strong correlation with the impact on the proximity/orientation of the ABCD domains.

The voltage-dependent phosphatase *Danio rerio* voltage sensing phosphatase (DrVSP) was used to address the impact on PIP_2 dependence. To avoid voltage errors associated with the large currents evoked at the extreme voltages required to activate DrVSP (see Fig. 6A), series resistance compensation for the patch electrode was set to >95% (Sherman et al., 1999). The comparison of current relaxations before and after DrVSP activation demonstrated that the L609R mutant was more resistant to activation of the voltage-dependent phosphatase (Fig. 6B). Furthermore, a similar increase in resistance to DrVSP activation was observed for wild-type channels under low CaM conditions, which is comparable to that in channels carrying the L609R mutation. Importantly, in contrast to wild-type channels, the response of the mutant channel to activation of DrVSP was insensitive to CaM elevation (Fig. 6C). Thus disruption of helix D coiled-coil changes voltage dependency and perturbs the adoption of additional CaM-binding modes and subsequent change on PIP_2 dependency in Kv7.2 channels.

DISCUSSION

Despite their fundamental importance in regulation and signaling, allosteric mechanisms are, in general, poorly understood (Motlagh et al., 2014). Here, we show that PIP_2 dependency is affected at a distance by the formation of a coiled-coil tetrameric bundle. The data are consistent with a mechanism involving different CaM-binding modes, which confer differential PIP_2 sensitivity to Kv7.2 channels.

The data reveal that the pathogenic L609R mutation [equivalent to L637R in the long Kv7.2 splice variant (Richards et al., 2004)] destabilizes the helix D-dependent tetramerization of the C-terminal region of Kv7.2. In addition, this mutation reduces the apparent affinity for CaM binding, and leads to increased resistance to the action of a voltage-dependent phosphatase that reduces PIP_2 concentration at the plasma membrane. A plausible consequence of the reduction of CaM affinity is that CaM occupancy of the channel is diminished, and, on average, not all four sites of the tetrameric channel would be engaged in a given instant. A similar reduction in the number of resident CaM molecules can be achieved by lowering CaM availability, which led to increased resistance to DrVSP action, similar to that seen for the helix D-mutated channels. In addition, both wild-type channels when CaM is scarce and L609R mutant channels under resting CaM levels present a >17 mV right shifted conductance–voltage relationship, meaning that two different situations that lead to low CaM occupancy converge towards a similar voltage dependency and increased resistance to PIP_2 depletion. Although results obtained with isolated domains may not apply to the full-length channel, the agreement between *in vitro* data and those obtained by using live cells favor the argument that these events are related, and are consistent with the idea that the effect on PIP_2 sensitivity is a consequence of the changes on CaM residence.

How can helix D affect CaM binding? Neither our new FRET data, nor previous studies using yeast two hybrid assays, or studies on Kv7.1 or Kv7.4, have exposed any hint of direct CaM interaction with helices CD (Yus-Nájera et al., 2002; Howard et al., 2007; Wiener et al., 2008; Xu et al., 2013). In addition, small angle X-ray scattering of the related Kv7.1 subunit (Sachyani et al., 2014) reveals that there is no physical contact between helix D and the [AB/CaM] complex. Therefore, we conclude that the impact of helix D in CaM binding is indirect. In addition to previous functional and structural data (Alaimo et al., 2013a; Sachyani et al., 2014), the helix D-dependent changes in CaM-binding affinity unveiled here support the concept of the occurrence of more than one binding mode. The decrease in FRET for the L609R mutant underscores the importance of coiled-coil formation by helix D in this process. The changes in homo-FRET efficiency between ABCD modules are a clear indication that the A helices re-orient, come closer, or both, when more CaM is available. Either new CaM molecules are entering the complex, or existing CaM molecules are engaging in new binding modes, such as intrasubunit and intersubunit binding modes.

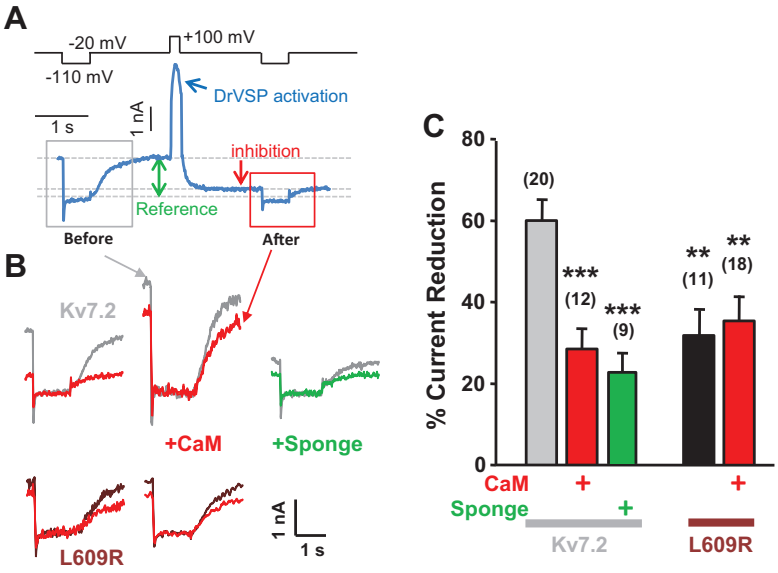

Fig. 6. Disruption of coiled-coil formation affects calmodulin-dependent regulation of PIP_2 sensitivity. (A) Scheme of the voltage protocol used for DrVSP activation (top) and exemplar current recorded from a cell expressing Kv7.2 channels to illustrate current inhibition quantification. (B) Exemplar current relaxations before (dark gray traces) and after DrVSP activation in resting conditions and overexpressing CaM (red traces) or overexpressing a CaM-binding protein –'sponge'– to sequester CaM (green). (C) Averaged current reduction after activation of DrVSP for the indicated Kv7 configurations, in resting conditions and with elevated (red) or reduced (green) CaM.

Journal of Cell Science (2015) 128, 4014-4023 doi:10.1242/jcs.176420

The CaM N-lobe has a significant preference to anchor to helix B, whereas the C-lobe binds more favorably to the IQ site located in helix A (Alaimo et al., 2014). In the context of the full-length channel, both helices in the [AB/CaM] complex could originate from the same subunit (intrasubunit binding) or from two adjacent subunits (intersubunit binding). Intersubunit binding requires placing AB helices from contiguous subunits within CaM reach, i.e. <4 nm (Villarroel et al., 2014). Indeed, Kv7.2 models derived from trigonometric restrictions obtained with pore blockers tethered to CaM as calipers, position the lobe anchoring sites of nearby CaM molecules under 4 nm (Mruk et al., 2012) (Fig. 1A). In addition, besides the precedents for bridged configurations in other channels (Schumacher et al., 2001; Sarhan et al., 2012; Villarroel et al., 2014), the crystallographic structure of Kv7.1 [AB/CaM] has been trapped with CaM embracing helices A and B from different subunits (Sachyani et al., 2014). We have previously shown by whole-cell recording that precluding CaM binding to helix A or to helix B results in non-functional channels, but, remarkably, both mutant channels complement each other, restoring function when co-expressed (Alaimo et al., 2013a). Furthermore, at submicromolar concentrations, CaM links two Kv7.2 AB domains *in vitro*, anchoring helix A of one subunit to helix B of another subunit (Alaimo et al., 2013a). Therefore, we consider reasonable the hypothesis that, by bringing together the AB helices from adjacent subunits thanks to helix D coiled-coil formation, each CaM lobe can engage with the complementary helix from a neighboring subunit.

Consideration of our new data together with prior work leads us to propose an extension of the CaM modulation hypothesis to include a switch between CaM binding-modes, which may correspond to intra- and intersubunit engagement or different degrees of occupancy of the multiple CaM-binding sites, providing distant control of PIP_2 sensitivity by the tetramerization domain. The structures of many configurations are presently unknown, but homology modeling confirms the plausibility of these arrangements. In the context of the full-channel, with the restrictions imposed by the pore-forming regions preceding helix A, the approximation of these helices caused by CaM elevation should translate in a movement of the whole [ABCD/CaM] complex relative to the pore. A doubling in FRET index in the presence of elevated CaM (Fig. 3) could be accounted for by less than 6% reduction in the separation of the fluorophores, i.e. a displacement <0.5 nm, a magnitude comparable to the vertical translation of the cytoplasmic domain observed between the structures of Kir2.2 channels with and without PIP_2 (Hansen et al., 2011).

It is not known if the helix D tetramer de-oligomerize and re-oligomerize as part of the normal channel function, allowing for physiological allosteric control of channel activity. Beyond supporting different CaM-binding modes and affecting channel assembly, the helix D coiled-coil domain may also serve as a scaffold for interactions with other proteins that regulate channel activity (Marx et al., 2002; Kass et al., 2003; Wiener et al., 2008). Thus, helix D may act as an antenna, funneling relatively distant interactions towards the pore by changing indirectly the way the channel engages with CaM.

The data provide a basis for theoretical generalization of an allosteric mechanism. Many ion channels, such as Kv7, Eag, Erg, SK, CNG and TRP, present multiple CaM-binding domains followed by a tetrameric coiled-coil bundle (Jenke et al., 2003; Tsuruda et al., 2006), but other elements could assume the equivalent conceptual roles. The ingredients are two bi-functional target–receptor components, plus a mechanism that brings two or more targets in close vicinity. By controlling at a long distance the proximity between the binding sites, the receptor could engage the target in different configurations, ultimately affecting activity.

PIP_2 is strictly required for the operation of Kv7 channels, and it is currently thought that parts of the channel from well-separated regions of the linear sequence fold to bring together several basic residues to create a binding pocket (Zaydman and Cui, 2014). The concept is that the interacting basic residues do not represent a structurally selective binding site; rather they form positively charged clouds that would attract any acidic lipid. PIP_2 would be the principal target because it is the most abundant multiply-phosphorylated lipid of the plasma membrane (Suh and Hille, 2008). By reconfiguring the CaM ring underneath the pore, the cloud envelope in contact with PIP_2 at the inner leaflet of the membrane could change, such that the orientation of lysine, arginine or histidine residues making electrostatic contacts with the charged phosphate groups will be controlled at a distance by helix D. A fuzzy organization of the PIP_2-binding surface like this may help to explain the puzzling similar effects in channel-PIP_2 sensitivity of low and elevated CaM levels. Defects in channel-PIP_2 sensitivity through interfering mutations can lead to disease (Logothetis et al., 2010). It is attractive to hypothesize that mutations not located at the binding site that disrupt channel-PIP_2 dependency, such as L609R described here and which was found in a patient with an epileptic condition (Richards et al., 2004), could also lead to disease.

MATERIALS AND METHODS

Molecular biology

The human isoform 3 Kv7.2 (Y15065) cDNA was provided by T. Jentsch (Leibniz-Institut für Molekulare Pharmakologie, Berlin, Germany) and the cDNA encoding rat CaM was provided by the group of J.P. Adelman (Vollum Institute, Portland, OR, USA). The subunits tagged at the N-terminal with CFP or YFP were cloned into pCDNA3.1 and we previously confirmed that these N-terminal tags have no impact on the electrophysiological properties of the channel (Soldovieri et al., 2006; Gómez-Posada et al., 2010; Gómez-Posada et al., 2011). Point mutations were constructed by polymerase chain reaction (PCR)-based mutagenesis. Dr-VSP-IRES-GFP from zebrafish was provided by Y. Okamura (Osaka University, Osaka, Japan). The CaM sponge, which has CFP and YFP flanking the apoCaM-binding site of neuromodulin, was provided by D.J. Black (University of Missouri, Missouri, USA). For *in vitro* co-expression experiments, CaM was subcloned into the pOKD4 vector. C-terminal channel sequences were fused to a custom-made circularly permuted Venus variant of YFP (Shinege; China) and subcloned into pPROEX-HTc vector. Rat neurogranin (NM_024140.2) tagged with a myc epitope at the N-terminus was cloned into pcDNA3.1 hys/myc A vector.

Homology modeling

The portrayed structure in Fig. 1 is an extension of model 3 proposed by Mruk et al., which places key residues of the CaM N- and C-lobes at a distance relative to the Kv7.2 pore compatible with the effects of a pore blocker tethered to CaM with chains of varying length (Mruk et al., 2012), and adequate for it being linked to S6, assuming that the IQ site adopts a similar disposition as that in the Kv7.1 [AB/CaM] complex (Sachyani et al., 2014), and presents a kink as predicted by sequence analysis (Alaimo et al., 2014). The structural models of [N-lobe/helix B] complexes from Kv7.1 and Kv7.4 nicely superimpose, and are consistent with nuclear magnetic resonance (NMR) data obtained for the Kv7.2 [AB/CaM] complex (Xu et al., 2013; Alaimo et al., 2014; Sachyani et al., 2014). In turn, the structural crystallographic X-ray-based model for the Kv7.1 [C-lobe/helix A] complex is compatible with NMR observations of the Kv7.2 [AB/CaM] complex (Alaimo et al., 2014; Sachyani et al., 2014), and is almost identical to every other solved complex of apo-C-lobe (Ca^{2+} free) with peptides containing an IQ motif (IQxxθR, θ=bulky apolar residue), a motif that is present in helix A of every Kv7 channel (Yus-Nájera et al., 2002; Villarroel et al., 2014).

Journal of Cell Science (2015) 128, 4014-4023 doi:10.1242/jcs.176420

Finally, helix D has been placed at a distance from the CaM-binding site, according to the envelope observed by small-angle X-ray scattering (SAXS) for the Kv7.1 [ABCD/CaM] complex in solution (Sachyani et al., 2014). This disposition places PIP_2 and L609 of helix D more than 10 nm apart.

Fluorescence spectroscopy

Recombinant proteins ABCD, ABCD-L609R (both fused to GST) and CaM were produced as described previously (Alaimo et al., 2009). Fluorometric experiments using dansyl-CaM (D-CaM), CaM dansylation, sample and buffers preparation and fluorescent measurements were performed as described previously (Alaimo et al., 2013b; Bonache et al., 2014).

Recombinant protein production, purification and native gel electrophoresis

Fusion proteins were expressed in *Escherichia coli* [BL21(DE3)] grown in lysogeny broth (LB) medium at 37°C and induced at $OD_{600\ nm}$=0.6–0.8 with 0.5 mM isopropyl β-D-1-thiogalactopyranoside (IPTG) for 5 h. Cells were harvested by centrifugation at 5000 ***g*** for 20 min at 4°C, and cell pellets were frozen at −20°C. Thawed cell pellets were lysed in lysis buffer (mM: 120 KCl, 3 imidazole, 1 phenylmethylsufonyl fluoride (PMSF), 10 K-HEPES; pH 7.4), and one tablet of protease inhibitor without EDTA (Roche Applied Science, Penzberg, Germany), and passed three times through a homogenizer (Emulsiflex). Insoluble material was precipitated by centrifugation for 30 min at 25,000 ***g*** at 4°C. The resulting soluble fraction, which contained the fusion protein, was applied to a 5 ml cobalt-charged column (no. 28-9537-67, GE Healthcare, Little Chalfont, UK), and pre-equilibrated in wash buffer (mM: 120 KCl, 10 K-HEPES; pH 7.4). Increasing amounts of imidazole were used for washing. Sample elution proceeded on a linear gradient from 30 to 300 mM imidazole on an ÄKTA fast protein liquid chromatography (FPLC) system. Imidazole was removed by dialysis overnight at 4°C in cellulose membrane tubing (no. D927-100FT, Sigma-Aldrich, St Louis, MO, USA) with agitation against 1 litre of fluorescence buffer (mM: 125 KCl, 5 NaCl, 1 $MgCl_2$, 10 EGTA, 10 Tris; pH 7.4. Fusion proteins were then applied to a Superdex 200 pg 26/600 column (no. 28-9893-36, GE Healthcare) and eluted in the same buffer. Positive fractions were pooled together and concentrated using a 3 kDa cut-off Amicon ultra-15 concentrator (no. UFC900308, EMD Millipore, Billerica, MA, USA) in a fixed angle rotor at 3500 ***g***. Protein concentration was measured at 462 nm, equalized to 4 µM and samples with 5% of glycerol were run in 7% non-denaturing ('native') gels (without SDS).

Cell culture and transfection

HEK293T cells (HEK 293T/17, ATCC, CRL-11268) were maintained in 5% CO_2 at 37°C in Dulbecco's modified Eagle's medium (DMEM, Sigma-Aldrich), supplemented with non-essential amino acids (Sigma, Madrid, Spain) and 10% fetal bovine serum (FBS; Lonza, Madrid, Spain). Transient transfection for imaging was performed using polyethylenimine (PEI) 25 kDa (no. 23966-22g, PolySciences, Eppelheim, Germany), whereas for electrophysiology experiments lipofectamine 2000 (Invitrogen) was used following manufacturer's instructions. All experiments were performed 48 h after transfection.

Electrophysiological measurements

Whole-cell patch recordings of HEK293T cells were obtained at room temperature (21–25°C). Cells were bathed in the following solution (mM): 140 NaCl, 4 KCl, 2 $CaCl_2$, 2 $MgCl_2$, 10 Na-HEPES and 5 D-glucose, adjusted to pH 7.4 with NaOH. The osmolarity was adjusted with mannitol to ∼315 mosmol/l. Pipettes were pulled from borosilicate glass capillaries (Sutter Instruments, USA) using a Narishige micropipette puller (PC-10; Narishige Instrument Company, Japan). All experiments to test the impact of DrVSP (0.5 µg cDNA per 35 mm dish) were carried out with 100% series resistance compensation using a VE-2 amplifier (Alembic Instruments, Canada) equipped with an Rs Compensator (Sherman et al., 1999).

We applied the traditional voltage protocol as in the original description of the M-current (Adams et al., 1982). This protocol takes advantage of the lack of inactivation of the M-channels, and allows removing potential 'invasion' of the signal by other inactivating currents. Our protocol to study the sensitivity to DrVSP activation is similar to that used by Hille and collaborators (Falkenburger et al., 2010). DrVSP was activated by a 200 ms jump to +100 mV, and the voltage was returned to the holding potential of −20 mV. Jumps to −110 mV, beyond the K^+ reversal potential, were applied to close the channels. Upon returning to the holding potential, an instantaneous current jump (corresponding to leak current) followed by a slowly developing outward relaxation (corresponding to the opening of the M-channels) was recorded. The size of the outward relaxation before and after the +100 mV jump was used to estimate the effect of DrVSP activation on M-current size (Adams et al., 1982; Villarroel, 1994).

Pipettes were filled with an internal solution containing (mM): 125 KCl, 5 $MgCl_2$, 5 EGTA, 5 Na_2ATP and 10 K-HEPES, adjusted to pH 7.2 with KOH and the osmolarity adjusted to ∼300 mosmol/l with mannitol (Gómez-Posada et al., 2010). The amplitude of the Kv7 current was defined as the peak difference in current relaxation measured at −30 mV after 500–1500 ms pulses to −110 mV (all channels closed) and to +30 mV (all channels opened). The data were acquired and analyzed using pCLAMP software (version 8.2), normalized in Excel (Microsoft, Madrid, Spain) and plotted using SigmaPlot (SPSS Corporation, Madrid, Spain). Data are shown as means±s.e.m. The differences between the means were evaluated using Student's unpaired *t*-test, where values of $P \leq 0.05$ were considered significant. The number of cells in each experiment is indicated in parentheses in the figures. The results are from two or more independent batches of cells. In all figures *, ** and *** indicate significance at $P<0.05$, $P<0.01$ and $P<0.001$, respectively.

Spectral FRET measurements

Single transiently transfected HEK293 cells were maintained in buffer solution composed of (mM): 140 NaCl, 5 KCl, 1 $MgCl_2$, 2 $CaCl_2$, 10 glucose and 10 Na-HEPES; pH 7.4 at room temperature. For CFP-CaM binding to YFP-tagged KV7.2 C-terminal region (devoid of any membrane anchoring region) the transfection ratio used was 1:5 with a total of 0.6 µg DNA per M35 dish. Control experiments expressing CFP alone or CFP together with YFP at a 1:5 ratio demonstrated that contamination of the CFP emission signal due to direct YFP excitation at 405 nm was <1% (Fig. S1). For assembly experiments, the ratio was 1:1 (1 µg of each FCP-tagged ABCD and 2 µg of CaM or 2 µg of empty pcDNA3.1 his/myc C vector). Images were recorded 48 h after transfection using a Nikon D Eclipse TE2000-U fluorescence microscope (Nikon Instruments, Tokyo, Japan) equipped with a confocal scanning head and a spectral detector module. Images were captured using a 60× oil objective (numerical aperture 1.43), with the pinhole opened (150 µm) and using the 405 nm laser line (Coherent, Santa Clara, CA, USA) or the 488 nm line (Melles-Griot, Rochester, NY, USA) for direct CFP or YFP excitation, respectively. Cytosolic regions of interest (ROI) from cells displaying a clear signal after excitation with the 488 nm laser line were included in the analysis. The spectral detector allows simultaneous recording of 32 images, each registering a 5 nm band of the spectrum, covering 450–610 nm. After spectral unmixing, the area under the spectra was measured and a FRET index was calculated as FRET index=YFP_{405}/CFP_{405}.

e-FRET measurements

Fluorescence intensities of YFP and CFP were recorded from single cells using a Leica DMI6000B inverted epifluorescence microscope and a dual emission photometric system (Till Photonics, Gräfelfing, Germany). Excitation was done at 436±7.5 nm or 500±7.5 nm, applied at 2 Hz using a Polychrome V as light source. Epifluorescence emission was detected by a photodiode, digitized (Mini Digi1B; Molecular Devices) and acquired using Clampex 10 software (Molecular Devices). FRET filter cubes were (excitation, long-pass beam-splitter, emission): CFP (ET436/20x; T455lp; ET480/40m), YFP (ET500/20x; T515lp; ET535/30m) and FRET (ET436/20x; T455lp; ET535/30m) (Chroma Technology). e-FRET efficiencies (E_D) were determined using $E_D=(S_{FRET}-R_{D1}\times S_{CFP}-R_A\times S_{YFP})/(S_{FRET}-R_{D1}\times S_{CFP}-R_A\times S_{YFP}+G\times S_{CFP})$. S_{FRET}, S_{CFP} and S_{YFP} denote fluorescence intensities derived from measurements in individual cells co-expressing YFP- and CFP-tagged proteins with the respective filter cube (excitation, emission): S_{FRET} (500±7.5 nm, 535±15 nm), S_{CFP} (436±7.5 nm, 480±20 nm) and S_{YFP} (500±7.5 nm, 535±15 nm). R_{D1} and R_A

are experimentally predetermined constants from measurements applied to single cells expressing only CFP- or YFP-tagged molecules that correct for donor bleed trough and acceptor cross excitation. G factor represents the ratio of sensitized acceptor emission to quenched donor emission due to FRET, and was experimentally determined to be 4.13 using CFP fused to YFP with linkers of varying length (4, 40 and 80 amino acids). The CFP/YFP ratio was between 1:5 and 5:1, which is expected to yield reliable results.

d-FRET measurements

Fluorescence intensities of YFP and CFP were recorded from single cells using a Leica DMI6000B inverted epifluorescence microscope and a 914 photomultiplier detection system (PTI, Canada). Excitation was done at 436±7.5 nm or 500±7.5 nm, applied with a DeltaRam X monochromator including an arc lamp (PTI, Canada) as light source. Epifluorescence emission was acquired using FelixGX software (PTI, Canada).

FRET efficiency for d-FRET (E_A), which is defined as the fractional increase in YFP emission caused by FRET, was calculated using $E_A=\{[S_{FRET}-(R_{D1})(S_{CFP})]/[(R_{A1})(S_{YFP})]-1\}\times(\varepsilon_{YFP}/\varepsilon_{CFP})$; S_{FRET}, S_{CFP} and S_{YFP} denote fluorescence intensities derived from measurements in individual cells co-expressing YFP- and CFP-tagged proteins with the respective filter cube.

FRET data were analyzed using Clampfit 10.0 (Molecular Devices), and Microsoft Office Excel software. Data plotting, curve fitting and statistical analysis were performed using Sigma-Plot 12 software (SPSS Corporation). All values are presented as means±s.e.m. for the indicated number (n) of experiments. Student's t-test was used to compare means of two groups from data with a normal distribution. Statistical analysis was performed using SigmaPlot software. $^*P<0.05$, $^{**}P<0.01$ and $^{***}P<0.001$ indicate significance.

Competing interests

The authors declare no competing or financial interests.

Author contributions

A.V. conceived the project. A. Alberdi, C.G.-P. and A.V. designed the experiments and analyzed the data. A.Alb., C.G.-P., G.B.-S., C.V., A. Alaimo, J.A. and C.L.-R. performed the experiments. A. Alberdi, C.G.-P., E.B. and C.W.-S. contributed analytical or experimental tools. A. Alberdi, C.G-.P., G.B-.S., A. Alaimo, P.A. and A.V. analyzed the data. A.V. wrote the paper with critical inputs from A. Alberdi, C.G.-P., P.A. and C.W.-S. All authors approved the final version of the manuscript. The experiments were performed at Unidad de Biofísica, Leioa, Spain and Department of Pharmacy, Center for Drug Research and Center for Integrated Protein Science Munich (CIPSM), Ludwig-Maximilians-Universität, Germany.

Funding

This work was supported by grants from the Spanish Ministry of Economy and Competitiveness (BFU2012-39883), the Spanish Ion Channel Initiative Consolider project (CSD2008-00005), and the Basque Government (SAIOTEK SA-2006/00023 and 304211ENA9). A. Alaimo was funded by a Universidad del País Vasco postdoctoral fellowship. A. Alberdi held a JAE-predoctoral Consejo Superior de Investigaciones Científicas fellowship co-financed with European Social Funds (JAEPre_2010_00711). G.B.-S. holds a fellowship from the Basque Country Government (BFI-2011-159). C.M. was funded by the Spanish Ministry of Economy and Competitiveness (PTA2012) and co-financed by Fundación Biofísica Bizkaia.

Supplementary information

Supplementary information available online at
http://jcs.biologists.org/lookup/suppl/doi:10.1242/jcs.176420/-/DC1

References

Adams, P. R., Brown, D. A. and Constanti, A. (1982). Pharmacological inhibition of the M-current. *J. Physiol.* **332**, 223-262.

Aivar, P., Fernández-Orth, J., Gomis-Perez, C., Alberdi, A., Alaimo, A., Rodríguez, M. S., Giraldez, T., Miranda, P., Areso, P. and Villarroel, A. (2012). Surface expression and subunit specific control of steady protein levels by the kv7.2 helix A-B linker. *PLoS ONE* **7**, e47263.

Alaimo, A., Gomez-Posada, J. C., Aivar, P., Etxeberria, A., Rodriguez-Alfaro, J. A., Areso, P. and Villarroel, A. (2009). Calmodulin activation limits the rate of KCNQ2 K^+ channel exit from the endoplasmic reticulum. *J. Biol. Chem.* **284**, 20668-20675.

Alaimo, A., Alberdi, A., Gomis-Perez, C., Fernandez-Orth, J., Gomez-Posada, J. C., Areso, P. and Villarroel, A. (2013a). Cooperativity between calmodulin-binding sites in Kv7.2 channels. *J. Cell Sci.* **126**, 244-253.

Alaimo, A., Malo, C., Areso, P., Aloria, K., Millet, O. and Villarroel, A. (2013b). The use of dansyl-calmodulin to study interactions with channels and other proteins. *Methods Mol. Biol.* **998**, 217-231.

Alaimo, A., Alberdi, A., Gomis-Perez, C., Fernández-Orth, J., Bernardo-Seisdedos, G., Malo, C., Millet, O., Areso, P. and Villarroel, A. (2014). Pivoting between calmodulin lobes triggered by calcium in the Kv7.2/calmodulin complex. *PLoS ONE* **9**, e86711.

Ben Johny, M., Yang, P. S., Bazzazi, H. and Yue, D. T. (2013). Dynamic switching of calmodulin interactions underlies Ca^{2+} regulation of CaV1.3 channels. *Nat. Commun.* **4**, 1717.

Bonache, M. A., Alaimo, A., Malo, C., Millet, O., Villarroel, A. and González-Muñiz, R. (2014). Clicked bis-PEG-peptide conjugates for studying calmodulin-Kv7.2 channel binding. *Org. Biomol. Chem.* **12**, 8877-8887.

Brown, D. A., Hughes, S. A., Marsh, S. J. and Tinker, A. (2007). Regulation of M (Kv7.2/7.3) channels in neurons by PIP_2 and products of PIP_2 hydrolysis: significance for receptor-mediated inhibition. *J. Physiol.* **582**, 917-925.

Cavaretta, J. P., Sherer, K. R., Lee, K. Y., Kim, E. H., Issema, R. S. and Chung, H. J. (2014). Polarized axonal surface expression of neuronal KCNQ potassium channels is regulated by calmodulin interaction with KCNQ2 subunit. *PLoS ONE* **9**, e103655.

Chen, H., Puhl, H. L., III, Koushik, S. V., Vogel, S. S. and Ikeda, S. R. (2006). Measurement of FRET efficiency and ratio of donor to acceptor concentration in living cells. *Biophys. J.* **91**, L39-L41.

Chung, H. J. (2014). Role of calmodulin in neuronal Kv7/KCNQ potassium channels and epilepsy. *Front. Biol.* **9**, 205-215.

Chung, H. J., Jan, Y. N. and Jan, L. Y. (2006). Polarized axonal surface expression of neuronal KCNQ channels is mediated by multiple signals in the KCNQ2 and KCNQ3 C-terminal domains. *Proc. Natl. Acad. Sci. USA* **103**, 8870-8875.

Devaux, J. J., Kleopa, K. A., Cooper, E. C. and Scherer, S. S. (2004). KCNQ2 is a nodal K^+ channel. *J. Neurosci.* **24**, 1236-1244.

Dvir, M., Peretz, A., Haitin, Y. and Attali, B. (2014a). Recent molecular insights from mutated IKS channels in cardiac arrhythmia. *Curr. Opin. Pharmacol.* **15**, 74-82.

Dvir, M., Strulovich, R., Sachyani, D., Ben-Tal Cohen, I., Haitin, Y., Dessauer, C., Pongs, O., Kass, R., Hirsch, J. A. and Attali, B. (2014b). Long QT mutations at the interface between KCNQ1 helix C and KCNE1 disrupt IKS regulation by PKA and PIP_2. *J. Cell Sci.* **127**, 3943-3955.

Edelstein, S. J. and Le Novère, N. (2013). Cooperativity of allosteric receptors. *J. Mol. Biol.* **425**, 1424-1432.

Etxeberria, A., Aivar, P., Rodriguez-Alfaro, J. A., Alaimo, A., Villace, P., Gomez-Posada, J. C., Areso, P. and Villarroel, A. (2008). Calmodulin regulates the trafficking of KCNQ2 potassium channels. *FASEB J.* **22**, 1135-1143.

Falkenburger, B. H., Jensen, J. B. and Hille, B. (2010). Kinetics of PIP_2 metabolism and KCNQ2/3 channel regulation studied with a voltage-sensitive phosphatase in living cells. *J. Gen. Physiol* **135**, 99-114.

Friedman, P. N., Chen, X., Bargonetti, J. and Prives, C. (1993). The p53 protein is an unusually shaped tetramer that binds directly to DNA. *Proc. Natl. Acad. Sci. USA* **90**, 3319-3323.

Gamper, N. and Shapiro, M. S. (2007). Regulation of ion transport proteins by membrane phosphoinositides. *Nat. Rev. Neurosci.* **8**, 921-934.

Gómez-Posada, J. C., Aivar, P., Alberdi, A., Alaimo, A., Etxeberría, A., Fernández-Orth, J., Zamalloa, T., Roura-Ferrer, M., Villace, P., Areso, P. et al. (2011). Kv7 channels can function without constitutive calmodulin tethering. *PLoS ONE* **6**, e25508.

Gómez-Posada, J. C., Etxeberria, A., Roura-Ferrer, M., Areso, P., Masin, M., Murrell-Lagnado, R. D. and Villarroel, A. (2010). A pore residue of the KCNQ3 potassium M-channel subunit controls surface expression. *J. Neurosci.* **30**, 9316-9323.

Haitin, Y. and Attali, B. (2008). The C-terminus of Kv7 channels: a multifunctional module. *J. Physiol.* **586**, 1803-1810.

Hansen, S. B., Tao, X. and MacKinnon, R. (2011). Structural basis of PIP_2 activation of the classical inward rectifier K^+ channel Kir2.2. *Nature* **477**, 495-498.

Hernandez, C. C., Zaika, O. and Shapiro, M. S. (2008). A carboxy-terminal inter-helix linker as the site of phosphatidylinositol 4,5-bisphosphate action on Kv7 (M-type) K^+ channels. *J. Gen. Physiol.* **132**, 361-381.

Hille, B., Dickson, E. J., Kruse, M., Vivas, O. and Suh, B. C. (2014). Phosphoinositides regulate ion channels. *Biochim. Biophys. Acta* **1851**, 844-856.

Howard, R. J., Clark, K. A., Holton, J. M. and Minor, D. L., Jr. (2007). Structural insight into KCNQ (Kv7) channel assembly and channelopathy. *Neuron* **53**, 663-675.

Jenke, M., Sánchez, A., Monje, F., Stühmer, W., Weseloh, R. M. and Pardo, L. A. (2003). C-terminal domains implicated in the functional surface expression of potassium channels. *EMBO J.* **22**, 395-403.

Kang, S., Xu, M., Cooper, E. C. and Hoshi, N. (2014). Channel-anchored protein kinase CK2 and protein phosphatase 1 reciprocally regulate KCNQ2-containing M-channels via phosphorylation of calmodulin. *J. Biol. Chem.* **289**, 11536-11544.
Kass, R. S., Kurokawa, J., Marx, S. O. and Marks, A. R. (2003). Leucine/isoleucine zipper coordination of ion channel macromolecular signaling complexes in the heart. Roles in inherited arrhythmias. *Trends Cardiovasc. Med.* **13**, 52-56.
Kosenko, A. and Hoshi, N. (2013). A change in configuration of the calmodulin-KCNQ channel complex underlies Ca^{2+}-dependent modulation of KCNQ channel activity. *PLoS ONE* **8**, e82290.
Kosenko, A., Kang, S., Smith, I. M., Greene, D. L., Langeberg, L. K., Scott, J. D. and Hoshi, N. (2012). Coordinated signal integration at the M-type potassium channel upon muscarinic stimulation. *EMBO J.* **31**, 3147-3156.
Liu, W. and Devaux, J. J. (2014). Calmodulin orchestrates the heteromeric assembly and the trafficking of KCNQ2/3 (Kv7.2/3) channels in neurons. *Mol. Cell. Neurosci.* **58**, 40-52.
Logothetis, D. E., Petrou, V. I., Adney, S. K. and Mahajan, R. (2010). Channelopathies linked to plasma membrane phosphoinositides. *Pflügers Arch.* **460**, 321-341.
Long, S. B., Campbell, E. B. and MacKinnon, R. (2005). Crystal structure of a mammalian voltage-dependent Shaker family K^+ channel. *Science* **309**, 897-903.
Lupas, A. N. and Gruber, M. (2005). The structure of α-helical coiled coils. *Adv. Protein Chem.* **70**, 37-38.
Maljevic, S. and Lerche, H. (2014). Potassium channel genes and benign familial neonatal epilepsy. *Prog. Brain Res.* **213**, 17-53.
Maljevic, S., Lerche, C., Seebohm, G., Alekov, A. K., Busch, A. E. and Lerche, H. (2003). C-terminal interaction of KCNQ2 and KCNQ3 K+ channels. *J. Physiol.* **548**, 353-360.
Marx, S. O., Kurokawa, J., Reiken, S., Motoike, H., D'Armiento, J., Marks, A. R. and Kass, R. S. (2002). Requirement of a macromolecular signaling complex for β adrenergic receptor modulation of the KCNQ1-KCNE1 potassium channel. *Science* **295**, 496-499.
Motlagh, H. N., Wrabl, J. O., Li, J. and Hilser, V. J. (2014). The ensemble nature of allostery. *Nature* **508**, 331-339.
Mruk, K., Shandilya, S. M. D., Blaustein, R. O., Schiffer, C. A. and Kobertz, W. R. (2012). Structural insights into neuronal K^+ channel-calmodulin complexes. *Proc. Natl. Acad. Sci. USA* **109**, 13579-13583.
Nakajo, K. and Kubo, Y. (2008). Second coiled-coil domain of KCNQ channel controls current expression and subfamily specific heteromultimerization by salt bridge networks. *J. Physiol.* **586**, 2827-2840.
Patterson, G. H., Piston, D. W. and Barisas, B. G. (2000). Forster distances between green fluorescent protein pairs. *Anal. Biochem.* **284**, 438-440.
Richards, M. C., Heron, S. E., Spendlove, H. E., Scheffer, I. E., Grinton, B., Berkovic, S. F., Mulley, J. C. and Davy, A. (2004). Novel mutations in the KCNQ2 gene link epilepsy to a dysfunction of the KCNQ2-calmodulin interaction. *J. Med. Genet.* **41**, e35.
Sachyani, D., Dvir, M., Strulovich, R., Tria, G., Tobelaim, W., Peretz, A., Pongs, O., Svergun, D., Attali, B. and Hirsch, J. A. (2014). Structural basis of a Kv7.1 potassium channel gating module: studies of the intracellular C-terminal domain in complex with calmodulin. *Structure* **22**, 1582-1594.
Sarhan, M. F., Tung, C.-C., Van Petegem, P. and Ahern, C. A. (2012). Crystallographic basis for calcium regulation of sodium channels. *Proc. Natl. Acad. Sci. USA* **109**, 3558-3563.
Schmitt, N., Schwarz, M., Peretz, A., Abitbol, I., Attali, B. and Pongs, O. (2000). A recessive C-terminal Jervell and Lange-Nielsen mutation of the KCNQ1 channel impairs subunit assembly. *EMBO J.* **19**, 332-340.
Schumacher, M. A., Rivard, A. F., Bächinger, H. P. and Adelman, J. P. (2001). Structure of the gating domain of a Ca^{2+}-activated K^+ channel complexed with Ca^{2+}/calmodulin. *Nature* **410**, 1120-1124.
Schwake, M., Athanasiadu, D., Beimgraben, C., Blanz, J., Beck, C., Jentsch, T. J., Saftig, P. and Friedrich, T. (2006). Structural determinants of M-type KCNQ (Kv7) K^+ channel assembly. *J. Neurosci.* **26**, 3757-3766.
Sherman, A. J., Shrier, A. and Cooper, E. (1999). Series resistance compensation for whole-cell patch-clamp studies using a membrane state estimator. *Biophys. J.* **77**, 2590-2601.
Soldovieri, M. V., Castaldo, P., Iodice, L., Miceli, F., Barrese, V., Bellini, G., del Giudice, E. M., Pascotto, A., Bonatti, S., Annunziato, L. et al. (2006). Decreased subunit stability as a novel mechanism for potassium current impairment by a KCNQ2 C terminus mutation causing benign familial neonatal convulsions. *J. Biol. Chem.* **281**, 418-428.
Soldovieri, M. V., Miceli, F. and Taglialatela, M. (2011). Driving with no brakes: molecular pathophysiology of Kv7 potassium channels. *Physiology* **26**, 365-376.
Suh, B.-C. and Hille, B. (2008). PIP_2 is a necessary cofactor for ion channel function: how and why? *Annu. Rev. Biophys.* **37**, 175-195.
Tsuruda, P. R., Julius, D. and Minor, D. L., Jr. (2006). Coiled coils direct assembly of a cold-activated TRP channel. *Neuron* **51**, 201-212.
Villarroel, A. (1994). On the role of arachidonic acid in M-current modulation by muscarine in bullfrog sympathetic neurons 61. *J. Neurosci.* **14**, 7053-7066.
Villarroel, A., Taglialatela, M., Bernardo-Seisdedos, G., Alaimo, A., Agirre, J., Alberdi, A., Gomis-Perez, C., Soldovieri, M. V., Ambrosino, P., Malo, C. et al. (2014). The ever changing moods of calmodulin: how structural plasticity entails transductional adaptability. *J. Mol. Biol.* **426**, 2717-2735.
Vogel, S. S., Thaler, C. and Koushik, S. V. (2006). Fanciful FRET. *Sci. STKE* **2006**, re2.
Wiener, R., Haitin, Y., Shamgar, L., Fernandez-Alonso, M. C., Martos, A., Chomsky-Hecht, O., Rivas, G., Attali, B. and Hirsch, J. A. (2008). The KCNQ1 (Kv7.1) COOH terminus, a multitiered scaffold for subunit assembly and protein interaction. *J. Biol. Chem.* **283**, 5815-5830.
Xu, Q., Chang, A., Tolia, A. and Minor, D. L., Jr. (2013). Structure of a Ca^{2+}/CaM: Kv7.4 (KCNQ4) B-helix complex provides insight into M current modulation. *J. Mol. Biol.* **425**, 378-394.
Yus-Nájera, E., Santana-Castro, I. and Villarroel, A. (2002). The identification and characterization of a noncontinuous calmodulin-binding site in non-inactivating voltage-dependent KCNQ potassium channels. *J. Biol. Chem.* **277**, 28545-28553.
Zaydman, M. A. and Cui, J. (2014). PIP_2 regulation of KCNQ channels: biophysical and molecular mechanisms for lipid modulation of voltage-dependent gating. *Front. Physiol.* **5**, 195.
Zaydman, M. A., Silva, J. R., Delaloye, K., Li, Y., Liang, H., Larsson, H. P., Shi, J. and Cui, J. (2013). Kv7.1 ion channels require a lipid to couple voltage sensing to pore opening. *Proc. Natl. Acad. Sci. USA* **110**, 13180-13185.

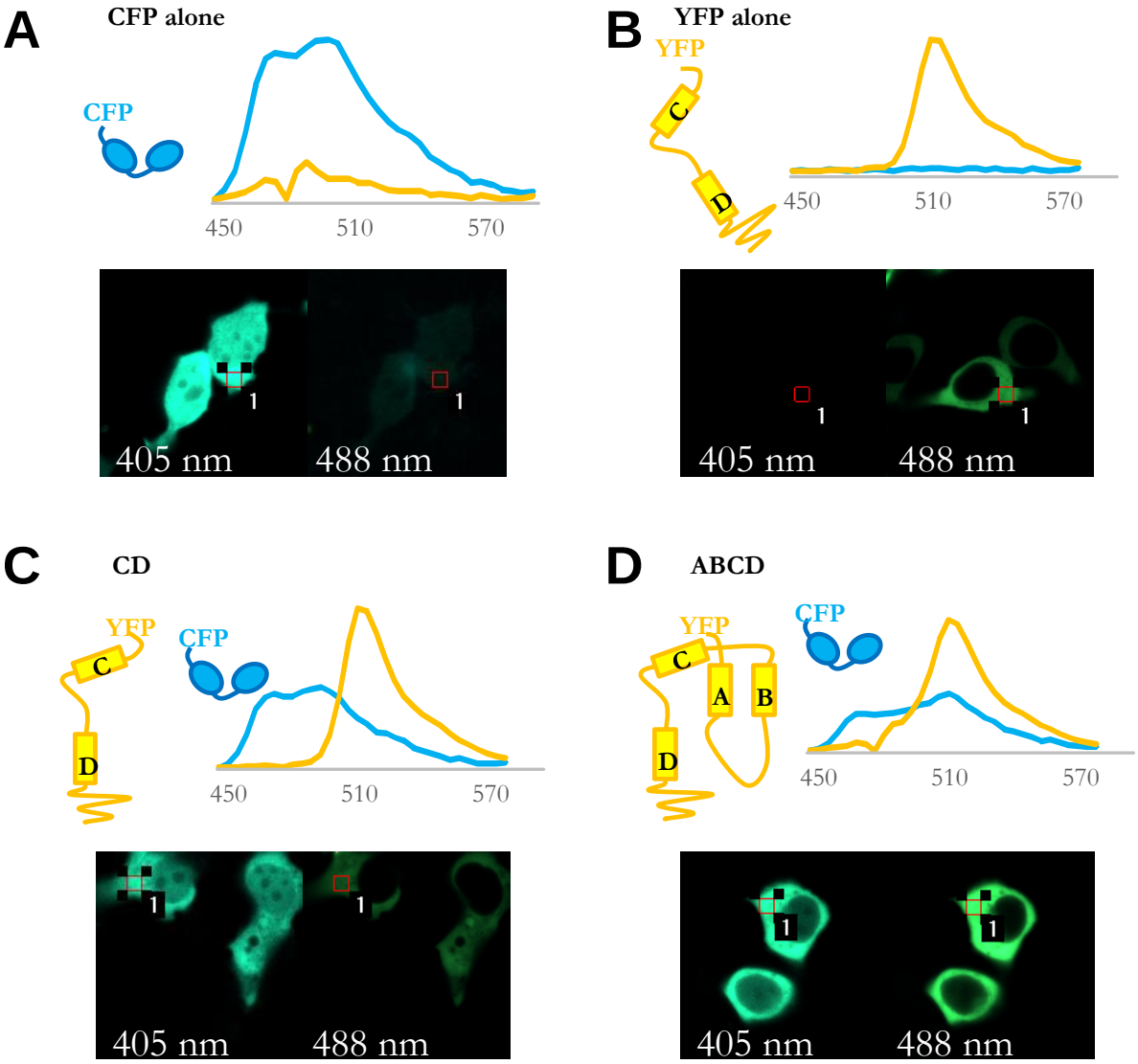

Fig. S1. Emission spectra of the different fluorophores excited at 405 nm (donor excitation wavelength, cyan trace, left image) or 488 nm (acceptor excitation wavelength, yellow trace, right image). The regions of interest selected to generate the spectra are indicated with red squares. Note that the presence of helices CD prevents the constructs from reaching the nucleus.

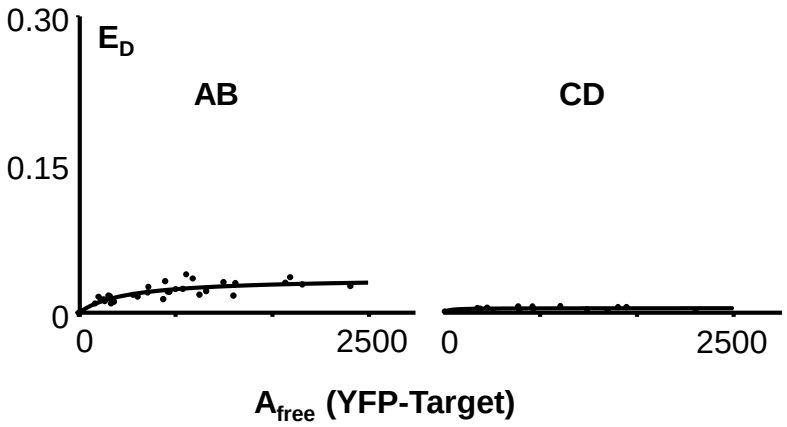

Fig. S2. The binding curve in which the FRET strength between CFP-CaM and YFP-AB or YFP-CD is plotted cell-by-cell versus concentration of free YFP-tagged acceptor (n >25).

nature COMMUNICATIONS

ARTICLE

Received 14 Mar 2014 | Accepted 10 Jul 2014 | Published 21 Aug 2014

DOI: 10.1038/ncomms5699

High susceptibility to fatty liver disease in two-pore channel 2-deficient mice

Christian Grimm[1], Lesca M. Holdt[2,*], Cheng-Chang Chen[1,*], Sami Hassan[1,*], Christoph Müller[3], Simone Jörs[4], Hartmut Cuny[1,*,†], Sandra Kissing[5], Bernd Schröder[5], Elisabeth Butz[1], Bernd Northoff[2], Jan Castonguay[6], Christian A. Luber[7,†], Markus Moser[7], Saskia Spahn[1], Renate Lüllmann-Rauch[8], Christina Fendel[9], Norbert Klugbauer[6], Oliver Griesbeck[10], Albert Haas[9], Matthias Mann[7], Franz Bracher[3], Daniel Teupser[2], Paul Saftig[5], Martin Biel[1] & Christian Wahl-Schott[1]

Endolysosomal organelles play a key role in trafficking, breakdown and receptor-mediated recycling of different macromolecules such as low-density lipoprotein (LDL)-cholesterol, epithelial growth factor (EGF) or transferrin. Here we examine the role of two-pore channel (TPC) 2, an endolysosomal cation channel, in these processes. Embryonic mouse fibroblasts and hepatocytes lacking TPC2 display a profound impairment of LDL-cholesterol and EGF/EGF-receptor trafficking. Mechanistically, both defects can be attributed to a dysfunction of the endolysosomal degradation pathway most likely on the level of late endosome to lysosome fusion. Importantly, endolysosomal acidification or lysosomal enzyme function are normal in TPC2-deficient cells. TPC2-deficient mice are highly susceptible to hepatic cholesterol overload and liver damage consistent with non-alcoholic fatty liver hepatitis. These findings indicate reduced metabolic reserve of hepatic cholesterol handling. Our results suggest that TPC2 plays a crucial role in trafficking in the endolysosomal degradation pathway and, thus, is potentially involved in the homoeostatic control of many macromolecules and cell metabolites.

[1] Department of Pharmacy—Center for Drug Research and Center for Integrated Protein Science Munich (CIPSM), Ludwig-Maximilians-Universität, 81377 München, Germany. [2] Institute of Laboratory Medicine—University Hospital Munich, 81377 Munich, Germany. [3] Department of Pharmacy, Ludwig-Maximilians-Universität München, 81377 München, Germany. [4] 2nd Department of Internal Medicine, Klinikum rechts der Isar, Technical University of Munich, 81675 München, Germany. [5] Institute of Biochemistry, Christian-Albrechts-Universität Kiel, 24118 Kiel, Germany. [6] Institute for Experimental and Clinical Pharmacology and Toxicology, Albert-Ludwigs-Universität Freiburg, Freiburg, Germany. [7] Max-Planck-Institute for Biochemistry, Am Klopferspitz 18, 82152 Martinsried, Germany. [8] Institute of Anatomy, Christian-Albrechts-Universität Kiel, 24098 Kiel, Germany. [9] Institute for Cell Biology, Rheinische Friedrich-Wilhelms-Universität Bonn, 53121 Bonn, Germany. [10] Max-Planck-Institute of Neurobiology, Am Klopferspitz 18, 82152 Martinsried, Germany. * These authors contributed equally to this work. † Present addresses: RMIT University, Melbourne, VIC 3001, Australia (H.C.); Novo Nordisk Research Center, Seattle, Washington 98109, USA (C.A.L.). Correspondence and requests for materials should be addressed to M.B. (email: martin.biel@cup.uni-muenchen.de) or to C.W.-S. (email: christian.wahl@cup.uni-muenchen.de).

Endo/lysosomal vesicle trafficking is important for many cells and organ systems. In the liver, receptor-mediated uptake of low-density lipoproteins (LDLs) and subsequent intracellular transport is essential for hepatic cholesterol homoeostasis and plasma lipoprotein metabolism. Dysfunction within this pathway results in liver disease such as non-alcoholic fatty liver disease (NAFLD), which is associated with increased cardiovascular and liver-related mortality[1]. NAFLD is the most common cause of chronic liver disease in Western Europe and the United States[2,3]. It has been estimated that as many as 30% of adults in these countries have NAFLD[2]. This liver disease has thus emerged as a substantial public health concern. The spectrum of NAFLD ranges from simple lipid accumulation in hepatocytes (steatosis) in absence of alcohol, which is considered relatively benign, to steatosis with liver damage, inflammation and fibrosis (non-alcoholic steatohepatitis (NASH)) and progressive liver disease, including cirrhosis and hepatocellular carcinoma[4]. The hallmark of NAFLD is hepatic neutral lipid accumulation, mainly triacylglycerol and cholesterol ester (CE). The roles of both triglycerides and free fatty acid accumulation in NAFLD have been elucidated in many studies[5]. By contrast, the role of cholesterol in NAFLD has been less extensively studied but is gaining increasing attention[1,6–8].

Recent studies have demonstrated that cholesterol metabolism and trafficking might play an important role in the pathogenesis of NAFLD and NASH[1]. Cholesterol is highly enriched in LDLs and is taken up by the liver via receptor-mediated endocytosis of the LDL–LDL receptor complex at the plasma membrane. After internalization, membrane vesicles containing this complex fuse to early endosomes. Subsequently, LDL receptors and its ligand LDL are separated in the sorting endosome and distributed by two major routes: the recycling pathway transports LDL receptor proteins back to the plasma membrane; the degradation pathway traffics LDL to late endosomes and lysosomes. This pathway involves maturation of early endosomes into multivesicular bodies/late endosomes which finally fuse with lysosomes[9–15]. LDL-cholesterol exits from late endosomes and lysosomes and is either metabolized to bile acids (BAs) and excreted, stored as CEs in lipid droplets or exported from hepatocytes into the plasma.

While the principle pathways of LDL transport in the endolysosomal vesicle system are well characterized, the distinct proteins involved in these processes are largely unknown. Interesting candidate proteins, which might regulate endolysosomal trafficking, and fusion processes are cation channels present in the membrane of endolysosomal vesicles. Recently identified cation channels that may generate Ca^{2+} signals during endolysosomal fusion events and thereby vesicle trafficking are the two-pore channels (TPCs)[16,17]. Two different TPC subtypes exist in mouse and man, TPC1 and TPC2. There is evidence that TPC1 is mainly present in the proximal endosomal system, and TPC2 is predominantly expressed on late endosomes and lysosomes[16,18,19]. The activation mechanism of TPCs is complex and has been suggested to involve the second messenger nicotinic acid adenine dinucleotide phosphate (NAADP) and the endolysosomal membrane lipidphosphatidylinositol (3,5)-bisphosphate ($PI(3,5)P_2$)[17,18,20–24]. Independent of what the nature of the endogenous ligand of these channels might be, there is substantial evidence that on activation TPCs mediate the release of Ca^{2+} from lysosomal stores. Patch-clamp[21,22,24], lipid bilayer and calcium imaging experiments[18,25,26] indicate that TPCs are Ca^{2+} permeable channels and, hence, may directly confer Ca^{2+} release from endosomes/lysosomes.

Here, we demonstrate that TPC2-deficient cells display profound trafficking defects in the endolysosomal degradation pathway. We provide evidence that TPC2 cation channels may directly be involved in Ca^{2+} signalling necessary for endolysosomal fusion processes. On the whole-animal level, we demonstrate that loss of TPC2 leads, as a result of the observed trafficking defects, to enhanced hepatic cholesterol accumulation, hyperlipoproteinaemia, and to NASH. These findings indicate a reduced metabolic reserve of hepatic cholesterol handling. Our results suggest that TPC2 plays a crucial role in endolysosomal trafficking in the endolysosmal degradation pathway and, thus, is potentially involved in the homoeostatic control of many macromolecules and cell metabolites.

Results

Loss of TPC2 impairs trafficking in the degradation pathway. To test whether TPC2 is implicated in endolysosomal trafficking, we disrupted the *Tpc2* gene in the mouse (Fig. 1a). In this mouse line, exon 7 of TPC2, which encodes TMD5 and part of the pore-loop of domain I, is globally deleted (Fig. 1a). This targeting strategy results in non-functional ion-channel proteins and is different from the strategies used for two mouse lines published before[17,18]. The deletion of the TPC2 gene was confirmed by genomic DNA analysis using Southern blot (not shown), PCR strategies, immunocytochemistry and western blotting (Supplementary Fig. 1a,b). Reverse-transcription PCR (RT–PCR) revealed the absence of exon 7 of TPC2 in $TPC2-/-$ murine embryonic fibroblasts (MEFs) and hepatocytes (Supplementary Fig. 1b). In addition, we generated a TPC2 antibody to detect TPC2 protein. In agreement with the RT–PCR results, TPC2 protein was totally absent in $TPC2^{-/-}$ MEFs in

Figure 1 | Generation and characterization of TPC2 knockout mice. (**a**) Targeting strategy for the generation of $TPC2^{-/-}$ mice and validation. The targeted exon 7 of the mTPC2 gene encodes TMD5 and part of the pore-loop of domain I. Exons 6–8 are represented by boxes. The targeting vector contains two *loxP* sites (green triangles), and a neo cassette flanked by two FLP recombination target (FRT) sites (blue triangles). (**b**) Representative immunofluroscence (IF) images of WT and $TPC2^{-/-}$ MEFs (stained with anti-TPC2 and Cy5) as well as WT and $TPC2^{-/-}$ liver cryosections (stained with anti-TPC2 and Alexa-488). Cell nuclei were visualized with Hoechst (MEFs) or 4′,6-diamidino-2-phenylindole (DAPI) (liver). Scale bars, 20 μm. (**c**) Current-voltage relations of currents recorded from single-WT and -$TPC2^{-/-}$ lysosomes in the presence of 50 nM NAADP or 10 μM $PI(3,5)P_2$. Lysosomes were isolated from vacuolin-treated WT and $TPC2^{-/-}$ MEFs before measurements. (**d**,**e**) Population data for current amplitudes at −200 mV obtained from experiments as shown in **a**; $^{**}P<0.01$, $^{***}P<0.001$, two-way analysis of varicane (ANOVA) followed by Bonferroni's *post hoc* test (**d**) or unpaired Student's *t*-test (**e**). (**f**) Expression and distribution of selected marker proteins for endosomes and lysosomes were unaffected in $TPC2^{-/-}$ compared with WT MEFs. Shown are representative confocal images of WT and $TPC2^{-/-}$ MEFs labelled with anti-EEA1, LAMP1 or LAMP2 and Alexa-488. Nuclei were visualized with DAPI. Scale bar, 20 μm. For additional markers, see Supplementary Fig. 1. (**g**) Representative electron microscope images of WT and $TPC2^{-/-}$ liver sections. BC, bile canaliculus; LY, lysosome; Mito, mitochondrion; RER, rough endoplasmic reticulum. Scale bars, 500 nm. (**h**,**i**) Measurement of endolysosomal pH in WT and $TPC2^{-/-}$ cells. Late endocytic compartments of WT and $TPC2^{-/-}$ MEFs were labelled with dextran-Oregon Green 514. (**h**) Fluorescence intensity ratios were calculated for defined pH values as described in the Methods section. (**i**) Lysosomal pH values in WT and $TPC2^{-/-}$ MEFs were calculated using the calibration curves presented in **h** and determined under basal conditions, without amino acids (−aa, EBSS), and without both, aa and glucose (−aa, −glc). Baf. A1 was used as positive control; n.s., not significant, unpaired Student's *t*-test. Data points in **d**,**e**,**h** and **i** are given as mean ± s.e.m.

immunocytochemistry experiments, while it could be detected in wild-type (WT) MEFs (Fig. 1b). Western blot analysis of WT and TPC2$^{-/-}$ liver samples confirmed absence of TPC2 protein in TPC2$^{-/-}$ livers (Supplementary Fig. 1b). In lysosomes prepared from TPC2$^{-/-}$ MEFs, currents elicited by postulated activators of TPC2, NAADP and PI(3,5)P_2 were strongly reduced (Fig. 1c–e). NAADP-dependent currents in WT lysosomes displayed a bell-shaped dose-response relationship (Fig. 1d) as reported previously[25,26].

Expression and distribution of the early endosomal markers EEA1, Rab4 and Rab5, the late endosomal/lysosomal markers LAMP1, LAMP2, LIMP2 and CD63 or the recycling endosomal markers TfR, Rab4 and Rab11 were comparable in WT and TPC2$^{-/-}$ cells (Fig. 1f and Supplementary Fig. 1c–e).

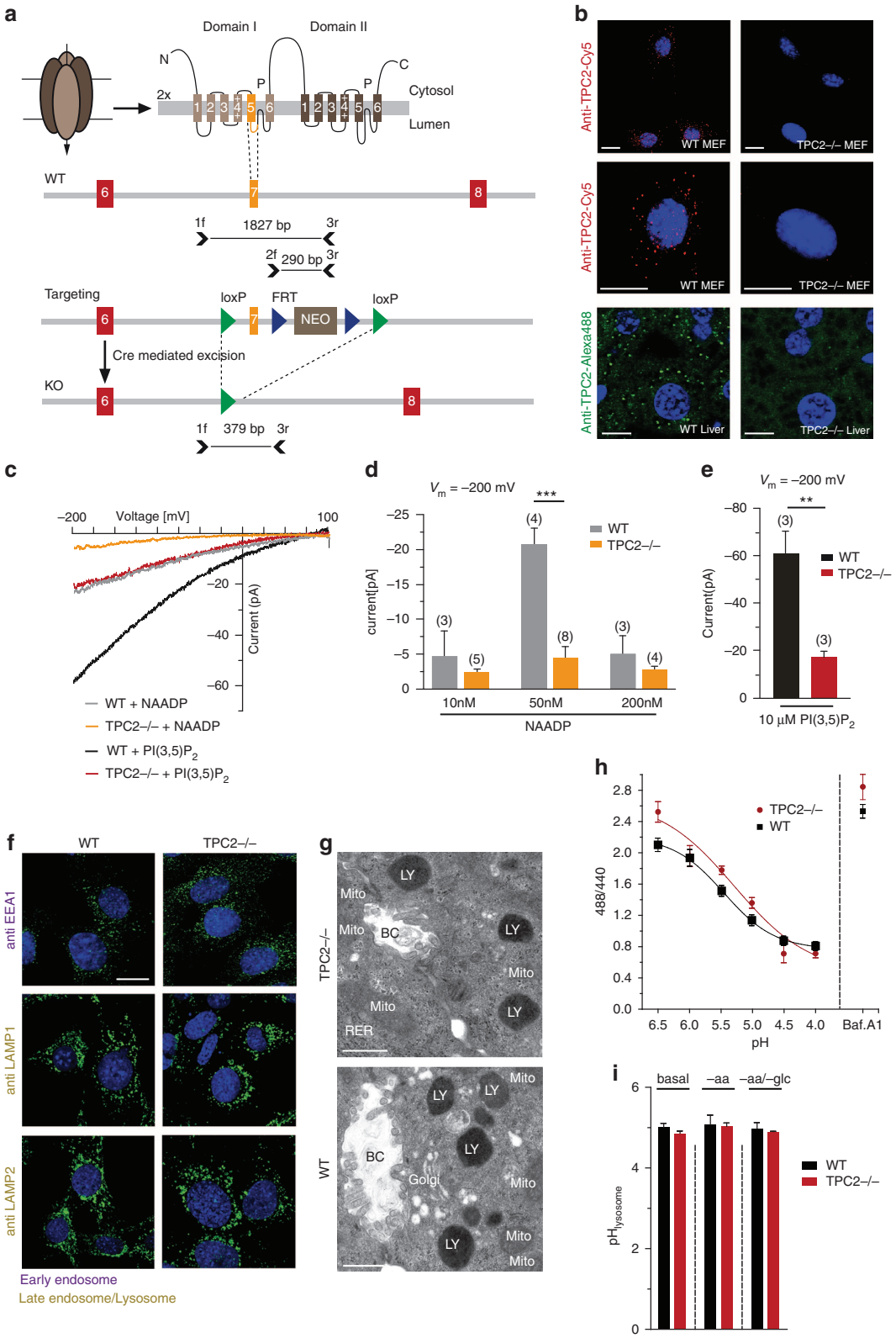

Overexpression of the constitutively active Rab5 variant Rab5(Q79L) induced the formation of characteristic enlarged Rab5-positive vesicles both in WT and TPC2$^{-/-}$ MEFs, indicating that early endosomal fusion is functioning normally (Supplementary Fig. 1f). Ultrastructural analyses of WT and TPC2$^{-/-}$ liver samples using electron microscopy revealed no obvious alterations in the endolysosomal system (Fig. 1g). In particular, the number of endolysosomal vesicles did not show any deviations between the two genotypes. Notably, lysosomal deposits which have been reported in lysosomal storage diseases such as mucolipidosis type IV[27,28] could not be detected in TPC2$^{-/-}$ mice.

Finally, steady-state endolysosomal pH values were similar in TPC2$^{-/-}$ and WT MEFs. This result was obtained in two different, independently generated WT and TPC2$^{-/-}$ batches of MEFs: 5.08 ± 0.1 for WT versus 4.93 ± 0.06 for TPC2$^{-/-}$ (batch-1) and 4.87 ± 0.03 for WT versus 4.89 ± 0.02 for TPC2$^{-/-}$ (batch-2) (Fig. 1h,i and Supplementary Fig. 1g–i). Even under starvation conditions (EBSS buffer ($-$aa) or starvation buffer ($-$aa/$-$glc)), no significant differences in endolysosomal pH between WT and TPC2$^{-/-}$ were observed (again two independently generated MEF cell lines (batch-1 and batch-2) were tested) (Fig. 1i and Supplementary Table 1). In addition, the pH dependent, endolysosomal processing of cathepsin D and cathepsin L was examined. In the acidic environments of late endosomes and lysosomes, the mature forms of cathepsin D and cathepsin L are produced after proteolytic removal of the propeptide. We found that the generation of mature forms of cathepsin D and L was not impaired in TPC2$^{-/-}$ MEFs compared with WT (Supplementary Fig. 1j). Specificity of the detected bands was controlled by analysing lysates from the respective cathepsin$^{-/-}$ MEFs in parallel.

Next, we assessed the functional consequences of a loss of TPC2 for trafficking processes in the endolysosomal degradation pathway (Fig. 2a), the main subcellular localization of TPC2. This pathway can be tested by using labelled LDL which binds to its receptor and is internalized into the cell via endocytosis[10]. Subsequently, LDL dissociates from the receptor and is passed on to late endosomes and lysosomes, from where cholesterol is released into the cytosol (Fig. 2a). A trafficking or fusion defect within this pathway would lead to accumulation of LDL in vesicles proximal to the defect. We used LDL-BodipyFL to test this hypothesis and found that the number of LDL-positive vesicles per cell was significantly increased in TPC2$^{-/-}$ compared with WT MEFs (Fig. 2b–d). This effect was observed at a broad range of LDL concentrations and after different pulse/chase times (Fig. 2c,d). LDLR expression in WT and TPC2$^{-/-}$ MEFs was found to be similar as determined by quantitative western blot experiments (normalized to glyceraldehyde 3-phosphate dehydrogenase) (Fig. 2e and Supplementary Fig. 2a). As an independent test for the same pathway, we performed experiments using labelled EGF (epithelial growth factor; AlexaFluor488-EGF)[29]. These experiments revealed that EGF accumulation is increased in TPC2$^{-/-}$ compared with WT MEFs (Fig. 2f–h). This finding was confirmed in independently generated MEFs (batch-2) (Supplementary Fig. 2b,c). In addition, in primary hepatocytes isolated from TPC2$^{-/-}$ mice, the number of EGF-positive vesicles per cell was also significantly increased compared with WT hepatocytes, whereas EGFR expression in WT and TPC2$^{-/-}$ livers was not significantly different (Fig. 2i and Supplementary Fig. 2d,e). To further assess whether the increased accumulation was caused by decreased degradation, the time course of EGF degradation after uptake was measured. MEFs were incubated with a saturating concentration of EGF ($4\,\mu g\,ml^{-1}$), followed by defined chase times before fixation (Fig. 2j,k). In TPC2$^{-/-}$ MEFs, the fluorescence decreased significantly slower compared with WT MEFs.

To further determine the identity of the endolysosomal vesicles where EGF accumulates in TPC2$^{-/-}$ cells, we co-labelled cells with markers for early endosomes (Rab5), late endosomes (Rab7), and late endosomes/lysosomes (LAMP1), and found that about 57% of the EGF-positive vesicles showed co-labelling with Rab7 and 41% with LAMP1, but only about 5% with Rab5, indicating that accumulation occurs rather in the late section of the endolysosomal system than in early endosomes (Fig. 2l,m).

Taken together, these results suggested that EGF/EGFR and LDL-cholesterol transport and degradation are impaired in TPC2$^{-/-}$ cells, and the endolysosomal transport machinery appeared to be saturated significantly faster in TPC2$^{-/-}$ than in WT cells.

Calcium and TPC2 channels are critical for trafficking. Endolysosomal trafficking defects can be caused by multiple factors. They can result from defects in enzymatic degradation of macromolecules, which is the underlying cause of most lysosomal storage disorders. Impaired trafficking can also be caused by defects in the acidification of endolysosomal organelles, defective ionic homoeostasis or defects in endolysosomal fusion and fission processes. Defects in acidification of endolysosomal vesicles have been reported before to be the primary cause for the observed trafficking abnormalities for example, in mucolipidosis type IV, which is caused by mutations in the lysosomal cation channel TRPML1 (refs 27,30,31). However, endolysosmal pH appears normal in TPC2$^{-/-}$ cells. Another attractive hypothesis for impaired endolysosomal trafficking is a defect in vesicle fusion or

Figure 2 | TPC2 deletion leads to LDL and EGF/EGFR trafficking defects in the degradation pathway. (**a**) Cartoon illustrating endolysosomal degradation and recycling pathways. In the degradation pathway (endo/lysosomal axis) EGF/EGFR and LDL are degraded. In the recycling pathway LDLR and Tf/TfR are recycled. Cholesterol can exit the endolysosomal system from late endosomes or lysosomes. LE, late endosome; LY, lysosome; C, free cholesterol. (**b**) Representative confocal images of WT and TPC2$^{-/-}$ MEFs incubated with $3\,\mu g\,ml^{-1}$ LDL-BodipyFL. Cell nuclei were visualized with Hoechst. (**c**) Average numbers of LDL-positive vesicles per cell after an incubation time of 30 min at concentrations as indicated. (**d**) Average numbers of LDL-positive vesicles per cell after different incubation times at a concentration of $1\,\mu g\,ml^{-1}$. (**e**) Quantitative western blot data showing average protein levels of LDLR in WT and TPC2$^{-/-}$ MEFs. (**f**) Representative confocal images of WT and TPC2$^{-/-}$ MEFs incubated with $0.3\,\mu g\,ml^{-1}$ AlexaFluor488-EGF. (**g**) Average numbers of EGF-positive vesicles per cell after an incubation time of 30 min at concentrations as indicated. (**h**) Average numbers of EGF-positive vesicles per cell after different incubation times at a concentration of $0.3\,\mu g\,ml^{-1}$, followed by a 2-h chase period. (**i**) Average numbers of EGF-positive vesicles per cell from similar experiments with freshly prepared WT and TPC2$^{-/-}$ hepatocytes. (**j**) Representative confocal images of TPC2$^{-/-}$ and WT MEFs incubated with $4\,\mu g$ AlexaFluor488-EGF for 30 min and chased for defined time intervals in EGF-free DMEM before fixation. (**k**) Time course of EGF degradation obtained from experiments as shown in **j**. (**l**) Representative confocal images of WT and TPC2$^{-/-}$ MEFs incubated with $1\,\mu g\,ml^{-1}$ AlexaFluor488-EGF for 30 min, fixed and stained with anti-LAMP1, anti-Rab5 and anti-Rab7 antibody, respectively, and Cy5 as secondery antibody. (**m**) Quantification of experiments as shown in **l**. All data points are given as mean ± s.e.m. of at least three independent experiments, each. At least two independently generated WT and TPC2$^{-/-}$ MEF cell lines were analysed; n.s., not significant, $^{***}P<0.001$, $^{**}P<0.01$, $^{*}P<0.05$ (**c**,**d**,**g**,**h** and **k**: two-way anlysis of variance (ANOVA) followed by Bonferroni's *post hoc* test; **e** and **i**: unpaired Student's *t*-test). All scale bars, 20 μm.

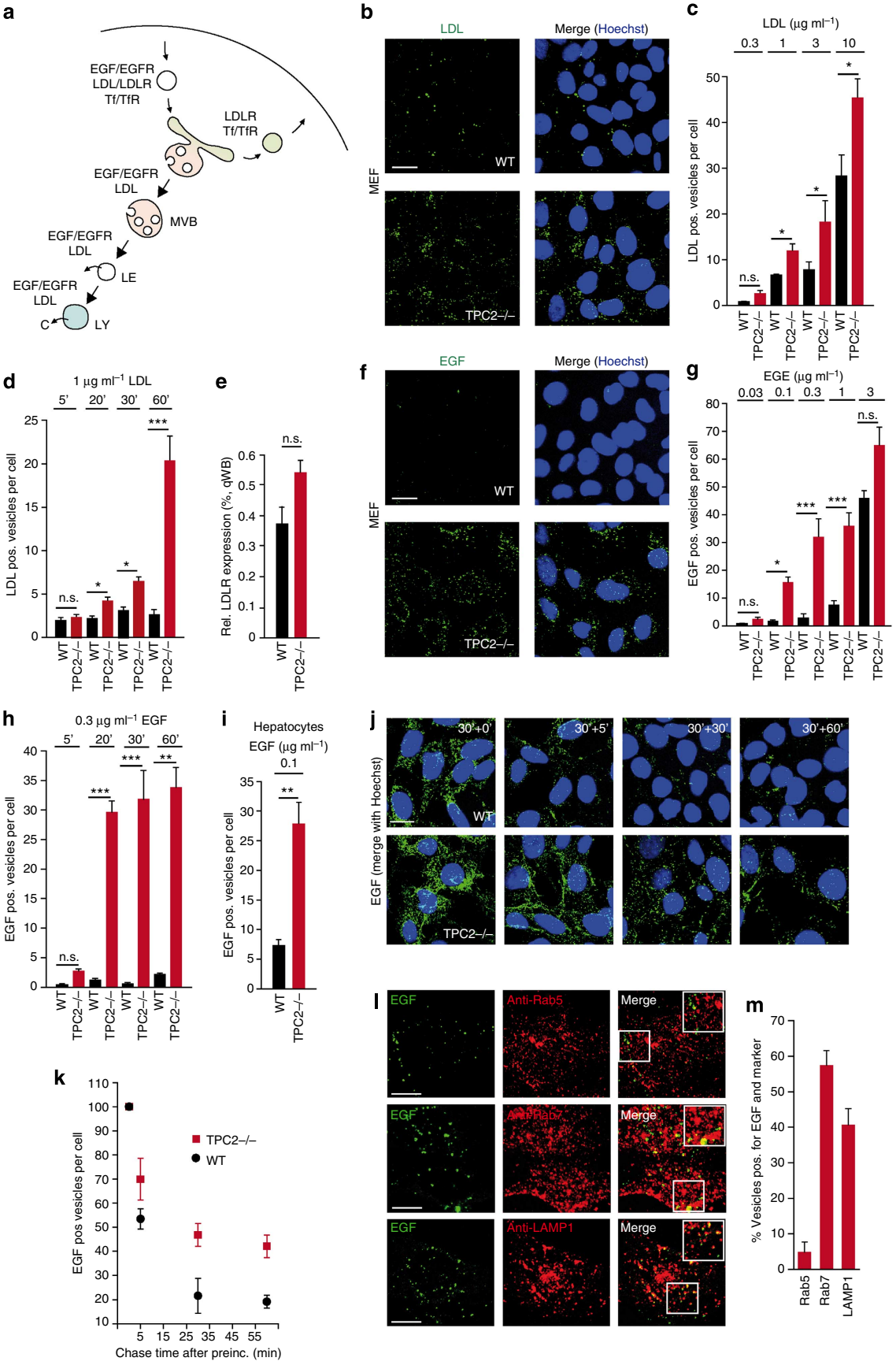

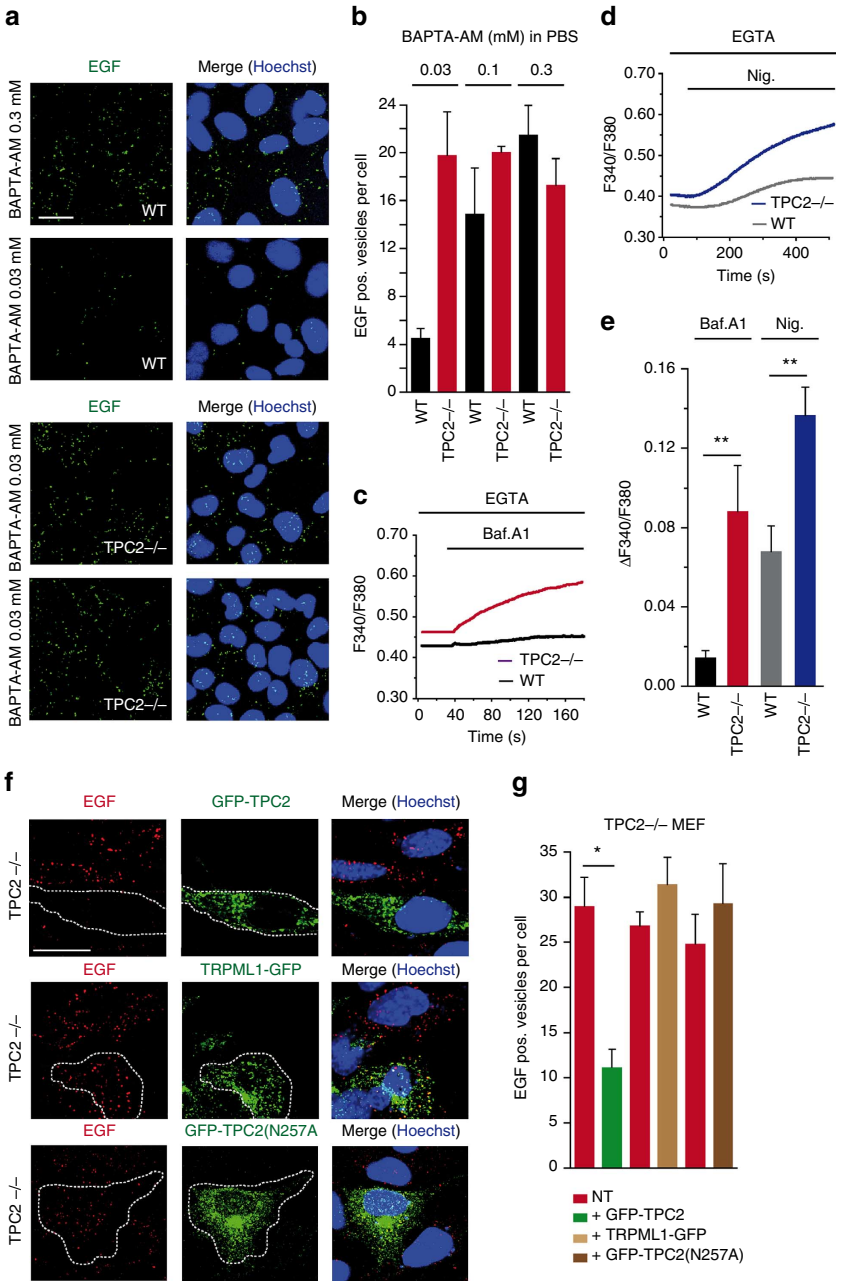

Figure 3 | Effects of BAPTA-AM or TPC2 overexpression on endolysosomal trafficking in WT and TPC2$^{-/-}$ MEFs. (**a**) Representative images of WT and TPC2$^{-/-}$ MEFs incubated with 0.1 μg ml^{-1} AlexaFluor488-EGF (5 min), followed by an incubation with 0.1 μg ml^{-1} AlexaFluor488-EGF in the presence of either 0.03 mM or 0.3 mM BAPTA-AM (25 min) in PBS. Cell nuclei were visualized with Hoechst. Scale bar, 20 μm. (**b**) Average numbers of AlexaFluor488-EGF-positive vesicles per cell after incubation with BAPTA-AM at different concentrations as described in **a**. (**c**,**d**) Effect of 2 μM bafilomycin A1 (Baf. A1; **c**) or 10 μM nigericin (Nig.; **d**) on cytosolic calcium levels in WT and TPC2$^{-/-}$ MEFs loaded with fura-2. Shown are representative calcium imging experiments (mean of $n=10$ cells, each). Measurements were performed in the presence of 2 mM EGTA. (**e**) Summary of Baf. A1 and Nig. experiments; bars represent values 150 s (bafilomycin) or 450 s (nigericin) after compound application ($n=$ at least five experiments with 5–10 cells, each). (**f**) TPC2 WT, the inactive TPC2 mutant TPC2(N257A), or TRPML1 WT were fused to green fluorescent protein (GFP), overexpressed in TPC2$^{-/-}$ MEFs and incubated with 1 μg ml^{-1} AlexaFluor555-EGF (red). Shown are representative images after fixation of the respective MEF cell line as indicated. Cell nuclei were visualized with Hoechst. Scale bar, 20 μm. (**g**) Average numbers of EGF-positive vesicles per cell taken from experiments as shown in **e**. Non-transfected (NT) TPC2$^{-/-}$ cells in close proximity to cells transfected with the respective cDNAs served as positive controls for each experiment. All data points are given as mean ± s.e.m. *$P<0.05$, **$P<0.01$, unpaired Student's *t*-test.

fission processes. It has been postulated before that Ca^{2+} is required for vesicular fusion processes and thereby regulates trafficking of vesicular cargo proteins[30,32,33]. In accordance with this hypothesis, we found that in WT MEFs chelation of cytosolic Ca^{2+} by 1,2-bis(2-aminophenoxy)ethane-*N*,*N*,*N*′,*N*′-tetraacetic acid tetrakis(acetoxymethyl ester) (BAPTA-AM) mimics the effect on EGF trafficking observed in TPC2$^{-/-}$ MEFs (Fig. 3a,b). This effect was dose dependent (Fig. 3a,b). By contrast, in TPC2$^{-/-}$ MEFs, EGF accumulation was not significantly changed by BAPTA-AM (Fig. 3a,b). Ethyleneglycol-bis(β-aminoethyl)-*N*,*N*,*N*′,*N*′-tetraacetoxymethyl ester (EGTA-AM), which has much slower binding kinetics than

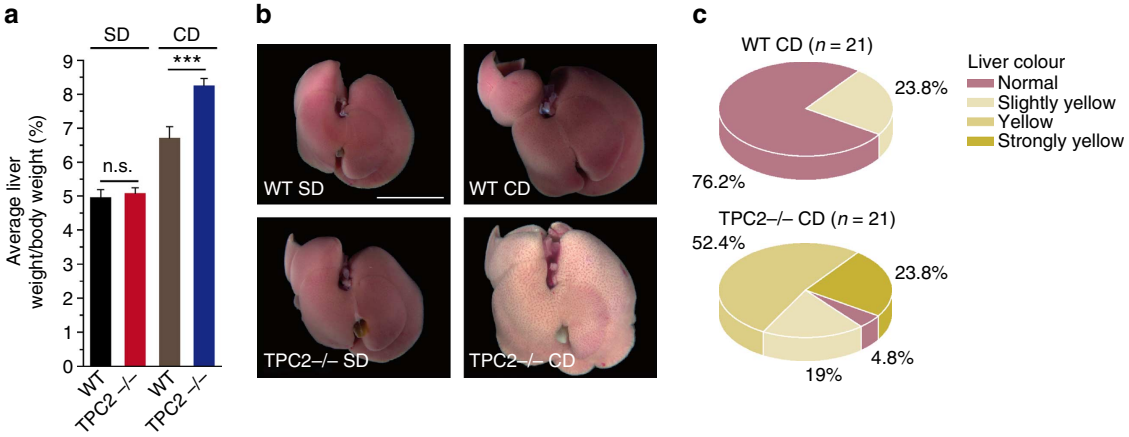

Figure 4 | Analysis of liver samples isolated from WT and TPC2$^{-/-}$ mice. (**a**) Bar diagram showing average liver weight/body weight ratios (in %) of WT and TPC2$^{-/-}$ mice treated for 6 weeks with SD or CD, respectively. $^{**}P<0.01$, two-way analysis of variance (ANOVA) followed by Bonferroni's *post hoc* test. (**b**) Shown are representative liver samples isolated from 10–12-week-old male WT and TPC2$^{-/-}$ mice, treated with either SD or CD for six consecutive weeks. Scale bar, 10 mm. (**c**) Pie charts showing the percentage of slightly to strongly yellow-stained liver samples isolated from WT and TPC2$^{-/-}$ mice treated with CD. Livers of SD-treated mice looked 100% normal.

BAPTA-AM, had no significant effect on EGF accumulation (Supplementary Fig. 2).

Bafilomycin A1 (Baf. A1)—a cell-permeant inhibitor of the vacuolar-type H^+-ATPase, results in loss of the lysosomal/late endosomal proton gradient and eventually leads to the depletion of luminal calcium[34]. By using Baf. A1 (in the absence of extracellular calcium), we demonstrate that loss of TPC2 (TPC2$^{-/-}$ MEF) causes a significant elevation in cytosolic calcium compared with WT, suggesting that loss of TPC2 may lead to an increased retention of calcium in the endolysosomal lumen (Fig. 3c,e). Similar results were obtained when the K^+/H^+ exchanger nigericin was used instead of Baf. A1 (ref. 35) (Fig. 3d,e). Taken together, these results suggest that a significantly higher amount of calcium is retained in intracellular acidic compartments in TPC2$^{-/-}$ compared with WT cells. To confirm that the Ca^{2+} required for EGF trafficking depends on the presence of TPC2, we performed rescue experiments in TPC2$^{-/-}$ MEFs and found that overexpression of WT TPC2 in TPC2$^{-/-}$ MEFs leads to a rescue of the EGF-trafficking defects (Fig. 3f,g). The remaining EGF accumulation was not significantly different from the amount of EGF accumulating in WT MEFs at the respective EGF concentration (Fig. 2g). Notably, a non-conducting TPC2 mutant (TPC2-N257A)[21] was not sufficient to rescue trafficking defects, suggesting that ion flux through TPC2 is necessary for the rescue. Furthermore, the rescue is specific for TPC2 because TRPML1, another Ca^{2+} permeable and $PI(3,5)P_2$-activated cation channel in lysosomes[36], did not rescue EGF-trafficking defects observed in TPC2$^{-/-}$ MEFs (Fig. 3f,g).

***In vivo* cholesterol accumulation in TPC2-deficient mice.** Given the pronounced impairments in LDL and EGF trafficking observed in TPC2$^{-/-}$ MEF cell lines and hepatocytes, we hypothesized that defects might also be present in an *in vivo* model. Therefore, WT and TPC2$^{-/-}$ mice were fed with a standard diet (SD) or a Western-type diet rich in cholesterol (CD) for 6 weeks, respectively[37]. Analysis of TPC2$^{-/-}$ mice fed with SD indicated that these mice appeared identical to their WT littermates as determined by morphological and histological studies. The lack of a gross phenotype in TPC2$^{-/-}$ mice on SD is not surprising, since SD contains relatively little cholesterol ($\leq$0.02% w/w). On this diet, the cholesterol requirement of the animals is achieved primarily through *de novo* biosynthesis[38].

We next tested the effect of a diet rich in cholesterol (1.25% cholesterol; CD). The intake of cholesterol per day on this diet is approximately 20–30 times above the amount an average animal synthesizes to maintain homoeostasis when its dietary needs are not being met[38]. The average liver weight/body weight ratio of TPC2$^{-/-}$ on CD was significantly increased compared with WT on CD (Fig. 4a), while this parameter was similar in WT and TPC2$^{-/-}$ on SD. Importantly, there was no difference in total body weight between the two groups of mice, suggesting the absence of obesity in the TPC2$^{-/-}$ mice. On macroscopic examination, more than 95% ($n=21$) of TPC2$^{-/-}$ livers (CD) displayed changes in colour ranging from slightly yellow to strongly yellow (Fig. 4b,c). Only about 5% of the livers looked normal. In contrast, 76% of WT livers (CD) looked normal while 24% displayed a light yellow colour ($n=21$). Livers from WT and TPC2$^{-/-}$ mice on SD did not display visible changes in colour ($n=13$ and $n=21$, respectively).

The prominent yellow colour of the livers from TPC2$^{-/-}$ mice on CD is highly suggestive for hepatosteatosis (fatty liver). An analysis of the free and total hepatic cholesterol levels (free cholesterol and CEs) revealed that in SD-fed WT and TPC2$^{-/-}$ mice, there was no difference in free and total liver cholesterol levels (Fig. 5a–c). After CD treatment, free and total cholesterol levels were elevated in both mouse lines. In TPC2$^{-/-}$ mice, cholesterol levels were significantly higher than in WT mice (Fig. 5a–c). In particular, total cholesterol levels including CEs were dramatically increased in TPC2$^{-/-}$ liver samples (Fig. 5a–c). In line with the biochemically observed hepatic overload of cholesterol and CEs in TPC2$^{-/-}$ mice on CD, liver paraffin sections from TPC2$^{-/-}$ mice on CD displayed strong accumulation of lipid droplets of different sizes predominantly in periportal hepatocytes (Fig. 5d). The histologic pattern is consistent with/resembles non-alcoholic fatty liver disease which is characterized by a microvesicular periportal hepatosteatosis. Signs of periportal and pericellular fibrosis were seen in liver sections from TPC2$^{-/-}$ mice on CD (Fig. 5e). The strong accumulation of lipid droplets was further confirmed by electron microscopy of liver sections from TPC2$^{-/-}$ mice on CD compared with WT on CD (Fig. 5f). Filipin[39–42] stainings further confirmed a strong accumulation of cholesterol in TPC2$^{-/-}$ hepatocytes after CD treatment (Fig. 6a). A macroscopic analysis of gallbladders isolated from WT and TPC2$^{-/-}$ mice on CD

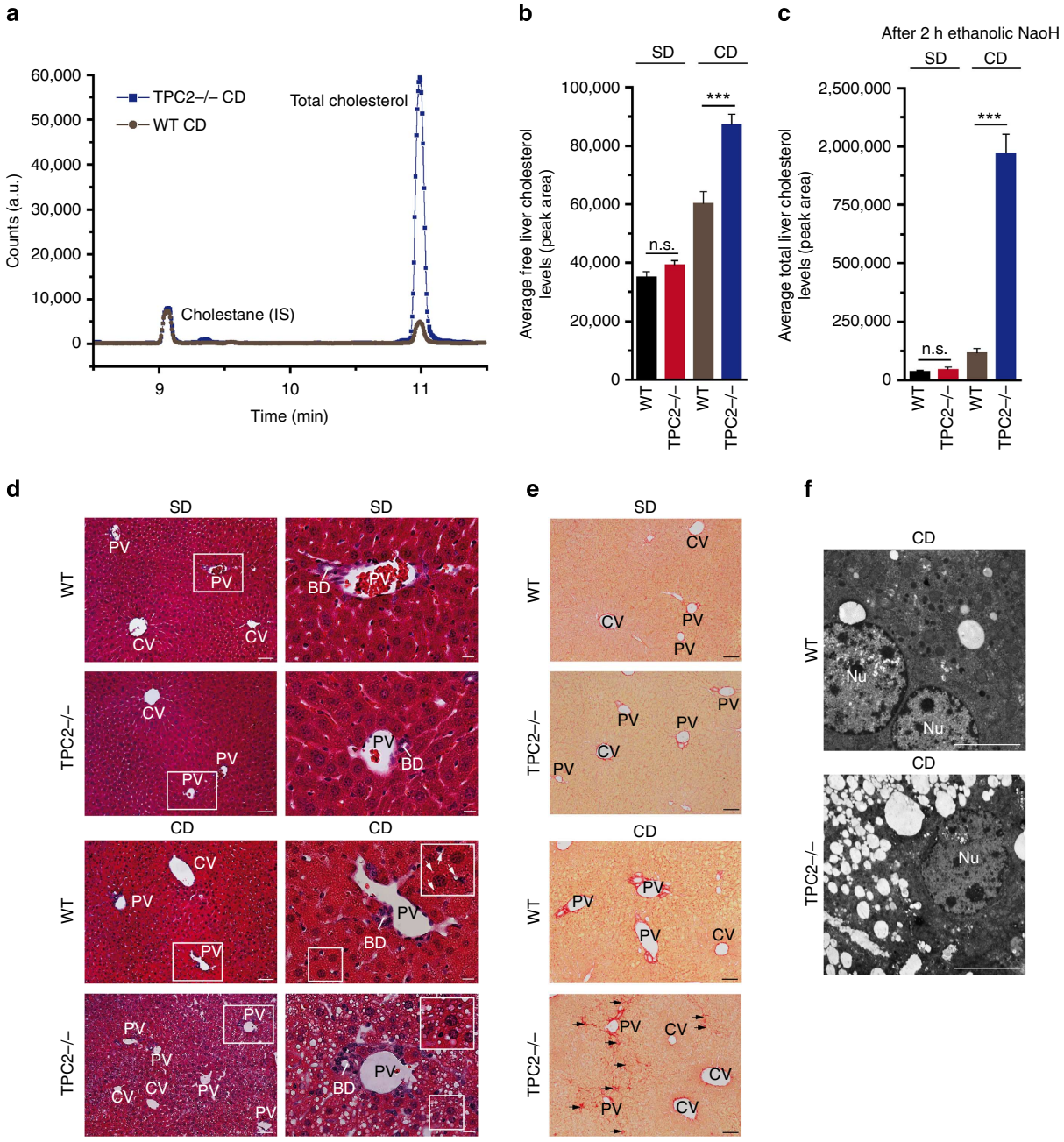

Figure 5 | Hepatic cholesterol overload, liver damage and hyperlipoproteinaemia in TPC2$^{-/-}$ mice. (**a**) Representative gas chromatogram (*m/z* 217 + 368) of total cholesterol and internal standard (IS) after alkaline hydrolysis in liver tissue prepared from male WT and TPC2$^{-/-}$ mice on CD. (**b**) Average hepatic levels of unesterified free cholesterol in male WT and TPC2$^{-/-}$ mice on SD or CD as indicated (GC split ratio 3). (**c**) Average total liver cholesterol levels, determined after alkaline ester hydrolysis (GC split ratio 15). (**d**) Representative images of liver paraffin sections of male WT and TPC2$^{-/-}$ mice on SD or CD diet, respectively, stained with haematoxylin–eosin (HE). BD, bile duct; PV, portal vein; CV, central vein. Scale bars, 100 μm (SD left, CD left) and 20 μm (SD right, CD right). White arrows point to some lipid droplets visible in CD WT sections. (**e**) Representative images of liver paraffin sections stained with Sirius Red. PV, portal vein; CV, central vein. Scale bars, 100 μm. Black arrows point to areas of pericellular fibrosis in CD-treated TPC2$^{-/-}$ livers. (**f**) Representative electron microscope images of WT and TPC2$^{-/-}$ liver sections after CD treatment. Nu, nucleus; scale bars, 5 μm. Data points in **b** and **c** are given as mean ± s.e.m. (**b** and **c**: two-way analysis of variance (ANOVA) followed by Bonferroni's *post hoc* test; n.s., not significant, ***$P<0.001$.

revealed the presence of large gallstones in TPC2$^{-/-}$ gallbladders (Supplementary Fig. 3a).

To test whether the severe cholesterol overload of TPC2$^{-/-}$ livers causes compensatory hepatic changes, a pathway analysis of differentially regulated genes was performed in TPC2$^{-/-}$ and WT mice on SD and CD diet. This analysis revealed significant enrichment of genes involved in lipid metabolism and molecular transport (Supplementary Table 2). In line with an increased hepatic pool of free cholesterol, transcriptional upregulation of hepatic enzymes involved in BA and CE synthesis as well as BA efflux was observed in TPC2$^{-/-}$ compared with WT mice on CD, while enzymes involved in hepatic cholesterol synthesis were downregulated (Fig. 6b)[43–45]. LDLR expression levels were comparable in livers from WT

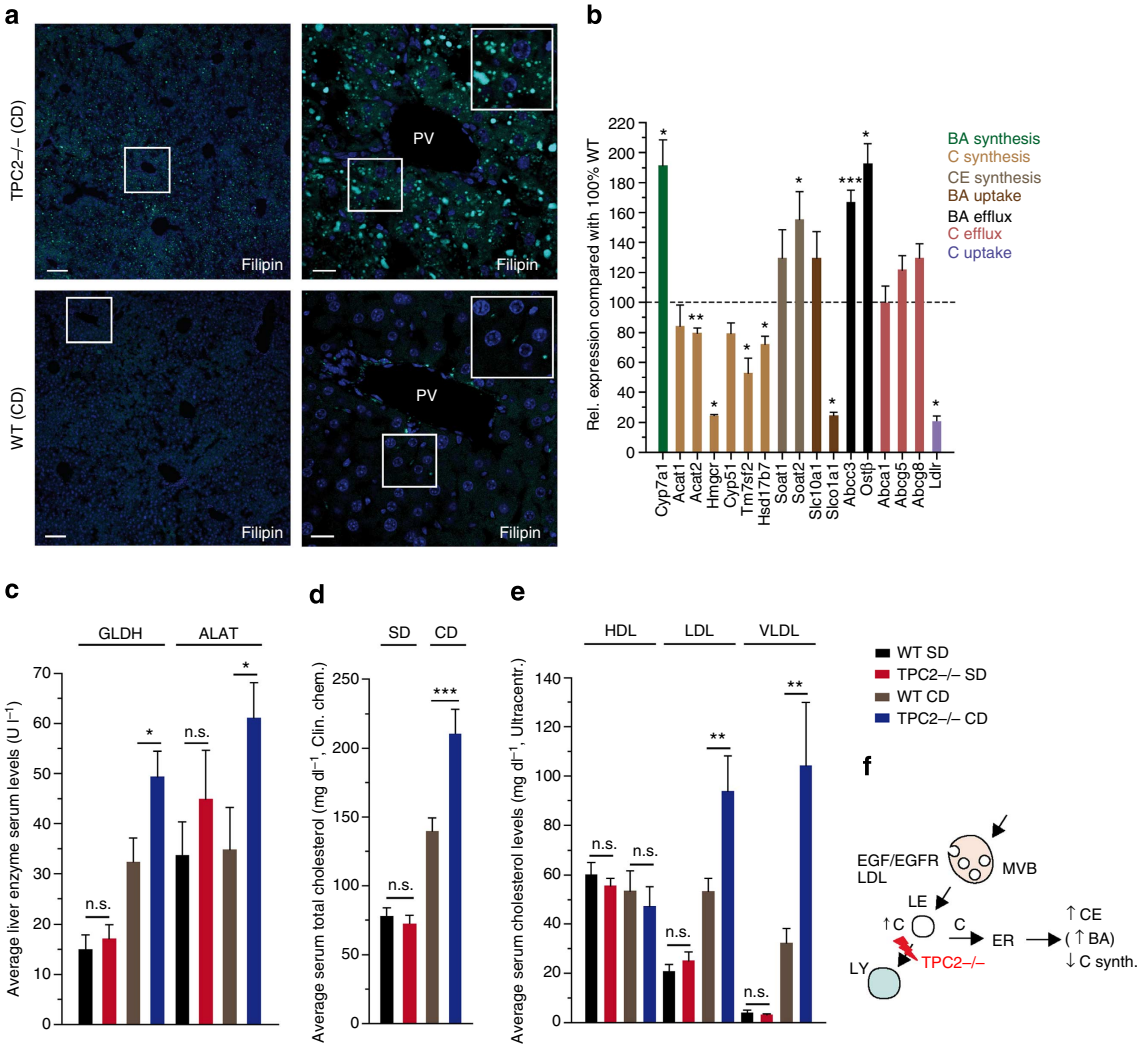

Figure 6 | Cholesterol accumulation in liver tissue isolated from TPC2$^{-/-}$ and WT mice and gene expression profile. (**a**) Representative images of liver cryosections of WT and TPC2$^{-/-}$ mice on CD diet, stained with filipin (0.05 mg ml^{-1} in PBS for 2 h) to visualize free cholesterol. Scale bars, 100 μm (left) and 20 μm (right). (**b**) Relative expression (WT compared with TPC2$^{-/-}$ on CD) of hepatic transcripts coding for proteins involved in: bile acid (BA) synthesis (Cholesterol-7-alpha-hydroxylase, Cyp7a1), cholesterol synthesis (Acat1 (acetyl-CoA acetyltransferase 1, mitochondrial), Acat2 (acetyl-CoA acetyltransferase 2, cytosolic), Hmgcr (HMG-CoA reductase), Cyp51 (Lanosterol 14α-demethylase), Tm7sf2 (delta(14)-sterol reductase), cholesterol ester (CE) synthesis (Soat1 and Soat2 (sterol O-acyltransferase 1 and 2)), BA efflux (Abcc3 (canalicular multispecific organic anion transporter 2), Ostβ (organic solute transporter beta)), BA uptake (Slc10a1 (Na^+-taurocholate cotransporting polypeptide, Ntcp), Slco1a1 (organic anion-transporting polypeptide, Oatp), sterol/cholesterol efflux transporters (Abca1, Abcg5, Abcg8) and cholesterol uptake (Ldlr). *$P<0.05$, **$P<0.01$, ***$P<0.001$, unpaired Student's *t*-test. Expression of Hmgcr and Ldlr was determined by quantitative RT-PCR and normalized to beta actin. (**c**) Average liver enzyme levels (GLDH (glutamate dehydrogenase) and ALAT (alanine transaminase) in male WT and TPC2$^{-/-}$ mice on SD or CD as indicated. (**d**) Average serum total cholesterol levels in male WT and TPC2$^{-/-}$ mice on SD or CD. (**e**) Average HDL-, LDL- and VLDL-cholesterol levels in serum of male WT and TPC2$^{-/-}$ mice on SD or CD diet. **$P<0.01$, ***$P<0.001$, two-way analysis of variance (ANOVA) followed by Bonferroni's *post hoc* test; n.s., not significant. (**f**) Cartoon illustrating hypothetical model of cholesterol accumulation. Cholesterol accumulates in LEs in TPC2$^{-/-}$ cells due to a delay or impairment of LE/LY fusion/trafficking processes (symbolized by the red flash); C, free cholesterol; CE, cholesterol ester; BA, bile acid. All data points are given as mean ± s.e.m.

and TPC2$^{-/-}$ mice on SD (data not shown), while a significant downregulation was observed in livers from TPC2$^{-/-}$ mice on CD compared with WT on CD (Fig. 6b). Expression of the ABC transporters ABCA1, ABCG5 (sterolin-1) and ABCG8 (sterolin-2) was not significantly upregulated (Fig. 6b). An analysis of faecal BA content and composition revealed an increase in BA excretion in CD compared with SD-fed animals, which was, however, independent of the genotype (Supplementary Fig. 3b). In liver, only one type of BA was consistently detectable: cholic acid. While desoxycholic acid was not detectable in liver samples of SD-fed animals, it was detectable in 40% of the investigated CD-fed TPC2$^{-/-}$ animals (Supplementary Fig. 3c).

We further assessed functional hepatic consequences of the measured cholesterol accumulation by determining liver-specific enzyme levels in the peripheral blood. While no differences in enzyme levels indicating liver damage such as glutamate dehydrogenase or alanine transaminase were found in mice on SD, significantly increased glutamate dehydrogenase and alanine transaminase values (Fig. 6c and Table 1) were detected in TPC2$^{-/-}$ mice compared with WT on CD. Taken together, these findings indicate that in addition to hepatic cholesterol

Table 1 | Summary of serum parameters.

	WT SD Mean ± s.e.m.	TPC2 −/− s.d. Mean ± s.e.m.	ANOVA	WT CD Mean ± s.e.m.	TPC2 −/− CD Mean ± s.e.m.	ANOVA
Total cholesterol (mg dl^{-1})	78 ± 5.8	72.0 ± 5.7	n.s.	139.5 ± 9.6	210.3 ± 18.0	***
GLDH (U l^{-1})	14.9 ± 2.8	17.1 ± 2.9	n.s.	32.3 ± 4.8	49.4 ± 5.0	*
ALAT (U l^{-1})	33.7 ± 9.6	44.9 ± 11	n.s.	34.9 ± 8.4	60.8 ± 7.7	*
ASAT (U l^{-1})	145.3 ± 34	199.4 ± 6.7	n.s.	118.6 ± 23	155.4 ± 34.5	n.s.
Total protein (g dl^{-1})	4.4 ± 0.2	4.1 ± 0.2	n.s.	4.4 ± 0.1	4.2 ± 0.2	n.s.
Glucose (mg dl^{-1})	163.9 ± 12.0	170.7 ± 12.0	n.s.	186.7 ± 14.0	183.2 ± 16.9	n.s.
Triglycerides (mg dl^{-1})	42.1 ± 3.4	41.1 ± 6.8	n.s.	33.8 ± 2.9	28.3 ± 5.0	n.s.

ANOVA, analysis of variance; ALAT, alanine transaminase; ASAT, aspartate transaminase; CD, cholesterol; GLDH, glutamate dehydrogenase; n.s. not significant; SD, standard diet; TPC, two-pore channel; WT, wild type.
Table summarizing data shown in Fig. 6 c,d and additional serum parameters in WT and TPC2$^{-/-}$ mice on SD and CD. Values are given as mean ± s.e.m. (two-way ANOVA followed by Bonferroni's *post hoc* test, *$P<0.05$, ***$P<0.001$).

overload, liver damage was present in TPC2$^{-/-}$ mice after CD treatment.

Since the liver is the key organ in regulating lipoprotein metabolism, we next determined systemic changes in lipoproteins. In WT and TPC2$^{-/-}$ mice fed with SD, we found no differences in total cholesterol as well as HDL- (high-density lipoprotein), LDL- or VLDL-cholesterol (very low-density lipoprotein cholesterol) plasma levels (Fig. 6d,e). However, in mice on CD, total blood cholesterol levels as well as LDL- and VLDL-cholesterol levels were strongly elevated. Notably, LDL- and VLDL-cholesterol levels were significantly more increased in TPC2$^{-/-}$ than in WT mice. Serum HDL-cholesterol levels as well as protein, triglyceride and glucose levels were similar within both groups (Table 1). Finally, faecal total cholesterol levels were increased in CD compared with SD-fed animals. However, here no significant differences were detectable between the genotypes (Supplementary Fig. 3d).

Discussion

Here, we show that TPC2$^{-/-}$ mice are more susceptible to cholesterol and CE accumulation in the liver than WT mice. This accumulation is not caused by extrahepatic factors, because similar accumulation is seen in single-cell experiments. The macroscopic and histological presentation of TPC2$^{-/-}$ livers, the increased cholesterol accumulation and increase in hepatic transaminases indicate fatty liver and liver damage, and are consistent with the clinical picture of NAFLD and NASH.

The clinical phenotype can be explained by specific defects in vesicle trafficking along the endolysosomal degradation pathway in the TPC2$^{-/-}$ mouse. In the absence of TPC2, receptors and cargoes such as LDL or EGF/EGFR, which are transported along the degradation pathway, accumulate rapidly in intracellular vesicles of TPC2$^{-/-}$ but not WT cells. This finding suggests that TPC2 channels are critically involved in the regulation of endolysosomal trafficking along this pathway. Since TPC2 channels are specifically expressed on late endosomes and lysosomes, it is likely that TPC2 regulates or enhances the final transport or fusion step between these two organelles. Consistent with this hypothesis, deletion of TPC2 leads to a partial block in transport and accumulation of LDL-cholesterol and LDL CEs proximal to the fusion defect in the prelysosomal vesicle pool, in particular late endosomes (Fig. 6f). LDL-derived CEs are normally hydrolysed to free cholesterol by lysosomal and late endosomal acid lipase and subsequently exported from the endolysosomal system. Due to prelysosomal accumulation, more cholesterol may exit via late endosomes in TPC2$^{-/-}$ mice and thus increase the free cholesterol pool in the cytosol. It is well known that an increased free cholesterol pool at the endoplasmic reticulum (ER) induces CE formation and deposition in lipid droplets as well as downregulation of endogenous cholesterol synthesis (Fig. 6f)[43,44]. In line with this theory, we found that CEs are increased in TPC2$^{-/-}$ mice. CEs are generated from free cholesterol by Soat1 and Soat2 (sterol O-acyltransferase 1 and 2). These enzymes are upregulated in livers of TPC2$^{-/-}$ mice. ER enzymes involved in endogenous cholesterol synthesis are downregulated. Finally, serum VLDL levels are elevated in TPC2$^{-/-}$ mice on CD (Fig. 6e). While this elevation could be caused by an increase in hepatic VLDL production, the possibility of a reduced VLDL clearance cannot completely be ruled out.

Together, these results indicate that in TPC2$^{-/-}$ hepatocytes, secondary ER-dependent processes are induced. This could either be caused by a globally increased free cholesterol pool or alternatively by misrouting of free cholesterol to the ER. Such a misrouting effect could be caused by a decreased flux of cholesterol from late endosomes to lysosomes with an upregulation of alternative trafficking pathways from late endosomes to the ER. In support of this notion, there is increasing evidence of contact sites between late endosomes and the ER[46–48], as well as evidence for direct vesicular and non-vesicular transport of cholesterol to the ER from late endosomes[49,50].

How could a proposed role of TPC2 for vesicular trafficking and fusion be explained mechanistically? We demonstrate that in MEFs, TPC2 is critically involved in the generation of a current specifically activated by the known TPC2 activators NAADP and $PI(3,5)P_2$. It has been shown that $PI(3,5)P_2$ concentrations increase from early to late endosomes[9,11,15]. Thus, in the absence or in the presence of very low levels of $PI(3,5)P_2$, TPC2 may conduct only very small currents and progressively start to open on maturation toward late endosomes as $PI(3,5)P_2$ gradually rises. Opening of TPC2 channels in late endosomes could initiate the final fusion between late endosomes and lysosomes. Here, we demonstrate that vesicle trafficking in the endo/lysosomal degradation pathway requires Ca^{2+} and ion flux through TPC2. The most likely interpretation is that Ca^{2+} flows directly through TPC2 channels. TPC2 has been shown previously to conduct Ca^{2+} (refs 18,21,22,24) and we confirm here that endogenous TPC2 channels are permeable to calcium (Supplementary Fig. 4). Opening of TPC2 channels may lead to Ca^{2+} efflux from vesicles directly into microdomains surrounding Ca^{2+}-dependent proteins of the fusion machinery and thereby induce fusion. Anchoring of TPC2 within the cellular fusion machinery is supported by interactions with specific SNARE proteins such as STX7 and additional protein components of SNARE complexes which were identified by proteomics-based interaction screens, and confirmed by fluorescence resonance energy transfer analyses and co-immunoprecipitation experiments (Supplementary Fig. 5a–g

and Supplementary Table 3)[51–53]. Alternatively, ionic flux through TPC2 channels could also be part of an indirect mechanism which provides Ca^{2+}. In this scenario, cations other than Ca^{2+} flowing through TPC2 would act on a downstream channel, which in turn provides Ca^{2+}. Na^+ and K^+ have also been shown to permeate through TPC2 channels[17,20]. Given the proposed close structural assembly of TPCs and the fusion machinery (Supplementary Fig. 5g), depolarization by Na^+ efflux through TPC2 may also electrostatically facilitate fusion between two vesicular membranes as suggested by the model of Wang *et al.*[17] Similar events may be relevant for TPC1 within the proximal endosomal pathway.

Defects in the endolysosomal trafficking and cellular processing of LDL-cholesterol have been implicated in human diseases such as Niemann Pick disease and Wolman's disease (CE storage disease) where CEs accumulate in late endosomes and lysosomes due to a severely diminished activity of cholesterol export proteins NPC1 and NPC2 or lysosomal acid lipase[54]. Here, we demonstrate that loss of TPC2 results in a defect which is more distally located in the endolysosomal LDL-cholesterol trafficking pathway. Loss of TPC2 increases the risk of developing NAFLD and NASH. These diseases themselves are independent of traditional cardiovascular risk factors and the metabolic syndrome associated with increased risk for cardiovascular disease. Furthermore, in obese individuals these diseases are markers of insulin resistance and diabetes. Notably, TPC2$^{-/-}$ mice are highly susceptible to NAFLD and NASH, while obesity and impaired glucose tolerance are not observed. This finding suggests that TPC2$^{-/-}$ mice have a reduced metabolic reserve in hepatic cholesterol handling, which leads to NAFLD even in the absence of obesity and impaired glucose tolerance. The increased susceptibility of TPC2$^{-/-}$ mice to NAFLD is clinically highly relevant because this disease affects up to one-third of the population worldwide and may cause adverse cardiovascular outcome and increased cardiovascular mortality.

Methods

Generation of TPC2$^{-/-}$ knockout mice. TPC2$^{-/-}$ mice were generated by deleting exon 7 and introducing an early stop codon. We generated a targeting vector that, after homologous recombination, resulted in a modified *TPC2* allele carrying two *loxP* sites flanking exon 7. A *neo*^{R} cassette, which was used for G418/geneticin selection, was removed with Flp recombinase before the ES cells were injected into host blastocysts to generate chimeric mice. After germline transmission and continued breeding, PCR with genomic DNA from progeny of WT, heterozygous and homozygous animals showed proper recombination and inheritance of the *TPC2*^{lox} allele. Subsequently, exon 7 was deleted by pairing *TPC2*^{lox} mice with mice expressing Cre-recombinase under a cytomegalovirus promoter. Exon 7 encodes TMD5 and part of the pore-loop in domain I of TPC2. Animals were used under approved animal protocols and University of Munich (LMU) Institutional Animal Care Guidelines.

Whole-lysosome planar patch-clamp experiments. For whole-lysosome planar patch-clamp recordings, isolated intact lysosomes from HEK293 cells or MEFs were prepared by differential centrifugation as described previously[21,22,55]. HEK293 cells stably expressing murine TPC2 or the TPC2 mutant TPC2(N257A), both N-terminally fused to green fluorescent protein and subcloned into pcDNA5FRT vector with hygromycin resistance (Invitrogen) were used. To investigate STX7 effects on TPC2, a double stable HEK293 cell line was generated coexpressing murine STX7, N-terminally fused to mCherry (in pcDNA3 vector with geneticin (G418) resistance) and TPC2 as described above. The planar patch-clamp technology combined with a fast internal perfusion system (Port-a-Patch, Nanion Technologies) was applied as described previously[21,22,55]. Currents were recorded using an EPC-10 patch-clamp amplifier and PatchMaster acquisition software (HEKA). Data were digitized at 40 kHz and filtered at 2.8 kHz. Mean endolysosomal capacitance was 1.01 ± 0.04 pF ($n = 47$). For all experiments, salt-agar bridges were used to connect the reference Ag-AgCl wire to the bath solution to minimize voltage offsets. Unless otherwise stated, cytoplasmic solution contained 60 mM KF, 70 mM K-MSA (methanesulfonate), 0.2 mM Ca-MSA, 4 mM Na-MSA, 10 mM HEPES (pH adjusted with KOH to 7.2). Luminal solution was 60 mM Ca-MSA, 85 mM Na-MSA, 1 mM $MgCl_2$, 10 mM HEPES (pH adjusted with NaOH to 4.6 (refs 17,20)). Mannitol was used to adjust osmolarity. For the application of $PI(3,5)P_2$ (A.G. Scientific) or NAADP (Tocris Bioscience), cytoplasmic solution was completely exchanged by $PI(3,5)P_2$- or NAADP-containing solution.

Endolysosomal trafficking experiments. For trafficking experiments, AlexaFluor488-EGF, AlexaFluor555-EGF or LDL-BodipyFL (Life Technologies) were used. MEFs from WT and TPC2$^{-/-}$ mice were seeded on glass coverslips in 24-well plates and grown in Dulbeccos modified eagles medium (DMEM) with 10% fetal bovine serum at 37 °C and 5% CO_2 for 48 h. Cells were treated with varying concentrations of labelled LDL or EGF and incubated for different time intervals at 37 °C and 5% CO_2. Cells were subsequently washed in DMEM containing no fetal bovine serum and fixed with ice-cold methanol for 5 min at − 20 °C or chased before fixation for defined time intervals at 37 °C and 5% CO_2 in DMEM containing no fetal bovine serum, as indicated in the respective figure legends. Hoechst nuclear staining (Hoechst 33342) was performed in PBS buffer (5 μg ml^{-1}). Cells were incubated at room temperature for another 30 min, washed twice with PBS and embedded in Cell Lab Fluoromount-G Slide Mounting Medium (Beckman Coulter). In the degradation format, cells were incubated as described above with a saturating concentration of AlexaFluor488-EGF (4 μg ml^{-1}) for 30 min, washed and incubated for different chase times as indicated. For data quantification, ImageJ software was used. In each experiment, numbers were calculated based on the total number of vesicles (dots) per image divided by the number of cells (nuclei) per image. The term 'cell' is used instead of 'confocal cell section'.

Endolysosomal pH measurements. Endolysosomal pH measurements were performed by ratiometric fluorescence imaging as described previously[56]. MEFs were seeded on imaging dishes (145 μm glass bottom, PAA Laboratories, Germany) and grown overnight in DMEM supplemented with 1 g l^{-1} bovine serum albumin in the presence of 500 μg ml^{-1} of the pH-sensitive fluorophore Oregon Green 514 conjugated to dextran (70,000 MW, Life Technologies). In order to allow clearance of early endocytic compartments and ensure specific localization of the dye in the late endocytic pathway, cells were chased in DMEM at 37 °C for 1 h in the presence of bovine serum albumin followed by 1-h incubation in serum-free medium before imaging for basal pH determination. To assess lysosomal pH under starvation conditions, the chase procedure was replaced by either 2-h incubation without amino acids (EBSS) or 2-h incubation without both, amino acids and glucose (110 mM NaCl, 45 mM $NaHCO_3$, 5 mM KCl, 2 mM $CaCl_2$, 1 mM $MgCl_2$, pH 7.4)[20]. As a control for increased lysosomal pH, 200 nM Baf. A1 (Sigma Aldrich) were applied during the 1-h incubation in serum-free medium under basal conditions. Ratiometric imaging was performed using an Olympus FV1000 confocal laser scanning microscope. Cells were excited alternately by light transmitted from a 440-nm laser diode or a multiline argon laser at 488 nm (Showa electronics model GLS3135). In both cases, images were acquired at an emission wavelength of 535 ± 20 nm using a charge-coupled device-camera. At the end of every experiment, an *in situ* calibration was performed for each genotype by incubating the cells with isotonic K^+ buffer solutions (145 mM KCl, 10 mM glucose, 1 mM $MgCl_2$ and 20 mM of either HEPES, MES or acetate, pH ranging from 4.0 to 7.0), containing 10 μg ml^{-1} of the ionophorenigericin. The resulting fluorescence intensity ratios (488/440) were fitted to the Boltzmann equation to interpolate pH values from the experimental ratio data.

Calcium imaging experiments. Calcium imaging experiments were performed using fura-2 as described previously[57]. Briefly, WT and TPC2$^{-/-}$ MEFs cells were plated onto glass coverslips, and after 24 h, cells were loaded for 1 h with the fluorescent indicator fura-2-AM (4 μM; Invitrogen) in a standard bath solution containing (in mM) 138 NaCl, 6 KCl, 2 $MgCl_2$, 2 $CaCl_2$, 10 HEPES and 5.5 D-glucose (adjusted to pH 7.4 with NaOH). Cells were washed in 2 mM EGTA for 30 min before measurement. Calcium imaging was performed using a monochromator-based imaging system (Polychrome IV monochromator, TILL Photonics). Compounds were applied in the presence of 2 mM EGTA.

Immunocyto- and immunohistochemistry, electron microscopy. Immunocytochemistry was performed as described previously[58]. Histology, immunohistochemistry and electron microscopy experiments were performed according to standard protocols. For further details, please refer to Supplementary methods.

Serum cholesterol levels and expression profiling in liver. Male TPC2$^{-/-}$ and WT mice were fed with standard chow diet (SD) or a high-cholesterol containing Western-type diet (1.25% cholesterol, 15% fat, 0.5% Na-cholate; ssniff GmbH, Soest, Germany) for 6 weeks. Throughout the text, we refer to this diet by calling it cholesterol diet or CD. On the day of euthanasia, food was removed from the cage and approximately 8 h later, mice were killed as described[59] and blood was drawn by left-ventricular puncture in EDTA-containing syringes. Cell counting was performed after 1:4 dilution with PBS in an automated hematology analyzer (Sysmex). Lipoproteins were isolated by sequential ultracentrifugation from 60 μl

of plasma at $d<1.006\,g\,ml^{-1}$ (VLDL) $1.006\leq d\leq 1.063\,g\,ml^{-1}$ (intermediate- and low-density lipoprotein (IDL and LDL, respectively)) and $d>1.063\,g\,ml^{-1}$ (high-density lipoprotein (HDL)) in a TL100 ultracentrifuge (Beckman). Cholesterol was determined enzymatically by using a colorimetric method (Roche).

RNA from liver samples of TPC2$^{-/-}$ and WT mice fed with SD (WT $n=4$; TPC2$^{-/-}$ $n=4$) or CD (WT $n=4$; TPC2$^{-/-}$ $n=4$) was isolated as described previously[60]. RNA was labelled and hybridized to Illumina Mouse Ref-8 v2.0 Expression Bead Chips and arrays were scanned with an Illumina iScan microarray scanner. Bead level data pre-processing was done in Illumina Genome Studio followed by quantile normalization and background reduction according to standard procedures in the software. Of the >25,600 annotated RefSeq transcripts that were covered by the arrays, a total of 4,598 transcripts were upregulated or downregulated in TPC2$^{-/-}$ mice with fold changes >20% compared with WT control. Of these, 2,159 transcripts were differentially regulated in livers of mice on SD and 3,288 partially overlapping transcripts were differentially regulated in livers of mice on CD. Using the Ingenuity Pathways Analysis software (www.ingenuity.com), most significantly enriched biological functions in WT and TPC2$^{-/-}$ mice were identified and levels of significance were determined using Fisher's exact tests implemented in the software[61]. Alternatively, expression of Ldlr (5′-primer 5′-TGGGTCATCGCCCTGCT-3′, 3′-primer 5′-TTCCTGCTGCATGA GTCTTCT-3′, probe 5′FAM-5′-CTGGCTGCTGCCGGAGTTGCA-3′TAMRA), Egfr (5′-primer 5′-CCTATGCCACGCCAACTGTAC-3′, 3′-primer 5′-GATGGCC ACACTTCACATCCT-3′, probe 5′FAM-5′-TATGGATGTGCTGGGCCAGGTC TTC-3′TAMRA) was assessed in liver samples by quantitative RT–PCR and normalized to glyceraldehyde 3-phosphate dehydrogenase (5′-primer 5′-TGTCCG TCGTGGATCTGACG-3′, 3′-primer 5′-CCAAGATGCCCTTCAGTGGG-3′, probe 5′FAM-5′-CGCCTGGAGAAACCTGCCAAGTATGATGAC-3′TAMRA).

Determination of hepatic cholesterol by gas chromatography mass spectrometry. Gas chromatography mass spectrometry analysis was performed on a Varian 3800 gas chromatograph coupled with a Varian Saturn 2200 ion trap. The stationary phase was an Agilent VF-5 ms capillary column with 30 m × 0.25 mm inner diameter and 0.25 µm film thickness. The mobile phase was helium at a constant flow rate of 1.4 ml min^{-1}. The inlet temperature was 250 °C, injection volume 1 µl (split ratio 3 for free liver cholesterol and 15 for total liver cholesterol after alkaline ester hydrolysis). The GC oven started at 70 °C, ramped up to 270 °C (heating rate 50 °C min^{-1}), followed by a gradient of 5 °C min^{-1} up to 310 °C. Transfer line temperature was 270 °C and the ion-trap temperature was 200 °C. MS scanned from 8.5 to 12.0 min at a mass range of 100–550 *m/z* (electron ionization, 70 eV). The peak areas of characteristic ions forcholesterol tetramethylsilane ether (368 *m/z*) and for cholestane (217 *m/z*) were used for data analysis. The mean value of each double-injected sample ($n=5$) was used for statistical analysis. For details of sample preparation, please refer to Supplementary methods.

Statistical analysis. Details of statistical analyses and *n* values are provided in the methods subsections or the figure legends. Statistical analyses were carried out using Origin 7.5 and GraphPad Prism 5. All error bars are depicted as mean ± s.e.m. Statistical significance was determined via Student's *t*-test, one-way analysis of variance followed by Tukey's post test, or two-way analysis of variance followed by Bonferroni's *post hoc* test, unless stated otherwise. Significance is denoted on figures as outlined in the legends. Statistics were derived from at least three independent experiments.

References

1. Min, H. K. *et al.* Increased hepatic synthesis and dysregulation of cholesterol metabolism is associated with the severity of nonalcoholic fatty liver disease. *Cell Metab.* **15,** 665–674 (2012).
2. Bhatia, L. S., Curzen, N. P., Calder, P. C. & Byrne, C. D. Non-alcoholic fatty liver disease: a new and important cardiovascular risk factor? *Eur. Heart J.* **33,** 1190–1200 (2012).
3. Tiniakos, D. G., Vos, M. B. & Brunt, E. M. Nonalcoholic fatty liver disease: pathology and pathogenesis. *Annu. Rev. Pathol.* **5,** 145–171 (2010).
4. Postic, C. & Girard, J. Contribution of *de novo* fatty acid synthesis to hepatic steatosis and insulin resistance: lessons from genetically engineered mice. *J. Clin. Invest.* **118,** 829–838 (2008).
5. Browning, J. D. & Horton, J. D. Molecular mediators of hepatic steatosis and liver injury. *J. Clin. Invest.* **114,** 147–152 (2004).
6. Chen, Y. *et al.* Inflammatory stress exacerbates hepatic cholesterol accumulation via disrupting cellular cholesterol export. *J. Gastroenterol. Hepatol.* **27,** 974–984 (2012).
7. Musso, G., Gambino, R. & Cassader, M. Cholesterol metabolism and the pathogenesis of non-alcoholic steatohepatitis. *Prog. Lipid Res.* **52,** 175–191 (2013).
8. Hendrikx, T., Walenbergh, S. M., Hofker, M. H. & Shiri-Sverdlov, R. Lysosomal cholesterol accumulation: driver on the road to inflammation during atherosclerosis and non-alcoholic steatohepatitis. *Obes. Rev.* **15,** 424–433 (2014).
9. Cullen, P. J. Endosomal sorting and signalling: an emerging role for sorting nexins. *Nat. Rev. Mol. Cell Biol.* **9,** 574–582 (2008).
10. Goldstein, J. L. & Brown, M. S. The LDL receptor and the regulation of cellular cholesterol metabolism. *J. Cell Sci. Suppl.* **3,** 131–137 (1985).
11. Gruenberg, J. Lipids in endocytic membrane transport and sorting. *Curr. Opin. Cell Biol.* **15,** 382–388 (2003).
12. Luzio, J. P., Parkinson, M. D., Gray, S. R. & Bright, N. A. The delivery of endocytosed cargo to lysosomes. *Biochem. Soc. Trans.* **37,** 1019–1021 (2009).
13. Luzio, J. P., Gray, S. R. & Bright, N. A. Endosome-lysosome fusion. *Biochem. Soc. Trans.* **38,** 1413–1416 (2010).
14. Saftig, P. & Klumperman, J. Lysosome biogenesis and lysosomal membrane proteins: trafficking meets function. *Nat. Rev. Mol. Cell Biol.* **10,** 623–635 (2009).
15. Wenk, M. R. & De Camilli, P. Protein-lipid interactions and phosphoinositide metabolism in membrane traffic: insights from vesicle recycling in nerve terminals. *Proc. Natl Acad. Sci. USA* **101,** 8262–8269 (2004).
16. Ruas, M. *et al.* Purified TPC isoforms form NAADP receptors with distinct roles for Ca(2+) signaling and endolysosomal trafficking. *Curr. Biol.* **20,** 703–709 (2010).
17. Wang, X. *et al.* TPC proteins are phosphoinositide-activated sodium-selective ion channels in endosomes and lysosomes. *Cell* **151,** 372–383 (2012).
18. Calcraft, P. J. *et al.* NAADP mobilizes calcium from acidic organelles through two-pore channels. *Nature* **459,** 596–600 (2009).
19. Rietdorf, K. *et al.* Two-pore channels form homo- and heterodimers. *J. Biol. Chem.* **286,** 37058–37062 (2011).
20. Cang, C. *et al.* mTOR regulates lysosomal ATP-sensitive two-pore Na+ channels to adapt to metabolic state. *Cell* **152,** 778–790 (2013).
21. Schieder, M., Rötzer, K., Brüggemann, A., Biel, M. & Wahl-Schott, C. A. Characterization of two-pore channel 2 (TPCN2)-mediated Ca2+ currents in isolated lysosomes. *J. Biol. Chem.* **285,** 21219–21222 (2010a).
22. Schieder, M., Rötzer, K., Brüggemann, A., Biel, M. & Wahl-Schott, C. Planar patch clamp approach to characterize ionic currents from intact lysosomes. *Sci. Signal.* **3,** pl3 (2010b).
23. Morgan, A. J. & Galione, A. Two-pore channels (TPCs): current controversies. *Bioessays* **36,** 173–183 (2014).
24. Jha, A., Ahuja, M., Patel, S., Brailoiu, E. & Muallem, S. Convergent regulation of the lysosomal two-pore channel-2 by Mg2+, NAADP, PI(3,5)P2 and multiple protein kinases. *EMBO J.* **33,** 501–511 (2014).
25. Pitt, S. J. *et al.* TPC2 is a novel NAADP-sensitive Ca2+ release channel, operating as a dual sensor of luminal pH and Ca2+. *J. Biol. Chem.* **285,** 35039–35046 (2010).
26. Zong, X. *et al.* The two-pore channel TPCN2 mediates NAADP-dependent Ca(2+)-release from lysosomal stores. *Pflugers Arch.* **458,** 891–899 (2009).
27. Miedel, M. T. *et al.* Membrane traffic and turnover in TRP-ML1-deficient cells: a revised model for mucolipidosis type IV pathogenesis. *J. Exp. Med.* **205,** 1477–1490 (2008).
28. Curcio-Morelli, C. *et al.* Functional multimerization of mucolipin channel proteins. *J. Cell. Physiol.* **222,** 328–335 (2010).
29. Carpenter, G. & Cohen, S. 125I-labeled human epidermal growth factor. Binding, internalization, and degradation in human fibroblasts. *J. Cell Biol.* **71,** 159–171 (1976).
30. Morgan, A. J., Platt, F. M., Lloyd-Evans, E. & Galione, A. Molecular mechanisms of endolysosomal Ca2+ signalling in health and disease. *Biochem. J.* **439,** 349–374 (2011).
31. Martina, J. A., Lelouvier, B. & Puertollano, R. The calcium channel mucolipin-3 is a novel regulator of trafficking along the endosomal pathway. *Traffic* **10,** 1143–1156 (2009).
32. Hay, J. C. Calcium: a fundamental regulator of intracellular membrane fusion? *EMBO Rep.* **8,** 236–240 (2007).
33. Pryor, P. R., Mullock, B. M., Bright, N. A., Gray, S. R. & Luzio, J. P. The role of intraorganellar Ca(2+) in late endosome-lysosome heterotypic fusion and in the reformation of lysosomes from hybrid organelles. *J. Cell Biol.* **149,** 1053–1062 (2000).
34. Wong, C. O., Li, R., Montell, C. & Venkatachalam, K. *Drosophila* TRPML is required for TORC1 activation. *Curr. Biol.* **22,** 1616–1621 (2012).
35. Moreno, S. N. & Zhong, L. Acidocalcisomes in Toxoplasma gondii tachyzoites. *Biochem. J.* **313,** 655–659 (1996).
36. Dong, X. P. *et al.* PI(3,5)P(2) controls membrane trafficking by direct activation of mucolipin Ca(2+) release channels in the endolysosome. *Nat. Commun.* **1,** 38 (2010).
37. Peet, D. J. *et al.* Cholesterol and bile acid metabolism are impaired in mice lacking the nuclear oxysterol receptor LXR alpha. *Cell* **93,** 693–704 (1998).
38. Osono, Y., Woollett, L. A., Herz, J. & Dietschy, J. M. Role of the low density lipoprotein receptor in the flux of cholesterol through the plasma and across the tissues of the mouse. *J. Clin. Invest.* **95,** 1124–1132 (1995).
39. Zhang, M. *et al.* Cessation of rapid late endosomal tubulovesicular trafficking in Niemann-Pick type C1 disease. *Proc. Natl Acad. Sci. USA* **98,** 4466–4471 (2001).
40. Soyombo, A. A. *et al.* TRP-ML1 regulates lysosomal pH and acidic lysosomal lipid hydrolytic activity. *J. Biol. Chem.* **281,** 7294–7301 (2006).

41. Lloyd-Evans, E. *et al.* Niemann-Pick disease type C1 is a sphingosine storage disease that causes deregulation of lysosomal calcium. *Nat. Med.* **14,** 1247–1255 (2008).
42. Shen, D. *et al.* Lipid storage disorders block lysosomal trafficking by inhibiting a TRP channel and lysosomal calcium release. *Nat. Commun.* **3,** 731 (2012).
43. Soccio, R. E. & Breslow, J. L. Intracellular cholesterol transport. *Arterioscler. Thromb. Vasc. Biol.* **24,** 1150–1160 (2004).
44. Martin, S. & Parton, R. G. Lipid droplets: a unified view of a dynamic organelle. *Nat. Rev. Mol. Cell Biol.* **7,** 373–378 (2006).
45. Alrefai, W. A. & Gill, R. K. Bile acid transporters: structure, function, regulation and pathophysiological implications. *Pharm. Res.* **24,** 1803–1823 (2007).
46. Eden, E. R., White, I. J., Tsapara, A. & Futter, C. E. Membrane contacts between endosomes and ER provide sites for PTP1B-epidermal growth factor receptor interaction. *Nat. Cell Biol.* **12,** 267–272 (2010).
47. van der Kant, R., Zondervan, I., Janssen, L. & Neefjes, J. Cholesterol-binding molecules MLN64 and ORP1L mark distinct late endosomes with transporters ABCA3 and NPC1. *J. Lipid Res.* **54,** 2153–2165 (2013).
48. Friedman, J. R., Dibenedetto, J. R., West, M., Rowland, A. A. & Voeltz, G. K. Endoplasmic reticulum-endosome contact increases as endosomes traffic and mature. *Mol. Biol. Cell* **24,** 1030–1040 (2013).
49. Hölttä-Vuori, M. & Ikonen, E. Endosomal cholesterol traffic: vesicular and non-vesicular mechanisms meet. *Biochem. Soc. Trans.* **34,** 392–394 (2006).
50. Du, X. & Yang, H. Endosomal cholesterol trafficking: protein factors at a glance. *Acta Biochim. Biophys. Sin. (Shanghai)* **45,** 11–17 (2013).
51. Antonin, W. *et al.* A SNARE complex mediating fusion of late endosomes defines conserved properties of SNARE structure and function. *EMBO J.* **19,** 6453–6464 (2000).
52. Mullock, B. M. *et al.* Syntaxin 7 is localized to late endosome compartments, associates with Vamp 8, and is required for late endosome-lysosome fusion. *Mol. Biol. Cell* **11,** 3137–3153 (2000).
53. Prekeris, R., Yang, B., Oorschot, V., Klumperman, J. & Scheller, R. H. Differential Roles of Syntaxin 7 and Syntaxin 8 in endosomal trafficking. *Mol. Biol. Cell* **10,** 3891–3908 (1999).
54. Rosenbaum, A. I. & Maxfield, F. R. Niemann-Pick type C disease: molecular mechanisms and potential therapeutic approaches. *J. Neurochem.* **116,** 789–795 (2011).
55. Schenkman, J. B. & Cinti, D. L. Preparation of microsomes with calcium. *Methods Enzymol.* **52,** 83–89 (1978).
56. Steinberg, B. E. *et al.* A cation counterflux supports lysosomal acidification. *J. Cell Biol.* **189,** 1171–1186 (2010).
57. Grimm, C., Jörs, S., Guo, Z., Obukhov, A. G. & Heller, S. Constitutive activity of TRPML2 and TRPML3 channels versus activation by low extracellular sodium and small molecules. *J. Biol. Chem.* **287,** 22701–22708 (2012).
58. Schröder, J. *et al.* Deficiency of the tetraspanin CD63 associated with kidney pathology but normal lysosomal function. *Mol. Cell Biol.* **29,** 1083–1094 (2009).
59. Teupser, D., Persky, A. D. & Breslow, J. L. Induction of atherosclerosis by low-fat, semisynthetic diets in LDL receptor-deficient C57BL/6J and FVB/NJ mice: comparison of lesions of the aortic root, brachiocephalic artery, and whole aorta (en face measurement). *Arterioscler. Thromb. Vasc. Biol.* **23,** 1907–1913 (2003).
60. Holdt, L. M., Thiery, J., Breslow, J. L. & Teupser, D. Increased ADAM17 mRNA expression and activity is associated with atherosclerosis resistance in LDL-receptor deficient mice. *Arterioscler. Thromb. Vasc. Biol.* **28,** 1097–1103 (2008).
61. Holdt, L. M. *et al.* Alu elements in ANRIL non-coding RNA at chromosome 9p21 modulate atherogenic cell functions through trans-regulation of gene networks. *PLoS Genet.* **9,** e1003588 (2013).

Acknowledgements

We thank Phuong Nguyen, Maximiliane Geerds, Berit Noack and Elisabeth Schulze (LMU Munich) for technical support. CathL$^{-/-}$ MEFs were provided by Dr Thomas Reinheckel (Institute of Molecular Medicine and Cell Research, Freiburg). Anti-LIMP2 antibody was provided by Dr Michael Schwake (Institute of Chemistry, Biochemistry III, Bielefeld). Mice expressing Cre-recombinase under a cytomegalovirus promoter were kindly provided by Professor Dr Freichel, Heidelberg. We further thank Professor Dr Fässler, Max-Planck-Institute for Biochemistry, München for his comments on the manuscript. This work was supported, in part, by funding of the German Research Foundation (DFG grants WA2597, GR4315 and SPP1580), the Bavarian Research Foundation, and by the SME innovation program 'ZIM' of the German Federal Ministry of Economics and Technology (BMWi).

Author contributions

C.G. designed, collected and analysed data, and wrote the manuscript. C.W.-S. and M.B. wrote and edited the manuscript. L.M.H., C.-C.C., S.H., S.J., H.C., S.K., B.S., E.B., B.N., C.M., J.C., C.A.L., S.S., M.M., R.L.-R. and C.F. designed, collected and/or analysed data. N.K., O.G., A.H., M.M., F.B., D.T. and P.S. edited the manuscript. All of the authors discussed the results and commented on the manuscript.

Additional information

Supplementary Information accompanies this paper at http://www.nature.com/naturecommunications

Competing financial interests: The authors declare no competing financial interests.

Reprints and permission information is available online at http://npg.nature.com/reprintsandpermissions/

How to cite this article: Grimm, C. *et al.* High susceptibility to fatty liver disease in two-pore channel 2-deficient mice. *Nat. Commun.* 5:4699 doi: 10.1038/ncomms5699 (2014).

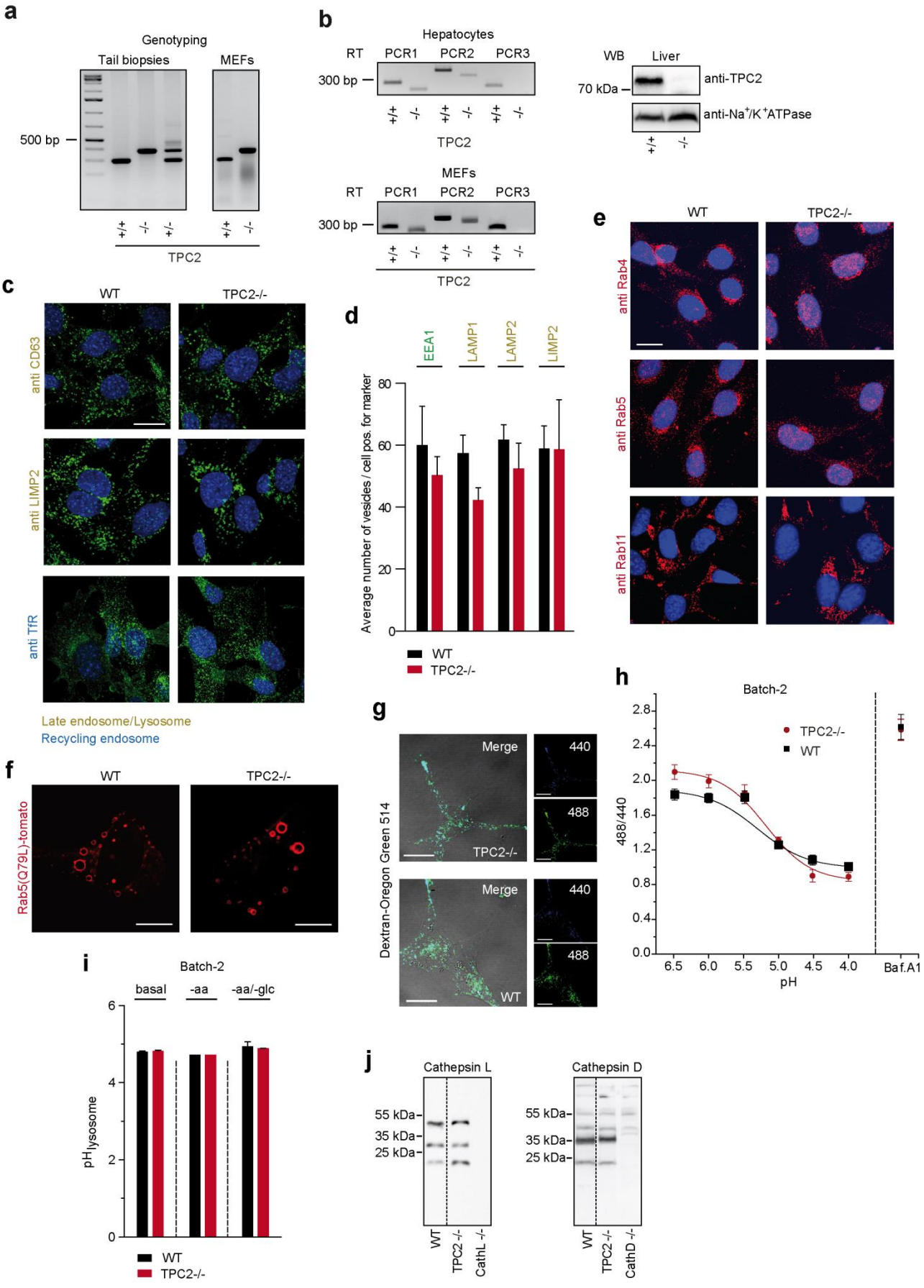
a
Genotyping
Tail biopsies
MEFs
500 bp
+/+ -/- +/-
+/+ -/-
TPC2
b
Hepatocytes
RT PCR1 PCR2 PCR3
300 bp
+/+ -/- +/+ -/- +/+ -/-
TPC2
WB Liver
70 kDa
anti-TPC2
anti-Na+/K+ATPase
+/+ -/-
MEFs
RT PCR1 PCR2 PCR3
300 bp
+/+ -/- +/+ -/- +/+ -/-
TPC2
c
WT TPC2-/-
anti CD63
anti LIMP2
anti TfR
Late endosome/Lysosome
Recycling endosome
d
EEA1 LAMP1 LAMP2 LIMP2
Average number of vesicles / cell pos. for marker
0 20 40 60 80
WT
TPC2-/-
e
WT TPC2-/-
anti Rab4
anti Rab5
anti Rab11
f
WT TPC2-/-
Rab5(Q79L)-tomato
g
Merge
440
488
TPC2-/-
Merge
440
488
WT
Dextran-Oregon Green 514
h
Batch-2
TPC2-/-
WT
488/440
0.0 0.4 0.8 1.2 1.6 2.0 2.4 2.8
6.5 6.0 5.5 5.0 4.5 4.0
pH
Baf.A1
i
Batch-2
basal -aa -aa/-glc
pHlysosome
0 2 4 6
WT
TPC2-/-
j
Cathepsin L
55 kDa
35 kDa
25 kDa
WT TPC2 -/- CathL -/-
Cathepsin D
55 kDa
35 kDa
25 kDa
WT TPC2 -/- CathD -/-

Supplementary Fig. 1. Characterization of TPC2 knockout mice. (**a**) Representative genotyping results obtained from samples prepared from tails and MEFs of WT, TPC2$^{-/-}$ and heterozygous mice. (**b**) RT-PCR (left) and Western blot (right) results obtained from WT and TPC2$^{-/-}$ samples prepared from MEFs, primary hepatocytes, or liver tissue lysates (membrane preparations). (**c**) Expression and distribution of selected marker proteins for endosomes and lysosomes were unaffected in TPC2$^{-/-}$ compared to WT MEFs. Shown are confocal images of WT and TPC2$^{-/-}$ MEFs labeled with antibodies against CD63 antigen, LIMP2, and TfR visualized with Alexa488 as secondary antibody. Nuclei were visualized with DAPI. Scale bar = 20 µm. (**d**) Average numbers of vesicles positive for selected markers shown in c and in Fig.1f. (**e**) Expression and distribution of different Rab proteins in TPC2$^{-/-}$ and WT MEFs. Antibodies against Rab4, 5, and 11 were used and proteins were visualized with Cy5 as secondary antibody. Nuclei were stained with DAPI. Scale bar = 20 µm. (**f**) Overexpression of the constitutively active Rab5(Q79L) variant in TPC2$^{-/-}$ and WT MEFs showing characteristic enlarged Rab5 positive vesicles. (**g-i**) Measurement of endolysosomal pH. Late endocytic compartments of WT and TPC2$^{-/-}$ MEFs were labeled with dextran-Oregon Green 514. *In situ* calibration procedure: Cells were bathed in extracellular solution of defined pH. After extracellular application of the ionophore nigericin intracellular pH was clamped to the pH value of the extracellular solution. (**g**) Fluorescence images are presented as overlay of fluorescence emission at 535 nm upon excitation at 440 nm (blue) and 488 nm (green), respectively. Scale bar = 20 µm. (**h**) Fluorescence intensity ratios were calculated for defined pH values and a calibration curve was constructed. (**i**) Lysosomal pH values in WT and TPC2$^{-/-}$ MEFs were calculated using calibration curves presented in f (Batch-2 MEFs; for Batch-1 MEFs see Fig.1h-i) and determined under basal conditions, without amino acids (-aa, EBSS), and without amino acids and glucose (-aa, -glc); n.s. not significant, unpaired Student's *t*-test. (**j**) Proteolytic processing of cathepsin D and cathepsin L in WT and TPC2$^{-/-}$ MEFs was analyzed by Western blotting. CathD$^{-/-}$ and CathL$^{-/-}$ MEFs were used as controls. All data points are given as mean ± SEM. For Western blotting the anti-TPC2 antibody was used as described in Fig.1b. For RT-PCR the following oligonucleotides were used for genotyping: 5'-atgcctaatccagatggctc-3' (sense), 5'-cctcagcctcaagatgagtg-3' (sense), and 5'-tggacatgcaacaggctctc-3' (antisense). Using a second forward primer that binds within the *loxP* sites, and therefore does not work in knockout mice/cells, results in three bands: 1827 bp (WT), 379 (TPC2$^{-/-}$), and 290 bp (WT). PCR conditions were chosen so that only the two shorter bands were amplified. The following oligonucleotides were used for RT-PCR: 5'-ctgctgcagaattcctccatgat-3' (forward) and 5'-aacaagcttcctatcaaggtgaa-3' (reverse) (PCR1: expected fragments: 322 bp for WT and 246 bp for TPC2$^{-/-}$), 5'-aacctgtggctgctggcctactt-3' (forward) and 5'- ggtagccacggaactgattatag-3' (reverse) (PCR2: expected fragments: 493 bp for WT and 417 bp for TPC2$^{-/-}$), and 5'-atccacctgtgtctcttcaccat-3' (forward) and 5'-ggtagccacggaactgattatag-3' (reverse) (PCR3). The latter forward primer binds to exon 7 which is lost in TPC2$^{-/-}$ animals. Expected fragment size for WT: 283 bp.

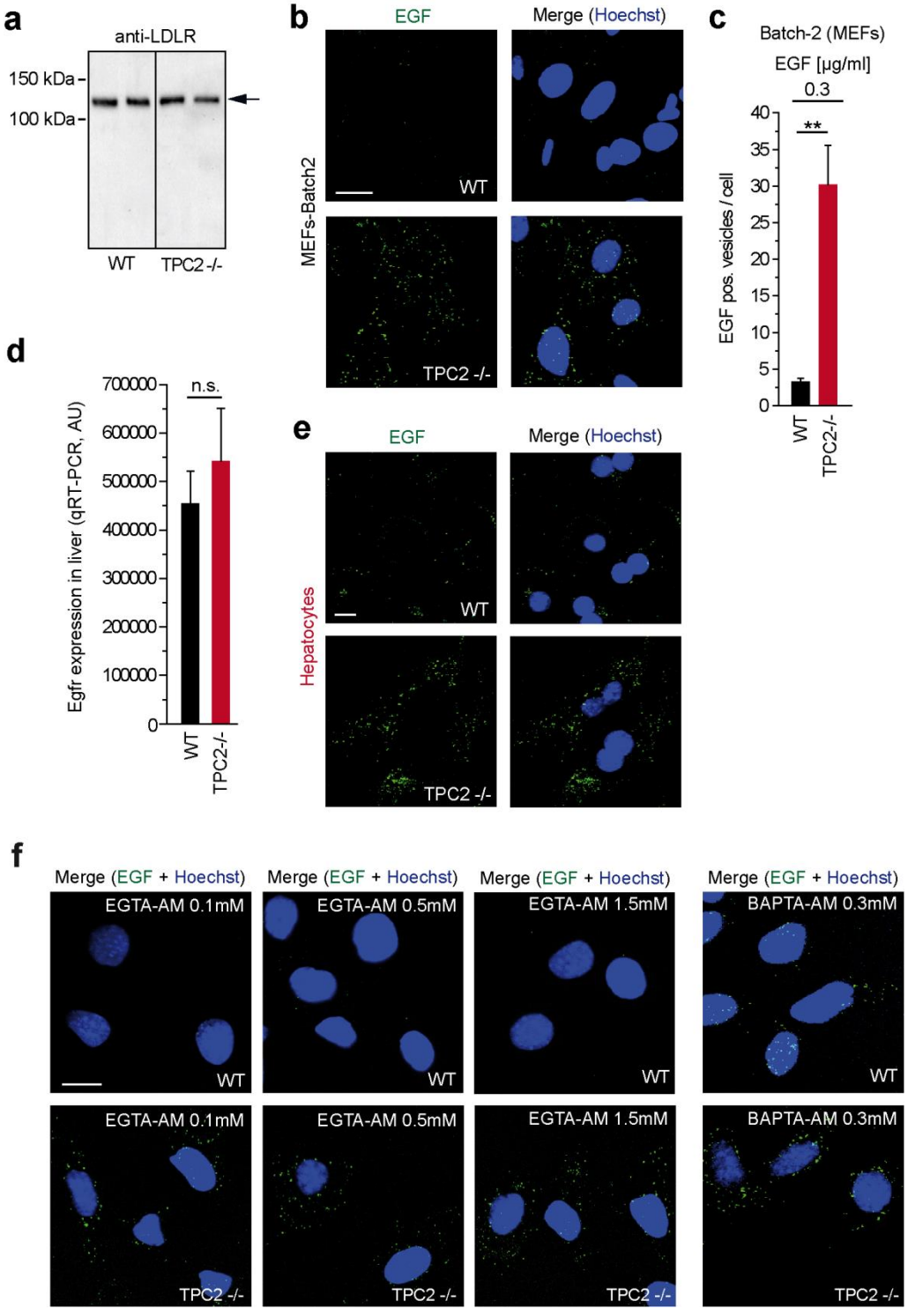
a
anti-LDLR
150 kDa
100 kDa
WT
TPC2 -/-
b
EGF
Merge (Hoechst)
MEFs-Batch2
WT
TPC2 -/-
c
Batch-2 (MEFs)
EGF [µg/ml]
0.3
**
EGF pos. vesicles / cell
40
35
30
25
20
15
10
5
0
WT
TPC2-/-
d
n.s.
Egfr expression in liver (qRT-PCR, AU)
700000
600000
500000
400000
300000
200000
100000
0
WT
TPC2-/-
e
EGF
Merge (Hoechst)
Hepatocytes
WT
TPC2 -/-
f
Merge (EGF + Hoechst)
EGTA-AM 0.1mM
EGTA-AM 0.5mM
EGTA-AM 1.5mM
BAPTA-AM 0.3mM
WT
TPC2 -/-

Supplementary Fig. 2. LDLR expression in MEFs, confocal images of EGF accumulation in TPC2$^{-/-}$ hepatocytes, Egfr levels in liver samples from TPC2$^{-/-}$ and WT mice, and effect of EGTA-AM on EGF trafficking. (**a**) Representative Western blot showing expression of LDLR protein in WT and TPC2$^{-/-}$ MEFs (calculated band size = 93 kDa; actual band size of 120 kDa is expected according to manufaturer's guidelines (http://www.abcam.com/ldl-receptor-antibody-ab14056.html)). Quantification was repeated in 3 independent experiments using GAPDH expression as reference. Western blot quantification was performed using ImageLab software (Bio-Rad Laboratories). (**b**) Confocal images of WT and TPC2$^{-/-}$ MEFs (Batch-2; MEFs were generated independently from MEFs used in Fig.2 (Batch-1)) incubated with 0.3 µg/ml AlexaFluor488-EGF for 30 min before fixation. Cell nuclei were visualized with Hoechst. Scale bar = 20 µm. (**c**) Average numbers of EGF positive vesicles/cell from experiments as shown in b. (**d**) Quantitative RT-PCR results showing average expression levels of Egfr in liver samples from WT and TPC2$^{-/-}$ mice, normalized to Gapdh. (**e**) Confocal images of WT and TPC2$^{-/-}$ primary hepatocytes incubated with 0.1 µg/ml AlexaFluor488-EGF for 30 min before fixation. Cell nuclei were visualized with Hoechst. Scale bar = 20 µm. Data points in c and d are given as mean ± SEM. **p<0.01, unpaired Student's *t*-test. (**f**) Representative images of WT and TPC2$^{-/-}$ MEFs incubated with 0.1 µg/ml AlexaFluor488-EGF (5 min), followed by an incubation with 0.1 µg/ml AlexaFluor488-EGF in the presence of either 0.1, 0.5 mM, 1.5 mM EGTA-AM, or 0.3 mM BAPTA-AM (25 min) in PBS. Cell nuclei were visualized with Hoechst. Scale bar = 20 µm.

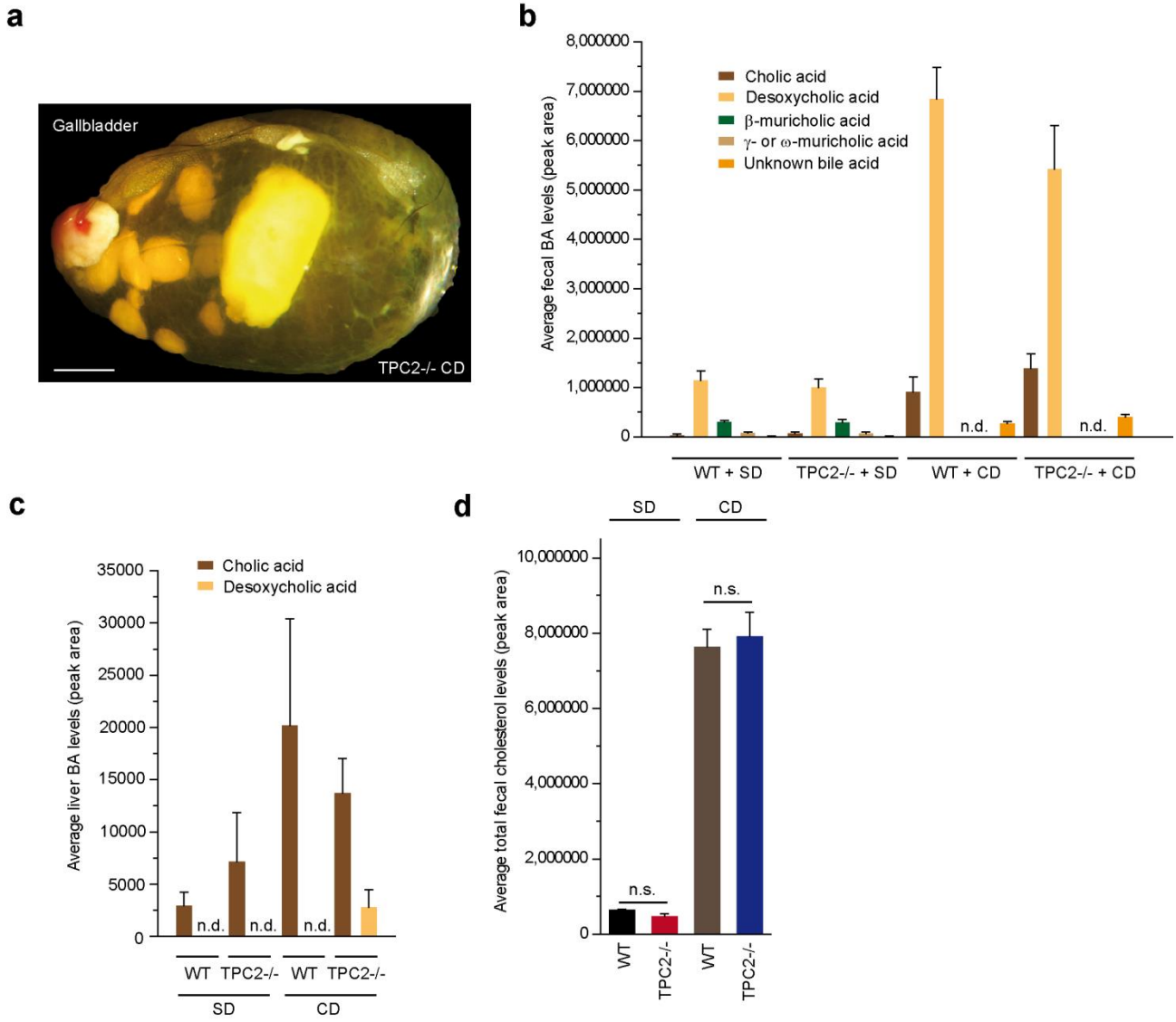

Supplementary Fig. 3. Macroscopic analysis of gallbladders, analysis of cholesterol content in feces, and analysis of BA content and composition in liver and feces. (**a**) Representative image of gallstone containing gallbladder isolated from CD fed TPC2$^{-/-}$ mice. Scale bar = 1 mm. (**b-c**) Average fecal (b) and liver (c) BA levels in WT and TPC2$^{-/-}$ mice on SD or CD as indicated; n.d. = not detectable. Unknown BA = ketocholic acid or cholic acid with an additional double bond. (**d**) Average fecal levels of unesterified free cholesterol in WT and TPC2$^{-/-}$ mice on SD or CD as indicated. All data points are presented as mean ± SEM.

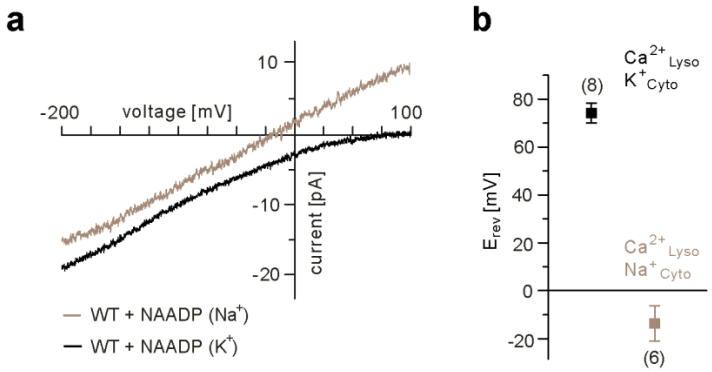

Supplementary Fig. 4. NAADP-activated TPC2 currents in WT MEFs are Na^+ and Ca^{2+} permeable. (**a**) Whole-lysosome recordings of NAADP-evoked TPC2-like currents (50 nM NAADP) under bi-ionic conditions with 107 mM luminal Ca^{2+}, 165 mM cytoplasmic K^+ or 165 mM cytoplasmic Na^+ at pH 4.6. (**b**) Current recordings revealed that E_{rev} is 77 ± 4 mV (n = 8) and -14 ± 7 mV (n = 6), respectively. Data are presented as mean ± SEM. The relative permeability of TPC2 for monovalent and divalent cations was assessed by determining the reversal potential with 107 mM luminal Ca^{2+} and 165 mM cytoplasmic K^+ or Na^+. NAADP evoked TPC2-like current recordings under these bi-ionic conditions revealed that the estimated permeability ratios for P_{Ca}/P_K and P_{Ca}/P_{Na} were about 340 (n = 8) and 0.7 (n = 6), respectively. These ion substitution analyses demonstrate that endogenous TPC2 is permeable for Ca^{2+} and Na^+ but much less for K^+. For further details see Supplementary Methods.

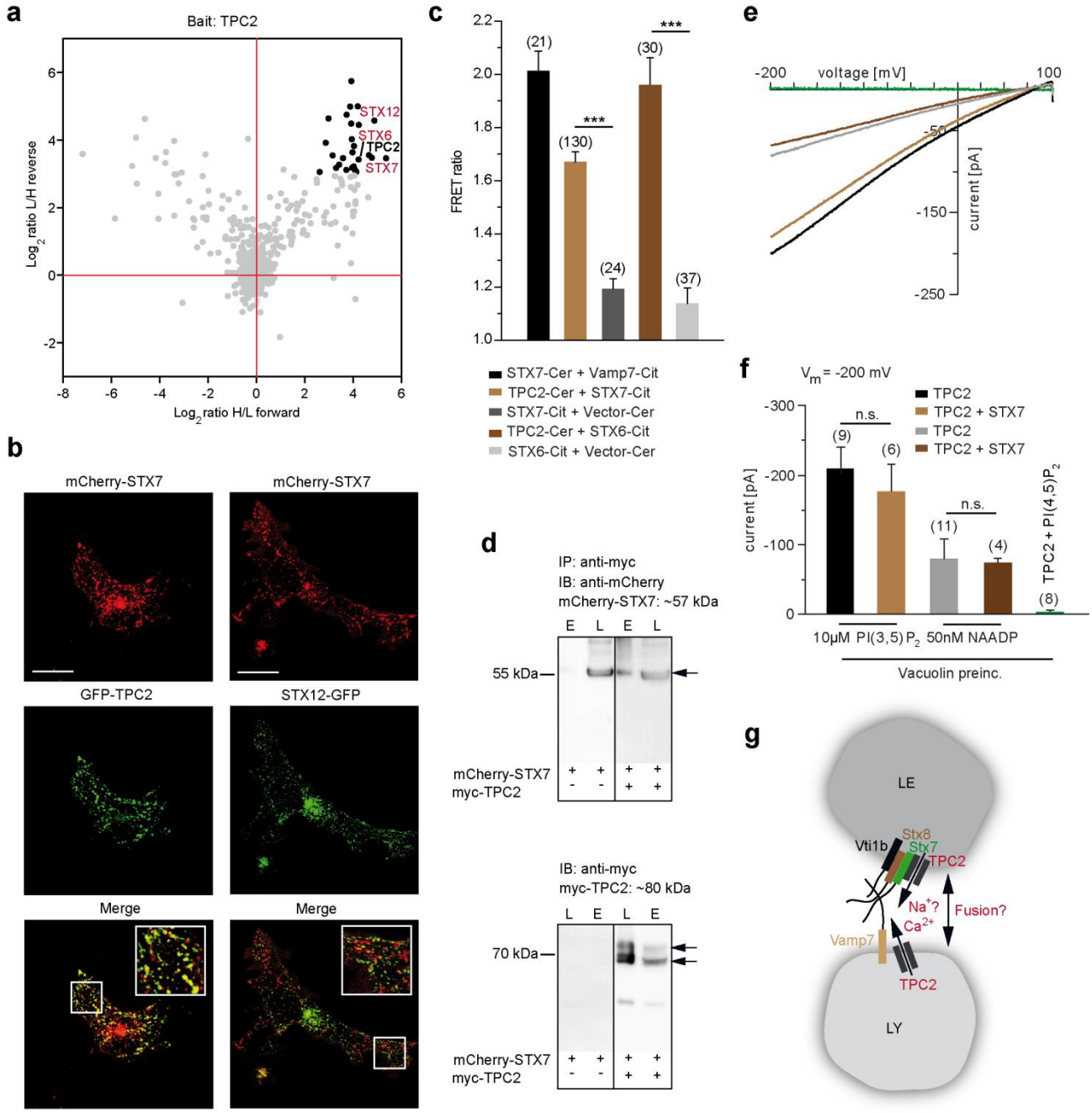
a
Bait: TPC2
STX12
STX6
TPC2
STX7
Log2 ratio L/H reverse
Log2 ratio H/L forward
b
mCherry-STX7
mCherry-STX7
GFP-TPC2
STX12-GFP
Merge
Merge
c
FRET ratio
(21)
(130)
(24)
(30)
(37)
***
***
STX7-Cer + Vamp7-Cit
TPC2-Cer + STX7-Cit
STX7-Cit + Vector-Cer
TPC2-Cer + STX6-Cit
STX6-Cit + Vector-Cer
d
IP: anti-myc
IB: anti-mCherry
mCherry-STX7: ~57 kDa
E L E L
55 kDa
mCherry-STX7
myc-TPC2
IB: anti-myc
myc-TPC2: ~80 kDa
L E L E
70 kDa
mCherry-STX7
myc-TPC2
e
-200
voltage [mV]
100
-50
-150
-250
current [pA]
f
Vm = -200 mV
current [pA]
n.s.
n.s.
(9)
(6)
(11)
(4)
(8)
TPC2
TPC2 + STX7
TPC2
TPC2 + STX7
TPC2 + PI(4,5)P2
10µM PI(3,5)P2
50nM NAADP
Vacuolin preinc.
g
LE
Vti1b
Stx8
Stx7
TPC2
Na+?
Ca2+
Fusion?
Vamp7
TPC2
LY

Supplementary Fig. 5. Identification of proteins associated with TPC2. (**a**) Logarithmized and normalized ratios of forward and reverse SILAC immunoprecipitation experiments of GFP-tagged murine TPC2 versus their corresponding control cell lines; annotated proteins shown as black dots were more abundant in the pull-down of the tagged cell line with $p<0.05$ (Significance B) in both the forward and reverse experiments. Grey dots represent proteins that were not significant interaction partners. For more details refer to Supplementary Table 2. (**b**) Confocal images showing colocalization of TPC2 and STX7 in a subset of intracellular vesicles of transiently transfected WT MEFs. For comparison, STX7 and STX12/13 did not colocalize in the same vesicles confirming that these proteins are confined to distinct vesicle pools. Scale bars = 20 µm. (**c**) FRET ratios between Cer-tagged TPC2 and Cit-tagged STX7 or STX6, and control combinations. Positive control: Cit-tagged STX7 and Cer-tagged Vamp7. Negative controls: Cit-tagged STX7 or Cit-tagged STX6 and Cerulean vector, respectively. ***$p<0.001$, one-way ANOVA followed by Tukey's post test, n = number of measured cells. (**d**) Representative co-immunoprecipiation experiment of HEK293 cells coexpressing myc-TPC2 and mCherry-STX7. Lysates (L) were immunoprecipitated (E) with anti-myc, blotted and probed with anti-mCherry or anti-myc. (**e**) Current-voltage relations of TPC2 currents from single lysosomes stably coexpressing TPC2 and STX7 in the presence of 10 µM $PI(3,5)P_2$ or 50 nM NAADP. Lysosomes were isolated from HEK293 cells pretreated with vacuolin (1 µM for 2 h). Further shown are control TPC2 currents activated by 10 µM $PI(3,5)P_2$, 10 µM $PI(4,5)P_2$, (negative control), or 50 nM NAADP, recorded from lysosomes expressing TPC2 only. These results suggest that TPC2 channel properties remain unaltered by the interaction with STX7, while close proximity to or direct interaction with endolysosomal SNARE proteins such as STX7 would allow spatially and temporally restricted Ca^{2+} signalling through TPC2 at the fusion complex. (**f**) Population data for current amplitudes at -200 mV obtained from experiments shown in f; n = number of measured cells, unpaired Student's *t*-test. (**g**) Cartoon displaying potential model of TPC2 involvement in fusion processes between late endosomes (LE) and lysosomes (LY) by directly or indirectly interacting with components of the fusion machinery such as syntaxins. Besides interaction with STX7, the proteomics and FRET results suggest possible interactions of TPC2 with other SNARE proteins and complexes containing e.g. STX6. Data points in c and f are presented as mean ± SEM.

Lysosomal pH	Batch-1 WT	Batch-1 TPC2-/-	Batch-2 WT	Batch-2 TPC2-/-
basal	4.93 ± 0.06	5.08 ± 0.1	4.89 ± 0.02	4.87 ± 0.03
-aa	5.1 ± 0.08	5.15 ± 0.23	4.79	4.79
-aa -glc	4.97 ± 0.01	5.05 ± 0.15	4.96 ± 0.01	5.01 ± 0.13
Baf.A1	> 6.5	> 6.5	> 6.5	> 6.5

Supplementary Table 1. Lysosomal pH measurements. Summary (mean ± SEM) for the conditions described in Fig. 1i and Supplementary Fig. 1i. Bafilomycin A1 (Baf. A1) was used as positive control.

Molecular and cellular functions	CD (p-value)	Molecules (n)	SD (p-value)	Molecules (n)
Lipid Metabolism	$1.47x10^{-09}$	399	$2.36x10^{-08}$	281
Molecular Transport	$1.47x10^{-09}$	397	$1.17x10^{-06}$	340
Small Molecule Biochemistry	$1.47x10^{-09}$	485	$2.36x10^{-08}$	331
Cell Death and Survival	$1.61x10^{-08}$	740	$5.88x10^{-08}$	512
Cell-To-Cell Signaling and Interaction	$1.59x10^{-06}$	347	$3.11x10^{-04}$	102
Cellular Movement	$2.67x10^{-06}$	454	$1.21x10^{-05}$	325
Carbohydrate Metabolism	$2.86x10^{-06}$	275	$9.57x10^{-08}$	195
Cellular Function and Maintenance	$4.14x10^{-05}$	292	$2.56x10^{-04}$	319
Cellular Development	$8.44x10^{-05}$	561	$2.80x10^{-05}$	301
Cellular Growth and Proliferation	$8.44x10^{-05}$	711	$2.80x10^{-05}$	501
Protein Synthesis	$1.18x10^{-04}$	370	$3.03x10^{-04}$	201
Cell Morphology	$4.82x10^{-04}$	165	$2.33x10^{-05}$	266

Supplementary Table 2. Gene set enrichment data. Gene set enrichment analysis of differentially regulated genes in livers isolated from $TPC2^{-/-}$ and WT mice on SD and CD, respectively. Molecular and cellular functions with ≥200 molecules are given. Data are sorted according to most significant p-value of enrichment in CD mice.

Gene name	Forward experiment		Reverse experiment	
	log_2 ratio H/L	Significance B	log_2 ratio L/H	Significance B
TPC2	**4.7**	**3.74E-13**	**3.6**	**1.69E-02**
SYNGR2	3.9	8.76E-10	5.7	6.99E-05
BCAP31	4.2	5.83E-11	5.0	5.99E-04
ARL8B	3.9	1.36E-09	5.0	6.00E-04
VAMP3;VAMP2	3.7	5.68E-09	4.7	1.14E-03
RTN4	3.0	3.26E-06	4.6	1.50E-03
STX12	4.9	2.58E-14	4.6	1.76E-03
RPN1	3.9	9.28E-10	4.5	2.18E-03
VTI1B	4.2	4.04E-11	4.4	2.39E-03
LMAN1	4.0	7.21E-10	4.0	6.38E-03
BAT3;BAG6	2.9	7.66E-06	3.9	8.01E-03
TMX1	4.0	2.99E-10	3.8	9.80E-03
HMGB2	4.0	5.48E-10	3.6	1.43E-02
RAB14	3.2	8.42E-07	3.5	1.72E-02
VPS45	4.8	9.18E-14	3.5	1.98E-02
RAB1A	3.6	2.26E-08	3.5	2.01E-02
TFRC	5.4	6.32E-17	3.5	2.03E-02
STX6	4.2	4.15E-11	3.4	2.19E-02
RAB1B;RAB1C	3.4	9.32E-08	3.3	2.90E-02
STX7	4.0	3.30E-10	3.2	3.18E-02
TMED10	4.0	6.21E-10	3.2	3.40E-02
RAB11A;RAB11B	3.3	2.72E-07	3.2	3.46E-02
SYNGR1	4.1	2.26E-10	3.1	3.76E-02
TMED9	3.7	6.36E-09	3.1	3.81E-02
ATP6V0D1	4.1	1.23E-10	3.1	4.23E-02
CPD	2.6	4.49E-05	3.1	4.26E-02
SCAMP3	4.1	1.29E-10	3.0	4.33E-02

Supplementary Table 3. Results of SILAC immunoprecipitation experiments. Logarithmized and normalized ratios of forward and reverse SILAC immunoprecipitation experiments of GFP-tagged murine TPC2 versus their corresponding control cell lines; Listed are the hits shown in Supplementary Fig. 3a as black dots. SNARE proteins including endolysosomal syntaxins are highlighted in red.

Supplementary Methods

Isolation of hepatocytes and MEFs from TPC2$^{-/-}$ and WT mice.

To generate primary hepatocyte cultures, livers from 8- to 12-week-old male TPC2$^{-/-}$ and WT mice were digested by a standard in situ 2-step retrograde collagenase-perfusion technique (Liberase-Blendzyme-3; Roche, Penzberg, Germany). Hepatocytes were separated from nonparenchymal cells by subsequent low-speed centrifugation (4x at 50 g for 2 minutes at 4°C). Isolated hepatocytes were seeded on collagen-coated glass cover slips in 24-well plates at a density of 2.5 x 10^5 cells/ml in Williams Medium-E (Sigma) supplemented with 5% FBS, 2 mmol/L L-glutamine, 100 U penicillin/ml, and 100 µg streptomycin/ml. Immortalized MEFs were generated as previously described[1, 2].

FRET measurements.

Measurements of single-cell FRET, based on aggregate (nonspatial) fluorescence recordings were performed and analyzed using the *Three-Cube*-FRET method as described previously[3].

For measurements, transiently transfected HEK293 cells were maintained in buffer solution composed of 140 mM NaCl, 5 mM KCl, 1 mM $MgCl_2$, 2 mM $CaCl_2$, 10 mM Glucose, 10 mM Na-HEPES pH 7.4 at RT. Fluorescence intensities of the GFP variants Citrine and Cerulean were recorded using an Axiovert 200 inverted epifluorescence microscope and a dual emission photometric system (Till Photonics). Excitation was done at 440 ± 7.5 nm or 505 ± 7.5 nm, applied with a frequency of 2 Hz with light from a Polychrome V. Epifluorescence emission was detected by a photodiode, digitized (MINI DIGI1B; Molecular devices) and analysed using Clampex 10 software. The FRET ratio, which is defined as the fractional increase in YFP emission caused by FRET, was calculated using $FR = [S_{FRET}-(R_{D1})(S_{CFP})]/[(R_{A1})(S_{YFP})]$. S_{FRET}, S_{CFP} and S_{YFP} denote fluorescence intensities derived from measurements in individual cells coexpressing Citrine- and Cerulean-tagged proteins with the respective filter cube (excitation, emission): S_{FRET} (440 ± 7.5 nm, 542 ± 13.5 nm), S_{CFP} (440 ± 7.5 nm, 483 ± 16 nm) and, S_{YFP} (505 ±

7.5 nm, 542 ± 13.5 nm). R_{D1} and R_{A1} are experimentally predetermined constants from measurements applied to single cells expressing only Cerulean- or Citrine-tagged molecules.

Co-immunoprecipitation and Western blotting.

For co-immunoprecipitation experiments, TPC2 and STX7 were N-terminally tagged with c-myc or mCherry, respectively. Anti c-myc MicroBeads (μMACS c-myc Isolation Kit) were used for co-immunoprecipitation and experiments were performed according to the manufacturer's protocol (Miltenyi Biotec GmbH). HEK293 cells were transiently transfected with single plasmids or with combinations of the expression vectors using calcium phosphate. Transfected cells were washed with cold PBS 48 h after transfection and lysed in ice-cold precipitation assay buffer consisting of Tris-HCl (50 mM), NaCl (150 mM), EDTA (1 mM), and Triton X-100 (1%). Western blots were incubated for 1 h at RT in 5% (w/v) dry milk powder (AppliChem GmbH) in TBST (milk). Subsequently the blots were incubated overnight at 4 °C with antiserum diluted in milk. The following antiserum dilutions were used: 1:1000 for monoclonal 9E10 anti c-myc antibody and 1:1000 for anti mCherry antibody (Clontech). The blots were washed four times for 10 min each at RT in TBST. Detection was performed with HRP coupled anti mouse secondary antibodies (1:1000; SantaCruz) and ECL solution using the BioRad ChemiDoc MP imaging system.

For detection of LDLR and GAPDH in WT and $TPC2^{-/-}$ MEFs the following antibodies were used in a dilution 1:1000, each: anti LDLR (abcam ab52818) and anti GAPDH (Cell signaling D16H11). For detection of TPC2 and Na^+/K^+-ATPase in WT and $TPC2^{-/-}$ liver membrane preparations the following antibodies were used in a dilution 1:1000, each: anti TPC2 (generated as described below) and anti Na^+/K^+-ATPase (Developmental Studies Hybridoma Bank).

Proteomics-based TPC2 interaction screens.

Cell Culture for SILAC experiments: For stable isotope labeling, HEK293 cells were cultured in SILAC-DMEM media (DMEM devoid of arginine and lysine) with 10% FBS, 100 U penicillin/ml and 100 μg streptomycin/ml. "Light" and "heavy" media were prepared by adding 84 mg/ml $^{13}C_6/^{15}N_4$ L-arginine and 146 mg/l $^{13}C_6/^{15}N_2$ L-lysine (Sigma Isotec) or the corresponding non-labeled amino acids, respectively[4]. Cells were grown for seven passages to ensure full labeling and "heavy" labeled cells were transfected with GFP-

TPC2. In parallel, a “reverse” experiment was performed by transfecting the “light” cells with GFP-TPC2 instead. Immunoprecipitation and in-gel digestion: Immunoprecipitation was performed using Chromotek’s GFP Trap according to manufacturer’s protocol. Immunoprecipitations of the corresponding SILAC conditions were combined, bound proteins eluted from beads by heating with 2x LDS-Sample buffer (NuPAGE, Invitrogen) at 70 °C for 10min and separated by 1D-SDS PAGE (4-12% Bis-Tris Mini Gel, Invitrogen). After visualization using Colloidal Blue Staining Kit (Invitrogen), gel pieces were excised from the gel and subjected to reduction, alkylation and in-gel digestion with sequence grade modified trypsin (Promega) as described[5]. After digestion, peptides were extracted with 30% acetonitrile/3% trifluoroacetic acid in water, concentrated in a *speedvac*, and desalted using StageTips before analysis by MS[6]. LC-MS/MS analysis: Peptides were separated by reverse phase chromatography using in house-made C_{18} microcolumns (75 µm ID packed with ReproSil-Pur C18-AQ 3 µm resin, Dr. Maisch GmbH) in a 130 min gradient from 9% to 45% acetonitrile in 0.5% acetic acid at a flow rate of 200 nl/min using a Proxeon EASY-nLC II, which was directly connected to a LTQ-Orbitrap VELOS mass spectrometer via a nanoelectrospray ion source (Thermo Fisher Scientific). The LTQ-Orbitrap VELOS was operated in the data-dependent mode to simultaneously measure full scan MS spectra in the Orbitrap and the ten most intense ions in the LTQ part by collisionally induced dissociation, respectively. Background ions were reduced by using an ABIRD device (ESI Source Solutions). Data processing and analysis: Raw files were analyzed with the in-house built software MaxQuant[7]. The derived peak list was searched with Andromeda[8] as a database search engine for peptide identifications against the human Uniprot database containing mouse TPC2 protein sequences combined with 248 common contaminants and concatenated with the reversed version of all sequences. Fixed modification of cysteine carbamidomethylation and variable modifications for methionine oxidation and protein N-acetylation were specified. Full tryptic specificity was required and a maximum of two missed cleavages accepted. The minimum peptide length was set to 6 amino acids. Parent MS masses and fragment MS/MS ions were searched with an initial mass tolerance of up to 7 ppm and 0.5 Da, respectively. Search results were processed with MaxQuant and filtered with a false discovery rate of 0.01. The re-quantification feature was enabled. Protein identification required at least one unique peptide for each protein group. Forward and reverse experiments were analyzed together and ratios of the

reversed experiment were inverted. Specific interactors were determined by using Significance B statistics as indicated in the figure. The p-value for the significance of enrichment had to be <0.05 in both the forward and reverse experiment.

Immunocytochemistry, histology, immunohistochemistry, and electron microscopy.

The following primary antibodies were used in immunocytochemistry experiments to label endo/lysosomal markers: anti EEA1 (C45B10, Cell Signaling), anti Rab4 (abcam ab13252), anti Rab5 (2143S, Cell Signaling or abcam ab18211), anti Rab7A (NBP1-87174, Novus Biologicals), anti Rab11 (abcam ab3612), anti CD63 antigen[9], anti LAMP1 (1D4B; Developmental Studies Hybridoma Bank), anti LAMP2 (ABL93; Developmental Studies Hybridoma Bank), anti LIMP2[10], and anti TfR (H68.4, Invitrogen). Briefly, cells grown on coverslips were fixed in 4% (w/v) paraformaldehyde in PBS and permeabilised with 0.2% saponin. Alternatively, cells were fixed with ice-cold methanol for 5 min at -20 °C. Alexa488 (MoBiTec) or Cy5 (Jackson ImmunoResearch) were used as secondary antibodies for detection. Nuclei were visualised with DAPI (4,6-diamidino-2-phenylindole, Sigma-Aldrich) that was included into the mounting medium containing Mowiol 4-88 (EMD Millipore) and the anti-fading reagent DABCO (1,4-diazabicyclo[2,2,2]octane, Sigma-Aldrich) or with Hoechst as indicated in the respective figure legend. Images from optical sections were acquired with an FV1000 confocal laser scanning microscope (Olympus) or with a Zeiss LSM 510.

For macroscopic analysis livers from TPC2$^{-/-}$ and WT mice were removed and imaged using the Zeiss Stemi SV11 microscope. Images were processed with Adobe Photoshop by extracting livers automatically and placing them on a black background.

For histological analysis, livers were removed, fixed in 4% PFA for 20 hours, embedded in paraffin, and sectioned. Serial 3.5 µm thick sections were stained with hematoxylin-eosin.

For immuohistochemical analysis, livers were fixed in 4% PFA for 2 hours at 4ºC, washed in PBS, cryoprotected with increasing concentrations of 10%, 20%, and 30% sucrose solutions prepared in PBS, and embedded in O.C.T. Tissue Tek. Serial 10 µm thick cryosections were stained with 0.05 mg/ml Filipin (Sigma F-9765) in PBS for 2h at RT, followed by nuclei co-staining with ToPro-3 (Invitrogen). Samples were washed in PBS and viewed by fluorescence microscopy using a UV filter set. Images were taken with a Zeiss Axiowert 200M microscope or confocal Olympus FV10i microscope.

For electron microscopic examination, tissues from TPC2$^{-/-}$ and WT mice were perfused transcardially with glutaraldehyde (6% in PBS). Tissue blocks of liver were rinsed in phosphate buffer, postfixed in OsO_4 for 2 h, and embedded in araldite according to routine procedures. Semithin sections were stained with toluidine blue. Ultrathin sections were stained with uranyl acetate and lead citrate, and examined with a Zeiss EM 900 microscope.

Generation of a TPC2 specific antibody.

To raise an antibody specific for TPC2, rabbits were immunized with a C-terminal peptide of the TPC2 protein (N-Cys_Phe[705]-His[726]-C). After immunization, complete serum was affinity purified against the peptide using the SulfoLink® Immobilization Kit for Peptides (Thermo Scientific) according to the manufacturer's protocol and an ÄKTAprime (GE Healthcare) plus chromatography system. Antibody elution was performed by applying a linear acid gradient starting from pH 7 to pH 2.

Sample preparation for the determination of hepatic cholesterol by GC-MS.

Sodium hydroxide solution (2 M) was added to aliquots of liver (40-120 mg) to obtain a final tissue concentration of 10 mg/ml. The vials were stored at 80° C for 2 h, and occasionally shaken. After cell lysis the content of every vial was partitioned into 50 µl samples for analysis of hepatic unesterified cholesterol and 100 µl samples for hepatic total cholesterol content analysis (n = 5). For alkaline hydrolysis aliquots were transferred into 4 ml glass vials containing 900 µl ethanolic NaOH solution (1 M) and stored at 60° C for 2 h. After saponication, 500 µl were transferred into 15 ml centrifuge tubes, and 5 ml water, 100 µl of internal standard solution (cholestane in MTBE, 10 µg/ml), and 900 µl MTBE were added. The mixtures were shaken and centrifuged at 2,500 x g for 5 min. The organic layer was transferred into 2.0 ml microcentrifuge tubes containing 40 mg of a mixture (7:1) of anhydrous sodium sulphate and PSA (Agilent Technologies). The lysate was extracted a second time with another 800 µl of MTBE. The second organic extract was also added to the microcentrifuge vial and the mixture was shaken and centrifuged at 9,000 x g for 5 min. Finally 900 µl of the purified organic phase were transferred into an autosampler vial and 100 µl of silylation reagent mixture MSTFA/TSIM (9:1) (Macherey-Nagel) was added.

Determination of bile acids in liver by gas chromatography-mass spectrometry.

Sample preparation: 1 ml of the cell lysate (n = 3) was transferred into 4 ml glass vials containing 1 ml ethanolic NaOH solution (1 M) for alkaline hydrolysis and stored at 60° C for 2 h. After saponication 1 ml was transferred into a 15 ml centrifuge tube, and 5 ml hydrochloric acid (1 M), 500 µl of internal standard solution (ergosterol in MTBE, 50 µg/ml), and 500 µl MTBE were added. The mixture was shaken and centrifuged at 2,500 x g for 5 min. Each lysate was extracted with another 1 ml of MTBE. The organic extracts were combined, 1 ml was transferred into an autosampler vial and evaporated to dryness under a gentle stream of nitrogen. The butyl ester formation of the free carboxylic group of bile acids was arranged according to literature[17]. Thus, the dried extract was mixed with 50 µl HCl (36%) and 200 µl n-butanol. The mixture was stored at 60 °C for 4 h. After esterification the solvents were removed under a stream of nitrogen. The silyation of free hydroxyl groups was carried out with 200 µl TSIM at 60 °C for 30 min. The resulting mixture was mixed with 300 µl MTBE and 1 µl was injected into the GC-MS system (see below).

Determination of bile acids and unesterfied cholesterol in feces by gas chromatography-mass spectrometry.

Sample preparation: the collected feces were comminuted after drying at 60 °C for 1 h. The samples (30-90 mg) were weighed into 4 ml glass vials and 4 M NaOH (water:ethanol; 1:1) was added to obtain a final solution of 25 mg/ml. The vials were stored at 80° C for 2 h and occasionally shaken. The mixtures were centrifuged at 2,500 x g for 5 min. Aliquots of 500 µl were transferred into 15 ml centrifuge tubes containing 5 ml HCl (1 M). The further work-up steps are described above.

Instrumental conditions: the inlet temperature was 270 °C, injection volume 1 µl (split ratio 3 for feces analyses and splitless for liver analyses). The GC oven started at 70 °C ramped up to 270 °C (heating rate 50 °C/min), followed by a gradient of 1 °C/min up to 290 °C, and of 50 °C/min to 310 °C (total run time 30 min). The MS was switched on for feces analyses after 14 min and for liver samples after 16 min (cholesterol cut-off). Transfer line temperature was 270 °C and the ion trap temperature was 200 °C. The MS scanned from a mass range of 70 to 650 m/z (EI, 70 eV). The peak areas of characteristic ions of TMS

ethers/butyl esters of bile acids and sterols were used for data analysis: cholesterol 368 m/z, ergosterol (internal standard) 468 m/z, cholic acid 410 m/z, chenodesoxycholic acid 412 m/z, desoxycholic acid 255 m/z, lithocholic acid 414 m/z, β/γ/ω-muricholic acid 195 m/z, and unkown BA (keto cholic acid or cholic acid with additional double bond). The muricholic acids were identified according to literature[18]. The mean value of each double injected sample was used for statistical analysis.

Calculation of relative cation permeabilites.

The reversal (zero-current) potential, E_{rev}, for NAADP-mediated currents in enlarged lysosomes was determined from current-voltage relations measured in response to NAADP during voltage-clamp ramp protocols (+100 to -200 mV, 500 ms). The relative permeability of P_{Ca}/P_x, where x is a monovalent ion (Na^+ and K^+), was estimated by the following bi-ionic equation (I)[11-13], derived from the Goldman-Hodgkin-Katz (GHK) voltage equation:

$$P_{Ca}/P_x = \gamma_X[X]_{Cyto}/(\gamma_{Ca}\ 4[Ca^{2+}]_{Luminal})\{\exp(E_{rev}F/RT)\}\{1+\exp(E_{rev}F/RT)\} \quad (I)$$

where R, T, E_{rev}, and γ are, respectively, the gas constant, absolute temperature (RT), Faraday constant, reversal potential, and activity coefficient. Activity coefficients of KF (γ_K) and NaF (γ_{Na}) were 0.75[14]. Activity coefficients of KMSA ($\gamma_{K'}$) and NaMSA($\gamma_{Na'}$) were likewise 0.75[15]. Activity coefficient of CaMSA was 0.52 similar to $CaCl_2$[16]. All results are presented as mean ± SEM. An unpaired *t*-test was performed for the comparison between two groups. Values of $p < 0.05$ were considered significant.

Supplementary references

1. Jat, P. S., Cepko, C. L., Mulligan, R. C., and Sharp, P. A. Recombinant retroviruses encoding simian virus 40 large T antigen and polyomavirus large and middle T antigens. *Mol. Cell. Biol*. **6**, 1204-1217 (1986).
2. Xu, J. Preparation, culture, and immortalization of mouse embryonic fibroblasts. *Curr. Protoc. Mol. Biol.* **28**, 28.1. (2005).
3. Erickson, M. G., Liang, H., Mori, M. X., Yue, D. T. FRET two-hybrid mapping reveals function and location of L-type Ca2+ channel CaM preassociation. *Neuron* **39**, 97-107 (2003).
4. Ong, S. E., Blagoev, B., Kratchmarova, I., Kristensen, D. B., Steen, H., Pandey, A., Mann, M. Stable isotope labeling by amino acids in cell culture, SILAC, as a simple and accurate approach to expression proteomics. *Mol. Cell. Prot.* **1**, 376-386 (2002).
5. Shevchenko, A., Wilm, M., Vorm, O., Mann, M. Mass spectrometric sequencing of proteins silver-stained polyacrylamide gels. *Anal. Chem.* **68**, 850-858 (1996).
6. Rappsilber, J., Ishihama, Y., Mann, M. Stop and go extraction tips for matrix-assisted laser desorption/ionization, nanoelectrospray, and LC/MS sample pretreatment in proteomics. *Anal. Chem.* **75**, 663–670 (2003).
7. Cox, J., Mann, M. MaxQuant enables high peptide identification rates, individualized p.p.b.-range mass accuracies and proteome-wide protein quantification. *Nat. Biotechnol.* **26**, 1367–1372 (2008).
8. Cox, J., Neuhauser, N., Michalski, A., Scheltema, R. A., Olsen, J. V., and Mann, M. Andromeda: a peptide search engine integrated into the MaxQuant environment. *J. Prot. Res.* **10**, 1794-1805 (2011).
9. Schröder, B., Wrocklage, C., Hasilik, A., and Saftig, P. Molecular characterisation of 'transmembrane protein 192' (TMEM192), a novel protein of the lysosomal membrane. *Biol. Chem.* **391**, 695-704 (2010).
10. Zachos, C., Blanz, J., Saftig, P., Schwake, M. A critical histidine residue within LIMP-2 mediates pH sensitive binding to its ligand β-glucocerebrosidase *Traffic* **13**, 1113-1123 (2012).
11. Fatt, P., Ginsborg, B. L. The ionic requirements for the production of action potentials in crustacean muscle fibres. *J. Physiol.* **142**, 516-543 (1958).
12. Hille, B. Ion Channels of Excitable Membranes, 3rd Ed., pp. 441–470, Sinauer Associates, Inc., Sunderland, MA (2001).

13. Xu, H., Jin, J., DeFelice, L. J., Andrews, N. C., Clapham, D. E. A spontaneous, recurrent mutation in divalent metal transporter-1 exposes a calcium entry pathway. *PLoS Biol.* **2**, e50 (2004).
14. Robinson, R. A. and Stokes, R.H. Electrolyte Solutions, Butterworth and Co. (Publishers) Ltd., London, 2nd edition (1965).
15. Bonner, O. D. Study of methanesulfonates and trifluoromethanesulfonates. Evidence for hydrogen bonding to the trifluoro group *J. Am. Chem. Soc.* **103**, 3262-3265 (1981).
16. Dani, J. A., Sanchez, J. A., Hille, B. Lyotropic anions. Na channel gating and Ca electrode response. *J. Gen. Physiol.* **81**, 255-281 (1983).
17. Batta, A. K., Salen, G., Rapole, K. R., Batta, M., Batta, P., Alberts, D., Earnest, D. Highly simplified method for gas-liquid chromatographic quantitation of acids and sterols in human stool. *J. Lipid Res*. **40**, 1148-1154 (1999).
18. Kumar, B. S., Chung, B. C., Lee, Y. J., Yi, H. J., Lee, B. H., Jung, B. H. Gas chromatography-mass spectrometry based simultaneous quantitative analytical method for urinary oxysterols and bile acids in rats. *Anal. Biochem.* **408**, 242-252 (2011).

TPC2 polymorphisms associated with a hair pigmentation phenotype in humans result in gain of channel function by independent mechanisms

Yu-Kai Chao[1], Verena Schludi[1], Cheng-Chang Chen[1], Elisabeth Butz[1], O. N. Phuong Nguyen[1], Martin Müller[1], Jens Krüger[2], Claudia Kammerbauer[1], Manu Ben-Johny[3], Angelika Vollmar[4], Carola Berking[5], Martin Biel[6], Christian Wahl-Schott[7], Christian Grimm[1]

[1]LMU Munich, [2]Universität Tübingen, [3]Johns Hopkins University, [4]University of Munich, [5]Ludwig-Maximilian University, [6]Ludwig-Maximilians-University Munich, [7]Center for Integrated Protein Science CIPS-M and Zentrum für Pharmaforschung

Submitted to Proceedings of the National Academy of Sciences of the United States of America

Two-pore channels (TPCs) are endolysosomal cation channels. Two members exist in humans, TPC1 and TPC2. Functional roles associated with the ubiquitously expressed TPCs include VEGF-induced neoangiogenesis, LDL-cholesterol trafficking and degradation, physical endurance under fasting conditions, autophagy regulation, the acrosome reaction in sperm, cancer cell migration, and intracellular trafficking of pathogens such as Ebola virus or bacterial toxins, e.g. cholera-toxin. In a genome-wide association study for variants associated with human pigmentation characteristics two coding variants of TPC2, rs35264875 (encoding M484L) and rs3829241 (encoding G734E), have been found to be associated with a shift from brown to blond hair color. In two recent follow-up studies a role for TPC2 in pigmentation has been further confirmed. However, these human polymorphic variants have not been functionally characterized until now. The development of endolysosomal patch-clamp techniques has made it possible to investigate directly ion channel activities and characteristics in isolated endolysosomal organelles. We applied this technique here to scrutinize channel characteristics of the polymorphic TPC2 variants in direct comparison with wild-type. We found that both polymorphisms lead to a gain of channel function (GOF) by independent mechanisms. We next conducted a clinical study with more than 100 blond and brown/black haired individuals. We performed a genotype/phenotype analysis and subsequently isolated fibroblasts from WT and polymorphic variant carriers for endolysosomal patch-clamp experimentation to confirm key in-vitro findings.

TPC | TPC2 | two-pore channel | polymorphism | pigmentation

Two-pore channels (TPCs) are endolysosomal cation channels which are distantly related to the endolysosomal TRP channels of the TRPML subfamily on the one hand and the voltage-gated calcium channels on the other hand. Two members exist in humans, TPC1 and TPC2. Functional roles associated with the ubiquitously expressed TPCs include VEGF-induced neoangiogenesis (1), endolysosomal LDL-cholesterol trafficking and degradation (2), physical endurance under fasting conditions (3), autophagy regulation (4-5), the acrosome reaction in sperm (6), intracellular trafficking of certain pathogens such as filoviridae, e.g. Ebola or Marburg virus (7), bacterial toxins, e.g. cholera-toxin (8), and a role in cancer cell migration (9). A few years ago, Sulem and colleagues (10) presented results from a genome-wide association study for variants associated with human pigmentation characteristics among 5,130 Icelanders, with follow-up analyses in 2,116 Icelanders and 1,214 Dutch individuals from which they claimed that two coding variants of hTPC2 (SNPs), rs35264875 (encoding M484L) and rs3829241 (encoding G734E), were associated with a shift from brown to blond hair color. Very recently, Ambrosio and colleagues (11) as well as Bellono et al. (12) confirmed a role for TPC2 in pigmentation by showing that TPC2 regulates the pH and size of melanosomes, thus controlling the amount of melanin produced. Consequently, loss of TPC2 activity by knockout or knockdown leads to a strong increase of melanin production and melanosomal pH.

Hence, it seemed intriguing to functionally investigate these polymorphic TPC2 variants. We investigated the activity of WT hTPC2 side-by-side with hTPC2(G734E) and hTPC2(M484L) as well as the double mutant isoform (M484L/G734E). First, we applied the endolysosomal patch-clamp technique in combination with small molecule activators and blockers of TPC2 to directly assess channel activity. Secondly, we performed molecular dynamics simulations of TPC2 based on the recently published structures of TPC1 (13-14) to investigate structural changes due to the SNPs. These results were corroborated by ion substitution experiments to assess pore sizes. Furthermore, we genotyped more than 100 blond and brown/black haired human individuals and isolated fibroblasts from selected donors to confirm key in-vitro findings and the results of the genome-wide association study by Sulem and colleagues (10).

Results

Human TPC2 WT and polymorphic variants show comparable subcellular distribution but differences in basal activity and their response to PI(3,5)P_2. Wild-type (WT) hTPC2 and the polymorphic variants containing either M484L, G734E, or both M484L and G734E show similar subcellular distribution when overexpressed in HEK293 cells (SI Fig. S1*A*). All variants localize

Significance

Polymorphisms in the endolysosomal cation channel TPC2 have been suggested to lead to a shift in human hair color from brown to blond. In two further studies a role for TPC2 in melanosomal pH-regulation was postulated. Electrophysiological data on how these polymorphisms affect channel gating and activity are however missing. We show here that both polymorphisms lead to a gain of channel function by different mechanisms. In M484L sensitivity to its endogenous ligand PI(3,5)P_2 is strongly increased while in G734E channel inactivation by ATP is reduced. These findings are corroborated by molecular dynamics and ion substitution experiments. Furthermore, >100 blond and brown/black haired human individuals were genotyped and fibroblasts isolated from selected donors to confirm key in-vitro findings.

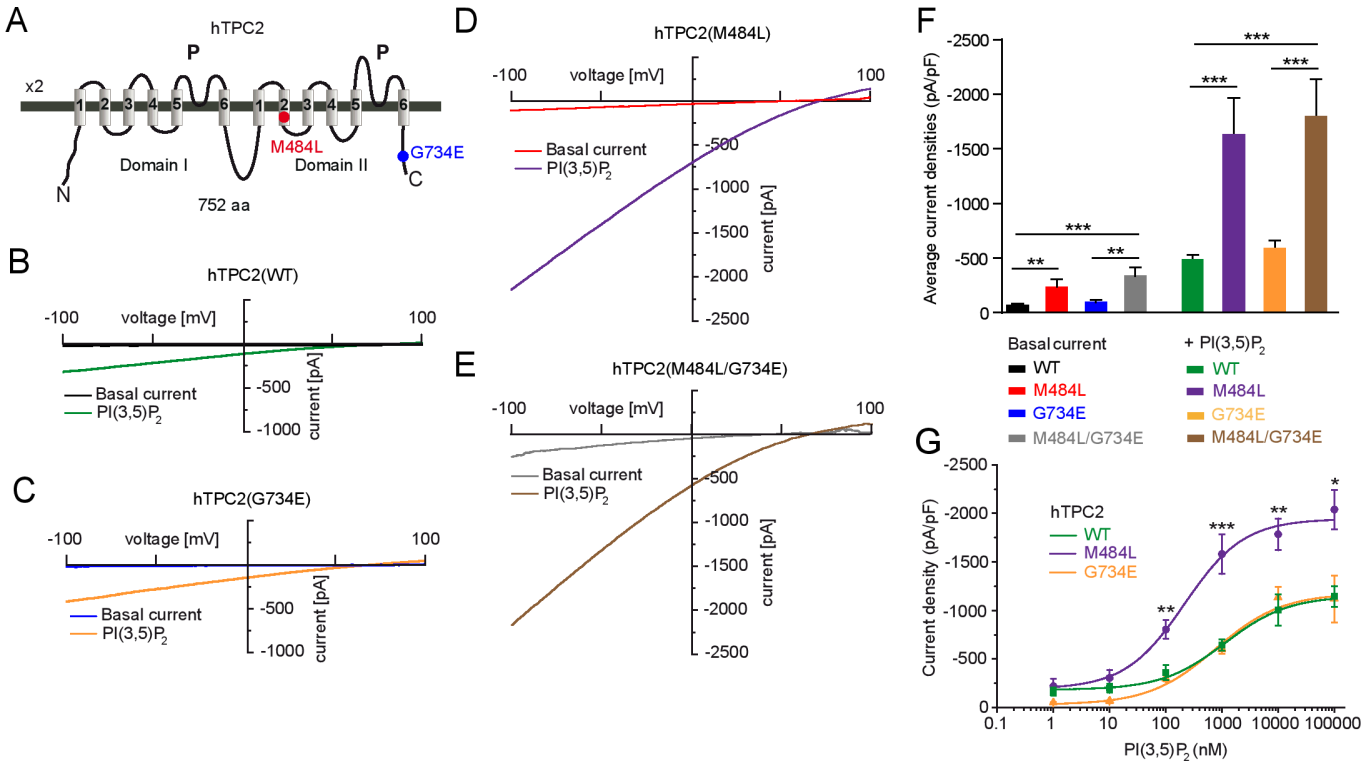

Fig. 1. Effect of PI(3,5)P_2 on endolysosomal vesicles expressing either human TPC2 WT or polymorphic variants. (*A*) Cartoon showing the estimated positions of the polymorphisms (SNPs) M484L and G734E. (*B-E*) Shown are representative basal and PI(3,5)P_2 (1 μM) activated currents in vacuolin enlarged endolysosomal vesicles expressing either hTPC2 WT, hTPC2(M484L), hTPC2(G734E), or hTPC2(M484L/G734E) C-terminally fused to YFP. (*F*) Statistical summary of data as shown in b-e. Shown are average current densities at -100 mV. (*G*) PI(3,5)P_2 dose-response curves for hTPC2 WT and hTPC2(M484L) and hTPC2(G734E). In all experiments, currents were elicited by applying 500-ms voltage ramps from -100 to +100 mV every 5 s. In all statistical analyses mean values of at least 5-10 independent experiments are shown, each. To test for statistical significance the one-way ANOVA test followed by Tukey's post-test was applied. ***,indicates p<0.001, **, indicates p<0.01.

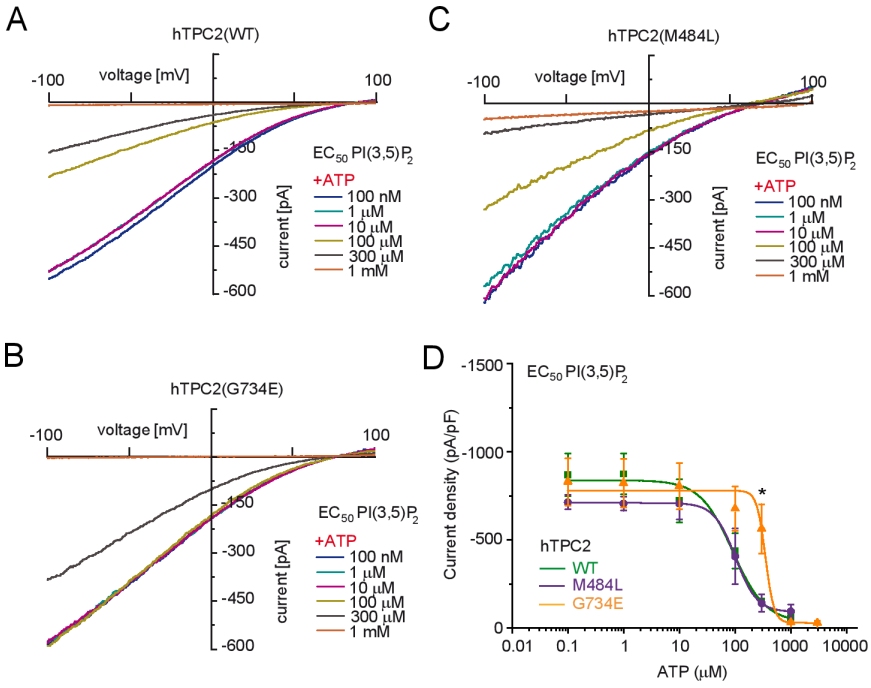

Fig. 2. Effect of ATP on human TPC2 WT and polymorphic variants using the respective EC_{50} values of PI(3,5)P_2 as activating concentrations. (*A-C*) Representative PI(3,5)P_2 (diC8) activated currents in vacuolin enlarged hTPC2 WT and hTPC2 SNP expressing endolysosomal vesicles using the respective EC_{50} values as activating PI(3,5)P_2 concentrations and different concentrations of ATP as indicated to block the currents. (*D*) ATP dose response curves from experiments as shown in *A-C*. In all experiments currents were elicited by applying 500-ms voltage ramps from -100 to +100 mV every 5 s. To test for statistical significance the Student's *t*-test, unpaired was applied. * indicates p<0.05.

to intracellular vesicular structures which are positively stained with Lysotracker (SI Fig. 1*A*). A calculation of the Pearson correlation coefficients (PCC) resulted in similar numbers for colocalization with Lysotracker for all variants (SI Fig. 1*B*). Western blot analysis demonstrated that expression levels of the different variants in endolysosomal membranes are not significantly differ-

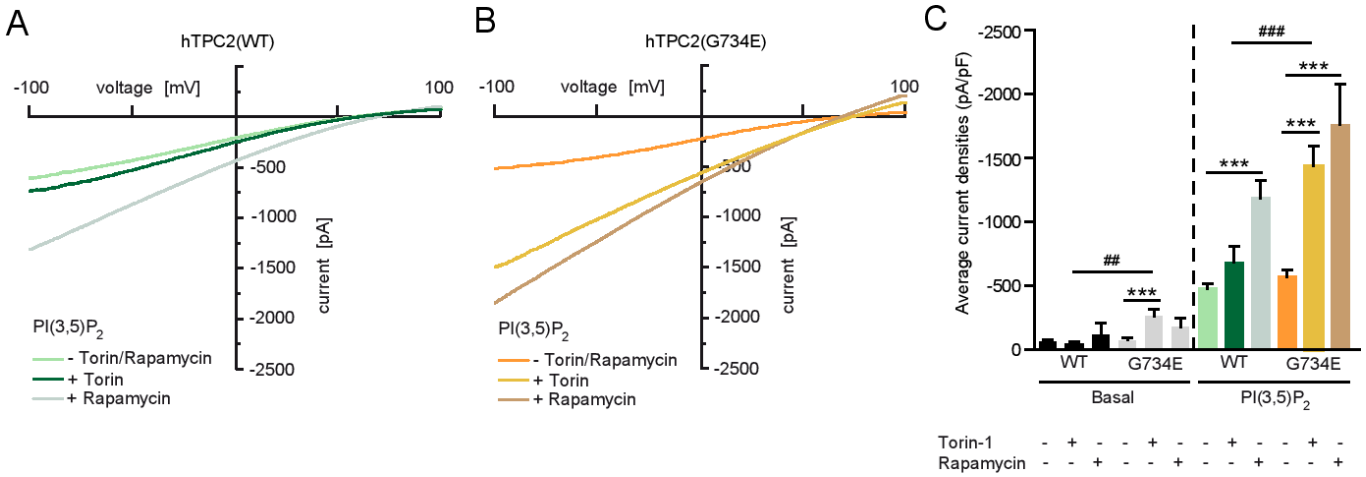

Fig. 3. Effect of rapamycin and torin-1 on human TPC2 WT and G734E. (*A-B*) Representative PI(3,5)P_2 (1 μM) activated currents in vacuolin enlarged hTPC2 WT and hTPC2(G734E) expressing endolysosomal vesicles and the respective blocking effects of 2 μM torin-1 or 1 μM rapamycin. Cells were incubated with torin-1 for 12 hours or with rapamycin for 10 minutes before experimentation. Currents were measured in the absence of ATP. (*C*) Statistical summary of data as shown in *A-B*including respective basal currents. Shown are average current densities at -100 mV. To test for statistical significance the one-way ANOVA test followed by Tukey's post-test was applied to basal and PI(3,5)P_2 conditions, respectively. ***, ### indicate p<0.001, ## indicates p<0.01.

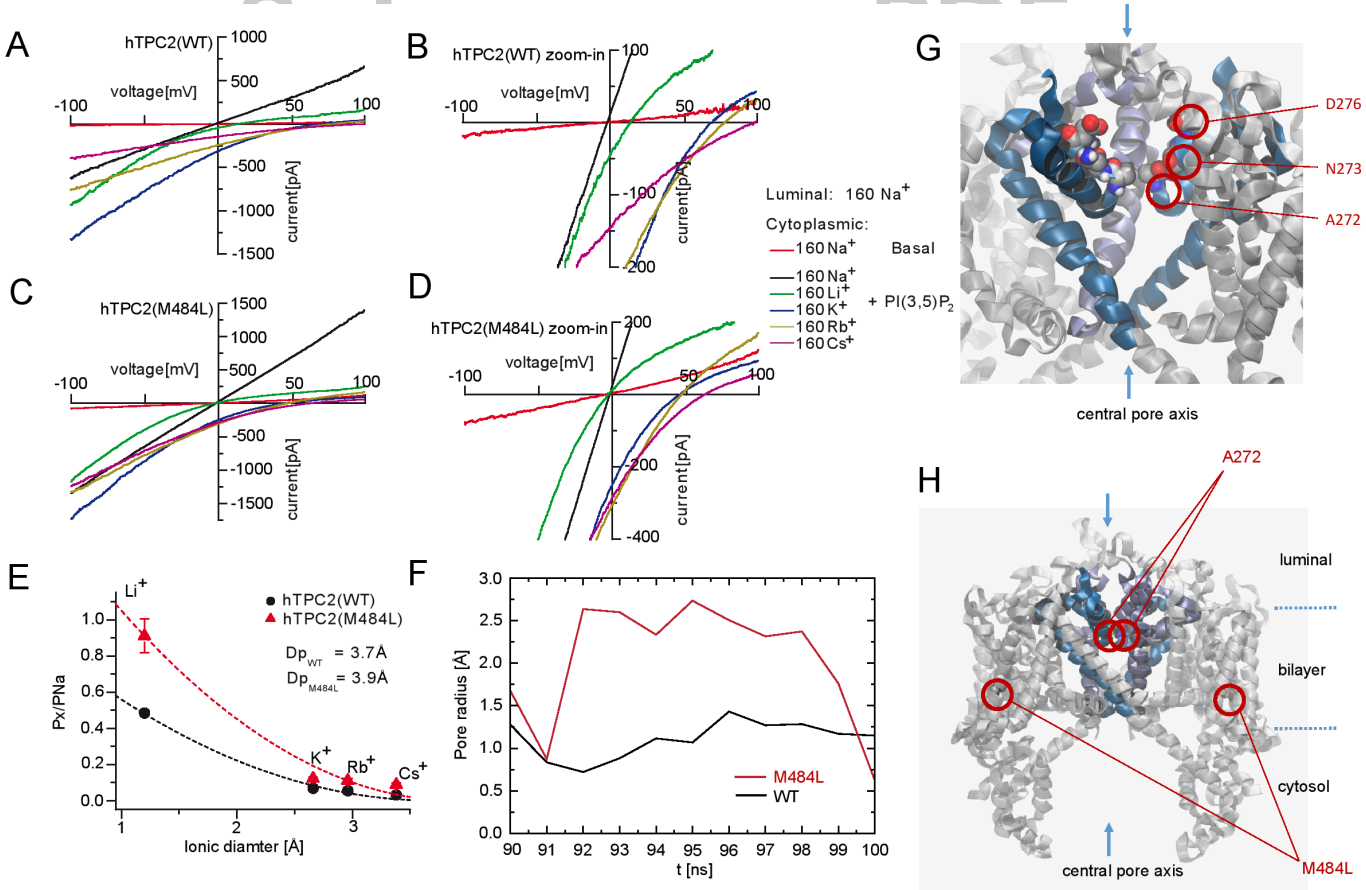

Fig. 4. Ion substitution experiments and molecular dynamics simulations. (*A-D*) Endolysosomal patch-clamp experiments showing PI(3,5)P_2-activated hTPC2 WT (*A-B*) or hTPC2(M484L) (*C-D*) currents under bi-ionic conditions with luminal Na^+ and bath solutions containing the following monovalent cations, respectively: Li^+, K^+, Rb^+ and Cs^+. (*B, D*) Expanded view of *A* and *C*, showing that the reversal potentials are shifted to negative voltage in M484L variant. (*E*) Summary of data as shown in *A-D*. Shown are the relative permeabilities (P_X/P_{Na}) of the different cations plotted against the diameter of cations. The dashed lines are fitted to Equation 1 (see method section for details). (*F*) Schematic representation of the TPC2 simulation system. The channel (grey) is embedded in a fully solvated POPC bilayer (transparent surfaces). As the channel has a conic shape the bilayer is bent locally. To cope with this effect always two channel models were embedded in antiparallel fashion into a larger bilayer patch. (*G*) Enlargement of the selectivity filter omitting part of the protein. D276, N273 and A272 which are present symmetrically on both subunits are shown in VdW representation. (*H*) The pore radius of TPC2 is shown at the height of A272 for WT (blue) and the M484L variant (red) simulated in presence of PI(3,5)P_2. A representative window at the end of the independent simulations was chosen which presumably resembles an opening event. One of two M484L pores showed a dilation of more than 1 Å for almost 10 ns.

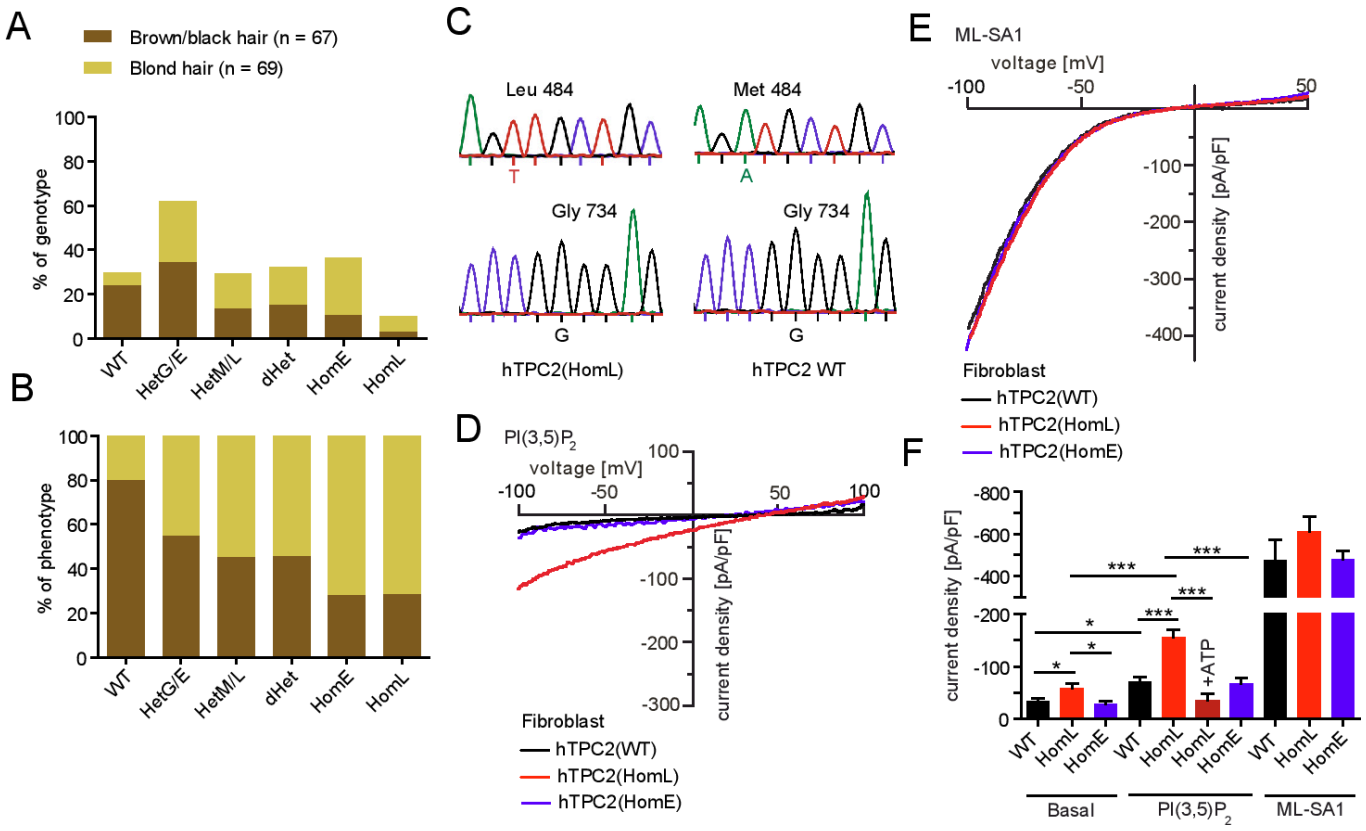

Fig. 5. Characterization of human fibroblasts isolated from TPC2 WT donors or donors carrying TPC2 polymorphisms. (*A-B*) Data summarizing sequencing results obtained from human genomic DNA samples. Shown in *A* is the genotype distribution (in %) of individuals with either blond hair or brown/black hair, e.g. 23.9% of the brown/black hair donors but only 5.8% of the blond hair donors are genotype WT. In contrast, 26.1% of the blond hair donors are homozygous for E (homE) at position 734 while only 10.4% of the brown/black hair donors are homE. Shown in *B* is the phenotype distribution (in %) of all genotyped individuals, e.g. 80% of all individuals with the genotype WT have brown/black hair while only 20% have blond hair. In contrast, 72% of all individuals with the genotype homE at position 734 and 71.4% of all individuals with the genotype L homozygous (homL) at position 484 are blond. The total numbers of donors were 67 (brown/black hair) and 69 (blond hair), respectively. (*C*) Examples of human donor genotyping results. Shown are respective sequences around position 484 (Leu/Met) and 734 (Gly).(*D-E*) Representative endolysosomal patch-clamp experiments showing $PI(3,5)P_2$ (10 μM) activated currents in vacuolin enlarged fibroblast endolysosomes isolated from donors homozygous for WT, M484L, and G734E. The TRPML channel activator ML-SA1 was used to demonstrate that TRPML currents were comparable in size in all fibroblast lines, in contrast to $PI(3,5)P_2$ mediated currents. (*F*) Statistical summary of data shown in *D-E*. Two independent donor fibroblast samples were used for each WT and M484L. One sample was used for G734E. Shown are the pooled average current densities at -100 mV of at least 5 independent experiments, each. To test for statistical significance one-way ANOVA test followed by Tukey's post-test was applied. ***,indicates p<0.001, *, indicates p<0.05.

ent (SI Fig. 1*C* and *D*). Treatment with vacuolin increased the size of endolysosomal vesicles to a similar extent in all variants (SI Fig. 1*E*). Finally, dimerization efficiencies of TPC2 WT and the polymorphic variants were comparable as assessed by FRET experimentation (SI Fig. 2).

The two polymorphisms are found in very different parts of the protein. While M484L resides in the second transmembrane domain of the second channel domain, G734E is found in the C-terminus of the protein (Fig. 1*A*), suggesting different functional consequences.

We next performed endolysosomal patch-clamp experiments. Here, we found striking differences between the respective variants. The polymorphic variant M484L as well as the double polymorphic variant showed, compared to WT, a significantly increased basal channel activity as well as a significantly increased channel activity after stimulation with $PI(3,5)P_2$ (3, 15). In contrast, G734E showed similar mean basal and stimulated activation levels as WT. (Fig. 1*B-F* and SI Fig. 3*A*). Average capacitance values were comparable for all variants indicating that differences in channel activity were not due to differences in the size of the patched vesicles (SI Fig. 3*B*). Dose-response measurements revealed an EC_{50} of 1138 ± 376 nM for WT compared to 216 ± 55 nM for M484L while G734E was not significantly different from WT with an EC_{50} of 827 ± 183 nM (Fig. 1*G*; increased potency). In addition, the maximum response level was increased by two to three fold, depending on the $PI(3,5)P_2$ concentration, in M484L compared to WT or G734E (Fig. 1*G*; increased efficacy).

Differences in ATP inhibition between TPC2 WT and polymorphic variants. We next assessed the inhibition of activated TPC2 WT and polymorphic variants by ATP. Block of TPC activity by ATP has been demonstrated before and was shown to be physiologically relevant during cell starvation (3). We confirm here that the channel activities of WT TPC2 and also the polymorphic variants M484L and G734E are efficiently blocked by applying high concentrations of ATP (1 mM). However, dose-response measurements revealed significant differences in the IC_{50} values which were generated for each variant based on their individual $PI(3,5)P_2$ EC_{50} values (Fig. 2*A-D*). When we used the individual $PI(3,5)P_2$ EC_{50} values to activate we obtained the following IC_{50} values for the ATP block: WT (91 ± 19 μM), G734E (351 ± 37 μM), and M484L (102 ± 6 μM). These data demonstrate that significantly less ATP is necessary to block WT TPC2 or M484L variant activities compared to the G734E variant. Similar results were obtained when we used the individual $PI(3,5)P_2$ EC_{80} values or a fixed concentration of 1 μM $PI(3,5)P_2$ to activate. The respective IC_{50} values for the ATP block were: WT (179 ± 15 μM)

and G734E (384 ± 39 μM) for $PI(3,5)P_2$ EC_{80} as well as WT (4 ± 2 μM) and G734E (133 ± 71 μM) for the fixed concentration of 1 μM $PI(3,5)P_2$ (SI Fig. 4).

In summary these data suggest that both M484L and G734E variants are gain of function (GOF) polymorphisms.

Effect of mTOR inhibitors. ATP is known to activate mTOR (mechanistic target of rapamycin (16)) and mTOR is the mediator that inhibits TPC2 by direct protein-protein interaction as recently shown (3). To further investigate the cross-talk between channel activity and ATP inhibition, we tested the effect of mTOR inhibitors such as rapamycin and torin-1 on TPC2 channel activity. Both compounds were found previously to enhance TPC2 channel activity by blocking the TPC2 inhibitor mTOR (3). We found that inhibition of mTOR increased TPC2(G734E) channel activity more efficiently than WT activity, suggesting a stronger effect of mTOR on WT compared to G734E. In contrast, the channel activity of the M484L isoform could not be further enhanced under the same conditions (for M484L a $PI(3,5)P_2$ concentration of 1 μM is a saturating concentration; EC_{50} = 216 ± 55 nM) (Fig.3*A-C* and SI Fig. 5*A-B*).

Ion substitution experiments. To further corroborate the findings obtained for the M484L variant, we performed ion substitution experiments and molecular dynamics simulations based on the recently published structures of AtTPC1 (13-14). In ion substitution experiments using the endolysosomal patch-clamp technique, we found differences in the estimated pore diameters between WT and M484L while there were no obvious differences between WT and G734E (Fig. 4*A-E* and SI Fig. 5*C-E*). We used monovalent cations (sodium, lithium, rubidium, and cesium) in a concentration of 160 mM, each, to estimate the pore diameters of TPC2 WT and the M484L variant (Fig. 4*A-E*). We determined permeability ratios relative to Na^+ (P_X/P_{Na}) from the bionic reversal potentials, which resulted in estimations of 3.7 Å and 3.9 Å for the minimum pore diameter of TPC2 WT and the M484L variant, respectively. The estimation for the G734E variant diameter resulted in the same value as for WT (3.7 Å) (SI Fig. 5*E*). These data suggest that M484L not only contributes to larger current amplitudes but also influences channel conformation and the narrowest part of the pore region.

Molecular dynamics simulations confirm dilated pore in hTPC2(M484L) variant. Multiple models of the TPC2 channel were submitted to prolonged molecular dynamics simulations of at least 100 ns, each. WT and M484L variant were simulated with $PI(3,5)P_2$ resembling the experimental layout. As each simulation system contained two channel models a total of over 800 ns was available for analysis. All models showed a high degree of stability preserving their overall structure and a continuous water column through the pore. For one of the two M484L models a dilation of the pore could be observed in the presence of $PI(3,5)P_2$ for ∼10 ns around position A272. The pore radii of the dilated M484L pore were compared with the WT pore (Fig. 4*F-H*). This finding suggests that the M484L mutation affects pore dynamics, further corroborating the data presented on the estimation of the pore sizes of TPC2 WT and M484L by ion substitution experimentation. Notably, Schieder et al. (17) had reported previously that TPC2 mutant isoform N273A (next to A272) shows a pore block and Wang and colleagues (15) reported that the D276K mutation likewise leads to a pore block and loss of $PI(3,5)P_2$ response, emphasizing the importance of this region for channel activity.

Endogenous TPC2 channel activity in human donor fibroblasts. Next, we screened, more than 100 blond and brown/black haired human donors for TPC2 polymorphisms and identified individuals which were either homozygous for WT, M484L, or G734E, or individuals which were heterozygous for the respective polymorphisms (Fig. 5*A-B*). The obtained genotyping results were found to correlate well with the data published by Sulem et al. (10). Thus, the percentage of DNA samples isolated from blond haired individuals which are homozygous for either M484L or G734E was 7.2% and 26.1% (n = 69), respectively, while DNA samples isolated from brown, dark brown, or black haired individuals were in only 2.9% of the cases homozygous for M484L and in only 10.4% of the cases homozygous for G734E (n = 67). Among the blond haired donors we found only 5.8% to be homozygous for WT. Vice versa among individuals with brown/black hair 23.9% were found to be homozygous for WT (Fig. 5*A*).

We subsequently isolated fibroblasts from selected individuals and analysed them using the endolysosomal patch-clamp technique (Fig. 5*C-F*). While we found only small endogenous $PI(3,5)P_2$ currents in WT or G734E fibroblast endolysosomes, significantly increased $PI(3,5)P_2$-mediated channel activity was detectable in endolysosomes isolated from donor fibroblasts homozygous for M484L, essentially confirming the in-vitro findings. For ATP dose-response measurements the $PI(3,5)P_2$-mediated currents in G734E endolysosomes were too small. As an activation control we used the TRPML-channel activator ML-SA1 (18). TRPML channel currents activated with ML-SA1 were not significantly different between M484L, G734E, and WT endolysosomes, suggesting that the differences in $PI(3,5)P_2$ response are not due to differences in TRPML channel activity (Fig. 5*C-E*). In summary, these data confirm the strong GOF found for the M484L variant in overexpressing HEK293 cells and the data further confirm the increased association of the M484L and G734E variants with blond hair color compared to the WT TPC2 isoform.

Discussion

We show here that the TPC2 variants M484L and G734E, reported previously to be associated with a shift in human hair color from brown to blond display distinct functional differences compared to WT. We used overexpressing HEK293 cells and endogenously expressing fibroblasts to functionally characterize the respective variants. In endolysosomal patch-clamp experiments we found that both variants show a gain of channel function compared to WT (SI Fig. 6). While basal activity and activation with $PI(3,5)P_2$ was increased in M484L, affecting both efficacy and potency of $PI(3,5)P_2$, inhibition of channel activity by ATP was less sensitive in G734E compared to WT (SI Fig. 6). The M484L polymorphism leads to structural changes affecting the pore diameter of TPC2. Thus, M484L displays a significant pore dilation compared to WT as demonstrated by molecular dynamics simulations and ion substitution experiments. The G734E variant is less responsive to ATP and more sensitive to mTOR inhibitors than WT, the latter one suggesting that the weaker ATP effect may be mediated by mTOR. While torin-1 is a selective ATP-competitive inhibitor of mTOR which effectively blocks phosphorylation of mTOR, rapamycin and related inhibitors form a complex with the intracellular immunophilin FKBP12; the resulting complex then interacts with and inhibits mTOR (19-20). Despite these different mTOR inhibitory mechanisms, both torin-1 and rapamycin result in a stronger increase in G734E activity compared to WT, further emphasizing that the differences in ATP block may be directly mediated via mTOR and downstream effects. Nevertheless, we cannot fully exclude the possibility of mTOR independent ATP effects.

Remarkably, human TPC2 cDNAs used for functional studies in past publications were often polymorphic variants. Thus, for example Calcraft et al. (21) had used a TPC2 variant cloned from HEK293 cells containing both polymorphisms: M484L and G734E. Pitt et al. (22) had used a variant of human TPC2 containing the G734E polymorphism (GenBank accession no. AY029200) and Brailoiu et al. (23) had used the IMAGE clone 5214862 (GenBank accession no. BC063008) which also contains the polymorphism G734E. Thus, it seems that WT hTPC2, at least in its recombinant form has not always been used as a reference in the existing publications.

In accordance with recent findings by Ambrosio et al. (11) as well as Bellono et al. (12), claiming that loss of TPC2 leads to increased melanin production, an increase in TPC2 channel activity as found here for the two SNPs would be expected to result in the opposite effect, a decrease in melanin production. Located in the basal epidermis and in hair follicles, melanocytes of the integument are responsible for hair coloration through production of melanin pigments in melanosomes (24). Two types of pigment are known to give hair its color: eumelanin and pheomelanin. Eumelanin has two subtypes, black and brown, which determine the darkness of the hair color. A low concentration of brown eumelanin results in blond hair, whereas a higher concentration of eumelanin will color the hair brown/black. Melanin production is strongly dependent on the activity of the enzyme tyrosinase (TYR). TYR activity is optimal at neutral pH (25-27). To achieve neutralization of melanosomal pH, the proper function of a cascade of ion transporters seems to be required (27). Consequently, polymorphisms in any of such transporters or ion channels rendering them dys- or malfunctional may lead to changes in melanosome pH and thus to changes in melanin production as suggested recently by Ito et al. (27). For TPC2 this hypothesis has now been supported by works published by Ambrosio and colleagues (11) and Bellono et al. (12). Thus, loss of TPC2 leads to an increase in melanosomal pH and melanin production while overexpression of TPC2 leads to a decrease in melanin production. Like TPC2 overexpression, an increase in TPC2 activity would be expected to result, in a decreased melanosomal pH and thus a decrease in melanin production. This would consequently explain the shift in hair color from brown to blond.

In addition to hair coloration, altered TPC2 channel activity may also impact human health, in particular under challenging conditions such as physical stress or infections. TPC2 knockout mice show an increased susceptibility to hypercholesterinemia and fatty liver hepatitis compared to WT when fed with a high cholesterol diet (2), they show a decreased physical endurance under fasting conditions (3), and they are less susceptible to distinct viral infections (7). Migration of cancer cells and the formation of metastases was recently found to be reduced in TPC2 knockdown cells or after pharmacological inhibition of TPC2 (9). We therefore speculate that humans carrying the GOF polymorphisms M484L or G734E or both may have, in particular under stress conditions, an altered susceptibility for diseases that are associated with the endolysosomal system. In addition, it may also be possible that changes in TPC2 activity affect melanosomes differently than lysosomes, e.g. due to differences in pH regulatory mechanisms with different consequences for human physiology and pathophysiology.

Materials and Methods

Molecular biology. All human TPC2 variants were generated from hTPC-2(M484L/G734E)-mCherry, a kind gift by Prof. Dr. Michael Zhu (Houston). Point mutations were removed from constructs by site-directed mutagenesis using QuikChange (Agilent) according to the procedures outlined in the manufacturer's manual or by overlap PCR-experimentation. C-terminally fused YFP versions of WT and the polymorphic TPC2 variants were generated from the respective mCherry constructs and subcloned into pcDNA3.1 vector. Constructs used for FRET experiments are described in the methods section and the figure legend in more detail.

Endolysosomal membrane preparations. To evaluate expression levels of TPC2 WT and variants in endolysosomal membranes, HEK293 cells were transfected with TPC2-constructs (YFP-tagged), respectively. Preparation of endolysosomes was performed as described previously (17, 28). For immunoblotting, antibodies were used in the following dilutions: rabbit anti-Rab7, 1:500 (cell signaling, 2094S); mouse anti-GFP, 1:2000, mouse anti-HRP 1:2000 (sc-2031, Santa Cruz), and rabbit anti HRP, 1:1000 (NA934V, GE Healthcare).

Molecular modeling. A model for TPC2 was constructed using Schrödinger Prime based on PDB_ID 5E1J (14) with the UniProt sequence Q8NHX9 (21). Default settings were used employing the multichain protocol modeling both subunits simultaneously. Always two of the resulting models were embedded into a POPC bilayer in antiparallel orientation to reduce lateral stress following protocols described earlier (29-30) and solvated with SPC water. $CaCl_2$ was added to balance the overall charge and to achieve nearly physiological ion concentrations. Employing GROMACS-5.1 the periodic system was energy minimized and constraints on the protein were gradually reduced (31-33). A total of 100 ns each were simulated with a time step of 2 fs for the WT, WT with $PI(3,5)P_2$, M484L and M484L with $PI(3,5)P_2$. Two equivalents per pore were placed in vicinity of M484L into the bilayer for the corresponding simulations. Neighbor searching was performed every 40 steps. The PME algorithm was used for electrostatic interactions with a cut-off of 1.2 nm and verlet cut-off scheme. A reciprocal grid of 192 x 120 x 120 cells was used with 4th order B-spline interpolation. A single cut-off of 1.2 was used for van der Waals interactions. Temperature coupling to 310 K was done with the V-rescale algorithm. Semiisotropic pressure coupling to 1 bar in the plane and perpendicular to it was done with the Berendsen algorithm. For all simulations the 53a6 force field were used with parameters for POPC adapted from (29) and adapted for $PI(3,5)P_2$ from (34). The analysis was performed using GROMACS tools, VMD, Schrödinger and hole2 (31, 35-37).

FRET experiments. Measurements of single-cell FRET, based on aggregate (nonspatial) fluorescence recordings were performed and analyzed using the three-cube-FRET method as described previously (38). For measurements, transiently transfected HEK293 cells were maintained in buffer solution composed of 140 mM NaCl, 5 mM KCl, 1 mM $MgCl_2$, 2 mM $CaCl_2$, 10 mM Glucose, 10 mM Na-HEPES pH 7.4 at room temperature (RT). Fluorescence intensities of YFP or the GFP variants Citrine and Cerulean were recorded using a LEICA DMI6000B inverted epifluorescence microscope and a photomultiplier detection system (PTI, Canada). Excitation was done at 436nm ± 2.5 or 500 nm ± 2.5 with a DeltaRam monochromator (Horiba, Canada). Epifluorescence emission was detected by a photomultiplier (PMT 914) and acquired on a personal computer using FelixGX software (Horiba, Canada). Three cube FRET filter cubes were as follows (excitation, longpass beamsplitter, emission): CFP/Cerulean (ET436/20x; T455lp; ET480/40m), YFP/Citrine (ET500/20x; T515lp; ET535/30m) and FRET (ET436/20x; T455lp; ET535/30m) (Chrome technology). The FRET ratio, which is defined as the fractional increase in YFP emission caused by FRET, was calculated using FR = [SFRET-(R_D)(S_{Cer})]/[(R_A)(S_{Cit})]. S_{FRET}, S_{Cer} and S_{Cit} denote fluorescence intensities derived from measurements in individual cells co-expressing Citrine- or Cerulean-tagged proteins with the respective filter cube (excitation, emission): S_{FRET} (436 nm ± 10, 535 nm ± 15), S_{CFP} (436nm ± 10, 480 nm ± 20) and, S_{YFP} (500nm ± 10, 535 nm ± 15). R_D and R_A are experimentally predetermined constants from measurements applied to single cells expressing only Cerulean- or Citrine-tagged molecules that correct for donor bleed through or acceptor cross excitation. FRET efficiencies (E_A) can be calculated from FRs using the following equation (39):

$$E_A = [FR - 1] \cdot \frac{\varepsilon_{citrine}(436)}{\varepsilon_{cerulean}(436)}$$

$\varepsilon_{citrine}$ and $\varepsilon_{cerulean}$ are the setup specific average molar extinction coefficients for citrine and cerulean, respectively, over the precise bandwidth of the FRET cube excitation filter. In our setup, the calculated molecular extinction coefficient ratio is $\varepsilon_{citrine}$ (436) / $\varepsilon_{cerulean}$ (436) = 0.0563. Data were analyzed using FelixGX (Horiba PTI, Canada) and Microsoft Excel (Microsoft).

Whole-endolysosomal patch-clamp experiments. For whole-endolysosomal patch-clamp recordings, isolated intact endolysosomes from HEK293 cells were manually isolated after vacuolin treatment for at least 2 hours. Human TPC2 WT and polymorphic TPC2 variants (C-terminally fused to YFP) were transiently transfected into HEK293 cells using TurboFect Transfection Reagent (ThermoFisher). Currents were recorded using an EPC-10 patch-clamp amplifier and PatchMaster acquisition software (HEKA). Data were digitized at 40 kHz and filtered at 2.8 kHz. Cytoplasmic solution contained 140 mM KMSA, 5 mM KOH, 4 mM NaCl, 0.39 mM $CaCl_2$, 1 mM EGTA and 20 mM HEPES (pH adjusted with KOH to 7.2). Luminal solution was 140 mM NaMSA, 5 mM KMSA, 2 mM CaMSA, 1 mM $CaCl_2$, 10 mM HEPES and 10 mM MES (pH adjusted with MSA to 4.6). For the application of $PI(3,5)P_2$ (A.G. Scientific) and ATP-Mg (Sigma), cytoplasmic solution was completely exchanged by compound containing solution. Torin-1 and rapamycin were purchased from Tocris and LC Laboratories, respectively. All recordings were performed at 23-25 °C. For experiments using ATP and mTOR inhibitors, cell density was 50-60 % and the time spent outside the incubator was 30 minutes.

To estimate the pore diameter of TPC2 WT and M484L, the relative permeability ratios of cations relative to Na^+ were plotted against the diameter of the respective monovalent cations as indicated in Fig.4. The following equation was applied (40):

$$\frac{P_{X^+}}{P_{Na^+}} = k\left(1 - \frac{a}{d}\right)^2$$

where *a* is the diameter of the permeating cation, *k* is a constant factor, and *d* is the pore diameter (41). The ionic radii of Li^+, K^+, Rb^+ and Cs^+ are 0.6, 1.33, 1.48 and 1.69 Å (42). To calculate the permeability ratios the following equation was used:

$$\frac{P_{X^+}}{P_{Na^+}} = \frac{[Na]_i}{[X^+]_o} e^{\frac{VF}{RT}}$$

where V is the reversal potential, R is the gas constant, F is the Faraday constant, and T is the temperature in Kelvin. To determine the relative Na^+ (P_{X+}/P_{Na+}) permeabilities of TPC2 WT and M484L, whole-endolysosome recordings were performed using ramp protocols (+100 to -100 mV with 500 ms increments). The bath solution contained 160 mM (pH 7.2, HEPES 5 mM) of the respective cations (as indicated in the Fig.) and the pipette solutions contained 160 mM NaCl (pH 7.2, HEPES 5 mM). The recordings were started with symmetric Na^+ solutions. The cytoplasmic solution was then exchanged with the respective monovalent cation containing solution.

Human donor DNA purification and sequencing. Human genomic DNA was obtained from adult male and female individuals using the Gentra Puregene Buccal Cell Kit (Qiagen), according to manufacturer's instructions. Briefly, buccal cells were collected by scraping the inside of the mouth 10 times. For cell lysis, the collection brush was incubated in lysis solution at 65 °C for at least 15 min. Proteins were precipitated and centrifuged. To precipitate DNA, the supernatant was added to isopropanol and glycogen solution. The pellet was washed with 70 % ethanol and air-dried before resuspension in DNA hydration solution. Samples were incubated at 65 °C for 1h, followed by incubation at RT overnight to dissolve the DNA. Genomic DNA fragments were amplified using gene-specific primers (hTPC2(M484L) genomic DNA-forward: 5'-GGTGTTCCTGGTGCTGGA-3'; hTPC2(M484L) genomic DNA-reverse: 5'-ACAGCCTCTAGTCCTCAGGG-3'; hTPC2(G734E) genomic DNA-forward: 5'-GGCCACCTACCAGATGACT-3'; hTPC2(G734E) genomic DNA-reverse: 5'-CGGACGTCACCTGCACAG-3'. All DNA sequencing services were done by Eurofins MWG Operon.

Isolation of human fibroblasts. Human genomic DNA sampling and human fibroblast isolation were approved by the LMU Ethics Committee (headed by Prof. Dr. Eisenmenger; reference number: 254-16). Acquisition of human material was performed after obtaining written informed consent by the donors. Primary fibroblasts were isolated by Prof. Dr. Carola Berking and colleagues, Department of Dermatology, LMU Munich from the skin of healthy adult donors. Epidermis was separated from dermis using dispase II (10 mg/ml in PBS pH 7.2 -7.4; Sigma #D4693) and dermis was digested in collagenase (1 mg/ml in DMEM Medium; Sigma #C0130) for 22 h at room temperature. Fibroblasts were cultured in DMEM with glutamine (Life Technologies, Inc.) and 10% FBS (FBS Superior, Biochrom #S0615). They were used for experiments at passage 3-7.

Statistical analysis. Details of statistical analyses and n values are provided in the methods subsections or the figure legends. Statistical analyses were carried out using Origin 7.5 and GraphPad Prism 5. All error bars are depicted as mean ± SEM. Significance is denoted on figures as outlined in the legends. Statistics were derived from at least three independent experiments.

1. Favia A, et al. (2014) VEGF-induced neoangiogenesis is mediated by NAADP and two-pore channel-2-dependent Ca2+ signaling. *Proc Natl Acad Sci USA* 111(44):E4706-4715.
2. Grimm C, et al. (2014) High susceptibility to fatty liver disease in two-pore channel 2-deficient mice. *Nat Commun* 5:4699.
3. Cang C, et al. (2013) mTOR regulates lysosomal ATP-sensitive two-pore Na+ channels to adapt to metabolic state. *Cell* 152:778-790.
4. García-Rúa V, et al. (2016) Endolysosomal two-pore channels regulate autophagy in cardiomyocytes. *J Physiol* 594:3061-3077.
5. Lin PH, et al. (2015) Lysosomal two-pore channel subtype 2 (TPC2) regulates skeletal muscle autophagic signaling. *J Biol Chem* 290(6):3377-3389.
6. Arndt L, et al. (2014) NAADP and the two-pore channel protein 1 participate in the acrosome reaction in mammalian spermatozoa. *Mol Biol Cell* 25(6):948-964.
7. Sakurai Y, et al. (2015) Ebola virus. Two-pore channels control Ebola virus host cell entry and are drug targets for disease treatment. *Science* 347(6225):995-998.
8. Ruas M, et al. (2010) Purified TPC isoforms form NAADP receptors with distinct roles for Ca(2+) signaling and endolysosomal trafficking. *Curr Biol* 20:703-709.
9. Nguyen P, et al. (2017) Two-pore channel function is crucial for migration of invasive cancer cells. *Cancer Res* 77:1427-1438.
10. Sulem P, et al. (2008) Two newly identified genetic determinants of pigmentation in Europeans. *Nat Genet* 40(7):835-837.
11. Ambrosio AL, Boyle JA, Aradi AE, Christian KA, Di Pietro SM (2016) TPC2 controls pigmentation by regulating melanosome pH and size. *Proc Natl Acad Sci USA* 2016 May 2. pii: 201600108. [Epub ahead of print]
12. Bellono NW, Escobar IE, Oancea E (2016) A melanosomal two-pore sodium channel regulates pigmentation. *Sci Rep* 6:26570.
13. Kintzer AF, Stroud RM (2016) Structure, inhibition and regulation of two-pore channel TPC1 from Arabidopsis thaliana. *Nature* 531(7593):258-262.
14. Guo J, et al. (2016) Structure of the voltage-gated two-pore channel TPC1 from Arabidopsis thaliana. *Nature* 531(7593):196-201.
15. Wang X, et al. (2012) TPC Proteins Are Phosphoinositide-Activated Sodium-Selective Ion Channels in Endosomes and Lysosomes. *Cell* 151:372-383.
16. Perl A (2015) mTOR activation is a biomarker and a central pathway to autoimmune disorders, cancer, obesity, and aging. *Ann N Y Acad Sci* 1346(1):33-44.
17. Schieder M, Rötzer K, Brüggemann A, Biel M, Wahl-Schott C (2010) Planar patch clamp approach to characterize ionic currents from intact lysosomes. *Sci Signal* 3(151):pl3.
18. Shen D, et al. (2012) Lipid storage disorders block lysosomal trafficking by inhibiting a TRP channel and lysosomal calcium release. *Nat Commun* 3:731.
19. Faivre S, Kroemer G, Raymond E (2006) Current development of mTOR inhibitors as anticancer agents. *Nat Rev Drug Discov* 5(8):671-688.
20. Hausch F, Kozany C, Theodoropoulou M, Fabian AK (2013) FKBPs and the Akt/mTOR pathway. *Cell Cycle* 12(15):2366-2370.
21. Calcraft PJ, et al. (2009) NAADP mobilizes calcium from acidic organelles through two-pore channels. *Nature* 459:596-600.
22. Pitt SJ, et al. (2010) TPC2 is a novel NAADP-sensitive Ca2+ release channel, operating as a dual sensor of luminal pH and Ca2+. *J Biol Chem* 285:35039-35046.
23. Brailoiu E, et al. (2009) Essential requirement for two-pore channel 1 in NAADP-mediated calcium signaling. *J Cell Biol* 186(2):201-209.
24. Borges CR, Roberts JC, Wilkins DG, Rollins DE (2001) Relationship of melanin degradation products to actual melanin content: application to human hair. *Anal Biochem* 290(1):116-125.
25. Ancans J, et al. (2001) Melanosomal pH controls rate of melanogenesis, eumelanin/phaeomelanin ratio and melanosome maturation in melanocytes and melanoma cells. *Exp Cell Res* 268(1):26-35.
26. Smith DR, Spaulding DT, Glenn HM, Fuller BB (2004) The relationship between Na(+)/H(+) exchanger expression and tyrosinase activity in human melanocytes. *Exp Cell Res* 298(2):521-534.
27. Ito S, Wakamatsu K (2011) Human hair melanins: what we have learned and have not learned from mouse coat color pigmentation. *Pigment Cell Melanoma Res* 24(1):63-74.
28. Chen CC, et al. (2014) A small molecule restores function to TRPML1 mutant isoforms responsible for mucolipidosis type IV. *Nat Commun* 5:4681.
29. Krüger J, Fischer WB (2008) Exploring the conformational space of Vpu from HIV-1: a versatile adaptable protein. *J Comput Chem* 29(14):2416–2424.
30. Sommer B, et al. (2011) CELLmicrocosmos 2.2 MembraneEditor: A Modular Interactive Shape-Based Software Approach To Solve Heterogeneous Membrane Packing Problems. *J Chem Inf Model*:110419120935062.
31. Abraham MJ, et al. (2015) GROMACS: High performance molecular simulations through multi-level parallelism from laptops to supercomputers. *SoftwareX* 1:19–25
32. Krüger J, Fischer WB (2010) Structural implications of mutations assessed by molecular dynamics: Vpu1-32 from HIV-1. *Eur Biophys J* 39(7):1069–1077.
33. Avbelj M, et al. (2014) Activation of lymphoma-associated MyD88 mutations via allostery-induced TIR-domain oligomerization. *Blood* 124(26):3896–3904.
34. Holdbrook DA, et al. (2010) Stability and membrane orientation of the fukutin transmembrane domain: a combined multiscale molecular dynamics and circular dichroism study. *Biochemistry* 49(51):10796–10802.
35. Humphrey W, Dalke A, Schulten K (1996) VMD: visual molecular dynamics. *J Mol Graph* 14(1):33–8, 27–28.
36. Jacobson MP, et al. (2004) A hierarchical approach to all-atom protein loop prediction. *Proteins Struct Funct Bioinforma* 55(2):351–367.
37. Smart OS, Goodfellow JM, Wallace BA (1993) The pore dimensions of gramicidin A. *Biophys J* 65(6):2455–2460.
38. Butz ES, et al. (2016) Quantifying macromolecular interactions in living cells using FRET two-hybrid assays. *Nat Protoc* 11(12):2470-2498.
39. Nguyen ON, et al. (2016) Peripherin-2 differentially interacts with cone opsins in outer segments of cone photoreceptors. *Hum Mol Genet* 2016 pii:ddw103.
40. Owsianik G, Talavera K, Voets T, Nilius B (2006) Permeation and selectivity of TRP channels. *Annu Rev Physiol* 68:685-717.
41. Bormann J, Hamill OP, Sakmann B (1987) Mechanism of anion permeation through channels gated by glycine and gamma-aminobutyric acid in mouse cultured spinal neurones. *J Physiol* 385:243-286.
42. Robinson RA and Stokes RH (2002) Electrolyte Solutions: Second Revised Edition (Dover Books on Chemistry) Second Edition, Revised Edition

Acknowledgements

We thank Kerstin Skokann, Melanie Wallisch, and Berit Noack (LMU Munich) for technical support. We thank Dr. Bernd Schröder (University of Kiel, Germany) for kindly providing the human TMEM192 cDNA. We further thank Prof. Dr. Michael Zhu (University of Texas Medical School at Houston, TX, USA) for kindly providing the human TPC2(M484L/G734E)-mCherry cDNA. This work was supported, in part, by funding of the German Research Foundation (SFB/TRR152 TP04 to C.G., TP06 to C.W.-S., and TP12 to M.B.) and by funding of the NCL Foundation Hamburg, Germany. **Author contributions** C.G. designed the study, collected and analyzed data, and wrote the manuscript. Y.-K.C., C-C.C., E.B., J.K., C.K., Y.S., M.M., M.B.-J., and O.N.P.N. designed experiments and/or collected, and/or analysed data. C.B. performed donor surgery. C.W.-S., M.B., and A.V. edited the manuscript and provided funding. In addition, F.B. designed syntheses. All of the authors discussed the results and commented on the manuscript. **Additional information Supplementary Information** includes three figures and can be found with this article online at http://www.pnas.org/ **Competing financial interests:** The authors declare no competing financial interests.

We thank Kerstin Skokann, Melanie Wallisch, and Berit Noack (LMU Munich) for technical support. We thank Dr. Bernd Schrőder (University of Kiel, Germany) for kindly providing the human TMEM192 cDNA. We further thank Prof. Dr. Michael Zhu (University of Texas Medical School at Houston, TX, USA) for kindly providing the human TPC2(M484L/G734E)-mCherry cDNA. This work was supported, in part, by funding of the German Research Foundation (SFB/TRR152 TP04 to C.G., TP06 to C.W.-S., and TP12 to M.B.) and by funding of the NCL Foundation Hamburg, Germany.

Author contributions

C.G. designed the study, collected and analyzed data, and wrote the manuscript. Y.-K.C., C-C.C., E.B., J.K., C.K., Y.S., M.M., M.B.-J., and O.N.P.N. designed experiments and/or collected, and/or analysed data. C.B. performed donor surgery. C.W.-S., M.B., and A.V. edited the manuscript and provided funding. In addition, F.B. designed syntheses. All of the authors discussed the results and commented on the manuscript.

Additional information

Supplementary Information includes three figures and can be found with this article online at http://www.pnas.org/

Competing financial interests: The authors declare no competing financial interests.

Chao et al.

Supporting information

TPC2 polymorphisms associated with a hair pigmentation phenotype in humans result in gain of channel function by independent mechanisms.

Yu-Kai Chao[1*], Verena Schludi[1*], Cheng-Chang Chen[1], Elisabeth Butz[1], O.N. Phuong Nguyen[1], Martin Müller[1], Jens Krüger[2], Claudia Kammerbauer[3], Manu Ben-Johny[4], Angelika Vollmar[1], Carola Berking[3], Martin Biel[1], Christian Wahl-Schott[1#], and Christian Grimm[1#]

[1]Department of Pharmacy - Center for Drug Research and Center for Integrated Protein Science Munich (CIPSM), Ludwig-Maximilians-Universität München, Germany; [2]High-Performance and Cloud Computing Group, Zentrum für Datenverarbeitung, Universität Tübingen, Germany; [3]Department of Dermatology, Medical Faculty, Ludwig-Maximilians-Universität München, Germany; [4]Calcium Signals Laboratory, Department of Biomedical Engineering, The Johns Hopkins University School of Medicine, Baltimore, Maryland, USA.

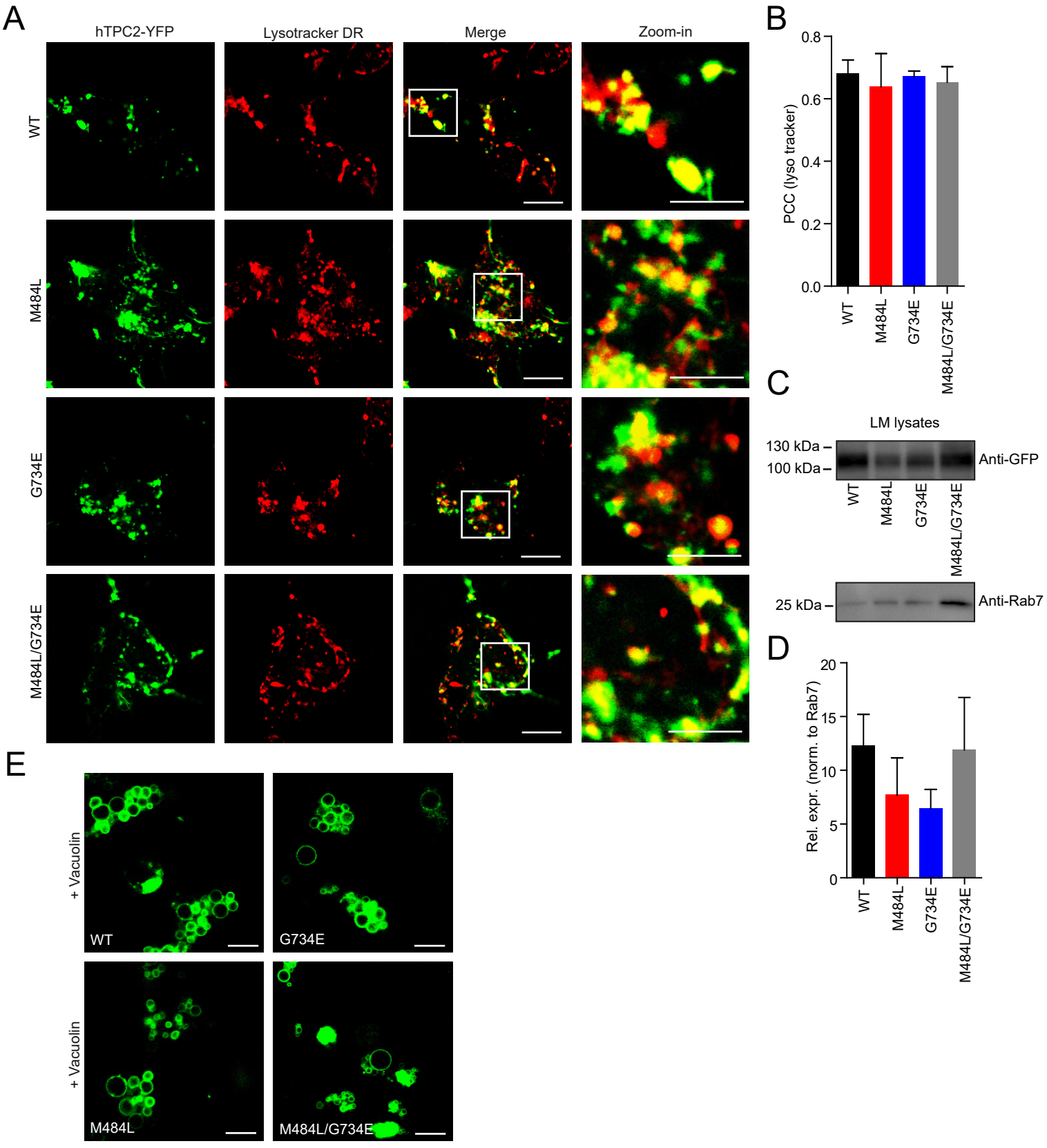
A
hTPC2-YFP
Lysotracker DR
Merge
Zoom-in
WT
M484L
G734E
M484L/G734E
B
PCC (lyso tracker)
0.8
0.6
0.4
0.2
0.0
WT
M484L
G734E
M484L/G734E
C
LM lysates
130 kDa
100 kDa
Anti-GFP
WT
M484L
G734E
M484L/G734E
25 kDa
Anti-Rab7
D
Rel. expr. (norm. to Rab7)
20
15
10
5
0
WT
M484L
G734E
M484L/G734E
E
+ Vacuolin
WT
G734E
+ Vacuolin
M484L
M484L/G734E

SI Figure 1

Human TPC2 WT and polymorphic variants: expression, subcellular distribution and vacuolin effect. (*A*) Shown are representative laser scanning images of hTPC2 WT and the polymorphic variants hTPC2(G734E), hTPC2(M484L), and hTPC2(M484L/G734E), all C-terminally fused to YFP and overexpressed in HEK293 cells using TurboFect. All isoforms showed a punctuated pattern and colocalized with Lysotracker DR (deep red). Scale bars = 10 µm (zoom-in images: scale bars = 5 µm). (*B*) PCC (Pearson correlation coefficients) calculated from images as shown in *A* using ImageJ software and the JACoP colocalization plugin (images were taken from n = 3 independent experiments). (*C-D*) Depicted in *C* are representative western blot data showing specific bands for hTPC2 WT and the polymorphic variants hTPC2(G734E), hTPC2(M484L), and hTPC2(M484L/G734E) fused to YFP, respectively, and detected with an anti-GFP antibody in lysosomal membranes (LM). LM were purified from whole cell lysates. The bands recognized with anti-Rab7 antibody were used as reference for the lysosomal preparations. Shown in *D* is the quantification of the data presented in *C* (n = 3 independent experiments) using Image Lab Software. All variants showed no significant differences in their relative expression levels. (*E*) The effect of vacuolin on all isoforms was comparable. Shown are representative laser scanning images of the respective variants overexpressed in HEK293 cells. Cells were treated for 4 hours with 1 µM vacuolin. Scale bars = 10 µm.

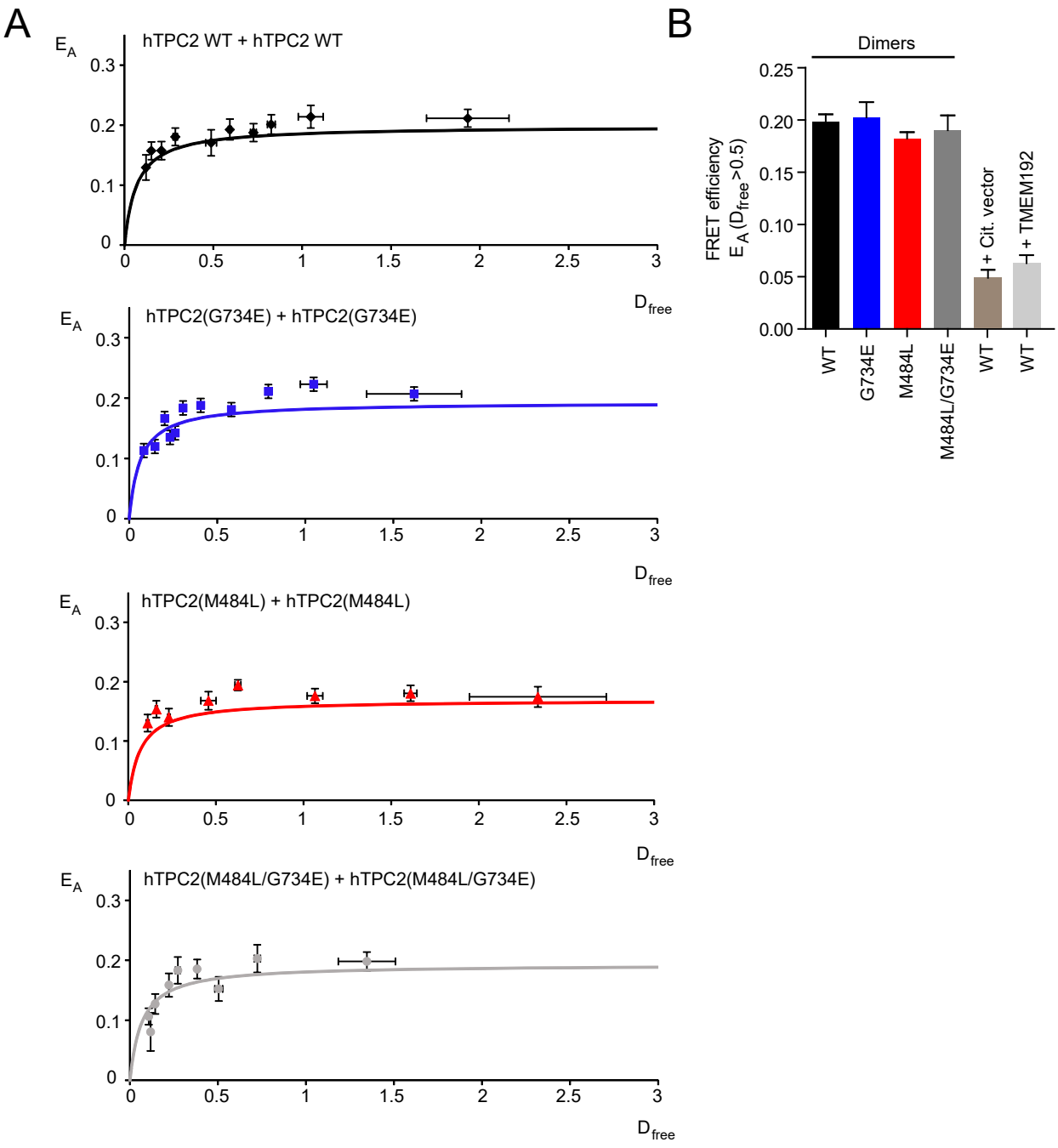
A
B
hTPC2 WT + hTPC2 WT
hTPC2(G734E) + hTPC2(G734E)
hTPC2(M484L) + hTPC2(M484L)
hTPC2(M484L/G734E) + hTPC2(M484L/G734E)
E_A
D_free
Dimers
FRET efficiency
E_A (D_free >0.5)
WT
G734E
M484L
M484L/G734E
WT + Cit. vector
WT + TMEM192

SI Figure 2

FRET experiments to assess TPC2 WT and polymorphic variant dimerization. (*A*) Shown are the respective FRET efficiencies (E_A) for binned groups of HEK293 cells overexpressing hTPC2 WT or the polymorphic variants hTPC2(G734E), hTPC2(M484L), or hTPC2(M484L/G734E), N-terminally fused to Citrine or Cerulean, respectively, plotted versus D_{free}, forming a binding curve. As negative control the lysosomal transmembrane protein hTMEM192 C-terminally fused to Cerulean was co-transfected with Citrine-hTPC2 WT. As a second negative control co-transfection of Cerulean-hTPC2 WT with empty Citrine-vector was used. (*B*) Statistical summary of data as shown in *A* using $D_{free} > 0.5$ as cutoff. In all statistical analyses mean values of at least 3 independent experiments (n = 10-15 cells each) are shown, each. To test for statistical significance one-way ANOVA test followed by Tukey's post-test was applied. No significant differences were found between the TPC2 variants.

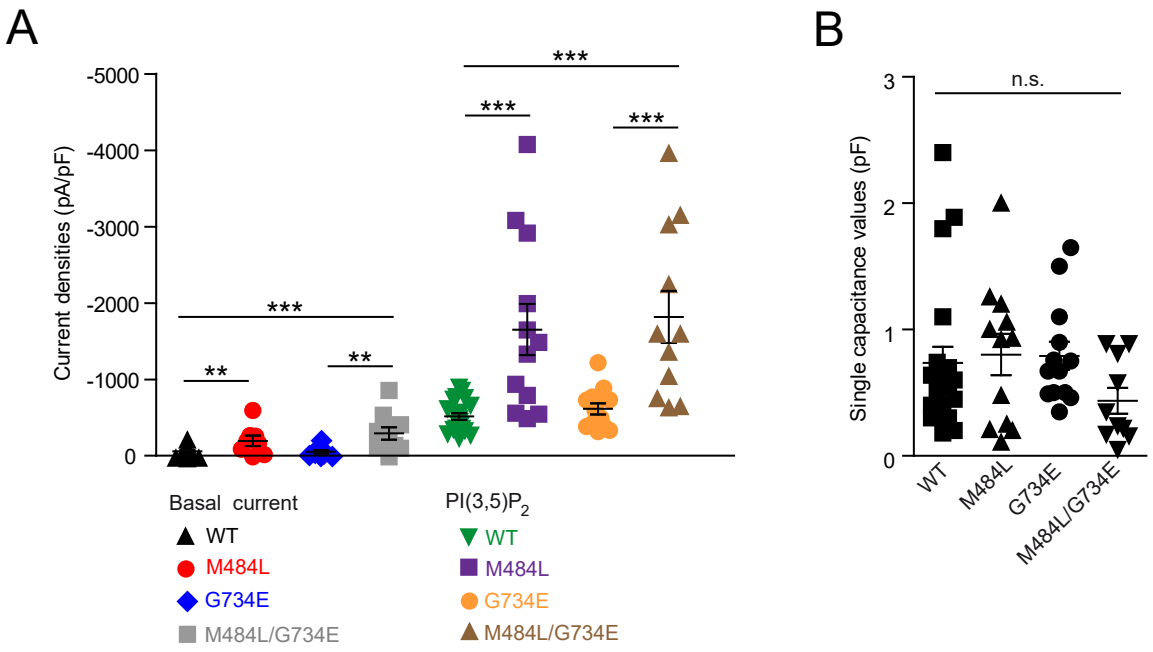
A
B
Current densities (pA/pF)
-5000
-4000
-3000
-2000
-1000
0
***
**
**
***
***
***
Basal current
WT
M484L
G734E
M484L/G734E
PI(3,5)P2
WT
M484L
G734E
M484L/G734E
Single capacitance values (pF)
3
2
1
0
n.s.
WT
M484L
G734E
M484L/G734E

SI Figure 3

Effect of PI(3,5)P_2 on endolysosomal vesicles expressing either human TPC2 WT or polymorphic variants. (*A*) Single values of current densities (at -100 mV) measured in endolysosomal patch-clamp experiments as shown in Fig.1. Currents were elicited with PI(3,5)P_2 (1 μM). To test for statistical significance the one-way ANOVA test followed by Tukey's post-test was applied. ***, indicates $p<0.001$, **, indicates $p<0.01$. (*B*) Single capacitance values for the vesicles measured in the experiments presented in Fig.1.

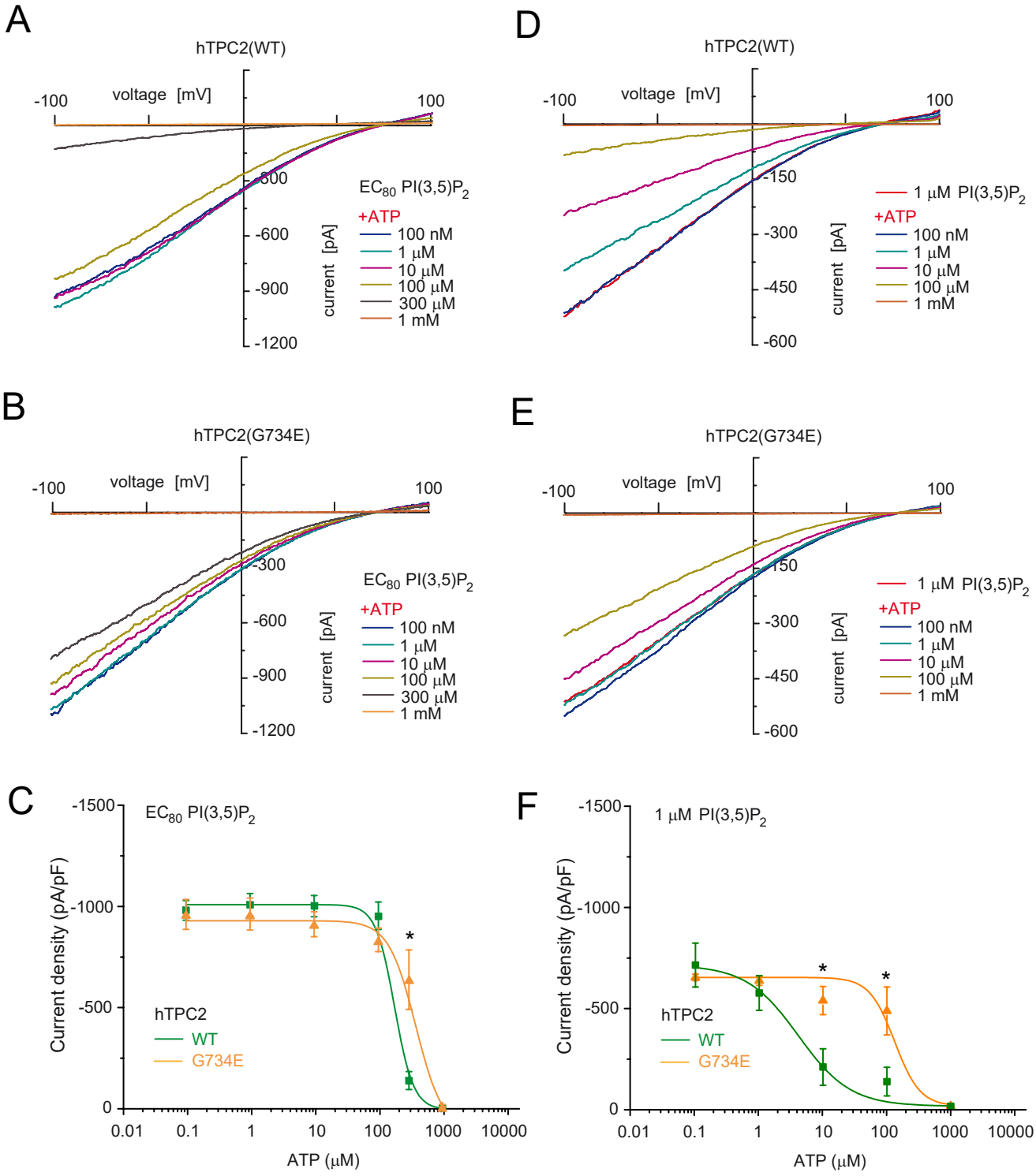
A
hTPC2(WT)
-100
voltage [mV]
100
-300
-600
-900
-1200
current [pA]
EC80 PI(3,5)P2
+ATP
100 nM
1 μM
10 μM
100 μM
300 μM
1 mM
D
hTPC2(WT)
-100
voltage [mV]
100
-150
-300
-450
-600
current [pA]
1 μM PI(3,5)P2
+ATP
100 nM
1 μM
10 μM
100 μM
1 mM
B
hTPC2(G734E)
-100
voltage [mV]
100
-300
-600
-900
-1200
current [pA]
EC80 PI(3,5)P2
+ATP
100 nM
1 μM
10 μM
100 μM
300 μM
1 mM
E
hTPC2(G734E)
-100
voltage [mV]
100
-150
-300
-450
-600
current [pA]
1 μM PI(3,5)P2
+ATP
100 nM
1 μM
10 μM
100 μM
1 mM
C
EC80 PI(3,5)P2
-1500
-1000
-500
0
Current density (pA/pF)
hTPC2
WT
G734E
*
0.01
0.1
1
10
100
1000
10000
ATP (μM)
F
1 μM PI(3,5)P2
-1500
-1000
-500
0
Current density (pA/pF)
hTPC2
WT
G734E
*
*
0.01
0.1
1
10
100
1000
10000
ATP (μM)

SI Figure 4

Effect of ATP on human TPC2 WT and G734E using the respective EC_{80} values of $PI(3,5)P_2$ as activating concentrations or a fixed concentration of 1 µM. (*A-B*) Representative $PI(3,5)P_2$ (diC8) activated currents in vacuolin enlarged hTPC2 WT and hTPC2(G734E) expressing endolysosomal vesicles using the respective EC_{80} values as activating $PI(3,5)P_2$ concentrations and different concentrations of ATP as indicated to block the currents. (*C*) ATP dose response curves from experiments as shown in *A-B*. (*D-E*) Similar experiments as in *A-B* using a fixed $PI(3,5)P_2$ concentration of 1 µM as activating concentration and different concentrations of ATP as indicated to block the currents. (*F*) ATP dose response curves from experiments as shown in *D-E*. In all experiments currents were elicited by applying 500-ms voltage ramps from -100 to +100 mV every 5 s. To test for statistical significance the Student's *t*-test, unpaired was applied. * indicates $p<0.05$.

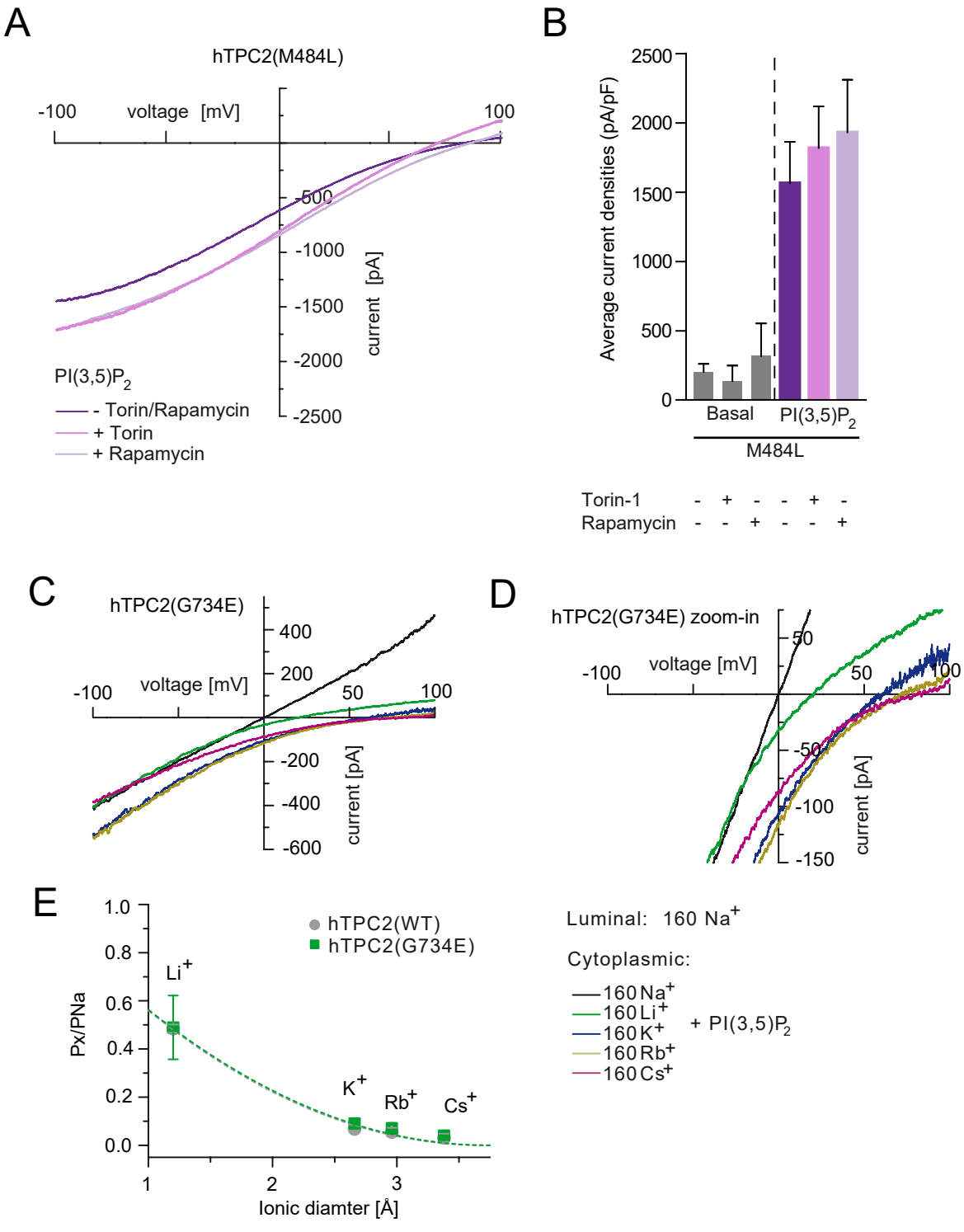
A
hTPC2(M484L)
-100
voltage [mV]
100
-500
-1000
-1500
-2000
-2500
current [pA]
PI(3,5)P2
- Torin/Rapamycin
+ Torin
+ Rapamycin
B
Average current densities (pA/pF)
2500
2000
1500
1000
500
0
Basal
PI(3,5)P2
M484L
Torin-1 - + - - + -
Rapamycin - - + - - +
C
hTPC2(G734E)
400
200
-100
voltage [mV]
50
100
-200
-400
-600
current [pA]
D
hTPC2(G734E) zoom-in
50
-100
voltage [mV]
50
100
-50
-100
-150
current [pA]
E
1.0
0.8
0.6
0.4
0.2
0.0
Px/PNa
hTPC2(WT)
hTPC2(G734E)
Li+
K+
Rb+
Cs+
1
2
3
Ionic diamter [Å]
Luminal: 160 Na+
Cytoplasmic:
160 Na+
160 Li+
160 K+
160 Rb+
160 Cs+
+ PI(3,5)P2

SI Figure 5

Effect of mTOR inhibitors on M484L and ion substitution experiments for G734. (*A*) Representative $PI(3,5)P_2$ (1 µM) activated currents in vacuolin enlarged hTPC2(M484L) expressing endolysosomal vesicles and the respective blocking effects of 2 µM torin-1 or 1 µM rapamycin. Cells were incubated with torin-1 for 12 hours or with rapamycin for 10 minutes before experimentation. Currents were measured in the absence of ATP. (*B*) Statistical summary of data as shown in *A* including respective basal currents. Shown are average current densities at -100 mV. (*C*) Endolysosomal patch-clamp experiments showing $PI(3,5)P_2$-activated hTPC2(G734E) currents under bi-ionic conditions with luminal Na^+ and bath solutions containing the following monovalent cations, respectively: Li^+, K^+, Rb^+ and Cs^+. (*D*) Expanded view of *C*. (*E*) Summary of data as shown in *C-D*. Shown are the relative permeabilities (P_X/P_{Na}) of the different cations plotted against the diameter of cations. The dashed lines are fitted to Equation 1 (see method section for details).

A

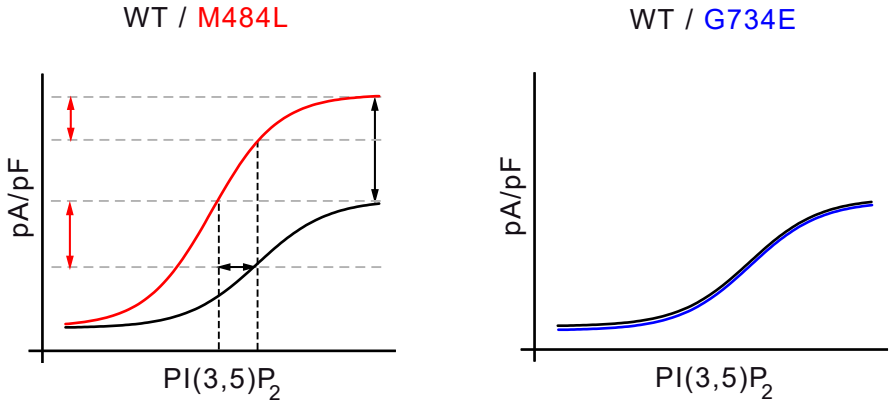
WT / M484L
WT / G734E
pA/pF
PI(3,5)P2
pA/pF
PI(3,5)P2

B

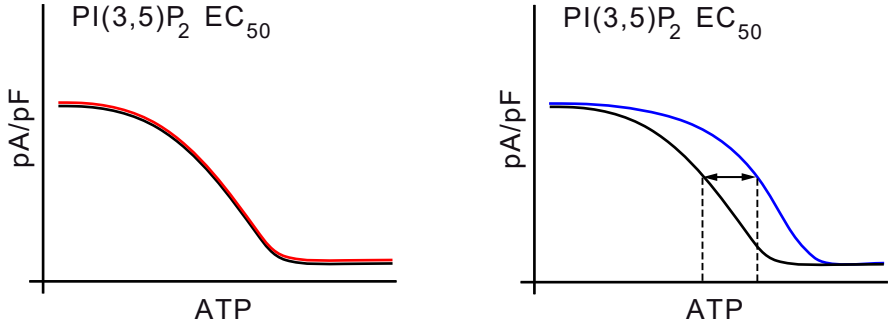
PI(3,5)P2 EC50
pA/pF
ATP
PI(3,5)P2 EC50
pA/pF
ATP

C

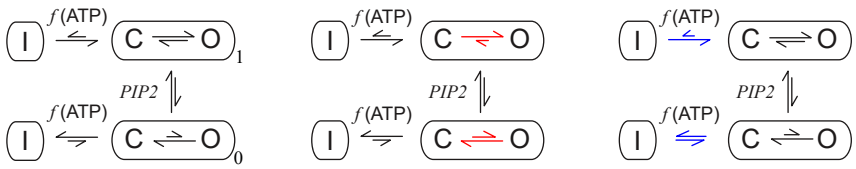
WT
M484L
G734E
I
C
O
f(ATP)
PIP2
1
0

SI Figure 6

Model for the different channel properties in TPC2 variants. (*A*) Shown are schematic $PI(3,5)P_2$ dose-response curves (DRCs) of WT versus M484L (*A*, left) and WT versus G734E (*A*, right). (*B*) Schematic ATP DRCs of WT versus M484L (*B*, left) and WT versus G734E (*B*, right) using the respective EC_{50} concentrations of $PI(3,5)P_2$ to activate. Compared to WT the DRC for $PI(3,5)P_2$ is changed in the M484L variant while the ATP inhibition curve is not. The opposite effect can be seen when comparing WT with the G734E variant: Compared to WT the DRC for $PI(3,5)P_2$ is unchanged in the G734E variant while the ATP inhibition curve is changed. Therefore, the overall system response is determined by the difference in DRC for $PI(3,5)P_2$ in the M484L variant while it is determined by the ATP inhibition curve in the G734E variant. Gain of function in the M484L variant is evident by the increased maximal $PI(3,5)P_2$ activation current density (increased efficacy) and by the lower EC_{50} for $PI(3,5)P_2$ (increased potency) compared to WT (*A*). At a fixed ATP concentration one would expect the same fractional block in WT and the M484L variant (inhibition curve is identical; *B*, left). However, this fractional block is determined by the DRC for $PI(3,5)P_2$ and depends on the $PI(3,5)P_2$ concentration. Inhibition of mTOR which likely mediates the ATP effect on TPC2 would revert the block and increase current density in both channel variants. The fractional increase would likewise be determined by the DRC for $PI(3,5)P_2$ and depend on the $PI(3,5)P_2$ concentration. The dashed grey lines and red double arrows (*A*, left) indicate the range for further increase in channel activity at the EC_{50} of WT. At this concentration M484L has almost reached its activation plateau. If the activating $PI(3,5)P_2$ concentration is at the EC_{50} of WT, then mTOR inhibition would result in a smaller increase in activity in M484L compared to WT. (A, right) In WT and G734E the DRC and EC_{50} values for $PI(3,5)P_2$ are similar. By contrast, the ATP inhibition curve is shifted to higher ATP concentrations in G734E (B, right). Thus, at the same ATP concentration (= activation of mTOR) WT would be blocked more efficiently than G734E. Inhibition of mTOR would increase channel activity in both WT and G734E. However, at the same $PI(3,5)P_2$ concentration (see Fig. 3) the increase in activity would be expected to be stronger in G734E than in WT. (C) Model of the effects shown in *A* and *B*. Left panel, WT: In the absence of $PI(3,5)P_2$, the channels can open but the openings are very rare. This is indicated by the equilibrium constant biased toward the closed state. Upon binding to $PI(3,5)P_2$, the channels can open much better as the equilibrium is biased towards the open state. Thus, addition of $PI(3,5)P_2$ will increase the currents substantially. Inactivation: ATP binding to mTOR triggers channel inactivation, possibly via a two-step process. First activated mTOR binds to an effector interface, and then that triggers a conformational change that manifests as inactivation. Moreover, channels unbound to $PI(3,5)P_2$ will preferentially enter the inactivated state. Center panel, M484L: C1 to O1 and C0 to O0 are enhanced as a result of the pore-dilation. Right panel, G734E: Activation process is not affected but the ATP sensitivity is reduced with no effect on the activation.

Human Molecular Genetics, 2014, Vol. 23, No. 22 **5989–5997**
doi:10.1093/hmg/ddu323
Advance Access published on June 24, 2014

Peripherin-2 couples rhodopsin to the CNG channel in outer segments of rod photoreceptors

Elvir Becirovic[1,2,†], O.N. Phuong Nguyen[1,2,†], Christos Paparizos[1,2], Elisabeth S. Butz[1,2], Gabi Stern-Schneider[3], Uwe Wolfrum[3], Stefanie M. Hauck[4], Marius Ueffing[4,5], Christian Wahl-Schott[1,2], Stylianos Michalakis[1,2] and Martin Biel[1,2,*]

[1]Munich Center for Integrated Protein Science CIPSM and [2]Department of Pharmacy, Center for Drug Research, Ludwig-Maximilians-Universität München, München, Germany, [3]Cell and Matrix Biology, Institute of Zoology, Johannes-Gutenberg Universität Mainz, Mainz, Germany, [4]Research Unit Protein Science, Helmholtz Center Munich, German Research Center for Environmental Health GmbH, München, Germany and [5]Center for Ophthalmology, Institute for Ophthalmic Research, Tübingen, Germany

Received May 5, 2014; Revised and Accepted June 19, 2014

Outer segments (OSs) of rod photoreceptors are cellular compartments specialized in the conversion of light into electrical signals. This process relies on the light-triggered change in the intracellular levels of cyclic guanosine monophosphate, which in turn controls the activity of cyclic nucleotide-gated (CNG) channels in the rod OS plasma membrane. The rod CNG channel is a macromolecular complex that in its core harbors the ion-conducting CNGA1 and CNGB1a subunits. To identify additional proteins of the complex that interact with the CNGB1a core subunit, we applied affinity purification of mouse retinal proteins followed by mass spectrometry. In combination with *in vitro* and *in vivo* co-immunoprecipitation and fluorescence resonance energy transfer (FRET), we found that the tetraspanin peripherin-2 links CNGB1a to the light-detector rhodopsin. Using immunoelectron microscopy, we found that this peripherin-2/rhodopsin/CNG channel complex localizes to the contact region between the disk rims and the plasma membrane. FRET measurements revealed that the fourth transmembrane domain (TM4) of peripherin-2 is required for the interaction with rhodopsin. Quantitatively, the binding affinity of the peripherin-2/rhodopsin interaction was in a similar range as that observed for rhodopsin dimers. Finally, we demonstrate that the p.G266D retinitis pigmentosa mutation found within TM4 selectively abolishes the binding of peripherin-2 to rhodopsin. This finding suggests that the specific disruption of the rhodopsin/peripherin-2 interaction in the p.G266D mutant might contribute to the pathophysiology in affected persons.

INTRODUCTION

Outer segments (OSs) of rod photoreceptors harbor all essential proteins of the phototransduction cascade including the G-protein-coupled receptor rhodopsin, the guanylyl cyclase, the phosphodiesterase and the rod cyclic nucleotide-gated (CNG) channel. Most of these proteins localize to highly structured intracellular membrane stacks (disks), which are physically separated from the plasma membrane (1). One exception is the CNG channel, which is exclusively found in the plasma membrane (2). Moreover, the periphery of disks facing the plasma membrane, referred to as disk rims, contains a set of proteins that differ from that of the remaining part of the disks. Previous studies revealed that the rod CNG channel is directly connected to the disk rims via a direct protein–protein interaction of the glutamic acid-rich (GARP) domain of the CNGB1a subunit and the disk rim-specific tetraspanin peripherin-2 (3,4). Peripherin-2 is a scaffolding protein reported to be responsible for the disk morphogenesis and for membrane fusion processes (5,6). Mutations in peripherin-2 are associated with severe retinal diseases (http://www.retina-international.org last accessed 26 June 2014). The vast majority of these mutations are linked to autosomal dominant retinitis pigmentosa (adRP), a degenerative retinal disease that affects rod photoreceptors and often results

*To whom correspondence should be addressed at: Department Pharmazie, Pharmakologie für Naturwissenschaften, Ludwig-Maximilians-Universität München, Butenandtstr. 5–13, D-81377 München, Germany. Tel: +49 89218077327; Fax: +49 89218077326; Email: mbiel@cup.uni-muenchen.de
† E.B. and O.N.P.N. contributed equally to this study.

in complete blindness. Here, we combined *in vivo* and *in vitro* biochemical, imaging and immunoaffinity methods to show that peripherin-2 in rod OSs binds to rhodopsin and the CNGB1a subunit of the CNG channel. Moreover, we demonstrate that the fourth transmembrane domain (TM4) of peripherin-2 is essential for its interaction with rhodopsin and that a single adRP-associated point mutation in TM4 of peripherin-2 abolishes this interaction while leaving the binding to CNGB1a unaffected. These results indicate that peripherin-2 operates as an adaptor protein in the disk rims that physically couples the rod CNG channel to the phototransduction cascade. This physical coupling between rhodopsin and the CNG channel suggests that phototransduction in rod OS is more spatially confined than it has been known so far and could help to gain new insights on the functional and structural role of the disk rim microcompartment in the rod OS. Finally, we conclude that the adRP phenotype in patients carrying a mutation in TM4 of peripherin-2 most probably results from the specific disruption of the peripherin-2/rhodopsin interaction in the disk rims.

RESULTS

Identification of CNGB1a-interacting proteins

To identify novel components of the rod photoreceptor, CNG channel complex of retinal lysates of light-adapted 6-week-old-mice were immunopurified using an antibody directed against the C-terminus of the CNGB1a subunit of the rod CNG channel and analyzed by quantitative mass spectrometry. Lysates of age-matched, CNGB1-deficient mice served as negative control. Among the list of OS-specific CNGB1a-interacting proteins, we identified rhodopsin and peripherin-2 (Supplementary Material, Table S1). Reciprocal co-immunoprecipitations (co-IPs) from retinal lysates using either an anti-rhodopsin antibody (Fig. 1A) or an anti-CNGB1a antibody (Fig. 1B) confirmed that rhodopsin, peripherin-2 and CNGB1a are present in the same channel complex. Importantly, no specific bands were observed when performing the co-IPs with retinal lysates from CNGB1-knockout mice (Fig. 1B, lane 2) or when a control IgG was used instead of the anti-CNGB1a antibody (Fig. 1A, lane 2). In addition to monomeric rhodopsin, the anti-rhodopsin antibody detected bands corresponding to rhodopsin oligomers (i.e. dimers, trimers and tetramers) pointing to a very tight interaction between rhodopsin molecules, which persisted under SDS–PAGE conditions. To get a more direct view on the localization of rhodopsin and CNGB1a in rod OSs, we employed immunoelectron microscopy in retinal sections (Fig. 1C). Immunogold particles of different diameters co-labeled with the anti-rhodopsin and anti-CNGB1a antibodies, respectively, revealed that CNGB1a is localized in close proximity to rhodopsin.

Analysis of the rod opsin/peripherin-2/CNGB1a complex in HEK293 cells

In previous studies, it was shown that peripherin-2 binds to the N-terminal GARP domain of CNGB1a (3,4). However, an interaction between peripherin-2 and rhodopsin or between rhodopsin and CNGB1a has not been reported so far. To address this issue, we performed co-IPs in HEK293 cells expressing different combinations of the chromophore-free rod apo-opsin (herein referred to as rod opsin), peripherin-2 and the rod CNG channel subunits (Fig. 2A and B). Surprisingly, in the absence of peripherin-2, rod opsin did not assemble with CNGB1a nor did it interact with this subunit when both subunits of the native CNG channel (CNGB1a + CNGA1) were present (Fig. 2A). In contrast, when peripherin-2 was co-expressed together with rod opsin and CNGB1a, the CNGB1a subunit could be co-immunoprecipitated with the anti-rhodopsin antibody (Fig. 2B). Moreover, peripherin-2 was binding to rod opsin in the absence of CNGB1a (Fig. 2B). Taken together, the co-IP experiments indicate that rod opsin requires peripherin-2 to interact with CNGB1a. We therefore postulated that peripherin-2 physically links rod opsin and CNGB1a by simultaneously binding to both proteins.

To test this hypothesis, we applied fluorescence resonance energy transfer (FRET) that allows detection and quantification of protein–protein interactions (Fig. 2C). We tagged the proteins C-terminally with either citrine or cerulean and then used the respective fusion protein pairs for FRET measurements. In agreement with the immunoprecipitation data, we obtained robust FRET signals for rod opsin/peripherin-2 and as well as for peripherin-2/CNGB1a. Quantitatively, FRET ratios (FRs) of these pairs were in a similar range. However, they were somewhat lower than FRs obtained for rod opsin or peripherin-2 homodimers (see also Fig. 1A and B). In agreement with previous findings (3,4), our FRET data also revealed a robust interaction between peripherin-2 and the soluble GARP2, which corresponds to the N-terminal portion of CNGB1a. Importantly, the FR obtained for the rhodopsin/CNGB1a FRET pair was only slightly above background confirming that there is no specific interaction between these two proteins.

In vitro FRET unveils binding characteristics of rod opsin and peripherin-2

To narrow down the region in peripherin-2 that is required for the interaction with rod opsin, we determined the FRs between the cerulean-tagged rod opsin and citrine-tagged peripherin-2 harboring C-terminal truncations (Fig. 3A). While deletion of the C-terminus downstream of the fourth transmembrane segment (Prph2_C1-citr) had no effect on the interaction with rod opsin, additional truncation of the TM4 domain (citr-Prph2_C2) abolished binding to rod opsin (Fig. 3A). In the latter truncation mutant (containing only three transmembrane segments), citrine was fused to the N-terminus to ensure that (like in C-terminally tagged peripherin-2 variants containing four transmembrane domains) citrine faces the cytoplasmic side of the cell. Importantly, the position of the tag did not interfere with the principal interaction with rod opsin because FRs of the peripherin-2/rod opsin pairs were in a comparable range for either N- or C-terminally tagged peripherin-2 (Fig. 3A).

In order to specifically examine protein interactions in the plasma membrane and to determine binding curves of the rod opsin/peripherin-2 interaction, confocal FRET experiments were performed in HEK293 cells (Fig. 3B and C). Maximal FR values (FR_{max}) obtained with this approach for rod opsin/peripherin-2 and rod opsin/rod opsin pairs, respectively, were in good agreement with the FR obtained in standard (non-confocal) FRET (Fig. 3A). As expected, confocal FR_{max} values were consistently higher than the corresponding

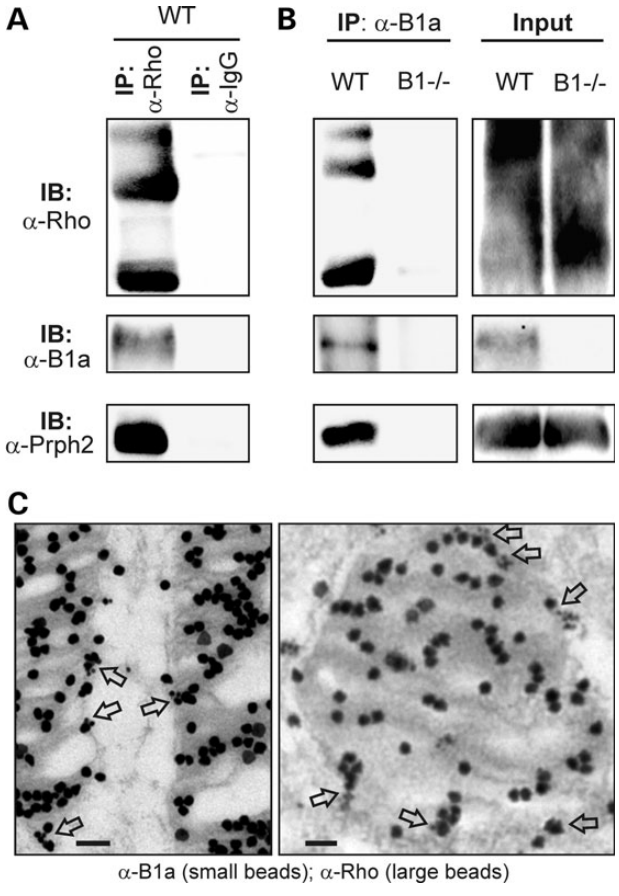

Figure 1. CNGB1a, peripherin-2 and rhodopsin are assembled in a protein complex in rod OS. (**A**) Retinal lysates of wild-type (WT) mice were immunoprecipitated with an anti-rhodopsin antibody (α-Rho) or a nonspecific control IgG (α-IgG). Precipitated samples were analyzed in immunoblots (IB) using α-Rho and antibodies directed against the CNGB1a subunit (α-B1a) and peripherin-2 (α-Prph2) as indicated. (**B**) *Left,* retinal lysates of WT and CNGB1-knockout mice (B1−/−) were immunoprecipitated with α-B1a and probed with α-Rho, α-B1a and α-Prph2. *Right*, loading control containing 10% of the protein lysate used for the co-IP in the left panel. (**C**) Immunoelectron microscopy images of longitudinal (left) and transversal (right) sections of rod OS co-stained with small-diameter immunogold particles coupled to α-B1a and large-diameter particles coupled to α-Rho, respectively. Co-localization of large and small particles is marked by arrows. Scale bar, 100 nm.

non-confocal FRs. On the basis of confocal FRET measurements, the relative binding affinity of the rod opsin/peripherin-2 interaction was calculated to be ∼80% of the rod opsin/rod opsin interaction.

FRET measurements in isolated rod OSs

To demonstrate that rhodopsin is bound to peripherin-2 in native rod photoreceptors, FRET constructs were expressed in the murine retina using AAV8-vectors, which contain the human rhodopsin promoter (Fig. 4A).Three to four weeks after subretinal injection of viral vectors, robust expression of individual constructs was observed (Fig. 4B). The expression was restricted to rod OSs indicating that the fluorophores did not interfere with the ciliary transport (Fig. 4B). OSs isolated using a self-designed quick protocol appeared to be intact with regard to their structure and shape (Fig. 4C). Figure 4D shows co-expression of a representative FRET pair (rhodopsin-cerulean and peripherin-citrin) in an isolated rod OS. As expected for a native system, FRs were throughout smaller as found upon heterologous expression in HEK293 cells (Fig. 4E). This difference most probably can be ascribed to the fact that the unlabeled wild-type proteins *in vivo* interfere with the FRET constructs leading to the reduction of the absolute FRET signal. Qualitatively, however, results in rod OSs were consistent with the results in HEK293 cells. Highest FRs were observed for the rhodopsin homomer. Importantly, there was also clear FRET between rhodopsin and peripherin-2 with the FR being slightly higher for the N-terminally as compared with the C-terminally tagged peripherin-2. In contrast, in good agreement with previous studies (4,7), no FRET was observed for rhodopsin and rod-specific GARP2 protein.

An adRP-linked mutation in TM4 of peripherin-2 disrupts binding to rhodopsin

As mentioned before, mutations in peripherin-2 have been associated with adRP. Thus, we were wondering whether some of these mutations may lead to an impaired rhodopsin binding. To address this issue, we analyzed whether some adRP-linked mutations are localized in TM4 of peripherin-2, the domain that we found to be crucial for binding to rhodopsin (cf. Fig. 3A). Indeed, one adRP-associated mutation (p.G266D) (8) was found in TM4 and was located in the transmembrane region most proximal to the intradiskal portion of peripherin-2 (Fig. 5A). Consequently, we tested whether this mutation interferes with the binding of peripherin-2 to rhodopsin. Using FRET (Fig. 5B) and co-IP (Fig. 5C) experiments from HEK293 cells, we demonstrate that the p.G266D mutant abolishes binding to rod opsin. To further demonstrate the specificity of this finding, we analyzed the effects of two additional peripherin-2 mutations on rhodopsin binding. Interestingly, the exchange of the glycine residue at position 266 and glutamate at position 276 by the neutral amino acid alanine (p.G266A and p.E276A, respectively) did not affect the binding to rhodopsin (Fig. 5B and C). Importantly, the interaction of single peripherin-2 mutants with CNGB1a was not affected as shown by additional co-IP experiments from HEK293 cells (Fig. 5D). This indicates that the lack of binding of the p.G266D mutant most probably is not due to its overall folding deficiency. Notably, for co-IP experiments, we used membrane preparations, and in the respective input controls, we could not observe any difference in the membrane expression levels of the mutants compared with the wild-type peripherin-2 (Fig. 5C and D, input controls), which argues against the lack of the membrane expression or transport deficits for any of the mutants analyzed.

DISCUSSION

In this study, we show that peripherin-2 forms a stable protein complex with both rhodopsin and the rod CNG channel in rod OS. Several lines of evidence support this conclusion. First, antibodies specific for the rod CNGB1a subunit immunoprecipitated rhodopsin from murine retinal lysates. Similarly, immunoprecipation with rhodopsin-specific antibodies pulled down CNGB1a. In both sets of experiments, peripherin-2 was

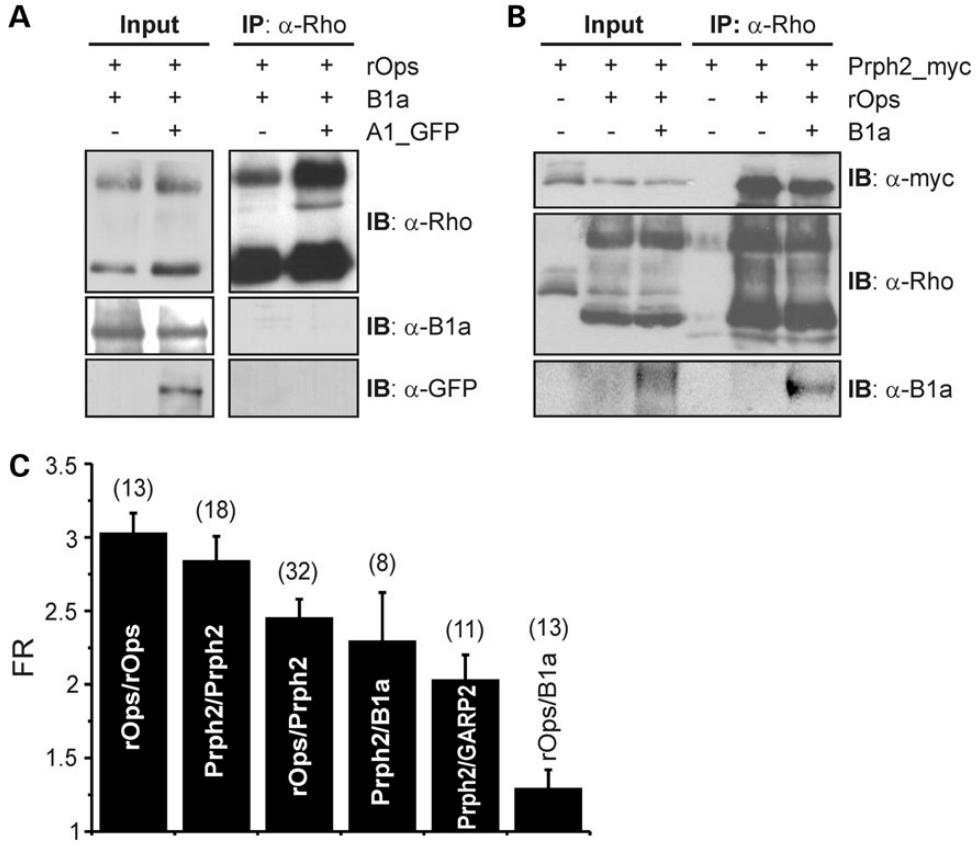

Figure 2. Peripherin-2 binds to both rod apo-opsin and CNGB1a. (**A**) Lysates from HEK293 cells co-transfected with rod apo-opsin (rOps), CNGB1a (B1a) and GFP-tagged CNGA1 (A1_GFP) were immunoprecipitated with α-Rho and probed with antibodies as indicated. (**B**) Co-IP from HEK293 cells co-expressing myc-tagged Prph2, rOps and B1a as indicated. Immunoprecipitates were analyzed with α-myc, α-Rho and α-B1a antibodies. Single transfection of peripherin-2 served as negative control for nonspecific binding to the beads (third lane from right). (**C**) FRET measurements from HEK293 cells co-transfected with different OS-specific proteins to monitor homomeric and heteromeric protein–protein interactions. Fret ratios for the single FRET pairs are as follows: rOps/rOps, FR = 3.03 ± 0.14; Prph2/Prph2, FR = 2.84 ± 0.17; rOps/Prph2, FR = 2.45 ± 0.13; Prph2/B1a, FR = 2.30 ± 0.33; Prph2/GARP2, FR = 2.03 ± 0.17; rOps/B1a, FR = 1.29 ± 0.13. Numbers of independent measurements (*n*) are given in brackets.

identified in the immunoprecipitated complex. Experiments in HEK293 cells revealed that rhodopsin does not directly bind to the CNG channel but rather requires peripherin-2 as a molecular linker to form a complex with the channel. FRET experiments strongly supported this 'bridging' function of peripherin-2. Based on our confocal FRET measurements, the relative binding affinity for the peripherin-2/rhodopsin interaction was in the similar range as for the rhodopsin/rhodopsin homomer. To the best of our knowledge, the absolute binding affinity of rhodopsin homomers was not determined so far. However, in our co-IP experiments, rhodopsin dimers and oligomers could be detected even under stringent SDS–PAGE and reducing conditions. Based on this, we expect the absolute binding affinity of rhodopsin homomers to be rather high. These results indicate that rhodopsin binds to peripherin-2 with a high affinity that is comparable with that of the rhodopsin homomer. Our biochemical and FRET experiments in isolated OSs strongly support the presence of rhodopsin dimers and oligomers in the native tissue. This is in line with recent studies providing strong evidence for the existence of rhodopsin dimers and oligomers in the native environment (9–11). In this study, we also identified the molecular determinants required for the rhodopsin/peripherin-2 interaction. As the major portion of both proteins is residing in the disk membrane of rod OS, it seems reasonable to assume that the interaction occurs via the transmembrane helices. In support of such a model, deletion of transmembrane domain 4 in peripherin-2 abolished binding to rhodopsin. Moreover, a single glycine to aspartate exchange at the position 266 in the TM4 of peripherin-2 that was previously reported in patients suffering from adRP (8) resulted in loss of binding to rhodopsin. Importantly, binding to CNGB1a was unaffected in the G266D mutant suggesting that the pathophysiological impact of this mutation relies on the impairment of the interaction with rhodopsin. The functional role of intradiskal and intracellular domains of peripherin-2 was examined in numerous studies (12). However, to our best knowledge, only one study addressed the role of a transmembrane domain of this protein showing that the glutamate residue at position 276 in TM4 was crucial for disk morphogenesis (13). Interestingly, the exchange of this charged amino acid to alanine (E276A) did not affect the interaction with rhodopsin. Similarly, the G266A mutation also had no effects on the peripherin-2/rhodopsin complex formation. These results suggest that introduction of charged residues on position 266 disrupts the binding of peripherin-2 to rhodopsin

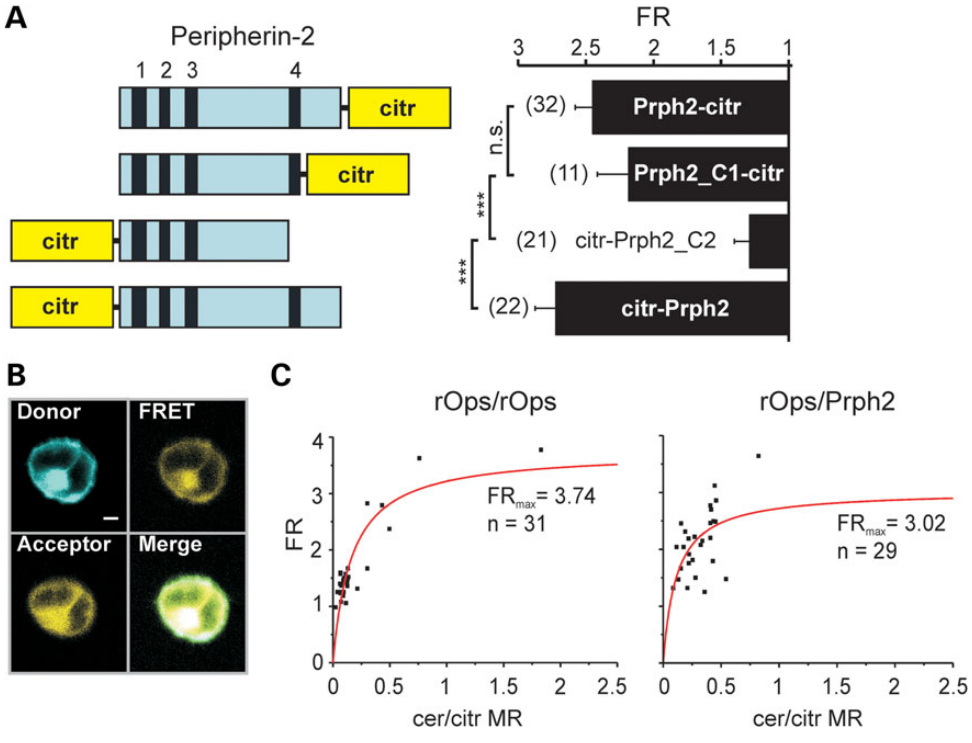

Figure 3. FRET-based determination of the binding characteristics of the rod opsin/peripherin-2 interaction. (**A**) *Left*, schematic representation of peripherin-2 constructs used to determine the FRs shown in the right panel. Citrine was fused to either the N- or C-terminus of peripherin-2. Numbered black boxes (1–4) represent the transmembrane domains of peripherin-2. *Right*, FR of the peripherin-2 constructs co-expressed with rOps-cerulean. Numbers of independent measurements (*n*) are given in brackets. Fret ratios for the single FRET pairs are as follows: rOps/Prph2-citr, FR = 2.45 ± 0.13; rOps/Prph2_C1-citr, FR = 2.19 ± 0.23; rOps/citr-Prph2_C2, FR = 1.29 ± 0.11; rOps/citr-Prph2, FR = 2.73 ± 0.15. (**B**) Representative confocal images of FRET channels (Donor, FRET, Acceptor and Merge) of single HEK293 cells used for the calculation of the FRs are shown in **C**. Scale bar = 3 μm. (**C**) Results of the confocal FRET imaging obtained from measurements of plasma membrane-restricted regions of single cells (black squares). FR was plotted against the cerulean/citrine molar ratio (cer/citr MR) to obtain FR_{max} and the binding curves.

whereas neutral amino acids at the same position do not affect this interaction. Taken together, our data point to a key role of TM4 for the peripherin-2/rhodopsin interaction and suggest that impaired binding to rhodopsin may contribute to the pathophysiology of peripherin-2 mutations.

As is evident in Figure 5C and D, two bands for wild-type peripherin-2 are detected in the inputs and co-IP experiments. The upper band of peripherin-2 is most likely not a result of glycosylation because our protein samples were deglycosylated prior to the SDS–PAGE. Intriguingly, the relative intensities of the two bands correlate with the number of negative charges in TM4. In the G266D mutant that contains two negative charges (E276 and D266), the upper band is stronger than the lower band. In contrast, in G266A and wild type containing one negative charge in TM4 (E276), the lower band is stronger than the upper band. Finally, in the E276A mutant containing no negative charge, only the lower band is visible. A potential effect of charges on the conformation and relative mobility of peripherin-2 would be in agreement with previous findings showing that single mutants can lead to a differential electrophoretic mobility of the corresponding protein (14).

Finally, we used FRET and immunoelectron microscopy to directly demonstrate that rhodopsin and CNGB1a are located in close proximity in rod OS. Overall, our results are consistent with the model shown in Figure 6. The novel aspect of this model is that peripherin-2 by binding to both, rhodopsin and the CNG channel, physically couples the most proximal protein of the light transduction cascade (rhodopsin) with the most distal protein (the CNG channel) in a narrow spatial microcompartment encompassing the disk rims and the neighboring plasma membrane. One could imagine two principal scenarios where the supramolecular organization of these proteins might be relevant. First, the complex could play a structural role in the formation and maintenance of rod OS structure. Mutations in peripherin-2 as well as in rhodopsin are associated with impaired disk morphogenesis and stability resulting in shortened and deteriorated rod OS (15–18). Structural impairments of OS are also seen upon mutation of ROM1, another photoreceptor-specific protein that binds to peripherin-2 (19), and in CNGB1a-knockout mice lacking the peripherin-2-binding GARP domain (20). Taken together, these findings imply that the integrity of the rhodopsin/peripherin-2/ROM1/CNG channel complex is crucial for morphogenesis and long-term stability of rod OS. Loss or functional impairment of any of the constituents of the complex will thus lead to more or less severe structural defects. In support to a structural role of the rhodopsin/peripherin-2 interaction, the addition of rhodopsin to the reconstituted peripherin-2/ROM1 complex in lipid vesicles was recently reported to induce the formation of disk rim-like structures *in vitro* (21).

The second scenario refers to a functional role of the complex in visual transduction. By binding to both, rhodopsin and the CNG channel, peripherin-2 helps to generate a microcompartment in

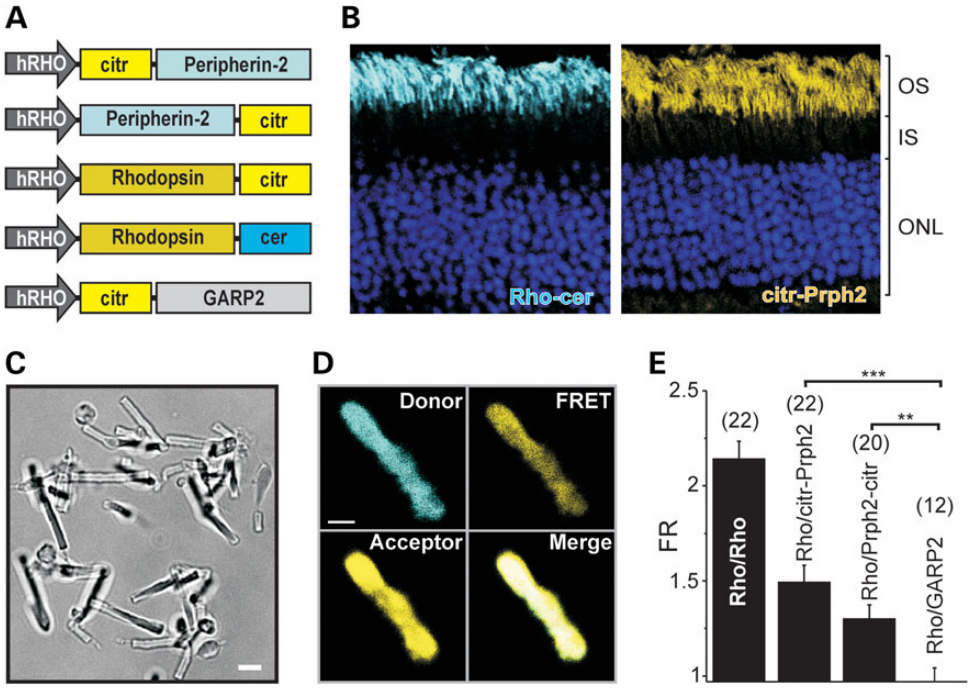

Figure 4. FRET in isolated rod OS from WT mice injected with different rAAV constructs. (**A**) Schematic view of the constructs used for the rAAV-mediated transduction of retinas from P14 C57/Bl6N WT mice. hRHO, human rhodopsin promoter. (**B**) Representative confocal images of retinal sections from mice expressing rhodopsin-cerulean (left) and citrin-peripherin-2 (right). OS, outer segment; IS, inner segment; ONL, outer nuclear layer. (**C**) Bright-field images of an isolated OS isolated from mouse retina. (**D**) Representative confocal image of a single OS used for FRET measurements and co-expressing rhodopsin-cerulean (donor) and peripherin-2-citrin (acceptor), respectively. Scale bar = 2 μm. (**E**) Results of the FRET measurements for different FRET pair combinations. Numbers of independent measurements (*n*) are given in brackets. FRET ratios for the single FRET pairs are as follows: Rho/Rho, FR = 2.14 ± 0.09; Rho/citr-Prph2, FR = 1.49 ± 0.09; Rho/Prph2-citr, FR = 1.30 ± 0.07; Rho/GARP2, FR = 0.97 ± 0.07.

the rim disk region that could have evolved to optimize the sensitivity and precision of light transduction. Recently, it was reported that a substantial portion of the rod phosphodiesterase (PDE6) is located at the disk rims of rod OS (22). GARP2 that was shown to bind PDE6, peripherin-2, and the CNG channel subunits (3,23,24) could serve as an adaptor protein that anchors PDE6 to the disk rim. Another study also reported a physical interaction of PDE6 and the rod CNG channel (25). The proposed complex would be exquisitely efficient because the distance between the light harvesting rhodopsin, the guanosine monophosphate (cGMP)-hydrolyzing PDE6 and the channel that translates changes in cGMP in changes of the Na^+/Ca^{2+} flux would be extremely short. In contrast to rhodopsin, the CNG channel and peripherin-2 were reported to be absent in the central disk region (2,26,27). Consequently, in this region, rhodopsin is physically uncoupled from the CNG channel. At the moment, only one can speculate about the exact functional role of the differential microcompartmentalization of rhodopsin in the central and peripheral part of the disks. Owing to the shorter diffusion distance for cGMP, however, the disk rim-associated complex is expected to operate at lower light intensities and faster kinetics. Such an optimization could be important in rods, which are tailored to detect extremely low light levels. In contrast, in the less light-sensitive cones, coupling of the light sensor to the channel seems less important. In agreement with this hypothesis, the cone CNG channel subunits lack the GARP domain that is required for the interaction with peripherin-2 (3,28,29).

MATERIALS AND METHODS

Animals

All procedures concerning animals were performed with permission of local authorities (Regierung von Oberbayern).

Molecular biology

Full-length CNGB1a, GARP2, peripherin-2 and rhodopsin were PCR-amplified from mouse retinal cDNA and subcloned into the pcDNA3.1Myc/His expression vector (Invitrogen). For FRET measurements and for *in vitro* co-IP studies, the FRET-optimized YFP and CFP derivatives citrine or cerulean (30–32) were introduced N- or C-terminally to the respective constructs by standard cloning procedures. Peripherin-2 deletion mutations were obtained by site-directed mutagenesis (QuikChange Lightning Mutagenesis Kit, Agilent Technologies) and overlap PCR techniques. All constructs amplified by PCR were completely sequenced prior to use. For the FRET studies on rod OS, the appropriate FRET constructs were subcloned to the previously described single-stranded pAAV2.1 vector (33) containing a human rhodopsin (hRHO) promoter.

Retina preparation and protein biochemistry

For *in vivo* co-IPs and for quantitative mass spectrometry, freshly dissected retinas were homogenized in 1% Triton X-100 solution under normal daylight illumination, which

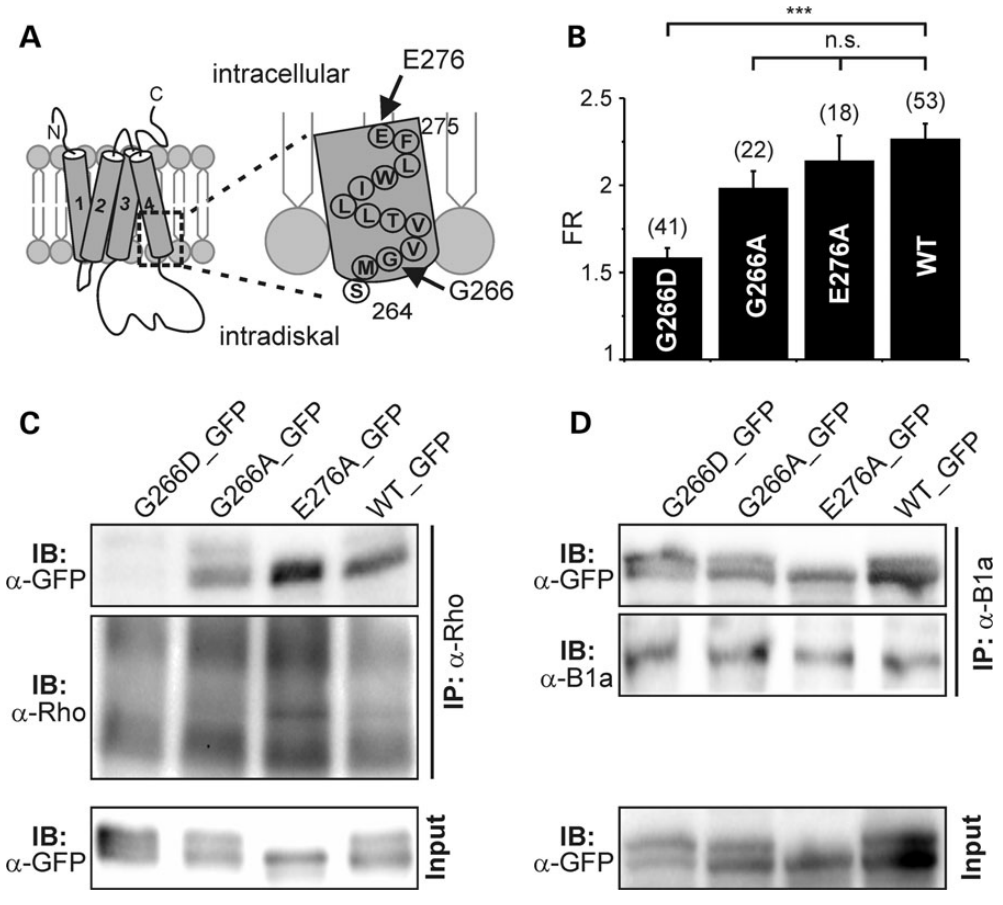

Figure 5. adRP-associated mutation in TM4 of peripherin-2 abolishes binding to rhodopsin. (**A**) Schematic view of the positions of the mutations in the TM4 of peripherin-2 analyzed in **B**–**C** (black arrows). (**B**) FRET experiment from HEK293 cells co-transfected with rod opsin and peripherin-2 wild-type (WT) or mutant constructs, respectively. FRET ratios for the single FRET pairs are as follows: Rho/G266D, FR = 1.58 ± 0.05; Rho/G266A, FR = 1.98 ± 0.09; Rho/E276A, FR = 2.14 ± 0.14; Rho/WT, FR = 2.26 ± 0.08. (**C**) Co-IP from HEK293 cells co-expressing rhodopsin and GFP-tagged wild-type or mutant peripherin-2 constructs. (**D**) Co-IP from HEK293 cells co-expressing CNGB1a and GFP-tagged wild-type or mutant peripherin-2 constructs. All peripherin-2 constructs in C and D were detected with the GFP-specific antibody (α-GFP).

results in bleached rhodopsin. Subsequently, cell debris was removed by 5000 × *g* centrifugation for 15 min, and protein concentration of the supernatant was determined by Bradford. For mass spectrometry, 50 µl of the magnetic beads (Dynabeads® Protein A, Invitrogen) were pre-incubated with 5 µg of the CNGB1 antibody (34) in a total volume of 500 µl of PBS for 2 h at 4°C. After the removal of PBS, the pre-coupled beads were incubated over night at 4°C with 500 µg of total retinal protein per single reaction. Next steps were performed according to manufacturer's instructions. After the removal of magnetic beads, the immunoaffinity purified proteins were analyzed via LC MS/MS as described previously (35).

For *in vivo* co-IP experiments, anti-B1a, anti-rhodopsin [mouse anti-Rho 1D4, Thermo Scientific) and anti-peripherin-2 (mouse anti-Prph2 2B7 (36)] antibodies were used followed by the same protocol as described earlier for the mass spectrometry. The anti-B1a antibody recognizes the distal C-terminus of the rod-specific CNGB1a and the olfactory-specific CNGB1b subunit (34). Immunopurified proteins were separated on a 6–12% SDS–PAGE gradient gel and proceeded for western blotting. Antibodies were used in the following dilutions: rabbit anti-B1a, 1 : 1000; mouse anti-Prph2, 1 : 1000; mouse anti-Rho, 1 : 2000; mouse anti-myc, 1 : 2000 (Cell Signaling); mouse anti-GFP (Clontech), 1 : 2000. *In vitro* co-IPs were performed as described previously (23). Rod opsin signals from untreated HEK293 protein lysates are detected as a smear on western blot owing to an extensive rod opsin glycosylation. Hence, prior to the sample loading to the SDS–PAGE gel, a deglycosylation step was included using PNGase F (New England Biolabs) according to the instructions of the manufacturer. For *in vitro* co-IPs with the anti-myc or anti-GFP antibody, the µMACS GFP or myc-tagged beads were used (Miltenyi Biotec). All steps were performed in accordance with the manufacturer's protocol.

Photometric FRET measurements

Digital FRET measurements were performed as described (37). For confocal FRET measurements, HEK293 cells were grown in 5-cm cell culture dishes (Greiner bio-one) and transiently transfected using the calcium phosphate method. After 24–48 h, the cells were washed and maintained in buffer solution composed of 140 mM NaCl, 5 mM KCl, 1 mM $MgCl_2$, 2 mM $CaCl_2$, 10 mM glucose, 10 mM Na-HEPES, pH 7.4, at room temperature.

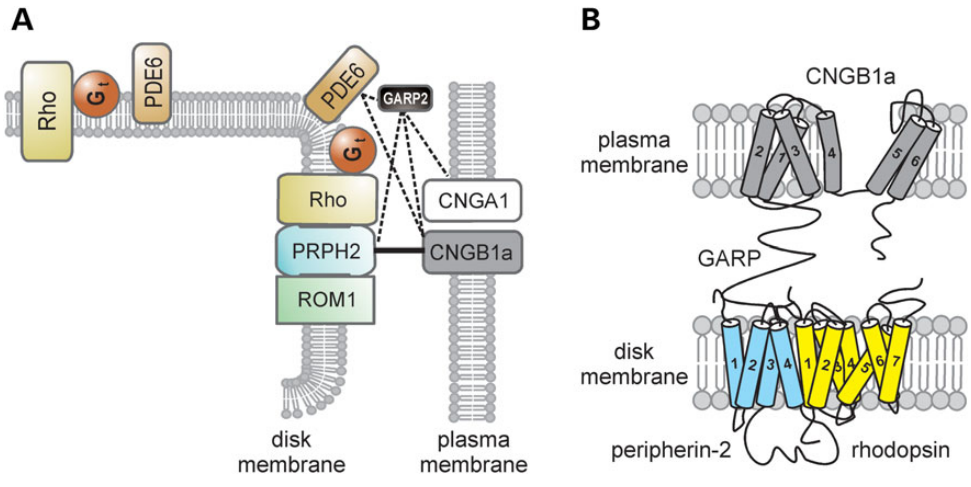

Figure 6. Peripherin-2 couples the CNG channel to the phototransduction cascade in rod OS. (**A**) Simplified paradigm of protein–protein interactions in the disk rim region of OS. Peripherin-2 simultaneously binds to its homolog ROM1, to CNGB1a and to rhodopsin. The soluble GARP2 undergoes multiple protein–protein interactions with CNGB1a, CNGA1, phosphodiesterase (PDE6) and peripherin-2 as indicated by the dashed line. Gt, transducin. (**B**) Tentative model of the CNGB1a/peripherin-2/rhodopsin complex. Note that the exact portion of rhodopsin that binds to TM4 of peripherin-2 is not known and is only tentatively assigned in this cartoon.

Cells were imaged using a Leica TCS SP8 confocal microscope with a 20× water objective (1.0 numerical aperture). Excitation of cerulean was performed with a 448-nm laser followed by emission measurements between 483 ± 16 nm. Citrine was excited with a 514-nm laser beam, and emission was measured between 542 ± 17 nm. FRET images were obtained by 448-nm excitation and 542 ± 17-nm emission. Cerulean, FRET and citrine images were acquired simultaneously, and all images were performed under the same laser intensity, photomultiplier gain and pinhole settings. The intensities of the signals were subtracted from the background, and FRs were calculated according to the three cube FRET equations described in (37). Cell membrane was defined as region of interest, and images of cells with over- or under-saturated cerulean or citrine signals were omitted from further analysis. For the conversion of fluorescence intensities obtained from measurements in cells expressing separate cerulean- and citrine-labeled proteins into molar cer/citr ratios, we used a correction factor, $R = 3$ (37). To calculate FR_{max} and to obtain the binding curves, FRs of the respective FRET pairs were plotted versus the cer/citr ratios and fitted to a hyperbolic function: $(P1 \times X)/(P2 + X)$. X is the FRET values of the single cells and P1 and P2 were calculated by 100 iterations for each FRET pair. P1 is the limiting value of the function and equals FR_{max}. For the determination of the relative binding affinity, the following equation was used: $(FR_{max}Prph2/FR_{max}rOps) \times 100$.

Statistics

All values are given as mean ± SE, and n is the number of animals or trials. Unless stated otherwise, an unpaired student's t-test was performed for the comparison between two groups. Statistical significance is given as follows: $^{*}P < 0.05$; $^{**}P < 0.01$; $^{***}P < 0.001$. If multiple comparisons were made, significance was tested by analysis of variance followed by Dunnett's test. For analysis of the LC MS/MS data, one-way ANOVA was used.

Preparation of OSs

Single retinas were dissected and transferred to 200 µl of PBS. The OSs were mechanically separated by mixing the solution for 10–20 s on a standard shaking device. The solution was spun for few seconds to remove cell debris. The supernatant containing the OSs was transferred to cell culture dishes (ibiTreat, ibidi, Martinsried, Germany). Prior to the FRET measurements, the OSs were allowed to sediment for ∼15 min.

rAAV preparation and subretinal injections

The production of single-strand AAVs and the procedure of subretinal injections were described previously (33). A total of 10^8–10^{10} rAAV particles were delivered by a single injection.

Immunoelectron microscopy

The preparation for immunoelectron microscopy was performed as previously described (38). Labeled LRWhite ultrathin sections were analyzed in a transmission electron microscope (Tecnai 12 BioTwin; FEI, Eindhoven, The Netherlands). Images were obtained with a charge-coupled device camera (SIS Megaview3; Surface Imaging Systems), acquired by analySIS (Soft Imaging System) and processed with Adobe Photoshop CS. Antibodies used were as follows: anti-B1a, anti-Rho and anti-Prph2 (PER5H2) (39).

SUPPLEMENTARY MATERIAL

Supplementary Material is available at *HMG* online.

ACKNOWLEDGEMENTS

We thank Berit Noack for excellent technical support. We also thank Muna Naash and Robert Molday for the gift of the peripherin-2 antibody.

Conflict of Interest statement. None declared.

FUNDING

This work was supported by the Deutsche Forschungsgemeinschaft; the FAUN-Stiftung, Nurnberg (to U.W.); the European Community FP7/2009/241955 (SYSCILIA) (to U.W.); and the Bundesministerium für Bildung und Forschung, (HOPE2) (grant number 0314106 to U.W.).

REFERENCES

1. Sung, C.H. and Chuang, J.Z. (2010) The cell biology of vision. *J. Cell Biol.*, **190**, 953–963.
2. Cook, N.J., Molday, L.L., Reid, D., Kaupp, U.B. and Molday, R.S. (1989) The cGMP-gated channel of bovine rod photoreceptors is localized exclusively in the plasma membrane. *J. Biol. Chem.*, **264**, 6996–6999.
3. Poetsch, A., Molday, L.L. and Molday, R.S. (2001) The cGMP-gated channel and related glutamic acid-rich proteins interact with peripherin-2 at the rim region of rod photoreceptor disc membranes. *J. Biol. Chem.*, **276**, 48009–48016.
4. Ritter, L.M., Khattree, N., Tam, B., Moritz, O.L., Schmitz, F. and Goldberg, A.F. (2011) In situ visualization of protein interactions in sensory neurons: glutamic acid-rich proteins (GARPs) play differential roles for photoreceptor outer segment scaffolding. *J. Neurosci.*, **31**, 11231–11243.
5. Boesze-Battaglia, K. and Goldberg, A.F. (2002) Photoreceptor renewal: a role for peripherin/rds. *Int. Rev. Cytol.*, **217**, 183–225.
6. Conley, S.M., Stuck, M.W. and Naash, M.I. (2012) Structural and functional relationships between photoreceptor tetraspanins and other superfamily members. *Cell Mol. Life Sci.*, **69**, 1035–1047.
7. Korschen, H.G., Beyermann, M., Muller, F., Heck, M., Vantler, M., Koch, K.W., Kellner, R., Wolfrum, U., Bode, C., Hofmann, K.P. *et al.* (1999) Interaction of glutamic-acid-rich proteins with the cGMP signalling pathway in rod photoreceptors. *Nature*, **400**, 761–766.
8. Sohocki, M.M., Daiger, S.P., Bowne, S.J., Rodriquez, J.A., Northrup, H., Heckenlively, J.R., Birch, D.G., Mintz-Hittner, H., Ruiz, R.S., Lewis, R.A. *et al.* (2001) Prevalence of mutations causing retinitis pigmentosa and other inherited retinopathies. *Hum. Mutat.*, **17**, 42–51.
9. Fotiadis, D., Liang, Y., Filipek, S., Saperstein, D.A., Engel, A. and Palczewski, K. (2003) Atomic-force microscopy: rhodopsin dimers in native disc membranes. *Nature*, **421**, 127–128.
10. Knepp, A.M., Periole, X., Marrink, S.J., Sakmar, T.P. and Huber, T. (2012) Rhodopsin forms a dimer with cytoplasmic helix 8 contacts in native membranes. *Biochemistry*, **51**, 1819–1821.
11. Suda, K., Filipek, S., Palczewski, K., Engel, A. and Fotiadis, D. (2004) The supramolecular structure of the GPCR rhodopsin in solution and native disc membranes. *Mol. Membr. Biol.*, **21**, 435–446.
12. Goldberg, A.F. (2006) Role of peripherin/rds in vertebrate photoreceptor architecture and inherited retinal degenerations. *Int. Rev. Cytol.*, **253**, 131–175.
13. Goldberg, A.F., Ritter, L.M., Khattree, N., Peachey, N.S., Fariss, R.N., Dang, L., Yu, M. and Bottrell, A.R. (2007) An intramembrane glutamic acid governs peripherin/rds function for photoreceptor disk morphogenesis. *Invest. Ophthalmol. Vis. Sci.*, **48**, 2975–2986.
14. Shi, Y., Mowery, R.A., Ashley, J., Hentz, M., Ramirez, A.J., Bilgicer, B., Slunt-Brown, H., Borchelt, D.R. and Shaw, B.F. (2012) Abnormal SDS-PAGE migration of cytosolic proteins can identify domains and mechanisms that control surfactant binding. *Protein Sci.*, **21**, 1197–1209.
15. Humphries, M.M., Rancourt, D., Farrar, G.J., Kenna, P., Hazel, M., Bush, R.A., Sieving, P.A., Sheils, D.M., McNally, N., Creighton, P. *et al.* (1997) Retinopathy induced in mice by targeted disruption of the rhodopsin gene. *Nat. Genet.*, **15**, 216–219.
16. Lem, J., Krasnoperova, N.V., Calvert, P.D., Kosaras, B., Cameron, D.A., Nicolo, M., Makino, C.L. and Sidman, R.L. (1999) Morphological, physiological, and biochemical changes in rhodopsin knockout mice. *Proc. Natl Acad. Sci. USA*, **96**, 736–741.
17. Sanyal, S. and Jansen, H.G. (1981) Absence of receptor outer segments in the retina of rds mutant mice. *Neurosci. Lett.*, **21**, 23–26.
18. Travis, G.H., Sutcliffe, J.G. and Bok, D. (1991) The retinal degeneration slow (rds) gene product is a photoreceptor disc membrane-associated glycoprotein. *Neuron*, **6**, 61–70.
19. Clarke, G., Goldberg, A.F., Vidgen, D., Collins, L., Ploder, L., Schwarz, L., Molday, L.L., Rossant, J., Szel, A., Molday, R.S. *et al.* (2000) Rom-1 is required for rod photoreceptor viability and the regulation of disk morphogenesis. *Nat. Genet.*, **25**, 67–73.
20. Zhang, Y., Molday, L.L., Molday, R.S., Sarfare, S.S., Woodruff, M.L., Fain, G.L., Kraft, T.W. and Pittler, S.J. (2009) Knockout of GARPs and the beta-subunit of the rod cGMP-gated channel disrupts disk morphogenesis and rod outer segment structural integrity. *J. Cell Sci.*, **122**, 1192–1200.
21. Kevany, B.M., Tsybovsky, Y., Campuzano, I.D., Schnier, P.D., Engel, A. and Palczewski, K. (2013) Structural and functional analysis of the native peripherin-ROM1 complex isolated from photoreceptor cells. *J. Biol. Chem.*, **288**, 36272–36284.
22. Chen, J., Yoshida, T. and Bitensky, M.W. (2008) Light-induced translocation of cyclic-GMP phosphodiesterase on rod disc membranes in rat retina. *Mol. Vis.*, **14**, 2509–2517.
23. Michalakis, S., Zong, X., Becirovic, E., Hammelmann, V., Wein, T., Wanner, K.T. and Biel, M. (2011) The glutamic acid-rich protein is a gating inhibitor of cyclic nucleotide-gated channels. *J. Neurosci.*, **31**, 133–141.
24. Pentia, D.C., Hosier, S. and Cote, R.H. (2006) The glutamic acid-rich protein-2 (GARP2) is a high affinity rod photoreceptor phosphodiesterase (PDE6)-binding protein that modulates its catalytic properties. *J. Biol. Chem.*, **281**, 5500–5505.
25. Bennett, N., Ildefonse, M., Crouzy, S., Chapron, Y. and Clerc, A. (1989) Direct activation of cGMP-dependent channels of retinal rods by the cGMP phosphodiesterase. *Proc. Natl Acad. Sci. USA*, **86**, 3634–3638.
26. Molday, R.S., Hicks, D. and Molday, L. (1987) Peripherin. A rim-specific membrane protein of rod outer segment discs. *Invest. Ophthalmol. Vis. Sci.*, **28**, 50–61.
27. Molday, R.S., Molday, L.L., Dose, A., Clark-Lewis, I., Illing, M., Cook, N.J., Eismann, E. and Kaupp, U.B. (1991) The cGMP-gated channel of the rod photoreceptor cell characterization and orientation of the amino terminus. *J. Biol. Chem.*, **266**, 21917–21922.
28. Conley, S.M., Ding, X.Q. and Naash, M.I. (2010) RDS in cones does not interact with the beta subunit of the cyclic nucleotide gated channel. *Adv. Exp. Med. Biol.*, **664**, 63–70.
29. Molday, R.S. and Molday, L.L. (1998) Molecular properties of the cGMP-gated channel of rod photoreceptors. *Vision Res.*, **38**, 1315–1323.
30. Griesbeck, O., Baird, G.S., Campbell, R.E., Zacharias, D.A. and Tsien, R.Y. (2001) Reducing the environmental sensitivity of yellow fluorescent protein mechanism and applications. *J. Biol. Chem.*, **276**, 29188–29194.
31. Rizzo, M.A., Springer, G.H., Granada, B. and Piston, D.W. (2004) An improved cyan fluorescent protein variant useful for FRET. *Nat. Biotechnol.*, **22**, 445–449.
32. Zacharias, D.A., Violin, J.D., Newton, A.C. and Tsien, R.Y. (2002) Partitioning of lipid-modified monomeric GFPs into membrane microdomains of live cells. *Science*, **296**, 913–916.
33. Koch, S., Sothilingam, V., Garcia Garrido, M., Tanimoto, N., Becirovic, E., Koch, F., Seide, C., Beck, S.C., Seeliger, M.W., Biel, M. *et al.* (2012) Gene therapy restores vision and delays degeneration in the CNGB1(−/−) mouse model of retinitis pigmentosa. *Hum. Mol. Genet.*, **21**, 4486–4496.
34. Huttl, S., Michalakis, S., Seeliger, M., Luo, D.G., Acar, N., Geiger, H., Hudl, K., Mader, R., Haverkamp, S., Moser, M. *et al.* (2005) Impaired channel targeting and retinal degeneration in mice lacking the cyclic nucleotide-gated channel subunit CNGB1. *J. Neurosci.*, **25**, 130–138.
35. Hauck, S.M., Dietter, J., Kramer, R.L., Hofmaier, F., Zipplies, J.K., Amann, B., Feuchtinger, A., Deeg, C.A. and Ueffing, M. (2010) Deciphering membrane-associated molecular processes in target tissue of autoimmune uveitis by label-free quantitative mass spectrometry. *Mol. Cell Proteomics*, **9**, 2292–2305.
36. Conley, S.M., Stricker, H.M. and Naash, M.I. (2010) Biochemical analysis of phenotypic diversity associated with mutations in codon 244 of the retinal degeneration slow gene. *Biochemistry*, **49**, 905–911.
37. Shaltiel, L., Paparizos, C., Fenske, S., Hassan, S., Gruner, C., Rotzer, K., Biel, M. and Wahl-Schott, C.A. (2012) Complex regulation of voltage-dependent activation and inactivation properties of retinal voltage-gated Cav1.4 L-type Ca2+ channels by Ca2+-binding protein 4 (CaBP4). *J. Biol. Chem.*, **287**, 36312–36321.
38. Wolfrum, U. and Schmitt, A. (2000) Rhodopsin transport in the membrane of the connecting cilium of mammalian photoreceptor cells. *Cell Motil. Cytoskeleton*, **46**, 95–107.
39. Connell, G., Bascom, R., Molday, L., Reid, D., McInnes, R.R. and Molday, R.S. (1991) Photoreceptor peripherin is the normal product of the gene responsible for retinal degeneration in the rds mouse. *Proc. Natl Acad. Sci. USA*, **88**, 723–726.

Human Molecular Genetics, 2016, Vol. 25, No. 12 2367–2377

doi: 10.1093/hmg/ddw103
Advance Access Publication Date: 30 March 2016
Original Article

ORIGINAL ARTICLE

Peripherin-2 differentially interacts with cone opsins in outer segments of cone photoreceptors

O.N. Phuong Nguyen[1,2], Sybille Böhm[1,2], Andreas Gießl[3], Elisabeth S. Butz[1,2], Uwe Wolfrum[4], Johann H. Brandstätter[3], Christian Wahl-Schott[1,2], Martin Biel[1,2,*] and Elvir Becirovic[1,2,*]

[1]Munich Center for Integrated Protein Science CIPS[M], 81377 München, Germany, [2]Department of Pharmacy—Center for Drug Research, Ludwig-Maximilians-Universität München, 81377 München, Germany, [3]Department of Biology, Animal Physiology, Friedrich-Alexander Universität Erlangen-Nürnberg, 91058 Erlangen, Germany and [4]Cell and Matrix Biology, Institute of Zoology, Johannes-Gutenberg Universität Mainz, 55128 Mainz, Germany

*To whom correspondence should be addressed at: Department Pharmazie—Pharmakologie für Naturwissenschaften, Ludwig-Maximilians-Universität München, Butenandtstr. 5-13, D-81377 München, Germany. Tel: +49-89-2180-77316; Fax: +49-89-2180-77326; Email: elvir.becirovic@cup.uni-muenchen.de (E.B); Department Pharmazie—Pharmakologie für Naturwissenschaften, Ludwig-Maximilians-Universität München, Butenandtstr. 5-13, D-81377 München, Germany. Tel: +49-89-2180-77328; Fax: +49-89-2180-77326; Email: martin.biel@cup.uni-muenchen.de (M.B)

Abstract

Peripherin-2 is a glycomembrane protein exclusively expressed in the light-sensing compartments of rod and cone photoreceptors designated as outer segments (OS). Mutations in peripherin-2 are associated with degenerative retinal diseases either affecting rod or cone photoreceptors. While peripherin-2 has been extensively studied in rods, there is only little information on its supramolecular organization and function in cones. Recently, we have demonstrated that peripherin-2 interacts with the light detector rhodopsin in OS of rods. It remains unclear, however, if peripherin-2 also binds to cone opsins. Here, using a combination of co-immunoprecipitation analyses, transmission electron microscopy (TEM)-based immunolabeling experiments, and quantitative fluorescence resonance energy transfer (FRET) measurements in cone OS of wild type mice, we demonstrate that peripherin-2 binds to both, S-opsin and M-opsin. However, FRET-based quantification of the respective interactions indicated significantly less stringent binding of peripherin-2 to S-opsin compared to its interaction with M-opsin. Subsequent TEM-studies also showed less co-localization of peripherin-2 and S-opsin in cone OS compared to peripherin-2 and M-opsin. Furthermore, quantitative FRET analysis in acutely isolated cone OS revealed that the cone degeneration-causing V268I mutation in peripherin-2 selectively reduced binding to M-opsin without affecting the peripherin-2 interaction to S-opsin or rhodopsin. The differential binding of peripherin-2 to cone opsins and the mutant-specific interference with the peripherin-2/M-opsin binding points to a novel role of peripherin-2 in cones and might contribute to understanding the differential penetrance of certain peripherin-2 mutations in rods and cones. Finally, our results provide a proof-of-principle for quantitative FRET measurements of protein-protein interactions in cone OS.

Introduction

Rod and cone photoreceptors are the light sensing cells of the retina conferring dim and daylight/color vision, respectively. The tetraspanin peripherin-2 (PRPH2) is a glycosylated membrane protein localized in the light detecting compartments of rods and cones referred to as outer segments (OS). Mutations in

Received: February 2, 2016. **Revised:** March 16, 2016. **Accepted:** March 17, 2016

PRPH2 are among the leading causes of autosomal dominant degenerative retinal disorders, which can either affect rod or cone photoreceptors (1,2). PRPH2 mutations primarily affecting the rods almost exclusively lead to autosomal dominant retinitis pigmentosa (adRP), a disease characterized by a progressive rod degeneration. In contrast, PRPH2 mutations primarily affecting the cones often result in adult vitelliform macular dystrophy (AVMD). Recently, we demonstrated that the differential penetrance of PRPH2 mutations in rods and cones can partially be explained by differential effects of the single mutations on mRNA splicing in the affected photoreceptors (3). However, some of the mutants did not exert an effect on mRNA splicing suggesting additional disease mechanisms. In another study, we identified the rod-specific light detecting G-protein coupled receptor rhodopsin as a novel PRPH2 interacting protein in OS of rods. In addition, we showed that the adRP-causing G266D mutation in transmembrane domain 4 (TM4) of PRPH2 specifically disrupted this binding (4). Other studies identified the soluble variant of the glutamic acid-rich protein (GARP2), the GARP-region containing rod cyclic nucleotide-gated (CNG) channel B-subunit (CNGB1a), the PRPH2 homologue ROM-1 and melanoregulin as proteins interacting with PRPH2 in rods (5–7). However, with the exception of ROM-1 (8,9), no additional PRPH2 interacting proteins were found in cones. Comprehensive analysis of protein-protein interactions in cones has been hampered by technical limitations as cones account for a very small percentage of photoreceptors in mammals (~3%, (10)). Furthermore, compared with rods, OS of cones are smaller in both, length and diameter (http://webvision.med.utah.edu/book/part-v-phototransduction-in-rods-and-cones/phototransduction-in-rods-and-cones/). Cone OS often contain phototransduction proteins which are homologous to the members of the rod phototransduction cascade. The rhodopsin homologous proteins in cones are referred to as cone opsins. Cones of most mammals express two different types of opsins, which differ in their light absorption spectra: the middle wavelength absorbing M-opsin and the short wavelength absorbing S-opsin (10). Based on the relatively low homology between rhodopsin and cone opsins, it is unclear whether PRPH2 binds to cone opsins *in vivo*. Here, using different methodological approaches including quantitative fluorescence resonance energy transfer (FRET) measurements in transduced cone OS, we provide evidence that PRPH2 binds to both, M-opsin and S-opsin, albeit the binding to M-opsin was significantly stronger throughout all experiments. We also show that the AVMD-linked V268I mutant in TM4 of PRPH2 selectively attenuates binding to M-opsin. These results provide novel insights into the physiology and pathophysiology of PRPH2 in cones. Finally, our study shows that FRET-based approaches are well suited to quantitatively analyze protein-protein interactions *in vivo* in small cellular compartments like cone OS.

Results

Co-immunoprecipitation analysis of the PRPH2/opsin interaction in transiently transfected HEK293 cells

In an attempt to examine the interaction of PRPH2 with cone opsins, we transiently co-expressed murine C-terminally myc-tagged PRPH2 with murine C-terminally GFP-tagged M- or S-opsin in HEK293 cells (Fig. 1A). Reciprocal co-immunoprecipitations (co-IPs) on membrane preparations with either a GFP- or myc-specific antibody revealed robust interaction of PRPH2 with both opsins (Fig. 1B–E). Importantly, no interaction was observed when co-expressing PRPH2 with C-terminally GFP-tagged HCN2, (hyperpolarization-activated cyclic nucleotide-gated cation channel, subunit 2), another unrelated transmembrane protein shown to be expressed in the retina (Fig. 1F and G) (11).

Given the high structural homology of photoreceptor opsins, it appeared reasonable to assume that cone disease-linked mutations in TM4 of PRPH2 might also interfere with binding to cone opsins. Screening of TM4-specific PRPH2 mutations identified one AVMD-associated mutant very close to the adRP-linked G266D mutation. This mutation leads to a valine to isoleucine exchange at position 268 (V268I, Fig. 2A). Cross-species alignment revealed a 100% conservation of this valine residue among mammals and birds, whereas zebrafish and *Xenopus laevis* contain methionine or leucine at this position (Fig. 2B). However, isoleucine is not present at position 268 in any of the species.

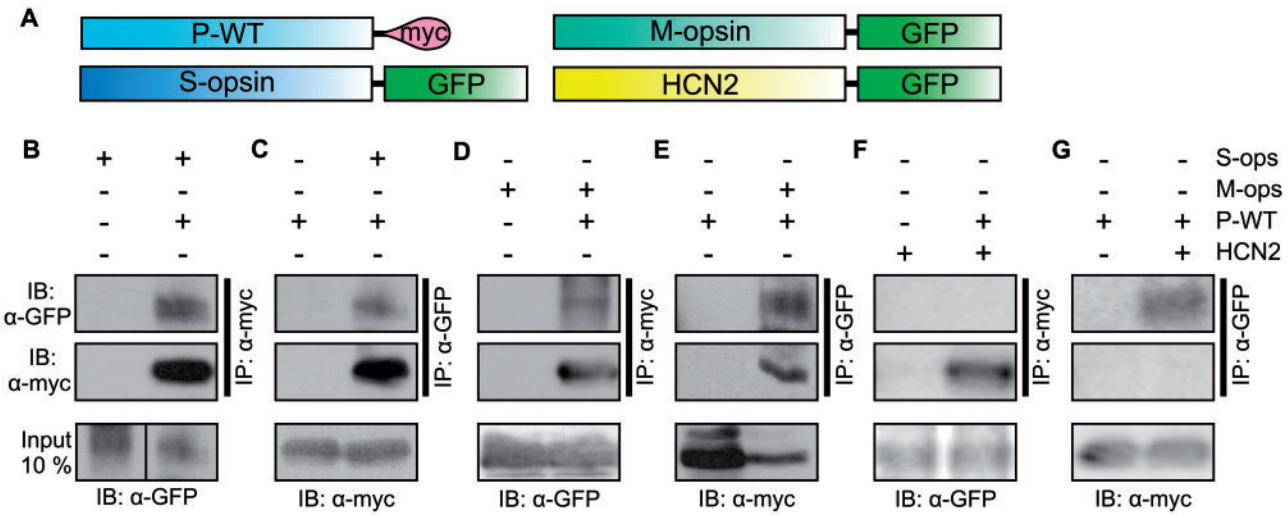

Figure 1. Reciprocal co-IPs from transfected HEK293 cells indicate stable PRPH2/cone opsin interaction. (**A**) Scheme of the C-terminally myc-tagged WT PRPH2 (P-WT) and C-terminally GFP-tagged M-opsin, S-opsin and HCN2 constructs used for the co-IPs shown in **B–G**. B–G, co-IPs using membrane preparations from HEK293 cells co-transfected P-WT/S-opsin (B and C), P-WT/M-opsin (D and E), and P-WT/HCN2 (F and G) combinations and the single transfected respective controls. For co-IPs, myc (α-myc, B, D and F) or GFP (α-GFP, C, E and G) specific antibodies were used. IB, immunoblotting; IP, immunoprecipitation.

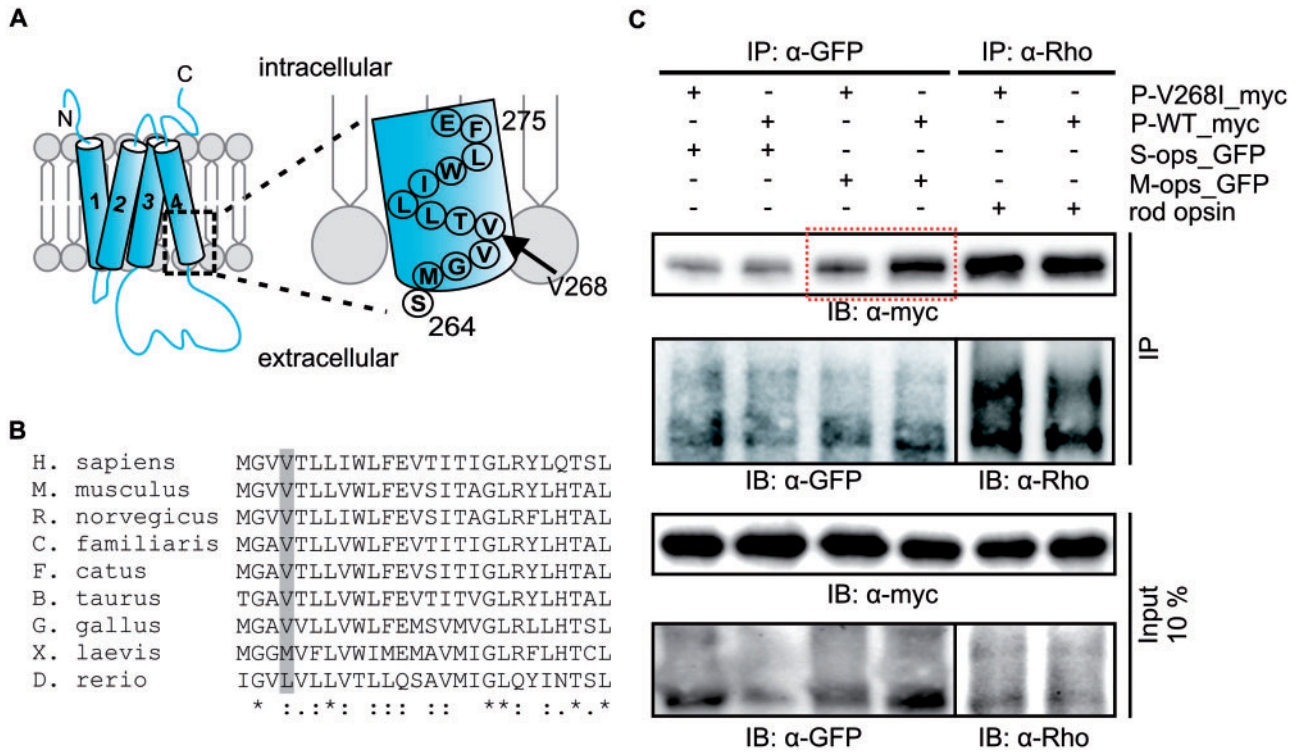

Figure 2. WT and V268I mutant differentially bind to cone opsins. (**A**) Schematic illustration of the mutant position in TM4 of PRPH2. (**B**) clustal cross-species sequence alignment (Clustal Omega 1.2.1) of TM4 shows high conservation of the valine at position 268 among representative mammals and birds. In Xenopus laevis and zebrafish, this position is occupied by methionine and leucine, respectively. (**C**) co-IPs using membrane preparations from HEK293 cells co-transfected with different combinations of C-terminally myc-tagged WT or V268I PRPH2 mutant and C-terminally GFP-tagged cone opsins or untagged rod opsin as indicated. PRPH2 constructs co-transfected with cone opsins were immunoprecipitated with a GFP antibody (left panel), those co-transfected with rod opsin were immunoprecipitated with a rhodopsin-specific antibody (α-Rho, Rho1D4). The IP showing the reduced binding of the V268I mutant to M-opsin is highlighted in a red dashed box.

Given that the cone dominant symptoms of the V268I mutant in affected individuals are caused by changes in binding to opsins, we hypothesized that such changes should be restricted to cone opsins and should not affect the PRPH2/rhodopsin interaction. To test this assumption, we co-expressed wild type (WT) PRPH2 and the V268I mutant with chromophore-free S-opsin, M-opsin and rod apo-opsin (herein referred to as rod opsin) in HEK293 cells and conducted another set of co-IP experiments. As expected, no differences in binding of WT and V268I mutant to rod opsin could be detected (Fig. 2C). However, this mutation revealed differential effects on the binding to cone opsins. Interestingly, whereas the interaction of the V268I mutant to M-opsin was significantly reduced, no significant changes could be observed with respect to its binding to S-opsin. In addition to these mutant-specific differences, we also detected differences in the binding of WT PRPH2 to the single opsins. In this context, the strongest binding was detectable for the PRPH2/rod opsin interaction followed by the PRPH2/M-opsin and PRPH2/S-Opsin interaction (Fig. 2C). Together, these results indicate that PRPH2 differentially binds to cone opsins and that the V268I mutant specifically deteriorates the PRPH2/M-opsin binding.

FRET-based quantification of WT and V268I PRPH2/opsin binding in transiently transfected HEK293 cells

To quantify the single interactions, we performed FRET measurements of the respective PRPH2/opsin combinations in transfected HEK293 cells. For this purpose, we used WT or mutant PRPH2 constructs C-terminally tagged with cerulean and C-terminally citrine-tagged opsins, respectively (Fig. 3A). The single PRPH2 and opsin constructs were robustly expressed and largely co-localized in HEK293 cells (Fig. 3B). Importantly, subsequent results of the FRET measurements in living HEK293 cells nicely confirmed our observations obtained from co-IP experiments. First, robust FRET signals, plotted as FRET ratios (FRs) (4), could be measured for all WT PRPH2/opsin interactions (Fig. 3C). Very similar to the co-IP results, the highest FR could be detected for the PRPH2/rod opsin interaction ($FR = 2.57 \pm 0.15$) and the lowest FR for the PRPH2/S-opsin FRET pair ($FR = 1.53 \pm 0.04$). Second, compared to the WT PRPH2/M-opsin FR ($FR = 2.01 \pm 0.11$), the V268I/M-opsin FR was significantly reduced ($FR = 1.34 \pm 0.14$). In contrast, no significant changes could be obtained when comparing WT and V268I mutant with regard to their binding to rod opsin or S-opsin (V268I/rod opsin, $FR = 2.54 \pm 0.18$, V268I/S-opsin, $FR = 1.13 \pm 0.10$). Taken together, FRET measurements from transfected HEK293 cells consistently confirm the co-IP results showing differential effects of WT and V268I mutant PRPH2 binding to rod or cone opsins.

In vivo co-IP and TEM studies of the PRPH2/opsin interaction in cones

To analyze if cone opsins also interact with PRPH2 *in vivo*, we conducted co-IPs from membrane preparations of 8-week old WT mice using the PRPH2-specific antibody (Prph2 2B7, (12)). This approach led to a robust enrichment of the M-opsin band and to a faint, but detectable band for S-opsin (Fig. 4A). This result is compatible with our data from HEK293 cells suggesting

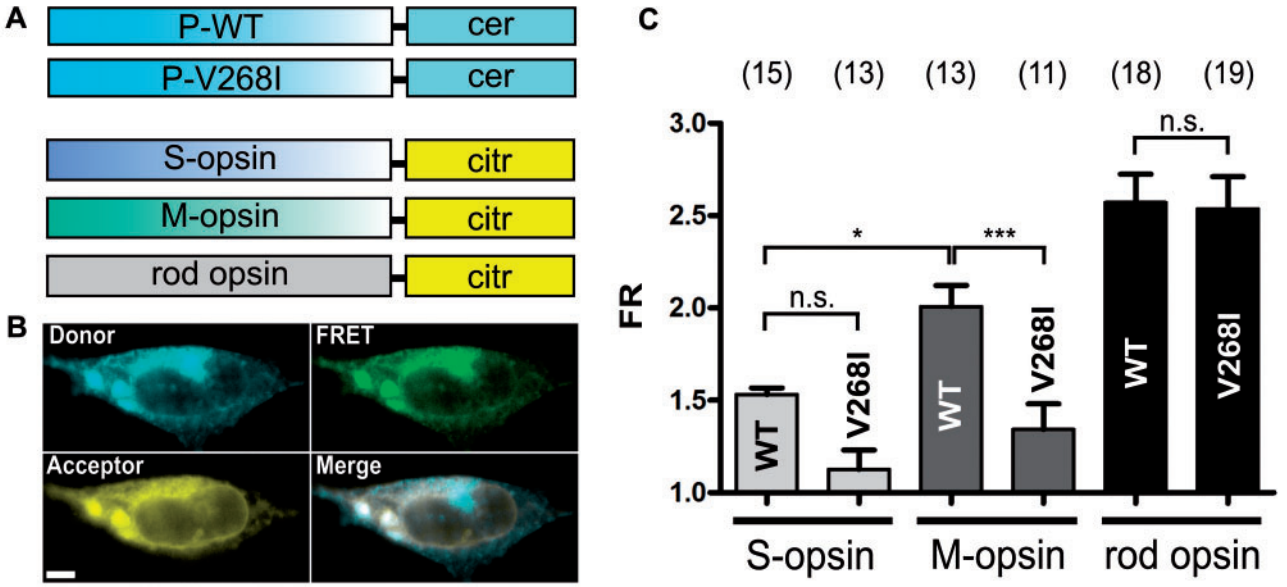

Figure 3. FRET-based quantification of WT and V268I mutant interactions with rod opsin and cone opsins. (**A**) Scheme of PRPH2 and opsin constructs used to determine the FRs shown in C. The FRET donor cerulean was C-terminally fused to WT or mutant PRPH2. The opsins were C-terminally fused to the FRET acceptor citrine. (**B**) Representative live confocal images showing FRET channels (Donor, FRET, Acceptor and Merge) from HEK293 cells co-transfected with one combination of the PRPH2 and opsin constructs shown in A. Scale bar represents 3 μm. (**C**) FRET-based quantification of the single combinations as indicated. The mean values of the single measurements are plotted as FRs with the number of independently measured cells for each construct given in brackets. Statistical analysis was performed using one way ANOVA followed by the Tukey's multiple comparison test. FRs and FRET efficiencies (E_A) for the single FRET pairs are as follows: P-WT/S-opsin, FR = 1.53 ± 0.04; E_A = 2.98% ± 0.08%; P-V268I/S-opsin, FR = 1.13 ± 0.10; E_A = 0.73% ± 0.06%; P-WT/M-opsin, FR = 2.01 ± 0.11; E_A = 5.69% ± 0.31%; P-V268I/M-opsin, FR = 1.34 ± 0.14; E_A = 1.91% ± 0.20%; P-WT/rod opsin, FR = 2.57 ± 0.15; E_A = 8.84% ± 0.52%; P-V268I/rod opsin, FR = 2.54 ± 0.18; E_A = 8.67% ± 0.61%;. *P*-values between the single FRET combinations are as follows, P-WT/S-opsin and P-V268I/S-opsin, $P = 0.0626$; P-WT/M-opsin and P-V268I/M-opsin, $P = 0.0002$; P-WT/S-opsin and P-WT/M-opsin, $P = 0.0106$; P-WT/rod opsin and P-V268I/rod opsin, $P = 0.8786$. *, $P < 0.05$; **, $P < 0.01$; ***, $P < 0.001$. n.s., not significant.

strong binding of PRPH2 to M-opsin and weaker binding to S-opsin. To confirm this finding with another method, we performed immunogold TEM-based staining on cone OS from 8-week old WT mice using the same PRPH2, M-opsin and S-opsin antibodies as for co-IPs (Fig. 4B). The specificity of each antibody was tested on post-embedded sections of photoreceptor OS using single antibodies coupled to immunogold particles. In line with previous studies, PRPH2 staining was almost exclusively observed in the rim regions of photoreceptor OS (Supplementary Material, Fig. S1A) (13,14). However, given the fact that PRPH2 is expressed in rods and cones, this approach does not allow to undoubtedly discriminate between the OS of these two photoreceptor types. Moreover, the identification of cone OS is strongly hampered by a very low number of this photoreceptor type in the mammalian retina. Hence, to identify cone OS among the photoreceptor OS, we performed immunogold stainings using M-opsin and S-opsin antibodies. In contrast to PRPH2, staining was restricted to few clearly shaped regions in the OS layer most likely representing cones (Supplementary Material, Fig. S1B and C). Having shown the specificity of the single antibodies, we next set out to identify and quantify PRPH2 and opsin co-localization in cone OS. To this end, we performed co-labeling experiments using immunogold particles of different size. Large particles were coupled to the PRPH2 antibody and small particles to M-opsin or S-opsin antibodies, respectively. Importantly, using this approach we could observe co-staining of PRPH2 with both opsin types (Fig. 4B). However, quantitative analysis of PRPH2 co-localizing with cone opsins revealed a co-labeling percentage of 49% ± 0.04% for PRPH2/M-opsin, which was significantly higher than the percentage of the PRPH2/S-opsin co-localization (29% ± 0.08%, Fig. 4C). Of note, our TEM data suggest that PRPH2 is present on both, opened and closed sites of the cone OS rims. This strongly indicates that PRPH2 localization in mammalian cone OS is not identical to that in Xenopus laevis, showing unilateral PRPH2 localization exclusively in the closed OS rims of cones (2,15). Taken together, *in vivo* co-IP and TEM data strongly support the results from HEK293 cells suggesting lower binding affinities for the PRPH2/S-opsin interaction compared with the PRPH2/M-opsin binding.

Ciliary transport and mRNA splicing of the V268I mutant in photoreceptors

The results from transfected HEK293 cells indicated that the V268I mutation selectively deteriorates the binding of PRPH2 to M-opsin. However, it is conceivable that the potential pathogenetic effects of this mutation are different *in vivo*. Some PRPH2 mutations have been shown to influence the transport of PRPH2 to the OS of rods or cones (3,8,16). To analyze the effects of the V268I mutant on protein transport, we expressed the mutant in rods and cones using recombinant adeno-associated virus (rAAV)-mediated gene transfer. The rAAV particles containing the C-terminally cerulean-tagged V268I mutant driven by rod- or cone-specific promoters (human rhodopsin, hRHO and mouse short wavelength opsin, mouse SWS (mSWS), respectively) were subretinally injected in 2-week old WT mice. Three weeks post injection, retinas were dissected and used for subsequent immunolabeling with the CNGB1a antibody as marker for rod OS and M-opsin and S-opsin antibodies as marker for cone OS, respectively. Importantly, the V268I mutant fully co-localized with rod or cone OS markers indicating no transport deficits for this mutant (Fig. 5A and B, Supplementary Material, Fig. S2A).

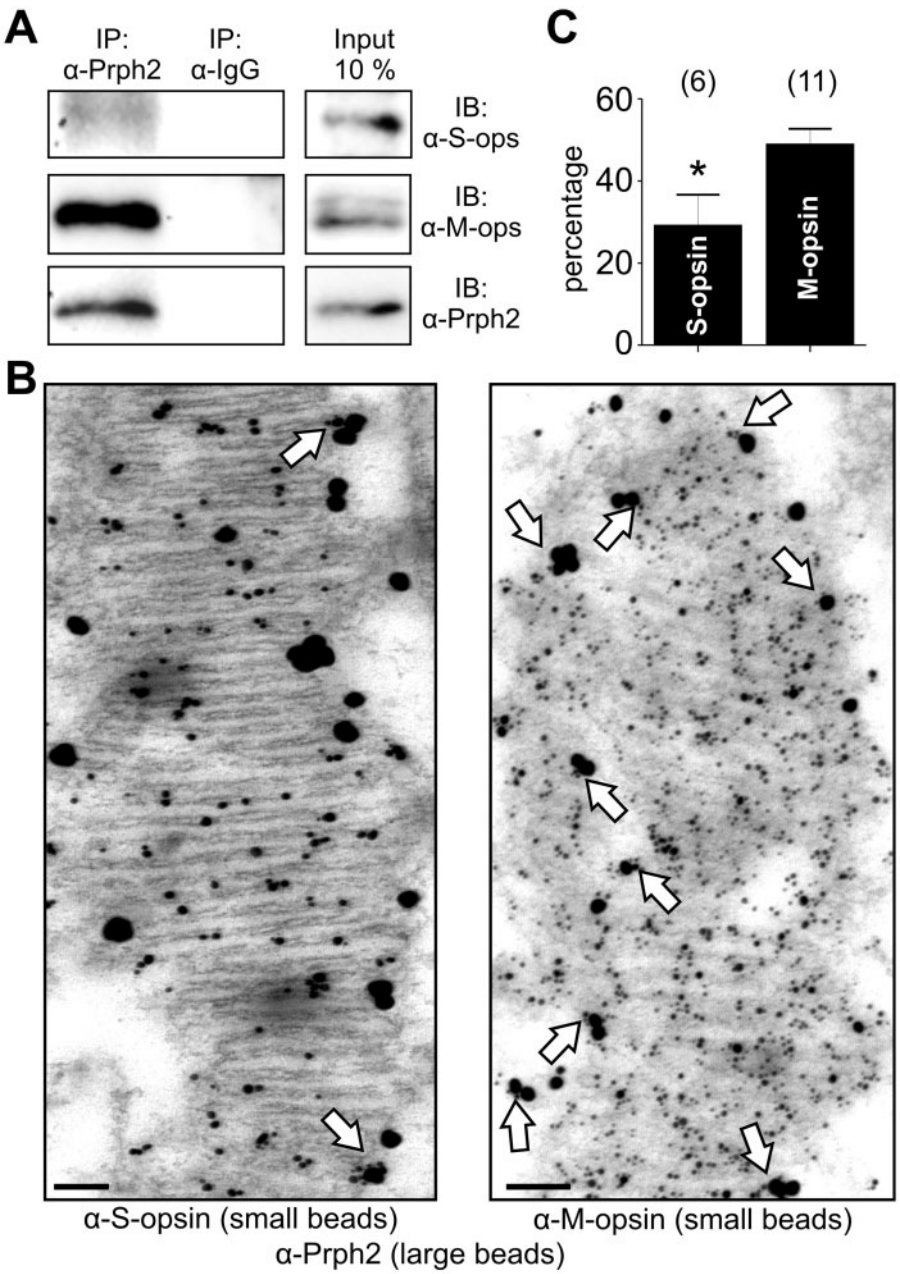

Figure 4. *In vivo* co-IP and TEM images of cone OS co-immunolabeled with PRPH2 and cone opsin antibodies. (**A**) co-IPs using membrane preparations from isolated retinas of light-adapted 8-week old C57/BL6J WT mice. Immunoprecipitation was conducted with the PRPH2-specific antibody (α-Prph2, Prph2 2B7). Control co-IP was performed with IgGs (α-IgG). (**B**) Representative TEM images of post-embedded longitudinal cone OS sections from 8-week old light-adapted WT mice co-labeled with large diameter gold particles coupled to the PRPH2 antibody and small diameter gold particles coupled to M-opsin (α-M-opsin) or S-opsin (α-S-opsin) specific antibody, respectively. The specificity of the antibodies was proven in Supplementary Material, Figure S1 showing TEM images of photoreceptor OS labeled with the single antibodies. White arrows indicate co-localization of large and small gold particles. Scale bar = 100 nm. (**C**) quantification of the PRPH2/cone opsin co-localization. Shown are the co-localization percentages of PRPH2/S-opsin and PRPH2/M-opsin gold particles originating from 6 (PRPH2/S-opsin) or 11 (PRPH2/M-opsin) different cone OS. The total number of gold particles counted was 58 for PRPH2/S-opsin and 178 for PRPH2/M-opsin, respectively. Statistical analysis was done with the unpaired Student's *t*-test, $P = 0.0195$.

Recently, we demonstrated that the cone dominance of some PRPH2 mutants goes along with their specific effects on mRNA splicing. In this context, we provided evidence for three different splice isoforms of PRPH2 to exist in rods and cones, which include the unspliced, the intron 1 retention, and the correctly spliced variant. In particular, some of the mutants associated with cone diseases led to increased splice efficiencies of the correctly spliced PRPH2 variant in cones, which represents the only splice isoform translated into protein (3). To exclude any effects of the V268I mutant on mRNA splicing, we performed splicing analysis in cones of WT mice transduced with the same PRPH2 minigenes under the same conditions as described (3). The analysis of mRNA splicing of all three PRPH2 isoforms revealed no changes between the V268I mutant and its WT counterpart (Supplementary Material, Fig. S3A–D). Taken together, we could exclude effects of the V268I mutation on

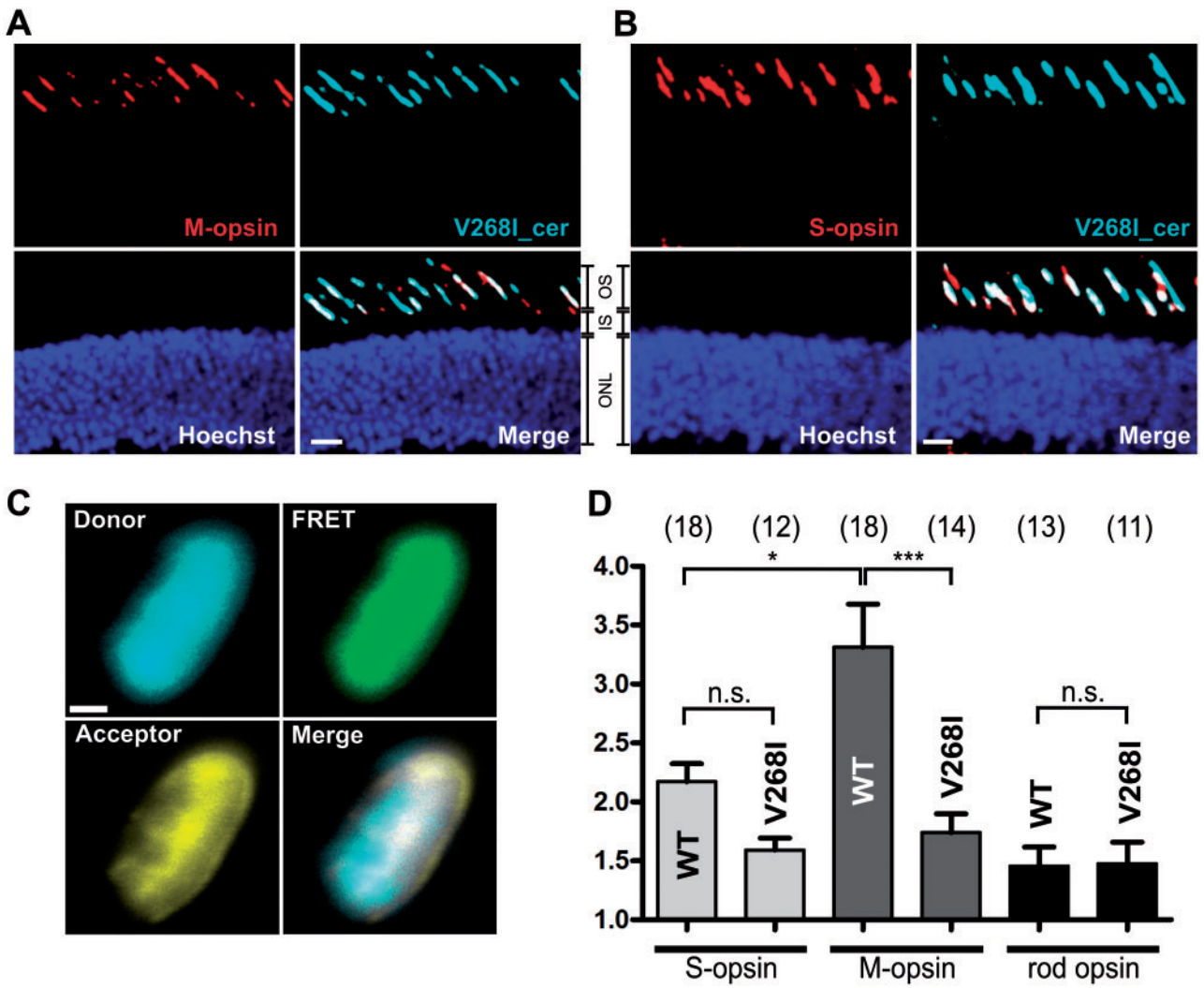

Figure 5. Expression of the V268I mutant in murine cones and FRET-based quantification of WT and V268I mutant interactions in isolated cone OS. (**A** and **B**) Representative confocal images of co-immunolabeled retinal sections from subretinally rAAV-injected C57/BL6J WT mice expressing C-terminally cerulean-tagged V268I mutant (V268I_cer) under the control of the mSWS promoter. Immunolabeling was performed on retinal cryosections of light-adapted animals 3 weeks post injection using M-opsin (A) or S-opsin (B) antibodies described in Figure 4. The expression of the mutant was visualized by cerulean fluorescence. OS, outer segment. IS, inner segment. ONL, outer nuclear layer. Scale bar = 5 μm. **C**, Representative confocal FRET channel images from isolated cone OS of rAAV-injected C57/BL6J WT mice co-expressing one combination of the FRET constructs described in Figure 3A under the control of the mSWS promoter. Scale bar = 1 μm. **D**, FRET-based quantification of the single combinations as indicated. The mean values of the single measurements are plotted as FRs with the number of independently measured cone OS for each combination given in brackets. Statistical analysis was performed using one way ANOVA followed by the Tukey's multiple comparison test. FRs and FRET efficiencies for the single FRET pairs are as follows: P-WT/S-opsin, FR = 2.17 ± 0.15; E_A = 6.59% ± 0.46%; P-V268I/S-opsin, FR = 1.59 ± 0.10; E_A = 3.32% ± 0.21%; P-WT/M-opsin, FR = 3.31 ± 0.37; E_A = 13.01% ± 1.45%; P-V268I/M-opsin, FR = 1.74 ± 0.16; E_A = 4.12% ± 0.38%; P-WT/rod opsin, FR = 1.46 ± 0.16; E_A = 2.59% ± 0.28%; P-V268I/rod opsin, FR = 1.48 ± 0.18; E_A = 2.70% ± 0.33%. *P*-values between the single FRET combinations are as follows, P-WT/S-opsin and P-V268I/S-opsin, $P = 0.4263$; P-WT/M-opsin and P-V268I/M-opsin, $P = 0.0001$; P-WT/S-opsin and P-WT/M-opsin, $P = 0.0126$; P-WT/rod opsin and P-V268I/rod opsin, $P = 0.9323$. *, $P < 0.05$; **, $P < 0.01$; ***, $P < 0.001$. n.s., not significant.

protein transport and mRNA splicing suggesting other disease mechanisms for this mutant.

FRET measurements of WT and V268I PRPH2/opsin interactions in murine photoreceptors

In our previous study, we demonstrated that quantitative FRET can in principle be used for analysis of protein-protein interactions in acutely isolated rod OS (4). Given the very low percentage of cones (~3%) and the smaller size of cone OS in the mammalian retina, it is unclear whether FRET measurements are also suitable for detection and quantification of protein-protein interactions in cone OS. Hence, we set out to establish FRET-based analysis of protein-protein interactions in isolated cone OS. To this end, we transduced cones with the same PRPH2/cone opsin FRET combinations as shown in Figure 3A using the rAAV-mediated gene transfer. All PRPH2/cone opsin FRET constructs were driven by the mSWS promoter. To analyze the effects of the V268I mutant on rhodopsin binding in rod OS, the respective WT and V268I FRET constructs were virally transduced to rods using the hRHO promoter. The titer-matched rAAV particles (10^{10} particles/injection) containing the FRET pairs were subretinally injected in 2-week old WT mice. Four weeks post injection, the OS of four pooled retinas for each FRET pair were isolated with the self-designed quick protocol as

described (4). Importantly, to ensure for comparability, FRET measurements of all constructs were conducted on the same day under the same conditions. The FRET approach addressing the PRPH2 WT or V268I/rhodopsin interaction in rods (Supplementary Material, Fig. S2B) led to a large number of labeled rod OS showing high co-expresssion rates of citrine and cerulean fluorophores up to 90%. Similar co-transduction rates in rods were observed in our recent study (4). As expected, in experiments addressing PRPH2 WT or V268I/cone opsin interaction, the vast majority of the isolated OS originated from rods and did not show any fluorescence (data not shown). Occasionally, we observed citrine or cerulean fluorescence in small-sized OS-like structures most likely representing the OS of cones (Fig. 5C). In contrast to rods, the percentage of cone OS co-expressing both FRET fluorophores was markedly lower (up to 30%). Despite the lower co-transduction efficiency of the FRET fluorophores, this approach led to the identification of a sufficient number of cone OS, enabling a comparative and quantitative analysis of the single protein-protein interactions. Overall, the resulting FRET measurements from isolated OS are largely comparable to those obtained from the HEK293 cells (Fig. 5D). First, for WT PRPH2, a robust FRET signal could be obtained with both M-opsin and S-opsin indicating that these proteins indeed interact *in vivo*. Quantitatively, however, the FR of PRPH2/M-opsin (FR = 3.31 ± 0.37) was significantly higher than that of the PRPH2/S-opsin (FR = 2.17 ± 0.15) FRET pair. Second, the FR of the V268I PRPH2/M-opsin (FR = 1.73 ± 0.16) was significantly attenuated compared with the FR of WT PRPH2/M-opsin. By trend, but not significantly, a reduction of the FR was also observed for the V268I PRPH2/S-opsin FRET pair (FR = 1.59 ± 0.10). Third, in rod OS, no significant differences could be measured when comparing the FRs between the WT PRPH2/rhodopsin (FR = 1.46 ± 0.16) and the V268I PRPH2/rhodopsin FRET pairs (FR = 1.48 ± 0.18). Notably, compared to the FRET results from HEK293 cells, the FRs were consistently higher for PRPH2/cone opsin interaction, and consistently lower for the PRPH2/rhodopsin FRET pair. The latter finding is in line with the results from our previous study (4). The consistently higher FRs for the PRPH2/cone opsin binding *in vivo* (in particular that for the PRPH2/M-opsin FRET pair) indicate that these interactions could have strong physiological relevance.

Discussion

In this study, we provide evidence for a stable interaction between PRPH2 and cone opsins. This finding is supported by several methodological approaches in living HEK293 cells and in cone OS. Consistently, co-IPs and quantitative FRET measurements in transiently transfected HEK293 cells and in cone OS suggested more stringent binding of PRPH2 to M-opsin in comparison to the PRPH2/S-opsin interaction. This was confirmed by TEM-studies on WT murine cone OS showing a significantly higher percentage of co-localization for PRPH2 and M-opsin when compared to PRPH2 and S-opsin. Overall, these findings are consistent with the model shown in Figure 6. The physiological importance of this differential interaction of PRPH2 with cone opsins remains unclear. Most cones express both opsin types, however, some of them contain either S- or M-opsin (10). Interestingly, S-opsin and M-opsin expressing cones are unequally distributed in the retina with M-opsin expressing cones (referred to as M-cones) being preferentially found in the dorsal part and S-opsin expressing cones (also known as S-cones) being present predominantly in the ventral part of the retina (10). It remains to be clarified if the differential binding of PRPH2 to cone opsins is related to the dorso-ventral gradient of M- or S-cones. In a recent study, it was shown that M-opsin and S-Opsin are mislocalized throughout the cone photoreceptor of a cone-dominant mouse model expressing a PRPH2 mutant that exhibits localization deficits (C150S) (8). Similar effects on protein localization were not reported for rhodopsin. One possible explanation for these observations is that the PRPH2/cone opsin interaction is specifically required for the concurrent transport of these proteins to the cone OS. The potential relevance of the PRPH2/M-opsin interaction in cone OS is supported by the fact that the V268I AVMD-linked mutant in TM4 of PRPH2 selectively attenuates the binding of PRPH2 to M-opsin without affecting other possible disease-causing parameters like protein localization or mRNA splicing. Interestingly, this mutant did not significantly alter the binding to rhodopsin or S-opsin. Given the same evolutionary origin and the resulting structural homology of photoreceptor opsins, it is not surprising that their binding to PRPH2 is mediated by the same domain. However, even though the V268I mutant is in very close proximity to the G266D mutation, only the latter interferes with the PRPH2/rhodopsin interaction. This finding implies that different molecular determinants within the same domain have evolved to ensure for the specificity of the PRPH2 binding to rhodopsin or cone opsins. The V268I mutant is associated with AVMD, a disease characterized by late onset degeneration of cones. In contrast to the adRP-linked G266D mutation, which almost completely abolishes binding of PRPH2 to rhodopsin (4), the V268I mutation results only in a moderate attenuation of its binding to M-opsin indicating that a portion of M-opsin still is able to form protein complexes with PRPH2. This finding is consistent with the mild and late-onset symptoms reported in AVMD patients carrying the V268I mutation (17). Transgenic mice expressing different PRPH2 mutations have been proven as a valid model to analyze the structural and functional importance of PRPH2 in rods and cones (9,18–21). The exact course of retinal degeneration caused by the V268I mutation requires the generation of appropriate transgenic mouse models and is beyond the scope of this study.

Comparative analysis of FRs from HEK293 cells and rod or cone OS revealed an inverse correlation between the PRPH2/rhodopsin and PRPH2/cone opsin interaction. Although the PRPH2/cone opsin FRs were higher in cone OS compared with HEK293 cells, the opposite was the case for the PRPH2/rhodopsin FRET pairs. The latter finding is in line with the results from our previous study (4). These differences in FRET between HEK293 cells and photoreceptor OS might be explained by the specific molecular composition of rod and cone OS. First, in our recent study using reverse transcriptase-polymerase chain reaction (RT-PCR) from fluorescence-activated cell (FAC)-sorted native rods, we demonstrated that the relative rhodopsin/PRPH2 mRNA expression is ~9:1 (3). Given the overwhelming evidence showing that rhodopsin forms dimers and high-order oligomers in rod OS (4,22,23) most of the labeled rhodopsin molecules used for FRET in our study most probably do not bind to PRPH2, but rather are assembled to rhodopsin di- and oligomers, leading to an overall reduction of the FRET signal. In contrast, RT-PCR from FAC-sorted native cones revealed that the mRNA expression levels for PRPH2 and cone opsins are very similar (3,24). This more or less balanced PRPH2/cone opsin mRNA expression is expected to result in similar PRPH2 and cone opsin protein levels and might explain the higher FRs for the PRPH2/cone opsin interaction in isolated cone OS when compared with the PRPH2/rhodopsin interaction in rod OS. Second, several studies have shown that PRPH2 interacts with the rod CNG channel B-subunit CNGB1a in the disc rim regions

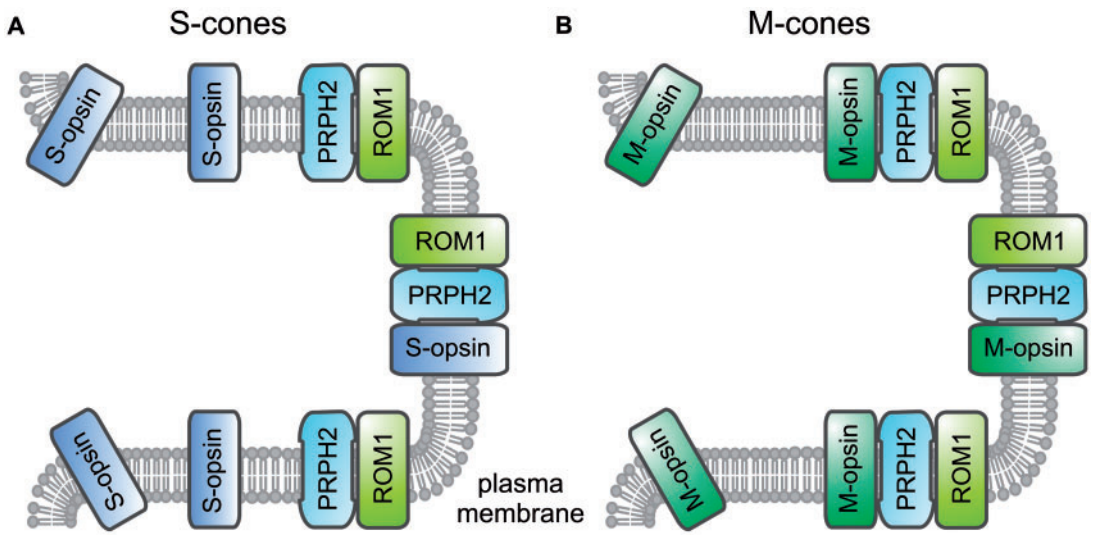

Figure 6. PRPH2 differentially interacts with M-opsin and S-opsin in cone OS. (**A** and **B**) Simplified paradigm of PRPH2 protein-protein interactions in the cone OS based on the results of this and previous studies. (**A**) In lamellar rim regions of S-opsin expressing cones (S-cones), PRPH2 presumably simultaneously binds to its homolog ROM-1 and to S-opsin. However, a large portion of the PRPH2/ROM-1 complexes probably remains unbound to S-opsin. (**B**) In lamellar rim regions of M-opsin expressing cones (M-cones), larger portions of the PRPH2/ROM-1 complexes are expected to be bound to M-opsin. Similar to S-opsin, M-opsin molecules outside of the rim regions are very likely not bound to PRPH2 complexes.

of rod OS (4,7,25). In contrast, PRPH2 does not bind to the CNGB1a homologous CNG B-subunit in cones (CNGB3) that lacks the N-terminal GARP domain (26). Based on this, it is tempting to speculate that PRPH2 is spatially less flexible in rods than in cones, thus allowing only a small portion of rhodopsin molecules to interact. Similar molecular constraints are not expected to occur in transiently transfected HEK293 cells, which are not known to express any of the OS-specific proteins analyzed herein. This might explain the higher FRs for the PRPH2/rhodopsin interaction obtained in these cells. Rods and cones show remarkable differences with respect to their light sensitivity or light response and adaptation kinetics. So far, the molecular determinants of the functional differences between these two cell types are not fully understood (27). This raises the option that the PRPH2/opsin interaction may also partially contribute to shaping the typical physiological features of cones. Conclusively, using different methodological approaches, this study identified cone opsins as novel interaction partners of PRPH2 in cone OS suggesting a novel physiological role of PRPH2 in these cells. In addition, the selective reduction of the PRPH2/M-opsin binding observed for the AVMD-linked, TM4-specific V268I mutant might contribute to explain the differential penetrance of some PRPH2 point mutations in rods and cones.

Materials and Methods

Animals

All procedures concerning animals were performed with permission of local authorities (Regierung von Oberbayern). Anesthesia was performed by subcutaneous injection of ketamine (40 mg/kg body weight) and xylazine (20 mg/kg body weight). Euthanasia was performed by cervical dislocation.

Molecular biology

Full-length sequences for M-opsin and S-opsin were RT-PCR amplified from mouse retinal cDNA and subcloned into the pcDNA3.1 expression vector (Invitrogen). For FRET measurements and for *in vitro* co-IP studies, GFP and the FRET optimized YFP and CFP derivatives citrine or cerulean (28–30) were C-terminally introduced to the respective constructs by standard cloning procedures. PRPH2 and rhodopsin FRET constructs were previously described (4). PRPH2 V268I mutation was obtained by site directed mutagenesis (QuikChange Lightning Mutagenesis Kit, Agilent Technologies). For mRNA splicing analysis, WT and V268I mutant PRPH2 minigene constructs were cloned as previously described (3). All constructs amplified by PCR were completely sequenced prior to use. For the FRET studies on rod or cone OS and the mRNA splicing analysis in cones, the respective FRET or PRPH2 minigene constructs were subcloned to the previously described single stranded pAAV2.1 vector (pAAV2/8 YF, (31)) containing a hRHO or mSWS promoter.

Protein biochemistry

For co-IPs in transiently transfected HEK293 cells (calcium phosphate transfection), cells were harvested 48 h post transfection and membrane preparations were conducted as described (32). co-IPs were performed with the anti-myc (9B11, Cell Signaling), anti-GFP (JL-8, Clontech) or anti-Rhodopsin (Rho1D4, ThermoScientific) antibody using Protein A or Protein G magnetic beads (novex by life technologies). All steps were performed in accordance to the manufacturer's protocol. Rod and cone opsin signals from untreated HEK293 membrane preparations are detected as a smear on western blot due to an extensive opsin glycosylation. Hence, prior to the sample loading to the SDS–PAGE gel, a deglycosylation step was included using PNGase F (New England Biolabs) according to the instructions of the manufacturer.

For *in vivo* co-IPs, freshly dissected retinas of light adapted WT C57 BL/6J animals were homogenized in membrane preparation buffer using the Potter S homogenizer (B. Braun). Subsequently, membrane preparations were performed followed by co-IPs using the anti- PRPH2 (mouse anti-Prph2 2B7,

(12)) antibody. The membrane preparation and co-IP protocols were identical to those described above for the HEK293 cells.

For immunoblotting, antibodies were used in following dilutions: mouse anti-Prph2, 1:1000; mouse anti-Rho, 1:2000; mouse anti-myc 1:2000; mouse anti-GFP, 1:2000.

Photometric FRET measurements

FRET measurements were performed as described (33). In short, HEK293 cells were transiently transfected using the calcium phosphate method. Twenty four to 48 h post-transfection, the cells were washed and maintained in buffer solution composed of 140 mM NaCl, 5 mM KCl, 1 mM $MgCl_2$, 2 mM $CaCl_2$, 10 mM glucose, 10 mM Na-HEPES, pH 7.4, at room temperature (RT). Isolated rod and cone OS were maintained in the same buffer solution at RT for 20 min to let the OS attach to the dish. Fluorescence intensities of cerulean and citrine were recorded using a Leica DMI6000B inverted epifluorescence microscope and a 914 photomultiplier detection system (PTI, Canada). Excitation was performed at 436 ± 2.5 nm or 500 ± 2.5 nm with a DeltaRam monochromator (Horiba, Canada) and emission was detected by a photomultiplier (PMT 914) and acquired on a personal computer using FelixGX software (Horiba, Canada). Three Cube FRET filter cubes were as follows (excitation, longpass beamsplitter, emission): CFP/cerulean (ET436/20×; T455lp; ET480/40m), YFP/citrine (ET500/20×; T515lp; ET535/30m) and FRET (ET436/20×; T455lp; ET535/30m) (Chroma technology). The fluorescence intensities (S) were measured in individual cells co-expressing cerulean-and citrine-tagged proteins with the respective filter cube (excitation, emission): S_{FRET} (436 ± 10 nm, 535 ± 15 nm), $S_{cerulean}$ (436 ± 10 nm, 480 ± 20 nm) and $S_{citrine}$ (500 ± 10 nm, 535 ± 15 nm). The intensities of the signals were subtracted from the background and FRs were calculated according to the three cube FRET equation described in (33). FRET efficiencies (E_A) can be calculated from FRs using the following equation:

$$E_A = [FR - 1] \cdot \frac{\varepsilon_{citrine}(436)}{\varepsilon_{cerulean}(436)}$$

$\varepsilon_{citrine}$ and $\varepsilon_{cerulean}$ are the setup specific average molar extinction coefficients for citrine and cerulean, respectively, over the precise bandwidth of the FRET cube excitation filter. In our setup, the calculated molecular extinction coefficient ratio is $\varepsilon_{citrine}(436)/\varepsilon_{cerulean}(436) = 0.0563$. FRET data were analyzed using FelixGX (Horiba PTI, Canada) and Microsoft Excel (Microsoft).

Preparation of OS

Preparation of rod OS was conducted as described (4). Cone OS were isolated using the same protocol.

rAAV preparation and subretinal injections

The production of single-strand AAVs (rAAV 2/8 YF) containing either the hRHO or mSWS promoter and the procedure of subretinal injections were described previously (31). 10^{10} rAAV particles were delivered by a single injection on postnatal day 14. Three weeks post injection, all injected retinas were analyzed for the fluorescence using scanning laser ophthalmoscopy (Spectralis, Heidelberg Eye Instruments).

Immunohistology

For immunohistology, WT C57 BL/6J mice were injected on P14 with the respective rAAV particles. Three weeks post injection, the retinas were dissected and processed for immunohistology as described (34). We used the rabbit anti-CNGB1a (1:2000, (35)), rabbit anti-M-opsin (1:300, EMD Millipore) or rabbit S-opsin (1:300, EMD Millipore) antibody as marker for rod and cone OS, respectively. Retinal images were obtained by the TCS SP8 confocal scan microscope (Leica), acquired with the LASAF software (Leica) and processed with the ImageJ software (National Institutes of Health).

Post-embedding immunoelectron microscopy

The isolated retinae were fixed in 0.1% glutaraldehyde and 4% paraformaldehyde for 3 h at RT and processed further as described previously (36). After dehydration and embedding in LR White Resin (Plano, Agar Scientific), retinas were briefly polymerized at 4 °C under indirect ultraviolet light (350 nm) for 48–60 h. After being sectioned on an ultramicrotome (Reichert Ultracut E), retina sections (60–70 nm) were collected on Pioloform coated nickel grids and etched with saturated sodium periodate solution (Sigma-Aldrich) at RT for 3–5 min. Following pre-incubation in 0.1% Tween 20 (Sigma-Aldrich), the sections were blocked in 50 mM NH_4Cl (Sigma-Aldrich) and blocking solution (0.5% cold-water fish gelatine and 0.1% ovalbumin, both Sigma-Aldrich). After incubating the retina in primary antibodies (4 °C, 60 h), the sections were washed once with PBS and twice in IgG-gold buffer (blocking solution including 0.01% Tween 20, 0.5 M NaCl) and incubated for 2 h with corresponding Fab-conjugated nanogold antibodies prepared with gold particles (Science Services, Aurion; diluted in IgG-gold buffer). Post-fixation in 1% glutaraldehyde for 10 min and air-drying was followed by silver intensification as described (37). All primary antibodies used for post-embedding (anti-Per 2B7, anti-M-opsin and anti-s-opsin) were described above.

Image preparation

Post-embedded immunoelectron sections were stained with uranylacetate and lead citrate (Leica). Ultrathin sections were examined and photographed by using a Zeiss EM10 electron microscope (Zeiss) and a Gatan SC1000 OriusTM CCD camera (Gatan) in combination with DigitalMicrographTM software (Gatan). Representative images were chosen based on the inspection of several hundred slices from independent experiments. Micrographs were adjusted for contrast and brightness by using Adobe Photoshop CS6 (Adobe Systems).

mRNA splicing analysis in cones

Splicing analysis of PRPH2 minigenes was performed as described (3). Briefly, WT C57 BL/6J mice were injected on P14 using respective WT or V268I PRPH2 minigenes. Three weeks post injection, the retina fluorescence was confirmed by fundus photography (see above). Subsequently, four of the dissected fluorescent retinas for each PRPH2 minigene were pooled and used for RNA isolation with the RNeasy Mini Kit (Qiagen) according to the instructions of the manufacturer. Equal concentrations (1 μg) of the isolated total RNA from each sample were applied for the subsequent cDNA synthesis (Revert Aid First Strand cDNA Sythesis Kit, Life Technologies). All experiments were performed on the same day under the same conditions. For semi-quantitative

analysis of the single PRPH2 minigenes, three RT-PCR reactions were conducted with variable number of cycles ranging between 30 and 33 cycles. The absolute intensities of the single splice bands were determined using the Image Lab software (BioRad).

Statistics

All values are given as mean ± SEM, and n is the number of trials. Unless stated otherwise, an unpaired Student's t-test was performed for the comparison between two groups. Statistical significance is given as follows: *, $P < 0.05$; **, $P < 0.01$; ***, $P < 0.001$. If multiple comparisons were made, significance was tested by analysis of variance (one way ANOVA) followed by the Tukey's multiple comparison test.

Supplementary material

Supplementary Material is available at *HMG* online.

Acknowledgements

We thank Berit Noack and Nadja Schröder for excellent technical support. We also thank Stylianos Michalakis for critical comments on this manuscript and Muna Naash for the gift of the peripherin-2 antibody.

Conflict of Interest statement. None declared.

Funding

This work was supported by the Deutsche Forschungsgemeinschaft [BE 4830/1-1].

References

1. Boon, C.J., den Hollander, A.I., Hoyng, C.B., Cremers, F.P., Klevering, B.J. and Keunen, J.E. (2008) The spectrum of retinal dystrophies caused by mutations in the peripherin/RDS gene. *Prog. Retin. Eye Res.*, **27**, 213–235.
2. Stuck, M.W., Conley, S.M. and Naash, M.I. (2016) PRPH2/RDS and ROM-1: historical context, current views and future considerations. *Prog. Retin. Eye Res.*, **52**, 47–63.
3. Becirovic, E., Bohm, S., Nguyen, O.N., Riedmayr, L.M., Koch, M.A., Schulze, E., Kohl, S., Borsch, O., Santos-Ferreira, T., Ader, M. et al. (2016) In Vivo analysis of disease-associated point mutations unveils profound differences in mRNA splicing of peripherin-2 in rod and cone photoreceptors. *PLoS Genet.*, **12**, e1005811.
4. Becirovic, E., Nguyen, O.N., Paparizos, C., Butz, E.S., Stern-Schneider, G., Wolfrum, U., Hauck, S.M., Ueffing, M., Wahl-Schott, C., Michalakis, S. et al. (2014) Peripherin-2 couples rhodopsin to the CNG channel in outer segments of rod photoreceptors. *Hum. Mol. Genet.*, **23**, 5989–5997.
5. Bascom, R.A., Manara, S., Collins, L., Molday, R.S., Kalnins, V.I. and McInnes, R.R. (1992) Cloning of the cDNA for a novel photoreceptor membrane protein (rom-1) identifies a disk rim protein family implicated in human retinopathies. *Neuron*, **8**, 1171–1184.
6. Boesze-Battaglia, K., Song, H., Sokolov, M., Lillo, C., Pankoski-Walker, L., Gretzula, C., Gallagher, B., Rachel, R.A., Jenkins, N.A., Copeland, N.G. et al. (2007) The tetraspanin protein peripherin-2 forms a complex with melanoregulin, a putative membrane fusion regulator. *Biochemistry*, **46**, 1256–1272.
7. Poetsch, A., Molday, L.L. and Molday, R.S. (2001) The cGMP-gated channel and related glutamic acid-rich proteins interact with peripherin-2 at the rim region of rod photoreceptor disc membranes. *J. Biol. Chem.*, **276**, 48009–48016.
8. Chakraborty, D., Conley, S.M., Stuck, M.W. and Naash, M.I. (2010) Differences in RDS trafficking, assembly and function in cones versus rods: insights from studies of C150S-RDS. *Hum. Mol. Genet.*, **19**, 4799–4812.
9. Chakraborty, D., Ding, X.Q., Conley, S.M., Fliesler, S.J. and Naash, M.I. (2009) Differential requirements for retinal degeneration slow intermolecular disulfide-linked oligomerization in rods versus cones. *Hum. Mol. Genet.*, **18**, 797–808.
10. Applebury, M.L., Antoch, M.P., Baxter, L.C., Chun, L.L., Falk, J.D., Farhangfar, F., Kage, K., Krzystolik, M.G., Lyass, L.A. and Robbins, J.T. (2000) The murine cone photoreceptor: a single cone type expresses both S and M opsins with retinal spatial patterning. *Neuron*, **27**, 513–523.
11. Muller, F., Scholten, A., Ivanova, E., Haverkamp, S., Kremmer, E. and Kaupp, U.B. (2003) HCN channels are expressed differentially in retinal bipolar cells and concentrated at synaptic terminals. *Eur. J. Neurosci.*, **17**, 2084–2096.
12. Conley, S.M., Stricker, H.M. and Naash, M.I. (2010) Biochemical analysis of phenotypic diversity associated with mutations in codon 244 of the retinal degeneration slow gene. *Biochemistry*, **49**, 905–911.
13. Arikawa, K., Molday, L.L., Molday, R.S. and Williams, D.S. (1992) Localization of peripherin/rds in the disk membranes of cone and rod photoreceptors: relationship to disk membrane morphogenesis and retinal degeneration. *J. Cell Biol.*, **116**, 659–667.
14. Molday, R.S., Hicks, D. and Molday, L. (1987) Peripherin. A rim-specific membrane protein of rod outer segment discs. *Invest. Ophthalmol. Vis. Sci.*, **28**, 50–61.
15. Han, Z., Anderson, D.W. and Papermaster, D.S. (2012) Prominin-1 localizes to the open rims of outer segment lamellae in Xenopus laevis rod and cone photoreceptors. *Invest. Ophthalmol. Vis. Sci.*, **53**, 361–373.
16. Loewen, C.J., Moritz, O.L., Tam, B.M., Papermaster, D.S. and Molday, R.S. (2003) The role of subunit assembly in peripherin-2 targeting to rod photoreceptor disk membranes and retinitis pigmentosa. *Mol. Biol. Cell*, **14**, 3400–3413.
17. Felbor, U., Schilling, H. and Weber, B.H. (1997) Adult vitelliform macular dystrophy is frequently associated with mutations in the peripherin/RDS gene. *Hum. Mutat.*, **10**, 301–309.
18. Akimoto, M., Cheng, H., Zhu, D., Brzezinski, J.A., Khanna, R., Filippova, E., Oh, E.C., Jing, Y., Linares, J.L., Brooks, M. et al. (2006) Targeting of GFP to newborn rods by Nrl promoter and temporal expression profiling of flow-sorted photoreceptors. *Proc. Natl. Acad. Sci. U S A.*, **103**, 3890–3895.
19. Ding, X.Q., Nour, M., Ritter, L.M., Goldberg, A.F., Fliesler, S.J. and Naash, M.I. (2004) The R172W mutation in peripherin/rds causes a cone-rod dystrophy in transgenic mice. *Hum. Mol. Genet.*, **13**, 2075–2087.
20. Kedzierski, W., Lloyd, M., Birch, D.G., Bok, D. and Travis, G.H. (1997) Generation and analysis of transgenic mice expressing P216L-substituted rds/peripherin in rod photoreceptors. *Invest. Ophthalmol. Vis. Sci.*, **38**, 498–509.
21. Stricker, H.M., Ding, X.Q., Quiambao, A., Fliesler, S.J. and Naash, M.I. (2005) The Cys214–>Ser mutation in peripherin/rds causes a loss-of-function phenotype in transgenic mice. *Biochem. J.*, **388**, 605–613.
22. Gunkel, M., Schoneberg, J., Alkhaldi, W., Irsen, S., Noe, F., Kaupp, U.B. and Al-Amoudi, A. (2015) Higher-order architecture of rhodopsin in intact photoreceptors and its implication for phototransduction kinetics. *Structure*, **23**, 628–638.

23. Koch, K.W. and Dell'Orco, D. (2015) Protein and signaling networks in vertebrate photoreceptor cells. *Front. Mol. Neurosci.*, **8**, 67.
24. Siegert, S., Cabuy, E., Scherf, B.G., Kohler, H., Panda, S., Le, Y.Z., Fehling, H.J., Gaidatzis, D., Stadler, M.B. and Roska, B. (2012) Transcriptional code and disease map for adult retinal cell types. *Nat. Neurosci.*, **15**, 487–495.
25. Ritter, L.M., Khattree, N., Tam, B., Moritz, O.L., Schmitz, F. and Goldberg, A.F. (2011) In situ visualization of protein interactions in sensory neurons: glutamic acid-rich proteins (GARPs) play differential roles for photoreceptor outer segment scaffolding. *J. Neurosci.*, **31**, 11231–11243.
26. Conley, S.M., Ding, X.Q. and Naash, M.I. (2010) RDS in cones does not interact with the beta subunit of the cyclic nucleotide gated channel. *Adv. Exp. Med. Biol.*, **664**, 63–70.
27. Kefalov, V.J. (2012) Rod and cone visual pigments and phototransduction through pharmacological, genetic, and physiological approaches. *J. Biol. Chem.*, **287**, 1635–1641.
28. Griesbeck, O., Baird, G.S., Campbell, R.E., Zacharias, D.A. and Tsien, R.Y. (2001) Reducing the environmental sensitivity of yellow fluorescent protein. Mechanism and applications. *J. Biol. Chem.*, **276**, 29188–29194.
29. Rizzo, M.A., Springer, G.H., Granada, B. and Piston, D.W. (2004) An improved cyan fluorescent protein variant useful for FRET. *Nat. Biotechnol.*, **22**, 445–449.
30. Zacharias, D.A., Violin, J.D., Newton, A.C. and Tsien, R.Y. (2002) Partitioning of lipid-modified monomeric GFPs into membrane microdomains of live cells. *Science*, **296**, 913–916.
31. Koch, S., Sothilingam, V., Garcia Garrido, M., Tanimoto, N., Becirovic, E., Koch, F., Seide, C., Beck, S.C., Seeliger, M.W., Biel, M. et al. (2012) Gene therapy restores vision and delays degeneration in the CNGB1(-/-) mouse model of retinitis pigmentosa. *Hum. Mol. Genet.*, **21**, 4486–4496.
32. Much, B., Wahl-Schott, C., Zong, X., Schneider, A., Baumann, L., Moosmang, S., Ludwig, A. and Biel, M. (2003) Role of subunit heteromerization and N-linked glycosylation in the formation of functional hyperpolarization-activated cyclic nucleotide-gated channels. *J. Biol. Chem.*, **278**, 43781–43786.
33. Shaltiel, L., Paparizos, C., Fenske, S., Hassan, S., Gruner, C., Rotzer, K., Biel, M. and Wahl-Schott, C.A. (2012) Complex regulation of voltage-dependent activation and inactivation properties of retinal voltage-gated Cav1.4 L-type Ca2+ channels by Ca2+-binding protein 4 (CaBP4). *J. Biol. Chem.*, **287**, 36312–36321.
34. Michalakis, S., Geiger, H., Haverkamp, S., Hofmann, F., Gerstner, A. and Biel, M. (2005) Impaired opsin targeting and cone photoreceptor migration in the retina of mice lacking the cyclic nucleotide-gated channel CNGA3. *Invest. Ophthalmol. Vis. Sci.*, **46**, 1516–1524.
35. Huttl, S., Michalakis, S., Seeliger, M., Luo, D.G., Acar, N., Geiger, H., Hudl, K., Mader, R., Haverkamp, S., Moser, M. et al. (2005) Impaired channel targeting and retinal degeneration in mice lacking the cyclic nucleotide-gated channel subunit CNGB1. *J. Neurosci.*, **25**, 130–138.
36. Gießl, A., Pulvermüller, A., Trojan, P., Park, J.H., Choe, H.W., Ernst, O.P., Hofmann, K.P. and Wolfrum, U. (2004) Differential expression and interaction with the visual G-protein transducin of centrin isoforms in mammalian photoreceptor cells. *J. Biol. Chem.*, **279**, 51472–51481.
37. Danscher, G. (1981) Localization of gold in biological tissue. A photochemical method for light and electronmicroscopy. *Histochemistry*, **71**, 81–88.

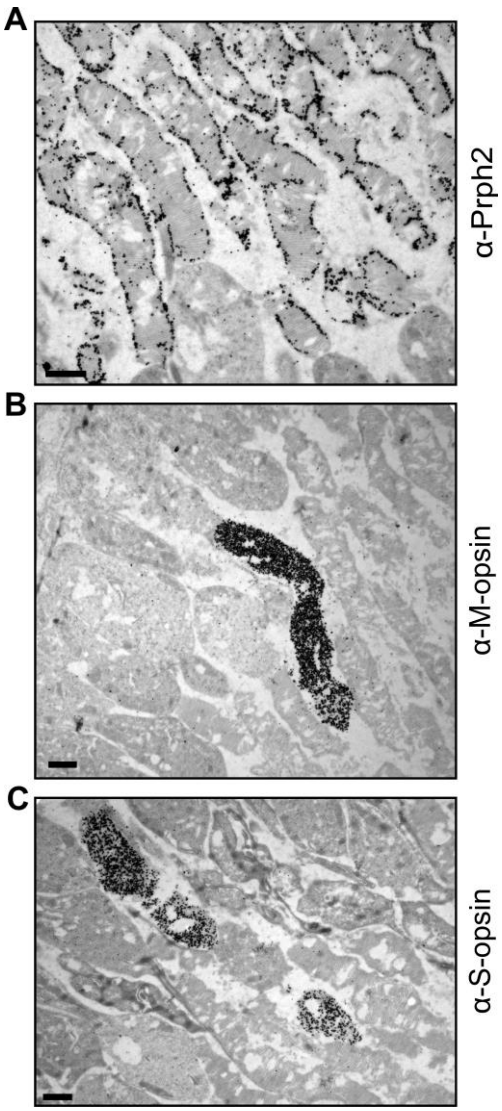

Suppl. Fig. 1 Immunogold TEM labeling of photoreceptor OS confirms the specificity of peripherin-2 and cone opsin antibodies. A-C, Representative TEM images of post-embedded rod and cone OS sections from 8-week old light-adapted C57/BL6J WT mice labeled with gold particles coupled to peripherin-2 (A), M-opsin (B), or S-opsin (A) specific antibodies. Note that the concentrations for S-opsin and M-opsin antibodies were higher than those used for co-labeling experiments shown in Fig. 2, resulting in stronger staining of cone OS. However, even under these high concentrations of M-opsin and S-opsin antibodies, no staining of rod OS was detectable, demonstrating the specificity of the respective antibodies.

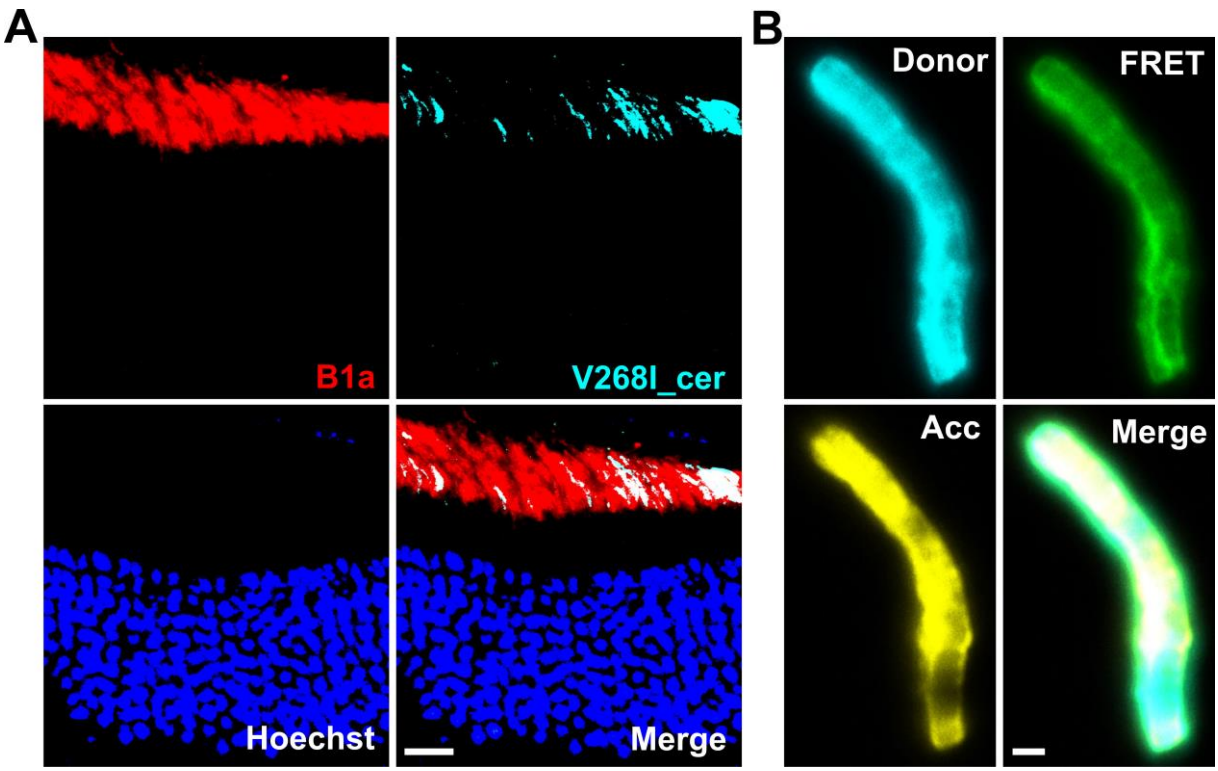

Suppl. Fig. 2 Immunolabeling of the V268I mutant in murine rods and confocal images of FRET channels in isolated rod OS. A, Co-immunolabeling of retinal sections from WT mice subretinally injected with rAAV particles containing C-terminally cerulean-tagged V268I mutant (V268I_cer) under the control of the human rhodopsin (hRHO) promoter. CNGB1a antibody (B1a) was used as marker for rod OS. Scale bar = 10 µm. B, Representative confocal FRET channel images from isolated rod OS of WT mice co-injected with rAAV particles containing the P-V268I_cer/Rhodopsin_citr FRET pair as described in Fig. 3A under the control of the hRHO promoter. Scale bar = 1 µm.

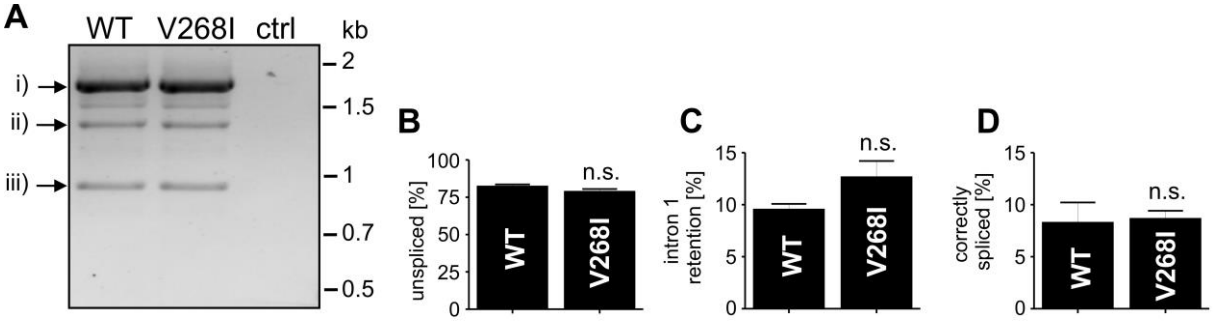

Suppl. Fig. 3 mRNA splicing of the V268I mutant in cones. A, Representative RT-PCR from retinal cDNA generated from total RNA of WT animals injected on P14 with rAAV PRPH2 minigene constructs harboring the mSWS promoter. The respective minigenes, RT-PCR primers, and detailed experimental conditions were recently described (1). Ctrl, control containing the cDNA from non-transduced retina. The single bands of the relevant splice products are highlighted by arrows: i) unspliced, ii) intron 1 retention, and iii) correctly spliced, respectively. (B-D) Semi-quantitative analysis of the relative signal intensity percentages of the unspliced (B), intron 1 retention (C), and correctly spliced (D) PRPH2 transcripts. For both, WT and V268I peripherin-2 minigenes, the mean percentage of the intensities of these three splice variants relative to the total intensity (given as sum of the single intensities) was calculated from five RT-PCR analyses. Significance was calculated using the unpaired student's t-test. P-values are as follows: unspliced, $p = 0.2075$; intron 1 retention, $p = 0.1332$; correctly spliced, $p = 0.8654$.

References

1 Becirovic, E., Bohm, S., Nguyen, O.N., Riedmayr, L.M., Koch, M.A., Schulze, E., Kohl, S., Borsch, O., Santos-Ferreira, T., Ader, M. *et al.* (2016) In Vivo Analysis of Disease-Associated Point Mutations Unveils Profound Differences in mRNA Splicing of Peripherin-2 in Rod and Cone Photoreceptors. *PLoS Genet*, **12**, e1005811.

frontiers in Neuroscience

PROTOCOLS
published: 28 July 2016
doi: 10.3389/fnins.2016.00356

AAV Vectors for FRET-Based Analysis of Protein-Protein Interactions in Photoreceptor Outer Segments

Elvir Becirovic[1,2], Sybille Böhm[1,2], Ong N. P. Nguyen[1,2], Lisa M. Riedmayr[1,2], Verena Hammelmann[1,2], Christian Schön[1,2], Elisabeth S. Butz[1,2], Christian Wahl-Schott[1,2], Martin Biel[1,2] and Stylianos Michalakis[1,2]**

[1] Department of Pharmacy – Center for Integrated Protein Science Munich (CiPSM), Ludwig-Maximilians-Universität München, Munich, Germany, [2] Department of Pharmacy – Center for Drug Research, Ludwig-Maximilians-Universität München, Munich, Germany

Fluorescence resonance energy transfer (FRET) is a powerful method for the detection and quantification of stationary and dynamic protein-protein interactions. Technical limitations have hampered systematic *in vivo* FRET experiments to study protein-protein interactions in their native environment. Here, we describe a rapid and robust protocol that combines adeno-associated virus (AAV) vector-mediated *in vivo* delivery of genetically encoded FRET partners with *ex vivo* FRET measurements. The method was established on acutely isolated outer segments of murine rod and cone photoreceptors and relies on the high co-transduction efficiency of retinal photoreceptors by co-delivered AAV vectors. The procedure can be used for the systematic analysis of protein-protein interactions of wild type or mutant outer segment proteins in their native environment. Conclusively, our protocol can help to characterize the physiological and pathophysiological relevance of photoreceptor specific proteins and, in principle, should also be transferable to other cell types.

Keywords: fluorescence resonance energy transfer, FRET, adeno-associated viral vectors, AAV, protein-protein interaction, photoreceptor, outer segment

OPEN ACCESS

Edited by:
Hildegard Büning,
University of Cologne, Germany

Reviewed by:
Peter Christian Kloehn,
University College London, UK
Jiajie Diao,
University of Cincinnati, USA

****Correspondence:***
Elvir Becirovic
elvir.becirovic@cup.uni-muenchen.de
Stylianos Michalakis
michalakis@lmu.de

Specialty section:
This article was submitted to Neurodegeneration, a section of the journal Frontiers in Neuroscience

Received: *20 April 2016*
Accepted: *14 July 2016*
Published: *28 July 2016*

Citation:
Becirovic E, Böhm S, Nguyen ONP, Riedmayr LM, Hammelmann V, Schön C, Butz ES, Wahl-Schott C, Biel M and Michalakis S (2016) AAV Vectors for FRET-Based Analysis of Protein-Protein Interactions in Photoreceptor Outer Segments. Front. Neurosci. 10:356. doi: 10.3389/fnins.2016.00356

INTRODUCTION

The outer segments (OS) of rod and cone photoreceptors are highly specialized cilia harboring all proteins involved in light-induced phototransduction (Arshavsky and Burns, 2012). Mutations in genes encoding these proteins lead to untreatable diseases that severely impair rod and/or cone structure and/or functionality (Berger et al., 2010). The majority of these genes encode proteins that are organized in large macromolecular complexes assembled by networks of homomeric and/or heteromeric protein-protein interactions (Roepman and Wolfrum, 2007). To decipher pathomechanisms underlying the retinal disorders and to develop appropriate treatments, the identification and characterization of these networks is inevitable. So far, the vast majority of OS protein-protein interaction studies in photoreceptors were performed using classical biochemical techniques (Goldberg et al., 1995; Loewen and Molday, 2000; Poetsch et al., 2001; Jastrzebska et al., 2004; Michalakis et al., 2011; Knepp et al., 2012). However, the biochemical techniques have several limitations: (i) They strongly rely on the availability of antibodies with high affinity and specificity, (ii) they do not necessarily reflect "true" interactions since, due to the tissue homogenization, some

proteins may randomly interact even though they are spatially separated *in vivo*, (iii) they do not allow for dynamic measurements, and (iv) exact quantification of interactions is rather difficult as many different technical parameters which might influence the interaction must be controlled rigorously.

With regard to these obstacles, FRET is superior to the biochemical approaches. One important constraint of FRET is the fact that it requires the co-expression of the fluorescently tagged molecules in a given cell type. This can be easily handled in heterologous expression systems, however, in complex organisms like mammals the application of FRET has been hampered by the laborious and time consuming generation of transgenic animals. Therefore, only a few FRET-based studies were performed *in vivo*, most of them using FRET biosensors for analysis of spatiotemporal dynamics of small signaling molecules (Hovan et al., 2010; Hirata et al., 2012; Wen et al., 2013; Kumagai et al., 2014). Here, we describe a protocol for systematic monitoring of protein-protein interactions without the necessity of generating transgenic animals. The technique utilizes adeno-associated virus (AAV) vectors that are valuable tools for *in vivo* gene transfer into brain and retinal neurons (Schön et al., 2013; Murlidharan et al., 2014; Trapani et al., 2014; Zacchigna et al., 2014). AAVs lead to long-term ectopic expression of the transgene in mammals and thus can be used as a rapid alternative to the generation of transgenic animals. We have already used AAV mediated viral gene expression in retinal neurons in our previous studies (Becirovic et al., 2014, 2016; Nguyen et al., 2016).

The protocol allows for rapid and robust measurements of sensitized acceptor emission FRET on isolated virally transduced murine photoreceptor OS. The complete procedure can be performed within 3 weeks on wild type animals and requires only limited expertise and special equipment (**Figure 1**). We show that this method is suitable for the detection and quantification of protein-protein interactions of proteins involved in the pathogenesis of hereditary degenerative retinal diseases. We propose the application of this method for FRET-based protein-protein interaction studies in other primary cilia of many cell types to study the pathogenesis of other ciliopathies.

Experimental Procedure

The genes of interest encoding each of the protein-protein interaction partners are C- and/or N-terminally fused to the genes encoding citrine or cerulean, two FRET-optimized derivatives of YFP and CFP, respectively (Griesbeck et al., 2001; Rizzo et al., 2004). Each of these constructs is then cloned into the multiple cloning site of a rAAV *cis*-plasmid containing the rod photoreceptor specific human rhodopsin (hRHO) (Allocca et al., 2007) or murine short wavelength opsin (mSWS) promoter (Michalakis et al., 2010a), a Woodchuck hepatitis virus posttranscriptional regulatory element (WPRE), and a bovine growth hormone polyadenylation signal (BGH pA). Subsequently, each rAAV *cis* plasmid is co-transfected with the *trans* (AAV helper and Adeno helper) plasmids into HEK293T cells using triple Ca^{2+} phosphate transfection. rAAV particles are then purified in a multistep procedure that yields high titers of approx. 10^{13} vector genomes (vg) per ml. For FRET measurements, 1×10^9 total vg of each construct is delivered into the subretinal space of anesthetized mice. For co-transduction experiments of two titer-matched constructs a total number of 2×10^9 total vg is injected. The co-transduction efficiency was up to 90% in rods and up to 30% in cones after co-delivery of mixtures of two rAAVs. The isolation of rod or cone OS was performed 10–14 days post-injection using a modified version of the mechanical share method (Mitchell et al., 2009). Three cube FRET measurements were carried out using a slightly modified version of the protocol described previously (Erickson et al., 2003; Shaltiel et al., 2012; Ben Johny et al., 2013). The isolated OS were stable for several hours after isolation, which in principle also allows for dynamic FRET measurements of single interactions.

Using this method, we were able to confirm several homomeric and heteromeric protein-protein interactions in rod OS that had been previously observed using other (biochemical) methods. In addition, we also identified novel protein-protein interactions in OS of rods and cones. Furthermore, we demonstrate that FRET is applicable to quantify the effects of disease associated point mutations on protein-protein interactions in these compartments. Conclusively, we show that our FRET protocol enables robust qualitative and quantitative measurements of protein-protein interactions in small cellular compartments like photoreceptor OS.

Advantages of the Method

Compared to FRET and other *ex vivo* measurements of protein-protein interactions, which are currently widely used, this method has several advantages:

(i) It can be performed within 3 weeks including the production of specific rAAVs. The isolation of OS can be carried out within a few minutes and yields a high quantity of OS of adequate quality and purity.
(ii) It allows for systematic analysis of protein-protein interactions *ex vivo* in a specialized small compartment with preserved native morphology.
(iii) It is principally transferable to analyses of protein-protein interactions in ciliary compartments of other tissues (e.g., respiratory cilia and olfactory cilia). This is of special importance for deciphering the disease mechanisms of a large group of diseases known as ciliopathies.
(iv) As isolated OS are stable for up to 6 h, the method can also be used for dynamic FRET measurements.
(v) The protocol was established in wild type mice. Thus, it allows for systematic analysis of disease mechanisms of single disease associated point mutations without the time consuming generation of transgenic animals.
(vi) It can in principle be used to determine the relative binding affinities of single interactions.
(vii) The co-transduction efficiency for two constructs was up to 90% for rod OS and up to 30% for cone OS. Hence, a sufficient number of OS co-expressing both proteins of interest can be isolated from a single animal.

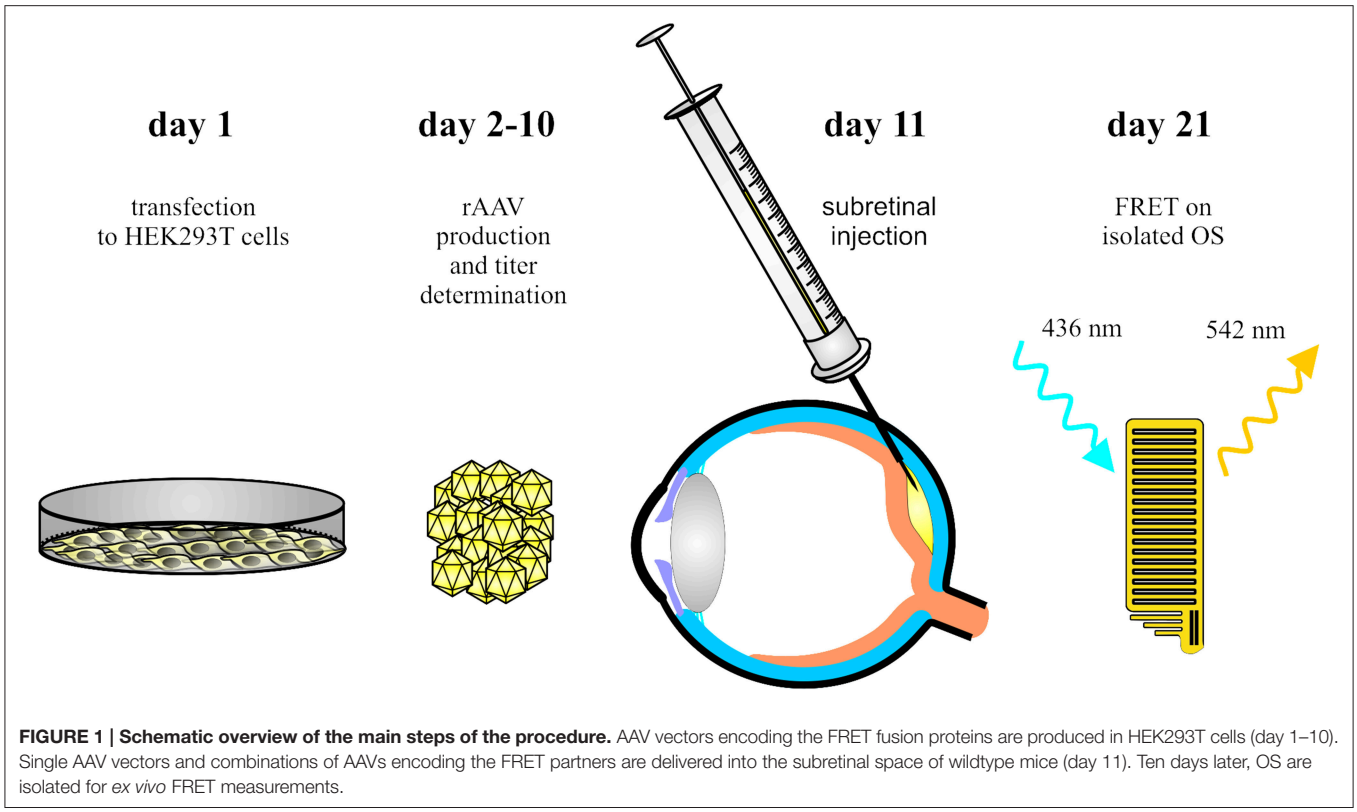

FIGURE 1 | Schematic overview of the main steps of the procedure. AAV vectors encoding the FRET fusion proteins are produced in HEK293T cells (day 1–10). Single AAV vectors and combinations of AAVs encoding the FRET partners are delivered into the subretinal space of wildtype mice (day 11). Ten days later, OS are isolated for *ex vivo* FRET measurements.

(viii) In principle, it can be adapted for the establishment of FRET measurements on retinas of living animals.
(ix) Due to its easy handling our protocol should also be transferable to other tissues or organisms.

Limitations of the Method

There are a few limitations of the method, which can be overcome by appropriate techniques or conditions:

(i) With respect to the packaging capacity of rAAVs (5 kb) (Trapani et al., 2014), this method seems less suitable for analysis of protein-protein interactions of large proteins. However, there are several approaches showing that larger transcripts can also be packaged into rAAVs, even though with lower efficiencies (Trapani et al., 2014).
(ii) The endogenous wild type proteins in the OS of transduced photoreceptors interfere with the labeled constructs and lead to overall lower FRET efficiencies than expected from *in vitro* experiments (incomplete labeling) (Becirovic et al., 2014). This limitation should be of relevance only if weak interactions are expected. This issue could be overcome by using appropriate single or double knock-out animals, which lack expression of the endogenous (unlabeled) proteins of interest.
(iii) So far, we found no short or long term toxic effects of the fluorophores on the structural integrity of the retina, which is consistent with previous studies (Bennett et al., 1999; Becirovic et al., 2014). However, we cannot exclude that large amounts of specific cerulean- or citrine-tagged proteins could have toxic effects that influence photoreceptor function and morphology. Therefore, to exclude any toxic effects, we suggest using histological analysis of retinal cross sections prior to the actual FRET measurements for each construct.
(iv) In the case of three cube FRET, in addition to the simultaneous delivery of two FRET partners, injections of single FRET constructs are also necessary. They serve as bleed-through and crosstalk controls for the determination of the FRET efficiencies.
(v) Overexpression of the tagged proteins by strong promoters might result in an artefactual FRET signal. To exclude this possibility, additional controls might be necessary. In this context, the most eligible control is to use point mutations within the protein-protein interaction site of one (or both) FRET partners. If the protein interaction interface is not known, artefactual FRET signal can be excluded by overexpressing other proteins not expected to interact with the respective FRET partner.
(vi) Bulky fluorescent tags could possibly hinder proper trafficking or localization of the fusion protein (Feilmeier et al., 2000). In addition, they might influence the proper folding and the stability of the protein. In turn, incorrect folding may also affect the fluorophore itself and lead to little or no fluorescence (Waldo et al., 1999). If these problems occur, they can be overcome by varying the position of the fluorescent tag within the protein or by placing a short linker sequence between tag and protein.

MATERIALS AND EQUIPMENT

Animals

All procedures were performed on P14-21 C57BL/6J mice with permission from local authorities (District Government of Upper Bavaria). Anesthesia was performed by subcutaneous injection of ketamine (40 mg/kg body weight) and xylazine (20 mg/kg body weight). Euthanasia was performed by cervical dislocation.

Reagents

- Sodium chloride (NaCl; VWR, cat. no. 27810.364)
- Potassium chloride (KCl; Carl Roth, cat. no. 6781.1)
- Magnesium chloride hexahydrate ($MgCl_2 \times 6H_2O$; Carl Roth, cat. no. 2189.1)
- Calcium chloride dihydrate ($CaCl_2 \times 2H_2O$; VWR, cat. no. 22317.230)
- Glucose monohydrate (Carl Roth, cat. no. 6887.1)
- HEPES sodium salt (VWR, cat. no. A16516.22)
- Sodium hydroxide, 5 M (NaOH; VWR, 28244.295)
- KAPA SYBR FAST Universal x2 qPCR MasterMix (peqlab, cat. no. 07-KK4600-01)
- Poly-L-lysine, 1 mg/ml (Sigma, cat. no. P2636)
- Polybrene/Hexadimethrine bromide (Sigma, cat. no. 107689)
- Dextran (Sigma, cat. no. 95771)
- BES sodium salt (Sigma, cat. no. B2891)
- AAV *cis* (for cloning of the expression cassette) and *trans* plasmids (encoding for Cap, Rep and adenoviral helper genes) can be obtained from various sources including Penn Vector Core (http://www.med.upenn.edu/gtp/vectorcore) or from UNC Vector Core (http://www.med.unc.edu/genetherapy/vectorcore,seealsoRef. Grieger et al., 2006)
- Benzonase (VWR, cat. no. 1.01695.0001)
- OptiPrep (Progen, cat. no. 1114542)
- Disodium hydrogen phosphate (Na_2HPO_4; Sigma, cat. no. S9763)
- Sodium dihydrogen phosphate (NaH_2PO_4; Sigma, cat. no. S5011)
- Tris(hydroxymethyl)aminomethane (TRIS; VWR, cat. no. 71003-490)
- Phenol red (Sigma, cat. no. P3532)
- Tween 20 (Sigma, cat. no. P2287).

Equipment for rAAV Preparation and Subretinal Injection

- Vortexer
- Microcentrifuge tubes, 1.5 ml
- Microcentrifuge tubes with screw cap, 1.5 ml
- ibidi μ-dish, 35 mm, low (ibidi, cat. no. 80131)
- Room temperature bench top centrifuge (1.5 ml tube rotor)
- Petri dishes, 3 cm
- Forceps
- Polystyrene tubes, 50 ml
- Cell culture dishes, 15 cm
- Cell scraper (VWR, cat. no. 734-1111)
- Liquid nitrogen
- Quick-Seal polypropylene tubes, 39 ml (Beckman, cat. no. 342141)
- Glass pipettes
- Peristaltic pump MINIPULS 3 (Gilson, cat. no. n/a)
- Quick-Seal Cordless Tube Topper kit, 50 Hz (Beckman, cat. no. 358313)
- Beckman Coulter J2-MC high speed centrifuge (Beckman, cat. no. n/a)
- JA-10 Rotor, Fixed Angle, Aluminum, 6 × 500 ml, 10,000 rpm, 17,700 × g (Beckman, cat. no. 369687)
- Beckman Coulter Optima LE-80K ultracentrifuge (Beckman, cat. no. n/a)
- 70 Ti Rotor, Fixed Angle, Titanium, 8 × 39 mm, 70,000 rpm, 504,000 × g (Beckman, cat. no. 337922)
- Syringe needle, 21-gauge
- Syringe, 5 ml
- Sterile syringe filters with acrylic housing, 0.2 μm, cellulose acetate (VWR, cat. no. 28145-477)
- HiTrap Q FF sepharose column, 5 ml (GE Healthcare, cat. no. 17-5156-01)
- Superloop, 50 ml (GE Healthcare, cat. no. 19-7850-01)
- ÄKTAprime plus chromatography system (GE Healthcare, cat. no. 11-0013-13)
- PrimeView 5.31 software (GE Healthcare, cat. no. 28-9949-61)
- Amicon Ultra-4 centrifugal filter units, 100 kDa (Millipore, cat. no. UFC810024)
- LightCycler 480 multiwell plate 96 (Roche, cat. no. 04729692001)
- LightCycler 480 Sealing Foil (Roche, cat. no. 04729757001)
- LightCycler 480 Instrument II real-time PCR amplification and detection instrument (Roche, cat. no. 05015278001)
- NanoFil syringe, 10 μl (World Precision Instruments, cat. no. NANOFIL)
- NanoFil 34-gauge beveled needle (World Precision Instruments, cat. no. NF34BV-2)
- Nanodrop 2000c UV-Vis spectrophotometer (peqlab, ca. no. 91-ND-2000C)
- Dexpanthenol eye and nose salve, 5% (Bepanthen, Bayer Vital GmbH, cat. no. 1578681)
- OPMI 1 FR pro surgical microscope (Zeiss, cat. no. n/a)
- Gentamicin 5 mg/g and dexamethasone 0.3 mg/g eye salve (Dexamytrex, Dr. Gerhard Mann GmbH, cat. no. 2747789)
- Dissection stereomicroscope Stemi 2000 (Zeiss, cat. no. 495005-0022-000)
- Epifluorescence microscope Axioplan 2 imaging (Zeiss, cat. no. n/a).

Equipment for Three Cube FRET Measurements

- Inverted fluorescent microscope (Leica, cat. no. DMI6000B)
- HC PL APO 63x/1.40-0.60 oil immersion objective (Leica, cat. no. 11506349)
- Cerulean filter cube, excitation: ET436/20x, Dichroic: T455lp, emission: ET480/40m, transmission rate 93–97% (Chroma Technology, cat. no. 49001)

- Citrine filter cube, excitation: ET500/20x, Dichroic: T515lp, emission: ET535/30m, transmission rate 93–97% (Chroma Technology, cat. no. 49003)
- FRET filter cube, excitation: ET436/20x, Dichroic: T455lp, emission: ET535/30m, transmission rate 93–97% (Chroma Technology, cat. no. 49052)
- DeltaRamX monochromator (Horiba, cat. no. n/a)
- D-104 B microscope photometer (Horiba, cat. no. n/a)
- Xenon short arc lamp type UXL-75XE (Ushio Inc. Japan, cat. no. n/a)
- PMT housing 914 (Horiba, cat. no. n/a)
- R1527 photomultiplier (Horiba, cat. no. n/a)
- FelixGX software (Horiba, cat. no. n/a)
- MATLAB® R2014b (MathWorks. Inc., cat. no. n/a)
- Excel software (Microsoft Corporation, cat. no. n/a).

Buffers and Solutions

2x BBS transfection solution Final component concentrations are 45 mM BES, 280 mM NaCl, 1.5 mM Na_2HPO_4. Adjust the pH to 6.95 and sterile filtrate. Prepare 50 ml aliquots and store them at 4°C for up to 1 year.

Lysis Buffer Final component concentrations are 150 mM NaCl, 50 mM TRIS. Adjust the pH to 8.5 and sterile filtrate. Prepare freshly before use.

15% iodixanol solution Final component concentrations are 1x PBS (phosphate buffered saline), 1 mM $MgCl_2$, 2.5 mM KCl, 1 M NaCl, 15% Optiprep. Add phenol red (use 1% solution) *ad libitum* until the solution is visibly colored. Store at 4°C for up to 1 week.

25% iodixanol solution Final component concentrations are 1x PBS, 1 mM $MgCl_2$, 2.5 mM KCl, 25% Optiprep. Add phenol red (use 1% solution) *ad libitum* until the solution is visibly colored. Store at 4°C for up to 1 week.

40% iodixanol solution Final component concentrations are 1x PBS, 1 mM $MgCl_2$, 2.5 mM KCl, 1 M NaCl, 40% Optiprep. The solution remains uncolored. Store at 4°C for up to 1 week.

60% iodixanol solution Final component concentrations are 1 mM $MgCl_2$, 2.5 mM KCl, 60% Optiprep. Add phenol red (use 1% solution) *ad libitum* until the solution is visibly colored. Store at 4°C for up to 1 week.

PBS-MK solution Final component concentrations are 1x PBS, 1 mM $MgCl_2$, 2.5 mM KCl. Sterile filtrate and store at 4°C for up to 1 week.

Buffer A Final component concentrations are 20 mM TRIS, 15 mM NaCl. Adjust the pH to 8.5. Store at 4°C for up to 1 week.

Buffer B Final component concentration is 2.5 M NaCl. Adjust the pH to 8.5. Store at 4°C for up to 1 week.

FRET imaging solution Final component concentrations are 140 mM NaCl, 5 mM KCl,

1 mM $MgCl_2$, 2 mM $CaCl_2$, 10 mM glucose, 10 mM HEPES sodium salt. Adjust the pH with 5 M NaOH to 7.4. Prepare 50 ml aliquots and store them at −20°C for up to 1 year. Store thawed aliquots at 4°C for up to 1 week.

FRET Imaging Setup

Imaging dishes We recommend the use of commercially available glass-bottomed cell-culture dishes for imaging. They should be coated with Poly-L-lysine to ensure complete adherence and immobilization of OS. In our hands, the use of pre-coated dishes (e.g., ibiTreat, ibidi) resulted in insufficient OS adherence.

Inverted epifluorescent microscope, excitation source, and detection All measurements were performed using a Leica DMI6000B inverted fluorescent microscope equipped with a motorized turret and a 63x oil objective. The microscope contains a motorized filter-wheel enabling rapid switching of filter cubes within 300 ms. Of note, the 40x oil objective is also suitable for FRET measurements on isolated OS. The fluorescent intensity is detected by a photomultiplier detection system including a photomultiplier tube (Horiba). As excitation source, we use a DeltaRam monochromator containing a 150W xenon high stability lamp. The use of a conventional LED lamp is also suitable. However, it is crucial to achieve a stable uniform illumination.

Excitation filter, emission filter, and dichroic mirror The following filter cubes are present in our microscope: A donor cube containing a cerulean excitation filter, T455lp dichroic mirror and a cerulean emission filter; an acceptor cube with a citrine excitation filter, T515lp dichroic mirror, and a citrine emission filter. Furthermore a FRET cube containing a cerulean excitation filter, T455lp dichroic mirror and a citrine emission filter. In case of using a monochromator as excitation source, the excitation filters are optional.

Software and data acquisition For photometric FRET measurements, we employ the three cube FRET method (Erickson et al., 2003; Shaltiel et al., 2012; Ben Johny et al., 2013) that utilizes the detection of fluorescence intensities from a specimen using three filter cubes. The excitation source (DeltaRam monochromator) and appendant excitation parameters (e.g., wavelength, pulse duration) are thereby controlled via the software FelixGX, whereas the filter switch is done manually. Fluorescence intensity signals are acquired with the FelixGX software and deciphered with a custom-written MATLAB script. Subsequent analysis is performed using Excel or an adequate data processing software.

STEPWISE PROCEDURES

Production and Titer Determination of rAAVs

Transfection, Harvesting, and Lysis of HEK293T Cells

The production and handling of recombinant pseudotyped AAV2-derived vectors is subject to biosafety level 1. For a detailed protocol on AAV production, see ref. (Grieger et al., 2006). 24 h before transfection, confluent 15-cm-dishes of HEK293T cells were split into 15 15-cm-dishes for each construct. For calcium phosphate transfection, the components listed in **Table 1** (the amounts are adjusted for transfection of 15 15-cm-dishes) were added in a 50-ml polystyrene tube. The following two equations are used to calculate the amount of pAd Helper plasmid and AAV2/8 Cap/Rep plasmid needed for the pre-transfection mix described in **Table 1**, respectively:

$$x\,(amount\ of\ pAd\ Helper) = \frac{m\,(transgene\ AAV) \times MM\,(pAd\ Helper)}{MM\,(transgene\ AAV)} = \frac{270\,\mu g \times 9509\frac{g}{mol}}{MM\,(transgene\ AAV)}$$

$$y\ \left(amount\ of\ AAV\ 2/8\,\mathrm{Rep/Cap}\right) = \frac{m\left(transgene\ AAV\right) \times MM\left(AAV\ 2/8\,\mathrm{Rep/Cap}\right)}{MM\left(transgene\ AAV\right)} = \frac{270\,\mu g \times 4523\frac{g}{mol}}{MM\left(transgene\ AAV\right)}$$

MM = molar mass of double stranded plasmid.

While vortexing the pre-transfection mix in the polystyrene tube at maximum speed, 15 ml 2x BBS was added dropwise. The mixture was incubated at room temperature for 4–5 min and 2 ml of the transfection mix was added dropwise to each 15-cm-dish of ∼80% confluent HEK293T cells. Transfected cells were then incubated at 37°C and 5% CO_2 atmosphere for 24 h. Subsequently, the medium from transfected cells was replaced and the cells were incubated at 37°C and 10% CO_2 atmosphere for additional 24 h. 48 h post transfection, the cells were harvested by scraping them from each 15-cm-dish. Cell suspensions were collected from 15 dishes in a 500-ml-centrifuge-tube. The cells were centrifuged at 2000 × g for 15 min at 4°C (4000 rpm in a J2-MC Beckman centrifuge using a JA-10 rotor). After medium removal, the cell pellet was gently resuspended in 7.5 ml lysis buffer (volume for cell pellet harvested from 15 15-cm-dishes) and transferred into 50-ml-polystyrene-tubes. The cell suspension was shock-freezed in liquid nitrogen and subsequently thawed at 37°C. Freeze-thaw cycle was repeated two additional times. The resulting cell suspension can be stored at −80°C overnight.

Gradient Centrifugation and Purification of rAAVs

Benzonase was added to the thawed cell suspension to a final concentration of 50 U/ml followed by an incubation at 37°C for 30 min. Subsequently, the cells were pelleted via centrifugation at 2000 × g for 25 min at 4°C. The virus-containing supernatant was transferred into a Beckman Quick-Seal polypropylene tube. To form the iodixanol gradient, a sterile, long glass pipette, and a Gilson MINIPULS3 pump were used. First, the virus-containing phase was underlaid with 7 ml 15% iodixanol, then with 5 ml 25% iodixanol, followed by 5 ml 40% iodixanol, and at last with 6 ml 60% iodixanol. To avoid mixing of the layers, the pump should be run at the slowest speed. Polypropylene tubes were filled up and accurately balanced with PBS-MK. Prior to centrifugation, the tubes were sealed with the Beckman Tube Topper. Centrifugation was performed at 361.000 × g for 1 h 45 min at 18°C (70.000 rpm in an Optima LE-80K Beckman ultracentrifuge using a 70 Ti rotor). During centrifugation, the virus-containing fraction should accumulate in the 40% phase. After centrifugation, the tube was pierced at the top near the seal for pressurization. To collect the virus-containing phase, a 21-gauge-needle was used with a 5-ml-syringe to pierce the tube through the side at the lower end of the 40–60% interface. During this step, the open site of the needle tip should face the 40% phase. Approximately 5 ml of the 40% phase were collected. The virus-containing phase can be stored in a 15-ml-polystyrene-tube at −80°C until proceeding with the purification step.

TABLE 1 | Reagents for a pre-transfection mix of one transgene AAV construct.

Reagent	Amount
Transgene AAV *cis* plasmid (Michalakis et al., 2010b; Koch et al., 2012)	270 µg
pAd Helper plasmid (pAdDeltaF6 Auricchio et al., 2001)	x µg
AAV2/5 (Hildinger et al., 2001) or AAV2/8 (Gao et al., 2002) Rep/Cap plasmid	y µg
Polybrene (8 mg/ml)	15 µl
Dextran (10 mg/ml)	1500 µl
2.5 M CaCl2	1500 µl
Double-distilled water	ad 15 ml

The listed amounts are for transfection of 15 15-cm-dishes of HEK293T cells.

For purification, the virus-containing phase was thawed on ice. HiTrap Q FF sepharose column and superloop were connected with the ÄKTAprime plus chromatography system. For collection of the purified fractions, 1.5-ml-centrifuge-tubes were loaded into the tube rack. Dropsync unit was adjusted to position 1. The HiTrap Q FF sepharose column was equilibrated with 25 ml of buffer A at 10 ml/min flow rate. Manual run mode was selected with 1.0 ml/min flow rate, 1 ml fraction size, and the measuring curves were put to starting point via autozero. Virus phase was diluted 1:1 with buffer A prior to application to the ÄKTAprime plus system with a 10 ml syringe to fill the superloop. The virus dilution from the superloop was injected into the ÄKTAprime plus system and 1 ml fractions were collected in 1.5-ml-tubes. During this step, the UV and conductance curves should be monitored via the Äktaprime software. When the conductance curve has reached basal values, the ÄKTAprime plus system was switched to 100% buffer B at 10 ml/min flow rate and 0 ml fraction size to purge the sepharose column from the remaining virus dilution. To wash out the remaining salt from the system, sterile, double-distilled water was used at 10 ml/min flow rate. When the conductance curve reached zero, the washing step was continued for additional 5 min. All of the collected 1-ml fractions within the plateau phase of the conductance curve were pooled. The purified and pooled virus fractions can be stored in a 15-ml-polystyrene-tube at −80°C until continuing with the virus concentration step.

Concentration of rAAVs

For virus concentration, the purified virus fraction was first thawed on ice. 4 ml of the fraction was then transferred to an Amicon centrifugal filter unit and was centrifuged at 2000 × g for 10 min at 20°C (4000 rpm in a Beckman centrifuge using a JA-10 rotor). The flow-through was discarded and the cycles of 4 ml virus fraction transfer and subsequent centrifugation were repeated until the complete virus was loaded to the column and ∼500 µl remained in the filter unit. The concentrated virus was

washed with 1 ml 0.014% Tween/PBS-MK by pipetting up and down five times. The virus suspension was then centrifuged at 2000 × g at 20°C until 100 µl of concentrated virus suspension remained in the filter unit. The supernatant was aliquoted and stored in 1.5-ml screw cap tubes. Virus suspensions were stored at −80°C until determination of virus titer and subretinal injection.

Titer Determination of rAAVs

For titer determination, the virus suspension was diluted 1:500 with double-distilled water. 5 µl of virus dilution, a standard sample, and double-distilled water were used for quantitative real-time PCR according to **Tables 2, 3**. For standard preparation, a small fragment within the WPRE (woodchuck hepatitis virus posttranscriptional regulatory element) of the pAAV2.1 vector was amplified via PCR. The corresponding primers are listed in **Table 4**. The PCR product was purified after gel electrophoresis and DNA concentration was determined with a spectrophotometer (Nanodrop 2000c). The concentration of the standard for 10^{10} copies per 5 µl was calculated according to the following equation:

$$c\left(\frac{pg}{\mu l}\right) = \frac{10^{10} \times 660 \times 10^{12}\,\frac{pg}{mol} \times fragment\ size}{6.022 \times 10^{23}\,\frac{1}{mol} \times 5\mu l}$$

c is the concentration of the standard for 10^{10} copies per 5 µl;

660 × 10^{12} pg/mol is the mean molar mass of a base pair (deoxyribosyladenosine with deoxyribosylthymidine or deoxyribosylcytidine with deoxyribosylguanosine);

6.022 × 1023/mol is the Avogadro constant;

The size of the amplified WPRE fragment is given in base pairs.

A 10-fold serial dilution was made to obtain standards at different concentrations. 5 µl of a standard were used to determine the virus titer via quantitative real-time PCR. Standards were stored at −20°C until use.

Subretinal Injection of rAAV Vectors

The procedure of subretinal rAAV injection was carried out as described by (Mühlfriedel et al., 2013) with slight modifications. The NanoFil 34-gauge beveled needle was sterilized before each experiment. The 10-µl NanoFil syringe was preloaded with the virus suspension under exclusion of air bubbles. The mouse was anesthetized via intraperitoneal injection of xylazine (20 mg/kg) and ketamine (40 mg/kg). Five percent dexpanthenol eye salve was applied to the non-injected eye and the anesthetized mouse was placed on a 37°C heating plate. The eye was dilated with 1% atropine and 0.5% tropicamide solution. The eye fundus was focused with a stereomicroscope until blood vessels became clearly visible. The outer layers of the eye (sclera, choroidea, and retinal pigment epithelium) were then penetrated with the needle in a 60° angle. When the needle was visible beneath the retina, 1 µl (containing approx. 10^9 rAAV particles) of virus suspension was gradually applied freehand. For the co-delivery of two constructs, a 1:1 mixture of titer matched rAAVs was used. The formation of a clearly visible injection bleb indicated a correct application to the subretinal space. The needle was slowly removed from the eye, which was subsequently treated with gentamicin 5 mg/g and dexamethasone 0.3 mg/g eye salve. The anesthetized mouse was placed under a heat lamp and was monitored until awaking from narcosis. If available, optical coherence tomography (OCT) was conducted immediately after subretinal injection to monitor the injection procedure and the degree of subretinal detachment (Mühlfriedel et al., 2013).

Dissection of Murine Retinas and Isolation of Photoreceptor Outer Segments

The mouse was sacrificed 10 days post injection and the injected eye was proptosed by placing blunt forceps around the optic nerve close to its exit from the eye. The globe was then transected along the equator with a sharp razor blade or scalpel and the vitreous body was removed by carefully pushing it out of the incision with a thin needle. The forceps was pushed upwards to detach the retina from the optic nerve and from the pigment epithelium. The upward movement was gradually continued until the retina lay free on the forceps. The isolated retina was transferred into a petri dish filled with phosphate buffered saline (PBS). The expression or co-expression of fluorescent fusion proteins was analyzed by an epifluorescence microscope (Axioplan 2 imaging, Zeiss). As described in **Figure 2A**, the retina was transferred into a 1.5-ml-microcentrifuge-tube containing 100 µl PBS. In case of weak expression or in case of isolating cone OS, two (or more) retinas can be pooled at this stage

TABLE 2 | Pipetting scheme for quantitative real-time PCR.

Reagent	Volume (µl)
Template plasmid (50–100 ng)/standard/double-distilled water (negative control)	5,0
KAPA SYBR FAST Universal x2 qPCR MasterMix	10,0
WPREqF (10 pmol/µl)	1,0
WPREqR (10 pmol/µl)	1,0
Double-distilled water	ad 20,0

TABLE 3 | Program steps of quantitative real-time PCR for titer determination.

Step	Phase	Temperature (°C)	Time	Cycle numbers
1	Initial Denaturation	95	10 min	1
2	Denaturation	95	10 s	40
3	Annealing	60	5 s	
4	Elongation	72	20 s	
5	Final elongation	72	5 min	1

TABLE 4 | Primer sequences for quantitative real-time PCR and standard preparation.

Primer for amplification of standard fragment	Sequence (5′ to 3′)
WPREqF	AGTTCCGCCGTGGCAATAGG
WPREqR	CAAGGAGGAGAAAATGAAAGCC

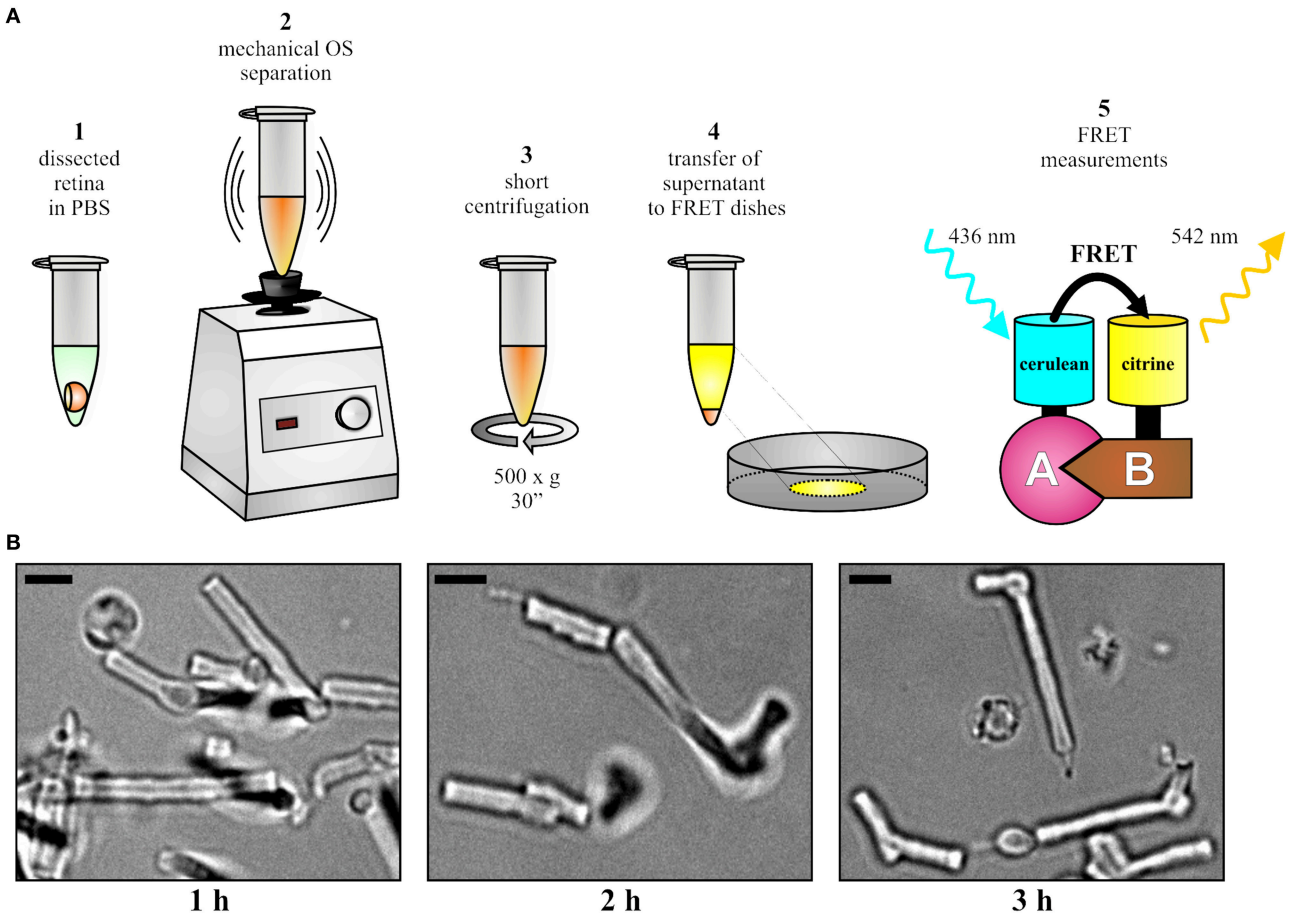

FIGURE 2 | OS preparation and FRET. (A) Overview of the protocol for the OS preparation and for the subsequent FRET measurements. **(B)** Representative images of isolated OS at different time points after the isolation. Scale bar, 3 μm.

to ensure a sufficient number of fluorescent OS. The OS were separated from the retina by vortexing for 15–30 s. Vortexing should not surpass 30 s as excessive shearing disrupts the shape of OS. Afterwards, centrifugation was conducted at 500 × g for 30 s and the supernatant was carefully transferred to a fresh 1.5-ml-microcentrifuge-tube without disturbing the pellet. The supernatant contained the OS fraction suitable for FRET measurements. If desirable, the quality and fluorescence of purified OS can be analyzed (**Figure 2B**) on a standard epifluorescence or confocal microscope by transferring 5–10 μl of supernatant on microscope slides topped with cover slips.

FRET Measurements on Isolated Outer Segments

Setup of FRET Microscope, Software, and OS Sample

Calculation of three cube sensitized acceptor emission FRET requires data for FRET donor (cerulean) only and acceptor (citrine) only samples (Erickson et al., 2003; Shaltiel et al., 2012; Ben Johny et al., 2013). Therefore, in addition to the fluorescence signals from OS co-expressing cerulean and citrine constructs, OS expressing cerulean- or citrine-tagged proteins only must be imaged as well. For optimized signal acquisition, we recommend to start the FRET measurements with OS co-expressing both cerulean- and citrine-tagged FRET partners (hereinafter referred to as FRET sample).

Purified OS solution was diluted in 400 μl FRET imaging solution and was transferred to the center of an imaging dish. FRET measurements should be performed on single OS as fluorescence from adjacent OS might interfere with the measurements. Therefore, the density of OS should be adjusted in order to allow for detection of single fluorescent OS within the defined region of interest on the imaging setup (image-plane pinhole). As the density of transduced OS varies with transduction and purification efficiency, it is necessary to individually adjust the amount of OS for each preparation. The OS were allowed to sediment to the bottom for 10–15 min at room temperature. The fluorescence lamp was turned on at least 30 min prior to the experiment to ensure stable illumination. The image-plane pinhole was set to an appropriate size that allows monitoring of a single OS, which was positioned in the center of the axial beam path. This position must not be changed throughout the entire FRET measurements performed on the same day. The FelixGX software was started to acquire the

fluorescence intensities. An oil-immersion and high-resolution objective (40x or higher) was used and immersion medium was applied. The imaging dish was placed onto the sample holder and bright field illumination was used to focus on OS. Individual OS were identified based on their characteristic morphology as shown in **Figure 2B**.

Measurements on the FRET Sample

For measurements of FRET samples, OS that express sufficient levels of both citrine and cerulean were used. A fluorescent OS was placed in the center of the optic field and fluorescence from adjacent cells invading the optic field was excluded. Gain and fluorescence intensity settings were adjusted in order to achieve an appropriate signal prior to the first signal acquisition. All subsequent data must be acquired under the same conditions. Fluorescence intensities were collected with the cerulean cube, FRET cube, and citrine cube. The settings for the single cubes are as follows:

For cerulean cube: 426–446 nm excitation filter, T455lp dichroic mirror, and 460–500 nm emission filter; for citrine cube: 490–510 nm excitation filter, T515lp dichroic mirror, and 510–550 nm emission filter; for FRET cube: 426–446 nm excitation filter, T455lp dichroic mirror, and 510–550 nm emission filter.

The data for a single OS was acquired according to the following sequence: cerulean excitation was started and the signals with the cerulean cube followed by the FRET cube were obtained. Then, citrine excitation was carried out and the signal with the citrine cube was obtained. 25–35 individual OS were measured. To subtract the OS autofluorescence, the same three cube protocol as described above was applied to ∼10 OS that do not express citrine or cerulean within the corresponding sample.

Cerulean-only Expressing Preparation

OS with varying expression levels of cerulean were used. For each OS, the fluorescence intensity was measured with the cerulean, FRET, and citrine filter cube according to the same protocol as described above for the FRET sample. Data from at least 15 OS were collected. To subtract the OS autofluorescence, the cerulean, FRET, and citrine cube were measured for ∼10 OS that do not express cerulean within the same sample.

Citrine-only Expressing Preparation

OS with varying expression levels of citrine were chosen. For each OS, the fluorescence intensity was measured with the cerulean, FRET, and citrine filter cube according to the same protocol as described above for the FRET sample. Data from at least 15 OS were collected. To subtract the OS autofluorescence, the cerulean, FRET, and citrine cube were measured for ∼10 OS that do not express citrine within the same sample.

Data Analysis

The data set consists of three data points per OS, i.e., one intensity value for each filter cube. As controls, we additionally included data points measured from non-fluorescent OS for background subtraction as well as from cerulean-only and citrine-only expressing OS for donor bleed-through and cross-excitation corrections, respectively. The data was transferred to an Excel sheet or an adequate data processing program. For the 10 non-fluorescent OS measured for each of the preparations, i.e. FRET, cerulean-only and citrine-only, the mean intensity values were calculated. These mean values were subtracted from each data point of the particular preparation to adjust for background fluorescence. In order to correct for donor bleed-through, the correction constant R_{D1} for each of the single data points gathered from the cerulean-only expressing preparation was calculated by dividing the intensities captured with the FRET-cube by those obtained from the cerulean-cube. In order to correct for acceptor cross-excitation, the correction constant R_A for each single data point gathered from the citrine-only expressing preparation was calculated by dividing the intensities captured with the FRET-cube by those obtained from the citrine-cube. The mean value for both constants, R_{D1} and R_A, was calculated. Usually, a value of ∼0.25 for cerulean (donor-bleed through) and 0.03 for citrine (acceptor cross-excitation) was obtained in our setup. However, these values might differ with fluorophore variant, protein tag, and imaging setup. The calculated constants were used for donor bleed-through and acceptor cross-excitation to evaluate the FRET ratio (FR) for each single measurement according to the following equation:

$$FR = \frac{S_{FRET} - R_{D1} \cdot S_{cerulean}}{R_A \cdot S_{citrine}}$$

$S_{cerulean}$, $S_{citrine}$, and S_{FRET} are intensity signals acquired with respective filter cubes (FRET, cerulean, and citrine) in a FRET specimen and R_A, R_{D1} are predetermined factors for calibration issues (R_A: Acceptor cross-excitation, R_{D1}: Donor bleed-through). Depending on the imaging setup and, in particular, the filter set used for experiments, a considerable amount of cerulean fluorescence may be detected by the citrine cube. To correct for this, an additional donor bleed-trough correction constant R_{D2} should be calculated by dividing the cerulean fluorescence intensity obtained with the citrine cube by the one detected with the cerulean cube. Accordingly, the FR equation was adjusted to: (Erickson et al., 2003)

$$FR = \frac{S_{FRET} - R_{D1} \cdot S_{cerulean}}{R_A \cdot (S_{citrine} - R_{D2} \cdot S_{cerulean})}$$

In our FRET setup, R_{D2} was negligibly small and could thus be ignored. However, it should be rigorously tested for each individual imaging setup. The mean value of the previously obtained data was calculated. The mean value represents the overall *FR*. Note that the *FR* values are instrumentation dependent. FRET efficiencies (E_A) (which are independent of the setup used) can be easily calculated from the *FR* using the following equation:

$$E_A = [FR - 1] \cdot \frac{\varepsilon_{citrine}(436)}{\varepsilon_{cerulean}(436)}$$

$\varepsilon_{citrine}$ and $\varepsilon_{cerulean}$ are the FRET setup specific average molar extinction coefficients for citrine and cerulean, respectively.

Troubleshooting

Problems, possible underlying reasons and advices concerning critical steps of the procedure can be found in **Table 5**.

TABLE 5 | Troubleshooting.

Problem	Possible Reason	Solution
Low titer.	Transfection reagents do not have sufficient transfection efficiency.	Test transfection reagents for their efficiencies. Requantify plasmid concentration used for transfection.
	pH of HEK293T cell medium is not optimal for transfection.	Remove HEK293T dishes from incubator immediately before transfection.
	The sequence of the ITRs (inverted terminal repeats) within the plasmid is not intact, thus replication and packaging of the rAAV vector is inefficient.	Check for the presence of *SmaI* and/or *Eam1105I* restriction sites within the palindromic ITR sequence. In case of unexpected restriction fragment band pattern, repeat cloning using an intact rAAV vector.
The injection bleb in the subretinal space is not visible under the surgical/stereomicroscope.	The eye shows damages or opacity of the cornea.	Make sure to choose only mice with clear, intact eyes for subretinal injection. Check the eyes under the stereomicroscope.
	Virus suspensions diluted with double-distilled water to adjust the particle concentration do not show optical refraction as clear as the virus suspension in 0.014% Tween/PBS-MK.	Dilute with 0.014% Tween/PBS-MK to adjust virus particle concentration. If the suspension is too viscous, dilute with double-distilled water at a maximum ratio of 1:2 (water-to-virus suspension).
	The injection angle is not optimal.	Adjust the injection angle to ∼60°.
Loss of many OS.	Removal of the pigment epithelium and ciliary body after retina isolation with forceps may result in loss of many OS.	Proceed with the next step without any removal of undesirable tissue.
Protein expression level is too low, thus leading to a too weak or absent fluorescence signal.	Virus suspension is not (completely) injected into the subretinal space.	Make sure to see a clear injection bleb as this indicates the correct injection to the subretinal space. An injection into the upper layers of the eye such as sclera or choroidea causes a bleb outside at the globe. If the needle is intravitreal, it can be clearly and sharply seen under the stereomicroscope. By contrast, a needle in the subretinal space (injection angle at ∼60°) appears rather blurred. Keep the injection needle for at least 20 s in the bleb to ensure proper delivery of the desired volume. If possible, perform OCT measurements on the anesthetized mouse after injection to confirm detachment of the retina at the injection position.
	Virus titer has not been determined correctly.	Double check the virus titer. Otherwise, repeat the virus production.

Time Schedule

- Transfection of HEK293T cells: 48 h
- Isolation of rAAV: 2–4 h (varies depending on number of dishes to be harvested)
- Gradient purification and rAAV concentration: 6 h (for 2 different rAAV constructs)
- Titer determination via quantitative real-time PCR: 2 h
- Preparation of standards for titer determination: 2 h
- Subretinal injection: 20 min (per mouse)
- rAAV transduction of murine retina and protein expression: 10 days
- Isolation of photoreceptor OS: 10 min (per eye)
- FRET imaging: 5–9 h (depending on number of retinas to be analyzed)
- Data analysis: 2–3 h (depending on number of measurements to be processed).

ANTICIPATED RESULTS AND DISCUSSION

In this protocol, we demonstrate that robust FRET signals can be measured for well-known homomeric and heteromeric interactions of different membrane and soluble proteins in OS of rod and cone photoreceptors. Representative results are found in our previous publications (Becirovic et al., 2014; Nguyen et al., 2016). Selected data from these publications are presented in the modified graphs shown in **Figure 3**. FRET is given as FRET efficiencies (E_A) which can be easily calculated from the FRET ratios (*FR*) as shown in the "Data Analysis" Section. It is noteworthy to mention that the mean value of E_A may not represent the maximal FRET efficiency ($E_{A\,max}$). $E_{A\,max}$ can be calculated if a relatively high variability of the cerulean/citrine molar ratios is present in FRET measurements. If this is the case, single FRET values can be plotted against the cerulean/citrine intensity ratios to obtain the binding curves and to calculate $E_{A\,max}$. A comparison of $E_{A\,max}$ between different constructs allows for the determination of relative binding affinities. Since $E_{A\,max}$ is directly proportional to the binding affinity, our method in principle should also allow for comparisons of relative binding affinities of single protein-protein interactions in an isolated subcellular compartment.

Taken together, our protocol enables the measurement of robust FRET signals *ex vivo* in small and highly specialized

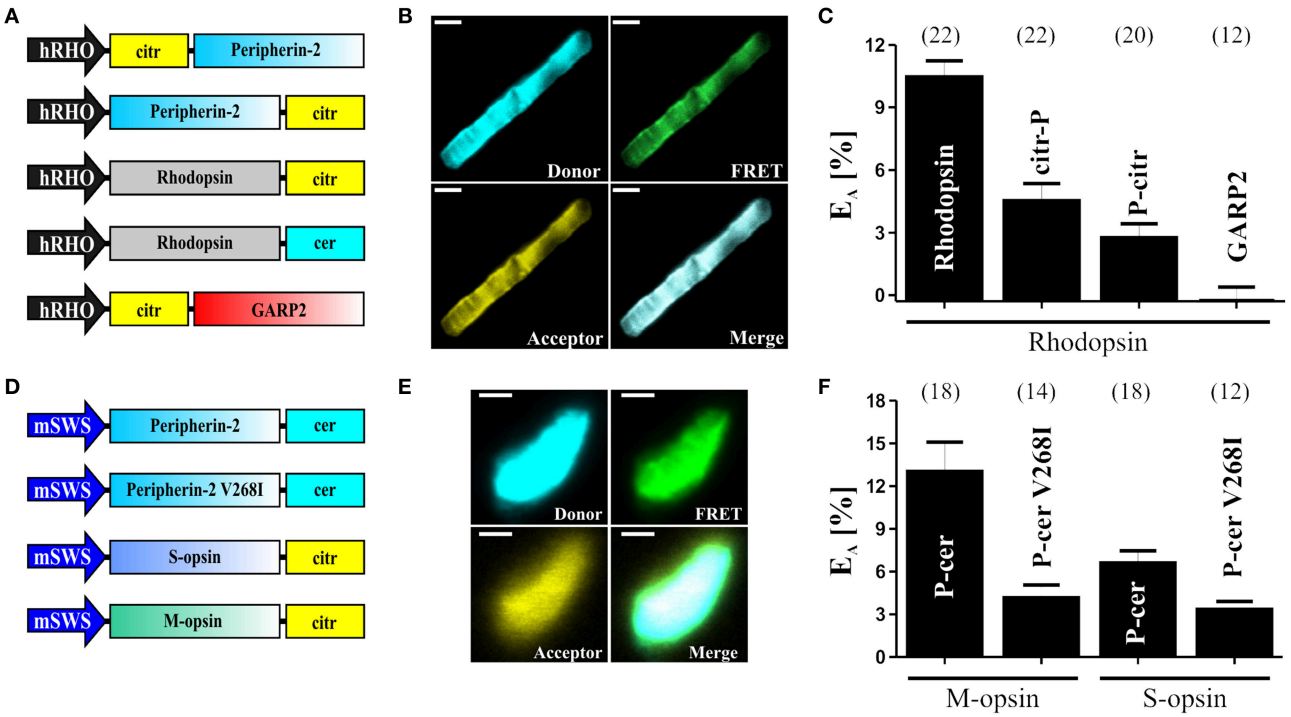

FIGURE 3 | FRET measurements in isolated photoreceptor OS. (A) Schematic depiction of the single constructs used for the subretinal injection and for the determination of the FRET efficiencies (E_A) shown in **(C)**. **(B)** Representative confocal images of single isolated rod OS co-expressing C-terminally tagged peripherin-2 and rhodopsin. The excitation wavelength and emission filter settings used to obtain the single channels (Donor, FRET and Acceptor) are summarized in the "Stepwise Procedures" section. Scale bar, 1.5 μm. **(C)** Results of the FRET measurements for different FRET pair combinations given as mean values ± standard error of the mean (SEM). Numbers of independent measurements (*n*) are given in brackets. E_A values for the single FRET pairs are as follows: Rho-Rho, $E_A = 10.45 \pm 0.78$; Rho-citr-P, $E_A = 4.52 \pm 0.82$; Rho-P-citr, $E_A = 2.76 \pm 0.65$; Rho-GARP2, $E_A = 0.26 \pm 0.65$; **(D)** Schematic view of the single constructs used for the subretinal injection and for the determination of the FRET efficiencies (E_A) shown in **(F)**. **(E)** Representative confocal images of single isolated cone OS co-expressing C-terminally tagged peripherin-2 and cone opsin. Scale bar, 1.5 μm. **(F)** Results of the FRET measurements (given as mean values ± SEM) for different FRET pair combinations as indicated. Numbers of independent measurements (*n*) are given in brackets. E_A values for the single FRET pairs are described elsewhere (Nguyen et al., 2016).

cellular compartments of mammalian cells like OS of murine photoreceptors. This allows for the systematic analysis of protein-protein interactions in a physiological or pathophysiological context of the photoreceptor biology. In particular, it can be used to analyze the effects of disease-associated mutations on protein-protein interactions. OS of photoreceptors are modified cilia. Ciliopathies encompass a very large group of genetic disorders compromising the functional or structural integrity of cilia. Since the isolation of ciliary compartments from other tissues (i.e. kidney, lung, brain, olfactory epithelium) is well-established (Mitchell et al., 2009), our protocol should also be transferable to analyses of protein-protein interactions in any other ciliated tissue. In non-dividing cells, rAAVs lead to an episomal and long-term expression of the respective gene for up to several years (Trapani et al., 2014). Thus, FRET measurements can be performed on several time points during the development of the tissue. Finally, our protocol could also provide an experimental basis for the establishment of FRET measurements in the retina of living animals by means of fundus ophthalmoscopy combined with e.g., conventional fluorescence imaging, 2-photon imaging, multiphoton FLIM-FRET, or near infrared-FRET fluorescence lifetime imaging (Abe et al., 2013; Johnsson et al., 2014).

AUTHOR CONTRIBUTIONS

EB designed the protocol with contribution from SM. EB, SB, ON, LR, VH, CS, and ESB performed the experiments, EB, SB, ON, and ESB analyzed the results. EB, ON, ESB, and SM wrote the manuscript with contribution from CW and MB.

FUNDING

This work was supported by the Deutsche Forschungsgemeinschaft (DFG, BE 4830/1 1).

ACKNOWLEDGMENTS

We thank Elisabeth Schulze and Berit Noack for excellent technical support.

REFERENCES

Abe, K., Zhao, L., Periasamy, A., Intes, X., and Barroso, M. (2013). Non-invasive *in vivo* imaging of near infrared-labeled transferrin in breast cancer cells and tumors using fluorescence lifetime FRET. *PLoS ONE* 8:e80269. doi: 10.1371/journal.pone.0080269

Allocca, M., Mussolino, C., Garcia-Hoyos, M., Sanges, D., Iodice, C., Petrillo, M., et al. (2007). Novel adeno-associated virus serotypes efficiently transduce murine photoreceptors. *J. Virol.* 81, 11372–11380. doi: 10.1128/JVI.01327-07

Arshavsky, V. Y., and Burns, M. E. (2012). Photoreceptor signaling: supporting vision across a wide range of light intensities. *J. Biol. Chem.* 287, 1620–1626. doi: 10.1074/jbc.R111.305243

Auricchio, A., Hildinger, M., O'Connor, E., Gao, G. P., and Wilson, J. M. (2001). Isolation of highly infectious and pure adeno-associated virus type 2 vectors with a single-step gravity-flow column. *Hum. Gene Ther.* 12, 71–76. doi: 10.1089/104303401450988

Becirovic, E., Bohm, S., Nguyen, O. N., Riedmayr, L. M., Koch, M. A., Schulze, E., et al. (2016). *In vivo* analysis of disease-associated point mutations unveils profound differences in mRNA splicing of peripherin-2 in rod and cone photoreceptors. *PLoS Genet.* 12:e1005811. doi: 10.1371/journal.pgen.1005811

Becirovic, E., Nguyen, O. N., Paparizos, C., Butz, E. S., Stern-Schneider, G., Wolfrum, U., et al. (2014). Peripherin-2 couples rhodopsin to the CNG channel in outer segments of rod photoreceptors. *Hum. Mol. Genet.* 23, 5989–5997. doi: 10.1093/hmg/ddu323

Ben Johny, M., Yang, P. S., Bazzazi, H., and Yue, D. T. (2013). Dynamic switching of calmodulin interactions underlies Ca2+ regulation of CaV1.3 channels. *Nat. Commun.* 4, 1717. doi: 10.1038/ncomms2727

Bennett, J., Maguire, A. M., Cideciyan, A. V., Schnell, M., Glover, E., Anand, V., et al. (1999). Stable transgene expression in rod photoreceptors after recombinant adeno-associated virus-mediated gene transfer to monkey retina. *Proc. Natl. Acad. Sci. U.S.A.* 96, 9920–9925. doi: 10.1073/pnas.96.17.9920

Berger, W., Kloeckener-Gruissem, B., and Neidhardt, J. (2010). The molecular basis of human retinal and vitreoretinal diseases. *Prog. Retin. Eye Res.* 29, 335–375. doi: 10.1016/j.preteyeres.2010.03.004

Erickson, M. G., Liang, H., Mori, M. X., and Yue, D. T. (2003). FRET two-hybrid mapping reveals function and location of L-type Ca2+ channel CaM preassociation. *Neuron* 39, 97–107. doi: 10.1016/S0896-6273(03)00395-7

Feilmeier, B. J., Iseminger, G., Schroeder, D., Webber, H., and Phillips, G. J. (2000). Green fluorescent protein functions as a reporter for protein localization in *Escherichia coli*. *J. Bacteriol.* 182, 4068–4076. doi: 10.1128/JB.182.14.4068-4076.2000

Gao, G. P., Alvira, M. R., Wang, L., Calcedo, R., Johnston, J., and Wilson, J. M. (2002). Novel adeno-associated viruses from rhesus monkeys as vectors for human gene therapy. *Proc. Natl. Acad. Sci. U.S.A.* 99, 11854–11859. doi: 10.1073/pnas.182412299

Goldberg, A. F., Moritz, O. L., and Molday, R. S. (1995). Heterologous expression of photoreceptor peripherin/rds and Rom-1 in COS-1 cells: assembly, interactions, and localization of multisubunit complexes. *Biochemistry* 34, 14213–14219. doi: 10.1021/bi00043a028

Grieger, J. C., Choi, V. W., and Samulski, R. J. (2006). Production and characterization of adeno-associated viral vectors. *Nat. Protoc.* 1, 1412–1428. doi: 10.1038/nprot.2006.207

Griesbeck, O., Baird, G. S., Campbell, R. E., Zacharias, D. A., and Tsien, R. Y. (2001). Reducing the environmental sensitivity of yellow fluorescent protein. Mechanism and applications. *J. Biol. Chem.* 276, 29188–29194. doi: 10.1074/jbc.M102815200

Hildinger, M., Auricchio, A., Gao, G., Wang, L., Chirmule, N., and Wilson, J. M. (2001). Hybrid vectors based on adeno-associated virus serotypes 2 and 5 for muscle-directed gene transfer. *J. Virol.* 75, 6199–6203. doi: 10.1128/JVI.75.13.6199-6203.2001

Hirata, E., Yukinaga, H., Kamioka, Y., Arakawa, Y., Miyamoto, S., Okada, T., et al. (2012). *In vivo* fluorescence resonance energy transfer imaging reveals differential activation of Rho-family GTPases in glioblastoma cell invasion. *J. Cell Sci.* 125(Pt 4), 858–868. doi: 10.1242/jcs.089995

Hovan, S. C., Howell, S., and Park, P. S. (2010). Forster resonance energy transfer as a tool to study photoreceptor biology. *J. Biomed. Opt.* 15, 067001. doi: 10.1117/1.3505023

Jastrzebska, B., Maeda, T., Zhu, L., Fotiadis, D., Filipek, S., Engel, A., et al. (2004). Functional characterization of rhodopsin monomers and dimers in detergents. *J. Biol. Chem.* 279, 54663–54675. doi: 10.1074/jbc.M408691200

Johnsson, A. K., Dai, Y., Nobis, M., Baker, M. J., McGhee, E. J., Walker, S., et al. (2014). The Rac-FRET mouse reveals tight spatiotemporal control of Rac activity in primary cells and tissues. *Cell Rep.* 6, 1153–1164. doi: 10.1016/j.celrep.2014.02.024

Knepp, A. M., Periole, X., Marrink, S. J., Sakmar, T. P., and Huber, T. (2012). Rhodopsin forms a dimer with cytoplasmic helix 8 contacts in native membranes. *Biochemistry* 51, 1819–1821. doi: 10.1021/bi3001598

Koch, S., Sothilingam, V., Garcia Garrido, M., Tanimoto, N., Becirovic, E., Koch, F., et al. (2012). Gene therapy restores vision and delays degeneration in the CNGB1(−/−) mouse model of retinitis pigmentosa. *Hum. Mol. Genet.* 21, 4486–4496. doi: 10.1093/hmg/dds290

Kumagai, Y., Naoki, H., Nakasyo, E., Kamioka, Y., Kiyokawa, E., and Matsuda, M. (2014). Heterogeneity in ERK activity as visualized by *in vivo* FRET imaging of mammary tumor cells developed in MMTV-Neu mice. *Oncogene* 34, 1051–1057. doi: 10.1038/onc.2014.28

Loewen, C. J., and Molday, R. S. (2000). Disulfide-mediated oligomerization of Peripherin/Rds and Rom-1 in photoreceptor disk membranes. Implications for photoreceptor outer segment morphogenesis and degeneration. *J. Biol. Chem.* 275, 5370–5378. doi: 10.1074/jbc.275.8.5370

Michalakis, S., Muhlfriedel, R., Tanimoto, N., Krishnamoorthy, V., Koch, S., Fischer, M. D., et al. (2010a). Restoration of cone vision in the CNGA3−/− mouse model of congenital complete lack of cone photoreceptor function. *Mol. Ther.* 18, 2057–2063. doi: 10.1038/mt.2010.149

Michalakis, S., Mühlfriedel, R., Tanimoto, N., Krishnamoorthy, V., Koch, S., Fischer, M. D., et al. (2010b). Restoration of cone vision in the CNGA3−/− mouse model of congenital complete lack of cone photoreceptor function. *Mol. Ther.* 18, 2057–2063. doi: 10.1038/mt.2010.149

Michalakis, S., Zong, X., Becirovic, E., Hammelmann, V., Wein, T., Wanner, K. T., et al. (2011). The glutamic acid-rich protein is a gating inhibitor of cyclic nucleotide-gated channels. *J. Neurosci.* 31, 133–141. doi: 10.1523/JNEUROSCI.4735-10.2011

Mitchell, K. A., Szabo, G., and Otero Ade, S. (2009). Methods for the isolation of sensory and primary cilia–an overview. *Methods Cell Biol.* 94, 87–101. doi: 10.1016/S0091-679X(08)94004-8

Mühlfriedel, R., Michalakis, S., Garrido, M. G., Biel, M., and Seeliger, M. W. (2013). Optimized technique for subretinal injections in mice. *Methods Mol. Biol.* 935, 343–349. doi: 10.1007/978-1-62703-080-9_24

Murlidharan, G., Samulski, R. J., and Asokan, A. (2014). Biology of adeno-associated viral vectors in the central nervous system. *Front. Mol. Neurosci.* 7:76. doi: 10.3389/fnmol.2014.00076

Nguyen, O. N., Bohm, S., Giessl, A., Butz, E. S., Wolfrum, U., Brandstatter, J. H., et al. (2016). Peripherin-2 differentially interacts with cone opsins in outer segments of cone photoreceptors. *Hum. Mol. Genet.* doi: 10.1093/hmg/ddw103. [Epub ahead of print].

Poetsch, A., Molday, L. L., and Molday, R. S. (2001). The cGMP-gated channel and related glutamic acid-rich proteins interact with peripherin-2 at the rim region of rod photoreceptor disc membranes. *J. Biol. Chem.* 276, 48009–48016. doi: 10.1074/jbc.M108941200

Rizzo, M. A., Springer, G. H., Granada, B., and Piston, D. W. (2004). An improved cyan fluorescent protein variant useful for FRET. *Nat. Biotechnol.* 22, 445–449. doi: 10.1038/nbt945

Roepman, R., and Wolfrum, U. (2007). Protein networks and complexes in photoreceptor cilia. *Subcell. Biochem.* 43, 209–235. doi: 10.1007/978-1-4020-5943-8_10

Schön, C., Biel, M., and Michalakis, S. (2013). Gene replacement therapy for retinal CNG channelopathies. *Mol. Genet. Genomics* 288, 459–467. doi: 10.1007/s00438-013-0766-4

Shaltiel, L., Paparizos, C., Fenske, S., Hassan, S., Gruner, C., Rotzer, K., et al. (2012). Complex regulation of voltage-dependent activation and inactivation properties of retinal voltage-gated Cav1.4 L-type Ca2+ channels

by Ca2+-binding protein 4 (CaBP4). *J. Biol. Chem.* 287, 36312–36321. doi: 10.1074/jbc.M112.392811

Trapani, I., Puppo, A., and Auricchio, A. (2014). Vector platforms for gene therapy of inherited retinopathies. *Prog. Retin. Eye Res.* 43C, 108–128. doi: 10.1016/j.preteyeres.2014.08.001

Waldo, G. S., Standish, B. M., Berendzen, J., and Terwilliger, T. C. (1999). Rapid protein-folding assay using green fluorescent protein. *Nat. Biotechnol.* 17, 691–695. doi: 10.1038/10904

Wen, L., Thunemann, M., Feil, S., Hillenbrand, M., Vachaviolos, A., Ott, T., et al. (2013). Analysis of cGMP signalling with transgenic mice expressing FRET-based cGMP sensors. *BMC Pharmacol. Toxicol.* 14, 1–2. doi: 10.1186/2050-6511-14-s1-p76

Zacchigna, S., Zentilin, L., and Giacca, M. (2014). Adeno-associated virus vectors as therapeutic and investigational tools in the cardiovascular system. *Circ. Res.* 114, 1827–1846. doi: 10.1161/CIRCRESAHA.114.302331

Conflict of Interest Statement: The authors declare that the research was conducted in the absence of any commercial or financial relationships that could be construed as a potential conflict of interest.

Despite hosting the research topic together with one of the authors of this manuscript, the handling Editor state that the process met the standards of a fair and objective review.

SCIENTIFIC REPORTS

OPEN

Peripherin-2 and Rom-1 have opposing effects on rod outer segment targeting of retinitis pigmentosa-linked peripherin-2 mutants

Received: 19 January 2017
Accepted: 12 April 2017
Published online: 24 May 2017

Sybille Böhm[1,2], Lisa M. Riedmayr[1,2], O. N. Phuong Nguyen[1,2], Andreas Gießl[3], Toni Liebscher[1,2], Elisabeth S. Butz[1,2], Christian Schön[1,2], Stylianos Michalakis[1,2], Christian Wahl-Schott[1,2], Martin Biel[1,2] & Elvir Becirovic[1,2]

Mutations in the photoreceptor outer segment (OS) specific peripherin-2 lead to autosomal dominant retinitis pigmentosa (adRP). By contrast, mutations in the peripherin-2 homolog Rom-1 cause digenic RP in combination with certain heterozygous mutations in peripherin-2. The mechanisms underlying the differential role of peripherin-2 and Rom-1 in RP pathophysiology remained elusive so far. Here, focusing on two adRP-linked peripherin-2 mutants, P210L and C214S, we analyzed the binding characteristics, protein assembly, and rod OS targeting of wild type (per^{WT}), mutant peripherin-2 (per^{MT}), or Rom-1 complexes, which can be formed in patients heterozygous for peripherin-2 mutations. Both mutants are misfolded and lead to decreased binding to per^{WT} and Rom-1. Furthermore, both mutants are preferentially forming non-covalent per^{MT}-per^{MT}, per^{WT}-per^{MT}, and Rom-1-per^{MT} dimers. However, only per^{WT}-per^{MT}, but not per^{MT}-per^{MT} or Rom-1-per^{MT} complexes could be targeted to murine rod OS. Our study provides first evidence that non-covalent per^{WT}-per^{MT} dimers can be targeted to rod OS. Finally, our study unravels unexpected opposing roles of per^{WT} and Rom-1 in rod OS targeting of adRP-linked peripherin-2 mutants and suggests a new treatment strategy for the affected individuals.

The tetraspanin peripherin-2 is exclusively expressed in outer segments (OS), specific light detecting compartments of photoreceptors. Peripherin-2 forms homo- and heteromeric protein complexes in OS. The core homomeric peripherin-2 unit is the non-covalent tetramer, which can also assemble into covalently linked octamers and higher-order oligomers[1–3]. These homomeric peripherin-2 complexes are crucial for proper OS morphology and architecture[4]. Peripherin-2 also forms heteromeric complexes with its homolog Rom-1, however, the functional importance of these complexes remained unclear[2,5,6]. Autosomal dominant retinitis pigmentosa (adRP) is the most frequent hereditary retinal disorder characterized by progressive loss of vision due to rod photoreceptor degeneration. Mutations in the peripherin-2 gene (*PRPH2*) are among the most common causes for adRP[7,8]. Interestingly, despite the high sequence identity (approx. 35%) and the high structural conservation of Rom-1 and peripherin-2[2,9], mutations in Rom-1 are not clearly linked to monogenic adRP. Some homozygous Rom-1 mutations, however, cause digenic RP in combination with a heterozygous mutation in *PRPH2*, suggesting that Rom-1 could function as genetic modifier that shapes the disease progression[10,11]. Nevertheless, the molecular mechanisms underlying the postulated modifier function of Rom-1 have not been determined yet[12]. The majority of adRP-linked peripherin-2 mutants are located within the large loop domain connecting the transmembrane domain 3 and 4, also known as EC2 or D2 loop domain[13,14]. Some adRP-linked peripherin-2 mutants in EC2 were shown to influence the subunit assembly[15,16]. In this context, it was postulated that peripherin-2 tetramerization

[1]Center for Integrated Protein Science Munich CiPSM, Ludwig-Maximilians-Universität München, Munich, Germany. [2]Department of Pharmacy – Center for Drug Research, Ludwig-Maximilians-Universität München, Munich, Germany. [3]Department of Biology, Animal Physiology, Friedrich-Alexander Universität Erlangen-Nürnberg, Erlangen, Germany. Sybille Böhm and Lisa M. Riedmayr contributed equally to this work. Correspondence and requests for materials should be addressed to E.B. (email: elvir.becirovic@cup.uni-muenchen.de)

is crucial for rod OS targeting. However, this conclusion was drawn from experiments addressing pure homotypic per^{MT} complexes[16]. Nevertheless, due to the autosomal dominant fashion of *PRPH2*-linked adRP, different combinations of peripherin-2 protein complexes (per^{WT}-per^{WT}, per^{MT}-per^{MT}, per^{WT}-per^{MT}, Rom-1-per^{WT}, and Rom-1-per^{MT}) can be formed in heterozygous patients carrying wild type and mutant *PRPH2* alleles. In addition, each of these complexes can exist in different equilibria of mono-, di- and tetramers and higher-order oligomers, respectively. This high complexity precluded a more accurate investigation of how subunit assembly might influence the rod OS targeting of the single peripherin-2 protein complexes.

In previous studies, we provided a proof-of-principle for FRET-based quantitative analysis of protein-protein interactions in isolated rod and cone OS[17–19]. Recently, we also reported that the two adRP-linked mutations (per^{P210L} and per^{C214S}) located within the highly conserved tetraspanin PxxCC motif are mislocalized to rod inner segments (IS) when expressed in wild type mice using adeno-associated virus (AAV) vectors[20]. Other studies demonstrated that per^{C214S} affects homotypic mutant interactions and the heteromerization with Rom-1[21,22]. Despite these findings, little is known about the specific binding characteristics of this and other peripherin-2 mutants to per^{WT} or Rom-1 in their native environment (e.g. rod OS). Moreover, the precise contribution of per^{WT} and Rom-1 on binding properties, subunit assembly, and rod OS targeting of the respective per^{WT}-per^{MT} and Rom-1-per^{MT} complexes is not clear. Nevertheless, such information is crucial to understand the full complexity of *PRPH2*-linked adRP and for developing successful treatments for the disease. Here, combining different methods we provide novel insights into the binding characteristics, subunit assembly, and rod OS targeting of per^{P210L} and per^{C214S} mutants. We show that per^{WT} and Rom-1 form heterodimers with both peripherin-2 mutants. However, only per^{WT}-per^{MT} but not Rom1-per^{MT} complexes could be targeted to rod OS suggesting unexpected opposing roles of peripherin-2 and Rom-1 in rod OS targeting of adRP-linked peripherin-2 mutants.

Results

per^{C214S} and per^{P210L} show reduced binding to per^{WT} and Rom-1. In our recent work, we demonstrated that, in contrast to per^{C214S} and per^{P210L}, eight additional disease-linked peripherin-2 D2 loop domain mutants did not affect rod OS targeting[20] (Fig. 1a). One possible mechanism, which might explain the mislocalization of per^{C214S} and per^{P210L} in rod photoreceptors, is that these mutants might affect binding to per^{WT} and/or to Rom-1. To examine this possibility, we performed co-immunoprecipitation (co-IP) experiments from HEK293T cells co-transfected with the respective peripherin-2 mutants and per^{WT} or Rom-1, respectively. Only per^{C214S} and per^{P210L} attenuated the binding to per^{WT}, while binding of other peripherin-2 mutants to per^{WT} remained unaffected (Fig. 1b). Very similar results were obtained in co-IPs addressing the binding of the single peripherin-2 mutants to Rom-1 (Fig. 1c).

P210 and C214 are crucial for the proper folding of the distal D2 loop. The proline at position 210 (P210) and the cysteine at position 214 (C214) are part of the highly conserved tetraspanin PxxCC motif, whose function has not been clearly determined yet. The reduced binding of per^{C214S} and per^{P210L} to per^{WT} suggests that these residues could either i) be crucial for proper folding of peripherin-2 or ii) represent the protein-protein interaction interface. Using CD spectroscopy, a recent study suggested that C214S impedes protein folding by increasing the percentage of ß-sheets concomitant with a decrease in helices in the D2 loop[23]. However, it remained unclear which part(s) of the D2 loop is (are) affected by this mutation. To address this issue more directly, we established a protease digestion assay on membrane preparations from HEK293T cells expressing citrine-tagged WT and mutant peripherin-2 transgenes. For this purpose, we took advantage of the fact that endogenously expressed proteases are regularly present in these preparations. In addition, membrane preparations are expected to retain the native protein structure as they are isolated without detergents or reducing agents. Protein cleavage occurs on the exposed domain regions, which are accessible for endogenous proteases. Accordingly, improper protein folding could lead to masking of existing or to an exposure of hidden protease cleavage sites. Using a GFP antibody that recognizes the N-terminal citrine tag of our peripherin-2 constructs, we could detect three peripherin-2 bands at 61.5 kDa, 52.4 kDa and 42.5 kDa (Fig. 1d). The calculated size of full-length citrine-tagged peripherin-2 is 66.5 kDa, however, even in presence of protease inhibitors, the full-length per^{WT} was always detected as a 61.5 kDa band. By contrast, the 52.4 kDa and 42.5 kDa could only be detected in the protease cleavage assay in the absence of protease inhibitors and upon incubation of the samples at 37 °C. Using the 61.5 kDa band as reference, we calculated the cleavage sites for the 42.5 kDa and for the 52.4 kDa band. The cleavage site for the 42.5 kDa band corresponds to the peripherin-2 region around the highly conserved tetraspanin CCG motif (Fig. 1a). This band was also present in all peripherin-2 mutants suggesting proper folding at this part of the protein. By contrast, the 52.4 kDa band was completely absent for per^{C214S} and per^{P210L}, whereas other mutations did not show any considerable differences to per^{WT}. The protease cleavage site for the 52.4 kDa band is calculated to be located within the distal part of the D2 loop domain next to the transmembrane domain 4 (Fig. 1a). Hence, these results suggest that per^{C214S} and per^{P210L} lead to a structural rearrangement of the distal part of the D2 loop domain.

A recent study suggested that peripherin-2 residues 165–182 are crucial for homomeric interactions[24]. However, it remained unclear whether the per^{C214S} and per^{P210L} residues or flanking regions might also contribute to this type of interactions. To test this possibility, we performed a peptide competition assay using a peptide corresponding to the residues 201–220 of native human peripherin-2. Provided that the positions P210 and C214 participate in peripherin-2 homomerization, this peptide should compete with the binding and, hence, result in a reduction of homomeric protein-protein interactions. However, in subsequent co-IP experiments even in the presence of a very high peptide concentration (10 mM), we could not detect any decrease in peripherin-2 binding compared to the peptide-free approach (Fig. 1e). This suggests that this region is not directly involved in homomeric peripherin-2 protein-protein interactions.

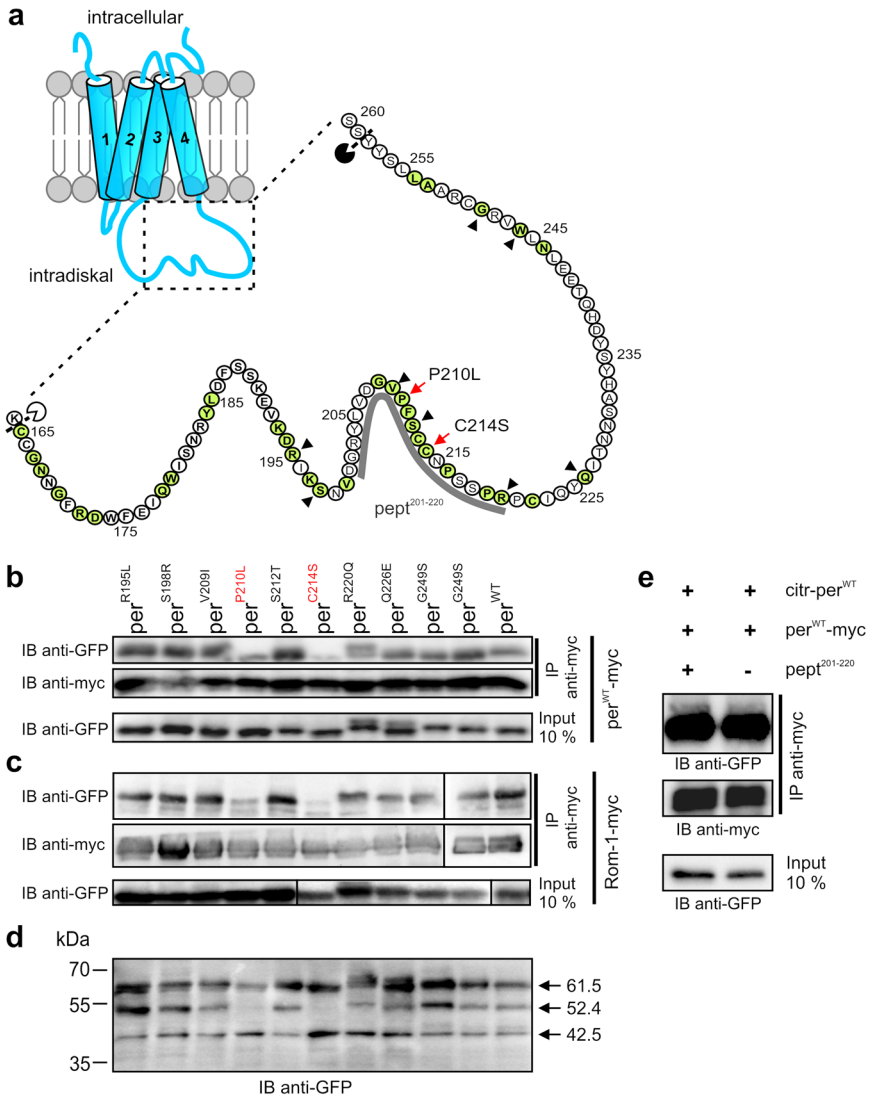

Figure 1. Effects of peripherin-2 mutants on protein-protein interactions and D2 loop folding. (**a**) left, Topology of peripherin-2. The dashed rectangle highlights the distal part of the D2 loop. Right, Schematical enlargement of the distal D2 loop showing the hitherto identified disease-linked peripherin-2 mutations in this region (highlighted in green). The position of mutants analyzed in (**b–d**) are marked by red arrows (for per^{P210L} and per^{C214S}) or by black arrowheads in case of the remaining mutants. The calculated protease cleavage sites from d are indicated by a white (corresponding to the 42.5 kDa band) or black (corresponding to the 52.4 kDa band) pacman. The position of the peptide (aa 201–220) used for the competition assay shown in (**e**) ($pept^{201-220}$) is highlighted by the gray line. (**b–c**) Co-Immunoprecipitations (co-IPs) from membrane preparations of HEK293T cells transiently transfected with the respective N-terminally citrine-tagged mutants and C-terminally myc-tagged per^{WT} (per^{WT}-myc) (**b**) or Rom-1 (Rom-1-myc) (**c**) using the myc-specific antibody (anti-myc). The single mutants were detected using the GFP-antibody, which also specifically recognizes citrine. IB, immunoblotting. (**d**) Protease cleavage experiments on membrane preparations from HEK293T cells transiently transfected with the single citrine-tagged peripherin-2 mutants as indicated. The molecular weight of the single bands (arrows) was calculated from five independent western blot experiments. (**e**) Co-IPs from membrane preparations of HEK293T cells co-transfected with myc- and citrine-tagged per^{WT} in presence (left lane, 10 mM) or absence of the peptide.

Quantification of per^{WT}, per^{MT}, and Rom-1 protein-protein interactions in HEK293T cells using FRET. Recently, we reported that three cube FRET is suitable for quantification of homomeric and heteromeric interactions of different photoreceptor specific proteins including peripherin-2. In particular, it has been demonstrated that FRET can be used to calculate the relative binding affinities of these proteins in HEK293T cells[17]. Consequently, using this approach we examined the binding properties of the different homo- and heteromeric per^{WT}, per^{MT}, and Rom-1 protein complexes. Binding curves can be calculated if the relative expression of the FRET fluorophores (given as molar ratio, MR) varies between the single FRET measurements. By plotting the FRET efficiency (E_A) values against the corresponding cerulean/citrine MR, we observed a sufficient variability

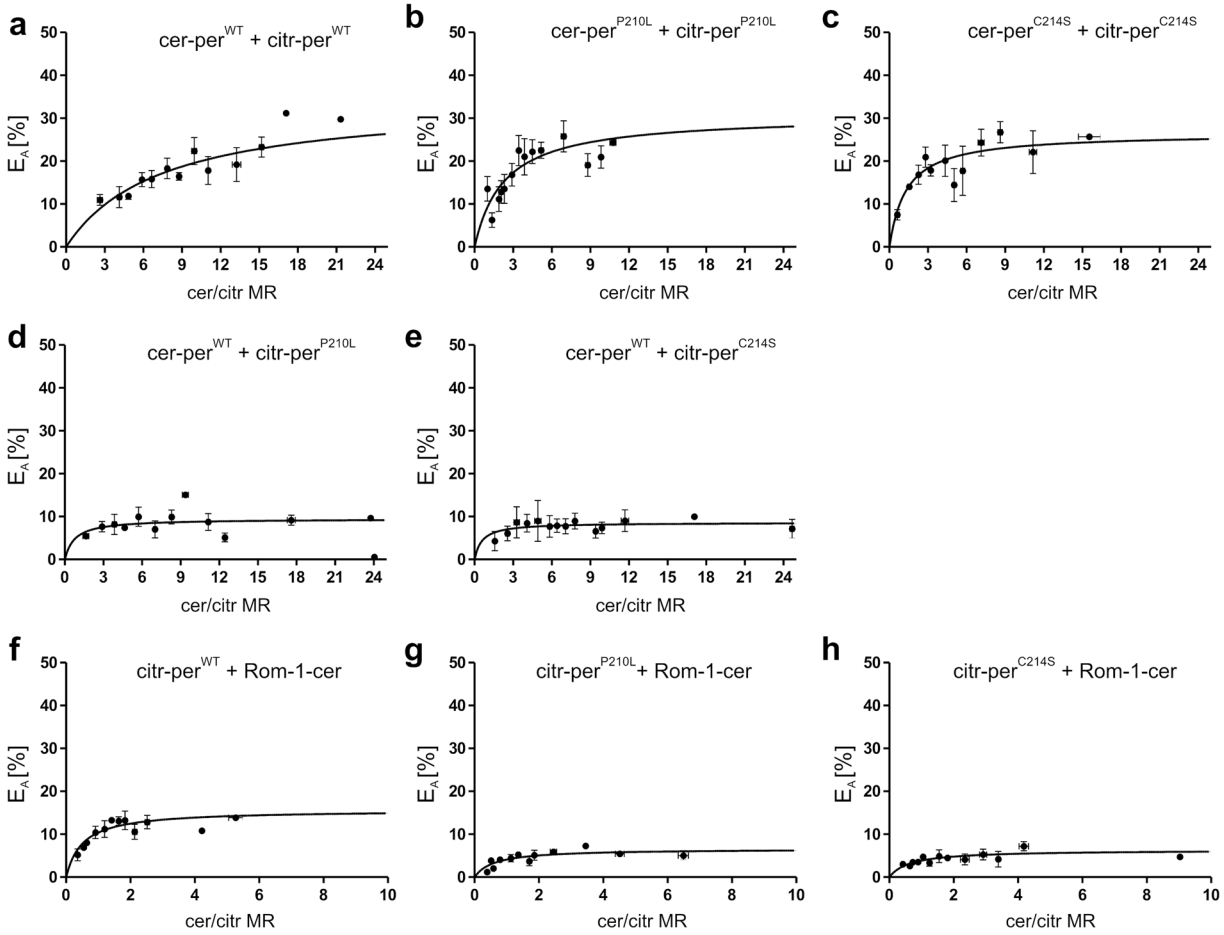

Figure 2. Quantification of homo- and heteromeric per^{WT}, per^{MT}, and Rom-1 protein-protein interactions using FRET. (**a–h**) FRET experiments from living HEK293T cells transiently co-transfected with the respective citrine- (citr) or cerulean (cer)-tagged peripherin-2 or Rom-1 constructs as indicated. To obtain the binding curves, FRET efficiency (E_A) was plotted against the cerulean/citrine molar ratio (cer/citr MR). The dots represent mean values of 1–7 single FRET measurements ± SEM. E_{Amax}, maximal FRET efficiency. The single E_{Amax}, values and the numbers of independent measurements (n) for each combination are summarized in Supplementary Table 1.

of the FRET fluorophore expression for each combination. The maximal FRET efficiency (E_{Amax}) was calculated from the binding curve for saturable binding as described previously[17] and is proportional to the binding strength of the respective protein complex in the equilibrium. Analysis of E_{Amax} for the different per^{WT} and per^{MT} combinations allowed us to draw several important conclusions. First, robust and unusually high E_{Amax} values could be observed for the per^{WT} only FRET pair (34.2%, Fig. 2a and Supplementary Table 1). These values are close to the highest theoretically possible 40% FRET efficiency for proteins tagged with bulky fluorophores like citrine or cerulean and highlight the strength of protein-protein interactions in homomeric peripherin-2 complexes. Second, E_{Amax} was only slightly decreased for the per^{P210L} only (30.7%) and per^{C214S} only (26.47%) FRET pairs when compared to per^{WT} only (Fig. 2b,c and Supplementary Table 1), suggesting that mutants are still largely capable of self-interacting. By contrast, both, per^{WT}-per^{P210L} (9.44%) and the per^{WT}-per^{C214S} (8.58%) combinations, led to a robust decrease in E_{Amax} (Fig. 2d,e and Supplementary Table 1). Next, we also determined the E_{Amax} values for Rom-1 co-expressed with each, per^{WT} and per^{MT}. When compared to per^{WT} only, E_{Amax} for the Rom-1-per^{WT} interaction was noticeably lower (15.64%) indicating that heteromeric Rom-1-per^{WT} complexes bind less tight than their homomeric per^{WT} only counterparts (Fig. 2f and Supplementary Table 1). Second, both, Rom-1-per^{P210L} and Rom-1-per^{C214S} combinations, led to reduced E_{Amax} values when compared to the Rom-1-per^{WT} interaction (6.58% and 6.32%, respectively, Fig. 2g,h and Supplementary Table 1). Finally, we also calculated the percentage of E_{Amax} reduction for both peripherin-2 mutants relative to per^{WT} only and to the per^{WT}-Rom-1 FRET pair. When compared to per^{WT} only, the E_{Amax} values were reduced to 28% for the per^{WT}-per^{P210L} and to 25% for the per^{WT}-per^{C214S} FRET pair, respectively. By contrast, relative to the Rom-1-per^{WT} FRET pair, the E_{Amax} values were reduced to 42% for the Rom-1-per^{P210L} and to 40% for the Rom-1-per^{C214S} combination, respectively (Supplementary Table 1). This suggests that binding of both peripherin-2 mutants to per^{WT} is more strongly affected than binding to Rom-1.

Taken together, our FRET results indicate that, although with reduced efficiencies, both mutants in principle retain their ability to self-interact and to form complexes with per^{WT} or with Rom-1.

Subunit assembly of homo- and heteromeric per^{WT}, per^{MT}, and Rom-1 complexes. Sucrose density gradient centrifugation (SDGC) allows for a separation of different covalently or non-covalently linked protein complexes across a sucrose gradient according to their specific molecular weight. Using SDGC, previous studies analyzed the impact of peripherin-2 mutants including per^{C214S} on homotypic per^{MT}-per^{MT} or heterotypic Rom-1-per^{MT} interactions on subunit assembly[16,21,22,25]. To examine the complexes which can be formed in heterozygous patients more systematically, we performed a set of sedimentation velocity experiments of differentially tagged per^{WT}, per^{MT}, and Rom-1 combinations (per^{WT} only, per^{P210L} only, per^{C214S} only, per^{WT}-per^{P210L}, per^{WT}-per^{C214S}, Rom-1-per^{WT}, Rom-1-per^{P210L}, and Rom-1-per^{C214S}) transiently expressed in HEK293T cells. In line with previous work, we found the per^{WT} complexes only in sucrose gradient fractions containing the non-covalent tetramers as well as in fractions containing the disulfide-linked octamers under non-reducing conditions (Fig. 3a). By contrast, when expressed alone, per^{P210L} was primarily detected as monomer, non-covalent dimer, and aggregates, but some complexes were also found as disulfide-linked tetramers and octamers (Fig. 3b). Similar to per^{P210L}, per^{C214S} was predominantly detected in monomer, non-covalent dimer, and aggregate fractions when expressed alone (Fig. 3c). In presence of per^{WT}, per^{P210L} was primarily detected in the fractions containing monomers and non-covalent dimers, and only weak signal was found in the non-covalent tetramer fractions (Fig. 3d). Moreover, in this combination the SDGC pattern for per^{WT} slightly differed from the per^{WT} only situation. The most striking difference was that a substantial per^{WT} signal could now also be seen in the non-covalent dimer fractions (Fig. 3d). Given that no considerable amounts of per^{WT} were detectable in this fraction for per^{WT} only (cf. Fig. 3a), we concluded that the non-covalent dimer fraction most likely consists of per^{WT}-per^{P210L} dimers. When co-expressed with per^{C214S}, per^{WT} reasonably decreased the percentage of per^{C214S} aggregates (Fig. 3e). Moreover, in presence of per^{WT} the majority of per^{C214S} was found in the non-covalent dimer fractions and as per^{C214S} monomers. However, in contrast to the per^{WT}-per^{P210L} combination, a strong per^{C214S} signal could also be detected in the non-covalent tetramer fractions. Finally, in the per^{WT}-per^{C214S} combination, we could also robustly detect per^{WT} in the non-covalent dimer fractions (Fig. 3e). Taking into account that per^{WT} alone does not homodimerize (cf. Fig. 3a) and that per^{C214S} alone does not form non-covalent tetramers (cf. Fig. 3c), we concluded that the non-covalent dimer and tetramer fractions in the per^{WT}-per^{C214S} combination most likely contain per^{WT}-per^{C214S} dimers and tetramers, respectively (Fig. 3e).

Next, we analyzed the SDGC fractions from HEK293T cells co-expressing Rom-1-per^{WT}, Rom-1-per^{P210L}, and Rom-1-per^{C214S} complexes. As expected, in the Rom-1-per^{WT} combination a robust Rom-1 signal was found in non-covalent tetramer fractions (Fig. 3f). In addition, Rom-1 was also detected in non-covalent dimer and monomer fractions. No considerable amounts of per^{WT} were found in these fractions suggesting that no Rom-1-per^{WT} heterodimers are present under these conditions (Fig. 3f). When analyzing Rom-1-per^{P210L} and Rom-1-per^{C214S} combinations, the per^{P210L} and per^{C214S} mutants were almost exclusively found in the non-covalent dimer and monomer fractions (Fig. 3g,h). In contrast to the Rom-1 signal from the Rom-1-per^{WT} combination, in presence of the per^{P210L} and per^{C214S} mutants Rom-1 was almost exclusively detected in dimer and monomer fractions (Fig. 3g,h). Based on this, we concluded that Rom-1 predominantly forms non-covalent dimers with both mutants.

Taken together, our SDGC results suggest that per^{WT}-per^{MT} and Rom-1-per^{MT} protein complexes are mainly built of non-covalent dimers.

Rod OS targeting of homo- and heteromeric per^{WT}, per^{MT}, and Rom-1 complexes. Our FRET and SDGC experiments from HEK293T cells strongly suggest that both peripherin-2 mutants are in principle capable of forming complexes with per^{WT} and Rom-1. This prompted us to analyze the protein targeting of these complexes in rod photoreceptors. For this purpose, we used rAAV vector gene delivery to express various combinations of per^{WT}, Rom-1, and per^{MT} and analyze their transport/localization in mouse photoreceptors. It has been shown previously that subretinal co-administration of two rAAVs encoding different transgenes results in very high co-transduction efficiencies in rods[17]. For delivery to rod photoreceptors, rAAV vectors with a rod specific human rhodopsin promoter were used. To allow for discrimination between per^{WT} or Rom-1 and per^{MT} expression, we fused cerulean to the N-terminus of per^{WT} and Rom-1, and citrine to the N-terminus of per^{MT}, respectively. The rAAVs containing the different peripherin-2 and Rom-1 constructs were subretinally injected to P14 wild type mice. Subsequent analysis of peripherin-2 localization was examined four weeks post injection by detecting citrine and cerulean fluorescence on retinal slices from injected animals. When expressed alone, citrine and cerulean were retained in the rod IS (Suppl. Fig. 1). In accordance with our previous observations[20], both mutants were also completely mislocalized to the IS (Fig. 4a,b). The localization pattern of per^{P210L} and per^{C214S} was remarkably different. per^{P210L} showed a spotted large vesicular-like expression, whereas per^{C214S} was distributed throughout the rod IS. Interestingly, however, simultaneous co-delivery of titer-matched per^{WT} and per^{MT} led to a noticeable rescue and substantial rod OS targeting of per^{P210L} and per^{C214S} (Fig. 4c,d). In addition, the rAAV-mediated co-delivery of per^{WT} also rescued the vesicle-like expression pattern of per^{P210L} in the rod IS (Fig. 4c). Finally, we also assessed whether co-administration of titer-matched rAAVs expressing transgenic Rom-1 together with per^{P210L} or per^{C214S} leads to a similar rescue effect. When co-expressed with per^{WT}, both, Rom-1 and per^{WT} were exclusively found in rod OS (Fig. 5a). However, transgenic Rom-1 did not noticeably promote per^{MT} protein targeting to the OS. By contrast, a substantial amount of transgenic Rom-1, most likely the Rom-1-per^{MT} heterodimers, was retained in the rod IS (Fig. 5b,c).

Taken together, these experiments demonstrate that simultaneous co-delivery of transgenic per^{WT} rescues the targeting of the per^{P210L} and per^{C214S} mutants to rod OS. However, simultaneous co-delivery of transgenic Rom-1 and per^{P210L} or per^{C214S} resulted in substantial retention of Rom-1 in the rod IS. In combination with the results obtained from SDGC experiments, these findings strongly indicate that per^{WT}-per^{MT}, but not Rom-1-per^{MT} heterodimers, can be efficiently targeted to rod OS.

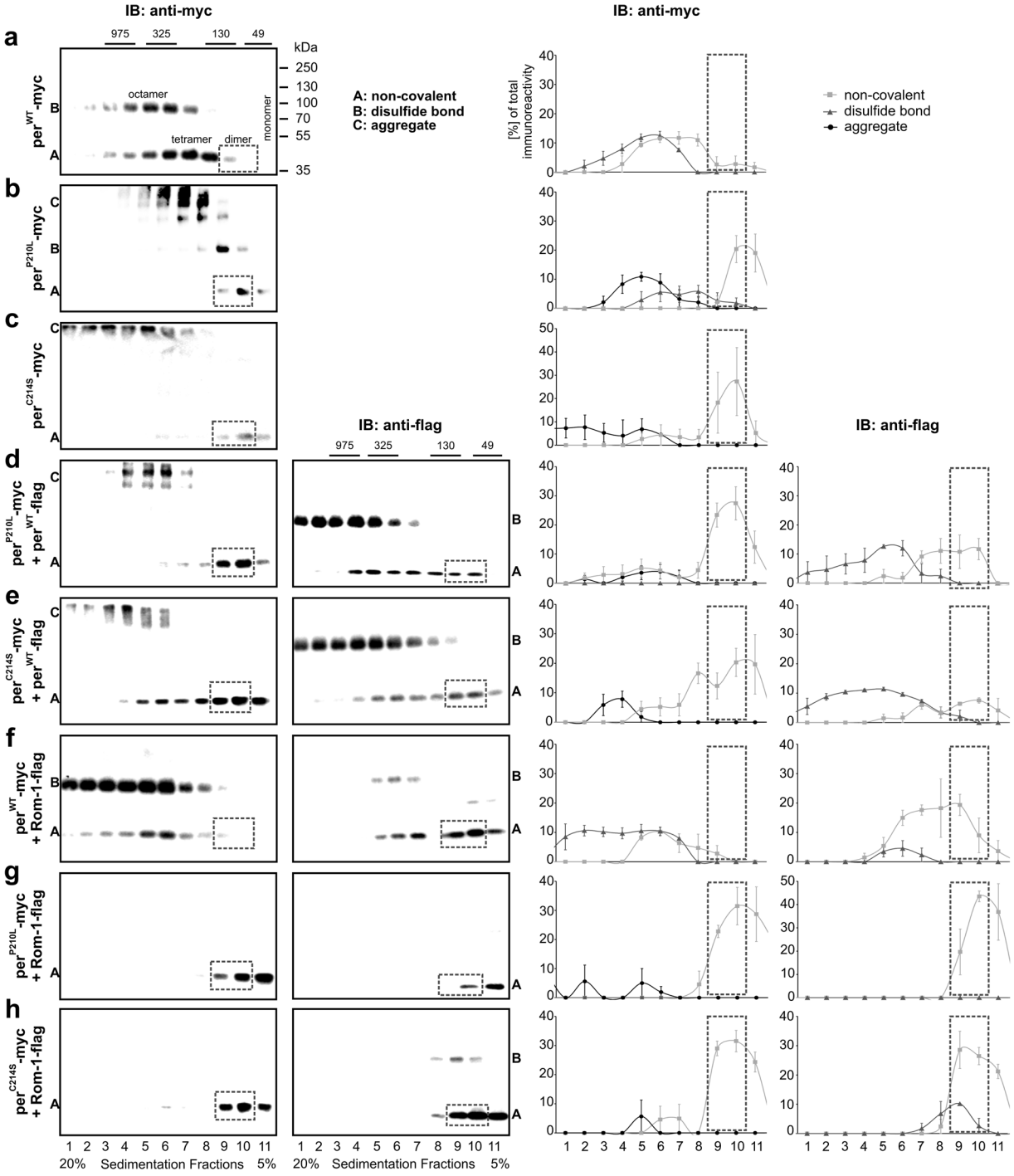

Figure 3. SDGC of different per^{WT}, per^{MT}, and Rom-1 combinations. Shown are representative immunoblots (left panel) and the corresponding statistics (right panel) for each C-terminally myc- or flag-tagged combination as indicated. Each blot consists of 11 fractions collected across the 5–20% sucrose gradient. All fractions were normalized to the DNA standard mixed to the protein solution prior to SDGC as described in the methods section. The single peripherin-2 or Rom-1 complexes can be found in following fractions: octamers: fraction 3–6; tetramers: fraction 6–8; dimers: fraction 9–10; monomers: fraction 10–11. Immunoblottings were performed with antibodies recognizing either the myc-tag (first row of the left panel) or the flag-tag (second row of the left panel), respectively. For quantification, the percentage of total immunoreactivity related to the number of single fractions for non-covalent or covalent complexes and aggregates was plotted against the 11 collected fractions. The fractions containing the non-covalent dimers are highlighted by a dashed rectangle. The single values (percentages and numbers of independent experiments) for all combinations are summarized in Supplementary Table 2. Fractions containing the DNA standards (975 kDa, 325 kDa, 130 kDa and 49 kDa) are marked accordingly.

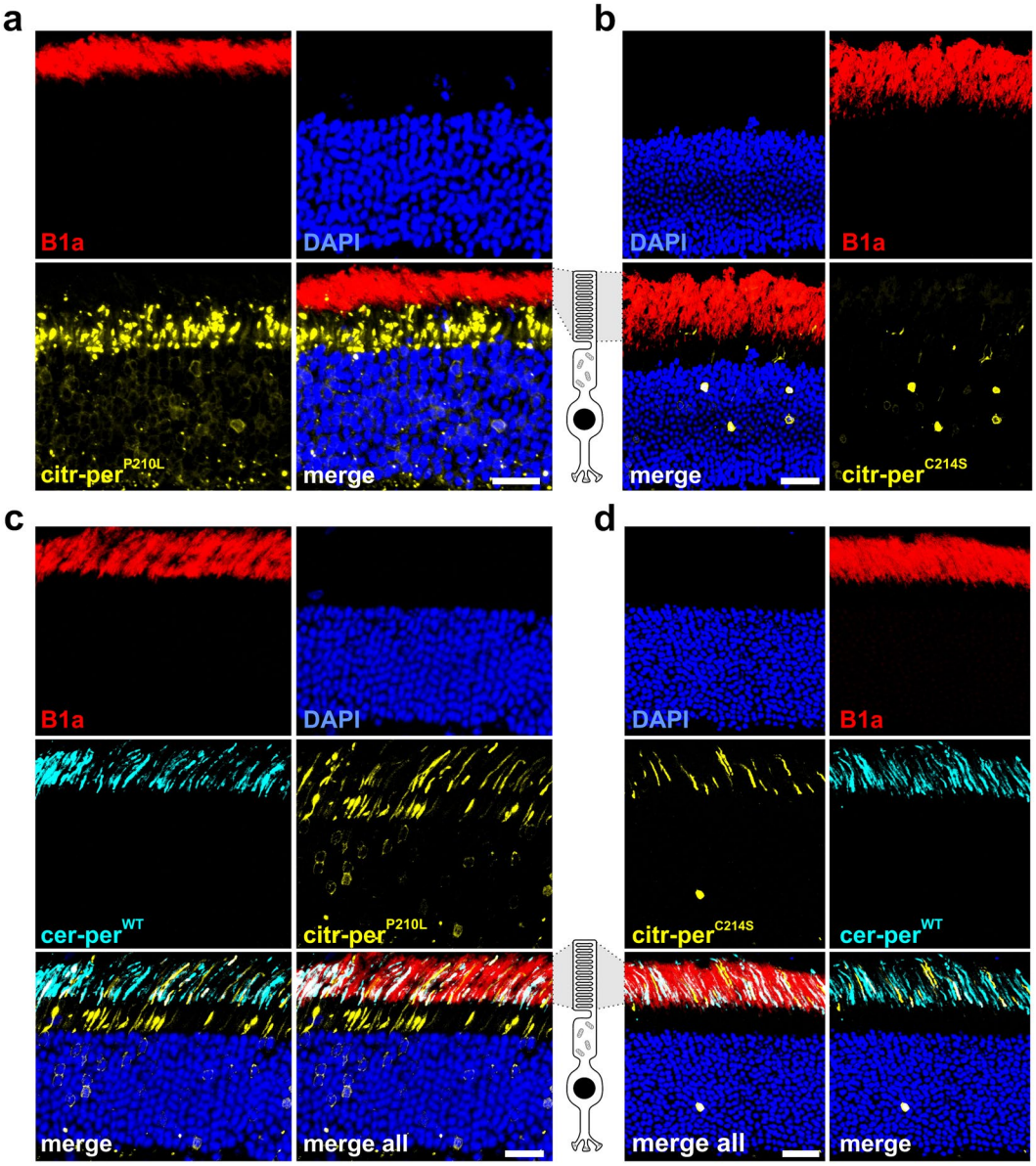

Figure 4. Rod OS targeting of per^{WT}-per^{MT} complexes. (**a–d**) Confocal images of immunostained retinas injected with citrine-tagged mutants (citr-per^{P210L} (**a**) and citr-per^{C214S} (**b**)), or co-injected with the respective mutants and the N-terminally cerulean-tagged per^{WT} (cer-per^{WT}, (**c–d**)). CNGB1a antibody (B1a, red) was used for specific staining of rod OS. Scale bar, 30 µm.

Analysis of the per^{WT}-per^{MT} binding properties in rod OS using FRET. FRET and co-IP experiments in HEK293T cells revealed a reduced apparent binding of both peripherin-2 mutants to per^{WT}. This finding could be best explained by decreased binding affinities of the per^{WT}-per^{MT} interaction and/or decreased initial binding kinetics of the mutants to per^{WT}. However, in HEK293T cells co-transfected with per^{WT} and per^{MT} each mutant can also exist as monomers or could undergo self-interactions (i.e. as dimers or aggregates, cf. Fig. 3b–e). As all these combinations would contribute to the overall FRET signal, the apparent reduction of E_{Amax} in HEK293T cells does not allow for discrimination between the mechanisms described above. To examine this issue directly, we took advantage of the fact that per^{MT} targeting to rod OS is rescued only upon co-delivery of transgenic per^{WT}. Consequently, in contrast to HEK293T cells, in rescued rod OS all per^{MT} protein must be arranged in complexes with per^{WT}. This happenstance allowed us to draw direct conclusions about the per^{WT}-per^{MT} binding properties under close-to-native conditions by measuring FRET in isolated "rescued" rod OS. For this purpose, we co-injected wild type mice on P14 with the respective per^{WT} and per^{MT} FRET pairs. At four weeks post injection we isolated the rod OS and measured FRET on single OS co-expressing both, cerulean-tagged per^{WT} and citrine-tagged per^{MT} (Fig. 6a–c). Robust FRET signals could be measured for all combinations. Importantly, the cerulean/citrine molar ratios substantially varied between the single rod OS, which also allowed us to calculate the binding curves. Remarkably, in contrast to the FRET results from HEK293T cells, the E_{Amax} from isolated rod

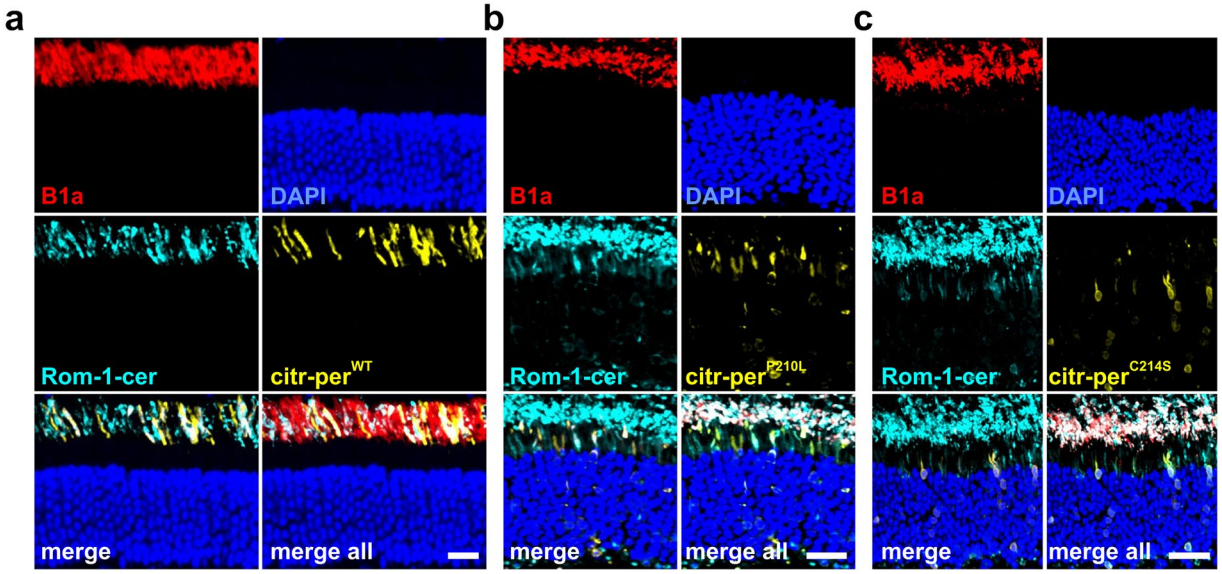

Figure 5. Rod OS targeting of Rom-1-per$^{WT/MT}$ complexes. Confocal images of immunostained retinas co-injected with C-terminally cerulean-tagged Rom-1 (Rom-1-cer) and citr-per^{WT} (**a**), citr-per^{P210L} (**b**), and citr-per^{C214S} (**c**). Scale bar, 30 µm.

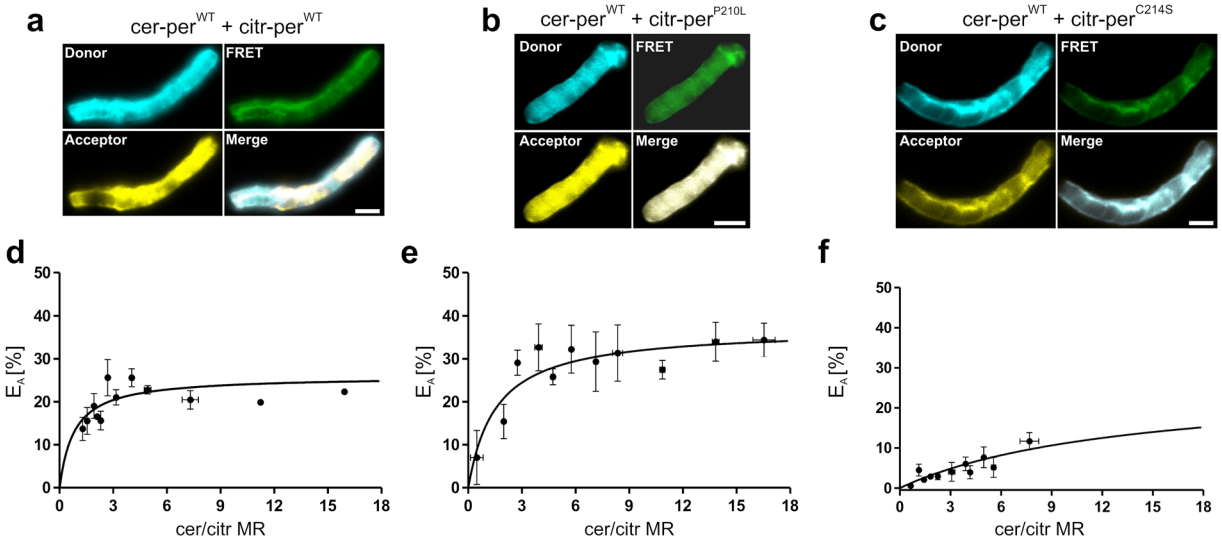

Figure 6. FRET experiments in rod OS of retinas co-injected with per^{WT} and per^{MT} AAV-vectors. (**a–c**) Representative confocal images of FRET channels showing a single OS co-expressing cer-per^{WT} and citr-per^{WT}(**a**), cer-per^{WT} and citr-per^{P210L} (**b**), or cer-per^{WT} and citr-per^{C214S} (**c**). Scale bar, 2 µm. (**d–f**) Binding curves of the corresponding FRET measurements for the single combinations displayed in (**a–c**). The dots represent mean values of 1–7 single FRET measurements ± SEM. The single E_{Amax}, values and the numbers of independent measurements (n) for each combination are summarized in Supplementary Table 1.

OS was either increased in case of the per^{WT}-per^{P210L} pair or very close to that of the per^{WT} only interaction for the per^{WT}-per^{C214S} combination (Fig. 6d–f and Supplementary Table 1). These findings indicate that the robust reduction in the per^{WT}-per^{MT} interaction observed from co-IP and FRET experiments in HEK293T cells does not result from reduced binding affinity, but is most likely caused by a decrease in initial binding kinetics of per^{MT} to per^{WT}.

Discussion

By analyzing the molecular mechanisms of two adRP-linked peripherin-2 mutants, we provide evidence for a novel role of peripherin-2 and its homolog Rom-1 in the pathophysiology of rod photoreceptors. We show for the first time that rod OS targeting of peripherin-2 mutants can be rescued *in vivo* by simultaneous co-delivery of per^{WT} using rAAV-mediated gene transfer. This finding is important for understanding the peripherin-2

biology in photoreceptors and has implications for the development of future gene therapies for patients with *PRPH2* mutations. Peripherin-2 is crucial for proper rod OS structure and development. This function was proposed to be dose-dependent in rods suggesting that reduced dosage of peripherin-2 (less than 60–80% of the wild type level) induces retinal degeneration[26,27]. In line with the postulated dose-dependency, transgenic mice expressing the per^{C214S} mutant show reduced amounts of mutant protein in rod OS (due to mislocalization or protein degradation) which results in haploinsufficiency[22]. Interestingly, genetic supplementation of per^{WT} on the per^{C214S} mutant background led to a noticeable rescue of the retinal function[28]. Although helpful in initial stages of therapy development, the application spectrum of genetic supplementation is restricted to model organisms. By contrast, rAAV-mediated gene delivery has proven to be a very promising technique for therapeutic intervention on retinal diseases like retinitis pigmentosa in mammals[29–32]. Our data suggest that rAAV-mediated gene supplementation of per^{WT} could support a rescue of per^{MT} targeting defects to rod OS in adRP patients carrying mislocalizing peripherin-2 mutations. We could not detect any detrimental effects on outer nuclear layer (ONL) thickness in fully developed retinas of WT animals co-injected with per^{WT} and per^{MT} transgenes six months post injection (Suppl. Fig. 2). However, we cannot exclude the possibility that rescue of per^{MT} rod OS targeting by per^{WT} gene supplementation would initiate retinal degeneration in patients heterozygous for these mutations. Consequently, prior to gene therapy, the long-term effects of the mutant rescue on retinal degeneration should be tested in appropriate animal models.

In mice co-injected with rAAVs expressing labeled peripherin-2 and Rom-1 transgenes, it is not possible to estimate the contribution of the endogenous murine peripherin-2 and Rom-1 on the per^{MT} rescue. However, our observation that both mutants are mislocalized to the rod IS and lead to reduced protein expression suggests that the endogenous protein levels were not sufficient to rescue per^{MT} localization. Of note, in heterozygous transgenic knock-in mice expressing per^{C214S}, the mutant protein remains in the inner segments and is highly prone to degradation[22]. These results are very similar to our observations from wild type mice injected with the transgenic per^{C214S} mutant. With respect to this finding, it can be concluded that the rAAV-mediated delivery of transgenic per^{C214S} mutant to wild type mice largely reflects the native situation in mice heterozygous for this mutant. The fact that per^{C214S} is not targeted to rod OS suggests that per^{WT}-per^{C214S} complexes most likely are not formed under these conditions. However, as discussed above, additional rAAV-mediated delivery of per^{WT} presumably exceeds the critical levels necessary for per^{WT}-per^{MT} complex formation, highlighting the critical role of peripherin-2 dosage in pathophysiology of photoreceptors.

Our study also provides novel insights into the structural impacts of per^{P210L} and per^{C214S} on folding of the D2 loop domain. We show that per^{P210L} and per^{C214S} lead to a structural rearrangement of the distal part of the D2 loop domain around the aa position 260. It is conceivable that per^{P210L} and per^{C214S} may also lead to structural changes in other parts of the D2 loop, which could not be covered by our assay. However, our data suggest that folding changes induced by per^{P210L} and per^{C214S} most likely do not elicit structural rearrangements of the proximal half of the D2 loop close to the highly conserved tetraspanin CCG motif.

P210 and C214 are located within the PxxCC motif, which is conserved among most tetraspanins[33]. While both cysteine residues of the motif were shown to be involved in intramolecular peripherin-2 disulfide bond formation[21,34], the role of the proline residue remained unknown. Peripherin-2 belongs to the subfamily of non-conventional tetraspanins[34], thus, it remains to be clarified if the PxxCC motif has a similar role on protein folding in other tetraspanins. Interestingly, other mutants in close proximity to the P210 and C214 position (i.e. per^{V209I} or per^{S212T}) did not change the accessibility of the proteases in our assay. This emphasizes the crucial role of the proline at position 210 and cysteine at position 214 for the proper folding of the D2 loop domain. Furthermore, our results suggest that the apparent reduction of per^{MT} binding to per^{WT} in co-IP and in FRET experiments from HEK293T cells is most likely caused by protein misfolding. Our FRET experiments on isolated rod OS indicate that this apparent decrease in binding to per^{WT} does not result from reduced binding affinities, but rather seems to be a consequence of reduced initial binding kinetics of per^{P210L} and per^{C214S} to per^{WT}. In other words, this suggests that the first step of per^{MT} binding to per^{WT} is impeded, however, once bound, the affinity of both mutants to per^{WT} remains largely unchanged. These results are well matched on our peptide competition assay indicating that the PxxCC motif does not represent the interface for homomeric peripherin-2 interactions. E_{Amax} values resulting from the transgenic per^{WT} were higher in HEK293T cells compared to the rod OS. This difference could be caused by non-labeled endogenous peripherin-2 or Rom-1 in the retina, which are also expected to bind to transgenic per^{WT} (incomplete labeling). However, the per^{WT} E_{Amax} values from isolated rod OS are still in a very high range highlighting the suitability of the FRET approach to addressing peripherin-2 oligomerization in these compartments.

When correlating our results from SDGC to those obtained from rod OS targeting experiments (Fig. 7 and Suppl. Fig. 3), two very important conclusions could be drawn: 1) Non-covalent per^{WT}-per^{MT} dimers can be formed and targeted to rod OS. 2) Non-covalent Rom-1-per^{MT} heterodimers are stacked in the inner segments. The first deduction is very surprising as non-covalent tetramerization was considered to be crucial for peripherin-2 targeting to rods[16]. This conclusion was drawn from different sets of experiments in previous studies: i) When analyzing per^{WT} complexes isolated from OS, no dimers could be detected[35]. ii) Tetramerization-deficient peripherin-2 mutants could not be targeted to rod OS[16]. iii) Peripherin-2 mutants which preferentially form homodimers are not targeted to rod OS[16]. However, none of these experiments is sufficient to state if per^{WT}-per^{WT} or per^{WT}-per^{MT} dimers can also be targeted to rod OS. First, per^{WT} does not form dimers in SDGC experiments when expressed alone, which explains its absence in rod OS under physiological conditions. Second, only rod OS targeting of pure per^{MT} complexes was examined so far[16]. Consequently, to the best of our knowledge, this is the first study addressing the principle capability of per^{WT}-per^{MT} dimers to be targeted to rod OS. The finding that Rom-1-perMT heterodimers cannot be targeted to rod OS suggests that Rom-1 cannot fully compensate for the peripherin-2 function in rods under these conditions. Currently, one can only speculate about the physiological role of these opposing effects of peripherin-2 and Rom-1 in terms of binding and targeting of misfolded

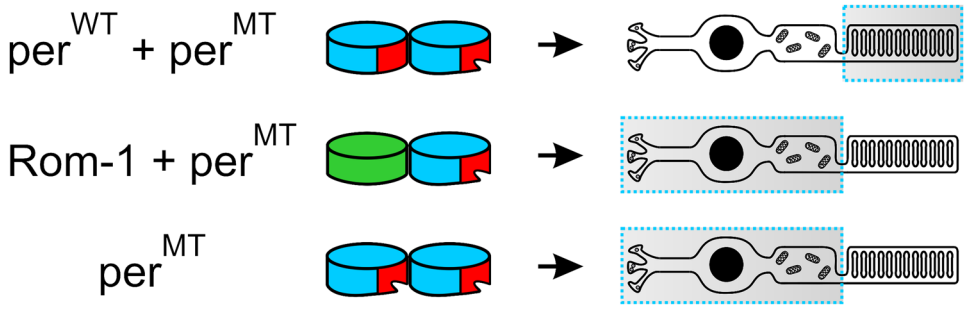

Figure 7. Rod OS targeting of per^{MT} dimeric complexes. The rod photoreceptor localization of different per^{MT}-containing dimers (per^{WT}-per^{MT}, Rom-1-per^{MT} and per^{MT} only) is symbolized by a dashed rectangle. The position of the D2 loop is highlighted in red and the D2 loop misfolding caused by per^{MT} is symbolized by an incision.

peripherin-2 mutants. A recent study revealed that Rom-1 promotes the trafficking of the Y141C peripherin-2 mutant *in vitro* and converts the cone-dominant pattern dystrophy to RP phenotype *in vivo*[12]. Similar effects are not expected to occur for the C214S or P210L mutation, as Rom-1 cannot promote targeting of these mutants to rod OS. Together, these findings indicate that Rom-1 might play a yet undefined role in pathophysiology of retinal diseases as a mutation-dependent disease modifier.

Rom-1 and peripherin-2 are also expressed in cones and many mutations in peripherin-2 (but not in Rom-1) are linked to retinal diseases primarily affecting cone photoreceptors[13]. Despite some advances, the molecular mechanisms underpinning this differential penetrance of peripherin-2 mutants in rods and cones are still not fully understood. In light of our results, it is tempting to speculate that Rom-1 might be one of the key players shaping the penetrance of peripherin-2 mutants in rods and cones. Finally, in the context of gene therapy, the postulated novel function of Rom-1 raises the possibility that the efficiency of gene supplementation therapy of adRP-associated peripherin-2 point mutations could be improved by co-delivering peripherin-2 with Rom-1.

Methods

Animals. The studies were carried out in accordance with the approved guidelines of the local committee of laboratory animal care (District Government of Upper Bavaria) and German Laws on animal welfare (Tierschutzgesetz). Anesthesia was performed by intraperitoneal injection of ketamine (40 mg/kg body weight) and xylazine (20 mg/kg body weight). Euthanasia was performed by cervical dislocation.

Molecular biology. For expression in rods, the single human peripherin-2[20] and Rom-1 transgenes were subcloned to the pAAV2/8 YF vector[30] containing the human Rhodopsin (hRHO) promoter using standard cloning techniques. For expression in HEK293T cells (LentiX 293 T Cell Line, Clontech Laboratories, Mountain View, CA, USA), the peripherin-2 and Rom-1 transgenes were subcloned to the standard pcDNA3.1 vector (Invitrogen, Waltham, MA, USA). Peripherin-2 mutants were introduced by site directed mutagenesis (QuikChange Lightning Site-Directed Mutagenesis Kit, Agilent Technologies, Santa Clara, CA, USA). All transgenes were sequenced prior to use.

Protein biochemistry. For co-immunoprecipitations (co-IPs) transiently transfected HEK293T cells were harvested 48 hours post transfection and membrane preparations were conducted as described[36]. Co-IPs were performed with the anti-myc antibody (9B11, Cell Signaling Technology, Danvers, MA, USA) using Protein G magnetic beads (Novex, Thermo Fisher Scientific, Waltham, MA, USA) according to the manufacturer's protocol.

For western blotting, injected retinas of light adapted wild type C57BL6/J animals were used four weeks post injection. The dissected retinas were homogenized in membrane preparation buffer using the Potter S homogenizer (B. Braun Diessel Biotech, Melsungen, Germany).

For peptide competition assay, the peripherin-2 peptide (peptide sequence CDGRYLVDGVPFSCCNPSSPR) was obtained from jpt Innovative Peptide Solutions (Berlin, Germany). The peptide was added to the respective membrane preparation and the solution was incubated with the myc-antibody-coupled magnetic beads for 30 min at room temperature. The co-IPs containing the peptide-free membrane preparations were processed under identical conditions. For the native protease cleavage assay, membrane preparations[36] of transfected HEK293T cells were incubated for 5 h at room temperature (RT) and processed for western blotting. No protease inhibitors were added to the membrane preparations prior to the incubation. For immunoblotting, antibodies were used in following dilutions: mouse anti-myc (see above), 1:2000; mouse anti-GFP (Clontec, Takara Bio Inc., Shiga, Japan), 1:2000; mouse anti-ATPase (anti alpha3, ab2826, Abcam, Cambridge, UK), 1:2000.

Sucrose density gradient centrifugation. For sucrose density gradient centrifugation, HEK293T cells were transiently transfected with the respective peripherin-2 constructs. Cells were harvested 48 h post transfection and homogenized in a lysis buffer comprising 0.5% Triton X-100, 150 mM NaCl and 2 mM $CaCl_2$ using the Potter S homogenizer (see above). Continuous density gradients of 5–20% (wt/vol) sucrose were prepared by underlayering 0.5 ml of 5%, 10%, 15% and 20% sucrose containing 0.1% Triton X-100 and 10 mM *N*-ethylmaleimide (Sigma-Aldrich, St. Louis, MO, USA). The gradient was left at RT for 1 h to facilitate diffusion

and chilled on ice for 30 min prior to sample application. To determine the weight of single peripherin-2 and Rom-1 protein complexes in each immunoblot, DNA standards of defined molecular weights (75 bp–20.000 bp, i.e. 49 kDa–13,000 kDa, GeneRuler 1 kb Plus (Thermo Fisher Scientific, Waltham, MA, USA)) were mixed to lysates containing 200 µg of the respective proteins. The mixture was carefully layered on top of the gradient and centrifuged at 46,700 rpm for 2 h at 4 °C in a Beckman Coulter Optima L-80K Ultracentrifuge (Beckman Coulter Biomedical GmbH, Munich, Germany). Afterwards, the centrifuge tube was punctured and fractions were collected dropwise (5 drops/tube). Fractions from each sucrose gradient were separately used for immunoblotting with myc- or flag-specific antibodies and for agarose gel electrophoresis to detect the DNA standards. The suitability of DNA standards was first validated for per^{WT} only. As shown in Fig. 3a, per^{WT} gives rise to well-defined fractions of non-covalent tetramers, covalent octamers, and high-order oligomers. The molecular weight of the DNA in the same fractions very nicely correlated with the molecular weights of the corresponding per^{WT} complexes. Therefore, for each of the remaining immunoblots, DNA standards were used to determine the fractions containing the different per^{WT}, per^{MT}, or Rom-1 complexes.

Photometric FRET Measurements. 3 cube FRET was performed as described in detail in Butz *et al.*[37] with modifications published in Becirovic *et al.* and Nguyen *et al.*[18,19]. Briefly, transfected HEK293T cells and isolated rod OS were measured in a FRET imaging solution comprising 2 mM $CaCl_2$, 10 mM glucose, 10 mM HEPES sodium salt, 5 mM KCl, 1 mM $MgCl_2$, 140 mM NaCl, pH 7.4, at RT. 3 cube FRET measurements were conducted using a Leica DMI6000B inverted fluorescent microscope (Leica, Wetzlar, Germany) in combination with a photomultiplier detection system including a photomultiplier tube (Horiba, London, Ontario, Canada). As excitation source, a DeltaRamX monochromator was used and FRET data were acquired with FelixGX software (Horiba, London, Ontario, Canada). FRET filter cubes were as follows (excitation, dichroic mirror, emission): cerulean/CFP (ET436/20 ×; T455lp; ET480/40m), FRET (ET436/20 ×; T455lp; ET535/30m) and citrine/YFP (ET500/20 ×; T515lp; ET535/30m) (Chroma technology, Vermont, USA). The fluorescence intensities were measured in single cells co-expressing varying, but sufficient levels of cerulean- and citrine-tagged proteins with the respective filter cube. Subsequent FRET ratios (FR) were calculated from the signal intensities according to the 3 cube FRET equation described in Shaltiel *et al.*[38]. Apparent FRET efficiencies (E_A) at given cerulean/citrine molar ratios (MR) were obtained from equation (1):

$$E_A = [FR - 1] \cdot \frac{\varepsilon_{citrine}(436)}{\varepsilon_{cerulean}(436)} \quad (1)$$

$\varepsilon_{citrine}$ and $\varepsilon_{cerulean}$ represent the setup specific average molar extinction coefficients for the fluorophores citrine or cerulean, respectively. FRET data were analyzed using FelixGX software (see above) and Excel (Microsoft Corporation, Redmond, Washington, USA).

Binding curves were calculated using equation (2):

$$E_A = \frac{E_{Amax} \cdot MR}{K + MR} \quad (2)$$

E_{Amax} is the maximal FRET efficiency that can be calculated for saturated donor concentrations and K is an analogon of the dissociation constant. *Ex vivo* FRET experiments were conducted on single rod OS isolated from six pooled retinas for each FRET pair.

rAAV preparation and subretinal injections. The production of single-strand AAVs (rAAV 2/8 YF) containing the hRHO promoter and the subretinal injection technique were described previously[30]. 10^{10} rAAV particles were delivered subretinally to wild type C57Bl6/J mice by a single injection on postnatal day 14. Four weeks post injection, all injected retinas were analyzed for fluorescence using scanning laser ophthalmoscopy (Spectralis, Heidelberg Engineering, Dossenheim, Germany).

Preparation of outer segments. A detailed procedure of rod OS preparation was described recently[17,19]. Briefly, mice were sacrificed four weeks post injection and the isolated retinas were collected in a 1.5-ml reaction tube containing 100 µl of PBS. The OS were separated from the retina by vortexing for 15–30 s and centrifuging for 30 s at 500 × g. Afterwards the OS containing supernatant was collected and used for subsequent FRET measurements.

Immunohistology and Confocal Microscopy. For immunohistology, wild type C57BL6/J mice were injected on P14 with the respective rAAV particles. Four weeks post injection, the retinas were dissected and processed for immunohistology as described[39]. Retinal and OS images were obtained by the TCS SP8 confocal scan microscope (Leica, Wetzlar, Germany), acquired with the LASX software (Leica, Wetzlar, Germany), and processed with the ImageJ software (National Institutes of Health, Bethesda, MD, USA). We used the rabbit anti-CNGB1a antibody (1:10.000[40]) as marker for rod outer segments. Citrine was excited with the 514 nm laser and detected with the Hybrid (HyD) detector using a 520–540 nm emission filter. Cerulean was excited using the 448 nm laser and detected via the HyD detector with a 460–480 nm emission filter. Images were taken using the 40x and 63x objectives.

Confocal scanning laser ophthalmoscopy and optical coherence tomography. Confocal scanning laser ophthalmoscopy (cSLO) and optical coherence tomography (OCT) were performed 6 months post injection using a modified Spectralis HRA + OCT system (Heidelberg Engineering, Dossenheim, Germany) as

described recently[41]. Fluorescence signals were examined at 488 nm excitation for citrine/cerulean detection (BP 550/49 nm emission filter).

Statistics. All values are given as mean ± SEM, and *n* is the number of trials. For multiple comparisons one-way ANOVA followed by the Tukey's test was used.

Data availability. All data generated or analyzed during this study are included in this published article (and its Supplementary Information files).

References

1. Goldberg, A. F. & Molday, R. S. Subunit composition of the peripherin/rds-rom-1 disk rim complex from rod photoreceptors: hydrodynamic evidence for a tetrameric quaternary structure. *Biochemistry* **35**, 6144–6149 (1996).
2. Stuck, M. W., Conley, S. M. & Naash, M. I. PRPH2/RDS and ROM-1: Historical context, current views and future considerations. *Prog. Retin. Eye. Res.* **52**, 47–63 (2016).
3. Goldberg, A. F. Role of peripherin/rds in vertebrate photoreceptor architecture and inherited retinal degenerations. *Int. Rev. Cytol.* **253**, 131–175 (2006).
4. Goldberg, A. F., Moritz, O. L. & Williams, D. S. Molecular basis for photoreceptor outer segment architecture. *Prog. Retin. Eye. Res.* **55**, 52–81 (2016).
5. Moritz, O. L. & Molday, R. S. Molecular cloning, membrane topology, and localization of bovine rom-1 in rod and cone photoreceptor cells. *Invest. Ophthalmol. Vis. Sci.* **37**, 352–362 (1996).
6. Loewen, C. J. & Molday, R. S. Disulfide-mediated oligomerization of Peripherin/Rds and Rom-1 in photoreceptor disk membranes. Implications for photoreceptor outer segment morphogenesis and degeneration. *J. Biol. Chem.* **275**, 5370–5378 (2000).
7. Daiger, S. P., Sullivan, L. S. & Bowne, S. J. Genes and mutations causing retinitis pigmentosa. *Clin. Genet.* **84**, 132–141 (2013).
8. Ferrari, S. *et al*. Retinitis pigmentosa: genes and disease mechanisms. *Curr. Genomics* **12**, 238–249 (2011).
9. Bascom, R. A. *et al*. Cloning of the cDNA for a novel photoreceptor membrane protein (rom-1) identifies a disk rim protein family implicated in human retinopathies. *Neuron* **8**, 1171–1184 (1992).
10. Dryja, T. P., Hahn, L. B., Kajiwara, K. & Berson, E. L. Dominant and digenic mutations in the peripherin/RDS and ROM1 genes in retinitis pigmentosa. *Invest. Ophthalmol. Vis. Sci.* **38**, 1972–1982 (1997).
11. Kajiwara, K., Berson, E. L. & Dryja, T. P. Digenic retinitis pigmentosa due to mutations at the unlinked peripherin/RDS and ROM1 loci. *Science* **264**, 1604–1608 (1994).
12. Conley, S. M., Stuck, M. W., Watson, J. N. & Naash, M. I. Rom1 converts Y141C-Prph2-associated pattern dystrophy to retinitis pigmentosa. *Hum. Mol. Genet*. (2017).
13. Boon, C. J. *et al*. The spectrum of retinal dystrophies caused by mutations in the peripherin/RDS gene. *Prog. Retin. Eye. Res.* **27**, 213–235 (2008).
14. Stenson, P. D. *et al*. The Human Gene Mutation Database: building a comprehensive mutation repository for clinical and molecular genetics, diagnostic testing and personalized genomic medicine. *Hum. Genet.* **133**, 1–9 (2014).
15. Goldberg, A. F. & Molday, R. S. Defective subunit assembly underlies a digenic form of retinitis pigmentosa linked to mutations in peripherin/rds and rom-1. *Proc. Natl. Acad. Sci. USA*. **93**, 13726–13730 (1996).
16. Loewen, C. J., Moritz, O. L., Tam, B. M., Papermaster, D. S. & Molday, R. S. The role of subunit assembly in peripherin-2 targeting to rod photoreceptor disk membranes and retinitis pigmentosa. *Mol. Biol. Cell* **14**, 3400–3413 (2003).
17. Becirovic, E. *et al*. Peripherin-2 couples rhodopsin to the CNG channel in outer segments of rod photoreceptors. *Hum. Mol. Genet.* **23**, 5989–5997 (2014).
18. Nguyen, O. N. *et al*. Peripherin-2 differentially interacts with cone opsins in outer segments of cone photoreceptors. *Hum. Mol. Genet.* **25**, 2367–2377 (2016).
19. Becirovic, E. *et al*. AAV Vectors for FRET-Based Analysis of Protein-Protein Interactions in Photoreceptor Outer Segments. *Front. Neurosci.* **10**, 356 (2016).
20. Becirovic, E. *et al*. *In Vivo* Analysis of Disease-Associated Point Mutations Unveils Profound Differences in mRNA Splicing of Peripherin-2 in Rod and Cone Photoreceptors. *PLoS Genet.* **12**, e1005811 (2016).
21. Goldberg, A. F., Loewen, C. J. & Molday, R. S. Cysteine residues of photoreceptor peripherin/rds: role in subunit assembly and autosomal dominant retinitis pigmentosa. *Biochemistry* **37**, 680–685 (1998).
22. Stricker, H. M., Ding, X. Q., Quiambao, A., Fliesler, S. J. & Naash, M. I. The Cys214–> Ser mutation in peripherin/rds causes a loss-of-function phenotype in transgenic mice. *Biochem. J.* **388**, 605–613 (2005).
23. Chakraborty, D., Rodgers, K. K., Conley, S. M. & Naash, M. I. Structural characterization of the second intra-discal loop of the photoreceptor tetraspanin RDS. *FEBS J.* **280**, 127–138 (2013).
24. Ding, X. Q., Stricker, H. M. & Naash, M. I. Role of the second intradiscal loop of peripherin/rds in homo and hetero associations. *Biochemistry* **44**, 4897–4904 (2005).
25. Ding, X. Q. *et al*. The R172W mutation in peripherin/rds causes a cone-rod dystrophy in transgenic mice. *Hum. Mol. Genet.* **13**, 2075–2087 (2004).
26. Kedzierski, W. *et al*. Deficiency of rds/peripherin causes photoreceptor death in mouse models of digenic and dominant retinitis pigmentosa. *Proc. Natl. Acad. Sci. USA*. **98**, 7718–7723 (2001).
27. Nour, M., Ding, X. Q., Stricker, H., Fliesler, S. J. & Naash, M. I. Modulating expression of peripherin/rds in transgenic mice: critical levels and the effect of overexpression. *Invest. Ophthalmol. Vis. Sci.* **45**, 2514–2521 (2004).
28. Nour, M., Fliesler, S. J. & Naash, M. I. Genetic supplementation of RDS alleviates a loss-of-function phenotype in C214S model of retinitis pigmentosa. *Adv. Exp. Med. Biol.* **613**, 129–138 (2008).
29. Rossmiller, B., Mao, H. & Lewin, A. S. Gene therapy in animal models of autosomal dominant retinitis pigmentosa. *Mol. Vis.* **18**, 2479–2496 (2012).
30. Koch, S. *et al*. Gene therapy restores vision and delays degeneration in the CNGB1(−/−) mouse model of retinitis pigmentosa. *Hum. Mol. Genet.* **21**, 4486–4496 (2012).
31. Petrs-Silva, H. & Linden, R. Advances in gene therapy technologies to treat retinitis pigmentosa. *Clin. Ophthalmol.* **8**, 127–136 (2014).
32. Ali, R. R. *et al*. Restoration of photoreceptor ultrastructure and function in retinal degeneration slow mice by gene therapy. *Nat. Genet.* **25**, 306–310 (2000).
33. Seigneuret, M., Delaguillaumie, A., Lagaudriere-Gesbert, C. & Conjeaud, H. Structure of the tetraspanin main extracellular domain. A partially conserved fold with a structurally variable domain insertion. *J. Biol. Chem.* **276**, 40055–40064 (2001).
34. Conley, S. M., Stuck, M. W. & Naash, M. I. Structural and functional relationships between photoreceptor tetraspanins and other superfamily members. *Cell. Mol. Life Sci.* **69**, 1035–1047 (2012).
35. Goldberg, A. F., Moritz, O. L. & Molday, R. S. Heterologous expression of photoreceptor peripherin/rds and Rom-1 in COS-1 cells: assembly, interactions, and localization of multisubunit complexes. *Biochemistry* **34**, 14213–14219 (1995).

36. Much, B. *et al*. Role of subunit heteromerization and N-linked glycosylation in the formation of functional hyperpolarization-activated cyclic nucleotide-gated channels. *J. Biol. Chem.* **278**, 43781–43786 (2003).
37. Butz, E. S. *et al*. Quantifying macromolecular interactions in living cells using FRET two-hybrid assays. *Nat. Protoc.* **11**, 2470–2498 (2016).
38. Shaltiel, L. *et al*. Complex regulation of voltage-dependent activation and inactivation properties of retinal voltage-gated Cav1.4 L-type Ca2+ channels by Ca2+ -binding protein 4 (CaBP4). *J. Biol. Chem.* **287**, 36312–36321 (2012).
39. Michalakis, S. *et al*. Impaired opsin targeting and cone photoreceptor migration in the retina of mice lacking the cyclic nucleotide-gated channel CNGA3. *Invest. Ophthalmol. Vis. Sci.* **46**, 1516–1524 (2005).
40. Huttl, S. *et al*. Impaired channel targeting and retinal degeneration in mice lacking the cyclic nucleotide-gated channel subunit CNGB1. *J. Neurosci.* **25**, 130–138 (2005).
41. Schon, C. *et al*. Loss of HCN1 enhances disease progression in mouse models of CNG channel-linked retinitis pigmentosa and achromatopsia. *Hum. Mol. Genet.* **25**, 1165–1175 (2016).

Acknowledgements

The authors thank Berit Noack and Nadja Gießl for their excellent technical support. This work was supported by the Deutsche Forschungsgemeinschaft, grant number BE 4830/1-1 (to E.B.), and Deutsche Forschungsgemeinschaft SFB 870 P05 and P15, TRR 152 P06 (to C.W-S). The funders had no role in study design, data collection and analysis, decision to publish, or preparation of the manuscript.

Author Contributions

E.B. designed research; E.B., S.B., L.M.R., O.N.P.N., A.G., T.L., and E.S.B performed research; E.B., S.B., L.M.R., C.S., S.M., C.W.S., and M.B. analyzed data; E.B., S.B., L.M.R., S.M., and M.B. wrote the paper.

Additional Information

Supplementary information accompanies this paper at doi:10.1038/s41598-017-02514-5

Competing Interests: The authors declare that they have no competing interests.

Publisher's note: Springer Nature remains neutral with regard to jurisdictional claims in published maps and institutional affiliations.

Peripherin-2 and Rom-1 have opposing effects on rod outer segment targeting of retinitis pigmentosa-linked peripherin-2 mutants

Sybille Böhm[1,2#], Lisa M. Riedmayr[1,2#], O.N. Phuong Nguyen[1,2], Andreas Gießl[3], Toni Liebscher[1,2], Elisabeth S. Butz[1,2], Christian Schön[1,2], Stylianos Michalakis[1,2], Christian Wahl-Schott[1,2], Martin Biel[1,2] and Elvir Becirovic[1,2*]

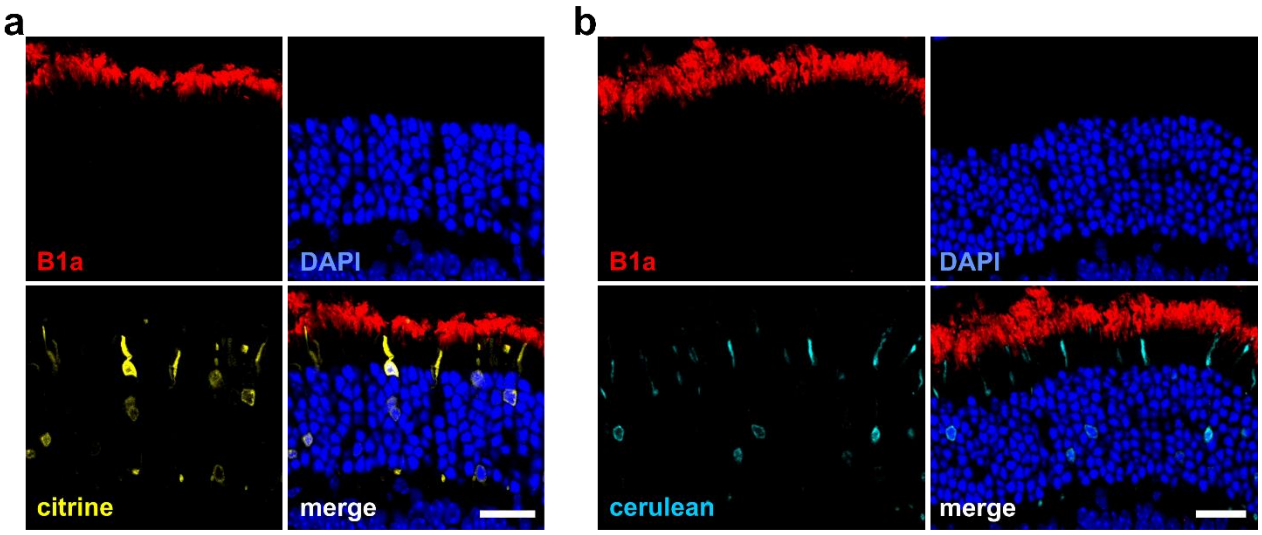

Supplementary Figure 1: Expression profile of citrine and cerulean in transduced photoreceptors. Scale bar, 30 µm.

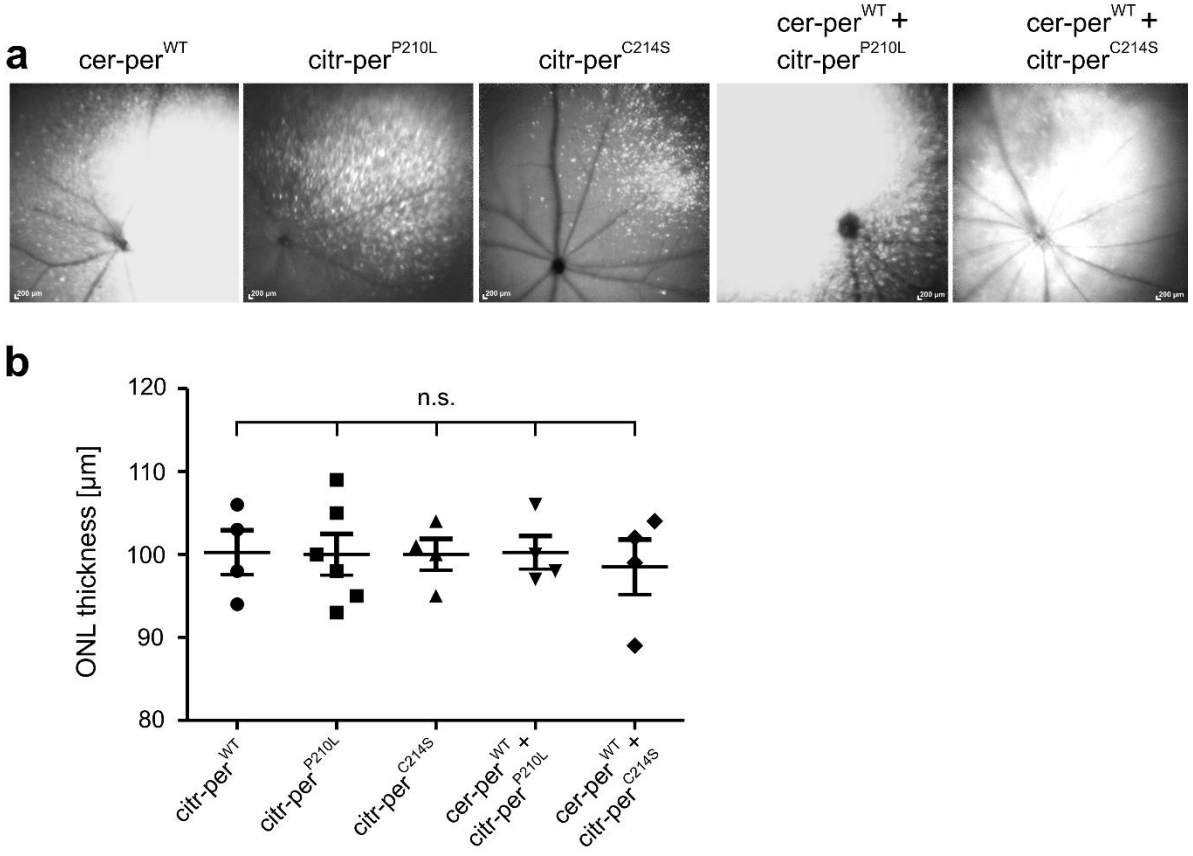

Supplementary Figure 2: Long-term effects of per^{WT} and per^{MT} expression on retinal degeneration in transduced murine photoreceptors. A, Representative confocal scanning laser ophthalmoscopy (cSLO) of mice injected with the single constructs as indicated. Note that, in contrast to the confocal microscope settings, citrine and cerulean fluorescence (white signal) cannot be distinguished using cSLO. B, measurements of the outer nuclear layer (ONL) thickness of injected animals using optical coherence tomography. The single values are as follows: citr-per^{WT} (n=4) 100.3 ± 2.7 µm; citr-per^{P210L} (n=6) 100.0 ± 2.5 µm; citr-per^{C214S} (n=4) 100.0 ± 1.9 µm; citr-per^{WT} + citr-per^{P210L} (n=4) 100.3 ± 2.0 µm; citr-per^{WT} + citr-per^{C214S} (n=4) 98.5 ± 3.3 µm. Statistical analysis was done with one-way ANOVA followed by the Tukey's test for multiple comparisons. n.s., not significant.

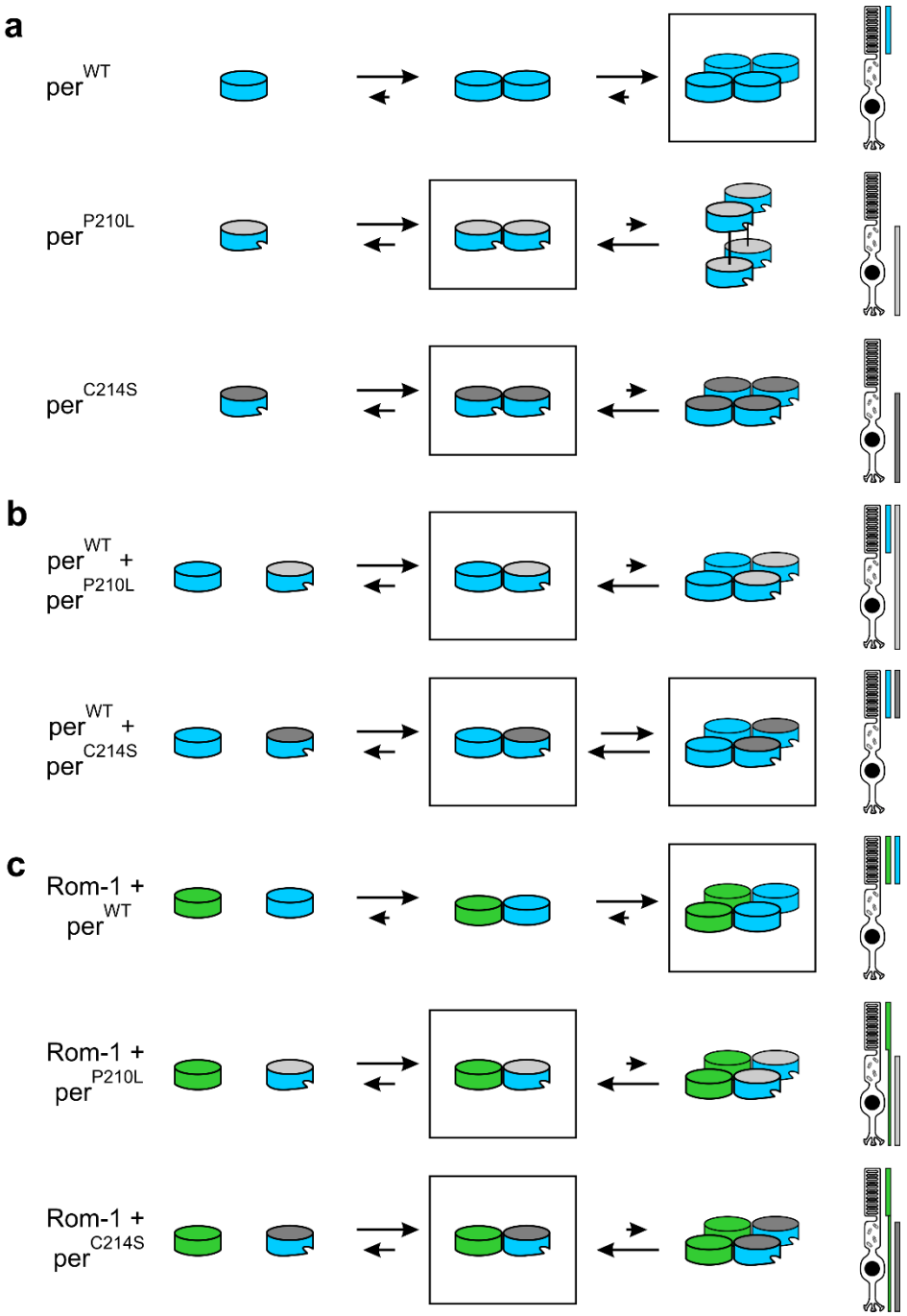

Supplementary Figure 3: Tentative model of per^{MT} protein assembly and rod OS targeting in presence or absence of transgenic per^{WT} and Rom-1. For reasons of clarity, octamers, higher-order oligomers, and aggregates are not included in this model. The rectangle highlights the major SDGC fraction(s) for the single homo- or heterogenic interactions and the arrow length correlates with the preferential direction within the equilibrium. The misfolding of the distal part of the D2 loop caused by both mutants is symbolized by an incision. The localization of the respective constructs in rod photoreceptors (right panel) is indicated by colored bars symbolizing color-coded per^{WT}, per^{MT}, or Rom-1 constructs. The bar thickness represents the estimated relative amount of the detected constructs in the respective compartment.

Supplementary Table 1: FRET measurements from HEK293T cells and from isolated rod OS.

	HEK293T								rod OS		
	WT-WT	**WT-P210L**	**WT-C214S**	**P210L-P210L**	**C214S-C214S**	**WT-ROM1**	**ROM-1-P210L**	**ROM-1-C214S**	**WT-WT**	**WT-P210L**	**WT-C214S**
E_{Amax}	34.2	9.44	8.58	30.7	26.47	15.64	6.58	6.32	25.96	37.12	26.47
% of WT-WT or WT-ROM-1		28	25	90	77		42	40		143	102
n	53	53	50	53	54	48	48	48	45	32	44

Supplementary Table 2: Quantification of the SDGC experiments. Values are given as mean values ± SEM.

Immunoreactivity (% of Total)												
			Fraction									
			1	2	3	4	5	6	7	8	9	10	11
n = 3	**WT**	Non-covalent	0.00	0.00	0.00	2.78 ± 2.78	9.33 ± 0.71	11.53 ± 1.38	11.70 ± 2.15	10.98 ± 2.06	2.65 ± 2.65	2.76 ± 2.76	1.68 ± 1.68
		Disulfide bond	0.00	2.05 ± 2.05	4.73 ± 2.39	7.97 ± 1.60	11.78 ± 1.26	12.46 ± 1.50	7.61 ± 0.57	0.00	0.00	0.00	0.00
n = 4	**P210L**	Non-covalent	0.00	0.00	0.00	0.00	0.00	0.00	0.00	0.00	2.10 ± 2.10	20.35 ± 4.66	19.00 ± 6.53
		Disulfide bond	0.00	0.00	0.00	0.00	2.86 ± 2.86	5.44 ± 3.16	4.81 ± 2.79	5.78 ± 2.13	2.67 ± 2.67	1.78 ± 1.78	0.00
		Aggregate	0.00	0.00	2.08 ± 2.08	8.28 ± 3.17	10.83 ± 1.53	8.80 ± 3.07	3.18 ± 2.67	2.02 ± 1.78	0.00	0.00	0.00
n = 3	**C214S**	Non-covalent	0.00	0.00	0.00	0.00	2.61 ± 2.61	4.36 ± 4.36	3.42 ± 3.42	3.34 ± 3.34	18.23 ± 13.07	27.29 ± 14.59	5.20 ± 5.20
		Aggregate	7.28 ± 3.77	7.65 ± 4.20	5.27 ± 5.27	4.03 ± 4.03	6.78 ± 6.78	4.53 ± 4.53	0.00	0.00	0.00	0.00	0.00
n = 5	**P210L + WT IB: anti-myc**	Non-covalent	0.00	1.74 ± 1.74	2.84 ± 2.84	3.13 ± 3.13	5.13 ± 3.15	4.33 ± 2.80	2.07 ± 2.07	4.45 ± 2.73	23.39 ± 4.14	27.42 ± 5.71	12.38 ± 5.53
		Disulfide bond	0.00	0.00	0.00	0.00	0.00	0.00	0.00	0.00	0.00	0.00	0.00
		Aggregate	0.00	1.36 ± 1.36	0.00	2.01 ± 1.27	3.57 ± 2.37	3.94 ± 2.49	2.23 ± 2.23	0.00	0.00	0.00	0.00
	P210L + WT IB: anti-flag	Non-covalent	0.00	0.00	0.00	0.00	2.37 ± 2.37	1.85 ± 1.85	9.13 ± 1.95	11.07 ± 4.26	10.79 ± 5.76	11.68 ± 3.67	0.00
		Disulfide bond	3.68 ± 3.68	4.67 ± 4.67	6.60 ± 3.45	7.86 ± 4.13	12.61 ± 0.59	11.95 ± 2.62	3.35 ± 3.35	2.40 ± 2.40	0.00	0.00	0.00
n = 4	**C214S + WT IB: anti-myc**	Non-covalent	0.00	0.00	0.00	0.00	4.45 ± 2.64	5.22 ± 3.09	5.91 ± 3.74	16.61 ± 3.49	12.33 ± 4.41	20.32 ± 4.78	19.65 ± 10.11
		Aggregate	0.00	0.00	5.87 ± 3.60	7.81 ± 2.74	1.82 ± 1.82	0.00	0.00	0.00	0.00	0.00	0.00
	C214S + WT IB: anti-flag	Non-covalent	0.00	0.00	0.00	0.00	1.45 ± 1.45	1.67 ± 1.12	5.95 ± 1.39	3.40 ± 1.90	6.41 ± 0.57	7.52 ± 0.92	4.11 ± 4.11
		Disulfide bond	5.51 ± 2.76	8.75 ± 1.12	10.40 ± 0.57	11.06 ± 0.38	11.38 ± 0.63	9.58 ± 0.63	7.24 ± 0.64	3.46 ± 1.90	2.11 ± 2.11	0.00	0.00
n = 3	**WT + Rom-1 IB: anti-myc**	Non-covalent	0.00	0.00	0.00	0.00	8.22 ± 0.86	10.20 ± 1.46	6.34 ± 3.17	4.70 ± 4.70	2.77 ± 2.77	0.00	0.00
		Disulfide bond	8.48 ± 4.42	10.61 ± 1.81	10.18 ± 1.60	9.69 ± 1.87	10.50 ± 2.20	10.41 ± 1.38	7.92 ± 0.20	0.00	0.00	0.00	0.00
	WT + Rom-1 IB: anti-flag	Non-covalent	0.00	0.00	0.00	1.45 ± 1.45	5.40 ± 2.89	14.96 ± 2.60	17.61 ± 1.74	18.26 ± 9.93	19.35 ± 3.61	8.99 ± 5.91	3.61 ± 3.61
		Disulfide bond	0.00	0.00	0.00	0.00	3.49 ± 1.85	4.55 ± 2.65	2.33 ± 2.33	0.00	0.00	0.00	0.00
n = 3	**P210L + Rom-1 IB: anti-myc**	Non-covalent	0.00	0.00	0.00	0.00	0.00	0.00	0.00	4.56 ± 4.56	22.76 ± 2.11	31.48 ± 6.45	28.67 ± 9.40
		Disulfide bond	0.00	0.00	0.00	0.00	0.00	0.00	0.00	0.00	0.00	0.00	0.00
		Aggregate	0.00	5.60 ± 5.60	0.00	0.00	5.01 ± 5.01	1.93 ± 1.93	0.00	0.00	0.00	0.00	0.00
	P210L + Rom-1 IB: anti-flag	Non-covalent	0.00	0.00	0.00	0.00	0.00	0.00	0.00	0.00	19.68 ± 9.84	43.50 ± 2.28	36.82 ± 12.12
		Disulfide bond	0.00	0.00	0.00	0.00	0.00	0.00	0.00	0.00	0.00	0.00	0.00
n = 3	**C214S + Rom-1 IB: anti-myc**	Non-covalent	0.00	0.00	0.00	0.00	0.00	4.59 ± 4.59	4.91 ± 4.91	0.00	29.00 ± 2.51	31.53 ± 3.67	24.34 ± 3.41
		Aggregate	0.00	0.00	0.00	0.00	5.64 ± 5.64	0.00	0.00	0.00	0.00	0.00	0.00
	C214S + Rom-1 IB: anti-flag	Non-covalent	0.00	0.00	0.00	0.00	0.00	0.00	0.00	2.43 ± 2.43	28.57 ± 6.38	26.46 ± 2.94	21.20 ± 2.41
		Disulfide bond	0.00	0.00	0.00	0.00	0.00	0.00	1.75 ± 1.75	6.79 ± 4.15	10.18 ± 0.14	2.60 ± 2.60	0.00